STUDY OF THE STRUCTURE OF PARTIAL REFLECTION RADAR SCATTERERS AND THEIR APPLICATION IN ATMOSPHERIC MEASUREMENTS

By

Drazen Lesicar, B.Sc. (Hons)

THESIS SUBMITTED FOR THE DEGREE OF

DOCTOR OF PHILOSOPHY

IN

THE UNIVERSITY OF ADELAIDE

(FACULTY OF SCIENCE)

(DEPARTMENT OF PHYSICS AND MATHEMATICAL PHYSICS)

July 1993

Preface

This work contains no material which has been accepted for the award of any other degree or diploma in any university or other tertiary institution and, to the best of my knowledge and belief, contains no material previously published or written by another person, except where due reference has been made in the text.

I give consent to this copy of my thesis, when deposited in the University Library, being available for loan and photocopying.

Drazen Lesicar, B.Sc. (Hons)

Date: 27 Jul 1993

Abstract

This thesis focuses on the study of lower and middle atmosphere dynamics, with particular emphasis being placed on the small dynamical regime. Furthermore, given that smaller scale motions, in particular high frequency gravity waves, can have important consequences for the mean flow, studies of the mean wind characteristics have also been undertaken.

All of the experimental data used has been obtained via radar techniques, and the thesis is unique because of its significant global coverage encompassing three separate sites. Furthermore, this work investigates and reports on radar studies of small scale structures embedded within turbulence regions of the middle atmosphere with a thoroughness not previously reported, and in addition studying not only their vertical but horizontal anisotropy.

Using three years of continuous data from our field station at Adelaide, South Australia, studies of both the climatology and short term structure of scatterers which cause partial radar reflections (1.98MHz) from the mesosphere have been made. These studies have included aspect sensitivity, horizontal correlation lengths, and energy dissipation rates. Comparisons of vertical and off–vertical beams show that there might co–exist several types of mesospheric scatterers, one at least which is highly anisotropic. These studies have important implications for the interpretation of wind measurements reported in subsequent chapters.

Adelaide is a mid–latitude site and has been shown to be in a low gravity–wave activity zone. In order to investigate a more dynamical region and provide direct comparisons with Adelaide, a partial reflection radar was established at Christmas Island (2° N 157° W). Calculations of the mean wind flows have shown that those at Christmas Island are strongly wave driven. Furthermore, studies of the small scale structures are quite different to those observed at Adelaide. To complement the results from Adelaide and Christmas Island, data from a radar site at Mawson, Antarctica was also analyzed to investigate high latitude inertial range scatterers. This has provided a unique opportunity to study small scale structures and dynamics over an extended period of time and large global coverage.

In March 1991, the partial reflection radar at Christmas Island was involved in a short campaign, ALOHA-90, which examined the short–term dynamics and behavior of the mesosphere utilizing various instruments. Amongst others was a Lidar system operated by the University of Illinois and mounted on an aircraft, which made several flights close to Christmas Island. This provided a direct comparison of measurements of gravity–wave activity as measured by the Lidar with those made by radar. and the investigation of any possible coupling with the behavior of radar scatterers and gravity–wave activity.

All the three sites use partial reflection radars which operate in the full correlation analysis mode, which not only calculates the wind flows, but a number of other parameters. A better understanding of the method, its limitations and accuracies was needed to have better conviction in the interpretation of the data. For this purpose a spaced–antenna model was used to investigate the accuracy of the full correlation analysis. This model simulates both the atmosphere in various degrees of motion/turbulence and a radar system operating in the spaced–antenna mode. Results from the model simulations indicate that the full correlation analysis is consistent and a reliable tool for measurements of atmospheric motions.

Acknowledgments

It is hard to try and thank all of the people that have helped me with this thesis, for so many have contributed in so many ways. I would first like to thank my supervisors, Wayne Hocking and Dr. Basil Briggs whose enthusiasm, guidance, and the opportunity to undertake this work in the first place will be fondly remembered. In addition their careful and prompt reading of the manuscript is very much appreciated.

Thanks must also go to the other academic staff, Bob Vincent, Graham Elford and Iain Reid for their suggestions and support, and the financial help of the Atmospheric Group in the production of this thesis.

I would also like to thank the Department of Physics and Mathematical Physics at the University of Adelaide for the financial support that was given to me in the form of a half–time tutorship.

Other members of the Department also made my work if not any easier then definitely more memorable. Thanks to John Smith, Brian Fuller, and Mike Shorthose of Electronic Services, for their help and allowing me to wear out their colour inkjet printer. To the general staff, especially Arlene Shaw and Janet Hobbs, many thanks for all those little things with a smile. Thanks also to the technical staff including Bob Hurn and Shane Dillon whose help and wit was refreshing.

Dallas Kirby and Lyn Birchby I wish to especially thank. Their help in so many ways too numerous to mention is greatly appreciated. Their patience, resilience, sense of humour and undercover work will be in years to come responsible for bringing many a smile to my face.

A special thanks goes to Laurence Campbell and Damian Murphy. Laurence was always willing to help, at times to the detriment of his own work. Damian, whose simple outlook on life (and weak tea) were a great calming influence I thank for organizing my trip to Mawson, which I think was just in time! Thanks must go to all my colleagues (Brenton, Dave, Dave, Deepak, Manuel, Simon, Trevor) who have provided a lot of memorable times and have sharpened my debating skills no end.

To Sandra, I would just like to thank for being there and for letting me not be there.

Finally, I would like to thank my parents whose tremendous support has never been unwavering or absent. It is easy to forget the sacrifices that others have made in the pursuit of your own goals. And yet without this support our own goals are unreachable. I will never be able to repay the sacrifices of my parents. I just hope to be able to offer my own children the opportunities that have been offered to me.

Contents

List of Tables

List of Figures

Chapter 1

Review of the Atmosphere

1.1 Introduction

This thesis is concerned with the study of the atmosphere, primarily in the altitude region of 60–100 km. To begin, it deals with the climatology and short-term variations of the structures which cause partial radar reflections in the MF band. Understanding of these structures and their interpretation when information about them is obtained by using atmospheric radars is vitally important, since better understanding of the nature of the radar scatterers will lead to better understanding of other measurements where radar data are used and interpreted. We subsequently present and discuss a variety of data, including wind data recorded at MF, and draw on our studies of the scatterers to interpret the results. While the study of the scatterers themselves is a rather specialized area of study, it is nevertheless necessary in order to understand the atmosphere as a whole.

For many years it has been customary to divide the study of the atmosphere into the dynamical/thermodynamical aspects, and the chemical/photochemical aspects. Only recently has it been appreciated that the two disciplines are inseparable and that their interactions play a vital role in the general circulation and chemistry. This chapter will briefly review the general atmosphere, dealing separately with its structure and dynamics. To treat each domain separately might be considered superficial, but it is necessary since the interrelations are so

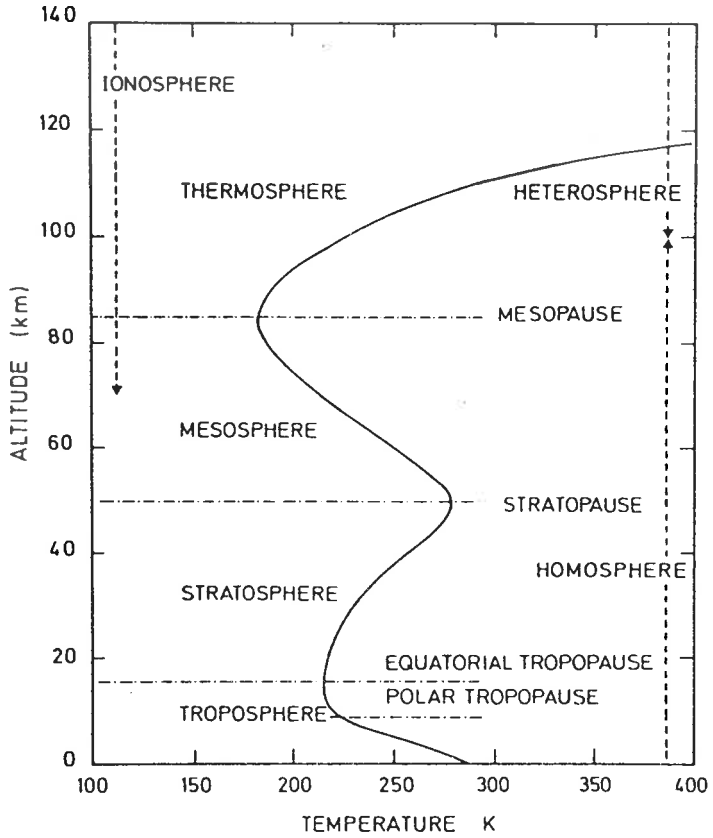

Figure 1.1: The vertical temperature structure of the Earth's atmosphere, showing the principal regions [after *Brasseur and Solomon*, 1986].

complex. We will also pay attention to the ionosphere, which is the primary region of interest in this dissertation.

1.2 The structure of the atmosphere

The most conventional classification of the atmosphere is based upon the vertical structure of the temperature. Figure 1.1 depicts the essence of the change in atmospheric temperature with height, which is typical of all latitudes and longitudes, except at polar latitudes during the winter darkness.

The distinct temperature structure of the lower and middle atmosphere[1] has led to the individual naming of the principal regions, which are distinguished from each other by a change in the sign of the temperature gradient. The individual regions in ascending order are known as the *troposphere*, *stratosphere*, *mesosphere* and *thermosphere* (for a historical review of the

[1]The lower and middle atmosphere is usually taken to be the region between the surface and an altitude of 100 km

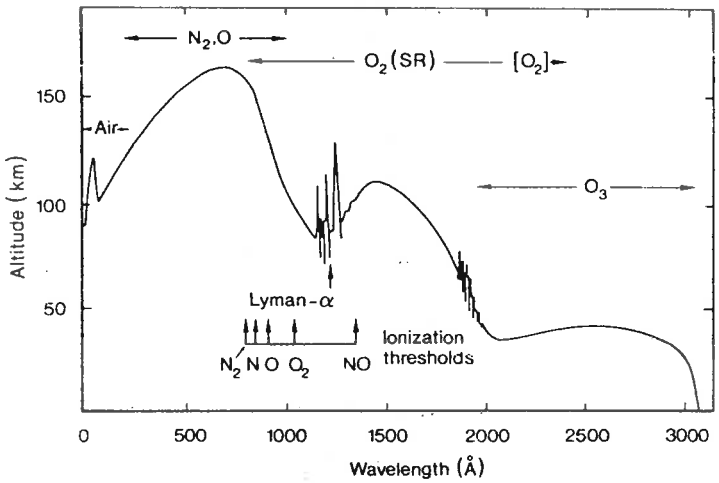

Figure 1.2: A plot of the altitude, as a function of wavelength at which the solar irradiation, is attenuated to e^{-1} of its value outside of the Earth's atmosphere, for vertical incidence. All the constituents contribute to attenuation in the region labelled "air", while wavelengths corresponding to the ionization thresholds of the important species are marked by arrows [after *Rees*, 1989].

naming of the regions see Appendix A). The temperature structure is governed mainly by the absorption of solar radiation and re–radiation of infra–red radiation, with different atmospheric species absorbing and radiating in different parts of the solar spectrum.

1.2.1 Effects of solar radiation

The interaction of the solar electro–magnetic spectrum both with the Earth's surface and its atmosphere produces heating effects in the atmosphere[2]. Although the solar spectrum extends from radio–waves to x–rays and beyond, the radiation that reaches and penetrates the terrestrial atmosphere below an altitude of about 100 km is mainly in the u–v, visible and infra–red parts of the spectrum. Figure 1.2 depicts the altitude at which incoming vertical solar radiation is attenuated to e^{-1} of its value outside the atmosphere, as a function of wavelength.

Since any planet's atmosphere is under the influence of the gravitational field, the atmospheric density falls off as a function of altitude, and is described by the *hydrostatic equation*[3]. In

[2]Interstellar cosmic rays are also known to play a part in atmospheric chemistry
[3]An equation equating the gravitational and buoyancy forces

an atmosphere devoid of any liquid particles, a vertically ascending parcel of air will cool at the *adiabatic lapse rate* for dry atmospheres. For the Earth's atmosphere this is approximately 9.8 Kkm^{-1}. The solar radiation which reaches the Earth's surface[4] heats it to $\sim$ 280 K. The Earth then re–radiates this heat, as a *black–body* spectrum, peaking in the infra–red. The troposphere, however, contains a number of gases which are absorbent in the infra–red, in particular water vapour and carbon dioxide (which are responsible for the *greenhouse effect*), and is therefore heated by the re–radiating Earth. To an observer outside of the Earth's atmosphere the Earth therefore appears as a black–body of $\sim$ 250 K. This absorption of the terrestrial radiation alters the lapse rate, which, on the average is $\sim$ 6.5 Kkm^{-1}, but can be greater than the dry adiabatic lapse rate (DALR). If the lapse rate is in fact larger than the DALR, it becomes superadiabatic, and a vertically displaced parcel of air continues in its direction of motion, leading to convective instabilities[5]. Other factors, such as surface cooling, large scale subsidences, and orography can not only effect the lapse rate, but induce other dynamical features such as turbulence. All of these factors make the troposphere very dynamic, with huge amounts of energy being exchanged. The upper limit of the troposphere, referred to as the *tropopause*, is at about 17 km at the equator and only 6–8 km at the poles. In the middle latitudes, the tropopause varies with atmospheric conditions, being higher in high pressure areas than in low pressure areas.

It is the increasing concentration of ozone with height which is responsible for the heating of the stratosphere. Figure 1.3 shows the concentration of the more important neutral constituents of the atmosphere as a function of height. Solar radiation in the 200-300 nm range dissociates ozone, and to a minor extent oxygen, thus heating the stratosphere. The balance is provided by cooling in the infra-red region by carbon dioxide. The concentration of ozone peaks at $\sim$ 40 km, [see figure 1.3] and quickly decreases at higher altitudes, so that the peak temperature of $\sim$ 270 K in the stratosphere is just above that height. As the temperature increases with altitude, the stratosphere is highly stratified and stable, and the large temperature gradients are responsible for large zonal[6] winds. [e.g. *Andrews et al.*, 1987].

[4] mainly in the short wave region
[5] convection is the vertical exchange of masses of air, each possessing unique heat, water vapour and momentum
[6] motion along the latitude contours; east–west

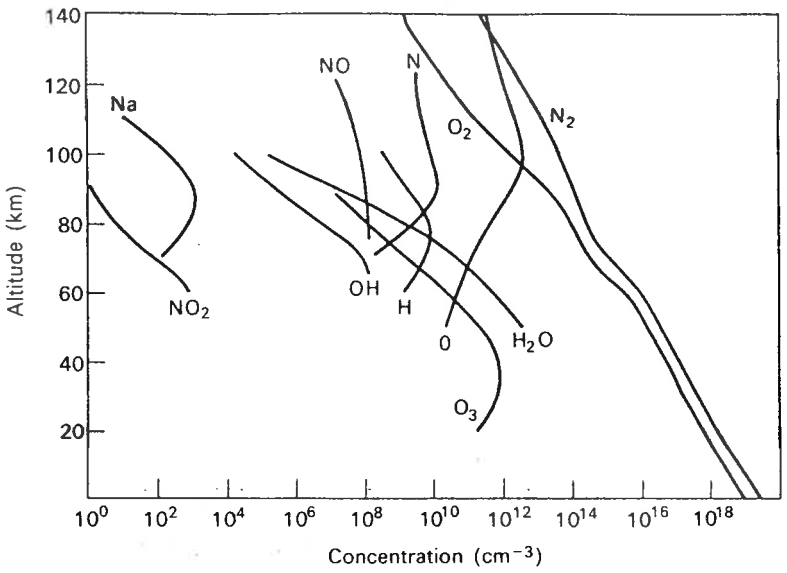

Figure 1.3: An altitude profile of the more important neutral species of the atmosphere, which is a qualitative description of their concentration rates. It is important to note, however, that these profiles are typical only, and that they do predictably vary with time of day, season, latitude and solar cycle [after *McEwan and Phillips*, 1975].

The mesosphere, due to decreasing ozone concentrations, absorbs very little solar radiation, and the heating rate decreases quite rapidly with altitude. In addition, radiation by CO_2 in the infra–red causes a temperature minimum to occur at $\sim$ 85–90 km; this is defined as the mesopause. Above the mesopause the thermosphere begins, where both atomic and molecular oxygen absorb the solar short u–v radiation, resulting in a subsequent increase in temperature. This trend persists for several hundred kilometers, with temperatures up to 2000 K, until reaching an essentially isothermal region, the exosphere [see figure 1.1]. The thermosphere is also the region where the small density means that molecular diffusion plays the dominant role in the transport of molecules themselves and for the transfer of heat. Molecular constituents are no longer well mixed by turbulence, but rather settle into layers according to their molecular weight. For this reason this region is also referred to as the heterosphere[7]. The thermosphere is also the region which is responsible for the air glows, that is the day glow, the night glow, and the auroras[8].

[7]The region where all the constituents are well mixed by turbulence is known as the homosphere
[8]borealis in the northern hemisphere and australis in the southern

1.2.2 The ionosphere

The ionosphere is defined as that region of the atmosphere which contains ions and electrons of sufficient concentration to affect the propagation of radio waves. There are two dominant processes which can ionize atoms and molecules; either energetic electrons, or short wavelength solar radiation[9]. Figure 1.4 shows the typical mid–latitude mean vertical distribution of electron density both for sunspot maximum/minimum, and for day/night. The electron concentration in all cases is far greater during the day than at night, since in the absence of solar radiation, electrons very quickly recombine or attach themselves to neutral molecules. This attachment is, however, very sensitive to photo–dissociation, and hence the electron concentration rapidly increases at sunrise. An additional source of ionization due to electron and proton precipitation[10] can also be important with primary auroral electrons producing secondary electrons by ionization of atmospheric gases [see, e.g. *Chamberlain and Jacka*, 1979; *Stamnes*, 1980; *Rees*, 1982].

The ionosphere is composed of a number of characteristic layers (regions) based upon the electron concentration profile. Of these layers we are mainly interested in the D and lower E regions, since they are responsible for partial radar reflections below 100 km. We shall now examine these individual layers in more detail.

The ionosphere below 100 km

The bottom region of the ionosphere, below 100 km, contains the D and the lower E region of the ionosphere [see figure 1.4]. At this altitude, most of the ionizing solar radiation has been absorbed with the exception of the Lyman α hydrogen emission line (121.6 nm) [see figure 1.2] which, together with extreme UV radiation, ionizes NO [see figure 1.3] in the lower region of 75–90 km. Lyman β and UV (0.2-0.8 nm) also ionize O_2, although at a smaller rate. Some ionization is also attributed to high energy cosmic rays[11], which ionize O_2 and N_2 below about

[9] UV and X-rays

[10] precipitation of high energy electrons and protons of solar and magnetospheric origin associated with the aurora

[11] galactic cosmic rays consist of about 83 % protons with the remainder being α particles

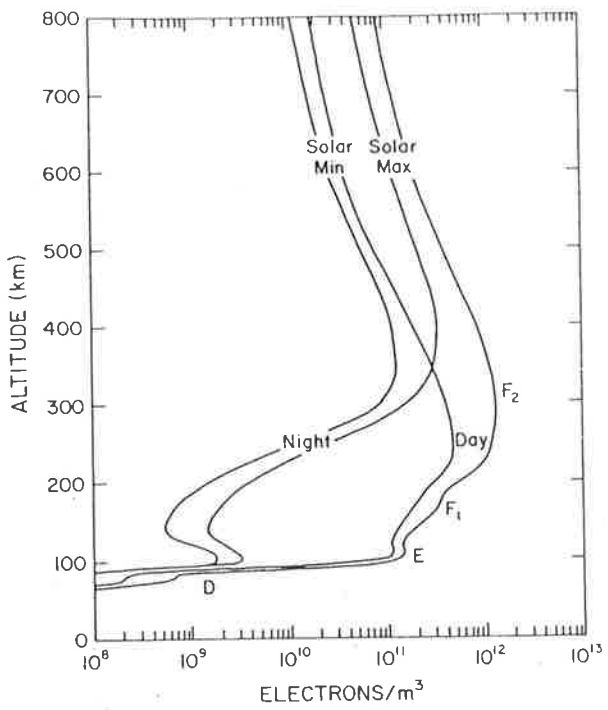

Figure 1.4: The ionospheric layers based on the vertical distribution of electron concentration, for night and day as well as solar maxima and minima, where the different regions of the ionosphere are labelled as D, E, F1, and F2 [after *Richmond*, 1987].

70 km. The rate of ion–pair production by cosmic rays increases exponentially with penetration into the atmosphere, reaching a maximum at around 10–15 km. The production is larger at high latitudes than in the tropics, and is also modulated by solar activity [see e.g. *Brasseur & Nicolet*, 1973]. High solar activity removes galactic cosmic rays due to the intense solar wind. The meridional gradient is due to cosmic rays following the magnetic field lines as they approach the earth, penetrating near the poles; this is particularly true for less energetic particles. The rate of pair production has been parameterized as a function of latitude, altitude, and solar activity [*Heaps*, 1978].

Figure 1.5 shows the mid-latitude day and night ionization production rates during quiet solar conditions, between an altitude of 60 and 100 km. Ionization due to high energy particles and galactic X–rays only becomes important in the absence of solar irradiation [see, e.g. *Thomas*, 1974; *Vampola and Gorney*, 1983]. A notable feature of the D region is the sharp increase in electron density observed between 80 and 90 km. This may be due to the change in rate of the dissociative recombination [*Reid*, 1970], or to the height distributions of the electron–ion

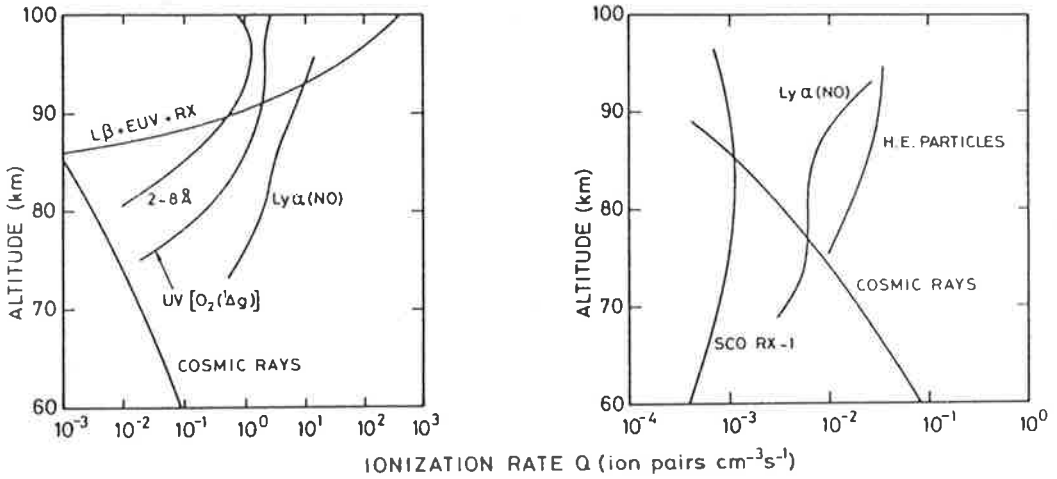

Figure 1.5: The ionization rates as produced by the different sources in the D and lower E regions for (*a*) day and (*b*) night, for quiet solar conditions [after *Thomas*, 1974]

production rates due to the ionization of O_2 and NO [*Chakrabarty et al.*, 1978].

There are several reasons why the D region is the most complex region of the ionosphere. Firstly, the presence of a large number of neutral species[12] is conducive to complex reaction paths between primary and product ions. Secondly, the pressure is still adequate for three-body reactions to be of significance. Thirdly, there are metal ions present and lastly, significant amounts of negative ions are attainable. Figures 1.6 and 1.7 exhibit some of the principal positive and negative ion chemistry effects in the D region as they are currently understood. It is beyond the scope of this thesis to pursue the chemistry of the ionosphere in any great depth, and there are numerous books which cover the area in detail [see, e.g. *McEwan and Phillips*, 1975; *Brasseur and Solomon*, 1986].

One aspect worth mentioning is the strong dependence of the ion chemistry on temperature, which in turn is dependent on the dynamics of the mesosphere. This importance can best be seen in the anomalous absorption of radio waves during winter, known as the winter anomaly. Normally, the absorption of radio waves is expected to vary systematically with respect to mean solar zenith angle, a fact observed in summer. However, during winter abnormally high absorption is observed, and this is directly attributable to increased electron concentration. Modelling studies, as well as the European winter anomaly campaign 1975/76, have suggested that the winter anomaly is predominantly due to large sporadic injections of nitric oxide from

[12] mainly NO, O_2, CO_2 and H_2O

the thermosphere to the mesosphere, in step with changes in atmospheric dynamics. An increase in turbulence can also increase NO concentration by transporting it down from higher altitudes. The increase of NO may also possibly be related to the horizontal transport processes occurring in planetary waves [*Offerman*, 1979; *Koshelev*, 1979; *Labitzke et al.*, 1979; *Kawahira*, 1982].

The ionosphere above 100 km

The E region, which extends up to 130 km, is ionized mostly from photoionization of atomic and molecular oxygen, and molecular nitrogen, in the 79.6–102.7 nm wavelength range – especially by the Lyman-β line, and by x–rays (0.1–14 nm). The sources of ionization at night–time are not yet understood, but are thought to be predominantly due to scattered solar radiation and stellar X–rays, except at high latitudes, where particle bombardment is thought to be important.

The F region which begins around 130 km ultimately terminates at heights of several Earth radii[13]. It reaches a peak electron concentration at around 250 km [see figure 1.3]. Occasionally the F layer is split into two, the F1 and F2, although the F1 layer contains no peak in ionization, and is basically a ledge at the base of the F2 layer. In the F region, the dominant ions are atomic, and hence ion interchange processes dominate the rate of electron loss as well as the chemistry of the region. With increasing altitude diffusion effects begin to dominate, and eventually control the ion distribution during daytime as well; in fact it is ambipolar[14] diffusion that is the major difference between the F1 and F2 layer. Above the F2 peak, hydrogen atoms are produced by charge transfer between ionized atomic oxygen and neutral hydrogen. At this altitude, the electric field is able to support the weight of hydrogen ions, but not that of oxygen. Thus the hydrogen ions accumulate and dominate the higher altitudes. Recombination is quite rapid in the F1 layer as compared with the F2 layer, in which the ionization remains large at night. At an altitude of $\sim$ 500 km the exosphere begins; this is a region where the mean free path becomes large enough that molecular escape becomes significant.

[13] One Earth radius is $\sim$ 6,370 km

[14] due to a concentration gradient in a partially ionized gas (plasma), thus influenced by electrostatic forces of the plasma

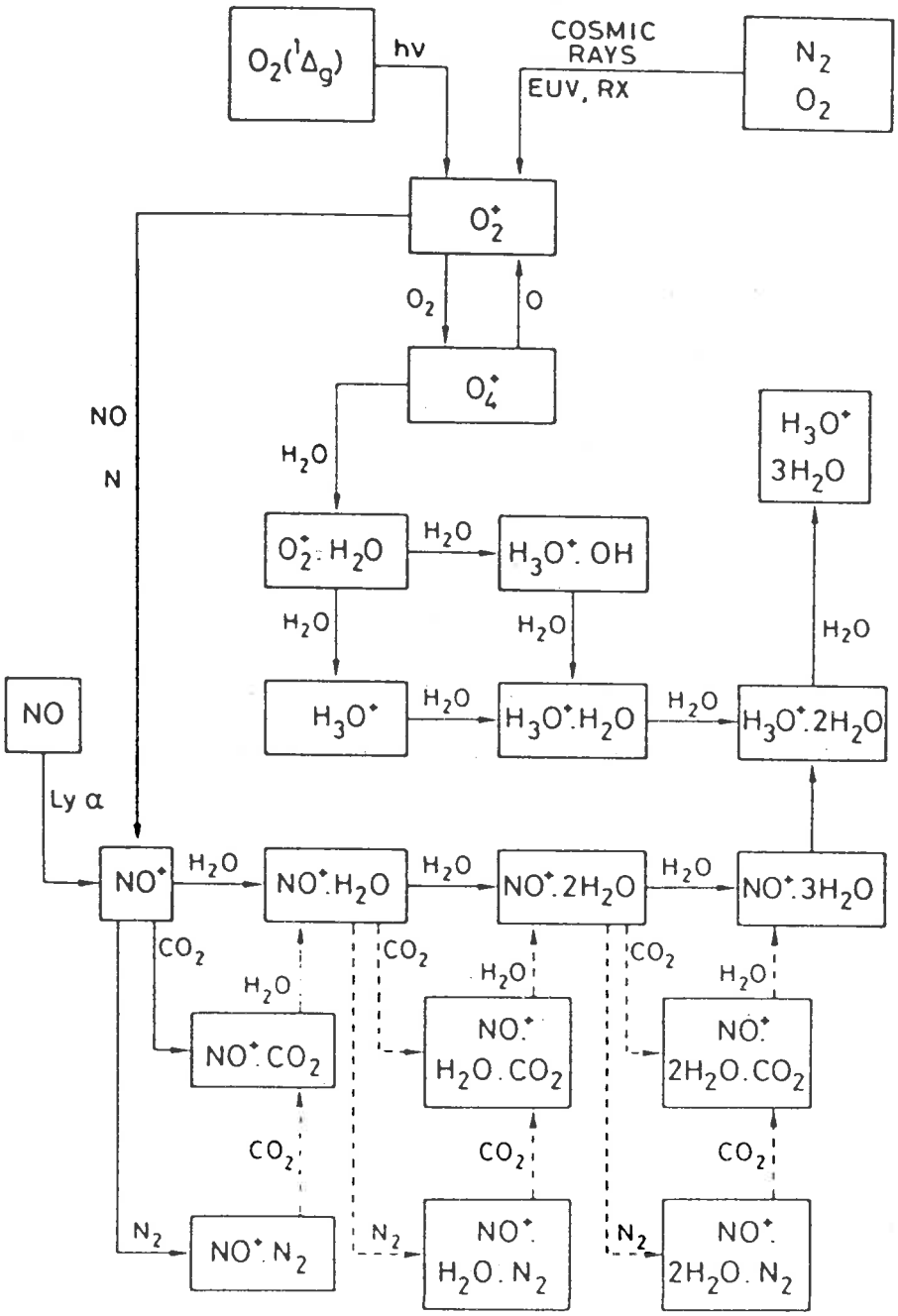

Figure 1.6: Schematic diagram of the D region positive ion chemistry as it is currently understood [after *Ferguson*, 1979].

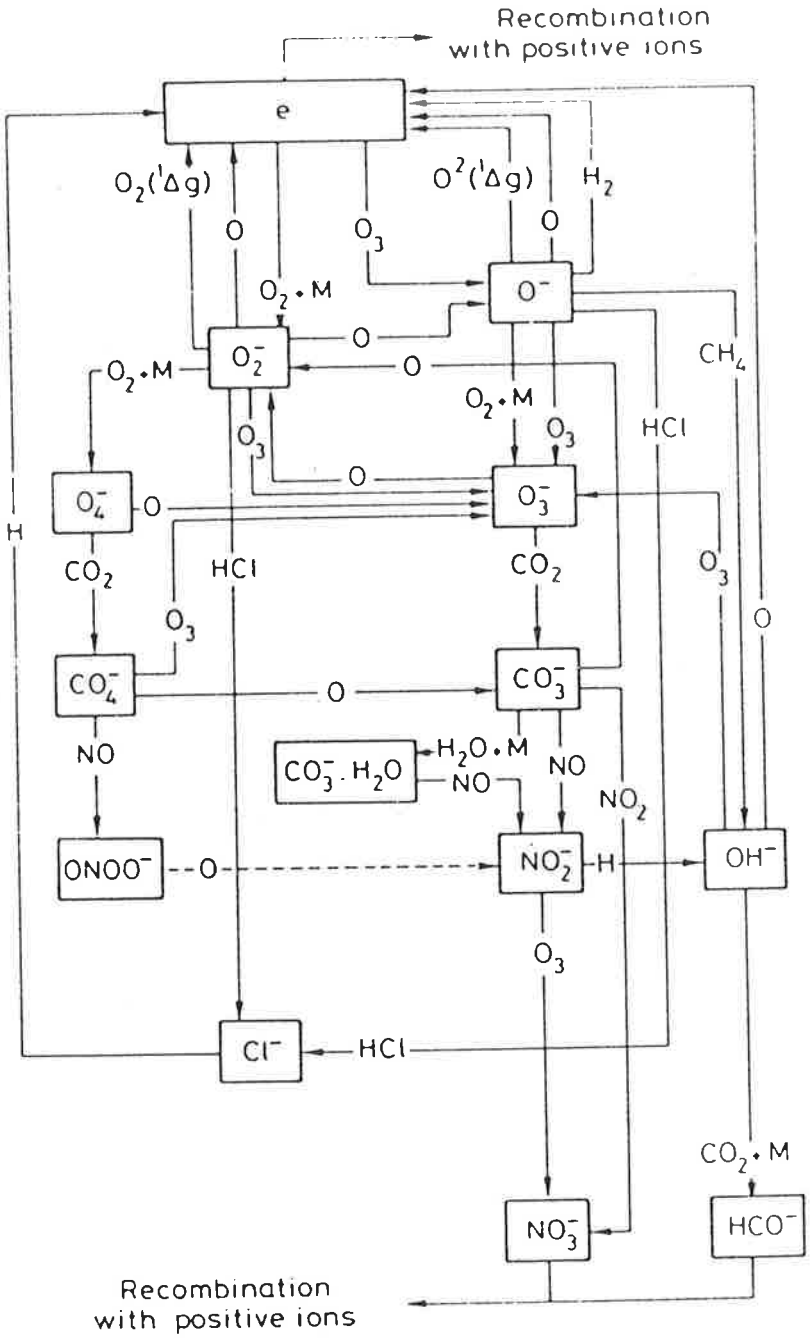

Figure 1.7: Schematic diagram of the suggested D region negative ion chemistry based upon intensive laboratory studies [after *Ferguson*, 1979].

1.3 Atmospheric dynamics

1.3.1 Introduction

The previous section of this chapter dealt with the discrete molecular nature of the atmosphere. This is ignored when we deal with atmospheric motions where the atmosphere is thought of as a continuous fluid medium. As such, the atmosphere is thought of as possessing at each point unique values of velocity, pressure, temperature, and density. These quantities are continuous both temporally and spatially, with the chemistry and the dynamics interacting with each other.

For many years it was thought that the general background wind motion could be inferred from atmospheric temperatures and that the influence of dynamical processes such as wave motions on the general circulation of the Earth's atmosphere was minimal. It was not until the early 1960's that, due to an increase in detailed measurements and better modelling, discrepancies arose which could not be explained by chemistry and chemical modelling alone. This led to a general awareness that atmospheric dynamics is not just a large scale solar and photochemically induced response, but that dynamical activity over a range of scales must also be considered for a proper understanding of the atmosphere [see e.g. *Fritts*, 1984; *Hines*, 1989].

In this section we will examine some of the atmospheric motions that are common in the atmosphere. To do that, though, requires some knowledge about the mathematical equations that describe motions in the atmosphere. We will therefore briefly examine these first.

1.3.2 Primitive equations

The three fundamental physical processes which describe motions in the atmosphere[15] are the basic conservation laws; conservation of mass, energy[16], and momentum. There are two distinct methods of dealing with these equations. The *Eulerian* frame of reference looks at the flux of fluid through a particular volume, while the *Lagrangian* follows individual particles and collects a detailed dynamical history of these particles. There are advantages and disadvantages of using either method. While the Lagrangian frame enables one to derive conservation laws in terms

[15] or any fluid
[16] first law of thermodynamics

of a particular mass of fluid, we will follow the Eulerian which allows the equation parameters to be related by a set of partial differential equations, such that the independent coordinates are the common x, y, z, and t. Another mathematical formalism which enables the description of the zonally averaged structure of the atmosphere by distinguishing between eddies and the mean meridional[17] circulation has been introduced by *Andrews and McIntyre* [1978]. Called the *Lagrangian mean averaging*, it computes horizontal averages following the path of a wave trajectory in both longitude and latitude. Although physically interpretable and mathematically elegant it is limited to scenarios where wave amplitudes are large [*McIntyre*, 1980]. We will only examine the basic equations, for there are many books dealing with fluid dynamics and it would serve no purpose to deal with detailed derivations here [see e.g. *Batchelor*, 1967; *Pedlosky*, 1979; *Andrews et al.*, 1987].

We start with the momentum equation (or the equation of motion),

$$\rho \frac{du_i}{dt} = \rho F_i + \frac{\partial \sigma_{ij}}{\partial x_j} \ , \tag{1.1}$$

where the total time derivative is

$$\frac{d}{dt} = \frac{\partial}{\partial t} + \underline{u}.\underline{\nabla} \ , \tag{1.2}$$

and is defined as the total time rate of change of a fluid property following the motion of a fluid element. ρ is the density, u_i is the vector fluid velocity, F_i are the coordinates of the external forcing per unit volume and σ_{ij} is the *stress tensor*. The equation of motion, in its most fundamental form, is a relation equating the rate of change of momentum and the sum of all forces acting on a volume of fluid.

The second equation is the continuity equation which simply states that for a particular volume of fluid, the rate of change of density within that volume is equal to minus the mass divergence;

$$\frac{d\rho}{dt} + \rho \underline{\nabla}.\underline{u} = 0 \ , \tag{1.3}$$

[17] wind flow along the longitude contours

where ∇ is the common gradient operator

$$\underline{\nabla} = \underline{i}\frac{\partial}{\partial x} + \underline{j}\frac{\partial}{\partial y} + \underline{k}\frac{\partial}{\partial z} .$$

Finally we have the energy equation

$$C_p\frac{dT}{dt} - \frac{1}{\rho}\frac{dp}{dt} = Q \ , \tag{1.4}$$

where C_p is the specific heat of air at constant pressure, T is the temperature and Q is the net heating rate per unit mass. The first two terms describe the expansion cooling, or adiabatic processes within a compressible fluid, while Q encompasses processes that produce nett heating or cooling of a volume of fluid (external forcing). In the upper atmosphere, the heating is provided by the absorption of u–v radiation, while the cooling is by infrared emission by ozone, carbon dioxide and water vapour.

An important equation in fluid dynamics is the *Navier-Stokes* equation, which is true for a viscous compressible Newtonian[18] fluid. Although gravity wave theory often requires a compressible theory, an assumption of incompressibility is often made for the atmosphere, and as can be seen from the continuity equation (equation 1.3), the velocity divergence $\underline{\nabla}.\underline{u}$ is then zero. The Navier–Stokes equation for a rotating planet is usually given in the following form,

$$\frac{d\underline{u}}{dt} = -\frac{1}{\rho}\nabla p + \frac{\mu}{\rho}\nabla^2\underline{u} - \nabla\psi - 2(\underline{\Omega}.\ \underline{u}) + g - \nu_{ni}(\underline{u}_i - \underline{u}) \tag{1.5}$$

where the individual terms are;

$-\frac{1}{\rho}\nabla p$ = pressure gradient force

$\frac{\mu}{\rho}\nabla^2\underline{u}$ = kinematic viscosity frictional force

$\nu = \frac{\mu}{\rho}$ = kinematic viscosity coefficient

$\nabla\psi$ = gravitational tidal term

$2\underline{\Omega}.\underline{u}$ = Coriolis force

g = effective gravity

$\nu_{ni}(\underline{u}_i - \underline{u})$ = ion drag

[18] Viscosity μ = constant, i.e. linear relationship between viscous force and velocity gradient

where μ is the viscosity coefficient, Ω is the angular velocity of rotation of the earth, ν_{ni} is the ion–neutral collision frequency, and the other terms are defined above.

Upon initial inspection one might be deceived into believing that solving these equations was a relatively simple problem. The equations are, however, highly non-linear, and no general solution is available. We therefore need to make several simplifications.

The first assumption made is that, for the Earth's atmosphere, ion drag plays no significant role below an altitude of $150km$, although it is important in the thermosphere. The term ion drag is in itself a little misleading because, depending on the relative magnitudes of the neutral wind velocity and the ion drift velocity, either can act as a drag or driver on the other. In fact, at high latitudes the externally applied electric field is large enough to accelerate the ions to a velocity larger than the neutral wind, and acts as a momentum source [*Heppner and Miller*, 1982; *McCormack and Smith*, 1984]. We can further ignore the gravitational tidal term, and also assume, at least for large scale motion, that the motion is purely in the horizontal plane. Finally we assume that there is a general background state upon which are superimposed small perturbations.

For synoptic scale motions in the lower atmosphere, we assume that the frictional forces are negligible (at least above the first kilometre), and that we have steady state flow ($d/dt = 0$). Thus the Coriolis force and the pressure gradient force are in approximate balance, leading to the *geostrophic* relationship,

$$fv \simeq \frac{1}{\rho}\frac{\partial p}{\partial x} \quad , \quad fu \simeq -\frac{1}{\rho}\frac{\partial p}{\partial y} \quad , \tag{1.6}$$

where $f \equiv 2\Omega sin\phi$ is called the *Coriolis parameter*. Thus we can describe the prevailing winds in the lower atmosphere from a knowledge of the pressure[19] distribution alone.

1.3.3 Waves in the atmosphere

Studies of winds and temperatures in the atmosphere have shown that there exist numerous oscillations and wave–like motions superimposed on the general atmospheric circulation, and that these waves have periods ranging from minutes to hours. These waves can be classified in

[19] or temperature distribution utilizing the thermal wind equation

Wave type	Typical period	λ_h
Internal gravity waves	$5 - 300min$	$100 - 1000km$
Atmospheric Tides	solar - $24, 12, 8hr$	Global
	lunar - $12.4hr$	
Planetary waves	> 2 days	$\geq 10^4km$

Table 1.1: Principal wave motion characteristics prevalent in the atmosphere

numerous ways, according to their physical or geometrical properties [*Andrews et al.*, 1987]. The main classification is based on their restoring mechanisms: gravity waves due to the stratification of the atmosphere, inertio-gravity waves due to the combination of stratification and Coriolis parameter, planetary waves due the Coriolis effect. These waves are all solutions of the Navier-Stokes equation (equation 1.5), but in each case different terms dominate. For example if we ignore the contribution due to gravity, Coriolis force and viscosity, we end up with acoustic waves. Consideration of the gravity term only leads to gravity waves, while if we maintain the Coriolis term we deal with planetary waves.

Waves can also be distinguished on the basis of being a forced or free mode; an example of forced waves are the solar thermal tides while a free–mode wave is the two-day wave [*Salby*, 1981]. Another classification can be made according to the propagation characteristics of the waves; those that can propagate only in some general horizontal directions are said to be vertically evanescent. An example of these are the equatorial waves which are trapped and prevented from propagating latitudinally (see section 7.3). Waves can also be separated into stationary and travelling waves; the former are those that maintain a fixed phase relationship with respect to the Earth. Finally, waves are classified according to their interaction with the mean flow. Those that do not accelerate the mean flow are linear, steady, frictionless and adiabatic (see Section 3.6, *Andrews et. al.*, 1987), while those that do are transient and nonconservative.

Although it is the same physical processes that govern the propagation of all waves within the atmosphere, the Coriolis effect can be ignored when dealing with larger wavenumbers, thus allowing the adoption of Cartesian coordinates. Table 1.1 shows the main characteristics of the more common atmospheric wave motions.

One type of wave which has not been mentioned arises when the contributions from viscosity

and thermal conduction are included in the solution of the equations of motion [see e.g. *Hooke and Jones*, 1986; *Hocking et al.*, 1991]. These solutions are known as *viscosity waves*. Although these types of waves are not commonplace and exist under specific conditions, they might explain some observations of the middle atmosphere and will be discussed further in chapter 5).

The following is a brief discussion on the main wave motions that are supported, and are evident everywhere throughout the Earth's atmosphere. Only the important attributes will be discussed, and no detailed wave solutions will be presented.

Internal gravity waves

The atmosphere contains a spectrum of waves. Of these, the highest frequency ones are the acoustic or sound waves, ranging above, through, and below the human audible range. These waves are longitudinal, compression waves in which the individual particle motion is parallel to the direction of propagation and where the gravitational forcing of the Earth plays no role [see e.g. *Houghton*, 1986]. Waves in which the oscillations have periods of a few minutes and more and whose motions are almost transverse to their line of propagation are known as gravity waves (the oscillation is actually elliptical with a small compressional component). These waves arise due to the buoyancy nature of the atmosphere. A parcel of air displaced from its equilibrium position will attempt to return to its original position - the oscillation resulting from gravity and buoyancy acting on the air parcel. For free unrestricted vertical oscillations the frequency is the well known Brunt-Väisälä frequency. Since the buoyancy force is the restoring force on these waves, they are also sometimes known as *buoyancy waves*. *Hines* [1960], initially proposed that the existence of gravity waves in the middle atmosphere explained wavelike features which were evident in meteor wind profiles in the mesosphere and which were previously attributed to turbulence [see figure 1.8].

The atmosphere can sustain gravity waves with intrinsic periods (with respect to the mean motion of the atmosphere) which can not be greater in value than the inertial ($\approx 12hr/\sin\theta$) or smaller than the Brunt-Väisälä[20]. Since the atmosphere has no upper boundary, gravity

[20] $\approx 5min$ in the mesosphere and $10min$ in the troposphere

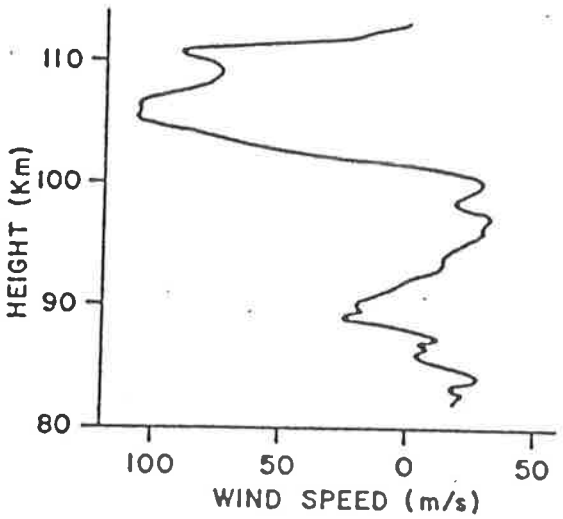

Figure 1.8: An initially puzzling result of a mesospheric wind profile obtained by photographs of meteor trails which was later easily explained when gravity waves were finally understood [after *Liller and Whipple*, 1954].

waves propagate vertically as well as horizontally, unlike the ocean where similar waves exist but in which the propagation is mainly in the horizontal. Vertically propagating waves in the atmosphere can also become trapped and form standing waves between temperature inversions. Atmospheric gravity waves are also commonly referred to as *internal waves*, with their phase being a function of height. Gravity waves can possess any combination of horizontal and vertical wavelengths, provided that they satisfy the following dispersion relationship [see e.g. *Gossard and Hooke*, 1975]

$$m^2 = k_h^2 \left(\frac{N^2 - \omega^2}{\omega^2 - f^2} \right) - \frac{1}{4H_\rho^2} + \frac{\omega^2}{C_s^2} \ , \tag{1.7}$$

where

$$k_h^2 = k^2 + l^2, \tag{1.8}$$

$$\omega = \sigma - k\bar{U} - l\bar{V} \ , \tag{1.9}$$

$$N^2 = \frac{g}{T} \left(\frac{dT}{dz} + \frac{g}{C_p} \right) \ , \tag{1.10}$$

$$f \approx \frac{4\pi}{24\text{hrs}} \sin\theta \ , \tag{1.11}$$

where m is the vertical wavenumber, k_h the horizontal wavenumber, N the Brunt-Väisälä frequency, ω the intrinsic frequency, f the Coriolis or inertial frequency, H_ρ the density scale-height, C_s the speed of sound, T the background temperature, g the gravitational acceleration, C_p the atmospheric specific heat at constant pressure, θ the latitude, σ the ground–based wave

frequency (as measured from a fixed position on the ground, not including the effects of mean atmospheric motion), and $\overline{U}$ and $\overline{V}$ are the mean background wind vectors. When one includes the polarization relations [see e.g. *Vincent and Eckermann*, 1990], they, together with the dispersion relationship are sufficient to describe the physical nature of gravity waves.

In the middle atmosphere the last term in equation 1.7 is negligible, and H_ρ is only important in the case where the vertical wavelength is larger then $\approx$ 40 km. Thus, the only important term in equation 1.7 is the first, where f and N are the boundary limits on ω, the intrinsic wave frequency. We do note, however, that the density scale–height is important when considering second order effects like Stokes' diffusion [*Walterscheid & Hocking*, 1991]. There is, however, one constraint on the lower limit of the vertical wavelength. Small vertical wavelength waves can be "smothered" by eddy diffusion and the motions tend to become intermediate between quasi-linear gravity waves and isotropic turbulence, and belong to a region of scales defined either as saturated gravity–wave fields or as buoyancy subrange turbulence [*Hines*, 1964; *Weinstock*, 1978a; *Sidi and Dalaudier*, 1989].

Gravity waves can transport energy and momentum upward into the atmosphere [see e.g. *Hines*, 1960], because the most important sources are near the ground. An important property of gravity waves is that the group velocity and energy propagation are orthogonal to the direction of phase propagation. The direction of the energy propagation also depends on the period, small period gravity waves propagating energy almost vertically, and long period waves almost horizontally.

For many years, the mean state of the mesosphere, as measured experimentally, could not be adequately modelled. Experiments showed that it departs significantly from radiative equilibrium[21]. This departure is now directly attributed to the effect of gravity waves in the mesosphere. As the density of the atmosphere decreases with height, the amplitude of an individual gravity wave increases until it breaks and dissipates. At this point the wave momentum and energy are transferred to the background flow [e.g. *Booker and Bretherton*, 1967]. That gravity–wave dissipation made a large contribution to the state of the mesosphere was

[21] the net incoming solar energy flux is balanced by the net outgoing long wave energy flux

initially proposed by *Houghton* [1978] while the mathematical ideas were developed by *Lindzen* [1981]. These ideas were then incorporated into general circulation models, and the results were at last found to agree with experimental observations [see e.g. *Matsuno*, 1982; *Dunkerton*, 1982; *Holton and Zhu*, 1984]. Quantitative measurements of momentum flux and mean–flow accelerations due to gravity waves have been measured by e.g. *Vincent and Reid* [1983] and *Reid* [1984], who concluded that the measured values were of the order required to explain the anomalies in the mean flow.

Figure 1.9 shows three plots of zonal wind contours. The top figure (*a*) is the predicted zonal wind structure (latitude-height) based on extensive computational modelling but excluding any gravity wave drag. The middle figure (*b*) is the observed mean zonal winds, while the bottom figure (c) is also modelled data, but this time including the effect of gravity wave drag. As can be seen the modelled data which do not include the effect of gravity–wave drag show very little agreement with the observed geostrophic winds, while modelled winds which do include the effects of gravity–wave drag agree remarkably well with the observed structure. Thus gravity waves are not only the cause of fluctuations in the observed winds, but they significantly affect the mean flow as well.

The deposition of momentum into the middle atmosphere by dissipating gravity waves also contributes significantly to the mesospheric meridional circulation. In radiative equilibrium the pressure gradient force driving a North–South flow from the summer to winter pole, is converted by a Coriolis force into a purely zonal flow so as to conserve angular momentum. This zonal flow also experiences a Coriolis force which opposes the original pressure gradient force, resulting in a nett zero meridional flow. However, if this zonal flow is reduced by gravity wave drag, the pressure gradient force is no longer balanced by the Coriolis–induced force acting in the opposite direction, resulting in a nett meridional flow [*Houghton*, 1978]. Furthermore, this meridional flow forces vertical motion with warm air rising and therefore cooling, resulting in a mesopause which is warmer in winter than in summer, again in conflict with radiative equilibrium theory which suggests that there should be a net motion from the summer to the

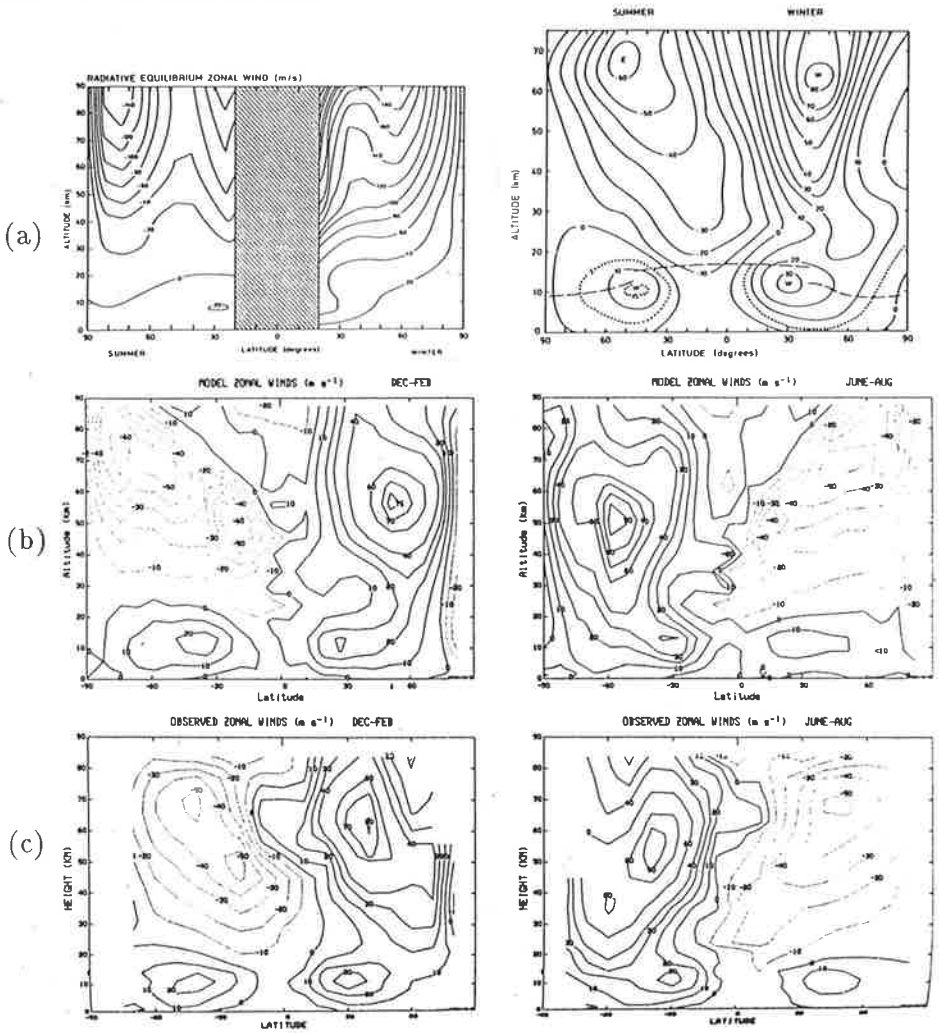

Figure 1.9: Plots of the zonal winds (a) modelled without incorporating the effects due to gravity wave drag [after *Brasseur and Solomon*, 1986], (b) the observed winds [after *Murgatroyd*, 1969], (c) modelled, but including the effects of gravity–wave drag [after *Rind et al.*, 1988].

winter mesospheric hemispheres, where the flow from the summer hemisphere is upwards and conversely downwards for the winter hemisphere [see e.g. *Dunkerton*, 1978; *Barnett and Corney*, 1985]. Gravity waves are also often associated with the formation of turbulence and this point will be further discussed in the following chapter.

It now seems evident that gravity waves pervade the whole atmosphere, and are produced by many different sources, generated either at the Earth's surface or within the atmosphere. Orography can be a source of gravity waves, as airflow over topographic features like mountains can produce progressive waves [see e.g. *Hines*, 1968b]. It has also been shown by *Eckermann* [1990], that strong gravity–wave motions occurred throughout the troposphere as cold fronts moved across southern Australia. Other sources include cyclones, jet streams, wind shear,

convection, turbulence, volcanic eruptions, nuclear explosions, plus auroral sources like Joule heating, and Lorentz forcing[22] which are confined principally to the high–latitudes [see e.g. *Gavrilov and Shved*, 1982; *Fritts*, 1989; *Rees*, 1989].

Atmospheric tides

Atmospheric tides are essentially internal gravity waves but influenced by the Earth's sphericity and rotation. Moreover, their periods and origins are known more precisely and completely than those for internal gravity waves. The first tides that were observed by man were ocean tides whose causes were correctly attributed to the Moon and Sun, even though gravity was not yet understood. It was *Newton* who correctly inferred that gravitational tides existed in the atmosphere, although he surmised that they would be of such low amplitude as to be undetectable.

Tides are the response of the atmosphere to some type of forcing. This forcing can be due to the lunar and solar gravitational fields, or to solar insolation. Tides are classified according to their propagation with respect to the Earth's surface; we thus have *migrating* and *nonmigrating* tides. Nonmigrating tides are due to local topography and geographically–fixed heating sources, and unlike migrating tides do not follow a predictable cycle. They are of no relevance to this thesis and hence will not be considered further. Migrating tides are due to the gravitational attraction of the atmosphere by the moon and the sun, as well as solar heating of the atmosphere [see e.g. *Lindzen*, 1974; *Groves*, 1976]. Herein we will consider tides due to solar heating only, since they are by far the dominant tides. For a discussion of lunar and solar gravitational forcing see e.g. *Chapman and Lindzen* [1970].

The absorption of UV by stratospheric ozone and tropospheric water vapour heats the lower atmosphere. Since the solar heating, due to the spherical nature of Earth, is differential, the atmosphere is continually in a state of thermodynamic imbalance. Solar tides attempt to return the Earth to a state of thermodynamic equilibrium. To keep a fixed phase relationship with their driving force, they must therefore propagate westward.

[22] a force on charged particles due to electric and magnetic fields

The fundamental period of a tide in the Earth's atmosphere is 24 hours, and oscillations with this period are known as the *diurnal* tides. In addition there are two harmonics at periods of 12, (*semi-diurnal*), and 8 (*ter-diurnal*) hours. It would serve little purpose to go through the classical tidal theory of Laplace here, since there are a number of works dealing with the subject [see e.g. *Chapman and Lindzen*, 1970; *Lindzen*, 1974; *Kato*, 1980], and we will deal rather with the main points qualitatively.

Classical tidal theory due to Laplace attempts to predict the behaviour of the tides, assuming, to a first approximation, that the Earth is a smooth sphere, and the atmosphere a non–viscous, hydrostatic, uniform temperature gas. Consideration of the momentum, mass, and energy equations, and assuming tidal motions to be but a small perturbation of a basic state, leads to the linearization and analytical solution of the tidal equations. These solutions yield a set of eigenvalues and eigenfunctions, (for any particular latitude and longitude), and allow tides to be described in terms of modes and equivalent depths. Modes describe the horizontal structure while, equivalent depths fix the vertical structure. Thus each tidal mode has a unique vertical wavelength based on the eigenvalues of the atmosphere for that particular mode, which can be calculated from

$$\lambda_z \approx 2\pi \left(\frac{N^2}{g h_e} - \frac{1}{4 H_\rho^2} \right)^{-\frac{1}{2}} \tag{1.12}$$

where λ_z is the vertical wavelength, N is the Brunt-Väisälä frequency, g gravitational acceleration, and H_ρ the density scale height. Modes which are excited over a vertical region which has a depth equal to or greater than their vertical wavelengths will self-interfere resulting in only weak excitation. Since the diurnal tide has a vertical wavelength of about 25 km, while the semidiurnal is about 200 km, the semi-diurnal tide often has a much larger amplitude than the diurnal even though it is not the primary mode. This explains why the semidiurnal tide measured experimentally can be as strong if not stronger than the diurnal, even though it is not the primary mode of forcing. In addition, it should be noted that the forcing function is not sinusoidal with a 24 hr period, but rather has Fourier components.

Winds due to tides in the atmosphere can be resolved into a zonal and a meridional flow,

with a phase difference between them which results because the wind vector rotates with respect to time. In the Northern hemisphere the meridional wind vector generally lags the zonal resulting in a clockwise rotation of the wind vector. Conversely, in the Southern hemisphere the meridional wind vector generally leads the zonal resulting in an anticlockwise rotation of the wind vector.

Since tides can propagate vertically they transport energy and momentum into the atmosphere, thus having an influence on its dynamics and temperature. It has been found, for example, that the amplitude of mesospheric tidal temperature variations can exceed 10 K [*Andrews et al.*, 1987]. It should also be noted that below 100 km, tidal motions can be calculated quite accurately by using classical tidal equations, provided that a knowledge of the solar thermal forcing and the surrounding atmosphere is known. Above 100 km, however, effects due to viscosity, ion drag and thermal conduction must be included [see e.g. *Richmond*, 1971]. For a review of tidal motions below 80 km see e.g. *Forbes and Groves* [1990], above 80 km see e.g. *Forbes* [1990].

Planetary waves

Planetary waves, also known as *Rossby waves*, are large scale waves whose wavelength is comparable to the dimensions of the Earth. Planetary waves arise due to the existence of the variation of the Coriolis force with latitude[23], and are a motion which conserves absolute vorticity. They propagate in a westward direction relative to the air stream, so that their motion may therefore be either eastward or westward relative to the ground. Their phase velocity increases with wavelength and thus they are highly dispersive. Planetary waves can be either forced or free normal modes of the atmosphere and are usually classified by their wave number, which is defined as the number of complete cycles around the globe for a given latitude.

Forced planetary waves, with periods of between 5 and 30 days and vertical displacement amplitudes of between 2 and 10 km, have been observed in the northern hemisphere up to heights of 110 km [see e.g. *Brown & John*, 1979], although during summer, they are precluded

[23] also known as the β–effect

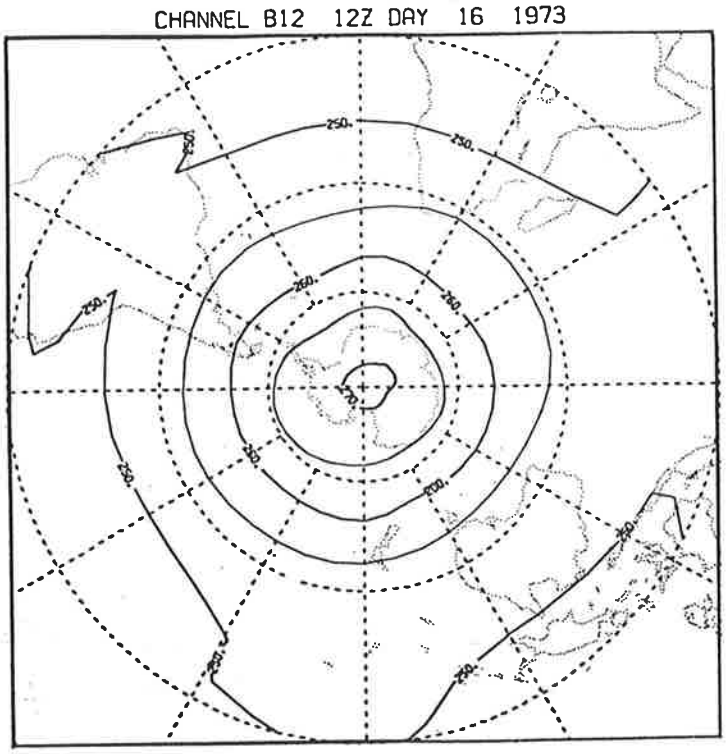

Figure 1.10: Brightness temperature contours observed by the Selective Chopper radiometer on the *Nimbus* 5 satellite measured on January 16, 1973 at an altitude of 42 km clearly showing the 2-day wave (zonal wave number 3) [after *Rodgers & Prata*, 1981].

from the upper atmosphere by stratospheric easterlies (westward flow) [*Charney & Drazin*, 1961]. A dominant planetary wave is the $5-day$ wave (wave number 1), a westward travelling normal mode whose period is very close to 5 days. It is symmetric about the equator and peaks in mid-latitudes.

Other planetary waves are the 2–day (wave number 3), and the 16–day (wave number 1) wave [see e.g. *Madden*, 1978; *Madden & Labitzke*, 1981; *Salby*, 1984; *Smith*, 1985; *Hirota & Hirooka*, 1984; *Daley & Williamson*, 1985; *Hirooka & Hirota*, 1985, 1989]. Figure 1.10 shows brightness temperature contours clearly showing the 2-day wave (zonal wave number 3) [after *Rodgers & Prata*, 1981]. Figure 1.11 shows the power spectral density found by the maximum entropy method [for a review of this method see *Hayashi*, 1971, 1977] of the s=1 component at 75° N, found at 1 and 200 mb using three months of data. Two notable peaks can be seen; one near 9 and the other near 17 days in the westward travelling regime. The 9–day peak is due to the (1,2) mode (10–day wave), while the 17–day peak was classified as that of the (1,3)

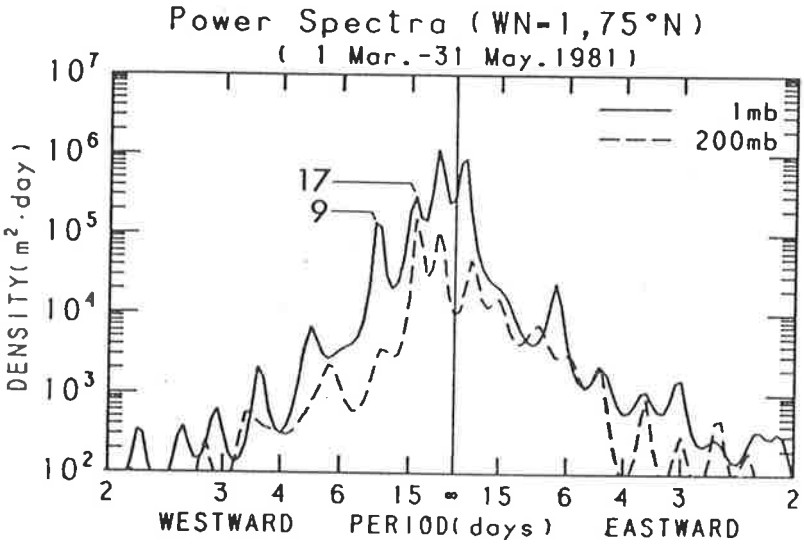

Figure 1.11: Maximum entropy method power spectral density of s=1 wave component at 75° N for March 1 to May 31, 1981. The solid line is the spectrum at 1 mb while the dashed line is at 200 mb [from *Hirooka & Hirota*, 1989].

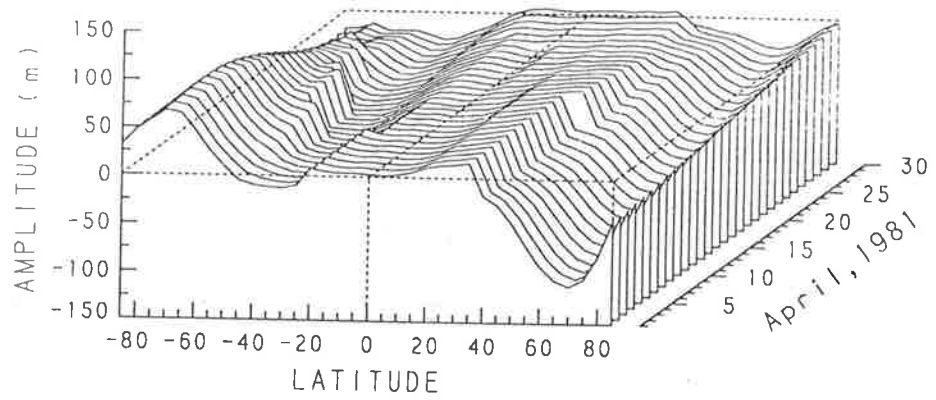

Figure 1.12: Three–dimensional plot of a 100 mb (1,4) mode amplitude versus latitude and time for April 1981 [from *Hirooka & Hirota*, 1989].

mode (16–day wave). Figure 1.12 illustrates the meridional structure and time evolution of a (1,4) wave at 100 mb over April 1981 [from *Hirooka & Hirota*, 1989]. One can clearly see the almost antisymmetric structure with three nodes between the two poles during the first half of the month. The kink near the equator was attributed by the authors to be mainly due to the error resulting from the small amplitude of the wave.

Although planetary waves are evanescent in the vertical, low wavenumbers can propagate vertically during the winter westerly (eastward) flow [*Salby*, 1984; *Houghton*, 1986]. In the mesosphere they can be strongly attenuated and contribute momentum to the mean flow, [*Eliassen & Palm*, 1960]. For further reading see e.g. *Salby* [1984], *Andrews et al.* [1987]. Planetary waves have also been recognized as important in their affect on the distribution of chemical species, like ozone, N_2O, and N_2O_5 and NO_2 [*Berggren & Labitzke*, 1968; *Schmidt*, 1982; *Solomon & Garcia*, 1983].

1.3.4 Turbulence

Until now we have concentrated on large scale motions which are prevalent in the atmosphere. These motions are the result of energy being pumped into the atmosphere, which is eventually dissipated as heat. Before that though, these large scale motions become turbulent. In fact, the most common state of any fluid is turbulent flow, and only some of the flow can be termed laminar. It is only because the atmosphere is turbulent that we can use partial reflection radars to study it. For this reason we shall not deal with turbulence here, but devote the following chapter to it.

Chapter 2

Atmospheric Turbulence

2.1 Introduction

This thesis concentrates on the study of the structure and dynamics of the mesosphere using the remote sensing capabilities of partial–reflection radars. These radars rely on inhomogeneities in the atmosphere to scatter the radar signal and thus provide information about the scatterers and the medium in which the scatterers exist. Turbulence is one of the primary generators of both spatial and temporal variations in the refractive index of the atmosphere; it creates a medium which scatters electromagnetic radiation, thereby enabling one to probe the atmosphere and study both the long–term and short–term dynamics as well as turbulence itself. Atmospheric turbulence is an extremely complex subject and although it is well beyond the scope of this thesis to study it in detail, an elementary treatment is desirable if not mandatory. This chapter will look at some basic features of turbulence and its relevance to the atmosphere.

The author is indebted to an unpublished series of lectures on atmospheric turbulence given by *W.K. Hocking* [1988b]. There are also a number of excellent texts dealing with turbulence to which the reader is referred, such as: *Batchelor* [1953], *Tatarski* [1961], *Lumley & Panafosky* [1964], *Bradshaw* [1971], *Tennekes & Lumley* [1972], and *Panafosky & Dutton* [1984].

2.2 Properties of turbulence

Any fluid motion, whether it be an ocean current, lava flow, or wind, can be regarded as being composed of a steady (slowly varying) component on which a fluctuating component is superimposed. The definition of the steady component is arbitrary, for the temporal scales are defined by the needs of the study. One could be examining the expansion of the universe where the steady flow could be averaged over millions of years and the fluctuating component over periods of hundreds of thousands, or one could look at atmospheric jets where turbulence occurs in fractions of a second. For most purposes, however, turbulence is the term used when one cannot predict the detailed evolution of the flow and can only use statistical descriptors to describe the fluctuating component.

Since the definition of turbulence is rather a difficult one, it makes more sense to define the properties of turbulence, which are as follows:

(1) The velocity of the fluid is chaotic, and a random function of both space and time. It is usually the result of some instability developing within a fluid which grows and breaks down.

(2) The flow is generally three–dimensional and rotational, with gradients in all three dimensions, although in special cases it can be two-dimensional and hence anisotropic.

(3) An essential part of turbulence is the non-linearity, which ensures structures which are continuous in both intensity and size, and a flux of energy from one scale to another.

(4) Turbulence is a property of the flow of the fluid rather than a property of the fluid, where the flows are diffusive and chaotic. Almost all flows in nature are turbulent rather than laminar.

(5) Turbulence causes diffusion of any physical property carried by the fluid and is instrumental in momentum, heat and mass transfer. Viscous forces always result in the internal energy of the fluid increasing at the expense of turbulence, i.e. turbulent energy is converted into heat.

The last point is perhaps the most important in distinguishing atmospheric turbulence from other types of flow. For many years, all atmospheric motions which could not be clarified by

the (then) current dynamical theories were attributed to turbulence, and it is only since the 1960's that many of these have been been shown to be due to gravity waves and not turbulence. [see section 1.3.3]. This can be easily visualized when you consider that a spectrum of gravity waves can impart motion to a parcel of air which may make it appear chaotic. However, since no diffusion takes place the flow is not turbulent.

2.3 Description of turbulence

2.3.1 Basic theory of turbulence

Although turbulence is generally assumed to be a random motion of particles its roots are found in the basic fluid dynamic equations, the continuity and the Navier–Stokes equations. (equations 1.3 and 1.5). The solution of these equations is very difficult because of their non-linearity and it is much easier to deal with fluid energetics and correlation terms rather than with actual fluid flow velocities. We therefore re–arrange the Navier–Stokes equations to give an equation in terms of energies [*Dutton & Panafosky*, 1970], which describes the change in the turbulent kinetic energy with respect to time, viz,

$$\frac{dE}{dt} = M + B + T - \epsilon \ . \tag{2.1}$$

M is the mechanical generation of turbulence, B is the buoyancy term, and T is the transport (advection) of energy, both into and out of the relevant region. ϵ represents the rate of turbulent energy loss through viscous dissipation, and is always positive, implying that there is an energy sink in the above equation. The buoyancy term B can either be positive or negative depending on the current atmospheric temperature structure. If positive, it acts as an energy source since the rate of lapse of temperature is less than the adiabatic lapse rate. In this scenario of a stable atmosphere, energy is radiated away by the generation of gravity waves. If it is negative, it acts like an energy sink and damps out the existing turbulence.

One can alternatively view turbulence in the spectral domain, where the velocity and density fluctuations caused by turbulence are thought of as a Fourier sum; i.e. a sum of a number of

different sinusoidal fluctuations, or scales. This is a very useful approach when looking at the structure of turbulence [see e.g. *Bolgiano*, 1968]. Each scale is designated a wavenumber k, which is of a magnitude $\frac{2\pi}{\lambda}$, where λ is the wavelength. The energy equation can then be re–written as [*Weinstock*, 1978a]

$$\frac{\partial E(k)}{\partial t} + \frac{\partial Q(k)}{\partial z} = S(k) - \frac{\partial \epsilon(k)}{\partial z} + Bk - 6\nu k^2 E(k), \tag{2.2}$$

where

(1) $E(k)$ is the spectral kinetic energy density.

(2) $\frac{\partial Q(k)}{\partial z}$ is the vertical transfer of energy in physical space purely caused by turbulence, where z is the vertical co-ordinate.

(3) $S(k)$ is the spectrum of the Reynolds stress, $- < u'w' >$[1], where u' is the horizontal velocity fluctuation in the direction of the mean flow velocity U_o and w' is the vertical velocity fluctuation. Thus $S(k)\frac{\delta U_o}{\partial z}$ represents the energy transferred from the mean flow to turbulence by the Reynolds stress.

(5) $B(k)$ is the spectrum of the buoyancy flux $(-\frac{g}{\rho_o}) < w\rho' >$, where ρ' is the density fluctuation, ρ_o is the average density at height z, and g is the acceleration due to gravity.

(6) $2\nu k^2 E(k)$ is the rate of energy dissipation by the molecular viscosity ν.

2.3.2 Turbulence generation

Turbulence in the atmosphere exists over a large range of scales, but before discussing the spectrum further, it is worthwhile spending some time discussing situations that are conducive to the generation and existence of turbulence. Following from equation 2.1, it is intuitive that turbulence can exist only if energy available for its generation is greater than the buoyancy effects which inhibit turbulence. This ratio is known as the *Flux Richardson number*, and is given by

$$R_f = \frac{-B}{M} \ . \tag{2.3}$$

[1] <> indicates averaging

R_f represents the ratio of the rate of destruction of turbulence by stable stratification to the rate of production of energy by a wind shear. Substituting this back into equation 2.1, we obtain

$$\frac{dE}{dt} = M(1 - R_f) - \epsilon \ . \tag{2.4}$$

The Flux Richardson number is then negative if the heat flux is upward, positive if the heat flux is downward, and zero when, in the absence of heat flux, only mechanical turbulence is being created. Its absolute value is usually a relative measure of the importance of convective to mechanical turbulence.

Experimentally, R_f is not the parameter which is usually measured, but rather another number, the *Gradient Richardson number* is used. This can be experimentally measured, and is related to R_f by,

$$R_i = \frac{K_m}{K_h} R_f \ , \tag{2.5}$$

where K_m and K_h are, respectively, the eddy viscosity and (heat) conductivity. The advantage of using R_i instead of R_f is that it can be computed from averaged quantities through the following equation for a horizontally stratified atmosphere where (a more general R_i has been derived by *Hines*, [1971].)

$$R_i = \frac{\omega_b^2}{\left(\frac{\partial \overline{U}}{\partial z}\right)^2} \ . \tag{2.6}$$

Not unlike R_f, R_i also represents the ratio of the relative importance of convective to mechanical turbulence. When R_i is positive and large, the temperature stratification is very large and inhibits turbulence. When positive and below a critical number, mechanical turbulence persists but is damped by temperature stratifications. Zero R_i implies purely mechanical turbulence, while increasing negative values indicate weaker mechanical turbulence and stronger convective turbulence as the temperature gradient becomes more unstable. The critical number at which turbulence can occur has been shown to be, both experimentally and theoretically, around 0.25 [see e.g. *Miles*, 1961; *Howard*, 1961; *Lyons et al.*, 1965; *Woods*, 1969; *Hines*, 1971]. One must bear in mind that $R_i < 0.25$ is a condition necessary for the existence of turbulence, but not a guarantee that it exists. Whilst R_i is mainly used within experimental work and

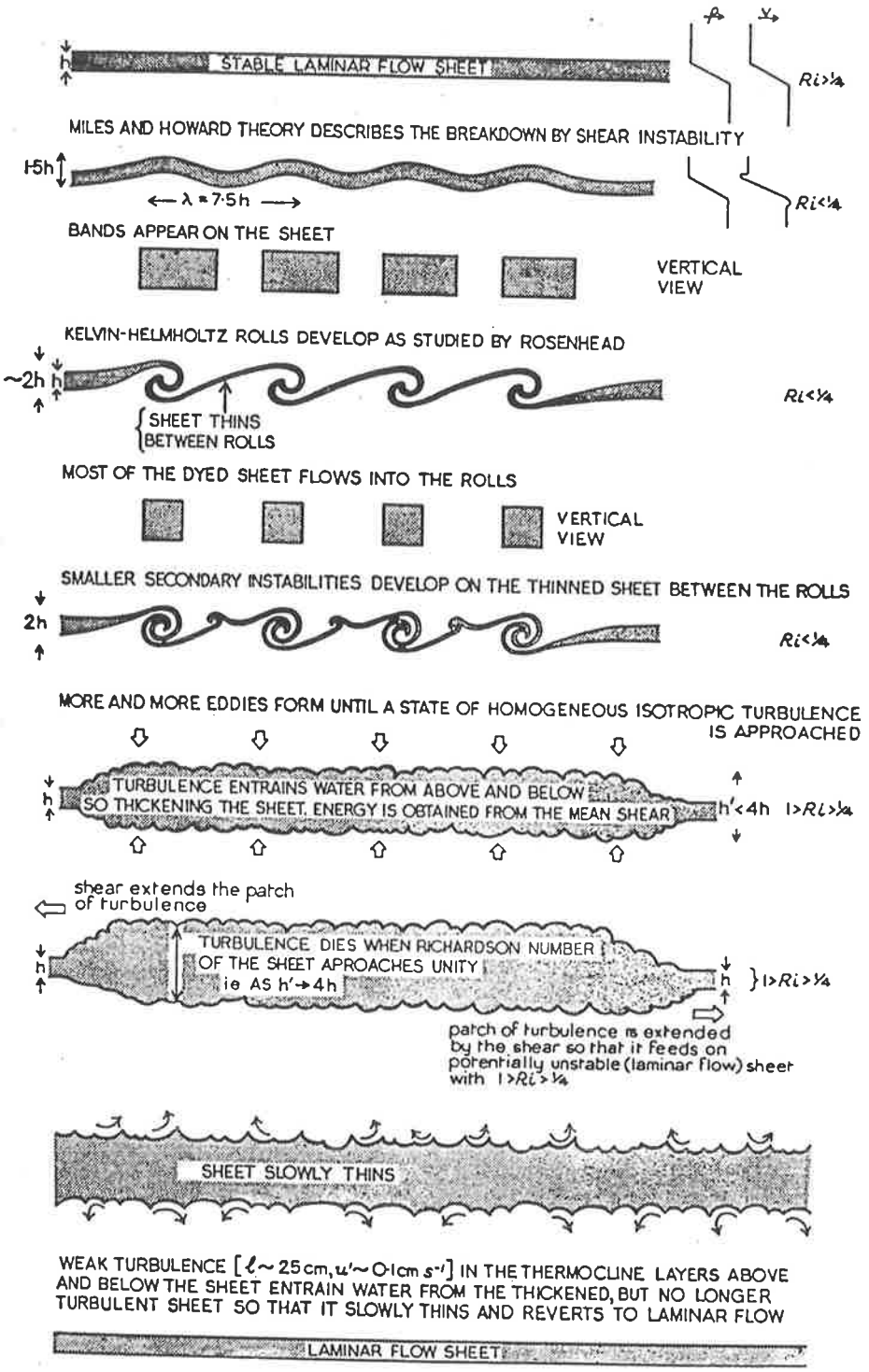

Figure 2.1: The development of turbulence *via* the Kevin-Helmholtz process in a stably stratified fluid [from *Woods*, 1969].

R_f in theoretical, the two are proportional if the abilities of turbulence to transport heat and momentum vertically are comparable.

A specific example of turbulence generation is the *Kevin-Helmholtz* instability which develops at the boundary of two fluids where waves develop and grow on a stably stratified shear layer, extracting kinetic energy from the shear. They grow until eventually breaking down into turbulence. Figure 2.1 illustrates the development of turbulence due to the Kevin–Helmholtz process in a stratified flow.

2.4 Atmospheric turbulence and the energy cascade

In the atmosphere the initial perturbation which leads to turbulence is usually due to shear instability, internal wave breaking or convection. Shears occur when the wind velocity changes rapidly with height; waves break as they grow in amplitude with increasing height; and convection leads to instability when cold air overlies hot. All three processes usually lead to rotational motion. Once rotation commences a local region of velocity shear develops, usually on a smaller scale than the original rotational motion. These rotational motions[2] in turn lead to smaller and smaller rotational motions. The end result is a cascade of energy where the energy is fed from larger scales into smaller ones until it is eventually dissipated as heat due to viscosity.

The determination of the structure of turbulence is often one of the primary objectives of any studies of turbulence. In that case, the velocity and density fluctuations can often be thought of as being composed of a number of sinusoidal fluctuations of varying scales[3], and varying spatial orientations. We can therefore, by Fourier analyzing the wind or density fluctuations, discover something about the spectrum of turbulence. Figure 2.2 describes the energy spectrum of atmospheric turbulence. The spectrum is divided into three distinct regions based on the distinct characteristics of turbulence within each region, known as the buoyancy range, inertial range and viscous range. We will now briefly discuss each region.

[2] known as eddies or vortices
[3] wavelengths

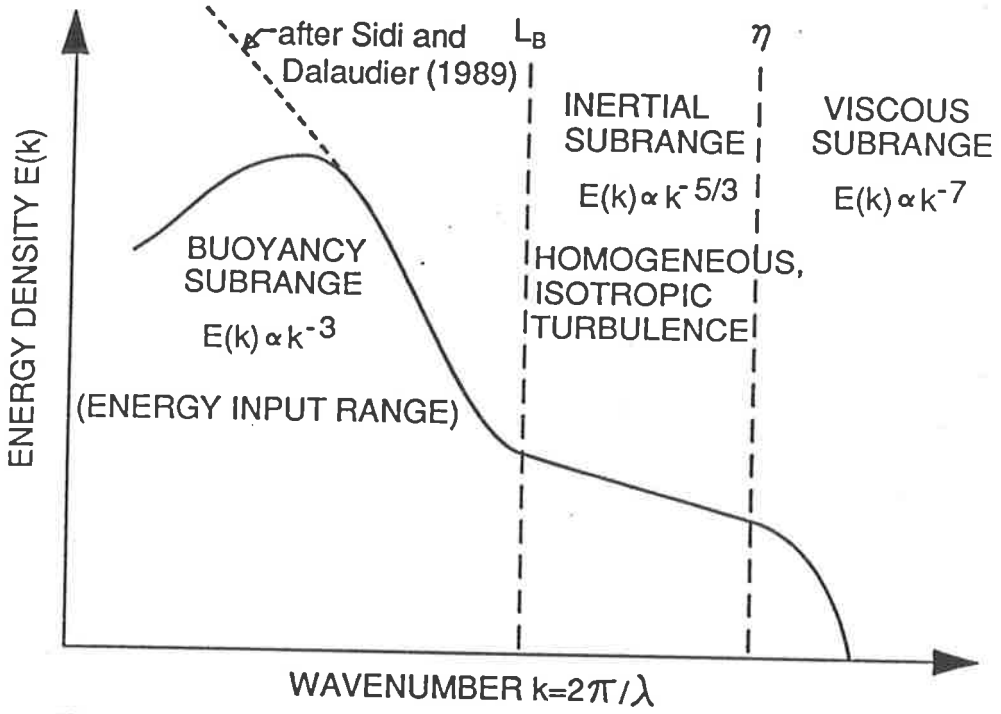

Figure 2.2: Turbulent energy spectrum [after *Blix*, 1988]. Energy is extracted by turbulence from the mean flow at large scales, is passed along into smaller and smaller scales until it is balanced by the viscous dissipation of energy at large wave numbers. It is currently thought that $E(k)$ does not fall off at small k in the upper atmosphere [*Sidi and Dalaudier*, 1989], [from *Murphy*, 1990].

Buoyancy range

The buoyancy subrange is the region where buoyancy effects dominate over inertia forces. It is one of the least understood regions, partly because of the difficulty of performing experimental measurements. Initial work proposed a scenario where the buoyancy range acts as an energy source, with the largest scales of motion feeding an energy cascade that transfers this energy through smaller and smaller scales until it is eventually dissipated as heat [*Shur*, 1962; *Lumley*, 1964]. Recent work has extended this to suggest that there may also be a reverse cascade of potential energy which is lost at low wavenumbers (large scales). These large scales then weakly oscillate and produce incoherent gravity waves [*Weinstock*, 1978a, 1985; *Gage*, 1979;

Sidi & Dalaudier, 1989]. Primarily though, the buoyancy range is where energy is extracted from the mean flow. Since the atmosphere is stratified at these large scales the turbulence eddies are thought to be both anisotropic and elongated [*Lumley*, 1964; *Bolgiano*, 1968; *Sidi & Dalaudier*, 1989]. The spectrum is thought to have the form $\propto k^{-3}$, although *Weinstock* [1978a] seems to feel that this power law depends on the flux Richardson number and the rms velocity, and is quite variable.

Inertial range

The range where energy is neither removed nor added to the spectrum is called the inertial subrange and is by far the most frequently studied range, especially in the mesosphere. In this range energy cascades at a constant rate from larger to smaller scales and is unaffected by viscosity. Since the energy flux across each wave number remains constant the vorticity of the smaller eddies increases with the increase in their energy obtained from larger eddies. There are various spectral forms for inertial range turbulence. One of these, according to *Kolmogoroff* theory [see e.g. *Tatarski*, 1961] is

$$E_K(k)dk = aC\epsilon^{\frac{2}{3}}k^{-\frac{5}{3}} \quad , \tag{2.7}$$

which describes the total kinetic energy spectrum for wave numbers whose scales are in the range $|k|$ to $|k + dk|$. a is equal to 0.76655 (=0.061(4π)), and C is a constant which has been experimentally determined to be very close to 2.0 [see e.g. *Kaimal et al.*, 1972; *Caughey et al.*, 1980]. ϵ is the rate at which energy is transferred through the spectrum; any particular wave number inertially transfers energy to larger wave numbers (smaller scales) at the same rate at which the energy is received by inertial transfer from still smaller wave numbers (larger scales). ϵ and is known as the *energy dissipation rate.* Hence it is also the rate at which turbulent energy is converted into heat at the very largest wave numbers.

As recently discussed by *Hocking* [1992], the potential energy per unit wave number in this range is

$$E_P(k) = \frac{1}{2}\,\frac{\omega_B^2}{M_N^2}\,\frac{6}{11}\,aC_N^2k^{-\frac{5}{3}} \quad , \tag{2.8}$$

where C_N^2 is the structure constant for electron density fluctuations, ω_B is the Brunt-Väisälä frequency (radians/sec), and M_N is the mean gradient of the electron density across the turbulent patch. *Thrane et al.* [1985] have suggested that the kinetic and potential energy should be equally partitioned within a turbulent patch. If this is so, then equating the above two equations gives us

$$\epsilon = \left[\frac{3C_N^2\omega_B^2}{22M_N^2}\right]^{\frac{3}{2}} \quad . \tag{2.9}$$

However, the equipartition assumption has been questioned by *Dalaudier & Sidi* [1987], *Sidi & Dalaudier* [1990], and *Hocking* [1992], who proposed that the ratio of the rates of flow of potential and kinetic energy down through the scales of the atmospheric turbulence spectrum varies, and is still not very well known. That the ratio is uneven and variable can be seen, for example, in the case where atmospheric turbulence exists in a region of an adiabatic temperature lapse rate. In such a scenario no temperature fluctuations are caused by turbulence and therefore E_P tends to zero even though E_K is finite. Recent work by *Hocking* [1992] has suggested that the ratio, and thus ϵ, should also depend on the Richardson number [see section 5.7].

The form of the spectra, given above, is based on the assumption that the turbulence sources and sinks are still active, and is not relevant, for example, for in the case of decaying turbulence where the turbulent sources are no longer active. Furthermore it does not describe unusual events, like fossil turbulence[4] , which persists long after the generating source has died. It is also assumed that turbulence eddies within the inertial range have lost all geometry relating to the initial (possibly anisotropic) eddies originally created in the buoyancy subrange. We therefore assume that eddies on average in the inertial range are essentially isotropic. This may not however be true in all cases, and will be discussed later on in section 2.6.2.

Viscous subrange

The range where the eddies are of such a small scale that molecular viscosity effects begin to dominate, and most of the turbulent energy is dissipated as heat, is called the viscous subrange. It is important to realize that viscosity plays no part in turbulence generation; it merely limits

[4] although at this stage there is no clear evidence that fossil turbulence does exist in the atmosphere

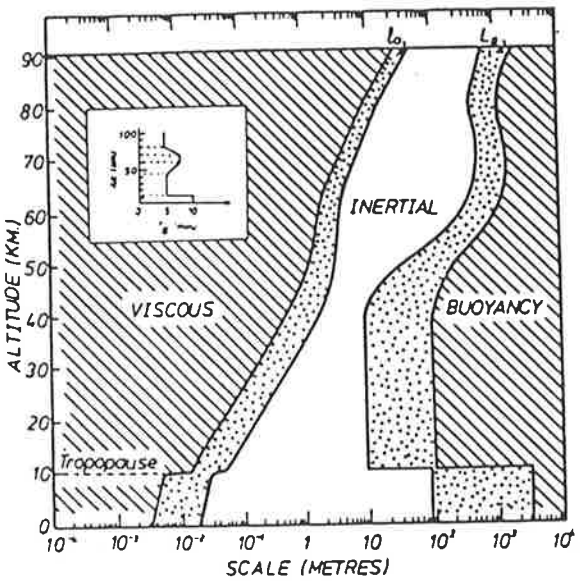

Figure 2.3: Typical values for the inner and outer transition scales of turbulence in the atmosphere, as well as the profile of the Brunt-Väisälä period (inset). ϵ was assumed to be $\sim 10^{-1}$ Wkg^{-1} at 90 km decreasing exponentially to $\sim 10^{-2}$ Wkg^{-1} at 80 km and remaining at this down to 60 km. The dotted areas define a region where ϵ was between a 1/3 and 3 times the mean value. Between 40 and 60 km ϵ was taken to vary smoothly, while from 40 km down to the tropopause it was assumed that $10^{-5} < \epsilon < 10^{-3}$ Wkg^{-1}. Below the tropopause ϵ was assumed to vary between 10^{-4} and 10^{-1} Wkg^{-1}. Larger estimates of ϵ would widen the inertial range, i.e. smaller l_0 and larger L_B [after *Hocking*, 1985].

the smallest scales at which turbulence can exist. A measure of the smallest scales at which turbulent eddies still exist is known as the *Kolmogorov microscale* and is given by

$$\eta = \left(\frac{\nu^3}{\epsilon}\right)^{\frac{1}{4}} \quad . \tag{2.10}$$

Inner and outer scales of turbulence

The Kolmogorov inertial range is separated from the buoyancy and the viscous ranges by two characteristic scales. The outer scale, L_B, is the boundary between the inertial and buoyancy ranges, and the inner scale l_0, is the boundary between the inertial and the viscous range [e.g. *Hill & Clifford*, 1978; *Weinstock*, 1978a]. These are given by

$$l_0 \approx 7.4\eta \ , \tag{2.11}$$

and

$$L_B \approx \frac{2\pi}{0.62}\epsilon^{\frac{1}{2}}\omega_B^{-\frac{3}{2}} \quad . \tag{2.12}$$

The inner scale constant 7.4 is only relevant for air and may in fact not be the same for all tracers in situations in which the Prandtl[5] number is not around 1.0[6]. Recent computer chemical modelling have suggested that the Prandtl number in the middle atmosphere may be higher than 3 [*Strobel et al.*[7], 1987; *Bevilacqua et al.*, 1990], while experimental rocket studies of *Justus* [1967] have suggested values of around 2 or more. Equation 2.12 also only applies in the case where the turbulence is shear generated within statically stable regions, since $\omega_B^2 < 0$ in the case of convective turbulence. Figure 2.3 exhibits typical values for the inner and outer scales in the atmosphere.

2.5 Mesospheric turbulence

Middle atmosphere turbulence (80–120 km) is thought to be due to gravity waves and tides, which generate turbulence through many different processes including non–linear breaking, shear instabilities, convective overturning, and critical level interactions [see e.g. *Jones & Houghton*, 1971; *Teitelbaum & Sidi*, 1976; *Sidi & Teitelbaum*, 1978; *Lindzen*, 1981; *Hocking*, 1987a]. Turbulence is important at these heights, for not only does it heat its environment, it is also a large contributor to the diffusion of momentum, heat and matter. Mesospheric turbulence can be both spatially and temporally intermittent and may occur in patches or in horizontal layers. The layers may be up to several kilometres thick and may be in a "sandwich" type arrangement such that the turbulent layers are bound by non–turbulent regions [see e.g. *Blamont & Barat*, 1967; *Lloyd et al.*, 1972, 1973; *Anandarao et al.*, 1978; *Röttger et al.*, 1979; *Ulwick et al.*, 1988]. Around an altitude of 110 km the molecular viscosity becomes large enough to damp out any turbulence, and this region is referred to as the turbopause. Whilst turbulence in the neutral atmosphere has been observed to heights of $\sim$ 130 km [*Rees et al.*, 1972], above the turbopause it only plays a minor physical role. Plasma turbulence is a different phenomenon

[5] ratio of momentum diffusion to temperature diffusion

[6] Prandtl numbers $\sim$ 100 can arise in oceans leading to a phenomenon called fossil turbulence. When the source of turbulence dies and momentum diffuses no velocity fluctuations remain, while temperature and density (salt) fluctuations do

[7] The results of Strobel et al. apply mainly below 80 km

which may be important at greater heights.

As discussed earlier in this chapter, atmospheric turbulence is characterized by the energy cascade, where large–scale features generate smaller circular motions, which in turn generate smaller ones until the smallest scales are finally dissipated as heat due to the molecular viscous forces. The rate of heating is denoted by ϵ, the energy dissipation rate. Measurements of ϵ from 80 km to the turbopause are difficult to make. In situ measurements by balloon or satellite are impossible, and satellite remote–sensing does not have sufficient vertical resolution.

The two most successful ways of measuring ϵ in this height range are rocket and radar techniques. One class of rocket techniques involve the release of chemoluminescent compounds which are released either by explosions producing instantaneous large luminescent clouds, or by a slow continuous release from the rocket resulting in long luminescent trails. The temporal behaviour of these compounds are then observed and photographed, and while the mean wind speed is deduced from the general drift, turbulence information is deduced by the change of form of the trail or cloud. These observations are not possible during the day because of the need to photograph the luminous trails, and are therefore only possible during twilight and at night [see e.g. *Blamont*, 1963; *Zimmerman*, 1968; *Rees et al.*, 1972; *Justus*, 1967]. More recent rocket measurements of the turbulent energy dissipation rates in the 65–120 km altitude range have been made as part of the MAP/WINE campaign (Middle Atmosphere Program/Winter In Northern Europe) [see e.g. *von Zahn*, 1987]. Measurements of ϵ were made by a neutral gas mass spectrometer, called BUGATTI[8], and a positive ion probe, PIP. Both instruments were mounted on the same rockets, although PIP measures on the upleg while BUGATTI measures on the downleg of the rocket trajectory [*Lübken et al.*, 1987]. Simultaneous measurements of ϵ were derived from foil cloud observations injected into the middle atmosphere.

Radar measurements of ϵ have been made from observations of meteor trails, utilizing fading times (spectral–width) and absolute back–scattered powers observed by MF radars, and by determining the decay of gravity–wave energy with height [see e.g. *Greenhow & Neufeld*, 1959; *Roper*, 1966; *Elford & Roper*, 1967; *McAvaney*, 1970; *Vincent & Stubbs*, 1977; *Manson et al.*,

[8] Bonn University Gas Analyzer for Turbulence Investigations

1981; *Fellous & Frezal*, 1981; *Vincent & Ball*, 1981; *Vincent*, 1984a; *Hocking*, 1988a]. It is not intended to go through the techniques listed above in detail; besides the references listed above the reader is also referred to the recent discussion by *Hocking* [1987a]. The MF radar techniques will be discussed in more detail in section 5.7.

2.6 Structure of inertial–range turbulence

Much of the theory of radar scattering and reflection mechanisms was initially developed by *du Castel* [1966] to explain over–the–horizon propagation of radio waves, although the scattering of electromagnetic waves by turbulence was proposed much earlier by *Booker & Gordon* [1950] to explain over–the–horizon tropospheric scattering. Soon afterwards, both theoretical and experimental studies documented the contribution of turbulence to radio–wave scattering in the troposphere [see e.g. *Chisholm et al.*, 1955; *Gjessing*, 1964; *Lane & Sollum*, 1965; *Hardy et al.*, 1966; *Kropfli et al.*, 1968; *Lane*, 1969]. Within a few years, turbulence had also been determined to be a major cause of radio propagation throughout the middle atmosphere [*Wheelon*, 1960; *Woodman & Guillén*, 1974; *Rastogi & Woodman*, 1974; *Rastogi & Bowhill*, 1976a, b, c; *Miller et al.*, 1978; *VanZandt et al.*, 1978; *Fukao et al.*, 1978; *Ecklund et al.*, 1979].

The modelling of radio–wave scatter from the turbulent atmosphere generally followed one of two approaches [for reviews see e.g. *Megaw*, 1957; *Wheelon*, 1959]. The first one, introduced by *Booker & Gordon* [1950], uses the Fourier transform of the radio refractive index spatial correlation function to describe the scattered signal, assuming an exponential decrease in the correlation function with spatial lag. Surfaces of equal correlation coefficients form spheres in the case of isotropic turbulence. The second approach uses the inertial–range theory developed by *Kolmogoroff* which has been applied to radio–wave scattering [*Silverman*, 1956; *Hardy et al.*, 1966; *Ottersten*, 1969a; *Tatarskii*, 1971]. However, although the predictions of the inertial–range theory are only sightly different to the Booker–Gordon theory, thie approach does not allow for the generalization to anisotropic turbulence.

2.6.1 Scatter from isotropic turbulence

Booker-Gordon [1950] proposed that turbulence in the atmosphere creates fluctuations in the refractive index which act to scatter electromagnetic waves. They assumed that the turbulence is isotropic in nature and that the correlation decreases exponentially with distance to become negligible beyond the scale of turbulence. The autocorrelation of the index of refraction is defined as

$$\rho = \frac{1}{V\overline{(\Delta n)^2}} \int_V (\Delta n)(\Delta n')^* dV \ , \tag{2.13}$$

where the asterix denotes the complex conjugate. This autocorrelation function has the functional form

$$\rho = \exp \frac{-r}{l} \ , \tag{2.14}$$

where r is the distance between the two points (P,P$'$) between which the autocorrelation is measured, l is the scale of turbulence, (Δn) and $(\Delta n')$ are the index of refraction variations at P and P$'$, and $\overline{(\Delta n)^2}$ is the mean-square departure of the index of refraction from its mean values over a volume V (where the turbulence within this volume is assumed to be uniform), i.e.

$$\overline{(\Delta n)^2} = \frac{1}{V} \int_V |\Delta n|^2 dV \ . \tag{2.15}$$

If a transmitted electric field illuminates such a volume, then an element of volume dV at P where the index of refraction varies from the mean by Δn, behaves as an electric dipole and re-radiates the electric field. If the electric field at P due to the transmitter is

$$E_0 \exp\left[j(\omega t - kR_0)\right] \ , \tag{2.16}$$

then the complete (Hertzian) potential at a receiver due to scattering from the whole volume V is given by

$$\frac{E_0}{4\pi R} \int_V \left(\frac{\Delta n}{n}\right) \exp\left[j(\omega t - k(R_0 + R))\right] dv \ , \tag{2.17}$$

where R_0 is the distance between the scattering volume of turbulence and the transmitter, while R is the distance between the same and the receiver. After some algebraic manipulation, using

the approach of *Booker & Gordon* [1950] the volume reflectivity is given by

$$\eta_{turb}(\Theta_s, \Psi) = 16\pi \overline{\left(\frac{\Delta n}{n}\right)^2} \cdot \frac{8\pi^3 l^3 \sin^2 \Psi}{\lambda^4 (1 + K^2 l^2)^2} \quad , \tag{2.18}$$

where Θ_s is the scattering angle (the angle between the incident electromagnetic radiation and the scattered electromagnetic radiation), and Ψ is the angle between the direction of the incident electric field and the direction of the receiver. The quantity $K = \frac{4\pi}{\lambda}\sin(\frac{\Theta_s}{2})$ is the Bragg wave number, important in forward scatter theory since for a given Θ_s the scatter is sensitive to vertical structures of size $\frac{\lambda}{2}(\sin(\frac{\Theta_s}{2}))^{-1}$. $\eta_{turb}(\Theta_s, \Psi)$ should not be confused with the Kolmogoroff microscale.

In the case of backscatter, $\Theta_s = \pi$, and $\Psi = \frac{\pi}{2}$ so that equation 2.18 simply becomes

$$\eta_{turb} = \overline{\left(\frac{\Delta_n{}^2}{n}\right)} \cdot \frac{1}{2l} \quad , \tag{2.19}$$

which is independent of λ.

The description of the backscattering by turbulence using the inertial–range theory is given by [*Tatarskii*, 1971]

$$\eta_{turb} = \frac{\pi^2}{2} K^4 \Phi_n(K) \tag{2.20}$$

where K is again the radar Bragg wave number ($= \frac{4\pi}{\lambda}$) and Φ_K is the three–dimensional wave number spectral density for the fluctuations in the refractive index [see e.g. *Gage & Balsley*, 1980]. In equation 2.20 the 3–D spectral density is normalized by the relation

$$\int\int\int_0^\infty \Phi_n(k) d^3k = \overline{(\Delta n)^2} \quad , \tag{2.21}$$

with

$$\Phi_n(k) = 0.033\, C_n^2 k^{-\frac{11}{3}} \quad , \tag{2.22}$$

where C_n^2 is the refractivity turbulence structure constant, defined by *Silverman* [1956] as

$$C_n^2 = 5.45\, \overline{(\Delta n)^2} L_0^{-\frac{2}{3}} \quad . \tag{2.23}$$

L_0 is the scale over which the change in the mean quantity if comparable to the RMS fluctuations ($L_B > L_0 > l_0$). Combining equations 2.20 and 2.22 we get

$$\eta_{turb} \;=\; 0.38\, C_n^2 \lambda^{-\frac{1}{3}} \quad , \text{ or,}$$

$$= \quad 2.07\,\overline{(\Delta n)^2}\,L_0^{-\frac{2}{3}}\lambda^{-\frac{1}{3}} \quad . \tag{2.24}$$

Comparison of the above expression for η_{turb} with the Booker–Gordon result shows that the ratio of the two alternative expressions is about $0.5\ L_0^{1/3}\lambda^{-1/3}$ if the integral scale l is related to the outer scale L_0 by $l = 0.12\ L_0$ as suggested to *Megaw* [1957]. Thus if the ratio of the outer scale to the wavelength is less than 8, the ratio is less than 1, while if it is greater than 8, then the ratio is greater than 1 [*Gage & Balsley*, 1980]. Hence, for most applications the two approaches will lead to backscattered signal strengths which agree within an order of magnitude. However, even this can be regarded as a relatively large error nowadays.

2.6.2 Scatter from anisotropic turbulence

It is now generally accepted that turbulence structures within the buoyancy subrange, and at larger scales are anisotropic [see e.g. *Crane*, 1980]. Anisotropic turbulence models for the buoyancy subrange have been developed by *Bolgiano* [1962], *Shur* [1962], *Lumley* [1967], and *Weinstock* [1978a], and show a great range of wavelength dependences. The turbulence in the inertial range, however, has been assumed to be generally isotropic, although at times experimental evidence for refractive index anisotropy had been presented [*Gjessing*, 1964].

Some early work in electromagnetic wave scatter did examine the theory of inertial–range atmospheric scatter for anisotropic turbulence (in the horizontal to the vertical scale). For example, *Staras* [1955] extended the theory of tropospheric scatter to include anisotropic turbulence. That study found that the various radio–wave parameters which only depend on the rate of decrease of scattered energy with zenith angle, such as the vertical correlation length, remained unchanged whether or not anisotropy was assumed. On the other hand, parameters like the horizontal correlation function which depend on energy from the "great circle plane" were found to be substantially influenced by anisotropy. Comparison of that theoretical work with the results of *Barsis et al.* [1954] suggested that the degree of anisotropy (vertical to horizontal) was $\approx 3/5$.

Booker [1956] used the general framework of the Booker–Gordon theory to develop an

anisotropic turbulence model, utilizing Gaussian correlation functions, which could explain the anisotropic radar echoes from the aurora. For axially symmetric ellipsoidal structures [after *Staras*, 1955]

$$\eta_{anisotropic} = \frac{8\pi^4 \overline{(\Delta n)^2}\, l_x l_y l_z}{\lambda^4[(l_x k_x)^2 + (l_y k_y)^2 + (l_z k_z)^2]^2} \quad , \tag{2.25}$$

where

$$\begin{aligned} k &>> \frac{1}{2}(l_x^2 + l_y^2 + l_z^2)^{\frac{1}{2}} \\ k_z &= k\cos\chi \\ k_y &= k\sin\chi\sin\phi \\ k_x &= k\sin\chi\cos\phi \quad . \end{aligned} \tag{2.26}$$

$(\Delta n)^2$ is the fluctuation of the refractive index n from its mean value, l are the correlation lengths of the permittivity variations along the x, y, and z axis, and k is the radar wave number component along these axes. The axes are those which fit the correlation ellipsoid of the permitivitty field. It is also assumed that one of these, z, is vertical (or sufficiently close to it). χ is the zenith angle and ϕ is the azimuth angle.

Gage & Balsley [1980] examined two cases of anisotropic scattering. One of these was an oblate spheroid (disk) where $l_x = l_y = l_h$ (l_h is the horizontal correlation distance) and $l_z = l_y$ (vertical correlation distance). In such a scenario $l_h > l_z$. The other structure considered was a prolate spheroid (cigar shape) where $l_z > l_x = l_y$. In both cases equation 2.25 can be re–expressed as

$$\eta_{anisotropic}(\chi) = \frac{\overline{(\Delta n)^2}\,\frac{l_z}{l_x}}{2l_x\,[\sin^2\chi + (\frac{l_z}{l_x})^2\cos^2\chi]^2} \quad . \tag{2.27}$$

From the above expression it is useful to define an anisotropy factor by

$$A(r_a,\chi) \equiv \frac{\eta_{anisotropic}}{\eta_{isotropic}} = \frac{r_a}{[\sin^2\chi + r_a^2\cos^2\chi]} \quad , \tag{2.28}$$

where

$$\begin{aligned} r_a &\equiv \frac{l_z}{l_x} < 1 \quad \text{for a disk} \\ r_a &\equiv \frac{l_z}{l_x} > 1 \quad \text{for a rod} \end{aligned}$$

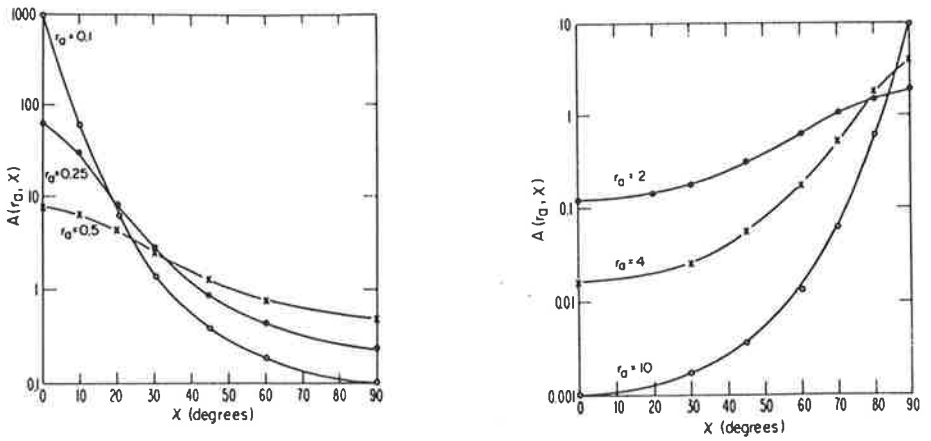

(a) (b)

Figure 2.4: Plots of the zenith angle dependence of the anisotropy factor A for (a) disks and (b) rods, both for several different ratios of r_a [from *Gage & Balsley*, 1980].

(2.29)

Figure 2.4 (a) and (b) show the dependence of A on zenith angle for a disk and a rod respectively. Both diagrams show that the angular dependence of backscattered reflectivity is strongly dependent on r_a. In the case of the disk, smaller r_a translates into a larger A when the zenith angle is 0°, and into a smaller A as the zenith angle approaches 90°. The converse is true for the rod, where viewing in the direction of the major axis of the rod results in minimum backscatter, and maximum backscatter when viewing orthogonal to it.

The Booker–Gordon theory is however derived under assumptions which may not be valid under certain situations [*Liu & Yeh*, 1980; *Wakasugi*, 1981]. In particular, the Booker–Gordon theory assumes phase coherence for the whole scattering volume. If this is true, the scattered power is proportional to the scattering volume multiplied by the turbulence spectrum which is $\Phi(0, 0, 2k)$ for the backscatter case. This is only true if the antenna beamwidth is much smaller than the angle of the coherence cone of the backscattered wave from the turbulent eddies. Fortunately, for turbulence with a power law spectrum the Booker–Gordon formula is a good approximation.

The work by *Gage & Balsley* [1980] attempted to explain VHF/UHF scatter from clear air as due to three mechanisms; anisotropic scatter, Fresnel reflection, and Fresnel scatter. It was assumed that the horizontal correlation lengths of the scatterers were much smaller than the Fresnel length. However, cases when both scatter and reflection have been found to co-exist were reported in the literature [see e.g. *Röttger*, 1980a]. A study by *Doviak & Zrnić* [1984], considered the case where the Fresnel zone radius was comparable to or smaller than the correlation length. They used a statistical approach that incorporated all of the three mechanisms mentioned above, and presented conditions under which reflection or scatter dominates. They suggested that only the temporal behaviour might distinguish between Fresnel reflection and anisotropic behaviour when the correlation length of the anisotropic turbulence is comparable to the first Fresnel zone radius. Furthermore, the inclusion of the Fresnel term in determining echo power is only dependent on the antenna diameter. Figure 2.5 shows the angular dependence of the observed mean backscatter for anisotropic irregularities as a function of zenith angle [*Röttger*, 1981a] to which *Doviak & Zrnić* [1984] fitted an anisotropic model. The model fitted the data quite well, and showed that the Fresnel term did not contribute significantly to the observed angular dependence, which on first observation might imply a reflection mechanism.

Another study by *Waterman et al.* [1985] attempted to compare an anisotropic scattering model against a quantitative study of the permittivity of the upper troposphere and lower stratosphere using the SOUSY 50 MHz radar. In that study they also began with equation 2.25 which describes the volume reflectivity for anisotropic turbulence, and which can be re-written as

$$\eta = \frac{\overline{(\Delta n)^2}\frac{l_x l_y l_z}{2}}{[(l_x \sin\chi\cos\phi)^2 + (l_y \sin\chi\sin\phi)^2 + (l_z\cos\chi)^2]} = \frac{B}{[\sin^2\chi + R^2\cos^2\chi]^2} \tag{2.30}$$

where

$$B = \frac{\overline{(\Delta n)^2}\, l_x l_y l_z}{2(l_x^2\cos^2\phi + l_y^2\sin^2\phi)^2} \tag{2.31}$$

and

$$R^2 = \frac{l_z^2}{l_x^2\cos^2\chi + l_y^2\sin^2\phi} \,. \tag{2.32}$$

B is thought of as an amplitude factor (not to be confused with the same term used earlier

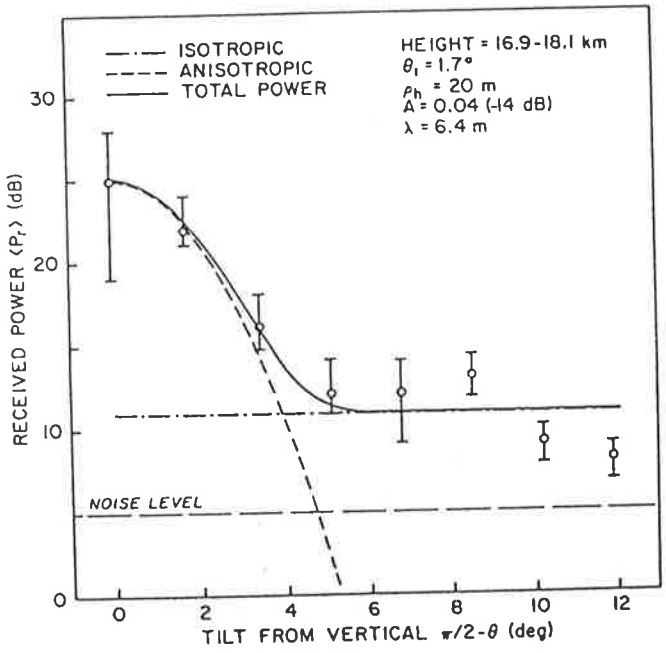

Figure 2.5: Angular dependence of observed mean backscatter power (open circles) from anisotropic irregularities as the radar beam axis is tilted away from the vertical [from *Röttger*, 1981a]. Fitted to the data is a model that consists of anisotropic turbulence with a two-dimensional (horizontal isotropy) correlation function in an isotropic background [from *Doviak & Zrnić*, 1984].

for buoyancy), and R as the measure of the anisotropy. In the case that there is horizontal isotropy, $l_x = l_y$, then the ratio $R = l_z/l_x$ is purely the ratio of the vertical minor axis to the horizontal major axis. *Waterman et al.* [1985] used two beams, one pointing north (N) and the other 90° to it, towards the east (E). The amplitude and anisotropy factors then become

$$\begin{aligned} B_E &= \frac{\overline{(\Delta n)^2}\,\xi\,\zeta(1+t^2)^2}{2l_x(1+\xi^2t^2)^2} \\ B_N &= \frac{\overline{(\Delta n)^2}\,\xi\,\zeta(1+t^2)^2}{2l_x(\xi^2+t^2)^2} \end{aligned} \tag{2.33}$$

and

$$R_E^2 = \frac{\frac{l_z^2}{l_x}\frac{1}{\cos^2\phi_E}}{1+\left[\frac{l_y}{l_x}\tan\phi_E\right]^2} = \frac{\xi^2(1+t^2)}{1+\zeta^2t^2}$$

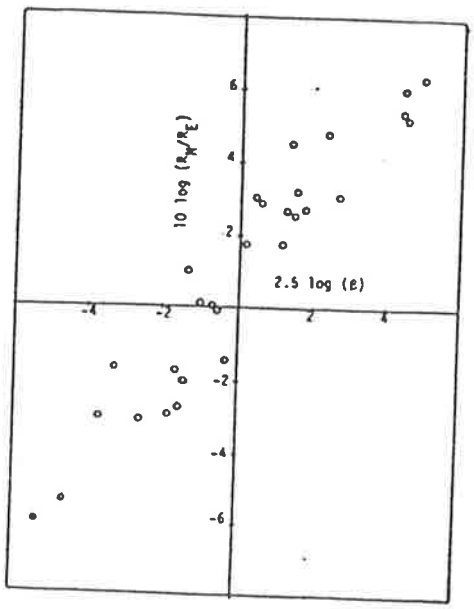

Figure 2.6: Check of the anisotropic model against tropospheric data which should fit equation 2.37. The points should all lie on a 45° line passing through the origin [from *Waterman et al.*, 1985].

$$R_N^2 = \frac{\frac{l_z^2}{l_x}\frac{1}{\sin^2\phi_E}}{1+\left[\frac{l_y}{l_x}\cot\phi_E\right]^2} = \frac{\xi^2(1+t^2)}{\zeta^2+t^2} \tag{2.34}$$

such that

$$\xi = \frac{l_z}{l_x}\,, \quad \zeta = \frac{l_y}{l_x}\,, \quad t = \tan\phi_E\ . \tag{2.35}$$

The ratio of the amplitude and anisotropy of the two azimuth beams can be defined as

$$\begin{aligned} \beta &= \frac{B_N}{B_E} = \left(\frac{1+\zeta^2t^2}{\zeta^2+t^2}\right)^2 \\ \rho &= \frac{R_N}{R_E} = \left(\frac{1+\zeta^2t^2}{\zeta^2+t^2}\right)^{\frac{1}{2}} \end{aligned} \tag{2.36}$$

so that

$$\beta = \rho^4\ . \tag{2.37}$$

This last relationship is true regardless of the structure of the permitivitty field, or the orientation and degree of anisotropy, either horizontal or vertical. Since the study used only two azimuths neither the ellipticity or the orientation of the horizontal ellipse could be measured. Rather, limits could be defined within which these must lie. Overall, the fit of the anisotropic model to the data collected showed that the anisotropic model has some merit. This is seen in figure 2.6 where equation 2.37 is tested, by plotting ρ against the fourth root of β. In that figure a fit to a 45° line is quite good, thus supporting the proposed anisotropic model.

After further algebraic manipulation *Waterman et al.* [1985] established a range of values within which the specific orientation ϕ_E and the minor–to–major axis anisotropy ratios ζ and ξ must lie. These are displayed in figure 2.7 where the shaded areas denote the permissible values. That diagram indicates that there is substantial anisotropy in both the vertical and horizontal, with only the height range between 13.2–13.6 km isotropic, although the authors conclude that that this may be due to weak signal/noise ratios. In addition, the vertical anisotropy is much more restricted in range than the horizontal and is also systematically smaller.

It must be remembered that all of these "anisotropic models" do not address the problem at a fundamental level. They just parametrize the degree of anisotropy and then examine the effect of this parametrization on electromagnetic scatter. On the other hand, the theory proposed by Kolmogoroff was a theory developed from one or two basic premises. A true anisotropic model where the degree of anisotropy can be related to some fundmental quantaties like buoyancy or the mechanical generation of turbulence is yet to be proposed.

Anisotropy of mesospheric turbulence

The growing evidence of experimental observations strongly suggested the existence of anisotropic turbulence throughout the atmosphere. Some of this evidence originally came from radar observations in the VHF and later MF bands, which found that the scatterers are aspect sensitive [aspect sensitivity is discussed in detail in section 5.3], particularly below 80 km [see e.g. *Golley & Rossiter*, 1971; *Lindner*, 1975a, b; *Vincent & Belrose*, 1978; *Fukao et al.* 1979, 1980a; *Hocking*, 1979, 1987b; *Czechowsky et al.*, 1984, 1988; *Sato et al.*, 1985; *Fritts & Vincent*, 1987;

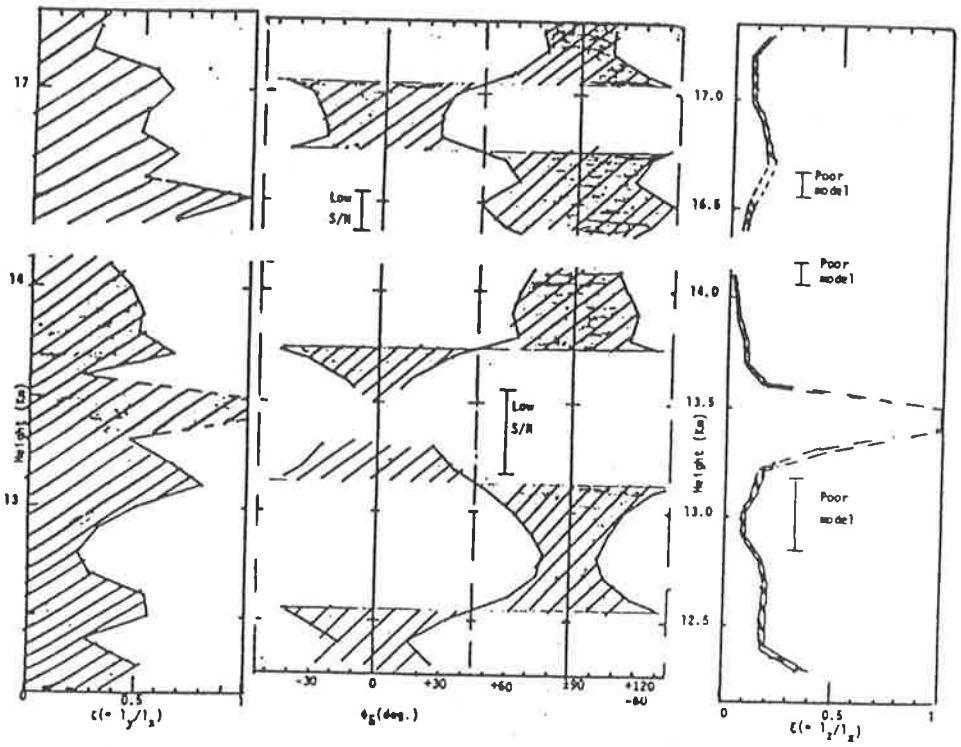

Figure 2.7: The degree ζ and orientation ϕ_E of horizontal anisotropy, and the degree ξ of vertical anisotropy using the SOUSY 50 MHz radar. The permissible range of values is indicated by the shaded areas. Low values of ζ and ξ indicate a high anisotropy. [from *Waterman et al.*, 1985].

Reid, 1988; *Adams et al.*, 1989; *Lesicar & Hocking*, 1992; *Lesicar et al.*, 1993].

It is important to remember that for volume scattering from the mesosphere the most likely source of irregularities in the electron density is the presence of turbulence. Fully developed turbulence can exist in the inertial range. The outer scale L_B (determined by the buoyancy forces) is typically from 500–1000 m in the mesosphere, while the inner scale l_o may vary from 1 m at 5 km to 30 m at 90 km [see e.g. *Hocking*, 1985].

A study by *Thrane et al.* [1987] found that for an MF radar operating at 2.75 MHz the radar echoes coincided with turbulence in about 70% of the cases where the turbulence was possibly created by gravity wave saturation. In addition, at other times they found that wind corners were associated with radar reflections in the MF band. A wind shear is commonly understood to be a region where the wind speed/direction changes with altitude. A wind corner is a special shear: a narrow altitude region (typically less than 0.5 km thick) where (a) rapid change of wind direction with altitude occurs and (b) the wind speed attains a minimum in comparison

with layers above and below [*von Zahn*, 1987]. They proposed that a laminar flow creates and maintains a gradient in electron density that can cause a Fresnel type reflection of MF radio–waves. Although such gradients must be very sharp, *Thrane et al.* [1987] felt that wind shears acting upon horizontal gradients in the electron density can create such gradients. They suggested that the horizontal gradients could themselves be caused by horizontal structure in the particle precipitation that often significantly contributes to the ion–production in the auroral D–region.

Other studies have also presented comparisons of radar measurements with *in situ* observations. First carried out by *Thrane et al.* [1981] and *Hocking & Vincent* [1982] these studies found that turbulent scatter and quasi–specular reflection were both important scattering mechanisms at MF/HF frequencies. Recently *Inhester et al.* [1990] and *Inhester & Ulwick* [1992] reported on the comparison of rocket–borne electron density measurements with those of the SOUSY VHF radar. Assuming that the mesospheric ions are a passive tracer of the turbulence and density fluctuations [see e.g. *Thrane & Grandal*, 1981], the authors determined a parameter which measures the anisotropy of the mesospheric turbulence both from radar aspect sensitivity and from the comparison of the radar and rocket observations. They found that the radar reflectivity is enhanced over what would be expected for the case of isotropic electron density fluctuations, where the electron density fluctuations were deduced from rocket data. The radar reflectivity η_{radar} at a range r was derived from the signal power P_s of a northward antenna beam using [*Inhester et al.*, 1990],

$$\eta_{radar} = 8\,\frac{r^2 k_{radar}^2}{G\Delta r}\cdot\frac{P_s}{\alpha P_t}\ , \tag{2.38}$$

where Δ_r is the range resolution ($\equiv$ 300 m), k_{radar} = 1.12 read/m is the radar wave number, $G = 10^{3.55}$ is its antenna gain, and α takes into account of losses in both transmission and reception of the radar system of about 3 dB. To compare the radar reflectivity and small scale density fluctuations observed by the rocket, *Inhester et al.* [1990] performed a power spectral

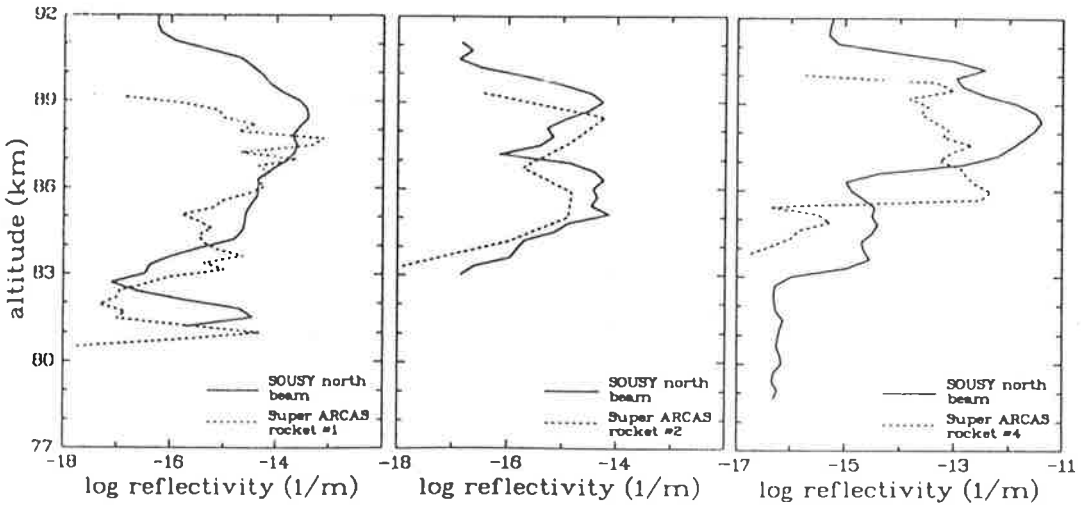

Figure 2.8: Height profiles of η_{radar} from the SOUSY northward beam (5.6°) and η_{rocket} estimated from simultaneous rocket observations under the assumption of isotropic turbulence, [from *Inhester & Ulwick* 1992].

density analysis of the electron density variations and used the following [*Ulwick et al*, 1988]

$$\eta_{rocket} = n8\pi^3 \left(\frac{r_e}{k_{||}}\right)^2 S_N \ . \tag{2.39}$$

where $r_e = 2.82.10^{-15}$ m is the classical electron radius, πS_N is the power spectral density of the electron density fluctuations at a wave number $2k_{radar}$ along the rocket trajectory over a height interval of 300 m and n is its power spectral index.

If the turbulence was homogeneous and isotropic than equations 2.38 and 2.39 would coincide. Figure 2.8 [from *Inhester & Ulwick*, 1992] show the resulting values of η_{rocket} and η_{radar}. Although the two volumes probed by the two methods are about 24 km apart, there is quite good agreement between the rocket and radar results concerning the general variation of reflectivity with altitude. The η_{rocket} values do seem slightly downplaced form the radar results. However, the general trend is for $\eta_{rocket} \leq \eta_{radar}$, in some heights by even 5–10 dB.

Inhester et al. [1990] suggest that the observations can be reconciled under the assumption of anisotropic turbulence. From the data, they conclude that an observed anisotropy (between the vertical and horizontal) of approximately 10 dB is consistent with the rocket and radar observations, with a similar anisotropy found from the aspect sensitivity of the radar echoes.

The spectral–width of the echoes also suggested an anti–correlation between the variation in anisotropy and the turbulence level. They propose that the most probable source of anisotropy at the radar wave number is the large anisotropy of gravity waves at scales of several hundred meters or more. As to the structure of the anisotropy, they suggest that the squared coherence length ratio (horizontal to the vertical coherence length) is approximately 40!

Other studies have also suggested the existence of anisotropic turbulence. For example, the extended von Kármán scalar (EVKS) model is formulated to estimate isotropic turbulence scalar spectral distributions at all wavenumbers as an arbitrary function of the Reynolds and the Schmidt (to be defined later) numbers [see e.g. *Hinze*, 1959]. However, although the model was shown to be in reasonable agreement with one–dimensional scalar data, it could not explain experimental observations for low wavenumbers [*Driscoll & Kennedy*, 1985]. This disagreement may be due to the anisotropy in the flow at low wavenumbers, since the EVKS model is formulated for isotropic turbulence only. Finally, *Sidi & Dalaudier* [1990] have also suggested that within large parts of the middle atmosphere, turbulence may have varying degrees of anisotropy and that the assumption of an ubiquitous small scales isotropic inertial domain in all atmospheric turbulence layers is an over–simplification.

Further discussion on the nature of atmospheric scatterers and the various methods of measuring their aspect sensitivity will be discussed in chapter 5.

Chapter 3

Radar and Data Analysis Techniques

3.1 Introduction

This chapter examines the use of radars for remote-sensing the atmosphere, and discusses the techniques used to make these studies. We concentrate on two of the most common methods, the Doppler and the spaced-antenna method. Both these methods have been extensively used in probing both the lower and upper atmosphere, and although on the surface they appear as independent techniques, it can be shown that, under some assumptions about the scattering medium, both should produce equivalent results [*Briggs*, 1980].

We start this chapter, however, with fundamental ideas on radio-wave propagation and scattering in the atmosphere.

3.2 Radar fundamentals

Atmospheric radars, as distinguished from weather radars for which the primary target is precipitation, observe the atmosphere by utilizing clear-air echoes produced by fluctuations in the refractive index of the atmosphere. In this section we discuss the radio refractive index for the

atmosphere, and then the radar equation for scatterers.

3.2.1 Refractive index of the atmosphere

The radio refractive index of the atmosphere, n, is defined as

$$n = \sqrt{\mu_r \epsilon_r} \quad , \tag{3.1}$$

where μ_r is the relative permeability of air, ≈ 1 for the atmosphere [*Bean & Dutton*, 1968], and ϵ_r is the dielectric constant of the medium. The refractive index as a function of height for the non–ionized atmosphere and for radio waves ranging from HF through to UHF is given by [e.g. *Tatarski*, 1961; *Larsen*, 1988]:

$$M = \frac{-77.6 \times 10^{-6}}{T^2} P \left[1 + \frac{15500}{T} q \right] \left[\frac{dT}{dz} + \Gamma_a - \frac{7800}{1 + \frac{15500}{T} q} \frac{dq}{dz} \right] \quad , \tag{3.2}$$

where P is the atmospheric pressure (millibars), T the temperature (degrees Celsius), Γ_a the adiabatic lapse rate, q the specific humidity, and z the height above ground. For the ionized atmosphere, the gradient of the potential refractive index can be written as [*Hocking*, 1985]

$$M_e = \frac{\partial n}{\partial N} \left[N \frac{w_B^2}{g} - \frac{dN}{dz} + \frac{N}{\rho} \frac{d\rho}{dz} \right] \quad , \tag{3.3}$$

where N is the electron density, n the refractive index, ρ the neutral density, w_B^2 the Brunt-Väisälä angular frequency, and g the gravitational acceleration.

An approximation to this equation has been given by *Gage & Balsley*, [1980], such that

$$n - 1 = \frac{3.75 \times 10^{-1} e}{T^2} + \frac{7.76 \times 10^{-5} P}{T} - \frac{N_e}{2N_c} \quad , \tag{3.4}$$

where e is the partial water vapour pressure (in millibars), P the atmospheric pressure (in millibars), T the temperature (degrees Kelvin), N_e the number density of electrons, and N_c is the critical plasma density. The first term in equation 3.4 is the contribution due to water vapour[1], and is only relevant within the troposphere. The second term is due to dry air and thus dominant above the tropopause. The third term is that due to free electrons, as opposed to bound ones for the first two cases, and is dominant at ionospheric heights.

[1] varies with frequency due to the dipole moment of the water molecule

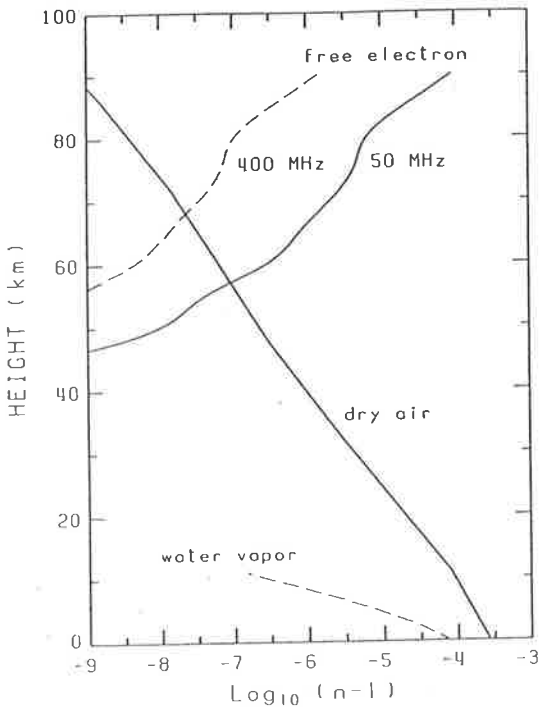

Figure 3.1: Typical altitude profiles of the three terms which determine the radio refractive index of the atmosphere [after *Sato*, 1988].

Figure 3.1 shows a typical altitude profile of the three terms that determine the radio refractive index of the atmosphere.

While it is large (macroscopic) changes in n that are responsible for refraction, it is small–scale changes of n in the atmosphere that are responsible for radar scattering. *Incoherent scatter*[2] occurs when there is sufficient electron density, for radio waves to be scattered by individual electrons and thus add up incoherently. It is mostly relevant for frequencies greater than 100 MHz. *Coherent scatter* is due to turbulent motion of air parcels of varying density, which contain the electrons (and molecules) which scatter radio waves and thus contribute conherently to the total scattered electric field. Unlike incoherent scatter, where the scattered echo power is proportional to the number density of free electrons, the backscattered power in coherent scattering depends upon the density gradients associated with the coherent scatterers, and if these gradients are large enough may be much greater than the power due to incoherent

[2] also known as Thermal scatter

scatter. This makes the design of MST[3] radars much simpler and relatively less expensive than incoherent scatter radars.

3.2.2 The radar equation

The radar equation for individual scatterers

If an antenna radiating power P_t, and with gain G_t, illuminates a target of cross–sectional area σ at a distance r away from the antenna, we can write the incident power, P_i, on the target as:

$$P_i = \frac{P_t\, G_t\, \sigma}{4\pi\, r^2} \quad . \tag{3.5}$$

The backscattered power received by the antenna, assuming a monostatic radar system, is then given as

$$P_r = \frac{P_t\, G_t\, A_e\, L\, \sigma}{(4\pi\, r^2)^2} \quad , \tag{3.6}$$

where A_e is the effective area of the antenna and L is the attenuation or efficiency factor. If the radar wavelength is denoted as λ, it can be shown that A_e and G_t are related viz:

$$G_t = 4\pi\, A_e\, \lambda^{-2} \quad , \tag{3.7}$$

so that equation 3.6 reduces to

$$P_r = \frac{P_t\, A_e^2\, L\, \sigma}{4\pi\, r^4\, \lambda^2} \quad , \tag{3.8}$$

which is the standard radar equation for a single scattering target situated in the antenna beam. It should be noted that the above equation assumes that the scatter is axially symmetric; i.e. independent of (θ, ϕ), the zenith and azimuth angle respectively. In a realistic equation this is not true, and all the above terms are a function of (θ, ϕ).

If there are a number of individual targets within the radar beam one must take into account the contribution from each target. Two cases present themselves. In the first case, if all the scatterers are uncorrelated (randomly distributed) the σ term in equation 3.8, is simply replaced by $\sum \sigma$, the summation of the echo power from individual scatterers; i.e. no new scatterers come

[3] Mesosphere–Stratosphere–Troposphere

into effect if the beam – width is increased. On the other hand, if the scatterers are uniformly distributed in some volume V, σ increases linearly with V. In this case it is useful to define the volume reflectivity, η, so that:

$$\eta \equiv \frac{d\sigma}{dV} \quad , \tag{3.9}$$

where V is determined by the radar spatial resolution

$$V = \pi(r\,\theta_{\frac{1}{2}})^2 \Delta r \quad , \tag{3.10}$$

$\theta_{\frac{1}{2}}$ is the antenna half–power half–width, and Δr the radar range cell. $\theta_{\frac{1}{2}}$ is related to the antenna gain [*Probert-Jones*, 1962]

$$G_t = \pi^2\, a^2\, \theta_{\frac{1}{2}}^{-2} \quad , \tag{3.11}$$

where a is a non–dimensional constant accounting for the non–uniform antenna illumination, and normally close to unity. Combining equation 3.8 with equations 3.7, 3.11, and 3.10, we obtain the backscatter power for the case of multiple targets:

$$P_r = \frac{P_t\, A_e^2\, L\, \pi\, a^2 \Delta r\, \eta}{64 r^2} \quad . \tag{3.12}$$

Comparison of the radar equations for the single target with that for multiple targets shows the major difference is the backscattered power dependence on the range; r^4 for the single target and r^2 for the multiple uniform targets.

The Radar equation for Specular targets

In the previous section we examined the case where discrete targets caused the radar scattering. We must also consider the case of specular targets, which occurs when reflection occurs from an extended horizontal layer whose refractive index differs slightly from its surroundings. Such a occurrence is termed *Fresnel (partial) scattering*, and may be treated as a mirror with reflectivity ρ for incident electromagnetic waves [*Friend*, 1949]. The radar equation is easily found since we consider the case of one–way transmission from the antenna to the image of the receiving antenna, as it would appear when reflected in the reflecting layer, i.e.

$$P_t = \frac{P_\epsilon\, G\, A_\epsilon\, L\, |\, \rho^2|}{4\, \pi\, 4\, r^2} \quad . \tag{3.13}$$

In reality, in the atmosphere, reflectors are not generally perfectly flat. Nevertheless, reflectors which show a tendency to reflect most signal straight back to the radar, and only small amounts to off–vertical angles, are termed "specular", i.e. their backscattered power falls off rapidly as a function of zenith angle [see e.g. *Röttger*, 1980a]. Another type of specular scatter occurs when stable, coherent structures, cause a sharp change in the gradient of the refractive index. This might arise from turbulence structures that are randomly distributed in the vertical direction but exhibit coherency in the horizontal direction. Alternatively, they might be due to reflective layers whose surface is corrugated by some dynamic processes. In all cases, the received amplitude is proportional to a convolution between the pulse and the reflection coefficient profile [*Hocking & Röttger*, 1983]. Figure 3.2 schematically represents the refractive index variation for different backscattering mechanisms. The scatter from anisotropic turbulence has already been discussed in the previous chapter.

3.3 Techniques to measure various parameters using radars

At least two radar techniques have been used to measure winds, as well as other parameters, in the lower and middle atmosphere. The first technique is the Doppler beam–swinging (DBS) technique which uses large arrays with narrow polar diagrams. By using a minimum of three beams pointing in various directions, one can determine the total wind vector [see e.g. *Briggs*, 1980; *Balsley*, 1981]. In most cases the preferred arrangement is one vertical beam to determine the vertical wind and two off-vertical beams to determine the horizontal wind. The second technique is the spaced–antenna (SA) technique [see e.g. *Briggs*, 1984; *Hocking et al.*, 1989; *Larsen & Röttger*, 1989] which uses a (generally) vertically pointing transmitting beam, and at least three spaced receiving antennas. By cross–correlating the received signals from the receivers the relative time displacement can be determined and used to infer the the horizontal wind. The spaced–antenna technique is sometimes also referred to as the partial reflection drift method (PRD).

It was once commonly believed that the two techniques were quite different, and that the

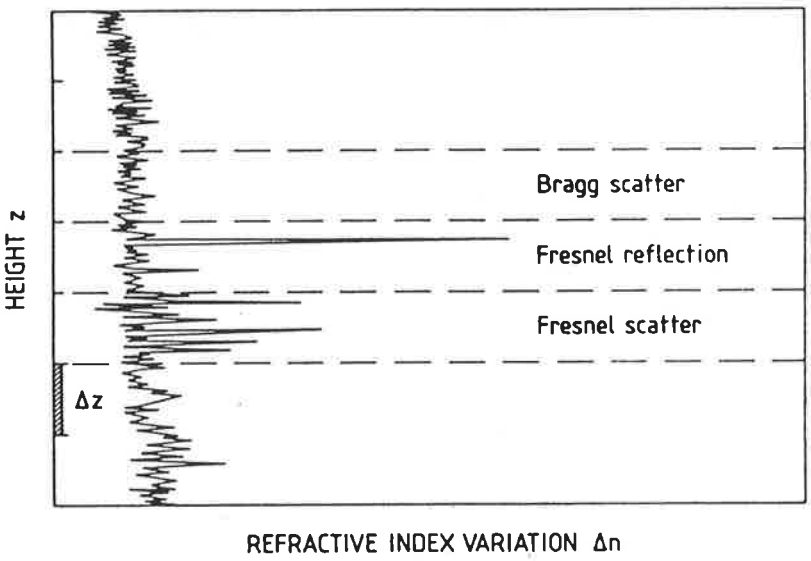

Figure 3.2: A diagram depicting the change of refractive index (Δn) with height z. Depending on the structure of n within the range gate Δz, the different processes of Bragg scatter, Fresnel scatter, and Fresnel reflection can occur. The abscissa n can also be interpreted as the relative horizontal extent of constant refractive index surfaces for the different processes. Bragg scatter occurs at every range where the variation in n is similar to that within the indicated range Δz. Thermal electron density fluctuations, which cause thermal scatter, are much weaker than the indicated variations of n [from *Röttger*, 1989].

Doppler method was a much more reliable and direct method. However, it has been shown by *Briggs* [1980] that, although experimentally different, the two techniques are very closely related, and in a fundamental sense identical. Thus the choice between the two techniques can not be made on theoretical grounds, but rather on practical considerations. We will now consider each of the techniques, but will concentrate on the spaced–antenna technique since it is by this method that the bulk of the data in this thesis were collected (for a detailed discussion of the Doppler technique see e.g. *Croft*, [1972]).

3.4 Doppler technique

The Doppler method is probably one of the most common methods of determining the relative velocity of targets; in our case we use it to determine atmospheric wind speeds. It does so by utilizing the change in phase of the scattered radio wave, which varies with time as the scatterer moves. One can think of the change of phase that occurs due to the motion of the scatterers as a rotation in the Argand plane of the electric field phasor. This rate of change of the phase is simply a measure of the scatterers radial velocity, i.e.

$$< v_{rad} >= -\frac{\lambda}{4\pi} < \frac{d\phi}{dt} > \quad . \tag{3.14}$$

Here, <> is the average value over the sampling time and radar volume, v_{rad} the radial velocity, λ the radar wavelength, ϕ the phase, and $\frac{d\phi}{dt}$ the rate of change of phase. It can easily be shown [see e.g. *Hocking*, 1988b] that the mean rate of change of phase for a number of scatterers can be found from

$$< \frac{d\Delta\phi}{dt} >= \frac{1}{2\pi\delta t} \tan^{-1}\left[\frac{Im(\rho(\delta t))}{Re(\rho(\delta t))}\right] \quad , \tag{3.15}$$

where $\rho(\delta t)$ is the autocovariance function of the complex time series at lag δt. Im and Re are the real and imaginary parts respectively. Another way of obtaining the value of autocovariance $\rho(\tau)$ at $\tau = \delta t$ is from the power spectrum $P(f)$, since by the Wiener–Kintchine theorem [see e.g. *Bracewell*, 1978], the power spectrum of a random process is the Fourier transform of the autocovariance function of the process, i.e.

$$\rho(\delta t) = \sum_{i=1}^{n} P(f_j) e^{2\pi i f_j \delta t}, \qquad f_j = \frac{j-1}{T} \quad . \tag{3.16}$$

T is the data length of the complex time series. Substituting into equation 3.15, we find that

$$v_{rad} = \frac{\lambda}{4\pi\delta t} \tan^{-1}\left[\frac{\sum_{i=1}^{n} P(f_j)\sin(2\pi f_j \delta t)}{\sum_{i=1}^{n} P(f_j)\cos(2\pi i f_j \delta t)}\right] \quad . \tag{3.17}$$

This can be simplified if the limit of the bracketed summation terms is $<< 1$, and the power spectrum contributions due to larger $|f_j|$ are small, so that

$$v_{rad} \approx \frac{\lambda}{2} \frac{\sum_{i=1}^{n} f_j P(f_j)}{\sum_{i=1}^{n} P(f_j)} \quad . \tag{3.18}$$

The above equation is in fact commonly used to provide estimates of the scatterers' radial velocities [see e.g. *Woodman & Guillen*, 1974; *Zrnić*, 1979; *Woodman*, 1985]. However, if the above assumptions are not true, the expression is no longer true, and one must use the more exact expression given in equations 3.15 or 3.17. The assumptions may be invalid if the signal is noisy, which will cause the radial velocities to be under–estimated, or when the spectral peak is close to the Nyquist frequency [see e.g. *Hocking*, 1988b]. Another method of extracting Doppler radial velocities involves fitting spectral shapes to the data, mainly Gaussian functions, and avoids some of the problems inherent in equation 3.18. We do not intend to discuss these here; for details of the method see e.g. *Woodman*, [1985].

Although the Doppler technique will in almost all cases measure the mean speed of the scatterers, there are potential problems in the interpretation of the measured velocity when dealing with atmospheric motions. One of these, albeit rare, may occur if the measured velocity is in fact not the mean motion of the scatterers, but rather the phase velocity of a wave or pulsation moving through the region. A more common problem is encountered when using off–vertical beams to infer the horizontal velocity. When using two beams which point in different directions to measure the total wind vector, one assumes that the wind is spatially homogeneous. This may not always be true if the wind divergence is significant [see e.g. *Warnock et al.*, 1978; *Fukao et al.*, 1988a,b; *Chang*, 1980].

Another common problem relates to the vertical velocity, w. If it is assumed that w is zero, then the horizontal wind component in the radar azimuthal direction is given by

$$v_{hor} = \frac{v_{rad}}{\sin\theta_T} \quad , \tag{3.19}$$

where θ_T is the beam tilt direction from the vertical.

By using orthogonal beams, the total horizontal wind vector can be determined. The assumption that there is no vertical motion is most likely to be false. This can be overcome by using a narrow vertical beam and measuring the vertical velocity. The radial velocity equation is now given by

$$v_{rad} = v_{hor}\sin\theta_T + w\cos\theta_T \quad , \tag{3.20}$$

which gives the horizontal velocity as

$$v_{hor} = \frac{v_{rad} - w\cos\theta_T}{\sin\theta_T} \quad . \tag{3.21}$$

Even if it is assumed that the wind field is non–divergent, the structure of the scatterers may cause an error in the measured wind velocity. If the scatterers are not isotropic, their backscatter polar diagrams will be anisotropic. Thus, radio waves which impinge on them vertically will be backscattered much more strongly than those which impinge at some off–zenith angle, and the angle θ_T in the above equation is no longer valid. This feature is commonly known as aspect sensitivity and will be discussed at length in section 5.3. Furthermore, the measured vertical velocity may be contaminated by the horizontal velocity if the scatterers possess a tilt from horizontal. Short–term measurements of the vertical velocity must therefore be treated with caution. More accurate measurements of w can be obtained when using bistatic[4] radars [*Waterman*, 1983].

Another physical event that can cause an error when using the Doppler technique occurs when a few discrete layers are separated by regions where there is no scatter. Then such layers can give "false" winds at radar ranges other than their true ranges, and this can lead to the appearance of false wind shears, and to temporal variations of wind, which do not exist in the real wind field. It may also lead to false wind oscillations if a thin scattering layer co–exists in several adjacent range volumes [*Hocking*, 1983a; *Fukao*, 1988a,b; *May et al.*, 1988].

3.5 Spaced–antenna technique

3.5.1 Introduction

Early researchers in the study of ionospheric radio wave propagation noticed that there existed fluctuations in the amplitude of the reflected signal. *Pawsey* [1935] found that the amplitude behaviour was sometimes similar at separated points, but with a time displacement. This led to the suggestion that the amplitude fluctuation was in fact due to the movement of a

[4] when the transmitting and receiving antennas are some distance apart

diffraction pattern resulting from the scattering of radio waves off scatterers (irregularities) in the ionosphere. The motion of the pattern over the ground was assumed to be due to the horizontal movement of the medium at the height sampled. The use of amplitude variations to measure the drift of such a pattern was first carried out systematically by *Mitra* [1949], who proposed the method of *similar fades.*

This method calculates the velocity of the pattern by dividing the vector distances by the fading timeshifts of receiver pairs. This, however, assumes that the amplitude contours are circular, and fade only as a result of the horizontal motion of the pattern across the receivers. The velocity calculated became known as the *apparent velocity* since it did not consider the possibility that the pattern may also change randomly as it moves.

Today there are two alternative methods for wind measurement based on the spaced–antenna technique; the full correlation analysis, and interferometer techniques (sometimes called IDI; Imaging Doppler Interferometry). The full correlation analysis (FCA) was developed by *Briggs et al.* [1950] to include the effect of random changes of the scatterers, and to measure some geometric parameters of the diffraction pattern. It was further extended by *Phillips & Spencer* [1955] to accommodate anisometric patterns. They assumed that the spatial correlation function was described by elliptical contours produced by some degree of elongation of the pattern in a preffered direction. For both the method of similar fades and FCA, a minimum of three spaced receivers non colinear is required. The interferometer technique uses groups of antennas which form an interferometer. By utilizing phase differences between groups of antennas, and using cross–spectral techniques one can determine the angle of arrival of the radio backscatter. The velocities are then determined using standard Doppler techniques. Thus individual scatterers can be "tracked" using this method, and horizontal and vertical motions determined [*Pfister*, 1971; *Farley et al.*, 1981; *Röttger & Ierkic*, 1985; *Adams et al.*, 1985]. There is, however, still much uncertainty whether preferred volumes of scatter with a narrow angular extent do actually exist. In the case where the scatter is widespread, and it is not possible to discern individual scatterers, the method might still provide effective angles of arrival although these results may

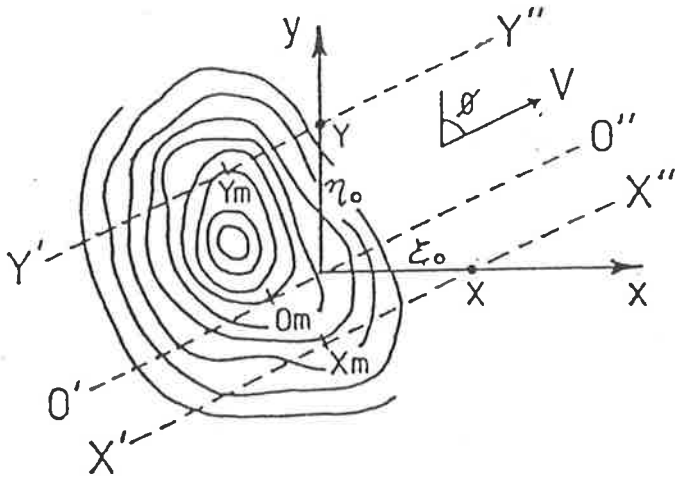

Figure 3.3: A typical unvarying contour pattern produced by the backscattering of electromagnetic radiation from irregularities in the atmosphere. The pattern is moving with speed V, in direction ϕ with respect to the y-axis [from *Briggs*, 1984].

well be difficult to interpret. The interferometer technique will not be discussed here since no data extraction in this thesis was performed using this technique. The full correlation analysis will be discussed in dètail. The following discussion is based on the reformulation of equations by *Briggs* [1977, 1980, 1984].

3.5.2 Measuring apparent velocity

If a pulsed radio wave is transmitted into the atmosphere, the scatterers backscatter the energy and create ground diffraction patterns of the backscattered electromagnetic field. It is useful to represent these patterns as contours, which are generally random. It is rather difficult to measure the entire pattern, and information about its motion and other characteristics must be measured by spaced receivers, the minimum useful number being three. Figure 3.3 shows a typical pattern, moving with a speed V and in a direction ϕ with respect to the y-axis, which is being sampled by three receivers, O, X, and Y. We assume for now that the pattern is unvarying.

The sensors O, X, and Y form a right–angled triangle with separations ξ_0 in the x–direction,

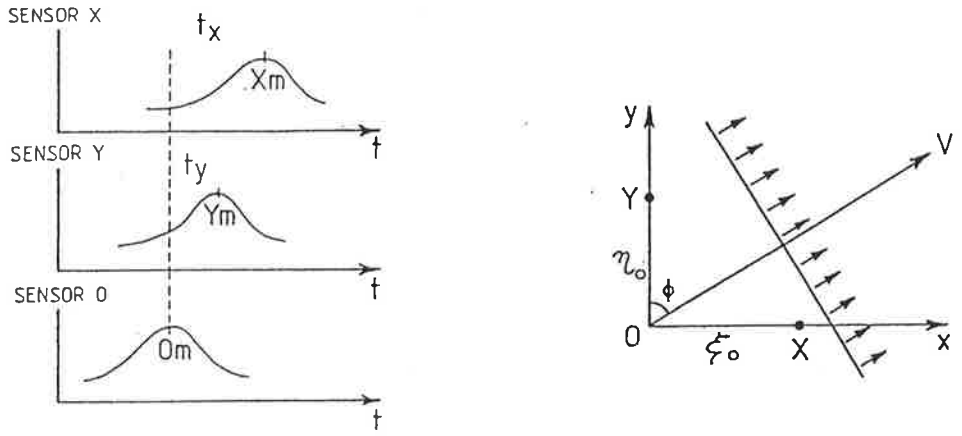

Figure 3.4: (a) A typical record obtained when sampling a diffraction pattern by three sensors, and (b) A simplification of the contour diagram based on the line of maxima [after *Briggs*, 1984].

and η_0 in the y–direction. We see that each of the sensors measures a section through the contours; 0 records along the line $0' - 0''$, X along $X' - X''$, and Y along $Y' - Y''$. The time series obtained might then look similar to figure 3.4(a), where the maxima recorded for each point are labelled O_m, X_m and Y_m. A line joining these three points is then called the line maximum, the accuracy of which increases with the number of individual sensors. Figure 3.3 is then replaced by the much simpler diagram shown in figure 3.4(b), where a solitary line of maximum moves perpendicular to V, at an angle ϕ.

Then, according to the geometry of figure 3.4, we find that

$$t_x = \frac{\xi_0 \sin\phi}{v}, \qquad t_y = \frac{\eta_0 \cos\phi}{v}, \tag{3.22}$$

and defining

$$v_x = \frac{\xi_0}{t_x}, \qquad v_y = \frac{\eta_0}{t_y}, \tag{3.23}$$

we obtain

$$v_x = \frac{v}{\sin\phi} \qquad v_y = \frac{v}{\cos\phi}. \tag{3.24}$$

Note that v_x and v_y known as trace velocities are not components of v but rather allow us to

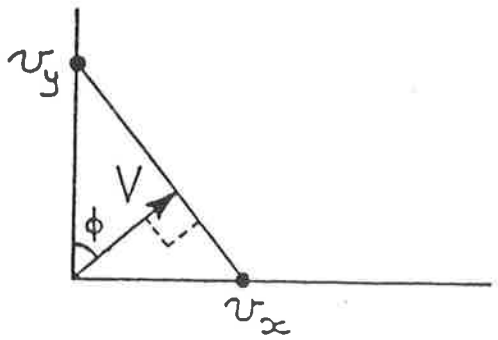

Figure 3.5: Determination of the apparent velocity from geometrical considerations. A line vector from the origin perpendicular to the line joining V_x and V_y, gives V, the velocity vector [from *Briggs*, 1984].

derive v *via* geometrical considerations as shown in figure 3.5, i.e.

$$v = \frac{v_x v_y}{v_x^2 + v_y^2} \quad , \qquad \tan\phi = \frac{v_y}{v_x} \quad , \tag{3.25}$$

where ϕ is measured clockwise from y. This type of argument equally applies when a number of distinct diffraction pattern features are measured by each sensor. In that case the various lines of maxima will not significantly depart from the perpendicular to the direction of motion, and will statistically average out, provided that the patterns are not systematically elongated. Thus the only parameters changed are the time displacements, which are now averages.

This speed and direction would truly represent the motion of the contour pattern provided that the pattern is not systematically elongated in a particular direction, and does not change in form as it moves. If the pattern is anisometric the apparent velocity will tend to be perpendicular to the axis of elongation. Another error occurs if the pattern is undergoing random changes as it moves. In that case the velocity calculated will be too large. This is obvious; consider a pattern which changes randomly but has no mean motion; in that case the above calculations would suggest that the pattern possessed an infinite velocity.

3.5.3 Full correlation analysis

To compensate for the errors mentioned above, a more sophisticated method, the *full correlation analysis* was developed which uses auto and cross-correlations functions rather than individual

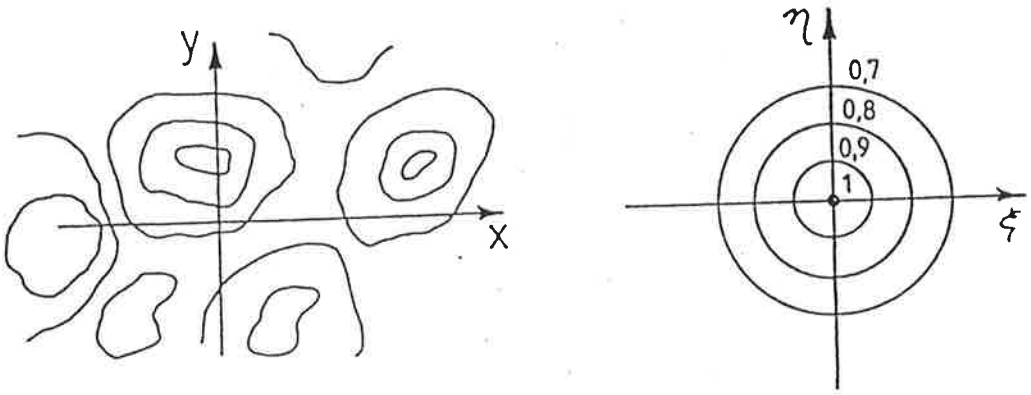

Figure 3.6: (a) An isometric contour pattern, and (b) contours of equal correlation for that pattern [from *Briggs*, 1984].

time delays. We will now examine this method in some detail. This will be done in stages; we will first consider a random stationary pattern, followed by a stationary, randomly changing pattern, followed by a moving randomly changing pattern.

Stationary non–changing random pattern

Consider a stationary, isometric[5] non–changing pattern. We can write the two–dimensional spatial correlation function between position (x, y), and $(x + \xi$,y+$\eta)$ (assuming a zero mean value) as

$$\rho(\xi, \eta) = \frac{< f(x, y) f(x + \xi, y + \eta) >}{< |f(x, y)|^2 >} \quad . \tag{3.26}$$

Figure 3.6(a) and (b) shows a typical isometric pattern, and its corresponding contours of equal correlation respectively. When ξ and η are both equal to zero, the correlation function is equal to one. As the pattern is displaced further from its original position, the correlation decreases until reaching a point where no correlation exists.

With unlimited sensors, the spatial correlation function could be very accurately determined. As this would be fairly laborious, we make some simplifying assumptions. We assume that the spatial averaging is equivalent to temporal averaging for a fixed pair of sensors with a known

[5] no systematic elongation

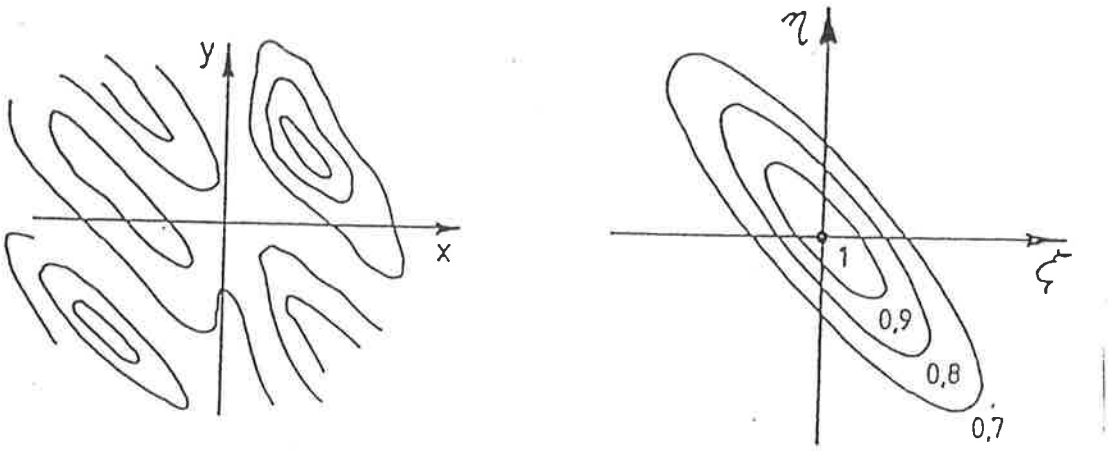

Figure 3.7: (a) An anisometric contour pattern, and (b) its corresponding correlation contours [from *Briggs*, 1984].

form and separated by (ξ, η). For example, since the pattern is isometric, the correlation depends only on the magnitude of ξ and η, and not the direction. The contours are therefore circles in the (ξ, η) plane, and sensors along any axis would be sufficient to determine the correlation coefficient. For an anisometric pattern, such as that in figure 3.7(a) we again make an assumption. In this case we assume that the contours are the result of simply stretching an isometric pattern in some preferred direction; i.e. the correlation function possesses ellipsoidal symmetry (figure 3.7(b)).

We write the functional form for a stationary non–changing pattern as

$$\rho(\xi, \eta) = \rho(A\xi^2 + B\eta^2 + 2H\xi\eta) \ . \tag{3.27}$$

Stationary randomly changing pattern

In the case of a pattern which changes in time, but still has no mean motion we introduce a time dependency, and equation 3.26 becomes

$$\rho_M(\xi, \eta, \tau) = \frac{< f(x, y, t) f(x + \xi, y + \eta, t + \tau) >}{< |f(x, y, t)|^2 >} \ . \tag{3.28}$$

Figure 3.8(a) shows such a pattern, with surfaces of constant ρ. The (x, y) plane moves upwards with respect to time, and the contours randomly change. If we set $\rho(\xi, \eta, \tau)$ to be constant, we

find the correlation coefficients to be ellipsoidal surfaces, with one of the axis being in the τ direction (figure 3.8(b)).

We can therefore describe the correlation surfaces viz

$$\rho_M(\xi,\eta,\tau) = \rho(A\xi^2 + B\eta^2 + 2H\xi\eta + K\tau^2) \ . \tag{3.29}$$

It is important to note that we have assumed that the temporal autocorrelation function and the spatial correlation function have the same functional form. This is true to a first approximation, but it should nevertheless be borne in mind when fitting to any experimental data.

Moving randomly changing pattern

We now consider the case where a pattern not only evolves in time, but it also has a mean velocity, V, in a direction ϕ (clockwise from the y–axis). Such a pattern is shown in figure 3.9(a), where its surfaces, $f(x,y,t)$, possess a systematic slope with respect to the time axis. Correspondingly, the correlation surfaces also possess a tilt with respect to the τ axis (figure 3.9(b)).

Consider an observer moving with this pattern. The co–ordinates of this frame of reference are represented by the primed quantities (x',y',t). The pattern is then $f(x',y',t)$ and its

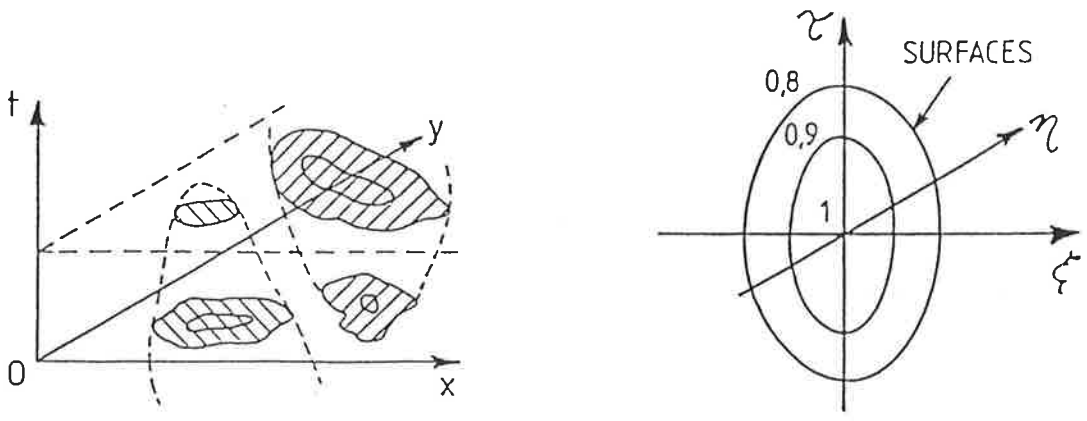

Figure 3.8: (a) A stationary pattern which evolves with respect to time, and (b) the corresponding correlation surfaces, in this case ellipsoids [from *Briggs*, 1984].

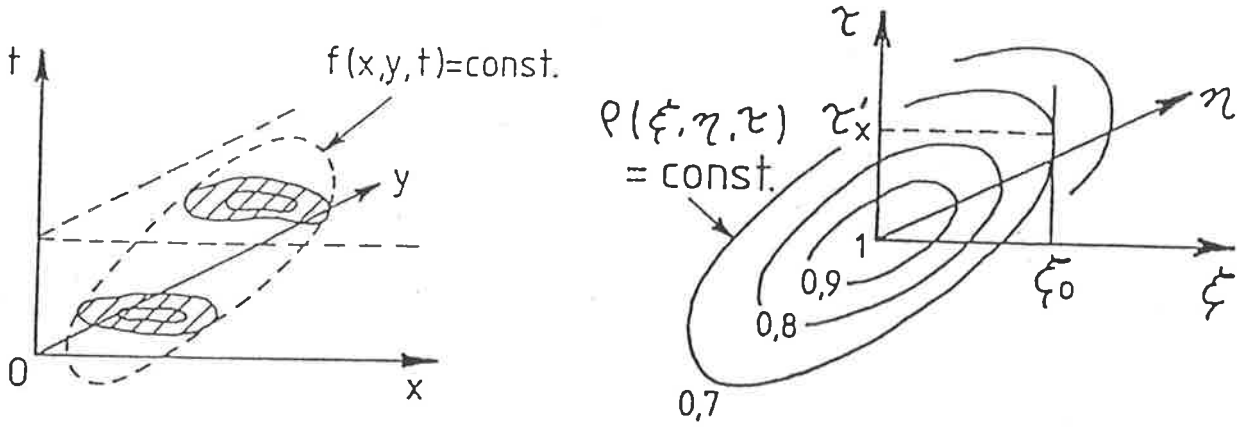

Figure 3.9: (a) A moving, randomly changing pattern, and (b) the corresponding correlation ellipsoids [from *Briggs*, 1984].

associated correlation function is

$$\rho_M(\xi', \eta', \tau') = \rho(A\xi'^2 + B\eta'^2 + 2H\xi'\eta' + K\tau'^2) \ . \tag{3.30}$$

The co–ordinates of a stationary observer are related to those of a moving observer by the following transformations,

$$\begin{aligned} x &= x' + Vt\sin\phi = x' + V_x t \\ y &= y' + Vt\cos\phi = y' + V_y t \ . \end{aligned} \tag{3.31}$$

In this case, the component velocities of the systematic motion can are defined as

$$V_x = V\cos\phi, \qquad V_y = V\sin\phi \ , \tag{3.32}$$

and it follows that

$$\xi = \xi' + V_x\tau \ , \ \text{and} \ \ \eta = \eta' + V_y\tau \ , \tag{3.33}$$

and simple substitution into equation 3.30 leads to the following:

$$\rho_G(\xi, \eta, \tau) = \rho(A(\xi - V_x\tau)^2 + B(\eta - V_y\tau)^2 + 2H((\xi - V_x\tau)(\eta - V_y\tau)) + K\tau^2 \ , \tag{3.34}$$

which has the following form

$$\rho(\xi, \eta, \tau) = \rho(A\xi^2 + B\eta^2 + C\tau^2 + 2F\xi\tau + 2G\eta\tau + 2H\xi\eta) \ . \tag{3.35}$$

Equations 3.34 and 3.35 are the basic equations used in FCA, and all the useful parameters can be calculated from them. We will now discuss how the individual coefficients can be derived.

Determination of FCA coefficients

If we want to measure velocity, or any other feature of a two–dimensional pattern, a minimum of three sensors is required. We consider an array of three sensors, arranged at the points of a right–angled triangle such as that depicted in figure 3.3, located at (0,0), (ξ_0,0), and (0,η_0). First consider the cross–correlation for two of the receivers, aligned along the x–axis (see figure 3.10(a)) and spatially separated by a distance ξ_0. We find that equation 3.35 reduces to

$$\rho_G(\xi, 0, \tau) = \rho(A\xi_0^2 + C\tau^2 + 2F\xi_0\tau) \ , \tag{3.36}$$

which is a maximum when

$$\tau_x' = -\frac{F}{C}\xi_0 \ . \tag{3.37}$$

Similarly, if we consider the two receivers along the y–axis, we find that:

$$\tau_y' = -\frac{G}{C}\eta_0 \ . \tag{3.38}$$

We now turn to each of the three sensors, and use the auto–correlation function, which should, theoretically, be equivalent for all three. Although experimentally there may be statistical variations between sensors the mean can be equated to the auto–correlation function determined from equation 3.35, i.e.,

$$\rho_G(0, 0, \tau) = \rho(C\tau^2) \ . \tag{3.39}$$

We now use the assumption that the spatial and temporal functions have the same form, and find the time at which the autocorrelation function has the same value as the value of cross–correlation between two sensors at zero lag ($\rho(\xi_0, 0, 0)$). Combining equations 3.35 and 3.39, we get,

$$\rho_G(\xi_0, 0, 0) = \rho_G(0, 0, \tau_x) \ , \quad \Longrightarrow \quad \rho(C\tau_x^2) = \rho(A\xi_0^2) \ ,$$

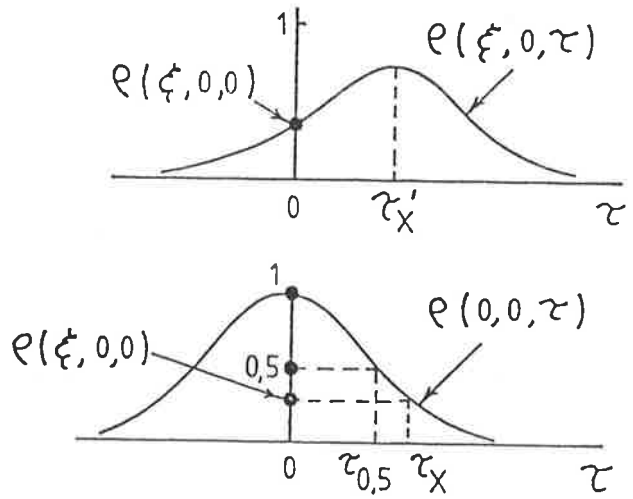

Figure 3.10: (a) Cross–correlation across two receivers separated spatially by a distance ξ_0, and (b) Auto–correlation for a single receiver, as a function of time τ [from *Briggs*, 1984].

and so

$$\frac{\tau_x^2}{\xi_0^2} = \frac{A}{C} \ . \tag{3.40}$$

Similarly, we can find the time delay, τ_y, with a pair of sensors along the y–axis, and hence

$$\frac{\tau_y^2}{\eta_0^2} = \frac{B}{C} \ . \tag{3.41}$$

Finally, if we consider the time delay between a pair of sensors at $(\xi_0, 0)$, and $(0, \eta_0)$ we find that:

$$\begin{aligned} \rho(-\xi_0, \eta_0, 0) = \rho(\xi_0, -\eta_0, 0) = \rho(0, 0, \tau_{xy}) \ , \\ \rho(C\tau_{xy}^2) = \rho(A\xi_0^2 + B\eta_0^2 - 2H\xi_0\eta_0) \ , \end{aligned} \tag{3.42}$$

which gives

$$-\frac{H}{C} = \frac{\tau_{xy}^2}{2\xi_0\eta_0} - \frac{A\xi_0}{2C\eta_0} - \frac{B\eta_0}{2C\xi_0} \ . \tag{3.43}$$

Equation 3.43 can be solved since the co–efficients $\frac{A}{C}$ and $\frac{B}{C}$ are already known (equations 3.40 and 3.41).

Thus the five ratios, $\frac{A}{C}$, $\frac{B}{C}$, $\frac{F}{C}$, $\frac{G}{C}$, and $\frac{H}{C}$, can be derived from the auto– and cross–correlation functions from the three spaced sensors. Generally, a right–angled sensor configuration would

not be used, as it might produce a directional bias. In practice, an equilateral triangle is preferred, although any spatial arrangement of sensors can be used. Denoting $\underline{r}_{ij}$ as the spatial separation between two receivers, such that $\underline{r}_{ij} = (\xi_{ij}, \eta_{ij})$, the cross–correlation between these two receivers, as a function of time lag τ_{ij} is given by

$$\rho(\xi_{ij}, \eta_{ij}, \tau_{ij}) = \rho(A\xi_{ij}^2 + B\eta_{ij}^2 + C\tau_{ij}^2 + 2F\xi_{ij}\tau_{ij} + 2G\eta_{ij}\tau_{ij} + 2H\xi_{ij}\eta_{ij}) \ . \tag{3.44}$$

This demonstrates a maximum for a particular time shift τ_i and is found by resolving $|\delta\rho/\delta\tau_{ij}| = 0$ which reduces equation 3.44 to

$$\tau_{ij} = \frac{-F}{C}\xi_{ij} - \frac{G}{C}\eta_{ij} \ . \tag{3.45}$$

By measuring the cross-correlation for a receiver pair at zero time shift and finding the time shift at which the auto-correlation function has the same value, then

$$\rho(0, 0, \tau_{ij}) = \rho(\xi_{ij}, \eta_{ij}, 0) \ . \tag{3.46}$$

From equation 3.35 we then find

$$\rho(C\tau_{ij}^2) = \rho(A\xi_{ij}^2 + B\eta_{ij}^2 + 2H\xi_{ij}\eta_{ij}) \ , \tag{3.47}$$

and thus

$$\tau_{ij}^2 = \frac{A}{C}\xi_{ij}^2 - \frac{B}{C}\eta_{ij}^2 + \frac{2H}{C}\xi_{ij}\eta_{ij} \ . \tag{3.48}$$

We again assume that the temporal and spatial correlation functions have the same functional form. This is not true in a rigorous sense, but is at least tolerable for most cross-correlation functions near their origin. From the above equations we see that all the pattern parameters can be uniquely evaluated. The coefficients will be generally overdetermined, and a least square technique is normally used, but this also allows some estimate of the statistical errors.

3.5.4 Determination of physical quantities

Although the previous section showed how a varying, anisometric contour pattern can be sampled and described by only three sensors, we now turn our attention to the determination of

useful physical quantities that can be obtained from the above equations. Another point to note is that radar systems now use complex signals to calculate the complex auto– and cross correlations (in contrast to measurements made 10–20 years ago, which were made using amplitude only data). Besides improving the signal–noise ratio, the use of complex auto–correlation enables the determination of the vertical velocity (see section 3.5.5).

True velocity

The most fundamental and basic parameter that is obtained from the FCA is the velocity of the pattern. By equating the $\xi\tau$ and $\eta\tau$ terms in equations 3.34 and 3.35 we obtain

$$\begin{aligned} AV_x + HV_y &= -F \\ BV_y + HV_x &= -G \ , \end{aligned} \tag{3.49}$$

which, when solved simultaneously, give the mean motion of the drift of the pattern. The velocity calculated,

$$|V|^2 = V_x^2 + V_y^2 \ , \tag{3.50}$$

in the direction

$$\tan\phi = \frac{V_x}{V_y} \ , \tag{3.51}$$

is termed the *true velocity* V_t, so as to distinguish it from the apparent (V_a) as it is corrected for the random changes and the anisometry of the pattern. In the case where the pattern is isometric and has no random change, the apparent and the true velocity will be equivalent. Otherwise the true velocity is always smaller than the apparent.

Both V_a and V_t describe the motion of the ground pattern. Hence, they should be halved if they are to represent the motion of the scatterers, to account for the point source effect [see e.g. *Ratcliffe*, 1956; *Felgate*, 1970].

Spatial properties of the pattern

The spatial properties of the pattern are themselves useful quantities to calculate. From equation 3.35, the spatial correlation function is

$$\rho_G(\xi, \eta, 0) = \rho(A\xi^2 + B\eta^2 + 2H\xi\eta) \ . \tag{3.52}$$

The constant correlation contours are a family of concentric ellipses. To physically describe the contour pattern size, we define the ellipse where $\rho = 0.5$ as the *characteristic ellipse*, which is defined by

$$\rho(A\xi^2 + B\eta^2 + 2H\xi\eta) = 0.5 \ . \tag{3.53}$$

The time lag value $\tau_{0.5}$ is defined as the time for which the auto-correlation function, for a stationary observer, falls to 0.5. i.e.

$$\rho_G(0, 0, \tau_{0.5}) = \rho(C\tau_{0.5}) = 0.5 \ . \tag{3.54}$$

Combining equations 3.53 and 3.54, we then define the characteristic ellipse as

$$A\xi^2 + B\eta^2 + 2H\xi\eta = C\tau_{0.5}^2 \ . \tag{3.55}$$

The characteristic ellipse is usually described by the magnitude of the major and the minor axes, and the orientation of the major axis with respect to the y–axis in the clockwise direction. To solve an ellipse of the form,

$$\frac{x'^2}{s'^2} + \frac{y'^2}{t'^2} = 1 \ , \tag{3.56}$$

we use rotation of coordinates,

$$\begin{aligned} x &= x' \cos\phi - y' \sin\phi \\ y &= x' \sin\phi + y' \cos\phi \ . \end{aligned} \tag{3.57}$$

Substitution and simultaneous solving leads to the derivation of the orientation of the major axis which can be shown to be,

$$\tan 2\theta = \frac{2H}{B - A} \ , \tag{3.58}$$

clockwise from the y–axis.

The major and minor axes, are, respectively;

$$a^2 = \frac{2C\tau_{0.5}^2}{(A+B) - \sqrt{4H^2 + (A-B)^2}}$$
$$b^2 = \frac{2C\tau_{0.5}^2}{(A+B) + \sqrt{4H^2 + (A-B)^2}} \quad . \tag{3.59}$$

The axial ratio, r, is another useful quantity, and is the ratio of the major to the minor axes, ie.,

$$r^2 = \frac{(A+B) + \sqrt{4H^2 + (A-B)^2}}{(A+B) - \sqrt{4H^2 + (A-B)^2}} \quad . \tag{3.60}$$

Random changes of the pattern

Using quantities already calculated, it is possible to estimate the mean lifetime of the irregularities which cause the diffraction pattern to change randomly. This parameter is the fading time which will be seen by an observer, who moves with the pattern, since in this case the auto-correlation function will change because of the random change of the pattern solely. The time it takes for this auto-correlation function to fall to 0.5, $T_{0.5}$, is called the *mean lifetime* or *time scale*, and is found from the function

$$\rho_G(0,0,\tau) = \rho(K\tau^2) \quad , \tag{3.61}$$

so that

$$\rho_M(0,0,T_{0.5}) = 0.5 \quad . \tag{3.62}$$

We now have two quantities which describe a fading time; the time $\tau_{0.5}$, for the auto-correlation function to fall to 0.5 for a stationary observer, and the time $T_{0.5}$, for the auto-correlation function to fall to 0.5 for an observer moving with the pattern. Since the spatial correlation is assumed to have the same functional form as the temporal correlation, the above two expressions can be equated, thus giving

$$T_{0.5} = \tau_{0.5}\sqrt{\frac{C}{K}} \quad . \tag{3.63}$$

As $\tau_{0.5}$ is directly observable, equating equations 3.54 and 3.62 and comparing τ^2 terms, we can solve for $\frac{K}{C}$ since all other variables have already been calculated:

$$\frac{A}{C}V_x^2 + \frac{B}{C}V_y^2 + \frac{K}{C} + \frac{2H}{C} \; .V_xV_y = 1 \; . \tag{3.64}$$

In the early days of SA analysis a quantity V_c was defined as the ratio of the diffraction pattern size to the pattern lifetime for an observer in the patterns reference frame. When the irregularity size was taken in the direction of motion it was defined that

$$\frac{(V_c)_v}{V} = \frac{d_{0.5}}{T_{0.5}} \; , \tag{3.65}$$

i.e., the irregularity size in the direction of motion divided by the irregularity lifetime. This quantity is evaluated from the spatial correlation function, and assuming $d_{0.5}$ is the distance in the direction of motion which has $\rho_{0.5}$ then,

$$\frac{d}{V} = \frac{\xi}{x} = \frac{\eta}{y} \tag{3.66}$$

and

$$\rho(d) = \rho[(AV_x^2 + BV_y^2 + 2HV_xV_y)\frac{d^2}{V^2}] \; . \tag{3.67}$$

The characteristic size of the irregularity, defined as $d_{0.5}$, is obtained when $\rho(d) = 0.5$, so that

$$\rho[(AV_x^2 + BV_y^2 + 2HV_xV_y)\frac{d_{0.5}^2}{V^2}] = 0.5 \; . \tag{3.68}$$

Combining with equation 3.62 we obtain

$$(V_c)_v = \frac{d_{0.5}^2}{T_{0.5}^2} = \frac{(V_x^2 + V_y^2)K}{AV_x^2 + BV_y^2 + 2HV_xV_y} \; , \tag{3.69}$$

where $V^2 = V_x^2 + V_y^2$. The quantity V_c can now be easily calculated since all the terms on the right hand side are known. The dimensionless ratio,

$$\frac{(V_c)_v}{V^2} = \frac{K}{AV_x^2 + BV_y^2 + 2HV_xV_y} \; , \tag{3.70}$$

is these days used, rather than V_c, as an indicator of the relative importance of the motion of the irregularity when compared with the internal randomness. The bigger the parameter, the more

important are the random changes. Naturally, if the parameter is zero, then the fluctuations that are observed by a stationary receiver are totally caused by the movement of the pattern as a whole. This now puts a new definition on the true velocity as the velocity of an observer who moves so as to maximize the width of the temporal auto-correlation function.

Rejection criteria

In some instances, it is necessary to question the reliability of data, and if necessary to reject it. To this end, several criterions have been developed and these are as follows [see e.g. *Ball*, 1981; *Briggs*, 1984];

(1) The mean signal is very strong during recording, thus predominantly saturating the receivers.

(2) The fading signal is very weak in amplitude.

(3) The signal–to–noise ratio is less than some pre–set limit (usually -6db).

(4) The mean auto-correlation function has not fallen to 0.5 in the number of lags used in the analysis, signifying low fading.

(5) No significant maxima for the cross-correlations $(\rho < 0.3)$ within the number of lags of the analysis, usually implying a very low wind velocity.

(6) The cross-correlation functions have several local maxima, thus making it impossible to identify the correct one (oscillatory).

(7) The sum of the time displacements for each of the cross-correlation maxima should ideally be zero. Due to random fluctuations this will generally not be so; hence the data are rejected if the quantity

$$\frac{|\Sigma t'|}{\Sigma |t'|} * 100\% \ , \tag{3.71}$$

known as the percentage time discrepancy (PTD), exceeds 30%. This criterion has been relaxed to around 50% [*May*, 1988].

(8) The calculated value of V_c^2 is negative, ie. V_c is imaginary. This criterion is not rigorously applied, since V_c describes the random motion, and if this is small, statistical fluctuations could

produce a negative value of V_c^2. This means that the true velocity should be approximately equal to the apparent.

(9) If the calculated pattern parameters indicate hyperbolic instead of elliptical contours. Rejection thus occurs if $H^2 < AB$.

(10) The polynomial interpolation procedures fail during any level (phase) of the analysis.

(11) Results for which the true velocity is significantly different from the apparent velocity are found to be questionable. The following criteria are generally used to reject data.

$$\begin{aligned} 3V_t &< V_a \\ V_t &> 2V_a \\ |\phi_t - \phi_a| &> 40^o \ . \end{aligned} \tag{3.72}$$

These criteria are not difficult to apply, because of the fast modern computer speeds, and are usually done interactively. The most important of these are criterions are number 3, 4, and 7.

3.5.5 Measuring vertical velocity

The angular power spectrum, W(l,m), where (l,m) are direction cosines, is just the Fourier transform of the spatial correlation function (equation 3.27), provided all length variables are measured in units of radar wavelength [*Ratcliffe*, 1956]. In the case that scatter is not centred on the zenith, and is centred on (l_1, m_1) the power spectrum is simply W(l–l_1, m–m_1), and by the 2-D shift theorem, the spatial correlation function of equation 3.27 becomes

$$\rho(\xi,\eta) = \rho(A\xi^2 + B\eta^2 + 2H\xi\eta) \, . \, exp\left(\frac{2\pi i \xi l_1}{\lambda}\right) \, . \, exp\left(\frac{2\pi i \eta m_1}{\lambda}\right) \ . \tag{3.73}$$

When we include the effect of a pattern velocity, V=(V_x, V_y), the spatial correlation function is simply equation 3.73 with ξ replaced by $(\xi - V_x\tau)$, and η by $(\eta - V_y\tau)$, i.e.;

$$\begin{aligned} \rho(\xi,\eta,\tau) = \rho \left[A(\xi - V_x\tau)^2 + B(\eta - V_y\tau)^2 + 2H(\xi - V_x\tau)(\eta - V_y\tau)\right] \\ \times exp\left(2\pi i(\xi - V_x\tau)\frac{l_1}{\lambda}\right) \, . \, exp\left(2\pi i(\eta - V_y\tau)\frac{m_1}{\lambda}\right) \ . \end{aligned} \tag{3.74}$$

The phase of this function, for an antenna pair (ξ_{ij},η_{ij}) is just the exponent in the exponential terms in equation 3.74. At $\tau = 0$ this is just

$$\psi_{ij}(0) = \frac{2\pi}{\lambda}(\xi_{ij}l_1 + \eta_{ij}m_1) \ . \tag{3.75}$$

In the case of the standard spaced–antenna configuration, we will have at least three receivers, and hence three equations like 3.75, from which we can determine the direction cosines l_1, and m_1. The slope of the phase of the temporal correlation function $\rho(0,0,\tau)$ is

$$\frac{d\psi_{ij}}{d\tau} = -\frac{2\pi}{\lambda}(V_x l_1 + V_y m_1) \ . \tag{3.76}$$

The pattern velocity will, however, be moving at twice that of the wind velocity due to the point source effect, ie.; $V_x = 2v_x$, and $V_y = 2v_y$. In that case our phase equation is simply

$$\frac{d\psi_{ij}}{d\tau} = -\frac{4\pi}{\lambda}(v_x l_1 + v_y m_1) \ , \tag{3.77}$$

where the RHS bracket is the line of sight radial component of wind velocity. If, besides the horizontal velocity there is a vertical velocity, v_z, this introduces an extra radial velocity component of $n_1 v_z = v_z(1 - l_1^2 - m_1^2)^{\frac{1}{2}}$. Since the phase slope is simply equal to a Doppler shift, equal to $\frac{2}{\lambda}$ times the radial velocity, v_z, then this will increase this Doppler shift by $-2v_z(1 - l_1^2 - m_1^2)^{\frac{1}{2}}/\lambda$. Thus the slope of the phase is increased by $-4\pi v_z(1 - l_1^2 - m_1^2)^{\frac{1}{2}}/\lambda$. The slope of the phase (which includes effects due to both a horizontal and a vertical motion) is then given as

$$\frac{d\psi_{ij}}{d\tau} = -\frac{4\pi}{\lambda}\left[v_x l_1 + v_y m_1 + v_z(1 - l_1^2 - m_1^2)^{\frac{1}{2}}\right] \ . \tag{3.78}$$

The standard full correlation analysis (using the modulus of $\rho(\xi,\eta,\tau)$) calculates the velocity components, v_x, and v_y, and we can easily determine l_1, and m_1 from equation 3.75. The phase slope can be found from the phase of the complex auto-correlation function, which should be the same for all three receivers. Thus the vertical velocity can be determined by solving equation 3.78. Furthermore, this velocity determination is not just limited to overhead scatter and we can use l_1 and m_1 to determine the mean direction of scatter.

3.5.6 Errors in the spaced antenna technique

Statistical errors

Initial investigations into statistical errors which arise when wind velocities are measured by the spaced–antenna technique did not give explicit expressions for the errors in the correlation parameters when using the full correlation technique. These early studies attempted to fit the observed correlation functions to classic functions such as the Gaussian, while others attempted to estimate errors from numerical simulations [*Awe*, 1964a, b; *Fedor*, 1967]. An expression for the error in the determination of the position of the maximum of a cross–correlation function was first obtained by *Buckley* [1971], and some aspects of the problem also discussed by others [see e.g. *Chandra et al.*, 1972].

Explicit expressions for the errors in the correlation function parameters were discussed by *May* [1988], who showed that if the functional form was Gaussian, relatively simple arguments lead to appropriate expressions. *May* [1988] found that a functional form for the error in the calculation of the maxima positions is given by

$$\sigma_{tau} = 0.52\ \tau_{0.5}[\frac{\tau_{0.5}}{T}]^{\frac{1}{2}}\ [\frac{(1-\rho^2)}{\rho}]\ , \tag{3.79}$$

where 0.52 is an empirical constant derived from numerical simulations. $\tau_{0.5}$ is the lag at which the auto–correlation function of the time series falls to 0.5 (fading time), T is the record length, while ρ is the modulus of the complex correlation coefficient. A further expression estimates the error σ_x in τ_x, which is complicated by the fact that the errors in the auto–correlation and cross–correlation functions are themselves correlated;

$$\sigma_x = 0.50\ (\frac{\tau_{0.5}^2}{\tau_x})\tau_{0.5}[\frac{\tau_{0.5}}{T}]^{\frac{1}{2}}\ [\frac{(1-\rho^2)}{\rho}]\ , \tag{3.80}$$

where again the constant (0.50) is empirically determined. Thus the two equations above can be used to estimate the standard deviation of two parameters; the position of the maximum in a cross–correlation function and the value of the lag at which the auto–correlation function falls to a pre–specified value. Two conditions are imposed on the use of these expressions. The

record length must be at least 50 times the fading period, and the data must not be filtered to remove noise.

These error estimates were subsequently tested by *May* [1988], both by numerical simulations and with real data. He found that useful estimates of the errors in spaced–antenna wind velocities were determined. In fact, the theoretical errors overestimated experimental ones by a factor of 1.5. This was attributed to the stringent rejection criteria of the full correlation analysis.

Systematic errors

The previously discussed errors might in fact be minor when compared with systematic errors which can arise in spaced–antenna wind measurements. There are three potential systematic error sources in spaced–antenna experiments.

The first of these involves the rejection of data where the calculated value of V_c^2 is negative. Where there is no natural fading it is probable that statistical fluctuations will cause the observed fading time to be different from that due to beam–broadening only (scatterers in different parts of the radar beam have different Doppler shifts, thus broadening the spectrum). A decrease in the width of the auto–correlation function will not stop the analysis, but too wide an auto–correlation function leads to a negative V_c^2, and the subsequent rejection of the data. This statistical variation can be significant, and the possible rejection of half of the data may lead to determination of winds which are systematically underestimated [*Hocking*, 1986]. Overall though, the percentage of data rejected on this condition is only a fraction of a percent, and it is unlikely that this has a major effect on the net result.

The second potential source of error is known as the *triangle size effect.* It has been found that the wind velocity measured is a function of the antenna spacing, and that there exists an optimal spacing. An early study was undertaken by *Golley & Rossiter* [1970] who found that the measured "true" velocity increases with increasing antenna spacing and approaches the real velocity when the spacings become larger. This agreed with the spatial pattern shift found on the large array (the array is discussed in chapter 6). They concluded that this effect

might be due to random noise which reduced the velocity measured and had more effect when correlations are high, which occurs with small antenna spacings. The same conclusion was later reached by *Chandra* [1978] who performed one–dimensional numerical simulations. An alternative cause was attributed to antenna coupling where the measured velocity changed depending on the magnitude and phase of the coupling [*Fedor & Plywaski*, 1972]. Recently, *Meek* [1990] suggested that noise is the only factor which affects the velocity and even the spatial properties of the pattern. This study found that the pronounced triangle size effect was removed when noise had been accounted for.

The third possible error is related to the vertical velocity. Since the antenna receives scattered signal from a variety of off–vertical angles a systematic difference in the vertical velocity through the radar volume will simulate an apparent horizontal wind [*Royrvik*, 1982]. Even so, unusual conditions have to exist for this to occur; for example high–frequency gravity waves with appropriate horizontal scales (10-20 km) enduring within the radar volume. Furthermore, as soon as the data is averaged even over short periods (say hourly) the effect will be negated.

3.5.7 Validity of the spaced–antenna technique

Although the spaced–antenna technique has been used for well over three decades, and numerous comparisons have shown that results obtained by it compare with other methods, from time to time objections to it are raised in literature [see e.g. *Bills et al.*, 1991; *Hines et al.*, 1992]. As stated in the previous section, the spaced–antenna and the Doppler techniques should measure the same velocity provided the sources of error previously mentioned are negligible. The primary difference between the two methods is in the direction of the beam. While the spaced–antenna method is generally limited to the vertical direction, the Doppler method uses beams which can be tilted at off–vertical directions. This may introduce further differences between measurements if the horizontal velocity field varies. In addition, the spaced–antenna radar may use a beam with a large half–width, whereas the Doppler beam is, by necessity, narrow. These problems are well known in the radar community and allowance for them is

usually built into any experiment.

The primary objection to the spaced–antenna method is much more fundamental, and is based on the scattering medium. If there is not one, but two types of scatterers within the radar volume, these scatterers may move at different velocities (the experimental validity of dual scatterers is discussed in Chapter 5). If one set of scatterers is of a specular[6] nature, and the other more isotropic, the specular reflectors cause the dominant reflections for vertical beams, while the isotropic scatterers contribute to the off–vertical beams. It is argued that any method which relies only on vertical scatter, such as the spaced–antenna method, will measure the motion of these specular reflectors only.

Gravity waves have been proposed as the most likely mechanism which may be responsible for the specular echoes. The effects of gravity waves on the spaced–antenna measurements has been discussed in literature, but the discussion concentrated on the E and F regions, which are by nature, highly specular [see e.g. Hines & Rao, 1968; *Hines*, 1972, 1976; *Brownlie et al.*, 1973]. The induced fading of the signal was caused by gravity waves curving the electron density isopleths thus inducing focusing, de–focusing, and interference effects. In the mesosphere and lower atmosphere this effect may not be as important, but should still be considered. The role of gravity waves in spaced–antenna measurements has been discussed in depth by *Hocking et al.* [1989], who considered two situations; one in which gravity waves dynamically effect specular scatterers, and the other where gravity waves themselves are the specular scatterers. These will now be discussed.

The effect of gravity waves on existing specular scatterers

Figure 3.11 illustrates the effect that a gravity wave might have on specular scatterers, at an initial time t_1, and some later time t_2. We assume that radar volume is filled with specular reflectors, forming a quasi–continuous sheet, and a single gravity wave co–exists in the scattering region. Radio reflections from two transmitters, Tx_1 and Tx_2 are *focused* and *defocused* respectively. As the gravity wave propagates, a fading is produced at either site, and this is

[6] aligned within the horizontal plane

interpreted by the spaced–antenna technique as a mean motion.

If this were a true representation of the atmospheric medium then this would present a serious problem. However, this may only be appropriate for the ionosphere where the electron density isopleths are continuous and the reflection absolute. In the lower atmosphere, including the troposphere and stratosphere, the specular scatterers do not fill the radar volume absolutely but are rather spatially and temporally variable, so that only a small part of the gravity wave cycle contains specular reflectors [see e.g. *Harper & Woodman*, 1977; *Röttger et al.*, 1979; *Jones*, 1982]. In addition, the gravity wave period will, in reality, be much longer than the data length[7], and the gravity wave tilting of the reflectors will be far too slow. The fading is then produced by the diffusivity or roughness of the reflectors and is measured as an accurate motion [*Röttger & Czechowsky*, 1980]. Nevertheless, situations may arise where the reflectors might be very smooth and mirror–like. In that case the data will be rejected by the analysis due to the slow fading rejection criteria discussed earlier on.

[7] the 2 MHz system at Adelaide collects data for 102.4 seconds

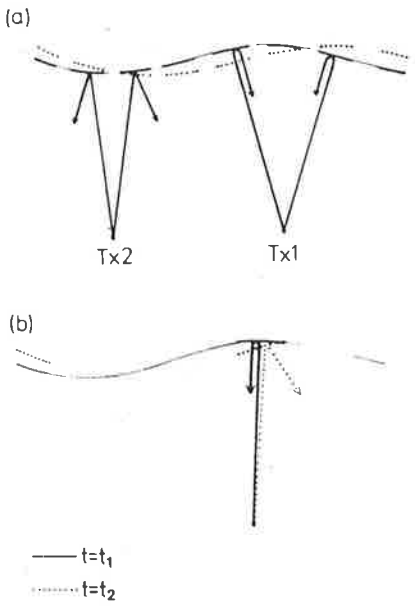

Figure 3.11: Two models of specular reflectors in the atmosphere. The heavy lines and dots are representative of the actual reflectors, while the light dots and lines are indicative of gravity wave isopleths, but with no scatterers present [after *Hocking et al.*, 1989].

Rare situations may arise when a spectrum of waves combine to produce a quasi–continuous reflecting layer, producing diffraction pattern scales much smaller than the gravity wave scales, referred to as *interference fading* [*Hines & Rao*, 1968; *Brownlie et al.*, 1973]. The fading times are subsequently fast and are not rejected by the spaced–antenna method, therefore producing incorrect winds. However, for MF, HF, and VHF D–region partial reflection radar winds, no examples of periodic interference–type fading has been found, although such evidence in the case of totally reflected waves has been found, [see e.g. *Felgate & Golley*, 1971]. This is not to say or imply that such situations may not arise, but that they are the exceptions to the rule and so do not influence general measurements. The scatterers in the middle atmosphere are, generally speaking, quite spatially and temporally variable.

One last point needs to be considered. As discussed by *Röttger* [1981a], if the gravity waves possess large amplitudes, this may tilt the specular reflectors to such an extent that even Doppler radars "see" only them, and thus measure the wave speed and not the mean motion. The built–in rejection criteria of the spaced–antenna technique are more likely to reject the measurement than if the Doppler technique was used. In addition, large amplitude gravity waves are rare, and usually occur in regions of critical–level interactions, where the mean wind and the horizontal phase velocity of the wave in the direction of phase propagation are the same [*Hines*, 1968b; *Röttger*, 1981a].

Finally, even in the case where the spaced–antenna technique erroneously interprets gravity wave motions as the wind speed, these points should be rare and should be easily discernible from the rest of the data. Indeed, if long term trends are the goal than these spurious points will not have any impact on the averages. Alternatively, these outliers may be "weeded" out before any further analysis is carried out [see e.g. *Larsen et al.*, 1982; *Murphy*, 1990].

Gravity waves acting as the specular echoes

The second case to consider is one where gravity waves do not perturb the scattering medium, but cause scatter themselves. For partial reflection radar scatter, the refractive index gradient has to change sufficiently over a quarter radar wavelength for efficient scatter to occur. If it is

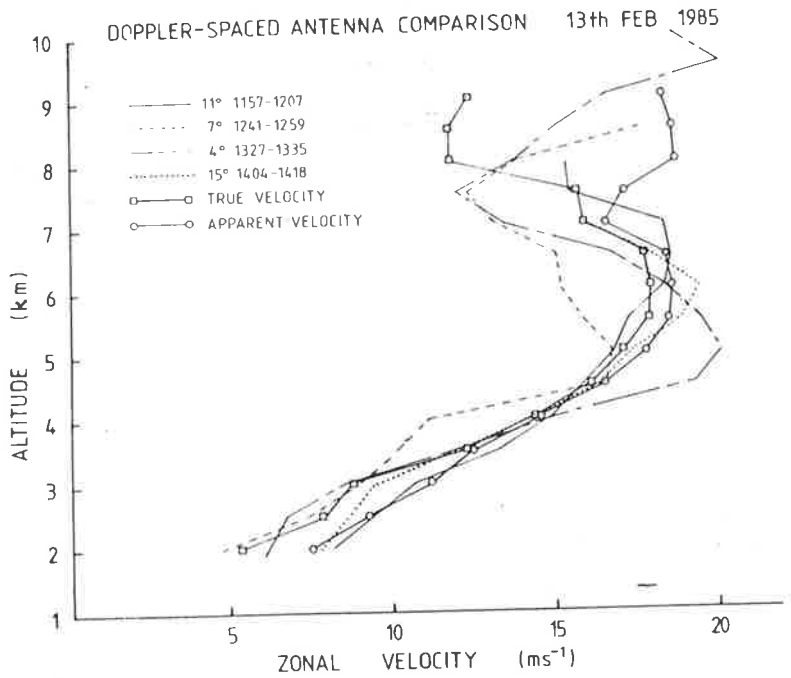

Figure 3.12: A comparison of tropospheric zonal velocities measured by the Doppler and spaced-antenna techniques. The Doppler beam was pointed at angles of 4°, 7°, 11°, and 15°. Data were collected by the Adelaide VHF radar [from *Vincent et al.*, 1987].

more than a quarter of a radar wavelength, the scatter will be quite inefficient. Thus, we need only worry about gravity waves whose wavelength is comparable to that of the radar[8].

Both *Hines* [1960] and *VanZandt & Vincent* [1983] have proposed a model in which the radar reflection occurs from gravity wave compressional wavefronts. The former attributes MF/HF mesospheric specular echoes to gravity waves whose vertical wavelengths are of the order of a hundred metres, while the latter propose that the mechanism causing VHF stratospheric scatter are gravity waves whose wavelength perpendicular to their wavefront is one half of the radar wavelength. The latter process is unlikely, since such wavefronts must possess a tilt which is a function of altitude,and should therefore produce strongest scatter at off-vertical angles; this has not been observed [see e.g. *Hines*, 1960; and discussion by *Hocking et al.*, 1989, 1991]. Even if the waves did have horizontal wavefronts, this implies that they have long periods. They would not have a bearing on measured winds when short term data sets are used, as is generally the case.

[8]The Adelaide radar's wavelength is about 150 metres

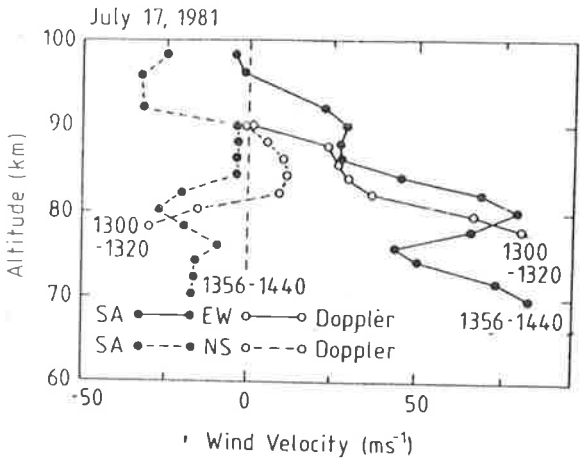

Figure 3.13: A comparison of mesospheric velocities measured by the Doppler and the spaced–antenna technique [from *Hocking et al.*, 1989].

Conclusion

Although situations may occur where gravity waves may be responsible for some of the observed specular echoes, these are rare, and will most likely be rejected by the criteria built into the full correlation analysis technique. Even if two types of scatterers moving at different velocities contributed equally to the reflected signal, the measurement would be rejected due to the cross–correlation having two local maxima. The most important criteria for using the spaced–antenna technique is the antenna separation and the data length. Accurate wind velocities are determined when the separation of the antennas is of the order of a radar wavelength and the sampling time of the order of minutes. On the other hand, when the antennas are separated by tens of kilometres, and the data length is of the order of tens of minutes the method is most suitable for measuring gravity wave phase speeds. Therefore, the spaced–antenna method does measure the net wind motion. Spurious events may be seen from time to time, but these types of events occur in any measuring technique.

Obviously the best way to test the spaced–antenna technique is to compare its results with those measured by other techniques. The first estimates of reliable MF and HF D–region wind velocities were found by *Fraser & Kochanski* [1970] and *Gregory & Rees* [1971]. Subsequently, *Stubbs & Vincent* [1973] and *Stubbs* [1973] showed that the space antenna technique compared well with meteor wind measurements (80–100 km altitude). Other comparisons have been

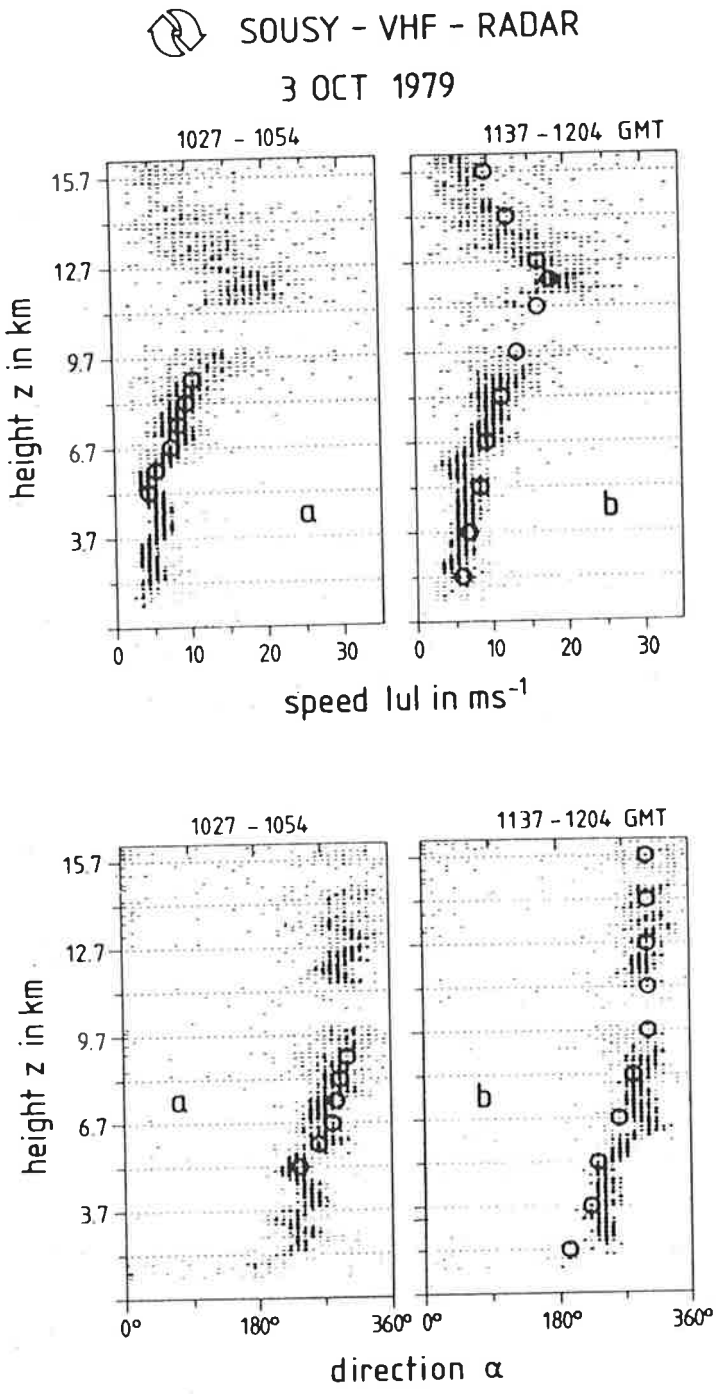

Figure 3.14: A comparison of lower atmospheric wind measurements made with the SOUSY VHF radar (scatter plot) with (represented as circles) (a) simultaneous aircraft wind measurements above the radar, and (b) radiosonde winds 100 km away. The spaced–antenna data are one–samples collected for a total time of 27 minutes [from *Röttger & Czechowsky*, 1980].

performed by numerous authors [see e.g. *Wright et al.* 1976; *Vincent et al.*, 1977, 1987; *Briggs*, 1977]. Daily mean winds have also shown agreement with accepted models of mesospheric circulation [see e.g. *Vincent & Ball*, 1981; *Manson et al.*, 1981, 1985; *Barnett & Corney*, 1985; *Koshelkov*, 1985].

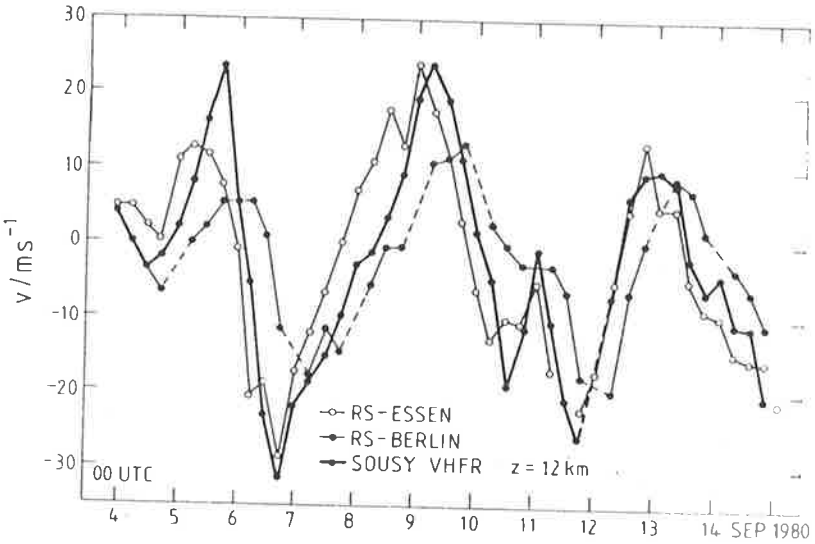

Figure 3.15: A comparison of daily meridional winds measured by the SOUSY VHF radar in the spaced–antenna mode with radiosonde measurements made at the stations of Essen and Berlin. Essen is west and Berlin is located east of the radar. The wind was measured every 6 hours at an altitude of 12km. The oscillating wind pattern is caused by a synoptic–scale wave moving eastward across the radar. Considering the time delay caused by the wave, the cross–correlations between radiosonde–radiosonde and radar–radiosonde are similar [from *Röttger*, 1983].

The spaced–antenna technique has been compared with meteorological techniques, including balloon and rawinsonde comparisons in the lower atmosphere, and again showing excellent agreement. The differences were of the same order as the estimated errors [see e.g. *Röttger & Vincent*, 1978; *Röttger & Czechowsky*, 1980; *Vincent & Röttger*, 1980; *Röttger*, 1981a, b, 1983; *Vincent et al.*, 1987]. Figures 3.12 to 3.15 are typical examples of the comparison between the spaced–antenna technique and other measurements. Figure 3.12 is a comparison of spaced–antenna measured velocities with several off–vertical Doppler velocities [from *Vincent et al.*, 1987]. Figure 3.13 shows a comparison of mesospheric winds using the Doppler and the spaced–antenna techniques [from *Hocking et al.*, 1989]. Figure 3.14 shows a comparison between wind

profiles measured by a VHF radar operating in the spaced–antenna mode and both aircraft and radiosonde measurements [from *Röttger & Czechowsky*, 1980]. Figure 3.15 is a daily wind comparison between the spaced–antenna technique and measurements made with a radiosonde at an altitude of 12 km [from *Röttger*, 1983]. All four figures show excellent agreement between the spaced–antenna measurements and other techniques at a number of altitudes and varying times.

Chapter 4

Spaced–antenna radar model

4.1 Introduction

The two primary radar remote sensing techniques of the atmosphere are the Doppler and the spaced–antenna techniques. In this thesis, most of the data collected has utilized the spaced–antenna technique using the full correlation analysis. Both these techniques were discussed in the previous chapter where it was shown that there is excellent agreement between spaced–antenna measurements and other techniques made at varying times, altitudes and sites. Nevertheless, objections to the spaced–antenna method do arise from time to time in the literature, where it is argued that the spaced–antenna technique does not consistently and accurately measure the neutral wind and may be at times affected by such things as gravity–waves and the structure of the reflecting layers [*Bills et al.*, 1991; Hines et al., 1992]. However, some modelling work has suggested that spaced–receiver measurements are accurate [see e.g. *Wernik et al.*, 1983].

To better understand the spaced–antenna technique and the full correlation analysis, a model was developed which simulates a complete partial reflection radar system, similar to the ones employed by the University of Adelaide. By comparing the various input parameters with those "measured" by the model, it was hoped to obtain a feel for the accuracy, and the strength and weaknesses of the spaced–antenna technique.

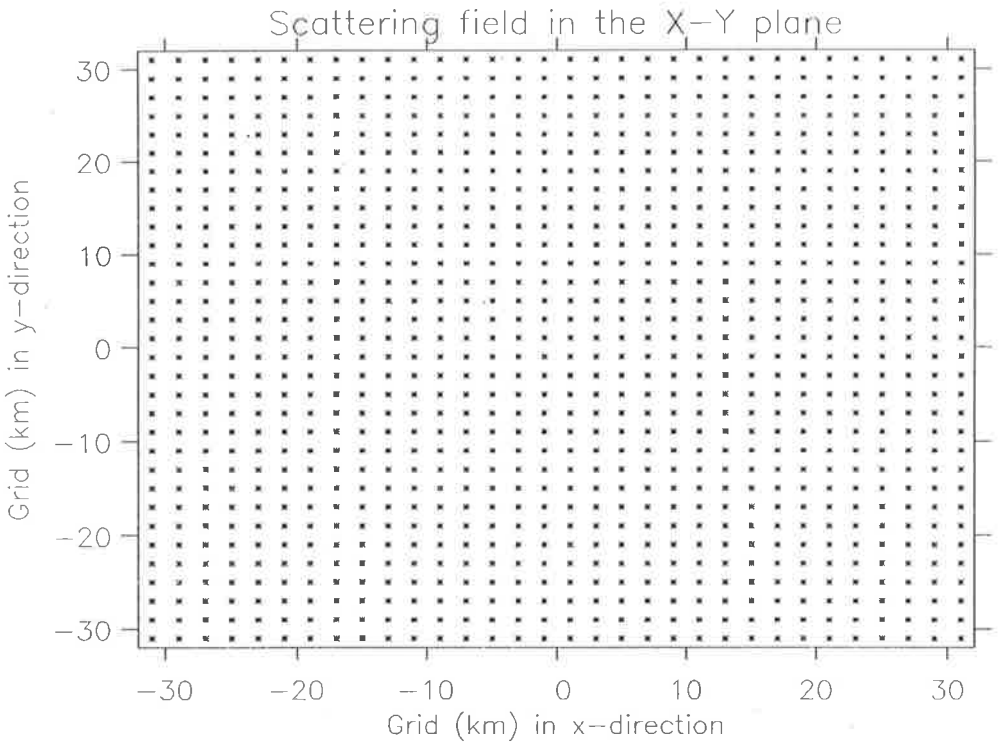

Figure 4.1: A symmetrical grid of scatterers used by the spaced-antenna model with no randomization. In the simulations the grid points were separated by 2 km.

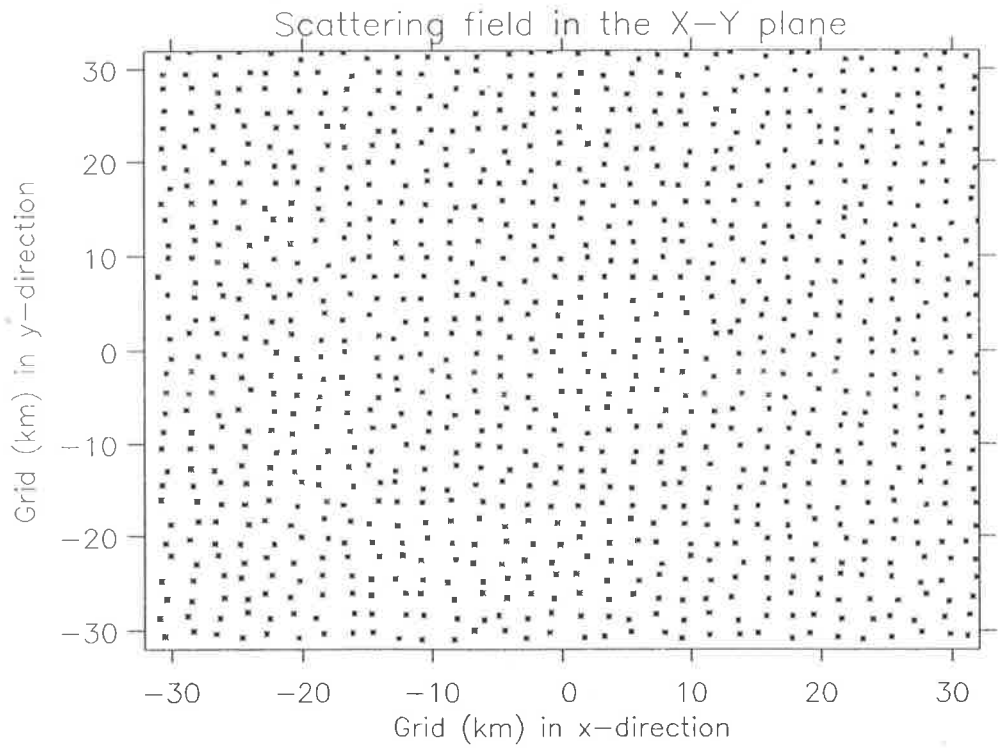

Figure 4.2: A symmetrical grid of scatterers used by the spaced-antenna model with 0.5 degree of randomization. The individual points were all within 1 km of their respective origins.

The model has been undergoing development for several years, and has had input from other workers, although it has greatly been expanded upon and tailored within this thesis. The results presented herein are the first time the model has been used to any degree. Here I will first discuss the various parts of the model followed by some simulations.

4.2 General description of the model

The first step in the model was to construct a scattering field where individual scatterers contribute to the total reflected signal, and which had the capacity to move at a pre–determined three–dimensional velocity with various degrees of turbulence. However, the first step involved selecting the initial relative positions of the scattering points on a grid.

Initial position of the scatterers

To simulate a group of scatterers it was decided to construct a grid of points which represent point scatterers whose initial positions could be either on a symmetrical grid, random (by varying amounts) around such a grid pattern, or completely random within a certain volume. The height range of the scatterers could also be pre–set within the model.

After initial investigation, a grid of 32×32 (1024) scatterers was found to be a suitable number, since more scatterers did not significantly change the results and took a large amount of computing time. The scatterers were placed on grid points 2000 m apart, so that the total area covered by the scattering field was some 64×64 km^2. Scatterers whose subsequent randomness around such a grid point was set to be 0.1 were therefore positioned within 200 m of the centre of their relative grid point, while those whose randomness was set at 0.5 were within 1000 m. Similarly, those scatterers whose randomness was 1.0 could be anywhere within the 2000×2000 m area allotted to each grid point and so on. In the case of pure randomness, the scatterers could be positioned anywhere within the 64×64 km^2 volume. Figure 4.1 shows a grid where the scatterers are purely symmetrical, while figure 4.2 shows a typical grid where the scatterers are randomized by 0.5. Figure 4.3 shows scatterers randomly positioned within the 64 km^2 area.

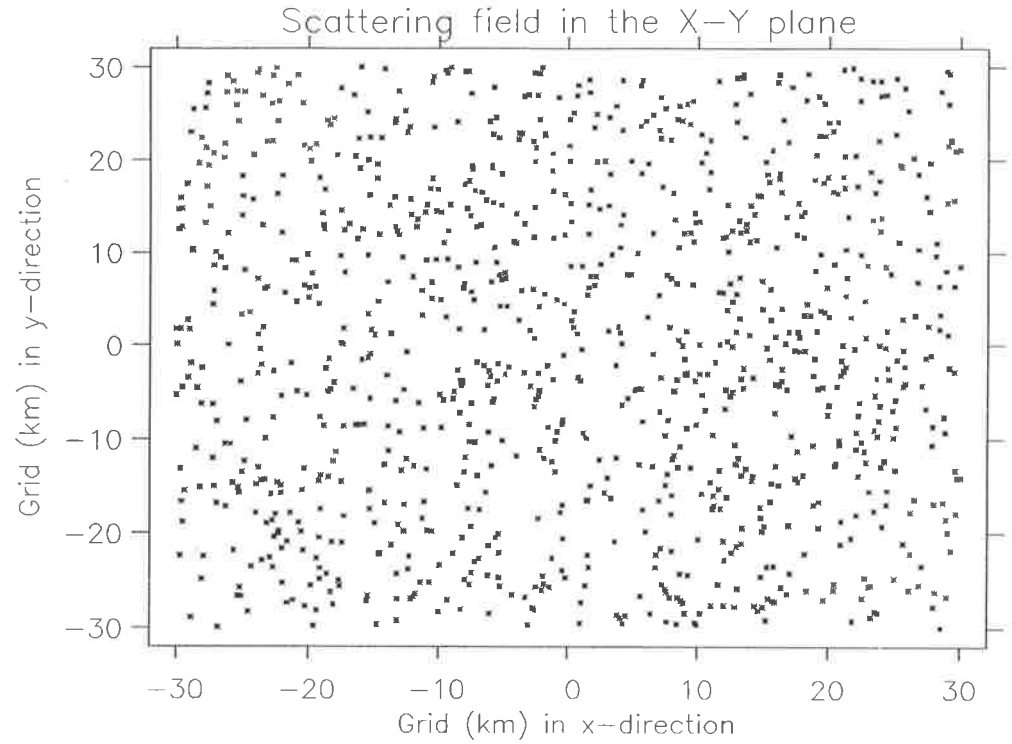

Figure 4.3: A symmetrical grid of scatterers used by the spaced-antenna model with completely random initial positioning within an area of 32×32 km.

The mean height of the scatterers was preset at 85 km. However, that resulted in the distance from each scattering point to a stationary ground point varying uniformly. This created an artificial phase variation. To avoid this problem the scatterers were randomized in the vertical plane so that their vertical position was within 2 wavelengths (±150 m) of a mean height of 85 km. Figure 4.4 shows a typical vertical cross-section of the scatterers which are randomly positioned (i.e. a view of figure 4.3 from above) in both the horizontal and vertical plane.

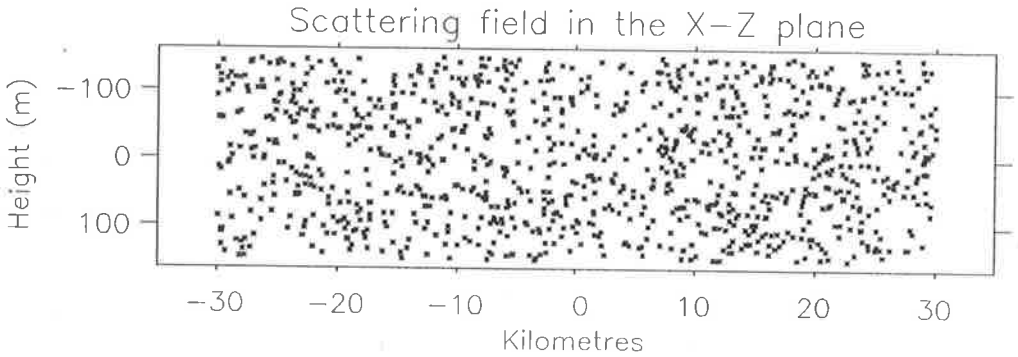

Figure 4.4: A vertical cross-section of the scatterers randomly distributed within a volume of 64×64×0.3 km.

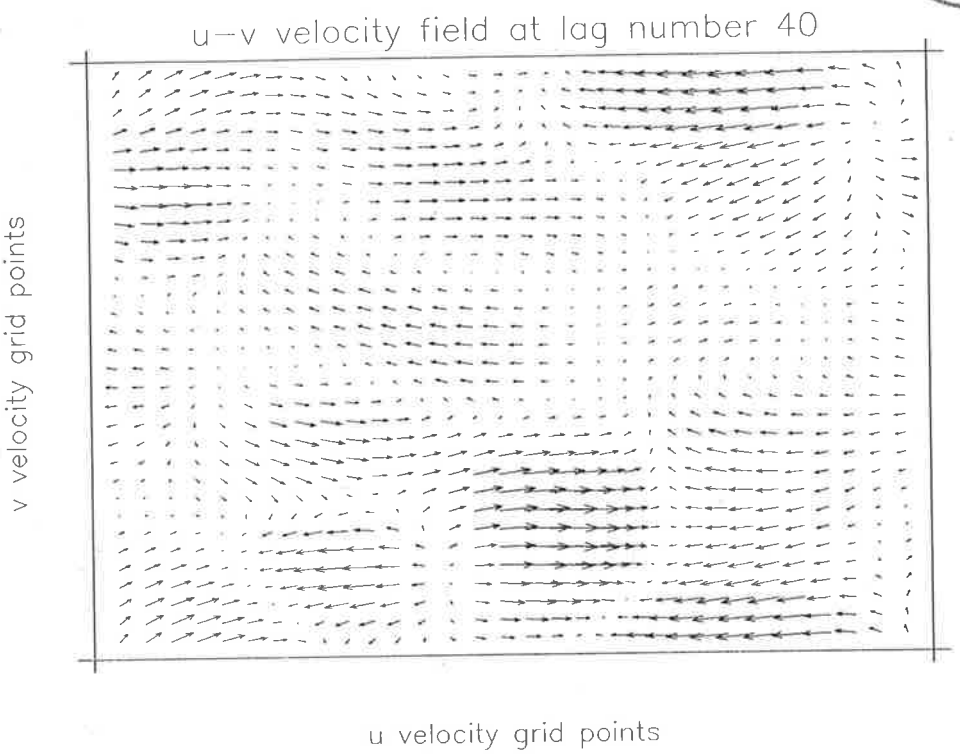

Figure 4.5: A two–dimensional turbulence field observed at 40 lags. The lengths are not the absolute values.

Such a volume of scatterers would be initially set up and then moved with a mean velocity and varying amounts of two–dimensional turbulence and wave activity. If the radar half–power half–width was about 9° this scenario meant that up to 50 scattering points were observed within the radar volume at any one time.

Turbulent velocity fields

In addition to a mean velocity with which the above scattering field could be moved, the model was also equipped to include a turbulence field (either large–scale 2-D or 3-D). Such a field consists of velocity vectors which simulate both the spatial and temporal structure of turbulence in the atmosphere. The generated velocity fields satisfy pre–determined correlation functions and thereby lead to smooth variations in both the spatial and temporal domain. Thus, three such velocity fields are all that is necessary to completely describe a vector field.

Figure 4.5 and 4.6 show a component of a turbulent velocity field at 40 and 60 time lags respectively. Such a velocity field would be an additional effect on the scattering field which

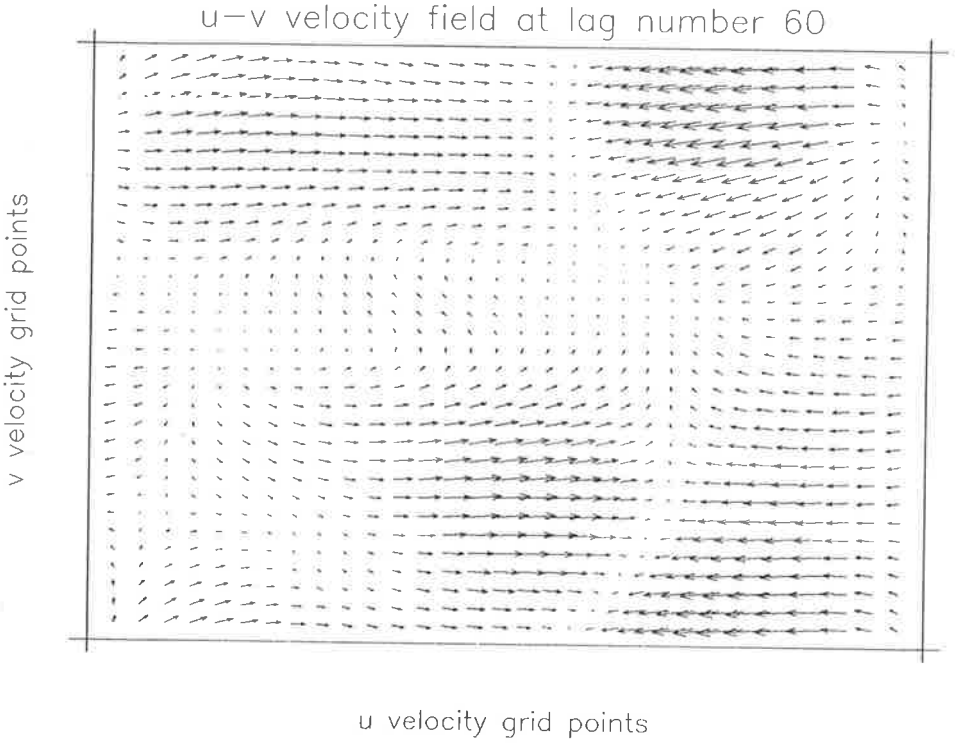

Figure 4.6: This is the same two-dimensional turbulence field as for figure 4.5 but at 20 lags later (lag 60). Comparison of the two shows a clear temporal evolution of the turbulent field.

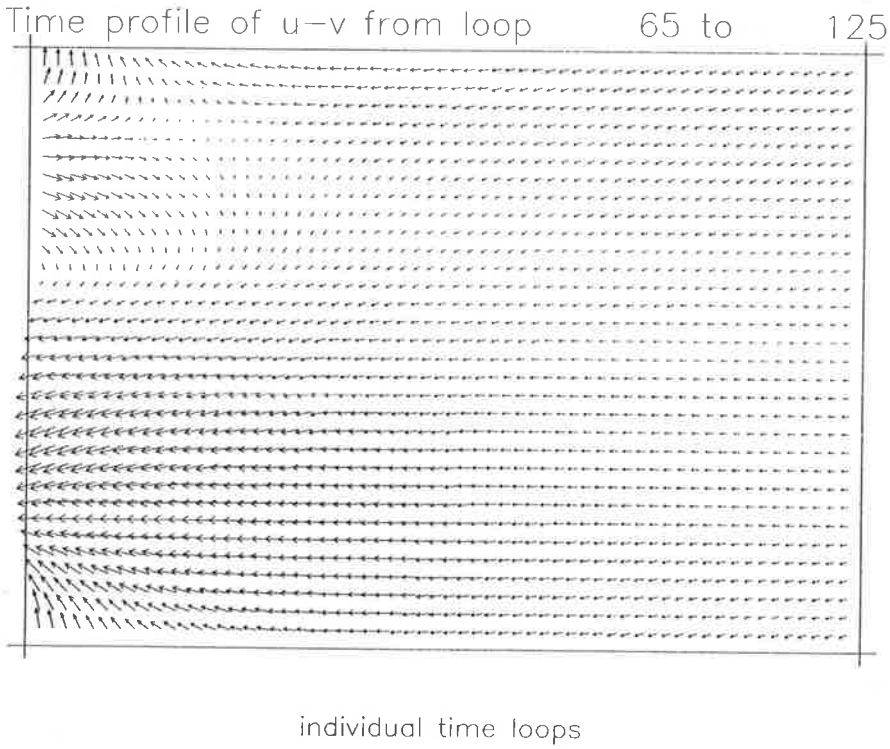

Figure 4.7: Temporal profile of one row of the horizontal vector velocity field over a total of 60 lags. One can clearly see the smooth variation in both direction and magnitude of the individual vectors.

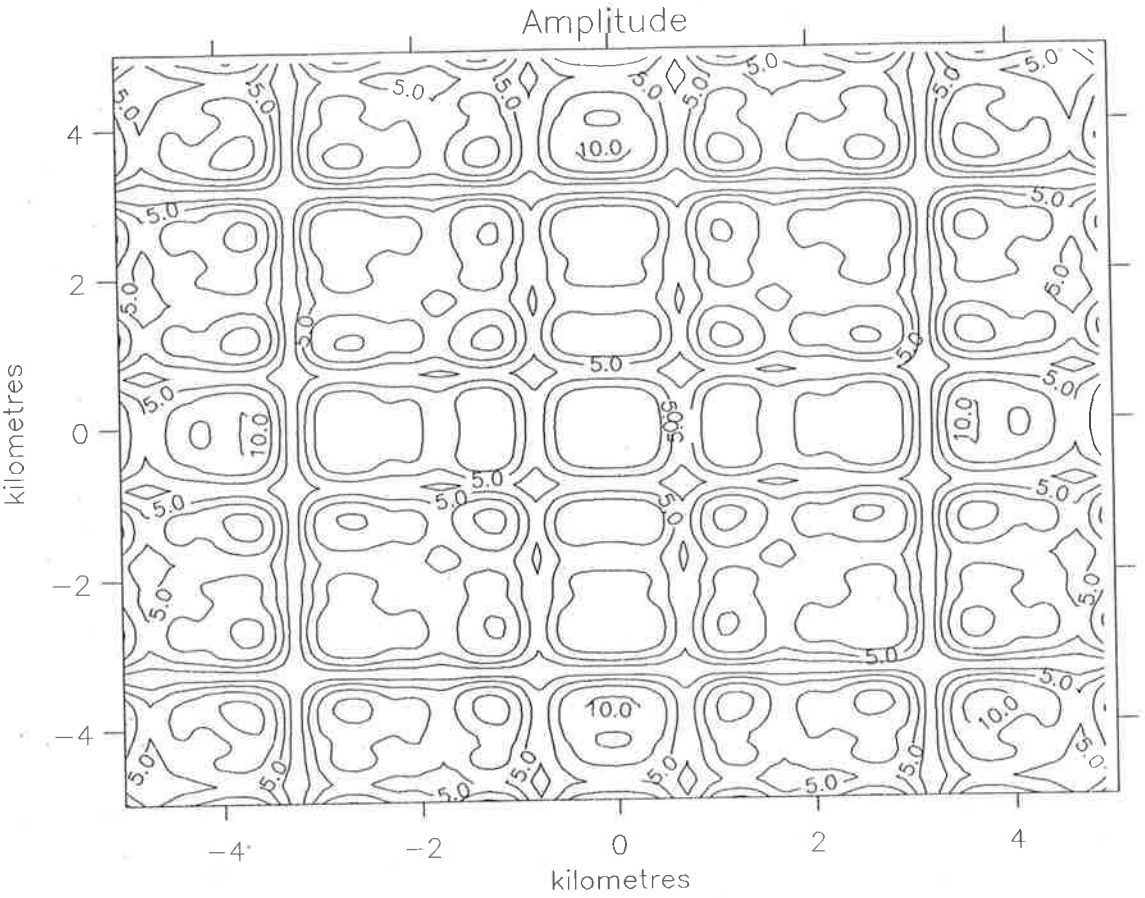

Figure 4.8: The amplitude diffraction pattern of the scattering grid displayed in figure 4.1. The contours are in arbitrary units. The pattern was constructed by sampling the complex contributions of each scatterer at 80×80 points covering an area some 10 km^2.

is already advected by some mean velocity. One can see that the turbulence field at 60 lags, although different to the one at 40 lags, still shows some resemblance to it. This temporal "continuity" is a better approach than the total randomization of a turbulent velocity field. Figure 4.7 is a plot which shows the temporal evolution of the horizontal turbulent velocity field of a single grid row over 60 lags. Each scattering point is seen to change smoothly in both direction and magnitude. The contribution by such a turbulent velocity field can also be weighted, that is, the magnitude of the contribution of the turbulence to the mean motion may be varied, but with the temporal and spatial evolution of the turbulence remaining undisturbed.

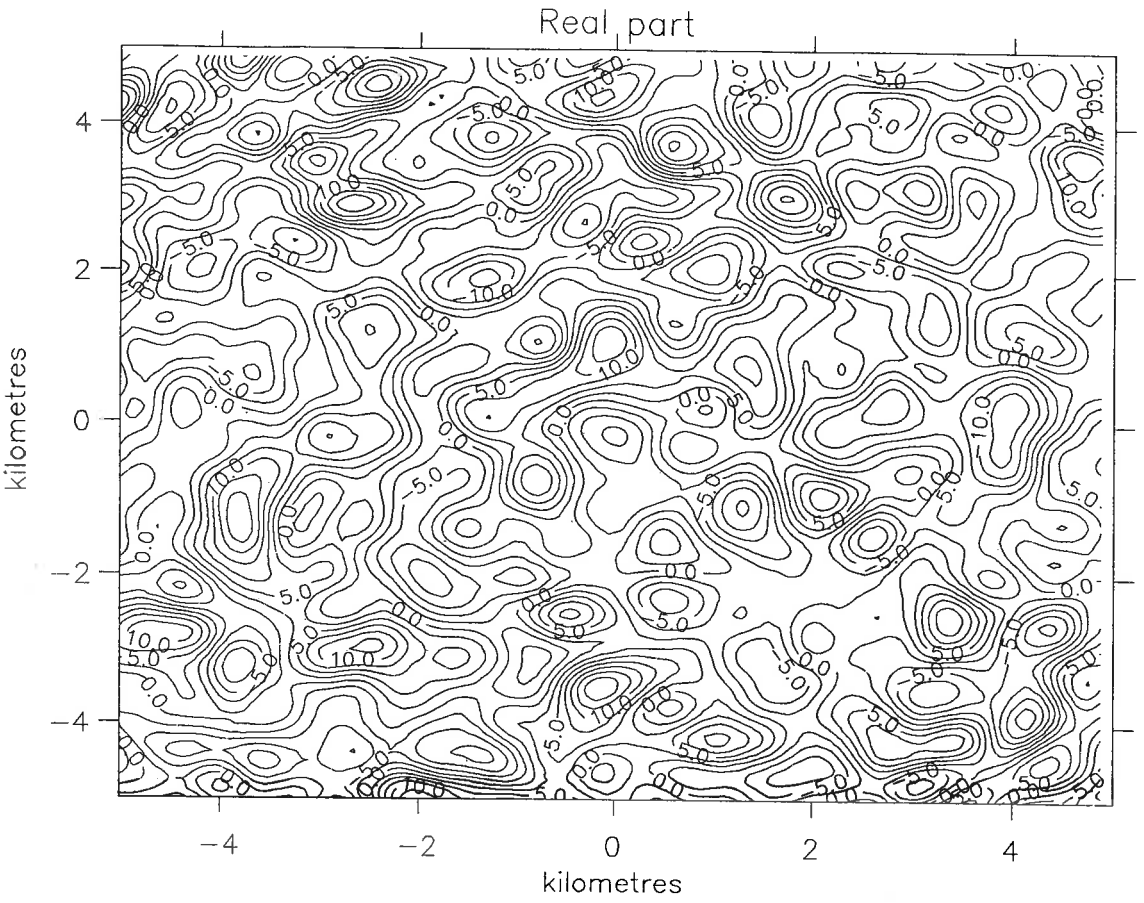

Figure 4.9: The real part of the electric field diffraction pattern of the electric field scattering grid displayed in figure 4.3. The contours are in arbitrary units. The pattern was constructed by sampling the real part of the contributions of each scatterer at 80×80 points covering an area of some 10 km^2.

4.2.1 Spaced–antenna time series generation

To simulate a spaced–antenna radar system the model used a single transmitter, and three receivers which could be positioned at any location on the ground plane. However in these simulations the transmitter was always placed at the centre of the 64×64 km^2 array, with the receivers being placed symmetrically at various distances around it. This made the system truly monostatic. The scattering grid was then used to reflect a transmitted signal at a frequency of 1.98 MHz (although any frequency could be used – this is the frequency used by our MF radars). The reflected complex signal made up of the contributions from each of the scatterers was then recorded at the three spatially–separated receivers. Both the transmitted and reflected signals were also modified by a function which simulated a Gaussian polar diagram describing both the transmitting and receiving system.

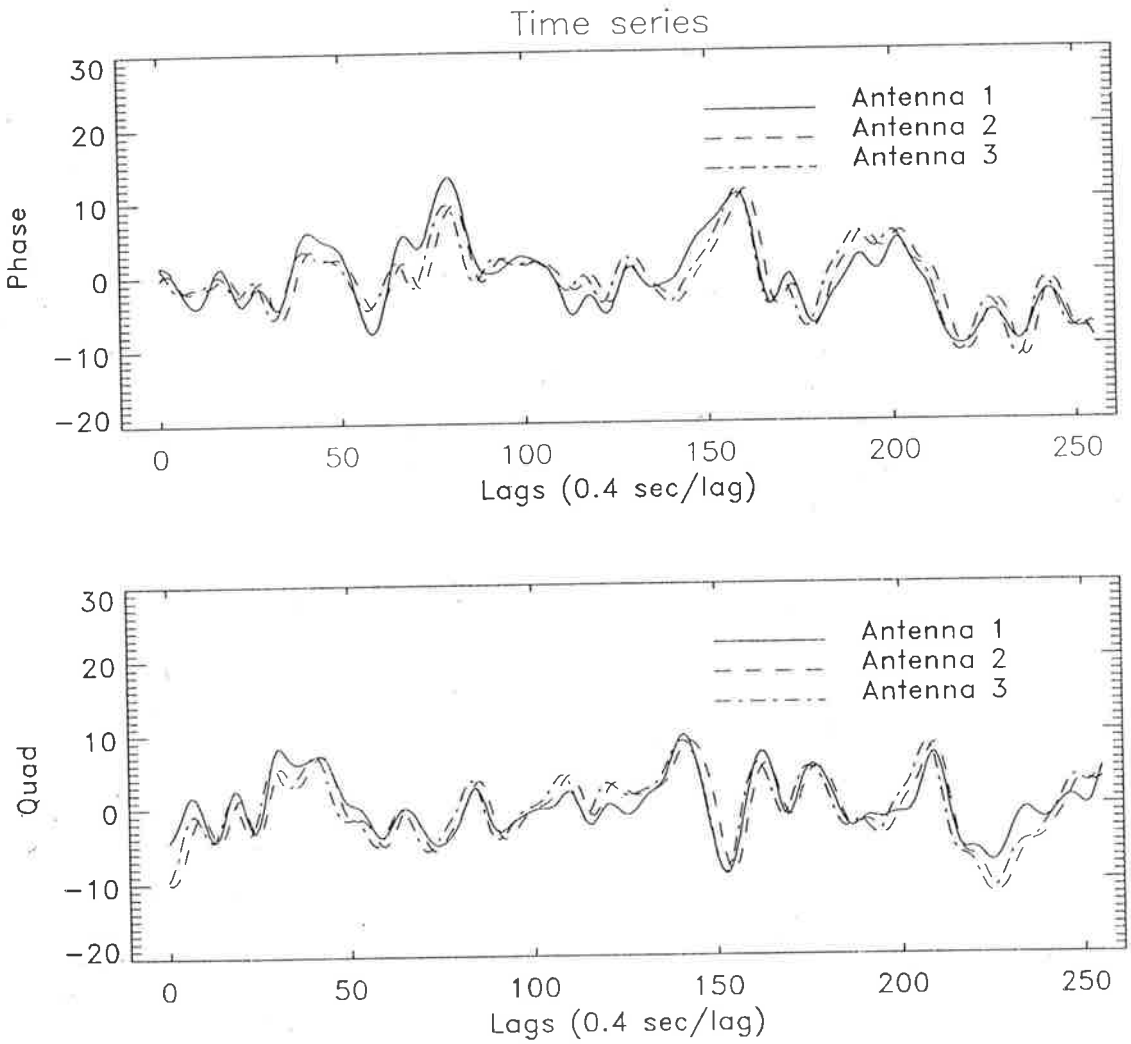

Figure 4.10: A typical complex time series measured by three spatially separated receivers moving at a velocity of 100 ms^{-1}.

Once the complex time signal for each of the receivers was calculated, the scattering grid was moved according to the pre–set mean velocity and turbulence level. Since the scatterers produce an electric field diffraction pattern (which could be measured on the ground), this pattern also moves, albeit at twice the velocity of the scatterers (the point source effect). A new complex signal was then re–calculated for each of the three receivers according to the new positions of the scatterers (shifting of the diffraction pattern). It should be noted that the simulation calculated the contribution from each individual scatterer, taking into account the transmitter–scatterer–receiver distance, and was not an approximation. This temporal sampling occurred

at 0.4 second intervals, for a total number of 256 samples. This made the total length of the time series 102.4 seconds.

Figure 4.8 is a typical contour plot of the amplitude of the electric field diffraction pattern produced by the non–randomized grid shown in figure 4.1. It clearly shows symmetry which would be expected for a symmetrical grid. Figure 4.9 shows the real component of the electric field diffraction pattern field for a completely random grid such as that in figure 4.3. The diffraction patterns were calculated by adding the contributions of each scattering point to a ground grid of size 80×80 points which covered an area of some 10 km^2. Small diffraction pattern maxima are clearly seen and it is the velocity of these "individual" diffraction patterns that is measured by the spaced–antenna system.

A typical complex time series showing the in–phase and quadrature components for three spatially separated receivers is shown in figure 4.10.

4.2.2 Full correlation analysis program

The full correlation analysis program used on the simulated data is the same program that has been used for a number of years to calculate the mean winds and other parameters from real data collected at the Buckland Park field station. The theory behind the full correlation analysis has already been covered in depth in the previous chapter which described how the various parameters were calculated. In its simplest form, the analysis program cross-correlates the complex signal from each of the three spatially–separated receivers to calculate the speed and direction of the scattering grid, while taking account of the "natural" change of the pattern. Figure 4.11 shows the auto–correlation function and the cross–correlation functions between the three receivers for the time series exhibited in figure 4.10.

4.3 Results obtained from simulations

In any model where a large number of variables can be changed, it is always difficult to decide which parameters to vary at any one time. However, since one of the primary reasons of

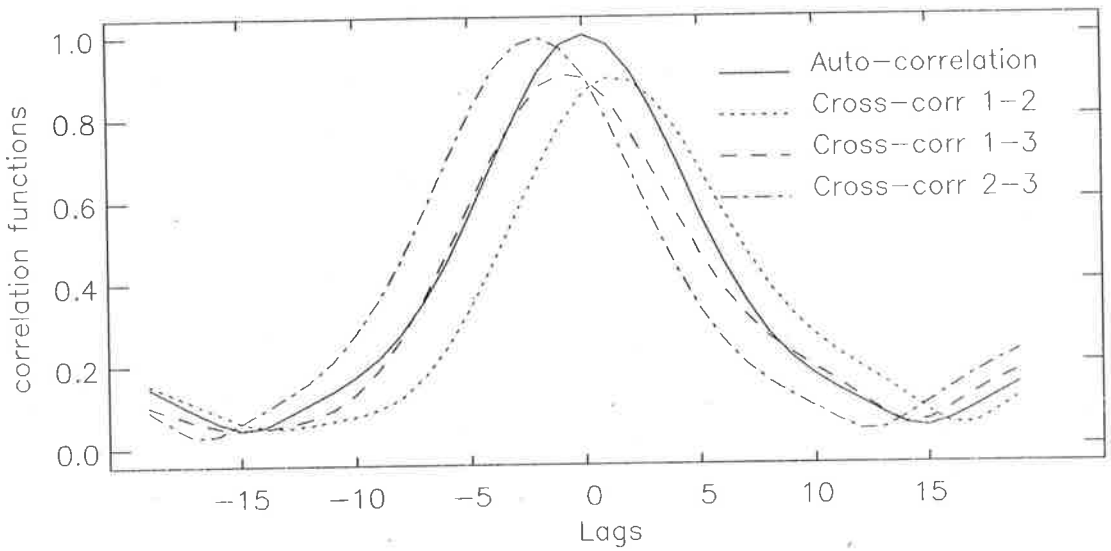

Figure 4.11: The auto– and cross–correlation functions for the time series collected by the three spatially–separated receivers which is shown in figure 4.10.

developing the model was to gauge the accuracy of the 1.98 MHz radar systems that were employed to collect the bulk of the experimental data used in the this thesis, this made the task somewhat easier.

The parameters that were not varied at any time during the modelling work included the number of scatterers (32×32), the mean height of the scatterers (~85000 m), the frequency of the radar (1.98 MHz), the location of the transmitter (centred), the sampling rate (0.4 sec), and the total length of the time series (102.4 sec).

A couple of factors which were initially kept constant included the half–power half–width of the transmitting and receiving polar diagrams (9°), and the relative positions of the receiving antennas. In the initial simulations the three receiving antennas formed an equilateral triangle whose centre was the transmitting antenna (centre of the grid). One antenna was positioned purely northward from the transmitter while the other two were at 120° clockwise and anti–clockwise from northward. Rather than changing the relative orientation of the antennas it was far easier to change the direction of the mean wind. However the mean distance between

the centre of such an arrangement and the antennas was varied. Altogether a large number of simulations were performed, and only a few typical examples will be presented here.

4.3.1 Initial test of the model

The obvious initial test is to see whether the model can correctly extract the velocity that the scattering grid is moved at, but assuming simple laminar flow (no two–dimensional turbulence). A large number of simulations were performed where two variables were varied. Firstly, the degree of randomization of the scattering grid was increased in steps of 0.25 from no randomization to total randomness within the scattering volume. Secondly, the distance from the centre of the receiving array to each of the receivers was increased in steps of 25 m, from 25 to 400 metres. Operating at a wavelength of ~150 m, the receiving antennas were one wavelength apart when their distance from the centre was about 87 m.

Figure 4.12 shows a typical set of apparent wind velocities and differences between the model and apparent wind directions (denoted as V_{app} and θ_{app}) calculated by the model for varying degrees of grid randomness and varying antenna separations. Similarly figure 4.13 shows a typical set of true velocities and differences in direction between the model and true velocity (denoted as V_{true} and θ_{true}), again as a function of grid randomness and antenna separation (denoted as D_{ant}). The model velocity and direction (V_{mod} and θ_{mod}) was 50 ms^{-1} moving eastwards. Both of these figures are for scattering grids which were all positioned in the one horizontal plane at 85 km, i.e. there was no randomness in the vertical.

V_{app} is seen to tend to V_{mod} as the antenna separation increases. However, two of the initial scattering grids (0.25 and 1.0) increased to approach V_{mod} while all the others, with the exception of the non–random grid (0.0) decreased towards V_{mod}. Only a few points were accepted by the analysis in the case of the non–random grid, and these themselves deviated markedly from V_{mod}. Examination of the raw output file for the non–randomized grid showed that the data were rejected due to hyperbolic contours (these can clearly be seen in figure 4.8).

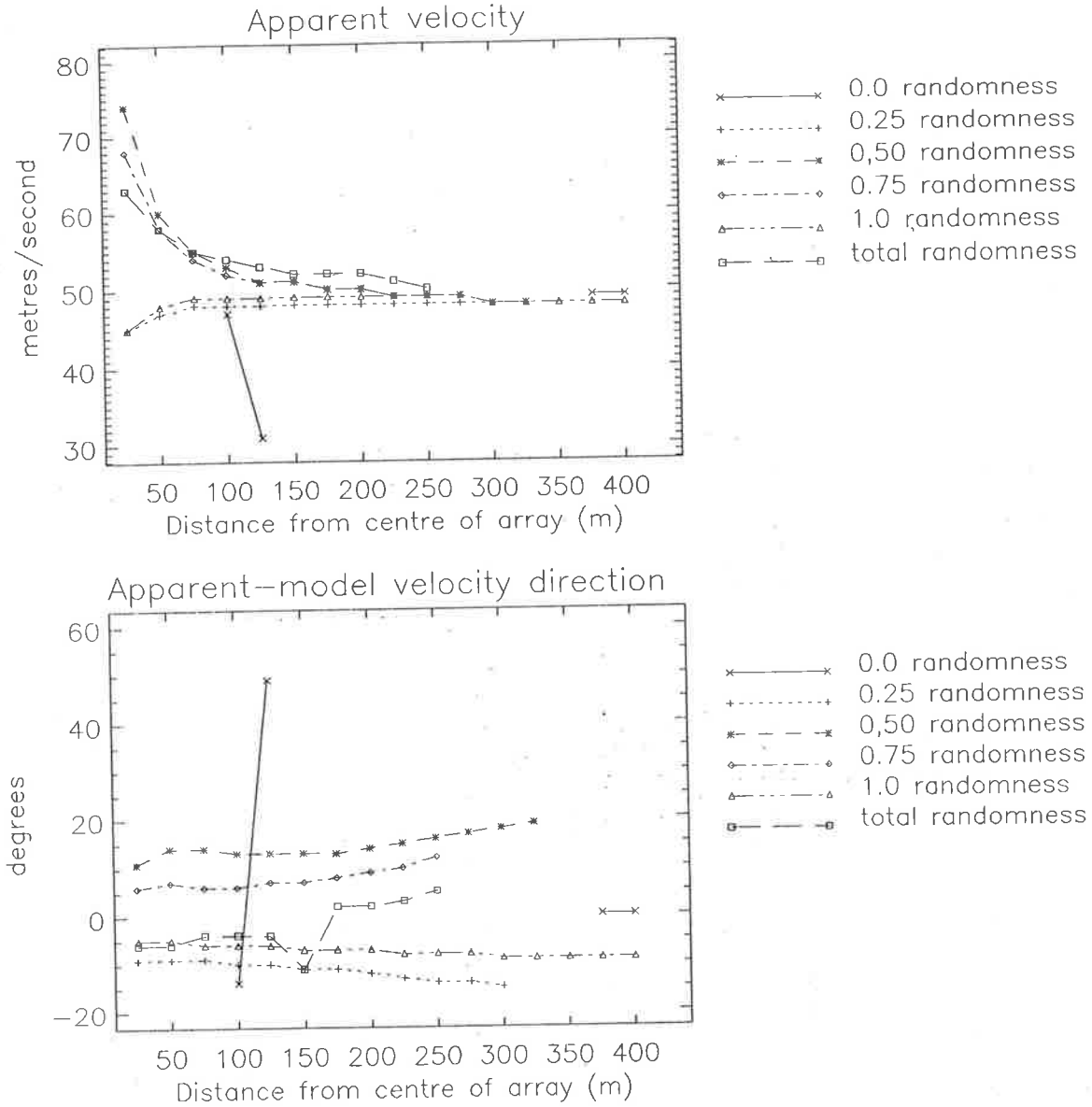

Figure 4.12: The modelled apparent velocity (top) and apparent–model direction (bottom) for varying degrees of scattering grid randomness and antenna separation, but fixed at a height of 85 km. The model velocity was 50 ms^{-1} moving eastwards. The interpretation of the degree of randomness has been discussed in a previous section.

The values of θ_{app} vary by around $\pm 10°$ from the θ_{mod}. Again, the exception is the non–randomized grid where the model struggles.

Unlike V_{app}, V_{true} is slightly overestimated and increases fairly constantly and slowly as a function of antenna separation when D_{ant}> 150 m. An exception to this is V_{true} observed from the 0.25 randomized grid. The distribution of θ_{true} is much narrower than θ_{app}, with the difference between it and θ_{mod} generally less than 5°. Again, the non–randomized grid

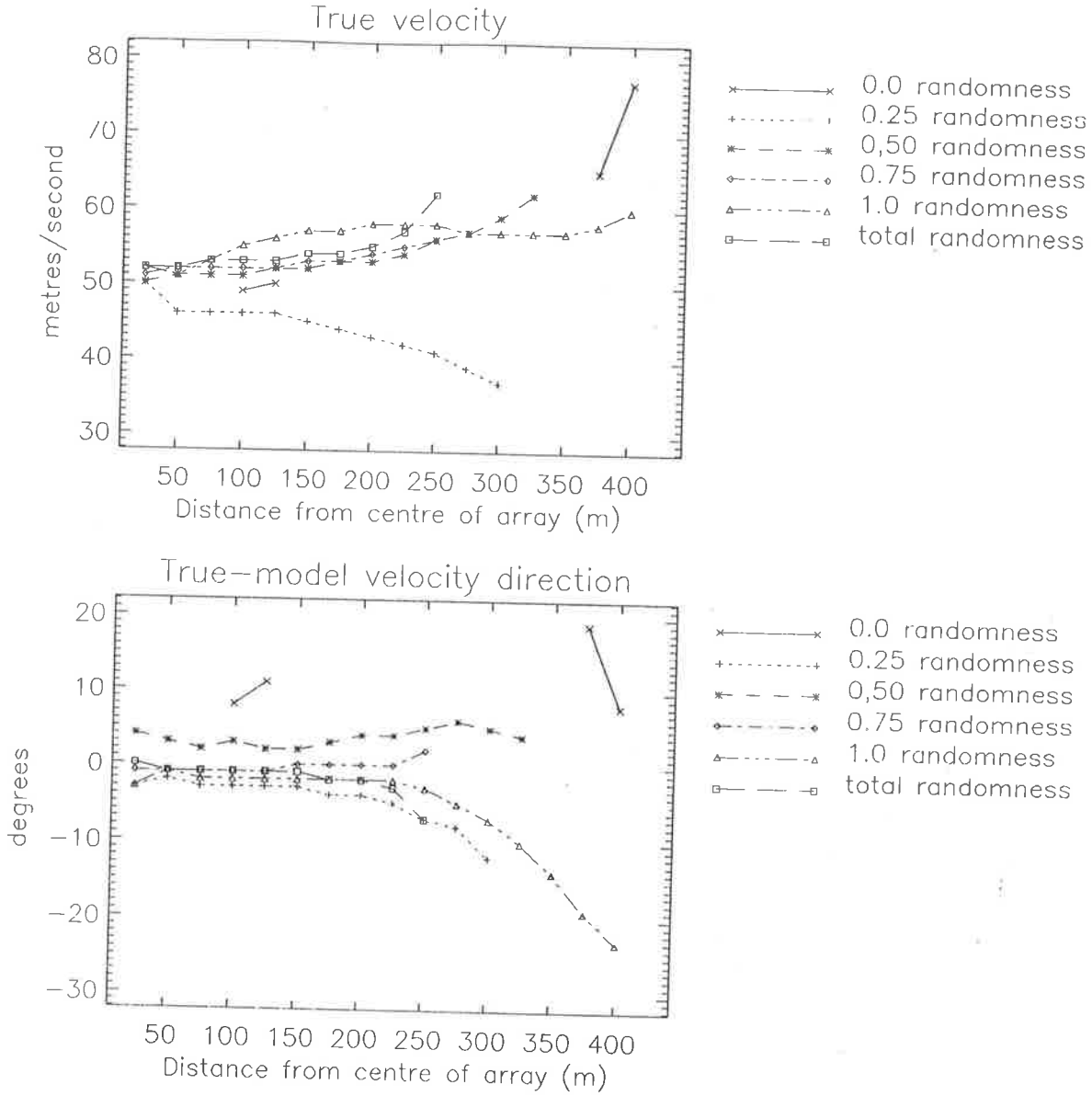

Figure 4.13: As for figure 4.12 but for the true velocity and true–model direction.

causes the most deviation, but such a grid must be considered a special case and not a true representation of a typical scattering grid.

These and other simulations involving non–turbulent two–dimensional but variable randomization fields showed that at times there existed systematic behaviour observed in both V_{app} and V_{true}. This was thought to be due to an artificial phase variation across the radar beam which occurs when the scatterers are two–dimensional, i.e. all positioned in the one horizontal plane (85 km in this case). To eliminate this possible contamination the simulations were repeated but with the scatterers additionally randomized in their height (and thus the phase) by $\pm$ 150

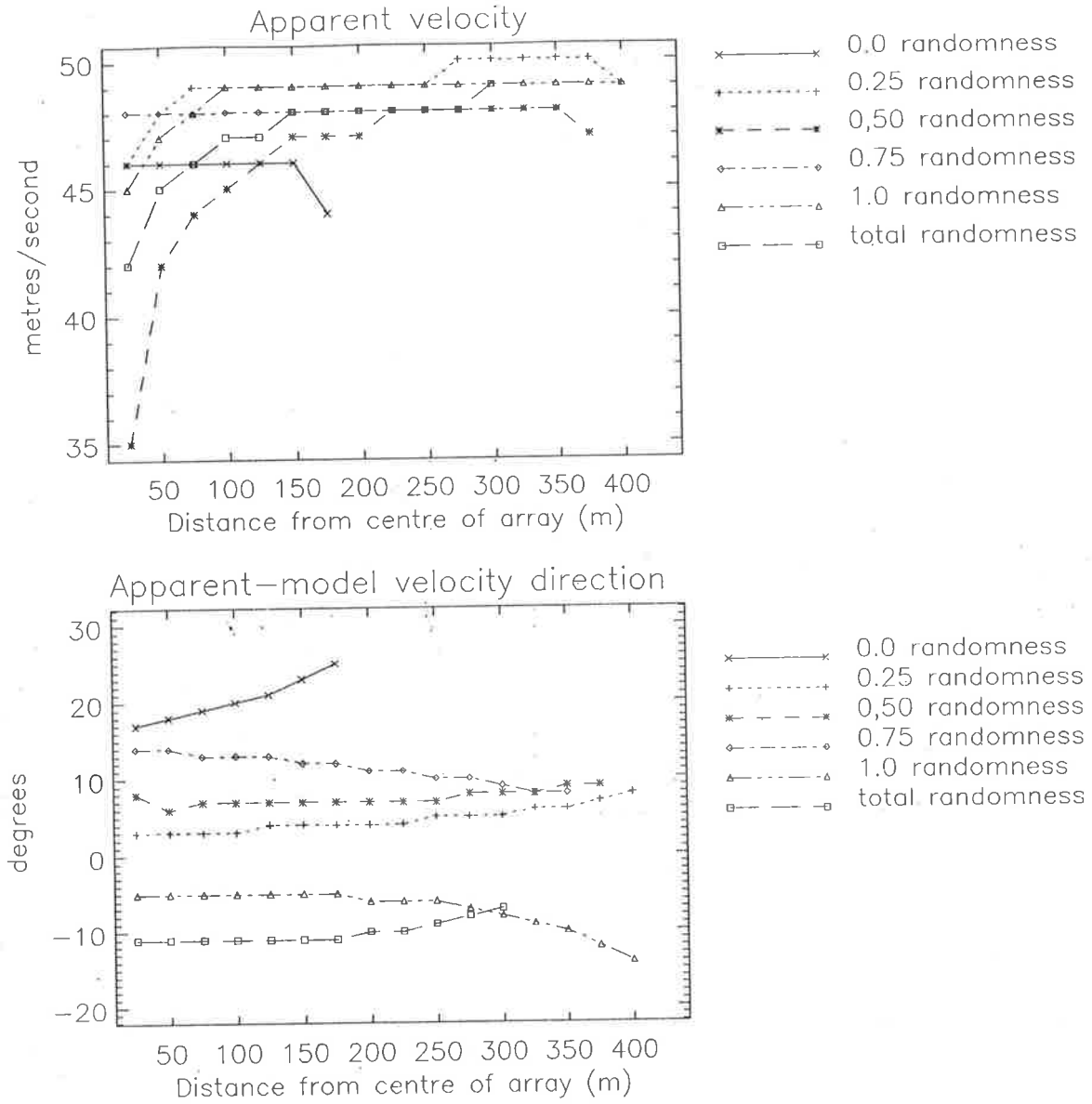

Figure 4.14: As for figure 4.12 but with the scattering fields being additionally randomized in the vertical to be within ±150 m of 85 km.

m (one wavelength) around a mean height of 85 km. These results are shown for V_{app} and θ_{app} in figure 4.14 and for V_{true} and θ_{true} in figure 4.15.

V_{app} is seen to increase tending towards V_{mod} although θ_{app} varies markedly by up to 20°. V_{app} in this case is slightly smaller than for the case where the scatterers were localized in the vertical, but are still within 5 ms^{-1} of V_{mod}. θ_{true} is also close to θ_{mod}, to within ±5°.

Although preliminary, and based on a number of pre-set parameters, the above results clearly show that the model is able to extract a true velocity which is quite close to that

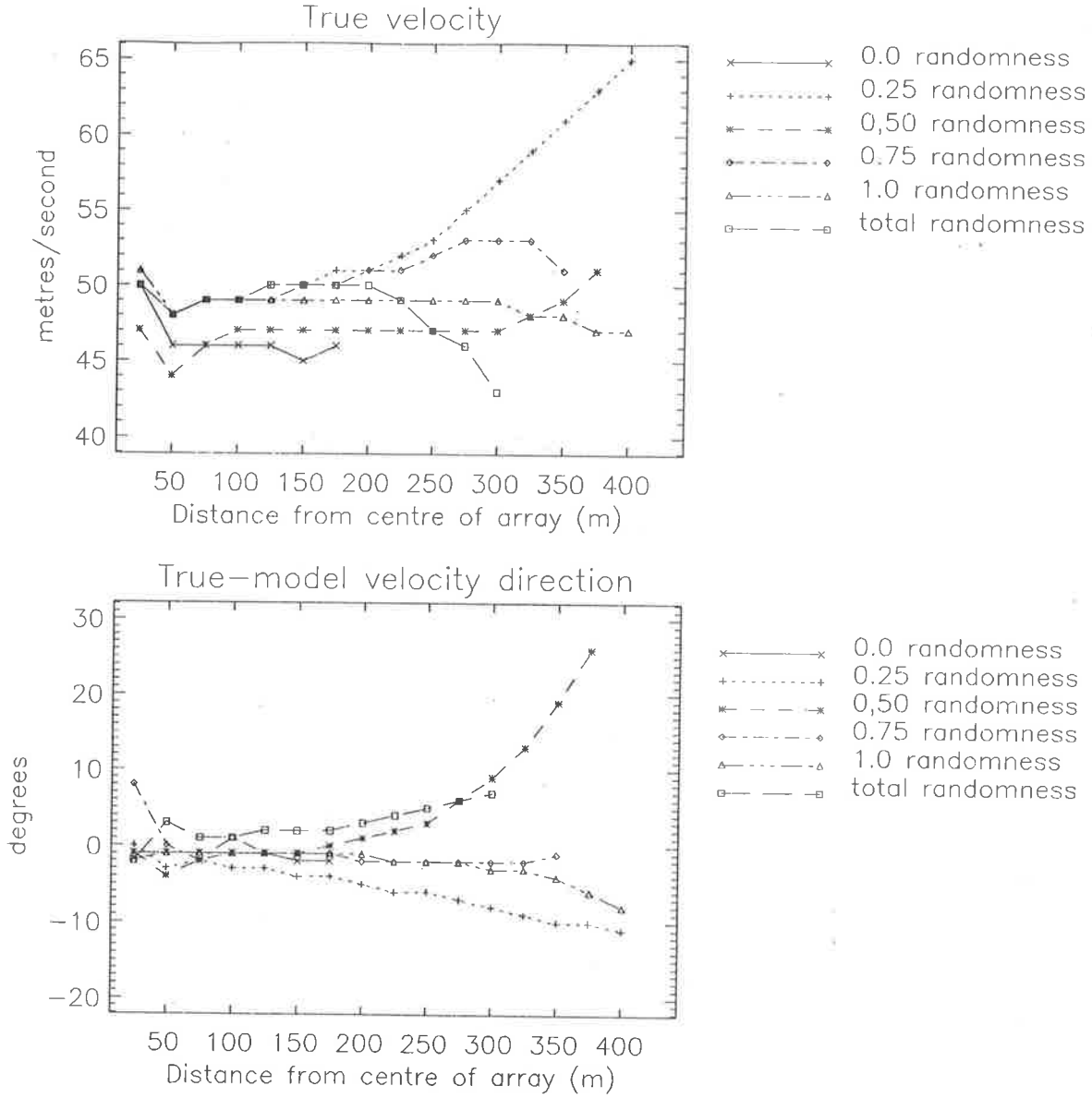

Figure 4.15: As for figure 4.13 but with the scattering fields being additionally randomized in the vertical to be within ±150 m of 85 km.

imparted to the scattering field. This itself shows that the point–source effect [see e.g. *Felgate*, 1970] is "real", i.e. the diffraction pattern produced by the scattering grid moves at twice the velocity of the scatterers.

None of the above results showed that there was a systematic variation in any velocity and direction which could be related to the degree of scattering field randomization. Therefore, the following simulations undertaken used scattering grids which, although constructed by different initial seeds, possessed the same degree of randomness.

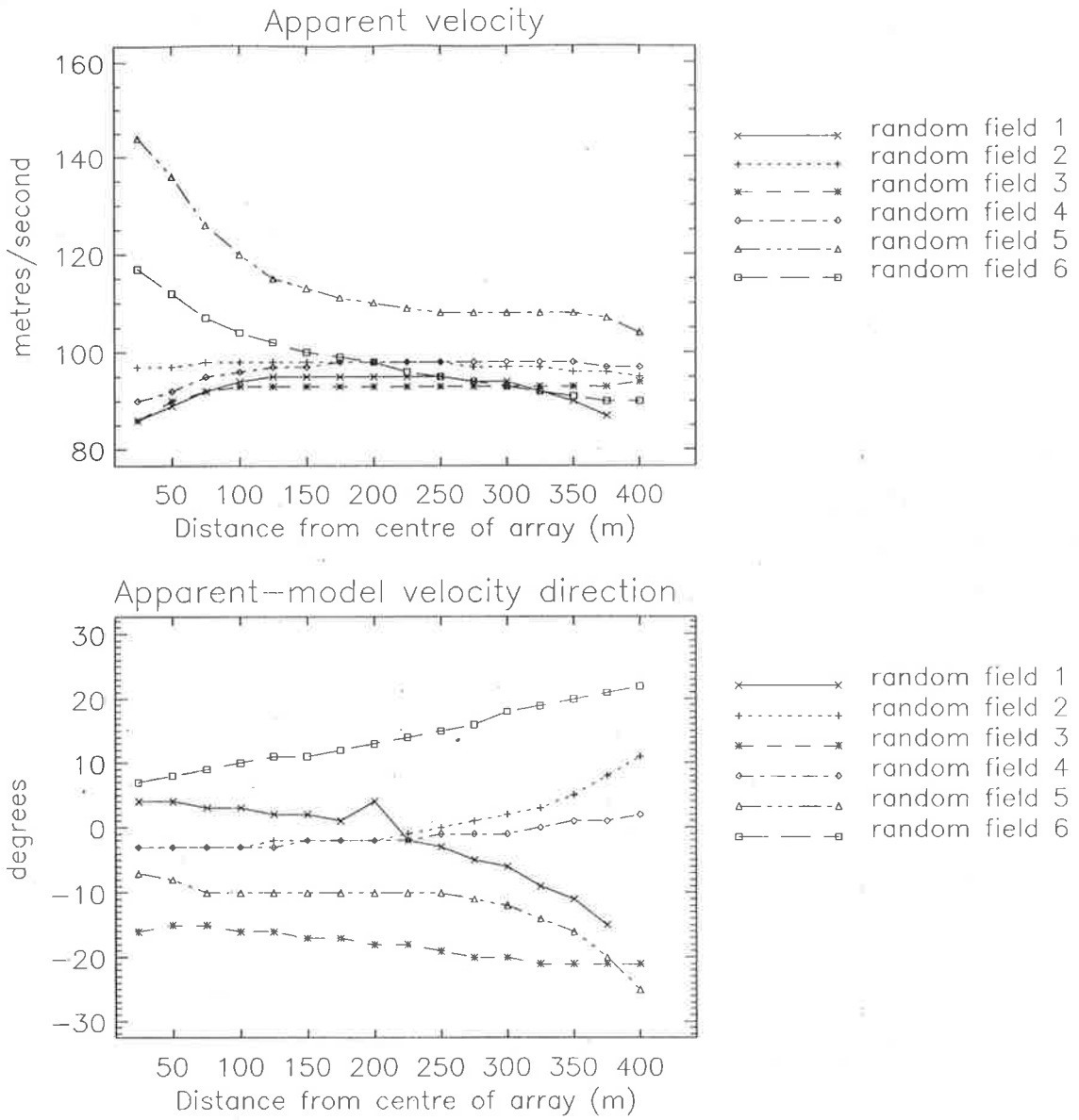

Figure 4.16: The modelled apparent velocity and apparent–model direction for six scattering grids as a function of antenna separation. The scattering grids are of 0.5 randomness and are moving at 100 ms^{-1} eastward.

4.3.2 Varying the model velocity

The next stage of modelling involved the use of six scattering fields all randomized by 0.5. The spaced–antenna simulations performed on these scattering fields again had various antenna separations, but in addition, the initial velocity of the scatterers was also varied from 50 ms^{-1} to 200 ms^{-1} in four 50 ms^{-1} steps. As before, the scatterers were not subject to any degree of turbulence. It was found that the general trends observed in the simulations were common for

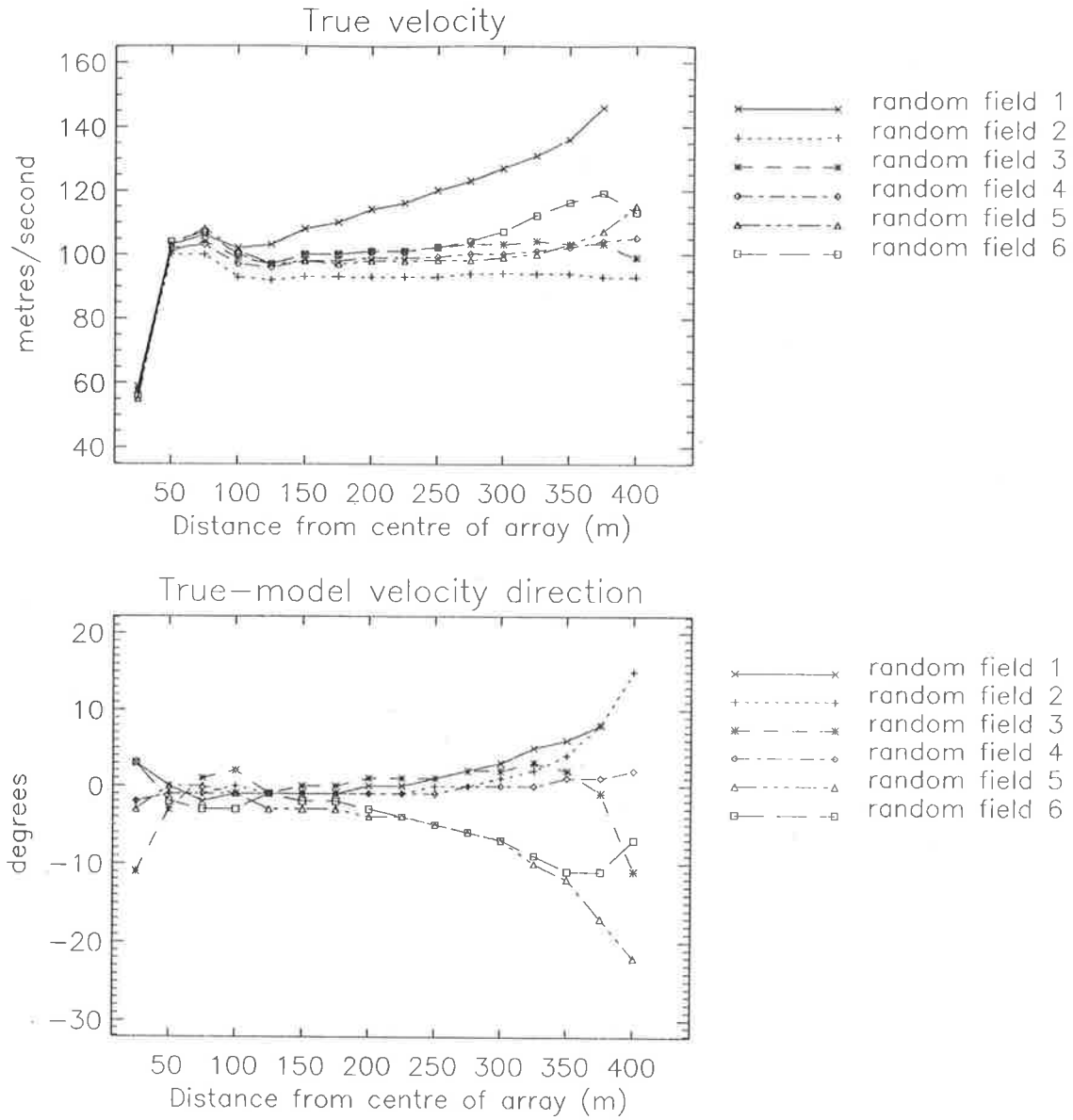

Figure 4.17: The modelled true velocity and true-model direction difference for six scattering grids as a function of antenna separation. The scattering grids are of 0.5 randomness and are moving at 100 ms^{-1} eastward.

the four different velocities, and for brevity only the results from the 100 ms^{-1} and 200 ms^{-1} velocity simulations are presented.

Figure 4.16 and 4.17 show V_{app}, θ_{app}, V_{true}, and θ_{true} respectively for a V_{mod} of 100 ms^{-1} eastward while figures 4.18 and 4.19 are the results for a model velocity of 200 ms^{-1} eastward.

For a V_{mod} of 100 ms^{-1}, V_{app} tends towards 100 ms^{-1} with increasing D_{ant} with the V_{app} measured using two of the grids being initially larger, and the other four smaller than V_{mod}. θ_{app} varies between -20°-10°. Calculations of V_{true} on the other hand are all underestimates of

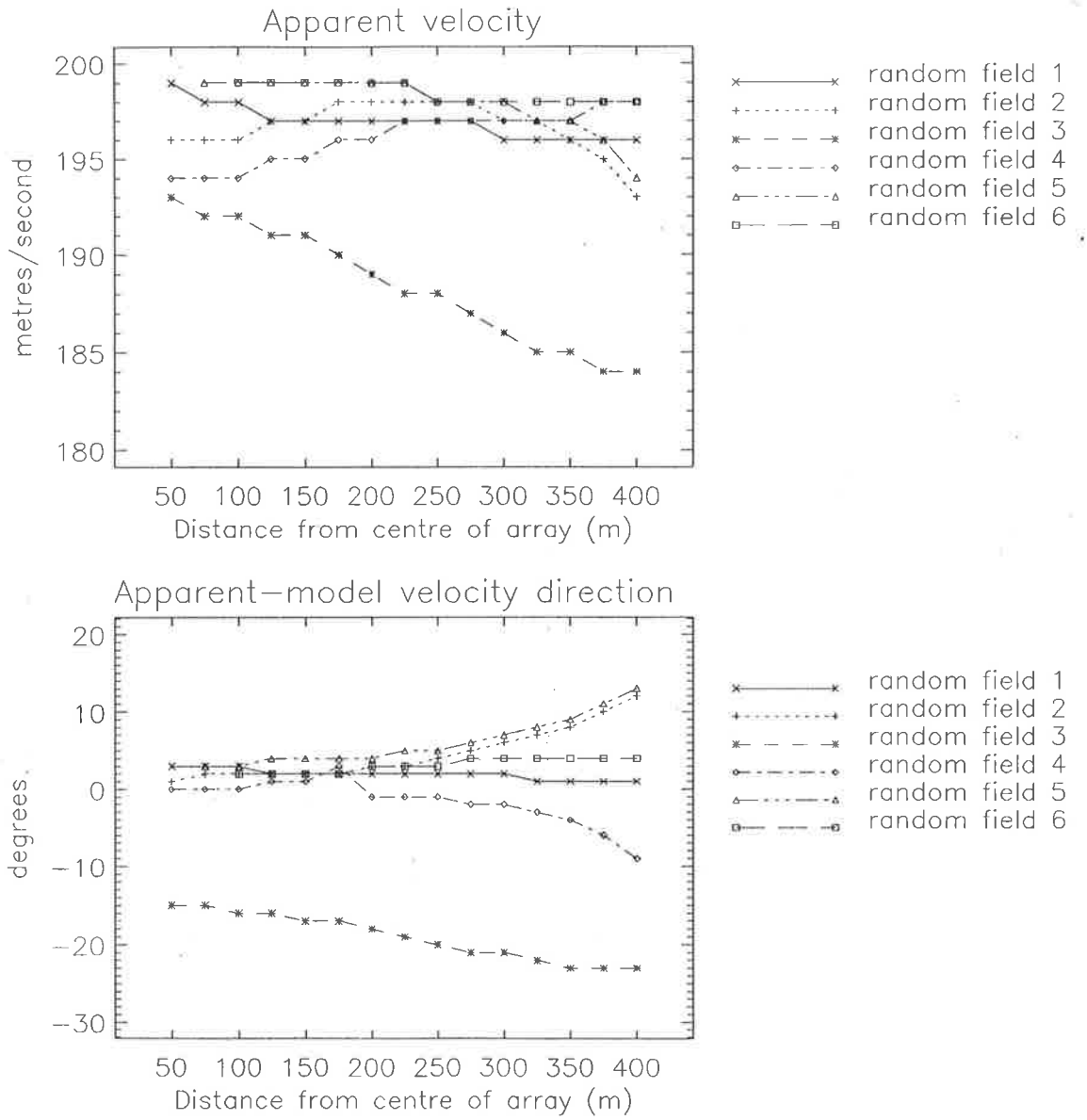

Figure 4.18: As for figure 4.16 but with the scattering fields all moving at 200 ms^{-1} eastwards.

V_{mod} for small D_{ant}, rapidly increase to be slightly greater than V_{mod} (~110 ms^{-1}) and then decrease to be within a few ms^{-1} of V_{mod} in all except data from one scattering grid in which V_{app} increased fairly linearly with D_{ant}. θ_{true} is also diverse at small D_{ant}, but this improves to be within a few degrees of θ_{mod} when D_{ant} is between 50–200 m.

Examining the case where V_{mod} is 200 ms^{-1} nearly all of the grids result in a slight underestimate for V_{app}. An exception occurs in one scattering field, which also shows the greatest deviation in θ_{app} from θ_{mod}. Otherwise, θ_{app} calculated from all the other scattering grids are

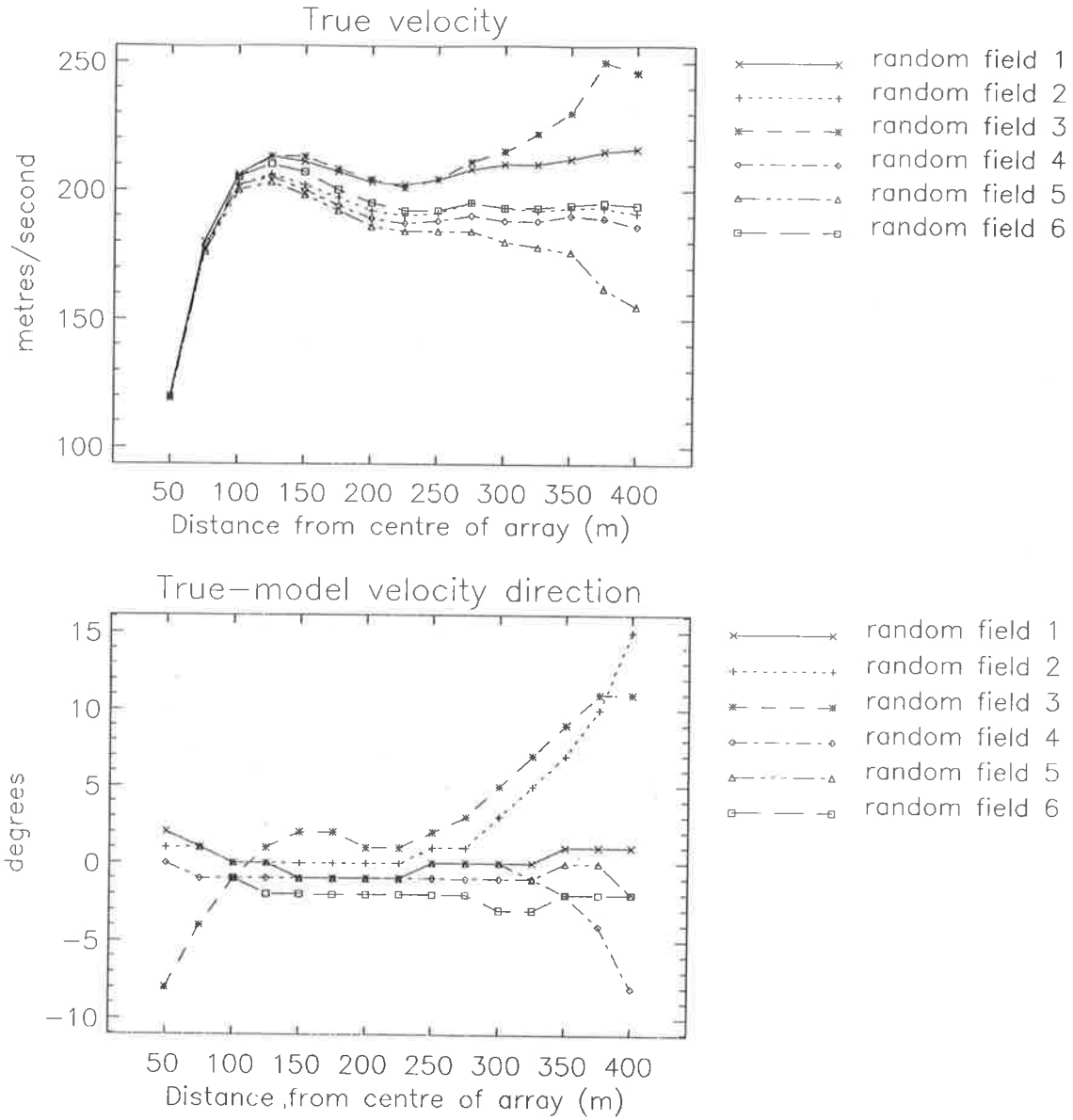

Figure 4.19: As for figure 4.17 but with the scattering fields all moving at 200 ms^{-1} eastwards.

very tightly clustered around 0°, and show no change as a function of D_{ant}. V_{true} at this velocity is very similar in behaviour to that at 100 ms^{-1} for small antenna separation up to about 150 m, where it is clearly underestimated. With increasing D_{ant}, V_{true} is "over-corrected", decreases and a finally exhibits a slow divergence for the various scattering fields. θ_{true} is again very close to θ_{mod}, the difference between the two being of the order of a few degrees only for smaller D_{ant} and slowly spreading as a function of increasing D_{ant}. A noticeable factor is that for D_{ant}< 125 m V_{true} measured from all the scattering grids are virtually identical, and show a sharp increase as a function of D_{ant}.

The optimum configuration for spaced–antennas has been reported to be of the order of one wavelength [see e.g. *Briggs & Vincent*, 1973] which in this model occurs when D_{ant} is close to 100 m. In the results presented above one can see that at that antenna separation both V_{true} and θ_{true} are not only just about equal to V_{mod} and θ_{mod}, they show the least spread in results between the different scattering fields.

Previous workers have found that the true velocity measured by the full correlation analysis tended to increase with an increasing receiving array geometry, approaching a limiting value, an effect known as the *triangle size effect* [*Golley & Rossiter*, 1970; *Chandra*, 1978]. These authors suggested that noise might be responsible for that effect since noise might have a greater reducing effect on the calculated velocities when the antennas are close to each other (large correlation). Another explanation, proposed by *Fedor & Plywaski* [1972], suggested antenna coupling as an explanation for the triangle size effect. These authors found both reductions and increases in V_{app} and V_{true} depending on the magnitude and phase of the coupling. The results presented here tend to suggest that perhaps one factor which might contribute to the triangle size effect, or even be responsible for it, is the full correlation analysis itself. That it depends on the analysis is supported by examining V_{true} as a function of D_{ant} when the model velocity was 100 and 200 ms^{-1}. The slow grid produces a correct velocity at an antenna spacing which is half that of the faster scattering grid. V_{true} in the case of the 100 ms^{-1} scattering grid reached 100 ms^{-1} at a D_{ant} of 50 m while V_{true} in the case of the scattering grid moving at 200 ms^{-1} reached that velocity when D_{ant} was 100 m, exactly double.

In the above simulations V_{app} was found to be relatively independent of D_{ant}, and fairly close to V_{mod}. The apparent velocity is calculated by the time–shifts between the cross–correlation maxima. Recent work by *May* [1988] has shown that the standard deviations in the calculations of the positions of the cross–correlation maxima depended on the fading time and record length. The fading time in these simulations was found to be remarkably constant and the record lengths were not varied. The calculations of V_{true} on the other hand depend on the determination of the time shift at which the auto–correlation has the same value as the cross–correlations at zero

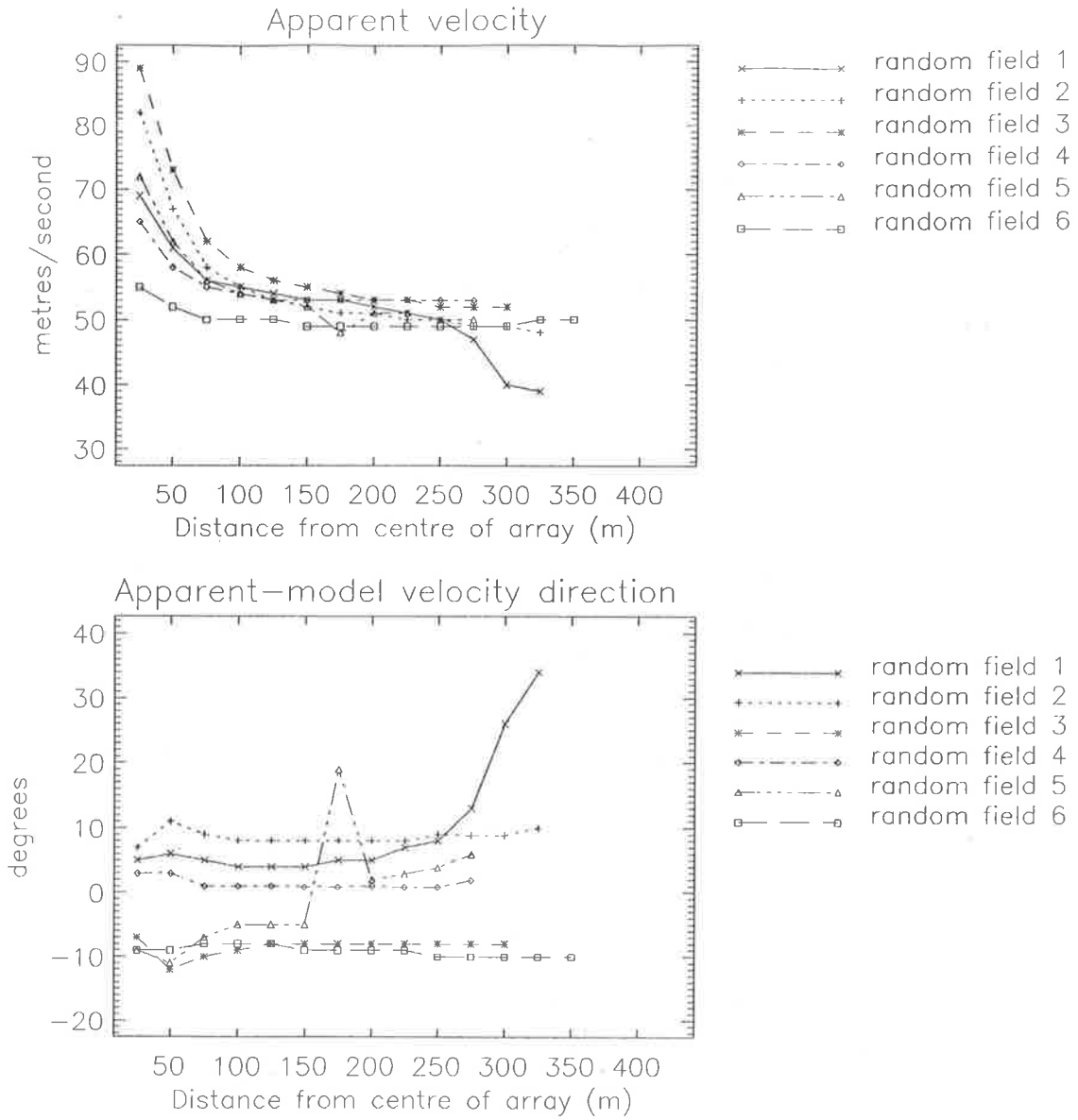

Figure 4.20: The modelled apparent velocity and apparent–model direction for six completely random scattering grids moving at 50 ms^{-1} eastward and with no turbulence.

shift. This would then suggest that large errors are found when these time–shifts are small.

4.3.3 Turbulent velocity fields

Having established that the spaced–antenna wind measurements technique using the full correlation analysis does extract a reasonable estimate of the velocity for larger antenna spacings and when the velocity is not extremely large, at least under conditions of no turbulence, various magnitudes of "turbulence" were introduced into the scattering fields. As mentioned before,

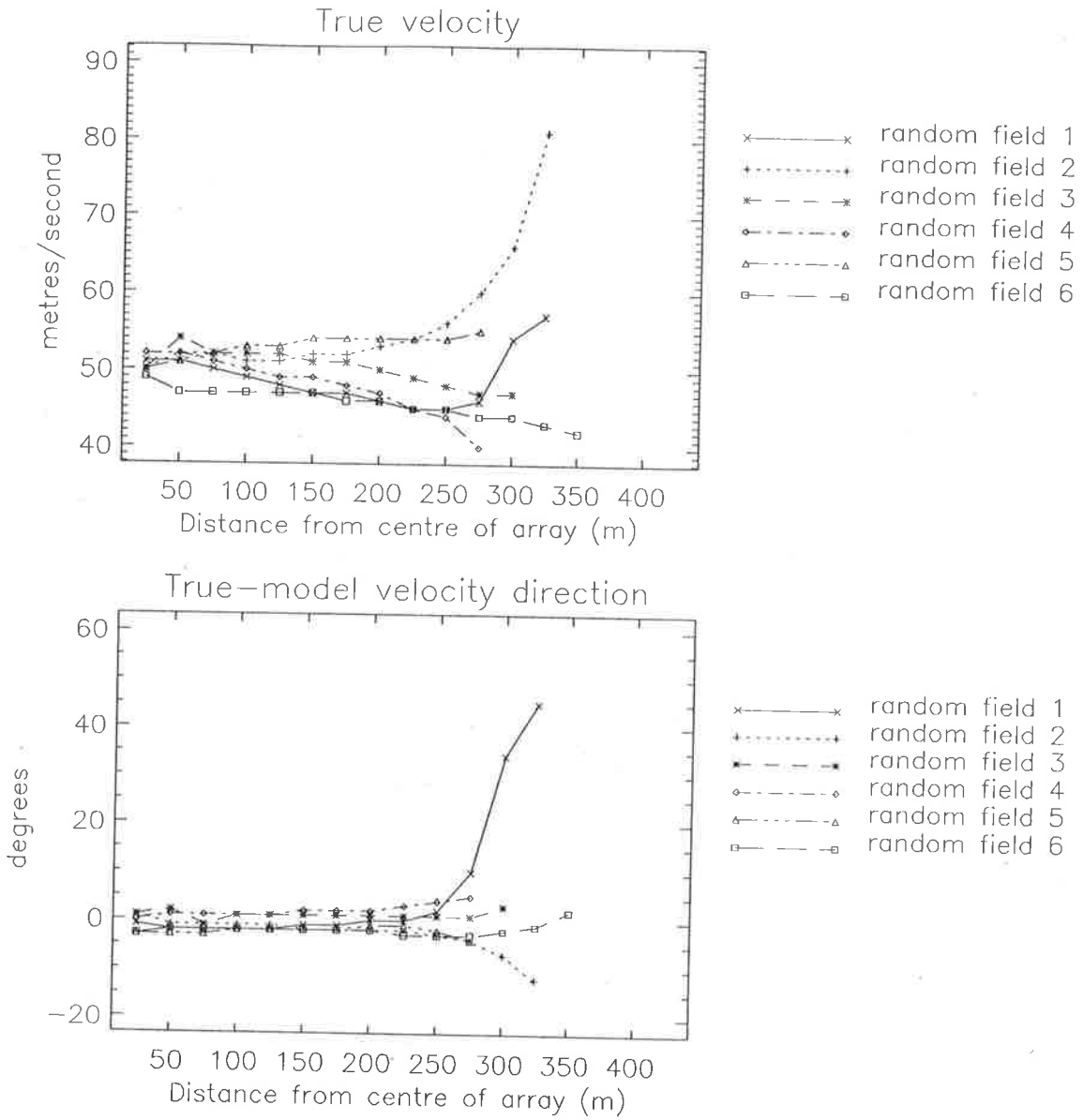

Figure 4.21: The modelled true velocity and true-model direction for six completely random scattering grids moving at 50 ms^{-1} eastward and with no turbulence.

the turbulence fields all consisted of vectors which vary both spatially and temporally. For the following set of data, the turbulent fields used were kept the same, and only the magnitude of the mean square turbulence contribution was varied. For these simulations new random scattering grids were also used, such that the randomness was total within the grid volume. The speed and direction of the grid was 50 ms^{-1} eastwards.

For a "control" we first present the simulation results where the scattering field has no turbulence added. Figure 4.20 shows V_{app} and θ_{app}, while figure 4.21 shows V_{true} and θ_{true}

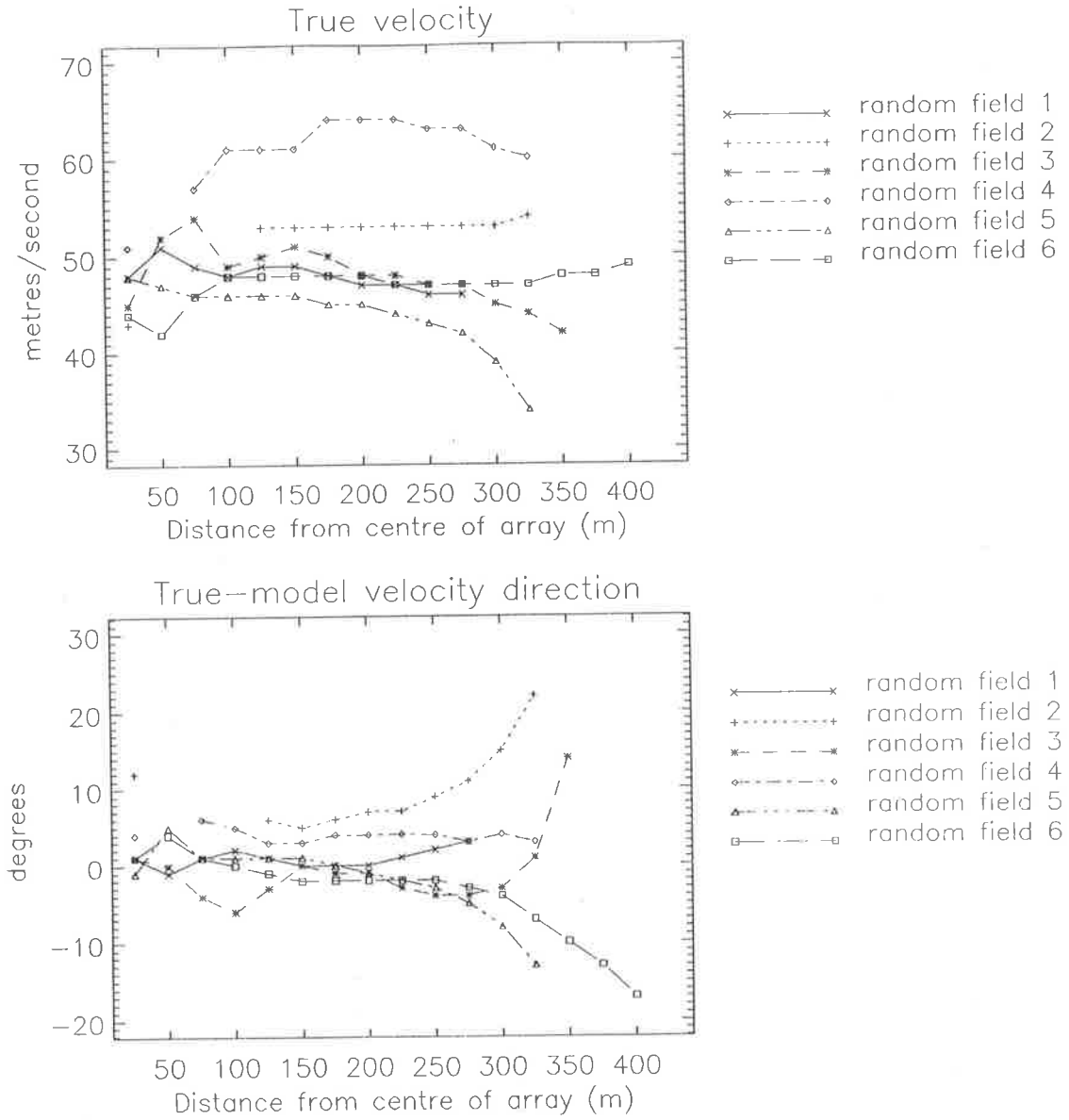

Figure 4.22: The modelled true velocity and true–model direction for six completely random scattering grids moving at 50 ms^{-1} eastward and with 1 $m^2s^{-2}$of turbulence.

for a group of six such non–turbulent fields. The apparent velocity is seen to decrease towards V_{mod} with increased antenna spacing, while θ_{app} varies to be within $\pm 10°$of $0°$. V_{true} varies by only a few ms^{-1}, and diverges with increasing antenna separation. However, θ_{true} is remarkably close to θ_{mod}, varying by only a few degrees, and much more accurate than θ_{app}.

Varying mean square turbulence magnitudes were now addedto this mean motion, with mean square fluctuating velocities ranging from 1 to 50 m^2s^{-2}. Initial inspection of V_{app} and θ_{app} showed not a large difference in their behaviour and mean values as a function of increased

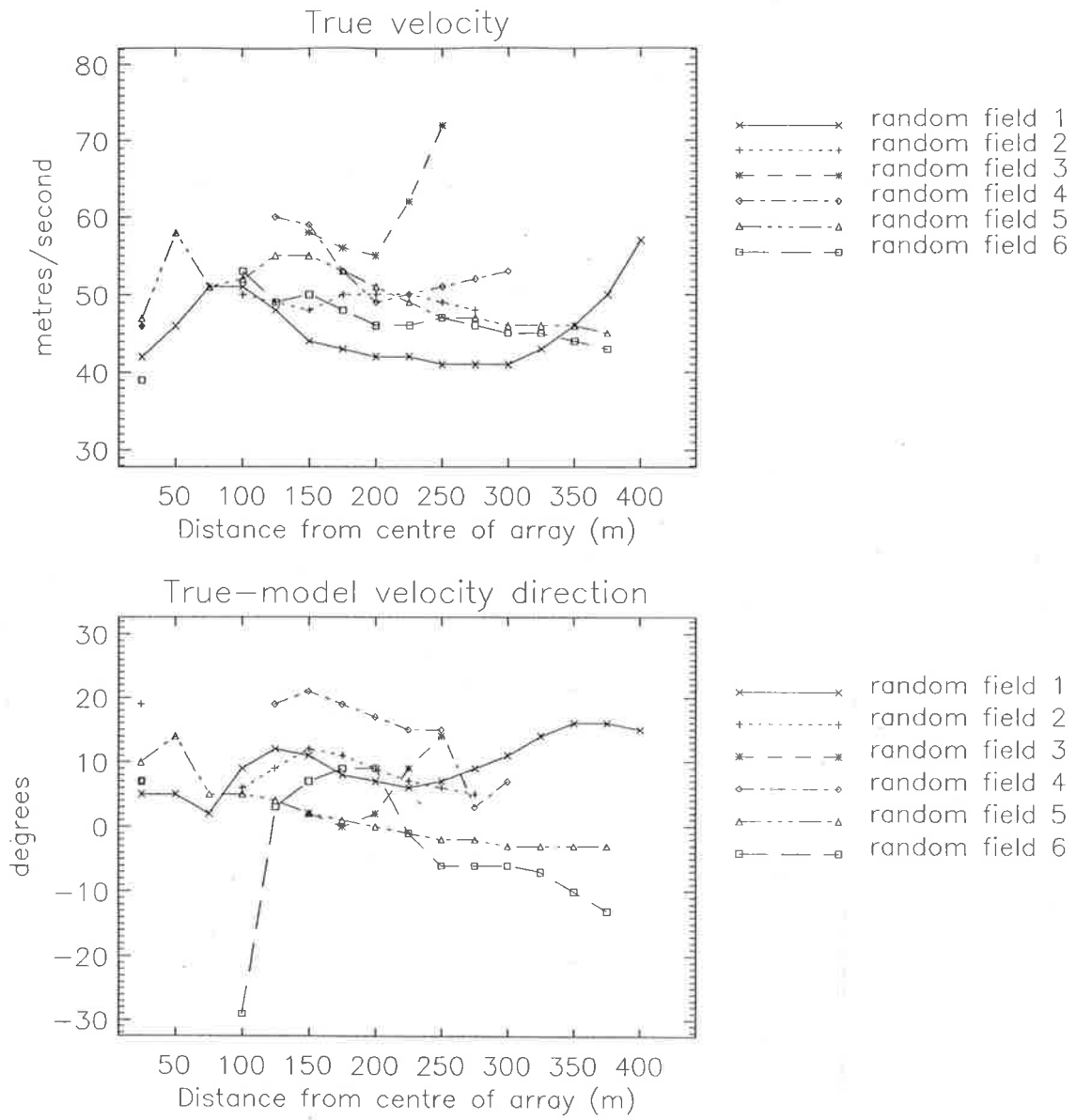

Figure 4.23: The modelled true velocity and true–model direction for six completely random scattering grids moving at 50 ms^{-1} eastward and with 5 $m^2s^{-2}$of turbulence.

turbulence. V_{app} generally decreased towards V_{mod} although the individual values as a function of antenna spacing became more ragged with increasing turbulence. θ_{app} also became more ragged, at times varying by up to $\pm 30°$. Therefore, only the V_{true} and θ_{true} results for varying degrees of turbulence as a function of antenna spacing will be presented here and even then, only for a few examples.

Figure 4.22 shows the spaced–antenna model results for V_{true} and θ_{true} with a mean square turbulence contribution of 1 m^2s^{-2}. Most of the V_{true} values vary by no more than 10 ms^{-1},

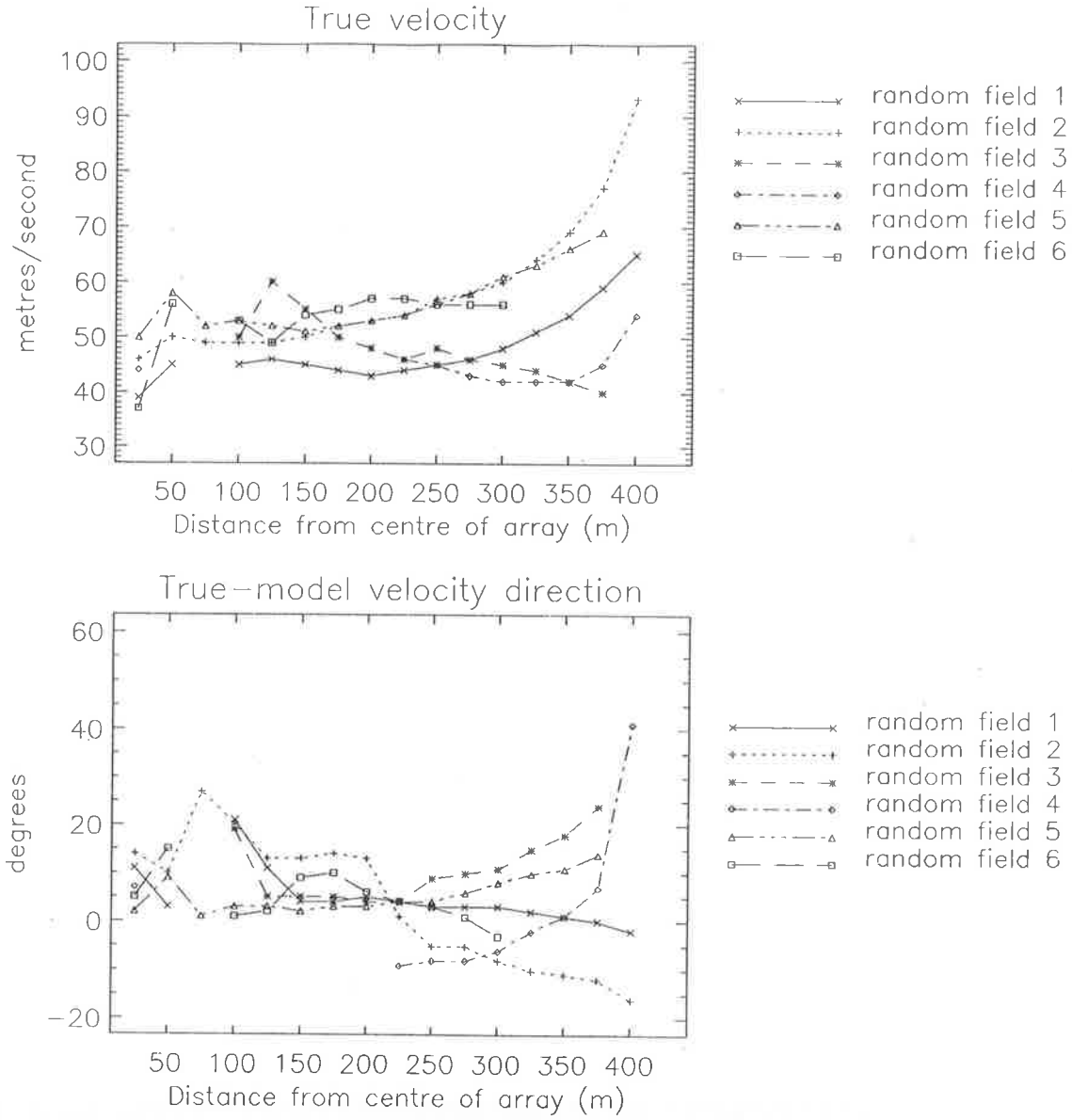

Figure 4.24: The modelled true velocity and true–model direction for six completely random scattering grids moving at 50 ms^{-1} eastward and with 10 $m^2s^{-2}$of turbulence.

although one grid is about 10 ms^{-1} "out". No triangle size effect is observed. θ_{true} is again quite close to θ_{mod}, although the accuracy decreases with increasing D_{ant}.

Figure 4.23 shows V_{true} and θ_{true} when the turbulence contribution is increased by 5 times (to 5 m^2s^{-2}). V_{true} again varies for the different scattering fields, but at most by 10 ms^{-1} from V_{mod}. However, a triangle size effect seems to have developed for all the scattering fields especially between about 100–200 metres where V_{true} seems to decrease within increasing D_{ant}. What is especially noticeable is the small spread of V_{true} at a D_{ant} of 100m, which is close to the

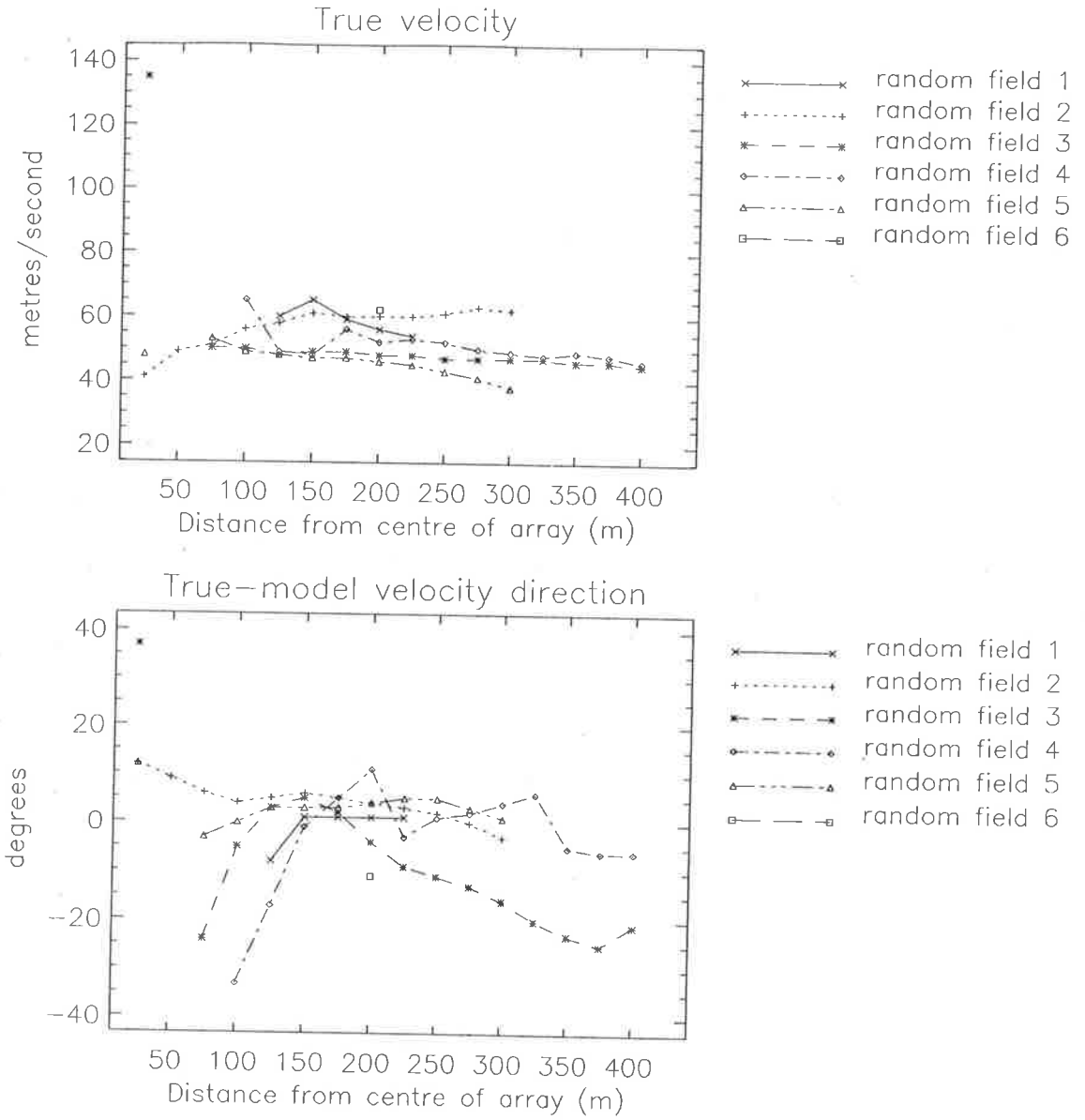

Figure 4.25: The modelled true velocity and true–model direction for six completely random scattering grids moving at 50 ms^{-1} eastward and with 50 $m^2s^{-2}$of turbulence.

one wavelength optimum separation. θ_{true} also varies slightly more with increased turbulence, and is also perhaps a function of D_{ant}.

Further increasing the level of turbulence to 10 m^2s^{-2}(figure 4.24), V_{true}as a function of D_{ant} and for all the different scattering fields, is initially underestimated, approaches V_{mod} and then varies (generally increases) as a function of D_{ant}. θ_{true} is not much different from that observed under conditions of less turbulence. At most it varies by 20°, although the average difference is perhaps 10°.

Finally, figure 4.25 shows the results where the turbulence contribution is of the same order as the mean velocity of the scattering grids (50 m^2s^{-2}). Here V_{true} is again close to V_{mod}, and is within a few ms^{-1} when D_{ant} is around 75 m. θ_{true} for small D_{ant} differs from θ_{mod} by up to 40°. However, this improves dramatically at an antenna spacing of about 150 m where θ_{true} is within 5° of θ_{mod}. With larger D_{ant} the difference starts to increase.

From the above simulations and others (not presented here) it can be concluded that for a number of varying turbulent scattering fields the mean velocity extracted is a very good estimate of the actual mean velocity of the scattering grids. At the optimum antenna spacing of 150 m, V_{true} is generally accurate to about ±10% while θ_{true} is accurate to within ±10°. The systematic bias is even less, so averaging of real data will tend to produce better estimates of the mean velocity.

4.3.4 Varying geometry of the receiving antennas

Equilateral triangle geometries

All of the above simulations involved an equilateral triangle receiving array geometry where one of the antennas was positioned exactly northward from the centre of the array. This meant that for an eastward wind, the time taken for the diffraction pattern to move across the receiver pairs was maximum. However, if the wind moves in such a direction such that its direction is perpendicular to a line joining one antenna pair, then the cross-correlation maxima will be extremely close and may lead to large errors. To see if this is a real effect the direction of the scattering grid motions was changed so as to be northward.

Figure 4.26 shows V_{true} and θ_{true} for six random grid fields as a function of D_{ant}, when V_{mod} was 100 ms^{-1} and θ_{mod} was northward. Figure 4.27 shows V_{true} and θ_{true} also for six random fields but when V_{mod} was 100 ms^{-1} at 64° (clockwise from north). One can see that V_{true} and θ_{true} in both figures are very similar to those exhibited in figure 4.17 where the scattering grids are moving eastward (including the triangle size effect). V_{true} approaches V_{mod} at small D_{ant}, slightly over–estimates, decreases, and then continues to increase with increasing D_{ant}. θ_{true}

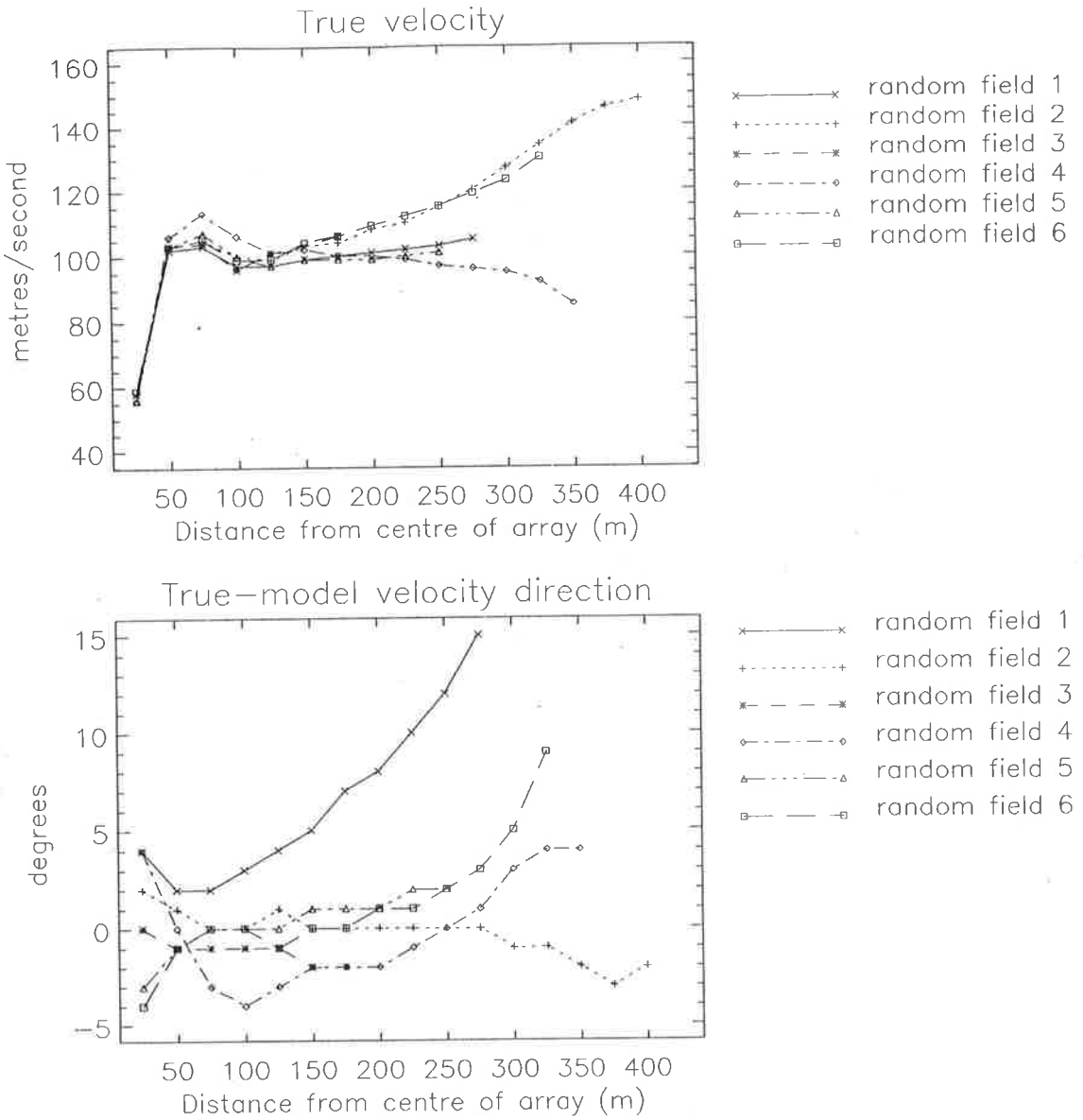

Figure 4.26: The modelled true velocity and true–model direction difference for six totally random scattering grids as a function of antenna separation, and moving at 100 ms^{-1} northward.

is within only a few degrees of θ_{mod} especially when one looks at the average, diverging only when D_{ant} is greater than 250 m.

The above and other simulation results (not presented here) supports the notion that the antenna orientation seems to have no noticeable effect on the extraction of the true velocity by the full–correlation analysis – at least for the case of an equilateral triangle.

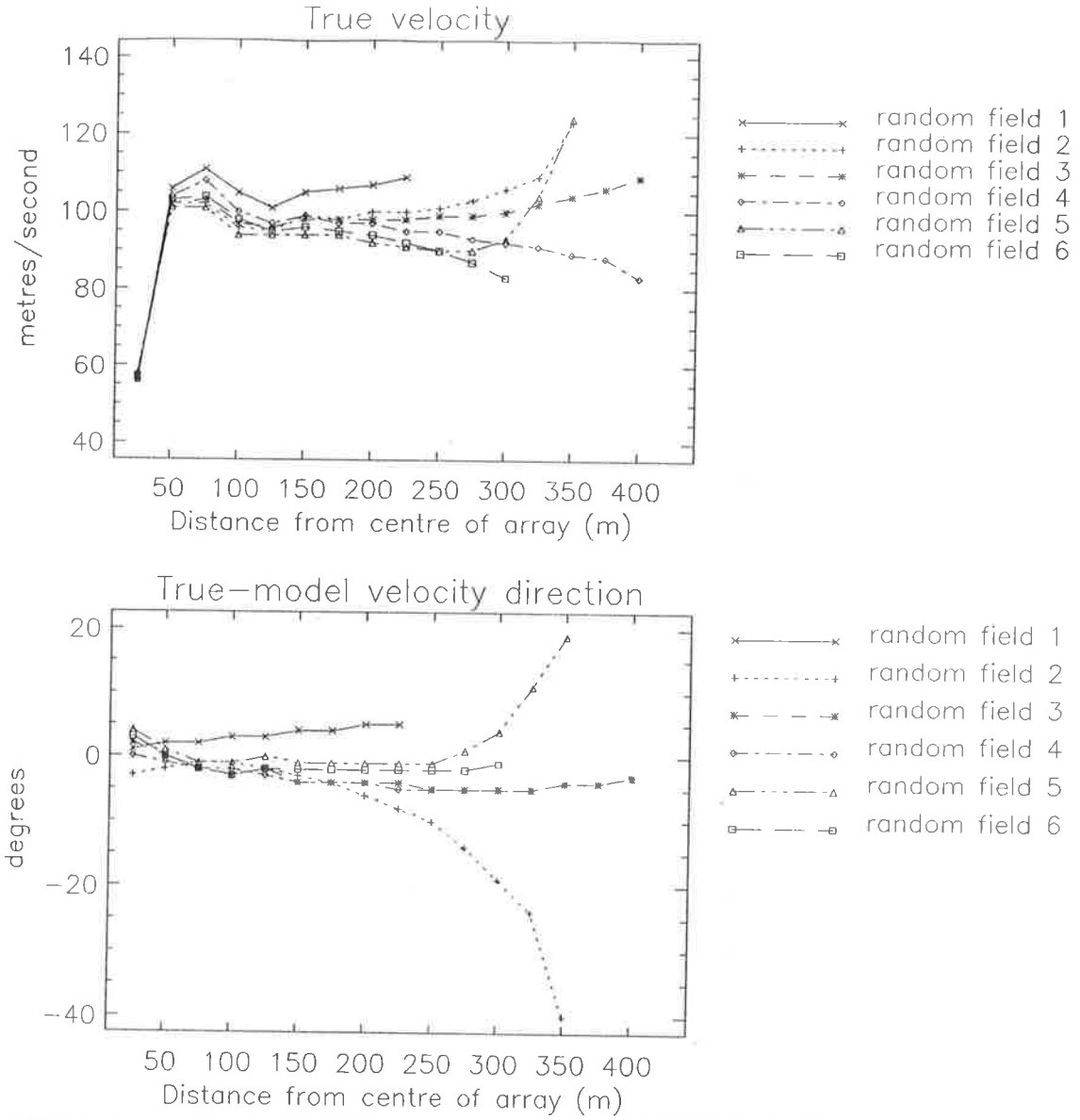

Figure 4.27: The modelled true velocity and true–model direction difference for six totally random scattering grids as a function of antenna separation, and moving at 100 ms^{-1} 64° clockwise from northward.

Isosceles triangle receiving antenna geometry

A bias initially found by *Beynon & Wright* [1969] and later by *Golley & Rossiter* [1970] showed that for a non–equilateral receiving array there is a preference for the ground diffraction patterns to be aligned along the longest side of the receiving array. It has recently been mathematically shown that this bias could be due to noise [*Meek*, 1990]. In this section I investigate the potential effect of various antenna array geometries on the full correlation analysis parameters, and see

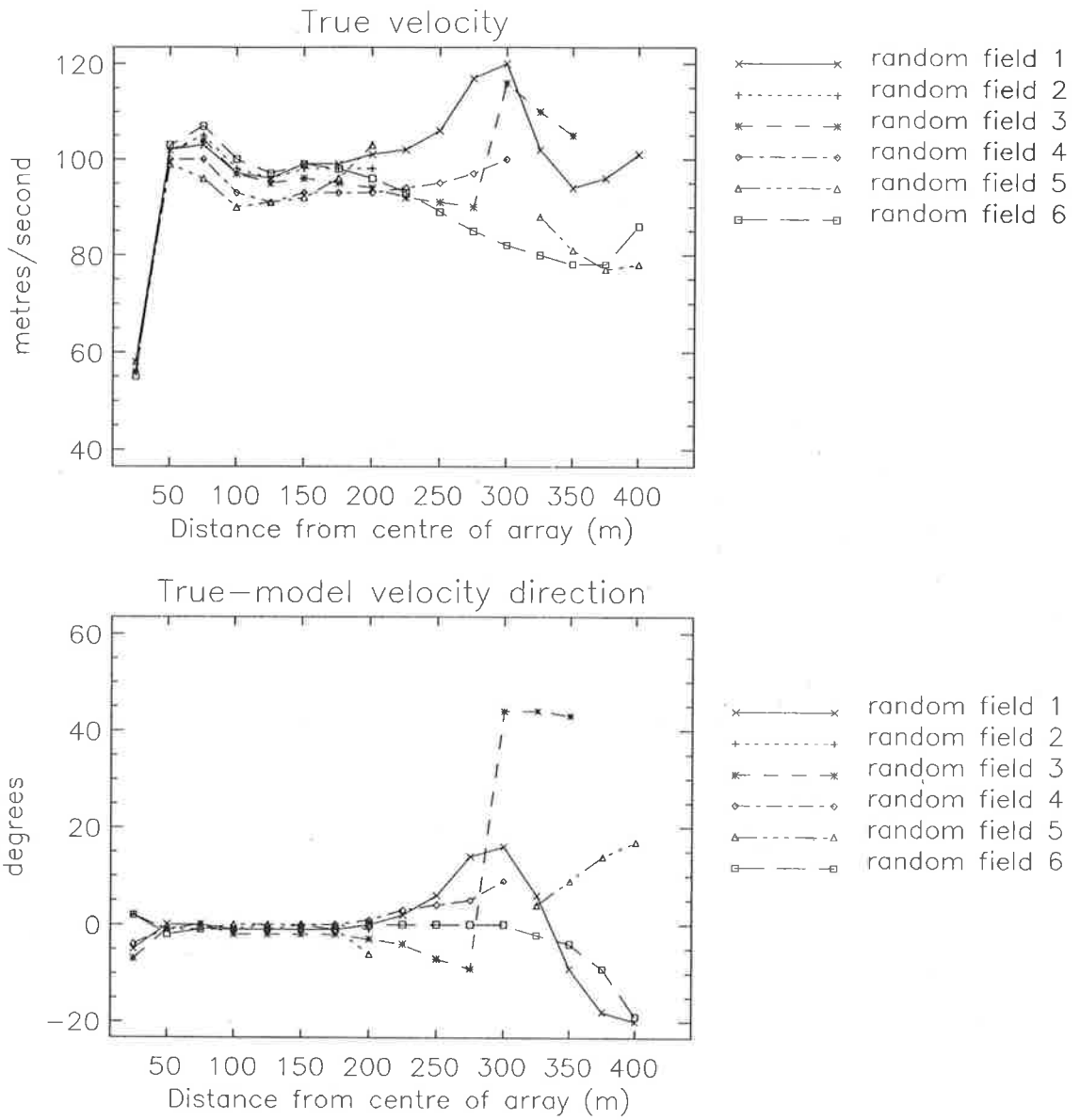

Figure 4.28: The modelled true velocity and true–model direction for six totally random scattering grids using a non–equilateral triangle receiving array geometry. The distance from the centre of the receiving array to the northward antenna was twice that to the other two. The bottom axis is the distance to the two unchanged antennas, i.e. the distance to the northward antenna is double that shown.

if the pattern alignment is affected by the receiving antenna array geometry.

The shape of the receiving–array antenna triangle used up till now has been equilateral. The ground diffraction pattern orientation characteristics for such a receiving array arrangement showed no preferential angle. Over a number of simulations, it was found that a number of different pattern angles were obtained with no observable bias in the pattern angle distribution. In addition, the pattern angle was not affected to any large degree by the antenna separation.

The geometry of the receiving array was then changed from an equilateral one to an isosceles triangle, so that the distance from the centre of the array to the northward antenna was twice that to the other two. The modelled true velocity and direction calculated using this triangle geometry and six random grids is shown in figure 4.28. The model velocity was 100 ms^{-1} eastwards. If the pattern was to be aligned along the longer side of the receiving antenna array triangle, then it should be preferentially oriented towards the north–south direction. However, no preferential distribution was observed and V_{true} and θ_{true} were not any different to those obtained by the equilateral triangle orientation. Thus any "preferred alignment" is not intrinsic to the full–correlation analysis, and other causes, e.g. noise as suggested by *Meek* [1990], must contribute to the experimental observations of bias.

The next triangle geometry involved was also an isosceles one, but one where the ratio of the distances from the centre to the northwards antennas was 1:2/3 that from the centre to the other two antennas. The results of such a triangular arrangement for V_{true} and θ_{true} are shown in figure 4.29. This result was one of the more unusual ones found, for V_{true} determined from all six different scattering fields were almost exactly the same. In addition a triangle size effect is observed extending to 150 m. This is the distance from the centre of the array to the northward antenna, whilst the distance between the two closer antennas was 2/3 that. This implies that all of the antennas should be at least one wavelength apart to avoid the triangle size effect.

Scalene triangle receiving antenna geometry

Finally, the last triangular shape tested for was a scalene triangle where the northward antenna geometry was the same as it was for the equilateral triangle, i.e. extending northward in 25 m steps. For the other two antennas, the x and y co-ordinates for the one initially positioned 120° clockwise were multiplied by 0.5, and for the one initially positioned 120° anti–clockwise by 1.5.

Figure 4.30 shows V_{true} and θ_{true} for such an antenna arrangement. Again, a triangle size effect is observed until the antenna spacing is of the order of one wavelength. For larger D_{ant},

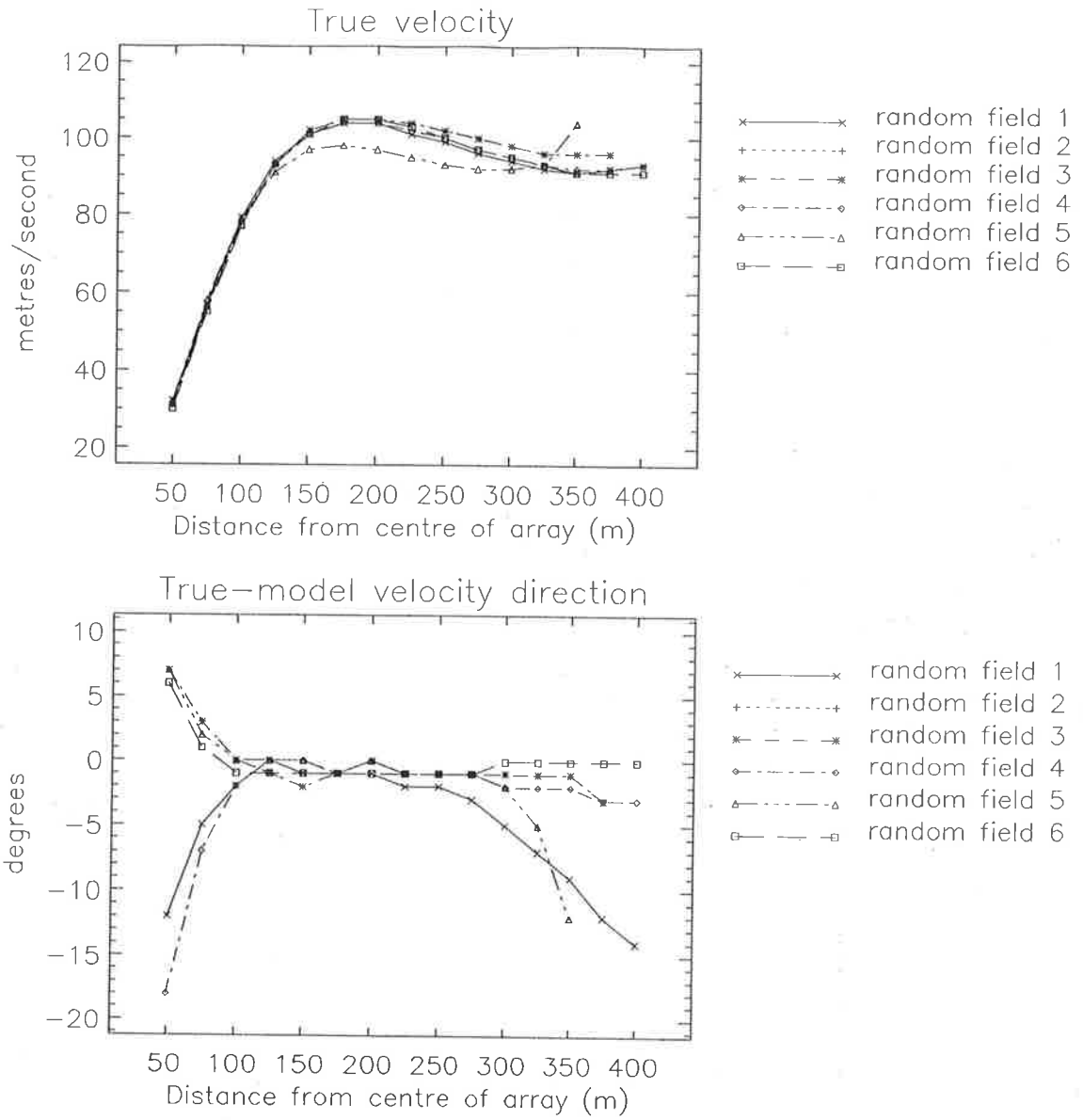

Figure 4.29: The modelled true velocity and true–model direction for six random scattering grids for an isosceles triangle receiving antenna array. The distance from the centre of the receiving array to the northward antenna was twice that to the other two (1:2/3). The bottom axis is the distance to the two unchanged antennas, i.e. the distance to the northward antenna is double that shown.

V_{true} is underestimated and diverges for the six different scattering fields. θ_{true} also shows a triangle size effect where the difference between it and θ_{mod} is only of the order of $\pm$ a few degrees at D_{ant} of $\sim$100 m. Larger D_{ant} also leads to greater dispersion for the various scattering grids.

It must therefore be concluded that the shape and relative orientation of the receiving array geometry has no significant effect on the determination of V_{true} and θ_{true}. As well, the triangle

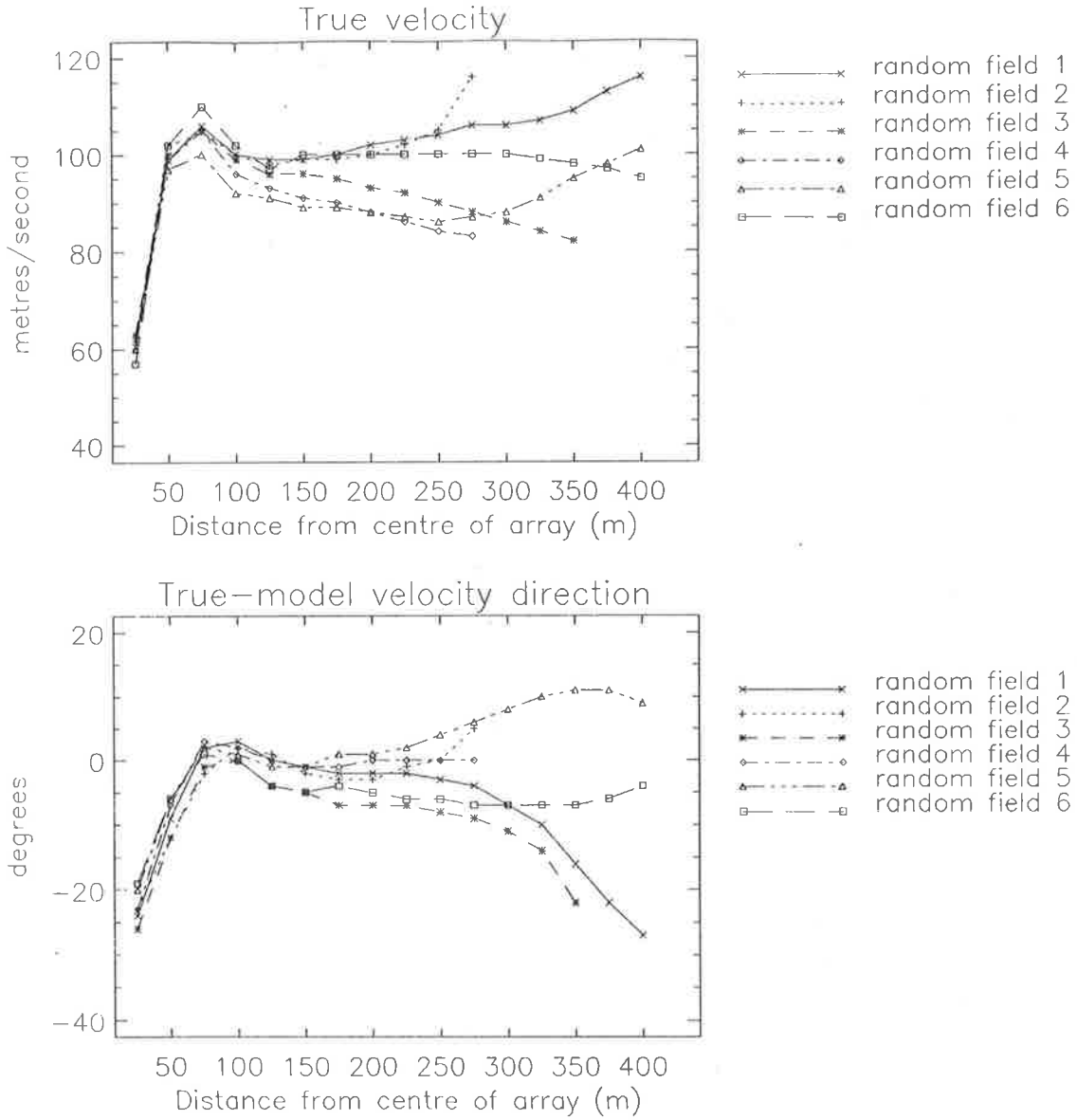

Figure 4.30: The modelled true velocity and true-model direction for six random scattering grids for a scalene triangle receiving antenna array. The distance from the centre of the receiving array to the northward antenna was twice that to the other two (1:2/3). The bottom axis is the distance to the two unchanged antennas, i.e. the distance to the northward antenna is double that shown.

size effect is also found in arrays where the antenna geometry for any one pair of receiving antennas is less than one wavelength.

Varying the polar diagram

Up till now, the simulations carried out all used a 9° polar diagram for the transmitting and receiving system. Under such conditions, approximately 50 scatterers are contained in the

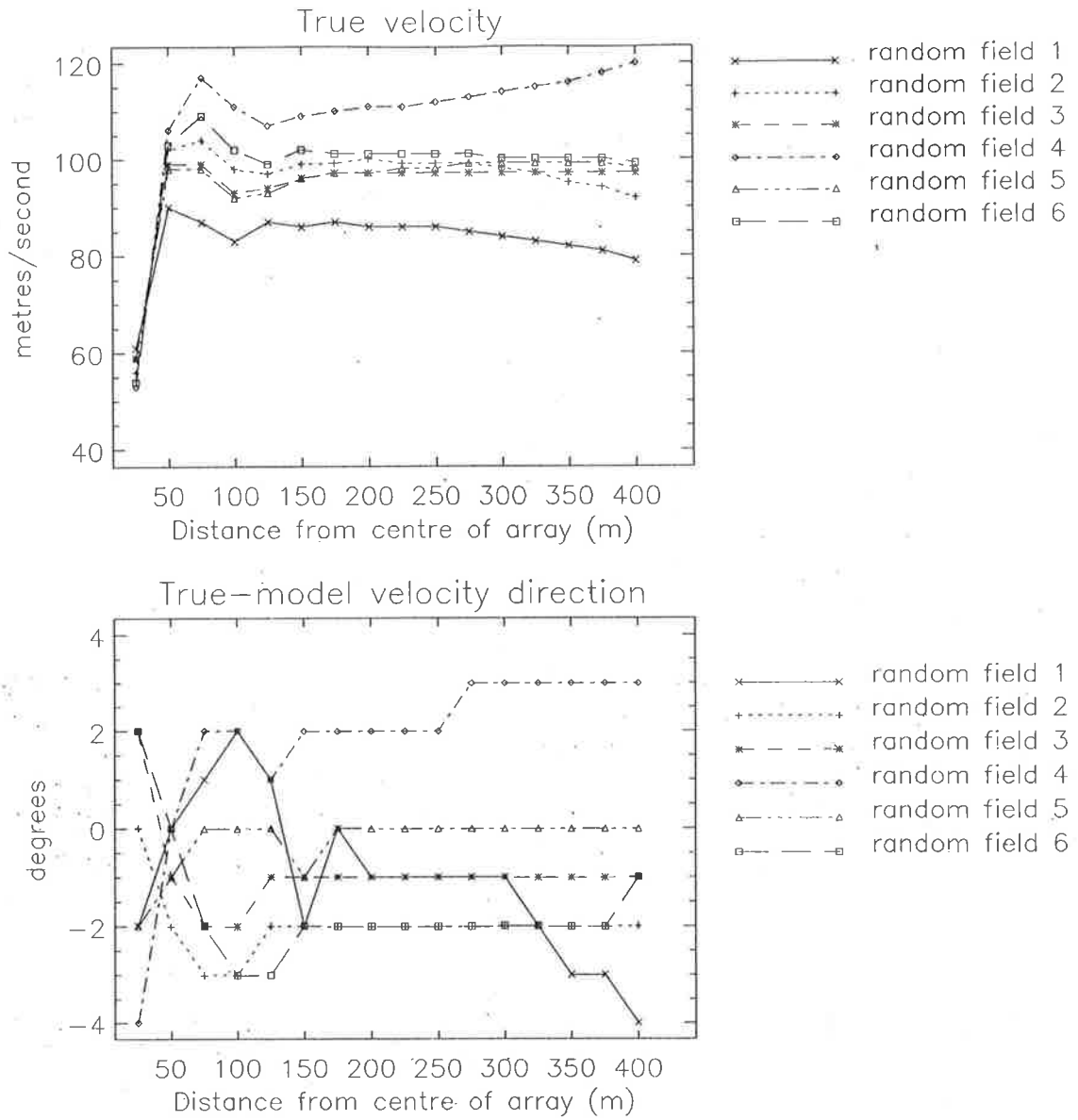

Figure 4.31: The modelled true velocity and true–model direction for six random scattering grids for a 4.5° total polar diagram (transmitting and receiving system).

radar volume at any one time. It has been shown that the spatial correlation as a function of receiver separation depends on the polar diagram of the transmitting and receiving arrays (see the following chapter) [*Briggs & Vincent*, 1973; corrected by *Briggs*,1991]. It predicts that for a polar diagram of about 10° the spatial correlation function should be ≈350 m, for 20° it should be around 200 m, and around 130 m for a 30°polar diagram. In these simulations it was found that the spatial ground diffraction pattern was larger than this by about 20% (an improvement on the original calculations of *Briggs & Vincent*, 1973), being of the order of 220–240 m for a

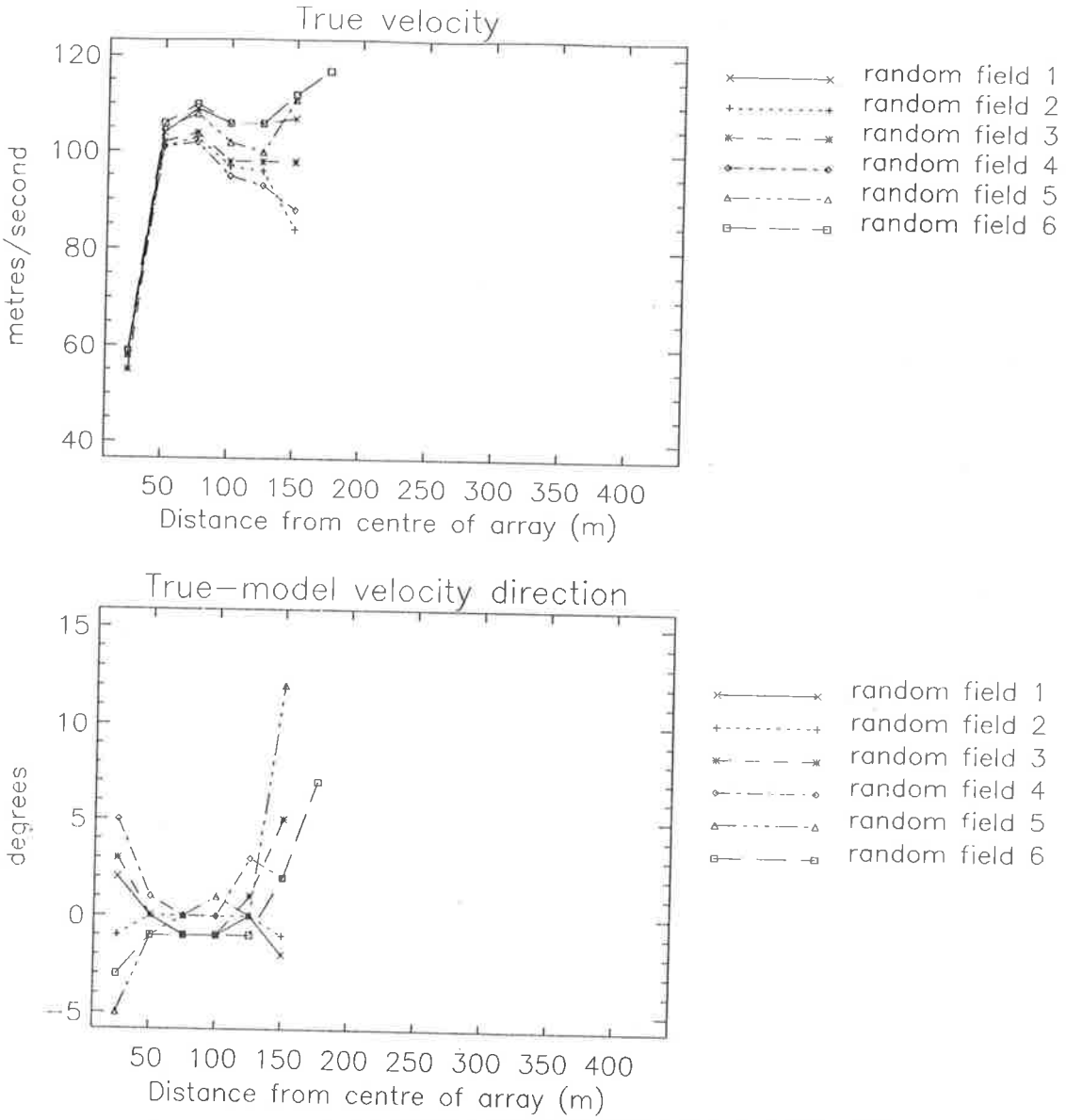

Figure 4.32: The modelled true velocity and true–model direction for six random scattering grids for a 30° total polar diagram (transmitting and receiving system).

20° polar diagram, and around 800 m for a 4.5° polar diagram. At this stage the reason for the difference between the theory and the above simulations is unknown. However, it does not seem to affect the accuracy of V_{true} and θ_{true}. In addition to a change in the size of the ground diffraction pattern with changing polar diagram one also finds that the fading time decreases with increasing polar diagrams. This is to be expected since the fading time is the time which defines the size of the ground diffraction pattern. Nevertheless, calculations of V_{true} and θ_{true} are still very close to V_{mod} and θ_{mod}. Figures 4.31 and 4.32 are plots of V_{true} and θ_{true} for a

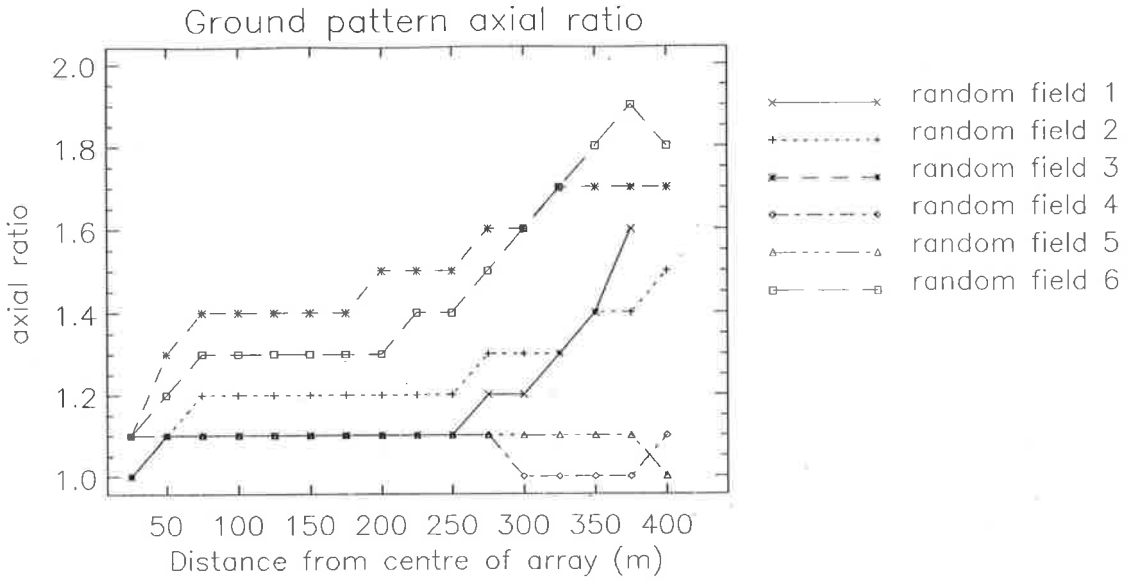

Figure 4.33: The ground pattern axial ratio as a function of antenna spacing.

transmitting/receiving polar diagrams of 4.5° and 30° respectively. Other simulations for other polar diagrams were also performed and exhibited the same trends.

Comparing the two diagrams shows that the spread of V_{true} around a mean of about 100 ms^{-1} is larger for the smaller polar diagram. In addition, as the polar diagram increases, the antenna spacing at which the data is accepted decreases. This was also observed in other examples of larger polar diagrams. Examination of the raw spaced antenna output file shows that for larger polar diagrams the full correlation analysis rejects data due to imaginary V_c and due to inaccurate cross–correlation peaks (t_{max}). At the same time θ_{true} is extremely accurate for the 4.5° polar diagram, varying only by several degrees. θ_{true} for the 30° polar diagram is also very accurate, but only when the antenna spacing is between 50–100 m (the optimum antenna spacing). At smaller and larger antenna spacings θ_{true} diverges by more than 5°.

4.3.5 The behaviour of other full correlation analysis parameters

Most of the uncertainty of the spaced–antenna method has been based upon its ability to measure the mean motion of the neutral wind. However, the other variables calculated by the

full correlation analysis can be used, and have been used extensively in this thesis to examine other properties of the partial–reflection radar scatterers. It is therefore interesting to compare the behaviour of some of these other parameters as calculated by the model.

As briefly mentioned earlier, the ground diffraction pattern orientation showed no preferential orientation that could be related to the longer side of a non–equilateral triangle or to the mean wind direction. However, no mention has been made of the pattern axial ratio. Figure 4.33 shows the ground pattern axial ratio as a function of antenna separation for a 100 ms^{-1} eastward wind and a 0.5 randomized grid. The mean axial ratio is seen to increase by about 0.2 to be about 1.2 at an antenna spacing of 100 m. It then remains essentially constant up to a D_{ant} of 200 m and then generally increases to a mean value of about 1.4, although for a couple of the grids it remains just barely above 1.0. This example is typical of the behaviour of the axial ratio, for various receiving array geometries and for turbulent fields.

Examining the fading time one finds that it does not change as a function of antenna separation, although it is inversely dependent on the mean speed of the scattering grid, i.e. decreases with increasing wind. It is also dependent, as noticed previously, on the size of the polar diagram of the transmitting and receiving antennas.

4.4 Conclusion

The spaced–antenna full correlation analysis simulations undertaken herein have shown that the true velocity and direction extracted by the full correlation analysis approximates the actual velocity very closely with an error usually less than $\pm 10\%$. This is true for various scattering grid randomizations, receiving antenna array geometry and orientation, and for varying polar diagrams (both transmitting and receiving arrays). It is also true for various magnitudes of turbulence, where the spaced antenna technique still performs well. It was found however, that the extracted velocity and direction do depend on the antenna separation. A triangle size effect is observed to occur up until, and even beyond the optimum antenna spacing ($\approx$ one wavelength).

At times the error in the individual measurements of V_{true} and θ_{true} are up to 20% (worst case). However, when a mean is constructed from the six different scattering grids presented in each simulation, V_{true} and θ_{true} are more accurate and very close in value and direction to V_{mod} and θ_{mod}.

In addition to the velocity, the simulations have shown that the pattern axial ratio is generally not greater than 1.3–1.4. This would be expected, since the scatterers are point scatterers. This fact is important for in the analysis of real data (done in the following chapters), it means that any observations of the axial ratio in excess of 1.4 can then safely be interpreted to imply that the scatterers possess a two–dimensionality.

The model has been used to examine and to support the feasibility of the spaced–antenna system under different conditions of velocity, turbulence, array geometry, and polar diagram size. This is however by no means the total extent of the model flexibility. Other tests performed could include the addition of various vertical velcoties and vertical turbulences. The scattering grids could also be changed to include propagating gravity waves. Various different types of scatteres within the scatter volume could also be incorporated and moved at different velocities.

In general, it can be concluded that individual measurements of the velocity field and other parameters should be interpreted with some care, although they are still a very good measurement. However, longer–term averages of data collected by the spaced–antenna systems (even hourly) should provide excellent mean winds and other full correlation analysis parameters.

Chapter 5

The nature of atmospheric scatterers

5.1 Introduction

Radar partial reflections are caused by refractive index irregularities which arise due to pressure, temperature and humidity fluctuations in the troposphere and stratosphere, and electron density fluctuations in the mesosphere. [*Röttger*, 1980a; *Gage & Balsley*, 1980; *Hocking*, 1985]. Mesospheric and lower thermospheric (60-100km) electron density irregularities can be caused by several different mechanisms [*Harper & Gordon*, 1980; *Gage & Balsley*, 1980; *Reid*, 1988], the main ones being turbulent scatter, Fresnel (partial) reflection, and thermal scatter. Turbulent scatter arises from spatial variations in the refractive index of half the probing wavelength in the direction of propagation, and occurs as a result of a turbulent process. Fresnel reflection occurs from horizontally stratified and stable regions which cover at least one Fresnel zone $(\lambda z)^{\frac{1}{2}}$ in horizontal extent, and with a vertical extent no greater than $\frac{\lambda}{4}$ where λ is the wavelength of the radar, and z is the height of the scatterer. Thermal scatter occurs due to fluctuations of electron density caused by thermal locomotion of ions and electrons. Also known as incoherent and Thompson scatter, thermal scatter at heights greater than 50 km is most important at frequencies greater than 100 MHz. Fresnel and turbulent fluctuations suffer major viscosity

damping at these scales, and hence incoherent scatter does not play a part in MF mesospheric scattering studies.

The physical shapes, and causes of these partial reflection scatterers is, as yet, an unresolved question. A better understanding of them will not only improve our ability to make and have faith in routine measurements such as the wind velocity, but it will also aid in the understanding of the dynamical processes which cause them in the first place. This chapter will review the proposed models which have been put forward to explain the experimental observations. We will also deal with the groundwork of the methods that are used in this thesis to determine the structure of these scatterers.

5.2 Structure of scatterers

Various models, ranging from stratified mirror–like layers, to individual scattering "disks", have been proposed to explain the experimental observations of partial reflection scatter. Any models proposed must, however, satisfy two criteria. Firstly, there must be a physical way to promote and sustain the shape of these scatterers, and secondly, the conditions for this to occur must be a common atmospheric feature, i.e., not a freak of nature. For radar partial reflections which occur when the antenna beam is pointed in a non-vertical direction (> a few degrees), the mechanism thought to be causing the scatter is turbulence embedded in a gradient of potential refractive index. This was proposed by *Booker & Gordon* [1950] to explain tropospheric over-the-horizon propagation of radio waves, and later by *Woodman & Guillen* [1974] for stratospheric and mesospheric echoes.

The shapes of the scatterers which are responsible for vertically pointing radar beams are still not clear. The partial radar reflections from these scatterers have shown that the back–scattered power decreases as a function of the off–zenith angle. This was shown for the troposphere and stratosphere by, (for example) *Gage & Green* [1978] and by *Röttger & Liu* [1978], and by *Fukao et. al.* [1979] for the mesosphere at VHF, although it has been known for MF studies since the 1970's. Commonly known as the *aspect sensitivity*, the rate of decrease of power as a function of

angle is often parameterized by a quantity θ_s. Small values of θ_s imply the existence of specular scatterers. A fairly common occurrence in atmospheric observations, specular reflectors have been found in numerous other studies [see e.g. *Röttger & Vincent*, 1978; *Röttger et al.*, 1981; *Sato et. al.*, 1985; *Waterman et al.*, 1985; *Hocking et. al.*, 1986; *Tsuda et. al.*, 1986; *Hocking*, 1989; *Lesicar and Hocking*, 1992]. A number of scatterer models which incorporate the observed aspect sensitivity have been proposed. Although quite varied, they can be grouped into two distinct camps [*e.g. Lindner*, 1975 a,b; *Briggs & Vincent*, 1973; *Röttger & Liu*, 1978; *Gage & Green*, 1978; *Hocking*, 1979; *Fukao et al.*, 1980a,b; *Röttger*, 1980b; *Gage et al.*, 1981; *Doviak & Zrnić*, 1984; *Waterman et al.*, 1985; *Hocking*, 1989; *Woodman & Chu*, 1989].

The first type of model proposes individual scatterers which range in their length–to–depth ratio as a function of scale. In the extreme, the scatterers may vary from being isotropic to highly elongated structures, where the length–to–depth ratio of the specular scatterers can even be of the order of 20:1. The most highly aspect sensitive scattering is due to these specular reflectors, claimed by some authors to be anisotropic turbulence [*Crane*, 1980; *Doviak & Zrnić*, 1984; *Woodman & Chu*, 1989]. Others argue that these types of scatterers cannot explain the sharp fall–off in power with respect to zenith angle, and that at other times the fading is too slow to be due to anisotropic turbulence alone. They propose a second type of model which consists of stratified horizontal layers, or steps, in which the refractive index varies vertically. Although this would imply a $\theta_s = 0$, the layers may at times be slightly distorted, thus inducing a non-zero θ_s, i.e. acting as diffuse reflectors [see e.g. *Röttger et al.*, 1979; *Gregory & Vincent*, 1970; *Hocking & Vincent*, 1982]. Three mechanisms which could produce the stratified reflecting layers have been put forward; they could be either the edges of a strongly turbulent layer, damped gravity waves with short vertical wavelengths, or viscosity waves [*Bolgiano*, 1968; *Hines*, 1960; *Van Zandt & Vincent*, 1983; *Hocking et al.*, 1991].

Since neither type of model can explain all of the observed features, models which combine the two type of structures have also been proposed. One of the first was that due to *Bolgiano* [1968], who envisaged atmospheric layers which were so strongly turbulent in some cases that

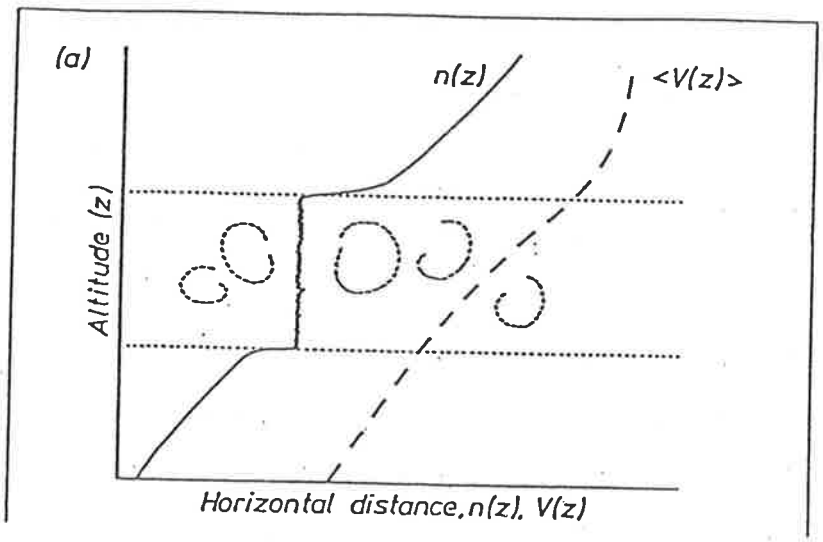

Figure 5.1: A model proposed to explain the observed partial radar reflections from the atmosphere. A strong layer of turbulence mixes a layer resulting in a constant refractive index across the layer while the edges have quite a sharp refractive index, n, variation. [after *Bolgiano*, 1968]

they have sharp refractive index edges at the top and bottom of the layer (see figure 5.1). These edges then cause the specular reflections.

There are, however, two reasons which make it unlikely that this model is an accurate representation, although the idea of turbulent layers is certainly not disputed. Firstly, it is difficult to envisage a mechanism which could contain strong turbulence with such a narrow edge. Secondly, no back–scatter due to the turbulent layer itself should be observed by the radar since the strong turbulence should, theoretically, mix the layer quite homogeneously and thus reduce the gradient of the potential index of refraction within this layer to zero.

Another model proposes a scenario where thin anisotropic turbulence exists at the edges of a more turbulent layer [see e.g. *Hocking et al.*, 1984; *Hocking*, 1989; *Woodman & Chu*, 1989]. Figure 5.2 depicts this type of scattering mechanism. The thin anisotropic turbulence causes radar partial reflections for a vertically pointing beam, and explains the observed aspect sensitivity, while the more isotropic turbulence contained within the layer is responsible for partial radar reflections from a off–zenith pointing beam. This type of model is more realistic, since turbulence is often more stable near the edges of the layer than within [*Peltier et al.*, 1978; *Klaassen & Peltier*, 1985]. If, in fact, there are two types of scatterers contained within the radar volume the resulting spectrum should not be Gaussian, but will consist of two distinct

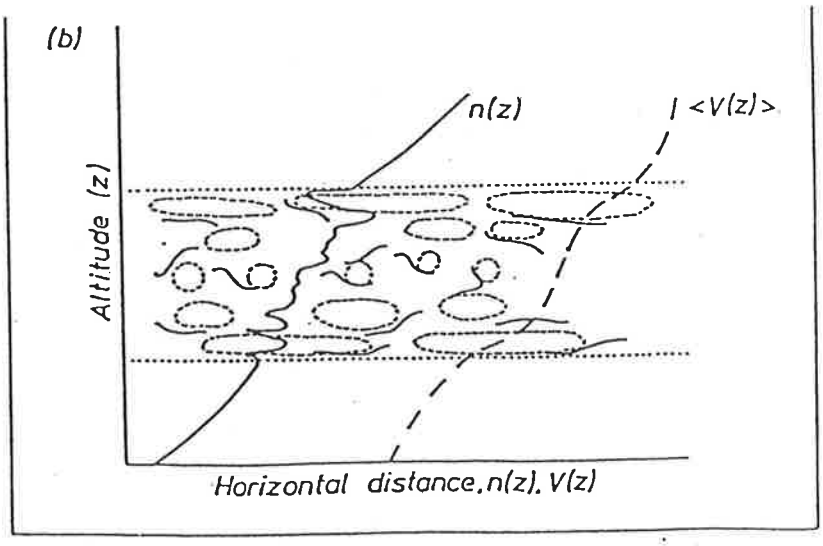

Figure 5.2: A model proposed to explain the observed partial radar reflections. For a turbulent scattering layer, whilst the scatterers contained within the layer are generally isotropic, those at the edges are anisotropic. A vertically pointing radar beam would therefore "see" the anisotropic scatterers, which would account for the observed aspect sensitivity. An off–vertical beam would back–scatter off the more isotropic turbulence [from *Hocking*, 1988b].

spectra; one due to the isotropic scatterers, and the other due to the more specular scatterers. There is some experimental evidence which supports the co–existence of both types of scatterers; for example such evidence has been found when using two separate receiving beams [*Hocking*, 1987b; *Czechowsky et. al.*, 1988; *Lesicar & Hocking*, 1992]. Figure 5.3 [from *Hocking*, 1987b] shows the power spectra recorded using two beams, one pointing vertically, and the other at 11.6° off–zenith, for an altitude of 70km. The power spectra recorded with the off–vertical beam were approximately 15dB less than those obtained with the vertical beam. There are two features in the figure which should be noted. Firstly, the spectra centred around 0 Hz are very similar, and secondly the spectra recorded with the off–vertical beam exhibits two components, a narrow and a broad component. The narrow component can be interpreted as being caused by isotropic scatter received from overhead leakage through both the edge of the main beam and the side lobes. The broad component, centered around -0.2 Hz, can be attributed to the more isotropic component received through the main lobe of the off–vertical beam. The shift in frequency was due to the large eastward wind which was evident at that time. This data clearly supports the idea that two types of scatterers can co–exist in the atmosphere, and that

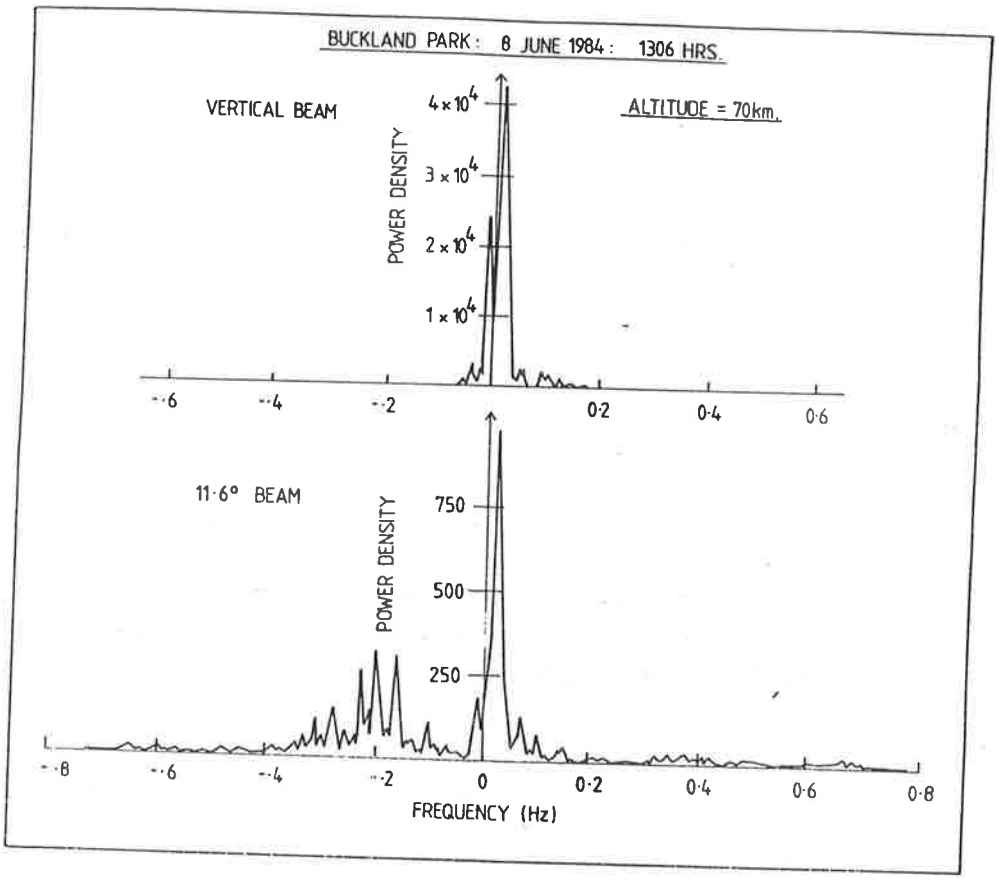

Figure 5.3: Spectra obtained with vertical and off–vertical beams observed at an altitude of 70km at Adelaide in 1984. The top diagram shows the narrow strong peak obtained by the vertical beam. The bottom diagram shows the spectra recorded when using the 11.6° off–vertical beam, which indicates two distinct components. The broader spectrum is due to isotropic backscatter received through the main lobe of the beam. The second component is very similar to the spectra observed by the vertical beam, and indicates leakage from the vertical. While the power comparison indicates that the specular component is very much stronger than the isotropic, the suggestion that two types of scatterers co–exist seems quite valid [after *Hocking*, 1987b].

one type is much more specular than the other. Further evidence supporting this is discussed in the following chapter. This type of investigation is best carried out by radars which possess a very narrow steerable radar beam. Such a radar system is in fact currently being developed by the Atmospheric Physics Group at the University of Adelaide, and will hopefully provide much more detailed and reliable data.

Another recent proposal argues that some of the observations cannot be explained by either anisotropic turbulence, or stratified layers as discussed above, and that the observed specularities are due to highly damped waves. As recently discussed by *Hocking et al.* [1991], the solution of the fluid dynamical equations can, besides the well known acoustic and buoyancy

waves, also lead to other wave modes. In particular, viscosity and thermal conduction waves can exist, which arise because of the balance between the acceleration term and the viscous drag term, somewhat analogous to simple harmonic motion within a lossy medium [see e.g. *Klostermeyer*, 1972, 1980; *Hooke & Jones*, 1986; *Pitteway & Hines*, 1963; *Yanowitch*, 1967a,b, 1969; *Myers & Yanowitch*, 1971]. Since they are highly damped, these waves must be created *in situ*, and there are two mechanisms which allow this.

First, to satisfy conditions of no–slip, zero normal velocity, and a continuous velocity profile, any reflection of waves from a rigid surface must involve creation of viscosity waves. They may therefore be created by reflection of waves from stratified changes in either the Brunt-Väisälä frequency or the mean wind speed, regions somewhat correlated with gravity wave reflections. Whilst the atmosphere is certainly not solid and any incident wave will distort the reflection boundary, this will only serve to reduce the production efficiency of viscosity waves. In fact, only small changes in the refractive index are needed to produce viscosity waves, and indeed even wind shear can generate them, as recently discussed by *Hooke & Jones* [1991]. One must also keep in mind that to account for the observed radar echo specularity, viscosity waves need only a fraction of the amplitude of the incident gravity waves. In addition, they can be long–lived, and provided that the flow remains non–turbulent, these waves will retain their structure for a time at least equal to their periods ($\approx$5–60 minutes).

Second, viscosity waves should also be generated in regions where gravity waves are highly non–linear, most likely at a critical level [see e.g. *Bowman et al.*, 1980]. Studies by *Hooke & Jones* [1991], who examined oceanic gravity wave–viscosity wave interactions in regions of large velocity shears, have shown that there is significant intermode coupling between the two, and that viscosity waves could easily be generated. They argue that the interaction is self–propelling, i.e., viscosity waves are initially generated by small perturbations on the shear, from which the wave coupling grows. On the other hand, a study by *Fritts & Geller* [1976] on critical level interactions, constructed a viscous solution in the vicinity of a gravity wave critical level. They argued that such modes always remove singularities, and would in fact damp out any

initial velocity perturbation, rather than creating them. *Hocking et al.* [1991] argued that this study did not have enough accuracy to detect stratospheric viscosity waves, which need only be around a few cm/s, and only 1–2 percent of the amplitude of the incident gravity waves. Figure 5.4 encapsulates the model, which contains both turbulent and laminar layers, and is congenial to the production of viscosity waves.

Hocking et al., [1991] have proposed that viscosity waves are responsible for some specular radar echoes by studying stratospheric partial reflection reflectors observed with the MU (VHF) radar at Shigaraki, Japan. They concluded that their experimental observations supported the existence of specular echoes which were due to some sort of horizontal stratification. However they also concluded that the reflectors could not be attributed to either steps in the refractive index or to long–period gravity waves with short vertical wavelengths, but rather were due to viscosity waves. Furthermore, their results have suggested that the typical scales of these viscosity waves, λ_v, correspond quite well with the observations of the heights of strongest specularity. For example, at an altitude of 20 km, $\lambda_v \approx 0.9$–3.0 m, whilst at 70 km, $\lambda_v \approx 20$–70 m. The Bragg back–scatter scale is ≈ 3 m for 50 MHz VHF radio waves, and ≈ 75 m for 2 MHz radio waves.

5.3 Aspect sensitivity

5.3.1 Introduction

In the previous section we have concentrated on the discussion of the possible structure of atmospheric scatterers, and how they might be produced. One distinguishing feature of these scatterers is that they are aspect sensitive. This implies that their structure is not isotropic and that their horizontal scales exceed their vertical ones. Their horizontal (length) to vertical (depth) ratio can, at times, be of the order of 20:1 or even more, in these cases indicating a strong level of stratification. The degree of aspect sensitivity, often denoted by θ_s, is a gauge of how quickly the back–scattered power falls off as a function of the zenith angle. A θ_s of close to 90° indicates highly isotropic scatter, while a θ_s of close to 0° indicates scatter mainly

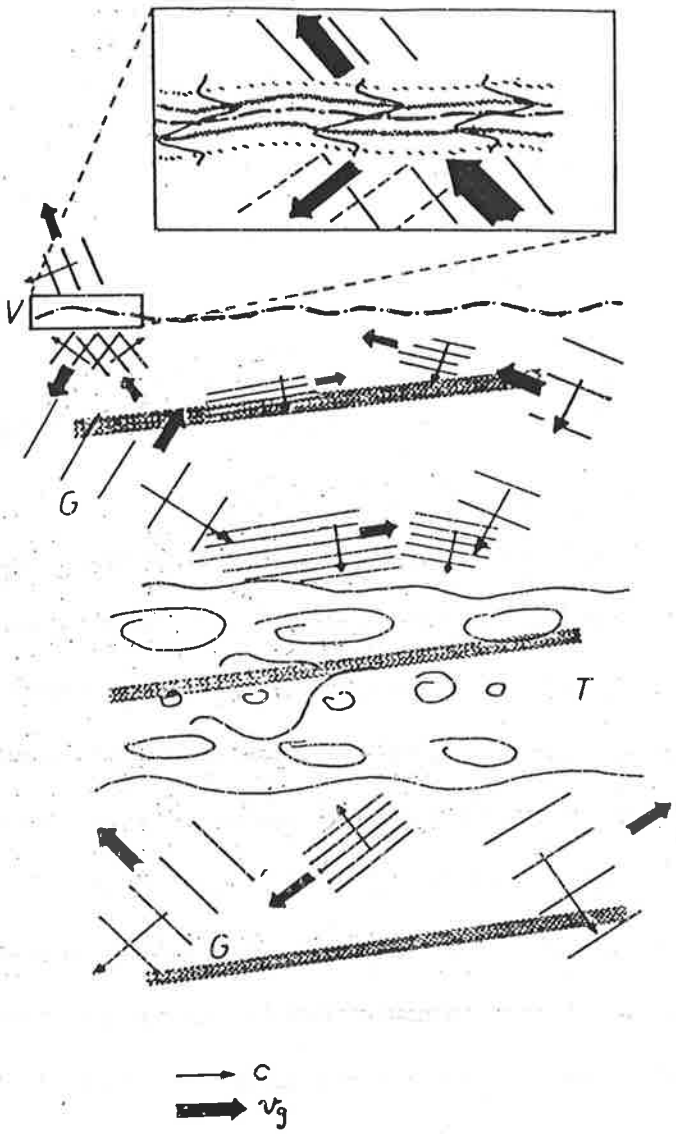

Figure 5.4: A scenario depicting the small–scale features of a dynamically active stratified atmosphere. The parallel lines indicate gravity wave packets (G), with phase velocities, c, and group velocities, v_g, indicated by the thin and thick arrows respectively. Longer gravity waves, such as those represented by the shaded wave fronts, generate turbulent layers (T), which are more anisotropic at the edges of the layer, and more isotropic towards the centre. Although most of the gravity waves are generated elsewhere, some may be generated by the turbulent layer. Next to the turbulence is a laminar region where either the Brunt-Väisälä frequency experiences a change, indicated by the dashed–dotted line, or there is a wind shear. This causes the partial reflection or critical absorption of gravity waves, and as indicated by the expanded diagram (V), produces viscosity waves, which are responsible for specular echoes as observed by partial reflection radars. The Brunt-Väisälä boundary may possess a slight tilt; this means that the viscosity waves can produce density perturbations. The boundary may also be undulated and thus responsible for weak off–vertical reflection [from *Hocking et al.*, 1991].

from the vertical, or highly aspect-sensitive scatter. Since aspect sensitivity is a clear measure of the stratification of the scatterers, it is obviously desirable to try and physically measure or quantify it. This section discusses various techniques, some of which are used later in this thesis, to determine the aspect sensitivity of the scatterers, and thus attempts to quantify the specularity of atmospheric scatterers. We start with the most common and obvious method.

5.3.2 Comparison of powers and velocities

The simplest and most obvious method of measuring aspect sensitivity is to measure the back–scattered power as a function of zenith angle; either by pointing a beam vertically and then at several off–vertical angles, or utilizing several beams simultaneously, where at least one is pointing vertically. However, because the beamwidth is always finite (non–zero), this may not give an accurate result. It has been shown by *Röttger* [1980a, 1981a], that an apparent beam direction occurs when the beams are pointed off–vertically. Figure 5.5 illustrates the case where the reflecting structures possess an angular dependence. We assume that the angular spectrum of the partially reflecting scatterers is centred at an angle ϕ_0, usually the zenith, and the physical off–vertical antenna angle to be pointing at an angle ϕ_b. The reflected echo power is then simply the product of the angular spectrum and the antenna beam pattern. In that case, an apparent beam direction is obtained at an angle ϕ_a, which is closer to the zenith than the physical pointing direction ϕ_b.

For a vertically pointing radar, the two-way polar diagram can be described as

$$P_r(\theta) \propto \exp\left[-\frac{\sin^2\theta}{\sin^2\theta_0}\right] , \tag{5.1}$$

while the polar diagram of the scatterers is parameterized as

$$P_s(\theta) \propto \exp\left[-\frac{\sin^2\theta}{\sin^2\theta_s}\right] . \tag{5.2}$$

For an off-vertical radar beam tilted by an angle θ_T at azimuth angle $\phi = 0$, the polar diagram at angle (θ, ϕ) is then described as

$$P_r(\theta,\phi) \propto \exp\left[-\frac{(\sin\theta\sin\phi)^2 + (\sin\theta\cos\phi - \sin\theta_T)^2}{\sin^2\theta_0}\right] . \tag{5.3}$$

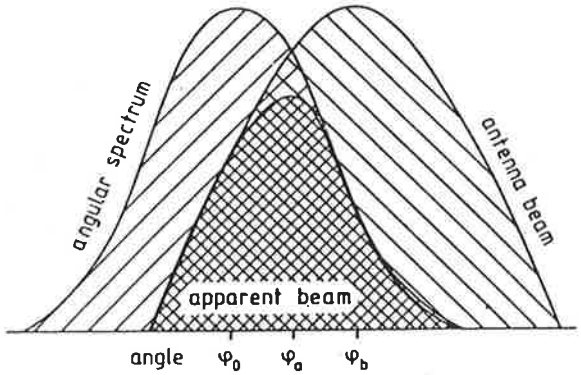

Figure 5.5: The formation of an apparent beam direction due to an angular dependence of the reflecting scatterers. The apparent beam direction is the product of the angular spectrum and the antenna beam pattern [from *Röttger*, 1981a].

Multiplying the polar diagram of the scatterers with that of the radar beam (equations 5.1 and 5.2) one obtains the effective polar diagram. The new effective pointing angle can then be determined when the derivative of the exponential is zero (with respect to $\sin\theta$), such that,

$$\sin\theta_{eff} = \sin\theta_T \left[1 + \frac{\sin^2\theta_0}{\sin^2\theta_s}\right]^{-1} . \tag{5.4}$$

Provided that θ_0 and θ_s are less than $\approx 10°$, this can be approximated to

$$\sin\theta_{eff} = \sin\theta_T \left[1 + \frac{\theta_0^2}{\theta_s^2}\right]^{-1} . \tag{5.5}$$

The effective pointing angle is thus given by equation 5.4, which directly implies that a Doppler radar will underestimate the radial velocities by a factor R_1 [*Röttger*, 1981a; *Hocking et. al.* 1986],

$$R_1 = \left[1 + \frac{\theta_0^2}{\theta_s^2}\right] . \tag{5.6}$$

If the scatterers are isotropic, this factor should be equal to one. It should be noted that equation 5.4 is only an approximation, and not an exact solution; it is however a very realistic result [see *Hocking*, 1983a; *Hocking*, 1988b].

The half-width of the effective beam is the angle at which the effective polar diagram, obtained by the product of equations 5.1 and 5.3, falls to half of its peak value. If we consider

the case where the azimuth is zero, we then write the product of equations 5.1 and 5.3 as,

$$\exp - \left[\frac{(\sin\theta - \sin\theta_T)^2}{\sin^2\theta_0} + \frac{\sin^2\theta}{\sin^2\theta_s} \right] \quad . \tag{5.7}$$

To determine the two angles, say $(\theta_{\frac{1}{2}})_{1,2}$, where this falls to half of the effective angles, θ_{eff}, value, one finds a quadratic solution so that

$$(\theta_{\frac{1}{2}})_{1,2} = \sin\theta_{eff} \pm \sqrt{ln2}\sin\theta_0 \left[1 + \frac{\theta_0^2}{\theta_s^2} \right]^{-\frac{1}{2}} \tag{5.8}$$

are the two roots when θ_0, and θ_s are ≤ 10 degrees. The effective half–power half–width of the radar is simply the half–width of the radar multiplied by the factor contained within the square brackets in the above equation. Alternatively, we can also relate the effective half–power half–width $\theta_{eff\frac{1}{2}}$, the half–power half–width of the radar beam $\theta_{\frac{1}{2}}$, and the half–power half–width of the back–scatter polar diagram of the scatterers $\theta_{s\frac{1}{2}}$ viz

$$\sin^{-2}(\theta_{eff\frac{1}{2}}) = \sin^{-2}\theta_{\frac{1}{2}} + \sin^{-2}\theta_{s\frac{1}{2}} \quad . \tag{5.9}$$

Now consider the power received by a radar beam, tilted at some angle θ_T. For a vertical beam, the power returned is found by integrating over the beam, which for a Gaussian polar diagram is proportional to $\theta^2_{eff\frac{1}{2}}$. When the beam is tilted this will be reduced by two factors; f_1 and f_2 so that

$$\begin{aligned} f_1 &= \exp\left[-\frac{(\theta_{eff} - \theta_T)^2}{\theta_0^2} \right] \quad , \\ f_2 &= \exp\left[-\frac{\theta^2_{eff}}{\theta_s^2} \right] \quad , \end{aligned} \tag{5.10}$$

where f_1 takes into account the fact that the returned power peaks at θ_{eff} rather than θ_T, and f_2 compensates for the fact that the scatterers may be specular. Hence, the total back–scattered power will be proportional to the product of f_1 and f_2, and we find that the ratio of the power received by the off–vertical beam to that received by the vertical is,

$$\frac{P(\theta_T)}{P(0)} = \exp\left[-\left(\frac{(\theta_{eff} - \theta_T)^2}{\theta_0^2} + \frac{\theta^2_{eff}}{\theta_s^2} \right) \right] \quad . \tag{5.11}$$

Measurements of $P(\theta)$ indicate a Gaussian fall–off to angles of $\approx$ 5–10°, and then remaining roughly constant; an indication that perhaps we are seeing more isotropic scatterers at the

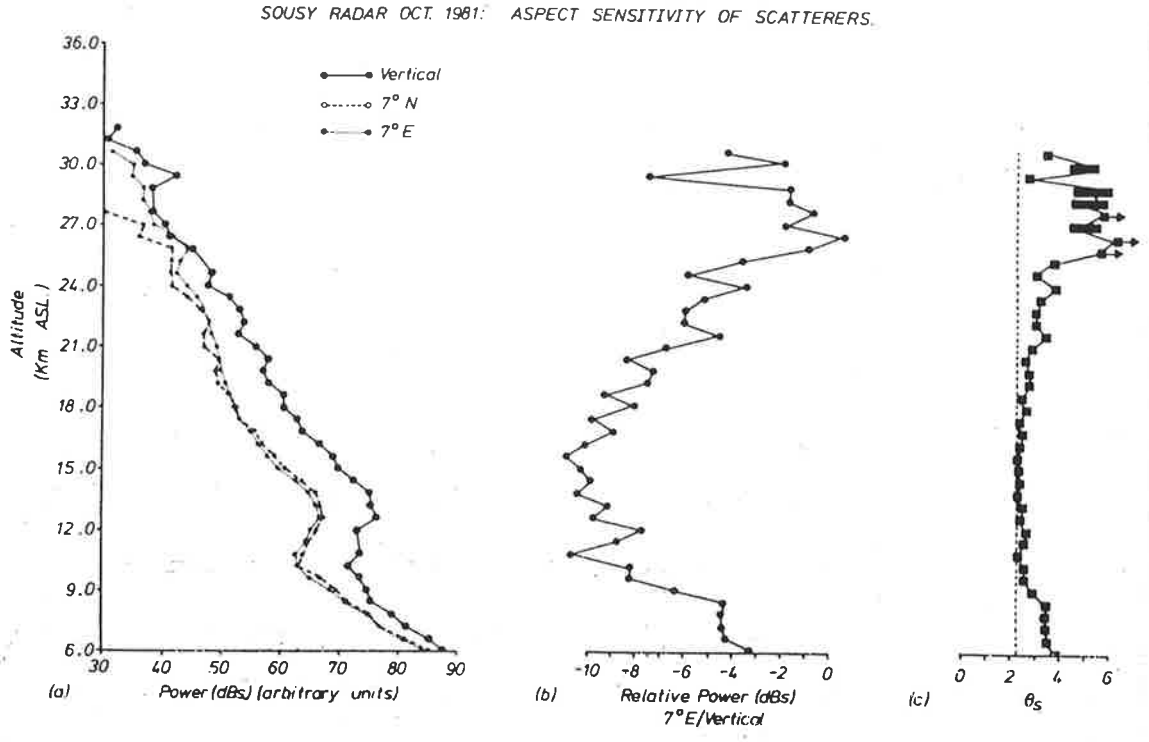

Figure 5.6: (a) A plot of three mean powers calculated over a 25 hour period using the SOUSY German radar. One profile was made using a vertical beam, while the other two are off-vertical, one at 7° N and the other at 7° E. (b) Ratio of the powers of the 7° E beam and the vertical beam. The 7° N beam signal had the most noise associated with it since Cassiopeia A passed through the beam. (c) The aspect sensitivity calculated for the scatterers, assuming that their back-scatter polar diagram was of the form described by equation 5.2. The minimum θ_s calculated is indicated by the broken line. Above an altitude of 18km, θ_s markedly increases. The black rectangles indicate the error due to a 1 dB increase in the power ratio [from *Hocking et al.*, 1986].

larger angles. Figure 5.6 represents a study made with the SOUSY German radar, using a vertical and two off-vertical beams; the calculations of θ_s have, however, been corrected since *Hocking et al.* [1986] did not consider the extra term induced due to the polar diagram of the scatterers [see *Hocking*, 1988b].

Another method of using powers to calculate θ_s was used by *Vincent & Belrose* [1978], who compared powers received on two vertical beams with different polar widths; one beamwidth was 21° and was produced by an array of 40 half-wave dipoles, while the other with a width of 48° was formed by an array of 4 dipoles. They found that the gain of the larger array over the smaller array was often variable in both time and altitude (50–95 km). These results were then used to estimate the off-vertical angles from which significant energy returns were obtained.

They concluded that at altitudes below 80 km these angles were limited to less than 10°, and increased to about 15–20° above this altitude.

5.3.3 Spectral–width method

The frequency spectrum determined from temporal variations in partially reflected radar signals is found to have a finite width, and this width was initially thought to be caused primarily by the random motion of the scatterers within the radar volume, resulting (for example) from turbulence [e.g. *Cunnold*, 1975; *Vincent & Röttger*, 1980]. If, within a volume probed by the radar beam, a number of scatterers have different velocities superimposed upon a mean speed, each scatterer will produce a slightly different Doppler shift. Consider the case where the scatterers have a Maxwellian distribution. In such a case the vertical velocity (w) has a Gaussian distribution which is proportional to $\exp\left[\frac{-w^2}{2w_{RMS}^2}\right]$. Because the Doppler shift for a vertical beam is $f = \frac{2}{\lambda}w$, the shape of the spectrum will be proportional to $\exp\left[\frac{-f^2}{2f_{RMS}^2}\right]$, where $f_{RMS} = \frac{2}{\lambda}w_{RMS}$. Whilst other causes were known to affect the spectral width, they were regarded as minor contributions. These include the effect due to the radar beam-width (see figure 5.7a), wind shears (figure 5.7b), buoyancy effects (figure 5.7c), and decay of turbulent eddies. Those assumptions have been subsequently found to be incorrect, as we will now see.

Variations in the horizontal velocity as a function of height, or wind shears, result in a range of frequencies received, which affect the spectra. However, depending on the sign of the wind shear, the total spectrum may be broadened or narrowed. Furthermore the effect of wind shears becomes more important as the radar beam is tilted.

Oscillations in both horizontal and vertical velocities due to buoyancy waves will also contribute to the spectral width, affecting both vertical and off–vertical beams. When the wave amplitudes are large, the radial components of velocity fluctuations which occur at the edge of the radar beam further add to the width of the spectrum. This effect is less important when using narrow beams. The effect is exacerbated when the beam is tilted; in this case not only do the horizontal velocity fluctuations due to buoyancy effects contribute to spectral broadening,

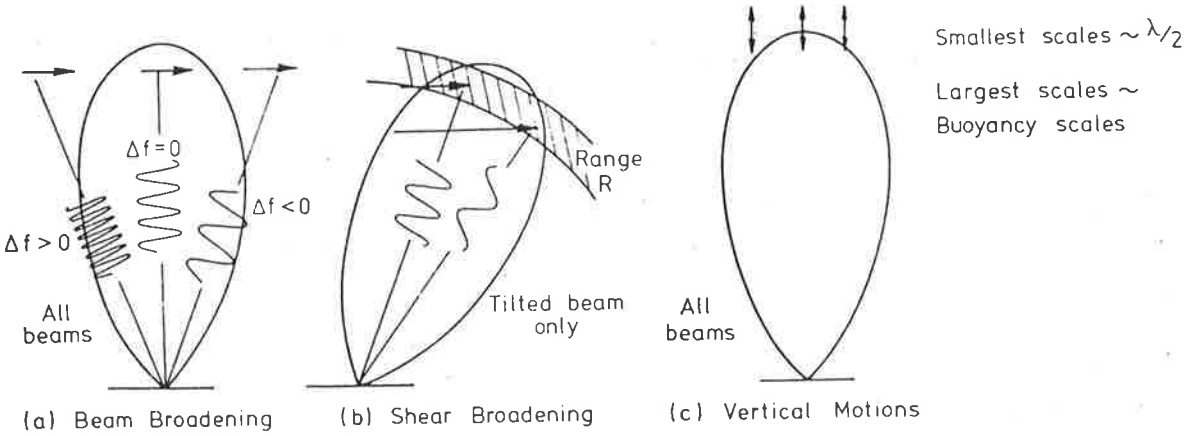

Figure 5.7: Contributions which might at any instant contribute to the spectral broadening. (a) Due to the finite width of the beam. (b) Due to altitude variation of horizontal velocity. (c) Caused by variations of velocity due to buoyancy waves [from *Hocking*, 1983a].

but the data sampling length also becomes important. For example, if the data is sampled over a time greater than say a couple of wave periods, the net effect will be a broadening of the spectrum without affecting the mean [see e.g. *Hocking*, 1983b]. Lastly, the contribution to the spectral broadening due to the decorrelation time associated with the finite lifetime of turbulent eddies can be ignored provided that the radar wavelength is smaller than the buoyancy scale (at least several times). In general the spectral width observed using an off–vertical beam will always be larger than that found by a vertical beam [e.g. *Countryman et al.*, 1981; *Hocking*, 1983b].

However, even in the case where the scatterers are all moving purely in a horizontal plane with the same velocity and no fluctuations of any type, there will be a range of Doppler shifts due to the finite width of the radar beam, producing a spectrum of finite width. This effect is known as *spectral beam–broadening*. Ray paths to the edge of the beam will not be purely parallel to the beam bore direction so that scatterers at the edge will induce Doppler shifts in the returned signal acting both in a direction towards and away from the net motion. Such an effect broadens the spectrum is illustrated in figure 5.8 [after *Hocking*, 1983a]. It is now accepted that for statistically isotropic scatterers, this so–called beam broadening is the largest contributor to the spectral width for a vertically pointing beam. The other contributions listed above are minor contributors [see e.g. *Atlas*, 1964; *Sloss & Atlas*, 1968; *Atlas et al.*, 1969;

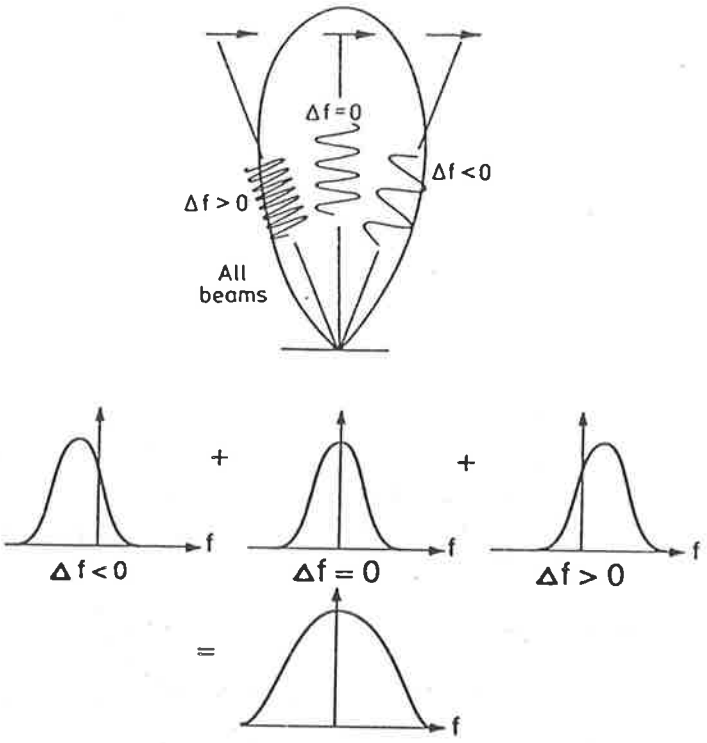

Figure 5.8: Spectral (beam) broadening due to the horizontal motion of wind in a vertical beam. At any instant, since echoes from the edge of the beam are not purely horizontal, there is an inherent Doppler shift. This acts at the edges of the beam pointing both towards and away from the direction of motion, resulting in a spectrum of finite width [from *Murphy*, 1990].

Hocking, 1983a,b, 1989].

Spectral broadening has been modelled, and it has been found that the spectral half–power half–width ($f_{0.5b}$ in units of Hz), for thick layers moving with uniform wind speed and where the beams are less then about five degrees half–power half–width, is fairly well approximated by [see, eg. *Hitschfield & Dennis*, 1956; *Atlas*, 1964; *Sloss & Atlas*, 1968; *Atlas et. al.*, 1969; *Hocking*, 1983a,b]

$$f_{0.5b} = \frac{2}{\lambda}(1.0)V_{hor}\theta_{0.5} \ , \tag{5.12}$$

where V_{hor} is the total horizontal wind vector, $\theta_{0.5}$ is the combined half–power half–width of the polar diagram due to both the radar beam and the scatterers (in units of radians), and λ is the radar wavelength. This approximation is also fairly accurate when using off–vertical beams, provided that one uses the total wind speed and not just the component in the direction of the beam. Since the Doppler spectrum of the partially reflected echoes is a convolution of the

spectrum due to turbulence and that due to beam broadening, we can isolate the individual contributions. The total spectral half–power half–width assuming a Gaussian form and ignoring wind shear is given by

$$f_{0.5}^2 = f_{0.5b}^2 + f_{fluct}^2 \ , \tag{5.13}$$

where $f_{0.5}^2$ is the total spectral half-power half-width and f_{fluct}^2 is the spectrum width due to the fluctuating velocity of the scatterers (turbulence). However, in the case of a relatively broad[1] radar beam, the spectral width is primarily due to beam broadening and only a small component is due to random fluctuating motions of the scatterers (i.e. $f_{0.5b} \gg f_{fluct}$). Equation 5.12 then becomes

$$\theta_{0.5} = \frac{\lambda}{2} \frac{f_{0.5}}{|V_{hor}|} \ , \tag{5.14}$$

where $\theta_{0.5}$ is now a very good estimate of $\theta_{0.5eff}$, the half–power half-width of the combined polar diagram of the radar beam and the scatterers. $\theta_{0.5}$ can be estimated by measuring $f_{0.5}$ and V_{hor} and applying equation 5.14.

For any radar system the effective polar diagram is just the product of the polar diagram of the radar and the back–scatter polar diagram of the scatterers. Denoting θ_{sb} as the e^{-1} half–width of the effective polar diagram and assuming that the polar diagrams have shape of the form $\exp(\theta^2/\theta_{sb}^2)$ we find that [*Hocking*, 1989],

$$\sin^{-2}\theta_{sb} = \sin^{-2}\theta_0 + \sin^{-2}\theta_s \ , \tag{5.15}$$

which is the combined upper limit of the half-power half-width of the polar diagram of the radar and the scatterers. Since we can approximate $\theta_{0.5eff}$ from $\theta_{0.5}$ we know that $\theta_{sb} = \frac{\theta_{0.5eff}}{\sqrt{ln2}}$. We can then use equation 5.15 to calculate θ_s. In the special case where a wide radar beam is used we can make the further approximation that $\theta_{sb} = \theta_s$, since $\theta_0 \gg \theta_s$.

Although this shows that it is relatively simple to determine θ_s, it should be borne in mind that this can only provide an upper limit since other factors, as discussed above can contribute to the spectral width. Nevertheless, it provides a good estimate when (as is usually

[1]The definition of broad can be a bit misleading since a narrow beam may only be 1-1.5° half–power half–width, so broad may indicate a beam as small as 2-3°.

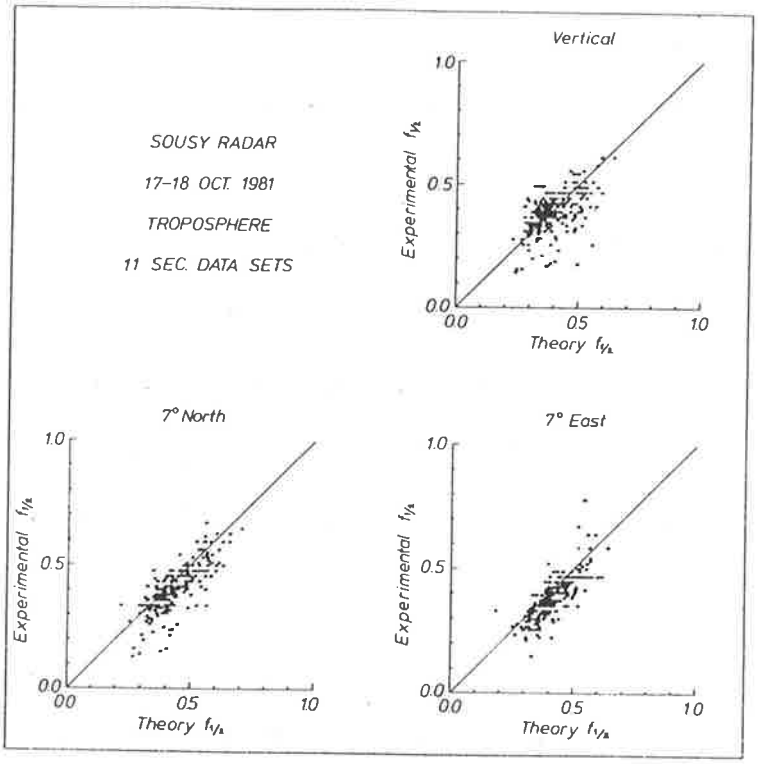

Figure 5.9: Scatter plots of tropospheric spectral half–power half–widths measured experimentally by a vertical and two off–vertical beams using 11 seconds of data vs. theoretical calculated values assuming that the spectral widths are due to beam and wind–shear broadening only [from *Hocking*, 1986].

the case) beam–broadening is the major cause of spectral broadening. For example, *Hocking* [1986] made both experimental observations and computer simulations to calculate spectral widths. The experimental observations were performed using the SOUSY 53 MHz radar in West Germany[2] over a 24 hr period. Three beams were used; a vertical one, one pointed at 7° off–vertical to the east, and one pointed at 7° off–vertical to the north. Each beam was used both for transmission and reception with a range resolution of ~600 metres, and all beams had narrow half–power half–widths; 1.8° for the vertical, and ~2° for the off–vertical beams. The theoretical work determined spectral half–power half–widths assuming that only beam and wind–shear broadening contributed to the spectra. This was achieved by using a computer program that has been described in *Hocking* [1983a]. Figures 5.9 and 5.10 [from *Hocking*, 1986], are scatter plots of the experimental spectral half–power half–widths obtained using 11 seconds of data vs the theoretical values for the troposphere and stratosphere respectively. It

[2] as known before German unification

is obvious that all of the points are clustered around the line of slope 1.0. This is a clear indication that most of the spectral width is due to wind and beam–broadening, and there is no clear indication that turbulent fluctuations contribute to the broadening. The spread of the scatter may be due to several factors; varying specular reflectors, and statistical fluctuations. In addition, the stratospheric spectra may have been biased by the dominant specular reflectors, which would have affected the effective off–vertical beam direction resulting in under–estimated wind velocities (by a factor R, defined in equation 5.6).

There are a number of ways to determine the spectral width. The method used in this thesis involves determining the lag at which the auto–correlation function (discussed in section 3.5.3) falls to one–half its peak value. This "fading" time is related to the spectral width by (see Appendix *D* for a derivation)

$$f_{0.5} = \frac{0.22}{\tau_{0.5}} \quad . \tag{5.16}$$

This expression has been shown to work quite well experimentally [*Hocking*, 1986], even in the case where the spectra may not be Gaussian. Figure 5.11 [from *Hocking*, 1986] is a scatter plot

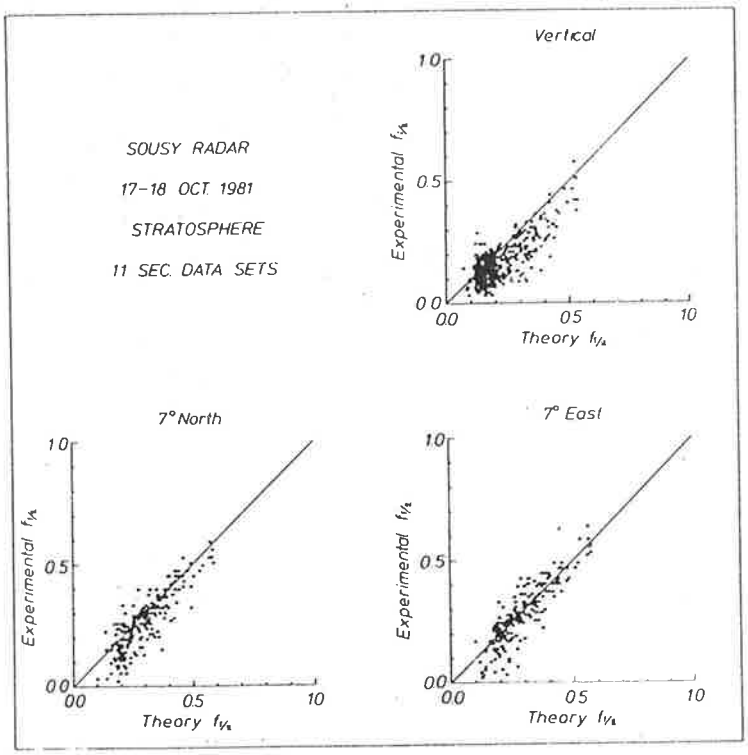

Figure 5.10: Same as figure 5.9 but for the stratosphere [from *Hocking*, 1986].

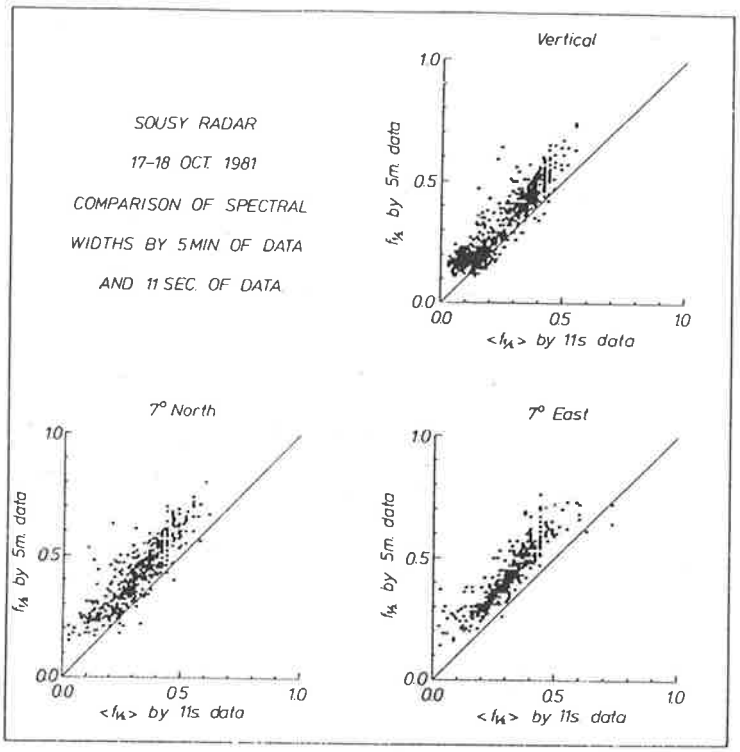

Figure 5.11: Scatter plot of experimental spectral half–power half–widths determined from 5 minutes of data versus those determined by fading times using 11 seconds of data. The obvious clustering of points around a straight line indicates that the spectral widths determined by the use of fading times is quite a reliable method. The off–set which shows that the 5 minutes spectral widths are generally wider is likely to be due to fluctuating motions with periods of ~5 minutes and much larger than 11 seconds; perhaps caused by gravity waves. [from *Hocking*, 1986].

of experimental spectra determined by fitting a Gaussian function and then "reading off" the spectral width for 5 minutes of data, versus the spectral width determined by the use of the auto–correlation fading time. Since the points seem to cluster around a straight line quite well, this seems a clear indication that the spectral width measured by use of the fading time is quite reliable.

There are a number of other methods that can be used to determine the spectral width. These include using the second lag of the auto–correlation function, or the second moment of the spectrum. We do not intend to discuss these in any detail, for a discussion see e.g. *Woodman* [1985].

The last points that need to be discussed are practical considerations that could improve

the accuracy of measuring spectral widths. For example, the effects of wind shears could be greatly reduced by the use of very short pulses, while the use of narrow beams could reduce the effects of beam–broadening (these widths need to be smaller than 1° in order to make the effect negligible). If these effects were reduced considerably, then the spectral widths could be interpreted as those mainly due to fluctuating motions. This could then be used to determine energy dissipation rates. The measurement of energy dissipation rates will be discussed later in section 5.7.

5.3.4 Spatial correlation method

A volume of scatterers which is probed with a radar beam will partially scatter the signal back to ground level. The back–scatter contributions from each of these scatterers will interfere and produce an electric field "shadow" or diffraction pattern on the ground. The study of this type of diffraction was originally developed to study characteristics of lower ionospheric irregularities [*Ratcliffe*, 1956], and was later applied to the study of winds in the middle and lower atmosphere [e.g. *Vincent et al.*, 1977; *Röttger & Vincent*, 1978]. It can easily be shown that for small off–zenith angles the spatial auto–correlation function of the diffraction pattern at ground level is just the Fourier transform of the combined power polar diagram of the transmitting and receiving arrays and the scatterers [*Ratcliffe*, 1956; *Briggs and Vincent*, 1973]. The mathematical methods used in remote probing of atmospheric irregularities, which lead to a description of scatterers, and taking into account geometrical factors and polar diagrams of the transmitter and receiver, are presented in the following subsections. The discussion follows that recently given by *Briggs* [1992].

Volume distribution of scatterers

In chapter 3 we briefly considered the radar equation for radar scattering, with the assumption that the scatter was azimuthally isotropic, and that the antennas were directly pointed at the target. We once again turn our attention to the radar equation, this time assuming that the radar is pointed vertically. Since back–scatter may occur from scatterers which are off–vertical

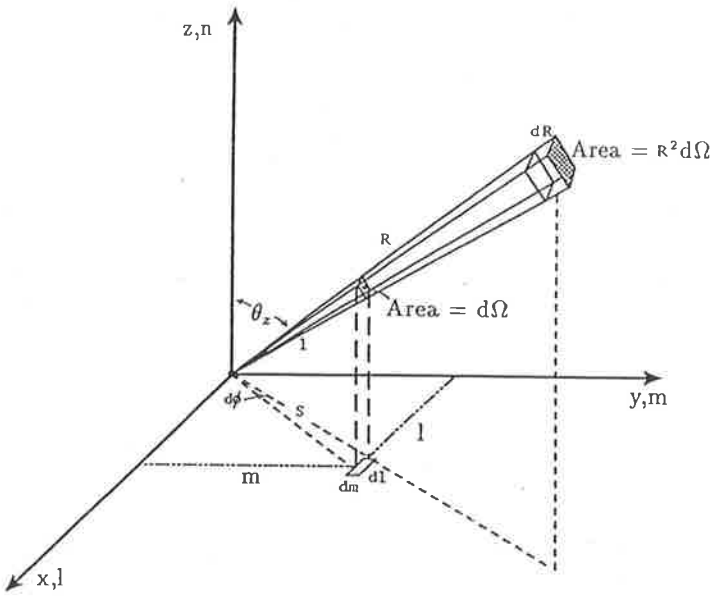

Figure 5.12: Geometrical representation of a volume distribution of scatterers encompassed by a range-gated (R to R+dR) radar [from *Briggs*, 1992]

we now consider the polar diagrams of both the transmitting and receiving antennas. The radar equation is therefore re-written as;

$$P_R = \frac{K}{R^4} G_T(l,m) G_R(l,m) \sigma(l,m) \ , \tag{5.17}$$

where K is a constant, while G_T and G_R are the gains of the transmitting and receiving antennas respectively, and (l,m) are direction cosines; if a given direction makes angles $(\theta_x, \theta_y, \theta_z)$ with the (x,y,z) axes, we then define $l = \cos\theta_x$, $m = \cos\theta_y$, $n = \cos\theta_z$. Note that G_T and G_R are now functions of direction. If we consider that the volume distribution of scatterers is random, we simply add the powers.

If we consider a volume of randomly distributed scatterers of volume density N, as depicted in figure 5.12, we find that the number of scatterers contained within the volume of the range gated radar beam is

$$NR^2 d\Omega dR = \frac{NR^2 dl dm dR}{(1-l^2-m^2)^{\frac{1}{2}}} \ , \tag{5.18}$$

where $d\Omega$ is an element of solid angle, and the scatterer volume is defined by dl and dm.

The back-scattered power from such a volume is denoted as $W(l,m)dldm$, and is found by

combining equations 5.17 and 5.18, i.e.;

$$W(l,m)dldm = \frac{KNdR}{R^2} \times \frac{G_T(l,m)G_R(l,m)\sigma(l,m)}{(1-l^2-m^2)^{\frac{1}{2}}}.dldm \ . \tag{5.19}$$

The total back–scattered power is then just the integral over the whole volume probed by the radar. The spatial correlation function, $\rho(\xi,\eta)$, (discussed in section 3.5), which is the correlation between two receivers with separation (ξ,η) in units of radar wavelength, is just the two–dimensional Fourier transform of $W(l,m)$ [*Ratcliffe*, 1956], so that

$$\rho(\xi,\eta) \ \propto \ \int_{-1}^{+1}\int_{-1}^{+1} W(l,m)\exp[2\pi i(l\xi+m\eta)]dldm \tag{5.20}$$

$$\text{or,}\rho(\xi,\eta) \ \propto \ \int_{-1}^{+1}\int_{-1}^{+1} \frac{G_T(l,m)G_R(l,m)\sigma(l,m)}{(1-l^2-m^2)^{\frac{1}{2}}}\exp[2\pi i(l\xi+m\eta)]dldm \ . \tag{5.21}$$

Since $W(l,m)$ is the reverse two–dimensional Fourier transform of $\rho(\xi,\eta)$, we can determine the scattering cross–section, $\sigma(l,m)$ which is of the form

$$\sigma(l,m) \propto \frac{(1-l^2-m^2)^{\frac{1}{2}}}{G_T(l,m)G_R(l,m)}\int_{-1}^{+1}\int_{-1}^{+1} \rho(\xi,\eta)\exp[-2\pi i(l\xi+m\eta)]d\xi d\eta \ . \tag{5.22}$$

Therefore, provided that the antenna polar diagrams are known, we can determine the aspect-sensitivity function $\sigma(l,m)$ by measuring the spatial correlation function which may be non–isotropic. As well, the above discussion allows for the case where $W(l,m)$ may be a function of both zenith and azimuth angle, a more than likely case. Furthermore, if the maximum of the angular power spectrum is found by a radar pointing at an off-zenith angle, the above treatment still applies; the only difference being that the spatial correlation will become a complex function.

If we consider the simplistic view that the scattering cross–section only depends on the zenith angle, θ_z, then the zenith angle becomes a function of $sin\theta_z = s = (l^2+m^2)^{\frac{1}{2}}$. Similarly if the antenna polar diagrams are azimuthally symmetrical they too will be functions only of s. We therefore replace terms in the previous equations that were a function of (l,m) with those that are a function of s, and write the total received power as:

$$\int_{-1}^{+1}\int_{-1}^{+1} W(l,m)dldm = 2\pi\int_0^1 W(s)sds \tag{5.23}$$

since $dldm = sd\phi ds$ (see figure 5.12). Equation 5.19 for the total received power then becomes

$$2\pi \int_1^0 W(s)sds = \frac{2\pi KNdR}{r^2} \times \int_1^0 \frac{G_T(s)G_R(s)\sigma(s)ds}{(1-s^2)^{\frac{1}{2}}} \quad . \tag{5.24}$$

Equation 5.21 becomes a Fourier–Bessel transform of the type

$$\begin{aligned} \rho(r) &\propto \int_1^0 W(s)J_0(2\pi rs)sds \\ &\propto \int_1^0 \frac{G_T(s)G_R(s)\sigma(s)ds}{(1-s^2)^{\frac{1}{2}}} J_0(2\pi rs)sds \quad . \end{aligned} \tag{5.25}$$

where $\rho(r)$ is the correlation for a separation r, in units of wavelength, and J_0 is the zero order Bessel function.

We again find $\sigma(s)$ from the inverse transform for $W(s)$, and equation 5.22 becomes

$$\sigma(s) \propto \frac{(1-s^2)^{\frac{1}{2}}}{G_T(s)G_R(s)} \int_0^\infty \rho(r)J_0(2\pi rs)rdr \quad . \tag{5.26}$$

In the scenario where the off–zenith angles are small, $(1-s)^{\frac{1}{2}}$ can be ignored, and $\sigma(s)$ can simply be found by dividing the angular power spectrum by the polar diagrams. Thus, if the scatterers were azimuthally isotropic, one would only need a collection of antennas aligned in a row to deduce $\rho(r)$, and hence $\sigma(s)$.

Plane distribution of scatterers

Until now we have considered the case where the radar volume density of scatterers is constant. However, in the atmosphere the scatterers may be confined to a thin horizontal layer; this can be due to stratification or a thin layer of horizontal turbulence. We assume that the layer has a constant density M, and is located at a height h, as depicted in figure 5.13. We again consider scatterers within the angular range l to $l + dl$ and m to $m + dm$.

The number of scatterers within that range is therefore

$$MA = \frac{MR^4}{h^2}.dldm \quad , \tag{5.27}$$

which, when combined with equation 5.17 gives the returned power viz:

$$W(l,m)dldm = \frac{KM}{h^2} G_T(l,m)G_R(l,m)\sigma(l,m)dldm \quad . \tag{5.28}$$

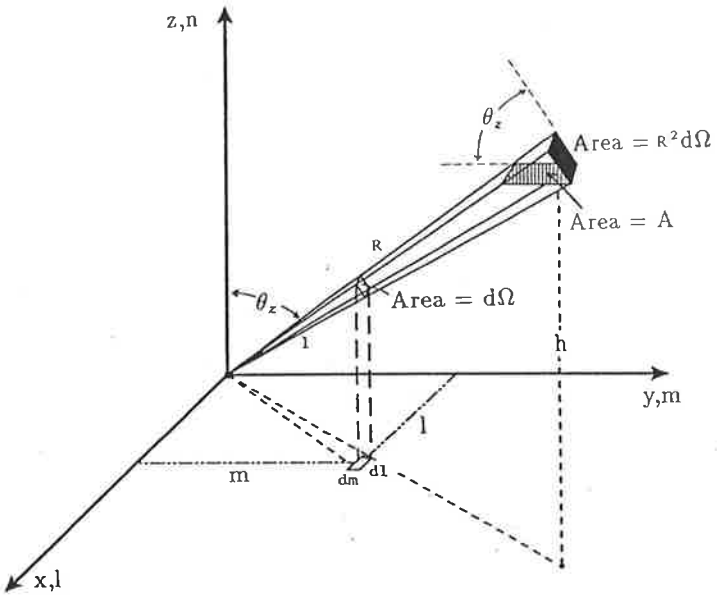

Figure 5.13: The geometry for the case of scatterers confined to a thin layer at a height h [from *Briggs*, 1992].

The total received power, assuming that the scatterers are contained within the radar range gate is then given as

$$\int_{-1}^{+1}\int_{-1}^{+1} W(l,m)dldm = \frac{KM}{h^2} \times \int_{-1}^{+1}\int_{-1}^{+1} G_T(l,m)G_R(l,m)\sigma(l,m)dldm \ . \qquad (5.29)$$

We already know that for a given angular pattern of echo power, the auto–correlation function of this complex wave field is just the two–dimensional Fourier transform of the angular pattern [*Ratcliffe* 1956], i.e.

$$\rho(\xi,\eta) \propto \int_{-1}^{+1}\int_{-1}^{+1} G_T(l,m)G_R(l,m)\sigma(l,m) \times \exp[2\pi i(l\xi + m\eta)]dldm \ , \qquad (5.30)$$

while the aspect sensitivity function is the reverse 2-D Fourier transform of the spatial correlation function, i.e.,

$$\sigma(l,m) \propto \frac{1}{G_T(l,m)G_R(l,m)} \int_{-\infty}^{+\infty}\int_{-\infty}^{+\infty} \rho(\xi,\eta) \times \exp[2\pi i(l\xi + m\eta)]d\xi d\eta \ . \qquad (5.31)$$

In the case where there is symmetry around the zenith, the above equations (which describe the total power, the spatial correlation, and the back–scatter cross–section) are re–written as

$$2\pi \int_0^1 W(s)sds \ = \ \frac{2\pi KM}{h^2} \int_0^1 G_T(s)G_R s\sigma(s)sds$$

$$\begin{aligned} \rho(r) &\propto \int_0^1 G_T(s)G_R(s)\sigma(s)J_0(2\pi rs)sds \\ \sigma(s) &\propto \frac{1}{G_T(s)G_R(s)}\int_0^{+\infty}\rho(r)J_0(2\pi rs)rdr \ . \end{aligned} \tag{5.32}$$

In the case where the scatterers are isotropic (i.e. $\sigma(s) = \text{constant}$), the back–scattered power depends only on the transmitting and receiving antenna polar diagrams. *Briggs & Vincent* [1973] examined such a case where they assumed that the polar diagrams possessed a Gaussian form, each with a e^{-1} half–width, s_0, so that:

$$\begin{aligned} G_T &\propto \exp\left[\frac{-s^2}{s_0^2}\right] \\ G_R &\propto \exp\left[\frac{-s^2}{s_0^2}\right] \\ W(s) &\propto \exp\left[\frac{-2s^2}{s_0^2}\right] \ . \end{aligned} \tag{5.33}$$

The spatial correlation is then given as

$$\rho(r) \propto \int_0^1 \exp(\frac{-2s^2}{s_0^2})J_0(2\pi rs)sds \ , \tag{5.34}$$

which gives

$$\rho(r) = \exp[-\frac{1}{2}\pi^2 s_0^2 r^2] \ . \tag{5.35}$$

In the original derivation by *Briggs & Vincent* [1973] W(s) was found by incorrectly assuming that the total power was proportional to $\int W(s)s^2ds$ instead of $\int W(s)sds$. In that case the spatial correlation function was

$$\rho(r) \propto \int_0^1 \exp(\frac{-2s^2}{s_0^2})J_0(2\pi rs)s^2ds \ , \tag{5.36}$$

the solution of which is a confluent hypergeometric function

$$\left\{\frac{\Gamma(\frac{1}{2}\nu + \frac{1}{2}\mu)(\frac{1}{2}\frac{b}{a})^\nu}{2a^\mu\Gamma(\nu+1)}\right\} M(\frac{1}{2}\nu + \frac{1}{2}\mu, \nu+1, \frac{-\frac{1}{4}b^2}{a^2}) \ , \tag{5.37}$$

which leads to the following normalized solution

$$\rho(r) = e^{-\left\{\frac{\pi r s_0}{\sqrt{2}}\right\}^2} M\left(-\frac{1}{2}, 1, \left\{\frac{\pi r s_0}{\sqrt{2}}\right\}^2\right) \ . \tag{5.38}$$

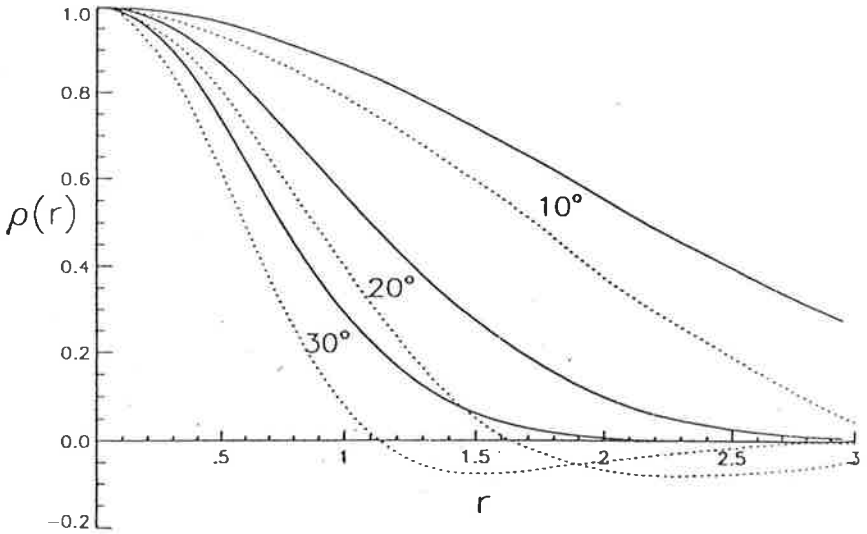

Figure 5.14: Spatial correlation functions, $\sigma(r)$, as a function of receiver separation, r, in units of wavelength. The scatterers are isotropic, and the antenna polar diagrams for both transmitting and receiving arrays are given by $\exp[-s^2/s_0^2]$, where $s = sin\theta_0$. Curves are for θ_0 values of 10°, 20°, and 30°. The solid line curves are from equation 5.39, while the dotted are from equation 5.38, and are incorrect, due to the extra s factor [from *Briggs*, 1992].

The *correct* result obtained from equation 5.35 is (much simpler)

$$\rho(r) = \exp[-\frac{1}{2}\pi^2 s_0^2 r^2] \quad . \tag{5.39}$$

The results for both equations 5.38 and 5.39 are compared in figure 5.14, for various θ_0 values [from *Briggs*, 1991].

If the scatterers are not isotropic and possess a back–scatter polar diagram with a Gaussian dependence we can similarly determine $\sigma(s)$:

$$\begin{aligned} \sigma(s) &\propto \exp[-\frac{s^2}{s_1^2}] \\ G_T(s) &\propto \exp[-\frac{s^2}{s_2^2}] \\ G_R(s) &\propto \exp[-\frac{s^2}{s_3^2}] \quad . \end{aligned} \tag{5.40}$$

In this case the returned power is proportional to

$$W(s) \propto \exp\left[-\frac{s^2}{s_4^2}\right] \text{ , where ,} \tag{5.41}$$
$$\frac{1}{s_4^2} = \frac{1}{s_1^2} + \frac{1}{s_2^2} + \frac{1}{s_3^2} \text{ ,}$$

which now defines the spatial correlation as

$$\rho(r) = \exp[-\pi^2 s_4^2 r^2] \text{ .} \tag{5.42}$$

This now enables us to determine s_1, the width of the polar diagram of the scatterers, provided that the antenna polar diagrams are known. We can relate the antenna separation, $r_{0.5}$ (in units of wavelength) at which the spatial correlation falls to one half its value, to the angle θ_4 measured in degrees where $s = sin\theta_4$. For small θ_4 this is

$$r_{0.5} \simeq \frac{15.2}{\theta_4} \text{ .} \tag{5.43}$$

If equation 5.38 was used to derive this result the constant would incorrectly be 12.0 as reported in some literature [*Hocking*, 1987b].

Determination of the spatial correlation function

To determine the spatial correlation function experimentally, one would normally need a large antenna array. *Felgate & Golley* [1971], used the 1 × 1 km Buckland Park 89 antenna 2 MHz array to examine the spatial correlation functions produced by total reflections from the E, E_s[3] and F layers, as well as partial reflections from D layers. They used a total of 89 antennas coupled to individual receivers, which unfortunately were not phase–sensitive so that the pattern sampled was amplitude only. This meant that $\sigma(l, m)$ could not be calculated, although the motion of the pattern and its scale and features could be obtained. Figure 5.15a and b shows the reflected amplitude pattern from the F–region and the D–region respectively [from *Felgate & Golley*, 1971]. The spatial pattern from the F–layer (figure 5.15a) shows an unvarying fringe–like pattern, with fringes aligned perpendicular to the direction of motion, while the D–region

[3]Sporadic E layers

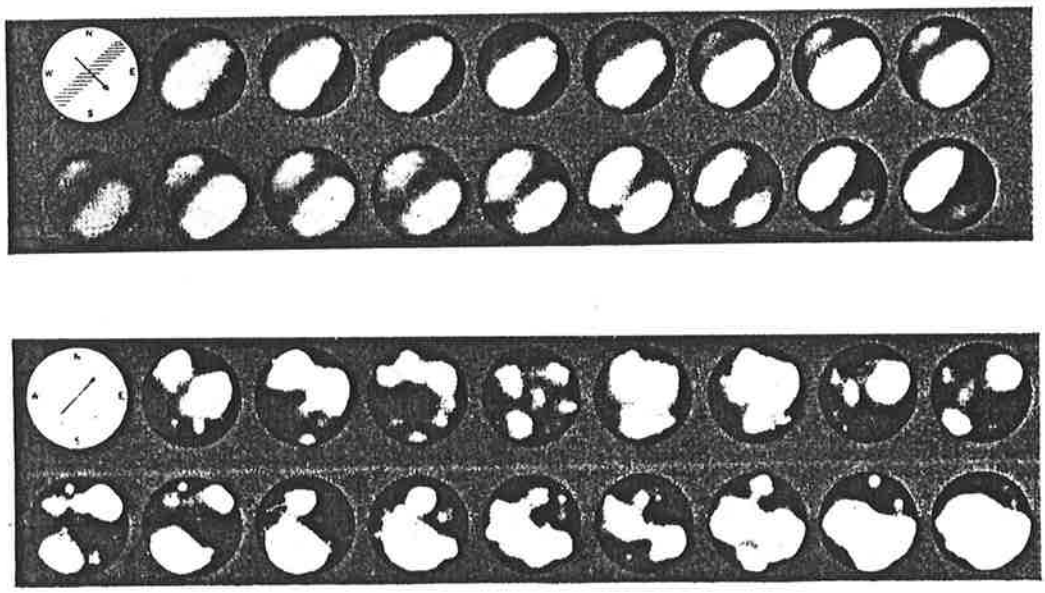

Figure 5.15: Spatial correlation patterns obtained by the 1km Adelaide array. Each of the 89 dipoles was connected to a separate receiver whose output was connected to a filament lamp. The brightness of the lamp was proportional to the amplitude of the reflected signal. The lamps were arranged in the same configuration as the receiving array, which meant that the pattern formed by the light duplicated that of the radio wave pattern. The motion of the pattern is indicated by the arrow. (a) represents the total reflection pattern from the night–time F–region (300km) sampled every 0.75 seconds. The nature of the fringes is an indication that the reflections might be caused by individual specular points (b) represents the partial reflection pattern from the D–region sampled every 0.5 seconds. The F–region pattern is unchanging in form as it moves, unlike that from the D–region [from *Felgate & Golley*, 1971].

pattern (figure 5.15b) is random and changes in form as it moves. This indicates that the reflections might be caused by individual specular points in the F region, but not in the D region.

The use of this large array was somewhat unique because of the large number of individual antennas used. Other studies also looked at these amplitude patterns, but used a much smaller number of antennas, ranging from 3 to 36 [see e.g. *Mitra*, 1949; *Harnischmacher*, 1963; *Kelleher*, 1966; *MacDougall*, 1966; *Beynon & Wright*, 1969].

Fortunately, if the primary objective is to determine $\rho(\xi, \eta)$, one need not use a large number of antennas, since many of the vectorial separations would be duplicated. If the ground

diffraction pattern is symmetrical one need only use a single antenna which measures a cross–section of the pattern as it moves. The velocity must be determined also. This idea has been used in the past to measure aspect sensitivity [see e.g. *Haug & Pettersen*, 1970; *Woodman & Chu*, 1989]. Unfortunately, the assumption of symmetry is unlikely to be true. In that case a useful approach is to parameterize the form of the spatial correlation function. This has been discussed in length in section 3.5, where the full correlation analysis determines the form of such a function from the use of three antennae only. Although the full correlation analysis is used primarily to determine the wind, as a byproduct it does determine the statistical properties of an (assumed) elliptical correlation function, including the orientation of the major axis, its length and the axial ratio. Since this ellipse is defined as the scale at which the modulus of the complex auto–correlation function falls to 0.5, we have the simple relationship

$$\theta_{sb} = \frac{15.2\lambda}{\sqrt{ab}} \ , \tag{5.44}$$

where θ_{sb} is e^{-1} the width of the effective polar diagram, λ is the radar wavelength, and a and b are the lengths of the major and minor axis respectively[4].

This method has been previously used by *Lindner* [1975a, b], who produced spatial auto–correlation functions using a 1.98 MHz radar, and then Fourier transformed them to determine the back–scatter polar diagrams. Values of θ_s of 10–15° were generally found above the mesopause and 2–5° below. The use of the spatial correlation functions is also unique, for in the case where $a \neq b$ it provides 2–dimensional information on the scatterers.

5.4 Amplitude distributions

Another technique, and perhaps one of the earliest used to determine the nature of radar scattering, involves amplitude distributions of scattered wave fields. First used to study the nature of the scattering mechanism in the D region, this method attempts to determine the nature of scattering by comparing measured amplitude distributions with theoretical probability density distributions, and is particularly useful when some of the scattering is assumed to be

[4]It is common to use $\sqrt{ab}$, as this is the radius of a circle with an area equal to that of the ellipse.

due to horizontal stratification, or to quasi–specular scatterers which are fairly long–lived, i.e.. in the order of at least minutes [see e.g. *Von Biel*, 1971, 1981; *Vincent & Belrose*, 1978; *Fukao et al.*, 1980b; *Röttger*, 1980a; *Rastogi & Holt*, 1981; *Sheen et al.*, 1985; *Kuo et al.*, 1987; *Hocking*, 1987c, 1988b]. Although the uses of amplitude distributions takes many different forms, all are based on a general theme. We will concentrate on the simplest technique.

If the scatter from the atmosphere is assumed to be due to a volume of similar scatterers, then the resulting amplitudes follow a *Rayleigh* distribution, where the probability of an amplitude in the range z to $z + dz$ is,

$$P_R(z).dz = \frac{2z}{k^2}.e^{-\frac{z^2}{k^2}}dz, \tag{5.45}$$

where k^2 is the received mean square amplitude and the variance of one component is $\sigma^2 = \frac{1}{2}k^2$. If, however, some of the scatter is also due to single, strong specular scatterers, the amplitude histograms are no longer Rayleigh. The resulting distributions have been compared with various known distributions, such as the Hoyt, log–normal, Nakagami–M, and Rice distributions [e.g. *Beckmann*, 1962; *Von Biel*, 1971, 1977, 1981; *Mathews et al.*, 1973; *Barakat*, 1976; *Newman & Ferraro*, 1976; *Chandra & Vincent*, 1977; *Vincent & Belrose*, 1978; *Röttger*, 1980a; *Rastogi & Holt*, 1981; *Sheen et al.*, 1985; *Hocking*, 1987c]. Of these, the most commonly used is the Rice distribution [*Rice*, 1944, 1945], which assumes that the received signal is a combination of a random component, and a single long–lived specular component. The resulting amplitude probability distribution is given as;

$$P'(z)dz = \frac{2z}{k^2}.\exp\left[-\frac{z^2 + L^2}{k^2}\right].I_0\frac{2Lz}{k^2}dz \ , \tag{5.46}$$

where L is the amplitude due to the specular component, and I_0 is the modified Bessel function of the first kind [*Hocking*, 1987c]. We parameterize such a distribution by the ratio of the strength of the specular component to the RMS or random component, and define this as the *Rice parameter*, denoted by α. When there is no specular component, and L is zero, the Rice probability density function (equation 5.46) reduces to the Rayleigh distribution. Figure 5.16 shows a collection of theoretical Rice distributions as the specular component increases, in steps of $\alpha = 0.5$.

Figure 5.17 shows plots of the mean power, mean fading time, and mean Rice parameters measured with a vertical beam (4.5° half–power half–width) for around one hour in August, 1979. It can be clearly seen that enhanced scattering layers exist at heights of around 86 km, 74–76 km, and 68–70 km, and this is well correlated with the Rice parameter which also peaks at these altitudes. While the 68–70 km, and the 86 km layers exhibit Rician tendencies, the 76 km layers shows $\alpha \approx 1$, which is that expected for a Rayleigh distribution. This, should, however not be interpreted as turbulence, as the fading time indicates that the scattering was quite specular. Indeed *Hocking* [1987c] interpreted this as evidence for a number of specular scatterers in the radar volume at one time.

Figure 5.18 is another calculation of the Rice parameter, but this time using the SOUSY VHF radar in Germany [*Hocking*, 1987c]. The Rice parameters were calculated using three beams; a vertical, a 7° North beam, and a 7° East beam. The vertical beam shows the Rice parameter increase just above the tropopause, which indicates the dominance of specular reflectors. An interesting feature is, however, the comparison of the Rice parameter for the two off-vertical beams, which are at right angles to each other. While the East beam indicates that the mean α is fairly constant with altitude and generally Rayleigh, α measured with the

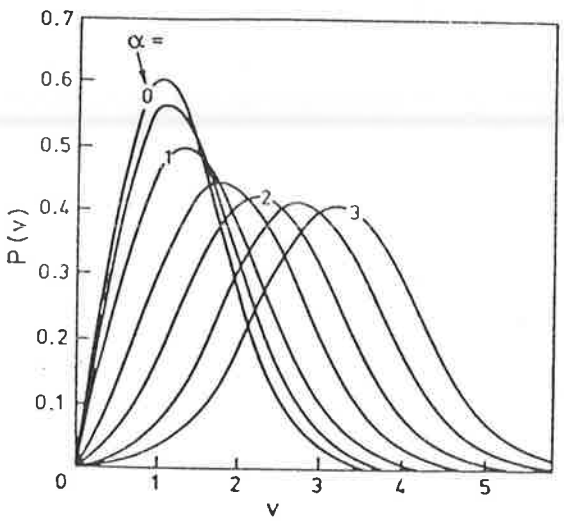

Figure 5.16: Rice distribution in steps of $\alpha = 0.5$, as a function of v, where $v = z/\sigma = \sqrt{2}z/k$, where z is the received amplitude, k is the RMS scattered power, and σ is the standard deviation of the in–phase and quadrature scattered signal components. An increasing α indicates an increasing specular contribution to the back–scatter amplitude signal [from *Hocking*, 1987c].

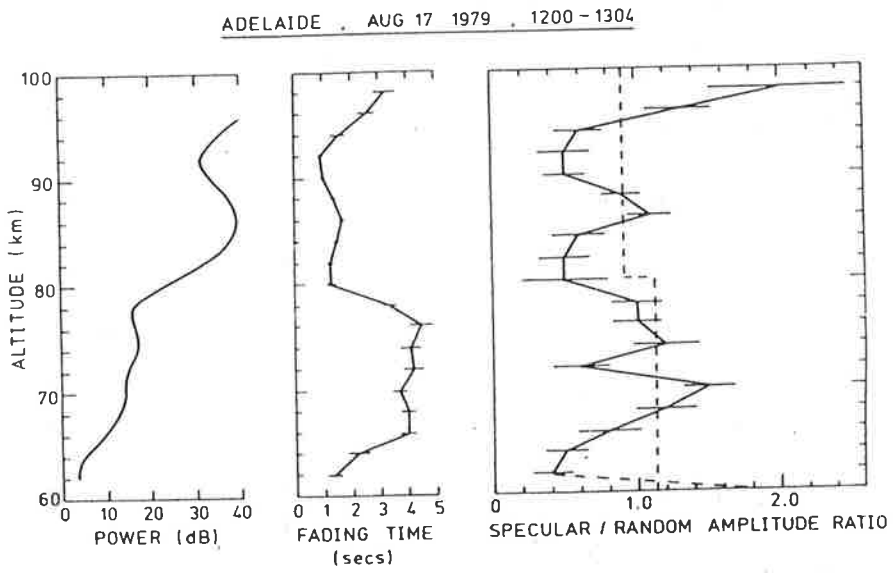

Figure 5.17: Profiles of mean power, fading time, and α, the Rice parameter, for altitudes of 60-100km, measured at Buckland Park in August, 1979, using a vertical beam (half–power half–width of 4.5°). The error bars associated with the fading time and α, are standard deviations of the mean. The expected mean Rice parameter, for a Rayleigh distribution based on the data length and the fading times, is shown as the dashed line superimposed on the plot of α. The large α values above 90 km are caused by the tail of the E–region, which causes the slow fading time, and subsequently large α values [from *Hocking*, 1987c].

North beam is appreciably larger. One possible reason for this asymmetry is that the wind, which was quite a strong easterly, physically affects the scatterers by stretching them along the wind direction; this would cause the back–scattering polar diagram of the scatterers to be wider in the N–S vertical plane. Another reason may be that the strong wind prevented the quasi–specular scatterers from tilting along the E–W direction, so that only the N–S aligned scatterers tilted, thus biasing the results in favour of the N–S plane. See *Hocking et al.*, [1986], for further experimental details.

Although a Rice distribution is a good indicator of the presence of specular scattering for individual or layered scatterers, and a Rayleigh distribution an indicator of turbulent scatter, these conclusions must be treated with some caution. In the case that several scatterers, which could even be specular, are contained within the radar volume, and possess different radial velocities, the resulting distribution might still appear Rayleigh. The Rice distribution only applies if there are only one or two dominant reflectors. Furthermore, if short data sets are

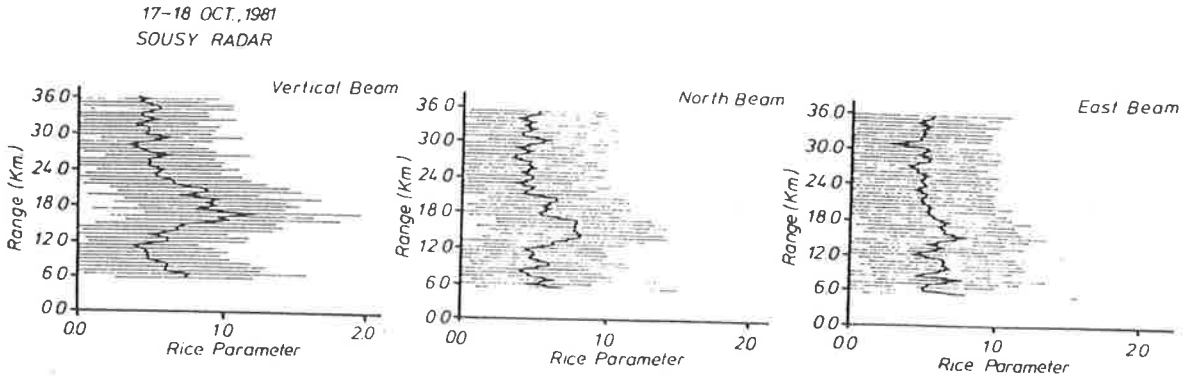

Figure 5.18: Mean Rice parameters, for an altitude spanning between 6 and 36km, measured with the German VHF SOUSY radar in October, 1981. Three beams were used, one vertical, two off–vertical at 7° N and 7°E. With a total observation period of 25 hours, the mean and the one sample standard deviations, here represented as horizontal bars, were constructed from between 20 to 50 individual measurements [from *Hocking*, 1987c].

used,larger Rice parameters can be obtained even when the original distribution was Rayleigh [see e.g. *Von Biel*, 1981; *Hocking*, 1987c]. At times the Rice parameter might not even be appropriate, for the amplitude statistics might neither be Rayleigh nor Rician. In that case other distributions might be better suited, for example the Nakagami–M, which is useful if the specular component possesses undulations and focuses and de–focuses the reflected radiation [see e.g. *Sheen et al.*, 1985]. Other, more complex models have also been proposed; for example *Vincent & Belrose*, [1978] compared measured amplitude distributions with those expected for several specular scatterers superimposed upon a weak background scatter. The use of phase distributions has been discussed by *Röttger*, [1980a].

5.5 Horizontal correlation lengths

If we assume that the scatterers are aspect–sensitive, and possess ellipsoidal shapes with a Gaussian radial variation of refractive index, then the above methods of observing θ_s enable us to directly calculate the ratio of the horizontal to vertical scales [see e.g. *Hocking*, 1987b].

Consider a Gaussian variation in the refractive index which takes the form $\exp-[\frac{x^2+y^2}{L^2} + \frac{z^2}{h^2}]$

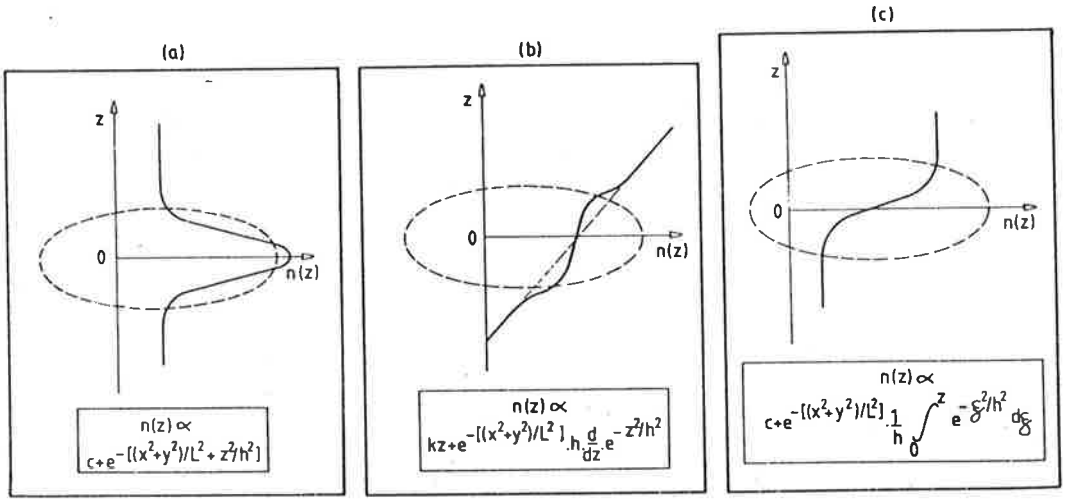

Figure 5.19: Some hypothetical refractive index variations; (a) falling off in a Gaussian manner. (b) Increasing linearly in height, but tending to be more constant across the scatterer. (c) A large change in a constant refractive index. [from *Hocking*, 1987b].

(see figure 5.19*a*). This has been considered by *Briggs & Vincent* [1973], who discussed the case where such scatterers were observed by a monostatic radar (similar studies have been done by *Doviak & Zrnić* [1984]). The back–scattered power as a function of zenith angle is then proportional to $(\pi^{\frac{3}{2}} L^2 h)^2 \, . \, P'$ where,

$$P' = \exp\left[-\frac{8\pi^2}{\lambda^2} \, . \, (L^2 s^2 \, + \, h^2(1 - s^2))\right] \, , \tag{5.47}$$

and $s = \sin\theta$. If such scatterers produce an angular variation of signal strength which is a function of $\exp[-\sin^2\theta / \sin^2\theta_0]$, it can easily be shown that

$$\begin{aligned} \frac{\sin^2\theta}{\sin^2\theta_s} &= \frac{8\pi^2}{\lambda^2} \, . \, [L^2 - h^2] \, . \, \sin^2\theta \, , \text{ or,} \\ \frac{L}{h} &= \sqrt{(\frac{\lambda}{h})^2 \, . \, \frac{1}{8\pi^2 \sin^2\theta_s} \, + \, 1} \, , \end{aligned} \tag{5.48}$$

where L is defined as the horizontal correlation length and h the vertical correlation length. Figure 5.20 is a plot of the back–scattered power for such a scatterer, as a function of the vertical scale of the irregularities measured in wavelengths [from *Briggs & Vincent*, 1973]. A resonance which is centered on 0.2λ indicates that irregularities of this vertical scale are preferentially scattered. This is analogous to the well known fact that only Fourier components of

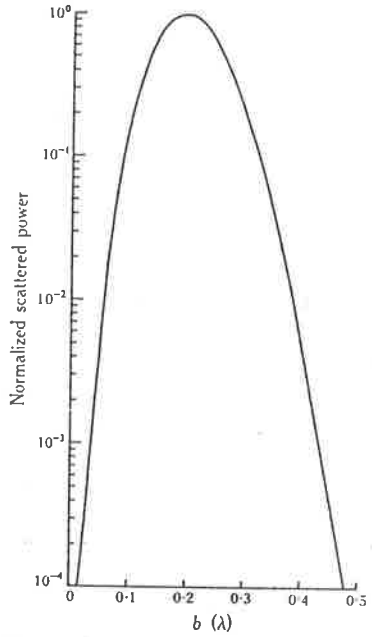

Figure 5.20: Normalized scattered power for an overhead irregularity of Gaussian form as a function of its vertical scale measured in wavelengths λ. The sharp resonance which is centered on 0.2λ indicates that irregularities of this scale are preferentially selected by an incident wavelength λ [from *Briggs & Vincent*, 1973].

wavelength $\frac{\lambda}{2}$ contribute to the back–scattered power for an incident wavelength λ. Furthermore, the resonance is sufficiently sharp to permit the assumption that, although other scales will contribute to the total back–scattered power, those with $h \approx 0.2\lambda$ dominate the observed back–scatter.

It could be argued that the scatterers may not possess a vertical Gaussian profile. For example, consider the cases such as in figure 5.19b and c, where in b the vertical refractive index increases linearly with height and tends more constant across the scatterer, while in c the refractive index varies markedly within the scatterer and is relatively constant otherwise. In both models, it has been assumed that the total change in refractive index across the scatterer is independent of vertical scale h. It can be shown that, even for such a diverse range of scattering profiles, the optimal vertical scale for back–scatter is around 0.2λ, ranging from 0.15λ to 0.3λ [*Hocking*, 1987b]. Therefore, even if θ_s can be the result of a range of (L,h) pairs, this range is fairly constrained. The relation between (L,h) and θ_s as defined in equation 5.48 is plotted in figure 5.21 for various values of h ranging from 0.15 to 0.32 [from *Hocking* 1987b].

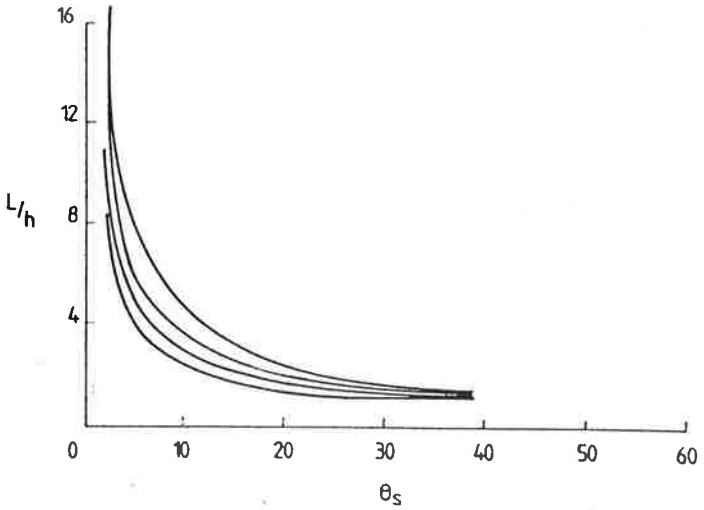

Figure 5.21: Aspect ratio of scatterers as a function of aspect sensitivity, plotted for various values of h from 0.15 λ to 0.32 λ, as described in equation 5.48. Although it would not be possible to deduce L/h precisely from θ_s values, a fairly small range of values can be determined [from *Hocking*, 1987b].

This makes it possible to determine a fairly narrow range of L/h for any θ_s value. In addition, if θ_s is $\leq 10°$, equation 5.48 can be approximated by

$$L = \frac{\lambda}{2\sqrt{2}\pi \sin\theta_s} \approx \frac{0.1125\lambda}{\sin\theta_s} \quad . \tag{5.49}$$

This expression enables a direct calculation of the e^{-1} horizontal scale (L) of the scatterers from small θ_s values, without any presumption about the ratio of horizontal to vertical scales. The auto-correlation function of the scattering medium is the same as the auto-correlation function of an individual scatterer and has a width $\sqrt{2}$ times that of the scatterer itself. The e^{-1} horizontal correlation length of the scattering or irregular medium is therefore $\sqrt{2}$L. If the correlation length of the irregular medium for a correlation of 0.5 is denoted as $\rho_{0.5}$, then this is given by

$$\rho_{0.5} = \sqrt{2} ln 2 L \simeq \frac{7.6\lambda}{\theta_s} \quad , \tag{5.50}$$

where θ_s is expressed in degrees.

This result seems intuitive, when compared with the expression relating to the spatial auto-correlation function (equation 5.43). The diffraction pattern measured by the receivers moves at a velocity twice that of the scatterers, the so called point source effect. In the same way, the size of the ground spatial autocorrelation function can be seen to be twice that of the scatterers.

Horizontal orientation of scatterers

As discussed in chapter 2, turbulence can not only be anisotropic in the vertical plnae, but it can also be anisotropic in the horizontal plane [e.g. *Gage & Balsley*, 1980; *Waterman et al.*, 1985]. In the full correlation analysis, one obtains a spatial diffraction pattern which is a two-dimensional feature. Besides the ground diffraction pattern scale one is also provided with information about its elongation and orientation within the horizontal plane. Whereas the geometrical mean of the ground diffraction pattern is used to determine θ_s, the orientation of the diffraction pattern can also be used to provide information on the preferential orientation of the partial reflection radar scatterers which are mirrored by the ground diffraction pattern [*Ratcliffe*, 1956].

5.6 Other measurements of θ_s

Observations of atmospheric scatterers have shown that the scatterers exhibit aspect sensitive behaviour. Small values of θ_s indicate that the scatterers are quite specular with the back–scattered power falling off rapidly with zenith angle. Larger values of θ_s imply that the scatterers are more isotropic. At times, both scatterer types might even co–exist. Figure 5.22 exhibits the measured back–scattered power as a function of 5 zenith angles [from *Czechowsky et al.*, 1988] for three different periods. It clearly shows the transition from quasi–specular scatter to more isotropic scatter at a zenith angle of about 13°, and supports other evidence such as that shown in figure 5.3.

Other θ_s values have recently been compiled by *Reid* [1988], who summarized measurements of various mesospheric θ_s values, at MF; [*Hocking*, 1987b; *Adams et al.*, 1989; *Lindner*, 1975a, b; *Golley & Rossiter*, 1971; *Hocking*, 1979; *Vincent & Belrose*, 1978; *Reid*, 1988; *Fritts & Vincent*, 1987], and at VHF; [*Czechowsky et al.*, 1984, 1988; *Fukao et al.* 1979, 1980a; *Sato et al.*, 1985]. The results obtained by *Hocking* [1987b] were deduced from back–scatter fading times and mean horizontal spaced–antenna winds observed by *Stubbs* [1977], *Manson & Meek* [1980], and *Manson et al.* [1985]. These results are plotted in figure 5.23, and although they are

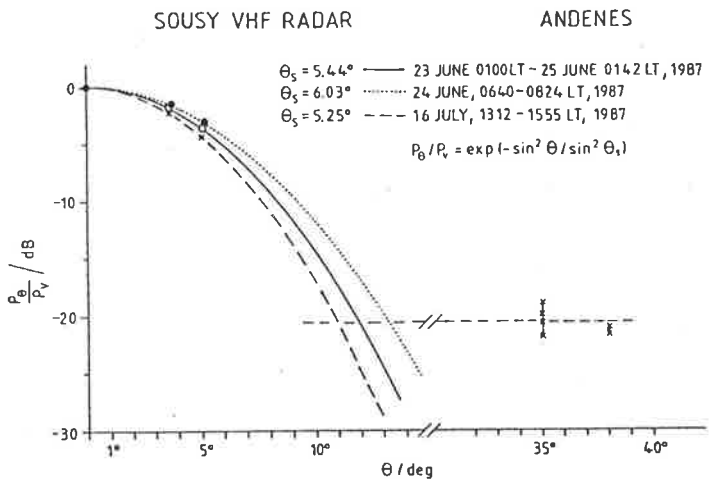

Figure 5.22: Variation in backscattered power as a function of increasing zenith angle measured at five different angles. At an angle of about 13° there seems to be a transition from quasi–specular to more isotropic scatter, which might indicate isotropic turbulent scatter [from *Czechowsky et al.*, 1988].

composed of various measurements at diverse times, locations, and made using varied methods, (suggesting that absolute values should be treated with caution), general tendencies can be seen. Firstly, for the MF studies, in most of the cases the majority of back–scatter occurs within a 20° zenith angle. Below around 80km most θ_s values tend to be less than 9° and all are below 16°, while θ_s is generally seen to decrease with decreasing height between about 65–95 km. Secondly, for the VHF studies, θ_s is generally small below about 75km, increasing above this height. The mid–latitude results from the Kyoto radar indicate quite isotropic scatter, quite different from high–latitudes summer results. The polar summer mesopause echoes (PMSE) are quite aspect sensitive and are similar to returns below 75 km at low–latitudes.

It is thought that the PMSE is either due to very intense turbulence [*Balsley et al.*, 1983; *VanZandt & Fritts*, 1989], or to the presence of heavy water cluster ions which extend the ionization irregularity scales to values less than the Kolmogorov microscale [*Kelley et al.*, 1987]. While the second reason seems to be more likely to account for the very high powers [*Czechowsky et al.*, 1988, 1989; *Reid et al.*, 1988], intense turbulence due to gravity wave supersaturation can occur when upward propagating gravity waves are compressed at temperature inversions, and subsequently dissipate as their amplitudes exceed the saturation limit when they grow again above the inversion [*Dewan et al.* 1984; *Smith et al.* 1987; *Fritts et al.*, 1988a, b]. The

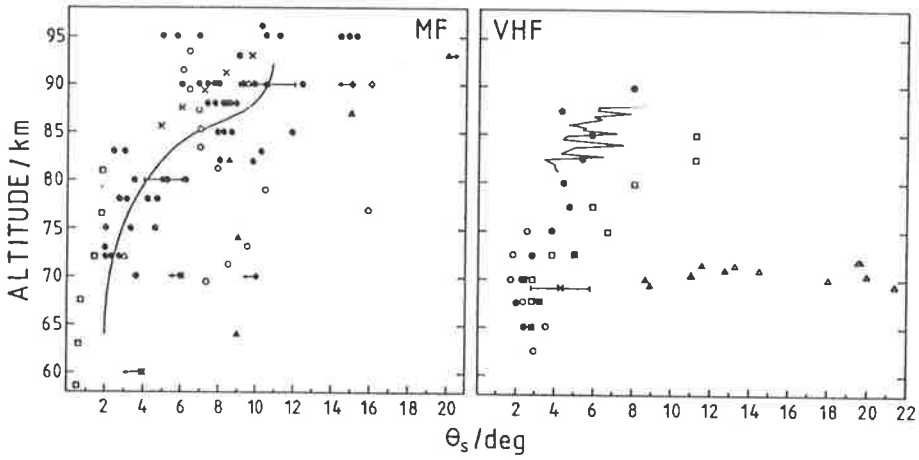

Figure 5.23: Values of mesospheric θ_s observed at MF (left) and VHF (right) at a number of locations. The MF results are obtained from the following studies: asterixes (Tromsø, 69° N), closed diamonds (Townsville, 16° S), closed squares (Adelaide, 35° S) [from *Hocking*, 1987b]; open squares (Boot Lake, 40° N) [*Adams et al.*, 1989]; closed circles and continuous line [*Lindner*, 1975a, b]; open diamond (Adelaide 35° S) [*Golley & Rossiter*, 1971]; open triangles (Adelaide 35° S) [*Hocking*, 1979]; closed triangles (Ottawa, 45° N) [*Vincent & Belrose*, 1978]; crosses (Adelaide, 35° S) [*Reid*, 1988], open circles (Adelaide, 35° S) [*Fritts & Vincent*, 1987]. The VHF results are obtained from the following studies: cross (Arecibo, 19° N) [*Czechowsky et al.*, 1984]; open and closed circles and squares (Jicamarca, 12° S) [*Fukao et al.* 1979, 1980a]; open and closed triangles (Kyoto, 35° N) [*Sato et al.*, 1985]; and continuous line (Andenes, 69° N, summer) [*Czechowsky et al.*, 1988]; [from *Reid*, 1990].

PMSE is, however, limited to high-latitude sites and has only been observed in the northern hemisphere. This should not be interpreted as meaning that the PMSE does not exist in the southern hemisphere. Rather, due to a lack of high resolution VHF radars, no observations of it have yet been made.

This thesis studies the seasonal and latitudinal behaviour of the aspect sensitivity of mesospheric scatter measured at three sites in the southern hemisphere over several years. These results will be presented and discussed in the following chapters.

5.7 Measuring turbulent energy dissipation rates

As mentioned earlier in this thesis, there are several distinct ways of measuring turbulence energy dissipation rates in the atmosphere. Two of these are *in situ* measurements, namely balloons and rockets, while a third involves remote sensing, utilizing radars. We will discuss only radar methods, of which there are two. One involves the measurement of the absolute

back–scattered power, and the other the spectral width as measured by the radar. We will discuss each method in turn.

5.7.1 Measuring energy dissipation rates from backscattered power

In the case of weak coherent scattering when using radars, we can write the back–scatter cross–section as [*Hocking*, 1985; after *Booker*, 1956]

$$\sigma = 0.00655\pi^{\frac{4}{3}} C_n^2 \lambda^{-\frac{1}{3}} \quad , \tag{5.51}$$

where C_n^2 is the potential refractive index structure constant, and λ is the radar wavelength. σ determines the total received power of a radar system P_R, [*Hocking*, 1985, 1989], through the relation

$$P_R = \frac{P_T e_T e_R G A_R}{4\pi z^4} \frac{V}{ln\, 2} \sigma \quad , \tag{5.52}$$

where P_T is the transmitted power, e_T the efficiency of the transmitting system and e_R that of the receiving system, G is the transmitter antenna gain, A_R is the effective area of the receiving array and z is the range or height of back–scatter. In the case of a monostatic[5] radar we can combine equations 5.51 and 5.52 to give

$$C_n^2 \approx \frac{66 P_R z^2 \lambda^{\frac{1}{3}}}{P_T A_R e_T^2 \Delta z} \quad , \tag{5.53}$$

where Δz is the spatial pulse length and is $\ll z$. Equation 5.53 can be used to determine the structure constant of turbulence, provided that the radar volume is completely filled with turbulence. As this is very rarely the case C_n^2 measured by the radar must be divided by a factor F_t which represents the fraction of the volume observed with the radar which actually contains turbulence. The refractive index structure constant for turbulence alone can be determined by

$$C_n^2(turb) = \frac{C_n^2(radar)}{F_t} \quad . \tag{5.54}$$

Estimating F_t within the mesosphere may at times be rather difficult, since the thickness of the scattering structures is quite variable and F_t can vary between 0.01 and 1 [*Czechowsky et al.*, 1979; *Gage & Nastrom*, 1985].

[5] one set of antennas used for both transmitting and receiving

An equation relating the energy dissipation rate, ϵ, to C_n^2 was initially proposed by *Tatarski* [1961], i.e.

$$C_n^2 = a^2 \alpha' K_m M_n^2 \epsilon^{-\frac{1}{3}} \quad , \tag{5.55}$$

where a^2 is a constant assumed to be 2.8, α' is the inverse of the Prandtl number, K_m is the momentum diffusion coefficient, and M_n^2 is the effective vertical potential refractive index gradient [see e.g. *Ottersten*, 1969a]. K_M is related to ϵ through the following

$$K_M = \frac{c_2 \epsilon}{\omega_B^2} \quad , \tag{5.56}$$

[e.g. *Weinstock*, 1978a, b; *Lilly et al.*, 1974] where c_2 is a constant thought to be $\sim$ 0.8. Combining equation 5.55 and 5.56 we finally come to an equation relating C_n^2 to ϵ:

$$\epsilon = \left\{ \frac{C_n^2 \omega_B^2}{a^2 \alpha' c_2 M_n^2} \right\}^{\frac{3}{2}} \quad . \tag{5.57}$$

Recently, the relationship between the strength of atmospheric radar backscatter and the intensity of atmospheric turbulence has been re–formulated by *Hocking* [1992], who proposes that the relation between the two quantities should have an extra dependence on the Richardson number. The above equation can be re-written as

$$\epsilon = [\gamma C_\xi^2 \omega_B^2 M_\xi^{-2}]^{\frac{3}{2}} \quad , \tag{5.58}$$

where γ is a constant, C_ξ^2 is the structure constant for fluctuations in any passive and conservative tracer ξ, and M_ξ is the mean gradient of the quantity ξ across the turbulent patch, and ω_B^2 is the Brunt-Väisälä frequency in radians per second. The constant γ has taken many forms in the literature, but it has always been assumed that it was just that, a constant [see e.g. *Tatarski*, 1961; *VanZandt et al.*, 1978; *Hocking*, 1985; *Luebken et al.*, 1987; *Blix et al.*, 1990]. *Hocking* [1992] argues that for γ to be a true constant, the ratio between the kinetic and potential energy spectra is a universal constant, an assumption that might be unreasonable. He proposes that the ratio of the potential and kinetic energy spectral densities is a function of the Richardson number, R_i, and that ϵ is given as

$$\epsilon = [\frac{3 C_N^2 \omega_B^2}{22 \frac{|R_i|}{|1-R_i|}} M_N^2]^{\frac{3}{2}} \quad , \tag{5.59}$$

for C=2.0. Thus γ is given as (for $R_i < 1.0$)

$$\gamma = \frac{3}{22}\frac{|R_i|}{|1 - R_i|} \ . \tag{5.60}$$

5.7.2 Measuring energy dissipation rates using radar fading times

The other method of calculating ϵ involves measuring the spectral widths of the returned signal. To obtain ϵ, data must first be filtered to reject signals due to specular reflectors. Usually this is fairly straight forward since such signals are seen as a spikes in the otherwise Gaussian spectrum, although in some rare cases most of the radar signal return is due to specular reflectors, and it is not feasible to extract meaningful spectral widths. Once the specular reflector contributions have been removed, it is necessary to remove the spectral width due to beam broadening, and for this an accurate knowledge of the profile of the wind with good temporal and height resolution is required. This can be obtained by either using the Doppler or spaced–antenna techniques [e.g. *Röttger*, 1981a; *Hocking*, 1985]. Although a detailed theory to estimate the resultant contribution has been given by *Hocking* [1983a, b], we can use simpler formulae. For relatively narrow beams ($\leq 5^o$ half-power half-width), the spectral half-power half-width due to effects other than turbulence is

$$f_{\frac{1}{2}}(Hz) = (1.0)\frac{2}{\lambda}\theta_{\frac{1}{2}}V_{hor} \ , \tag{5.61}$$

where λ is the radar wavelength, $\theta_{\frac{1}{2}}$ is the half-power half-width of the effective radar beam, and V_{hor} is the magnitude of the horizontal wind [see also *Atlas*, 1964; *Hitschfeld and Dennis*[6], 1956]. If the spectral width is experimentally measured and is denoted by f_{obs}, and one is using radars where the radar beam half–width is less then 5° we can then determine the experimental width that is due to the fluctuating motion of the scatterers only by [*Hocking*, 1985]

$$f_{turb}^2 = f_{obs}^2 - f_t^2 \ . \tag{5.62}$$

It is important to bear in mind that it will not always be possible to measure the spectral width due to the turbulence alone, especially if the horizontal wind motion is large. The mean square

[6] derived in an unpublished report

Effect	General comments
Beam broadening	Important for all beams, especially for beam widths $\geq 2°$. This may at times be the main contributor to the spectral width for vertical beams.
Shear broadening	Mainly important for off–vertical beams, increasingly so for larger zenith angles. Also relevant for long pulse lengths.
Vertical rms motions	Relevant for both vertical and off–vertical beams.
Horizontal rms motions	More relevant for off–vertical beams.
Anisotropic backscatter	Mainly relevant for vertical beams since specular reflectors tend to be mainly horizontally stratified.

Table 5.1: Contributors to the spectral width measured by radars [after *Hocking*, 1983a].

velocity of the scatterers is related to f_{turb}^2 by

$$V_{RMS}^2 = \frac{\frac{\lambda}{2}^2 f_{turb}^2}{2ln2} \quad , \tag{5.63}$$

which is related to ϵ through the following [*Hocking*, 1983a]

$$\epsilon = cV_{RMS}^2\omega_b \quad , \tag{5.64}$$

c being a dimensionless constant $\sim$ 0.4. Measuring V_{RMS} using Doppler radars has been discussed by *Hocking* [1983a, b], and we do not wish to go through his derivations here. What is of more interest in this case is measuring V_{RMS} using the spaced–antenna mode with full correlation analysis. This has been discussed in detail in section 3.5.3, and this procedure yields a parameter $T_{\frac{1}{2}}$, which is an estimate of the fading of a radar signal due to the random motion of the scatterers only, beam–broadening having already been removed. $T_{\frac{1}{2}}$ is related to V_{RMS} through [*Briggs*, 1977, 1980, 1984]

$$V_{RMS} = \frac{\lambda\sqrt{2ln2}}{4\pi T_{\frac{1}{2}}} \quad . \tag{5.65}$$

We can therefore find ϵ from $T_{\frac{1}{2}}$ by combining equations 5.64 and 5.65, i.e.

$$\epsilon = \frac{c\lambda^2 2ln2\omega_b}{16\pi^2 T_{\frac{1}{2}}^2} \quad . \tag{5.66}$$

5.7.3 Concluding Remarks

Although not initially obvious, the two methods of measuring turbulent energy dissipation rates described above do in fact measure different parameters. Whereas measurements of back–scattered power determine the mean ϵ within the radar volume, those measured via the spectral width method only involve ϵ within the scattering layer itself. Furthermore, the different techniques of measuring spectral widths may be biased. The main contributors to the spectral width have been summarized by *Hocking* [1983a], and these include beam broadening, shear broadening, both vertical and horizontal root mean square motions, and the effect of anisotropic scatterers (see table 5.1). For example *Schlegel et al.* [1978] made no attempt to remove these effects and they used quite arbitrary "constants" so their ϵ values are completely in error. Their seasonal variation may then just be the seasonal variation of the mean wind.

Other studies failed to distinguish between the horizontal and vertical fluctuations, and have also led to errors in estimation of ϵ [see e.g. *Manson et al.*, 1981; *Vincent et al.*, 1977; *Röttger & Vincent*, 1978; *Chakrabarty et al.*, 1981]. Furthermore there are two different techniques of measuring the spectral width, namely the Doppler and the full correlation analysis. Whilst both are prone to the spectral–width broadening effects as discussed above, the full correlation analysis, which utilizes spaced–antennas, may further over–estimate ϵ due to the wide radar beam–widths usually employed. As the radar beam–width increases, the contribution to the radial velocity by horizontal fluctuating motions increases. In the mesosphere, the volume encompassed by the radar beam can be several times greater than the gravity wavelength, the motion of which will thus broaden the spectrum even further. Thus estimates of ϵ can be over–estimated when employing the spaced–antenna system. Recent work has, however, suggested that the two methods are correlated to a degree, more so when looking at longer data sets, i.e. days as compared to hours [*Vandepeer and Hocking*, 1991].

Chapter 6

Seasonal results from Buckland Park

6.1 Introduction

This chapter examines the characteristics of various atmospheric parameters deduced from data obtained by an MF/HF radar located at Buckland Park[1], situated approximately 40 km north of Adelaide (35° 38'S, 138° 29'E). The system was constructed in the late 1960's to study the ionosphere and has since been used extensively to study the height range of approximately 60–100 km. It can be operated on two frequencies of 1.98 and 5.94 MHz, although in this work only 1.98 MHz was used.

The majority of the data used in this analysis were collected while the radar was operating in the spaced–antenna mode. This not only provided measurements of the mean winds, but it also provided information on the statistical properties of the ground diffraction pattern which is in turn related to the nature of the scattering medium. In this chapter we will discuss the various parameters that are deduced by the full correlation analysis method, and subsequently use these to determine various real physical properties of the radio wave scatterers in the mesosphere. We begin, however, with a brief description of the Buckland Park radar system.

[1]The unusual name stems from the nearby sheep station which once occupied the radar site

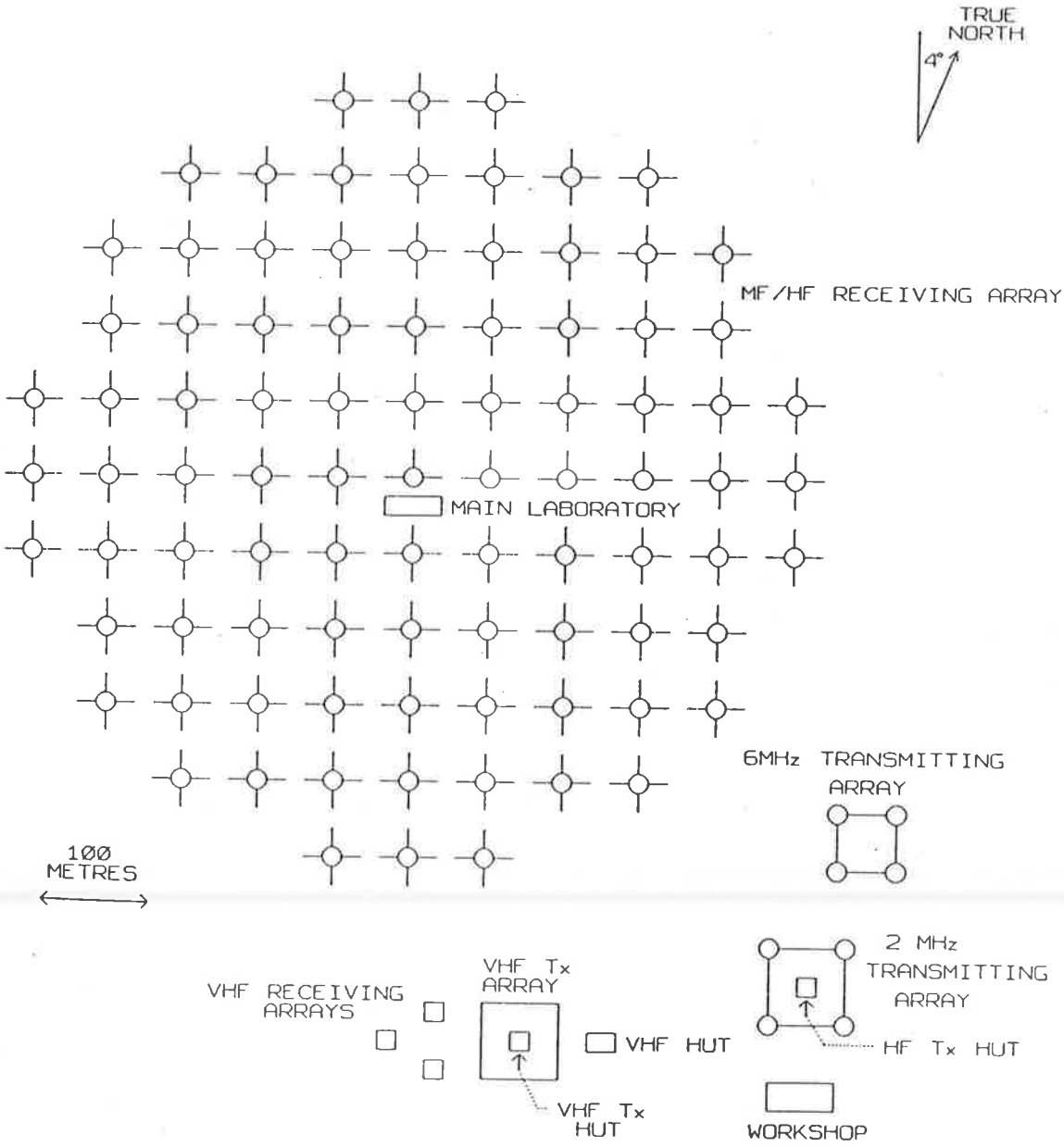

Figure 6.1: A ground layout of the Buckland Park site, showing the 89 MF/HF dipole antennas and the transmitting system [from *Murphy*, 1990].

6.2 Radar overview

The Buckland Park radar system is schematically shown in figure 6.1 [from *Murphy*, 1990]. The transmitting array consists of four centre–fed half–wave dipoles, arranged in a square, and suspended by towers at a height of 30 metres (approximately one–quarter wavelength). The dipoles are separated by approximately 75 metres. The resulting beam–width is about 40° half–power half–width. The dipoles are connected to a central transmitting hut by open twin–line transmission lines half a wavelength in length. Such an arrangement allows transmission of linear, left–hand[2] (E) or right–hand (O) circular polarization. Circular polarization is achieved by simply introducing a $\frac{\pi}{2}$ phase difference between the dipole pairs. During day–time, the O mode is generally used for transmitting, since the E mode is strongly absorbed above 80 km. Conversely, night–time observations use the E mode because of its better scattering characteristics.

The transmitter produces radio–frequency pulses with a Gaussian envelope and with a half–width of approximately 25 μs, giving a height resolution of about 4 km. The pulse repetition frequency is 20 Hz, and the peak power around 25 kW, the latter depending on the condition of the valves in the transmitter.

The receiving array is made up of 89 orthogonal dipoles, aligned 4° off north–south and 4° off east–west, and is also shown in figure 6.1. The whole array covers an area of approximately 1 km × 1 km. Each receiving dipole is 72 metres long, and these are suspended about 11 metres above ground level by wooden poles. Each dipole is independently connected to the main hut by a coaxial cable which is an integer number of wavelengths in length. With 89 dipoles connected in phase the receiving array has a beam–width of approximately 4.5° half–power half–width, with the first nulls at 11.6° off–zenith. Further details of the array can be found in *Briggs et al.* [1969].

The array can be used in two modes. Firstly, all of one set of 89 parallel dipoles can be coupled together to produce a large array with a very narrow polar diagram. This is achieved

[2] when looking in the direction of propagation, left–hand circularly polarized (southern hemisphere)

by phasing together dipoles within individual rows to produce a total of eleven outputs which can then be phased to swing the beam perpendicular to the orientations of the antennas. Since the first null of the whole polar diagram occurs at 11.6°, this is the angle often chosen for off–vertical beam experiments so that the strong scatter from overhead is minimized [*Hocking*, 1979]. In this configuration the array is used to measure both vertical and off–vertical Doppler velocities. Secondly, the array can be used in the 3 antenna spaced–antenna mode. In this case the usual configuration is such that each of the three antennas is made up of four adjacent dipoles (forming a square). The resulting time series are then analyzed using the full correlation analysis to determine mean winds and a statistical description of the scattering medium.

6.3 Experimental technique

The Buckland Park radar has been used to take observations of the mesosphere and ionosphere since the late 1960's, but has only operated on a continuous basis since 1984. Operating in the spaced–antenna mode with full correlation analysis, the horizontal wind velocities used in these analyses were obtained in two blocks, every 5 minutes, and at 2 km height intervals. During day–time the first five minutes covered the height range 60–78 km, while at night the program sampled 70–88 km in the first data block. During the second five minute block, data from day and night heights of 80–98 km were recorded. Thus, data were obtained for every height in ten–minute intervals, while night–time data for heights of 80–98 km were available every 5 minutes. Very few data were collected below 80 km at night because the signal level is below the noise level at this time. Although data rates below 80 km are quite sparse, the seasonal variation in the number of acceptable observations taken by the radar has been studied by *Hocking* [1988a]. He found that the lowest heights of useful echoes (more than 10 per 12 hour period) was around 78 km during night-time and 64 km during day–time, rising around the equinoxes. The full correlation analysis also rejects data for a variety of reasons (listed in section 3.5.4), so that only "good" data is used. This, however presents a possible problem which will be discussed further in this chapter.

Almost continuous measurements of winds and other parameters were available, and although the system did suffer down–time during which no data were collected, the data had fairly high temporal resolution. The raw winds and other parameters were first averaged into 24 hour means, thus averaging out any waves with periods less than 24 hours. Weekly means were then constructed from the daily averages of data from 1986 to 1988. This further averaged out any medium–period waves; for example the two–day wave is known to have a large peak in mid–summer [see e.g. *Craig et al.*, 1980]. Finally, the weekly means from all three years were averaged together to produce a "typical" year.

Figure 6.2 shows the total number of data points collected per week per unit height range over three years during 1986–1988. It is clear that the data rates are relatively low below about 80 km and above 95 km. While turbulence does affect the data rate, the scatterers below 80 km are known to be more specular and the data rate may not be due to turbulence activity alone. Above 95 km the data rates are also low due to the close proximity of the E region which simply saturates the receivers. Another feature to note is that the data rates around 80 km decrease during autumn and spring. It has been found by *Hocking* [1988a] that the minimum height of useful echoes observed during day–time is seasonal, rising at the equinoxes, while the night–time collection rates remain fairly constant.

6.4 Mean winds at Adelaide

Figure 6.3 shows the weekly–mean zonal wind at Adelaide constructed from three years of data, clearly showing the summer and winter circulation. The main feature of the zonal flow is the steady descent of easterly (westward) winds starting at the end of winter in the lower thermosphere, descending at a rate of 10 km per month, and climaxing in the summer mesospheric jet which peaks at 70 km in early January, a couple of weeks after solstice. Furthermore, the winter westerly winds exhibit significant fluctuations with temporal scales of more than a week, in contrast to the unfluctuating and methodical changes in the summer wind profile.

Figure 6.3 shows the weekly–mean meridional wind at Adelaide, again constructed from data

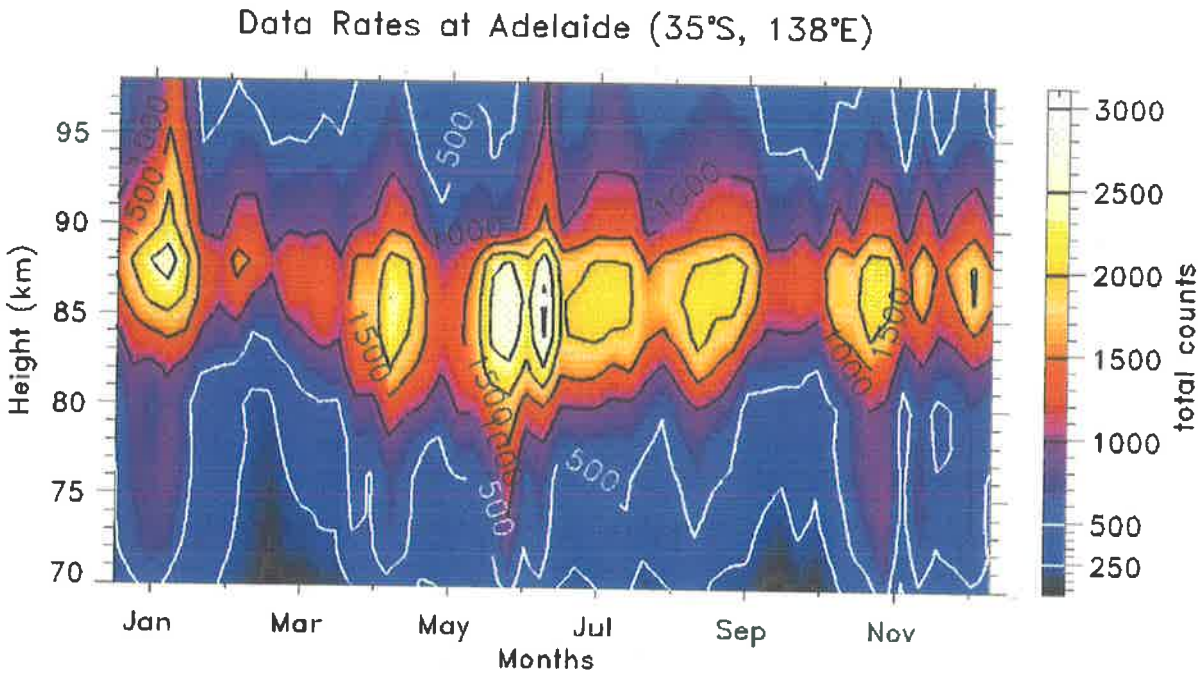

Figure 6.2: Data rates for the Adelaide MF radar during 1986–1988. The contours are labelled in the number of observations in any week that were subsequently used in further analysis. Although the system suffered some downtime the lack of usable data was primarily due to the rejection criteria of the full correlation analysis.

collected through 1986–1988. Above 85 km, the flow is generally southerly (northward) during all seasons except mid–winter, when a poleward flow penetrates up into the thermosphere. Conversely, below 85 km, the flow is generally northerly (poleward or southward), except during mid–summer when an equatorward flow penetrates downward into the mesosphere. An interesting feature is the "jet" like feature which occurs in mid–summer, at around 90km, close to the height at which the zonal winds undergo a reversal. At heights of around 80 km or below, winds in excess of 5ms^{-1} are observed during February–March and in August–October. This may be due to incomplete removal of the diurnal tide if there are insufficient data in a 24 hour period, often the case at Adelaide. It is further exacerbated by the fact that the diurnal tide attains its largest amplitude (10–20 ms^{-1}) at the equinoxes [*Vincent et al.*, 1988]. The incomplete diurnal sampling at night–time heights less than 78 km leads to the diurnal tide producing a southward bias. However, estimates of the overall effect of the diurnal tide, found

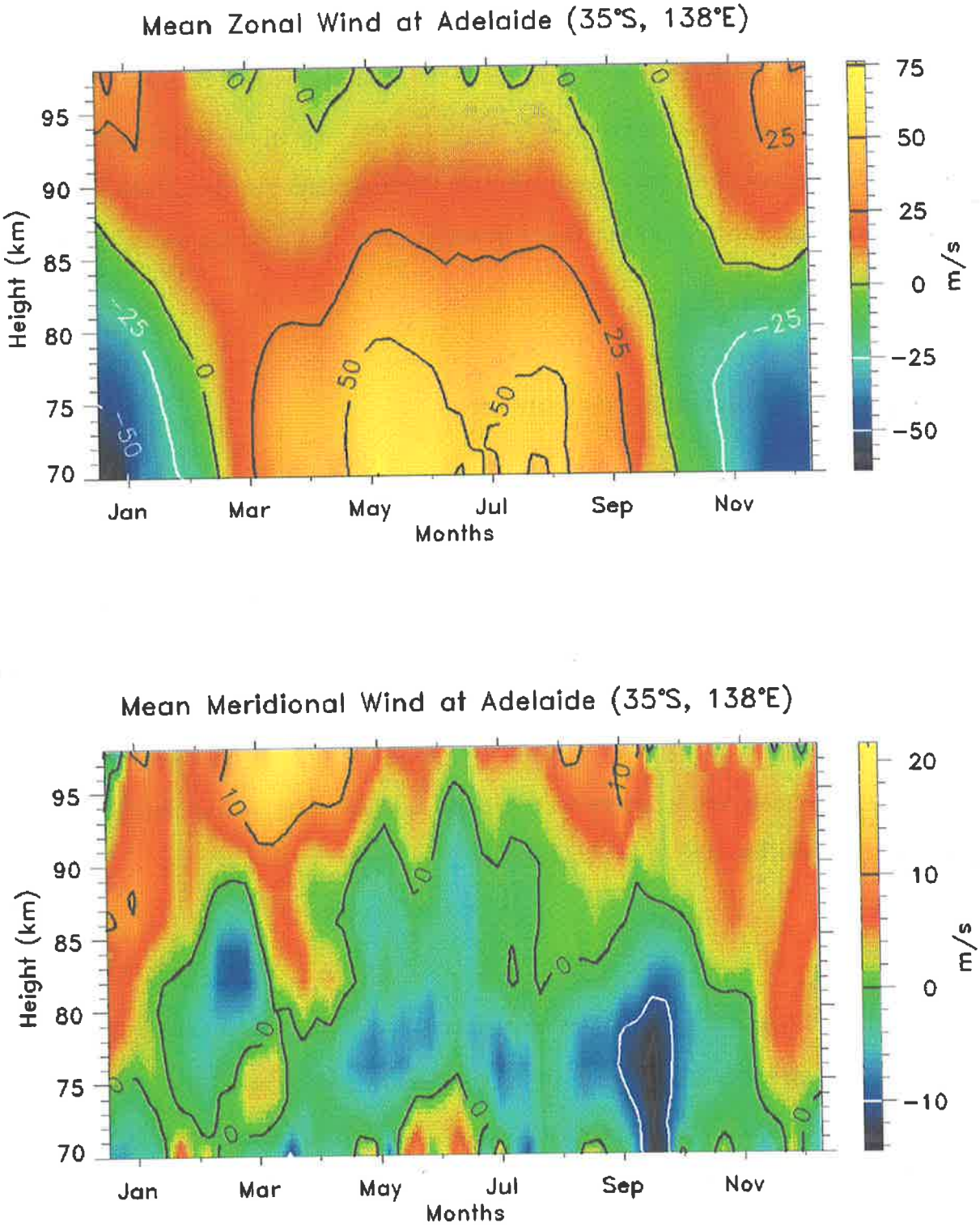

Figure 6.3: Mean zonal and meridional seasonal winds measured at Adelaide by the Buckland Park MF radar system over three years, 1986–1988. The contours are in labelled in ms^{-1}, positive for eastward and northward respectively.

by extrapolation of the phase and amplitude from 80 km to 75 km, indicate a net southward bias of around 2 ms^{-1} [*Phillips & Vincent*, 1989]. While this is not a negligible contribution it cannot account for values of 10 ms^{-1} observed at 75 km during August–October.

While incomplete averaging also leads to biasing of the zonal winds, it has a much smaller relative effect because of the larger zonal velocities. Estimates put the effect of the diurnal tide as a net westward bias of less than $5ms^{-1}$ at heights near 75 km during March–September[3] [*Phillips & Vincent*, 1989].

6.5 Spaced–antenna parameters

As discussed in chapter 3, the use of the full correlation analysis provides a number of parameters besides the mean winds. These were initially just a by–product of the analysis procedure, and little attention was paid to them other than to their general form. However, they have been shown to be not only useful quantities, but also can lead to determination of many other useful parameters which characterize on the general nature of the scattering medium. The determination of these useful parameters has been discussed at length in chapter 3, and the reader is referred there for the general mathematical methods. Here we concentrate mainly on the results; in particular their seasonal behaviour.

Fading time

The fading time, $\tau_{0.5}$, which is described by equation 3.54, is the time for which the directly observable auto–correlation function falls to 0.5 of its peak value. Figure 6.4 (top) is an image–contour plot of the weekly–mean fading times, measured by the Buckland Park radar, using three years of data, 1986–1988. Below about 80 km there is an obvious seasonal variation, where fading times of around 2–3 seconds become significantly longer during the equinoxes, typically reaching values of more than 5 seconds. At heights greater than 80 km, the equinoctial seasonal variation is quite small, $\tau_{0.5}$ is around only a second. Furthermore, the seasonal variation which

[3] i.e. causes the winter westerlies to be slightly underestimated

produces a maximum during September completely disappears above 85 km.

Other studies have also reported seasonal variations in the fading times. *Fraser & Vincent* [1970] found typical fading times of the order of 1–2 seconds in the 80–89 km height range, which increased in the 70–79 km height range during the equinoxes. A similar increase in fading times has also been reported by *Schlegel et al.* [1978], who found fading times above 80 km to be generally less than 3–4 seconds, tending to increase at lower heights, especially during spring.

The seasonal variation in the fading time of the signal can be partly attributed to the seasonal variation in the horizontal winds. As the wind velocity increases, the contribution by off–vertical scatter, due to an increase in the radial velocity component, broadens the Doppler spectrum. This effect, known as beam–broadening has been discussed in the previous chapters. Since the frequency spectrum and the auto–correlation functions are Fourier transforms of each other, the correlation time and the spectrum width are inversely related. Therefore, an increase in the spectral width translates into shorter fading times. When comparing the mean winds shown in figure 6.3 with the mean fading times in figure 6.4 (top) one can clearly see that they are inversely related. The largest fading times occur during the equinoxes, which is the time when the winds undergo a reversal.

Lifetime of ground pattern

When the beam–broadening effects of the horizontal wind have been removed from the fading time one is left with a time parameter $T_{0.5}$, which is known as the lifetime of the ground pattern. This lifetime is a measure of the random motions in the scattering centres, and is also calculated by the full correlation analysis [see section 3.5.3]. Besides giving a feel for the stability of the scattering medium, $T_{0.5}$ can also be used to determine the turbulent energy dissipation rates. This will be looked at in more detail later in this chapter (see section 6.8); for now we will concentrate on the seasonal behaviour of the lifetime of the ground pattern.

Figure 6.4 (bottom) is an image–contour three year weekly average plot of the lifetime parameter again using data from Buckland Park. A clear seasonal variation, exceptionally strong at lower heights (70–80 km), is evident where the equinoctial lifetimes are in excess of 8

seconds. This indicates that the scattering structures are particularly stable during this time. In addition, unlike the fading times, this maximum extends upwards in height during both spring and autumn. A seasonal variation of $T_{0.5}$ has previously been found by *Ball* [1981], but the data consisted of only a few observations and the seasonal variation was not considered to be conclusive. Other studies of $T_{0.5}$ have recently been undertaken [see e.g. *Fraser & Khan*, 1990], but these were based on data collected in Antarctica and will be discussed in chapter 8, which deals with Antarctic seasonal behaviour.

Pattern scale

A mean pattern scale may be defined as $\sqrt{ab}$ (see earlier) and the determination of this quantity by the full correlation analysis has already been discussed. Figure 6.5 (top) is an image–contour plot of the weekly average of the pattern scale using data from 1986–1988. Similarly to $\tau_{0.5}$ and to $T_{0.5}$, a seasonal behaviour in the pattern scale size is clearly evident, and is more pronounced at heights below 80 km. Below this height, the pattern scale exceeds 500 metres during the equinoxes, and decreases to less than 300 metres during the southern hemisphere summer. In addition, a slight increase evident from October to May is seen above 95 km. This may be partly due to the tail of the E–region which can cause total specular reflections.

Seasonal variations in the pattern scale have also been previously recorded by *Stubbs* [1977] who found maxima at the equinoxes, and by *Fraser & Vincent* [1970] who also found a semi–annual oscillation where the minimum pattern scale occurred at solstices.

Pattern axial ratio

The pattern scale discussed above was calculated from an average of the major and the minor axis of the ellipse which describes the ground diffraction pattern produced by the partial radar scatter. This pattern is however of a two–dimensional nature, and is often anisotropic in the horizontal plane.

Figure 6.5 (bottom) is an image–contour plot of the weekly average of the ratio of the major to the minor axis of the ellipse. Below about 80 km, there is some evidence of a semi–annual

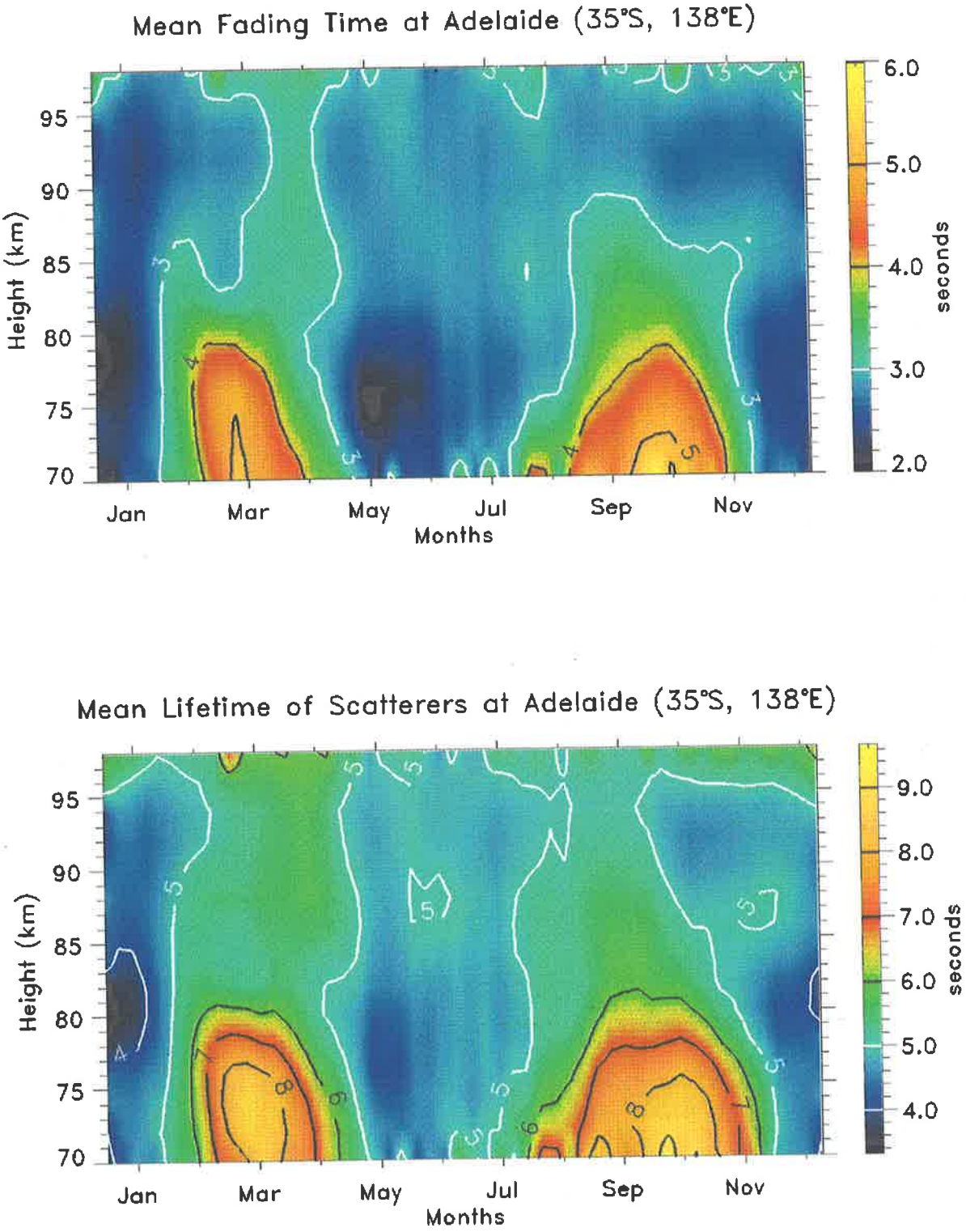

Figure 6.4: Weekly–mean fading time (top) and lifetime of ground pattern (bottom) at Adelaide, measured over three years, 1986–1988. The contours are in ms^{-1}.

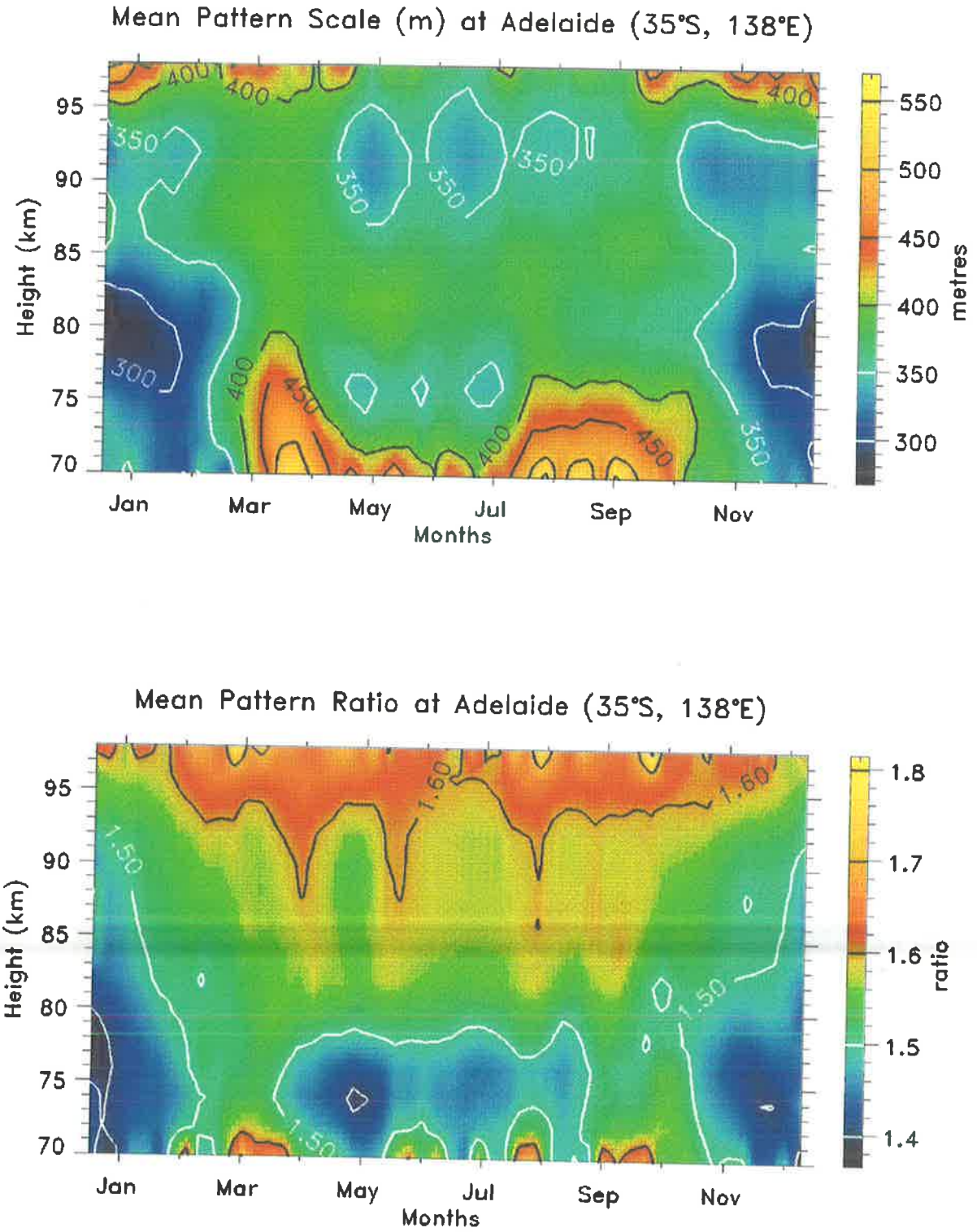

Figure 6.5: Weekly means of the scale (top) and axial ratio (bottom) of the ground diffraction pattern at Adelaide, calculated from three years of data, 1986–1988. The pattern scale contours are in labelled in ms^{-1}, while the axial ratio is the ratio of the semi–major to the semi–minor axis.

oscillation which increases from around 1.4 to more than 1.5 during the equinoxes; especially at around 72 km. Above 85 km, however, the evidence for an annual oscillation is much stronger with increasing height. While during the summer the ratio is around 1.5, it exceeds 1.6 at other times of the year.

Similar trends have previously been reported by other authors [see e.g. *Clemesha*, 1963; *Ball*, 1981]. An explanation of the increase in the axial ratio with height was attempted by *Stubbs* [1977], who proposed that the increase in axial ratio was due to anisotropic diffusion of ionization along magnetic field lines; an effect which should be most noticeable at the equator.

A study by *Wright & Pitteway* [1978] found that anisotropic ratios less than about 1.3 are not statistically different from isotropic ones with the record lengths normally used. This suggests that long–term averages, where the axial ratio is around 1.5 or greater, are significant and do indicate a real anisotropy in the scattering.

Conclusion

All of the above examples have shown that long term averages of various diffraction pattern parameters in the mid–latitude mesosphere and lower thermosphere exhibit seasonal variations. The largest values of $T_{0.5}$ and the pattern scale occurred at the equinoxes, while the axial ratio generally increased with height during most of the year.

A study of the diurnal variations of the various parameters was not undertaken with the Buckland Park data as data with much better temporal resolution and higher acceptance rates were obtained at another field station some 150 km from Adelaide. The diurnal changes of the various diffraction pattern parameters will be discussed in chapter 9.

6.6 Aspect sensitivity

In the previous sections we discussed the seasonal behaviour of the various parameters which are obtained as a by–product of the full correlation analysis when determining winds. It was shown in chapter 5 that these various parameters could be used to infer other properties of the

scattering medium besides its mean motion. In particular, it was shown how both the fading time of the signal and the spatial correlation pattern could be used to estimate the aspect sensitivity, θ_s, of the scatterers.

Here we discuss the behaviour of the aspect sensitivity of the partial reflection radar scatterers. These estimates were obtained by using three methods; spectral–width method, spatial–correlation method, and the velocity–ratio method. This work has been published [*Lesicar & Hocking*, 1992], and can be found in appendix *G*.

Spectral–width method

Figure 6.6 (top) represents weekly means of θ_s calculated by the spectral–width method. Looking down from 98 to 70 km, one can see that while there is no evident seasonal variation in θ_s at upper heights, whilst a clear seasonal variation exists at heights below about 85 km, with minima occurring at the equinoxes, and a maximum during the southern–hemisphere summer. These absolute values seem to decrease somewhat with height, with minima ranging from 12° at 82 km, to 8° at 70km, and the maxima ranging from 16° at 82 km to 13° at 70km. Furthermore, whilst no clear evidence of an annual oscillation above the mesopause exists, there is a hint of minima always occurring around the equinoxes. Above the mesopause θ_s is also much larger with values around 14°.

Figure 6.7 shows θ_s, calculated by the spectral–width method, plotted as a function of single heights; the error bars are the standard deviations of the plotted values. This not only shows that the seasonal behaviour of θ_s is real, but that the variability of θ_s is smallest around the mesopause.

Spatial–correlation method

Figure 6.6 (bottom) shows weekly means of θ_s calculated from the spatial correlation method. The mean of the semi–major and the semi–minor axis was used to calculate a mean correlation scale, from which θ_s was determined. The results are very similar in their seasonal behaviour, when compared with θ_s calculated by the spectral–width method. However, the actual values

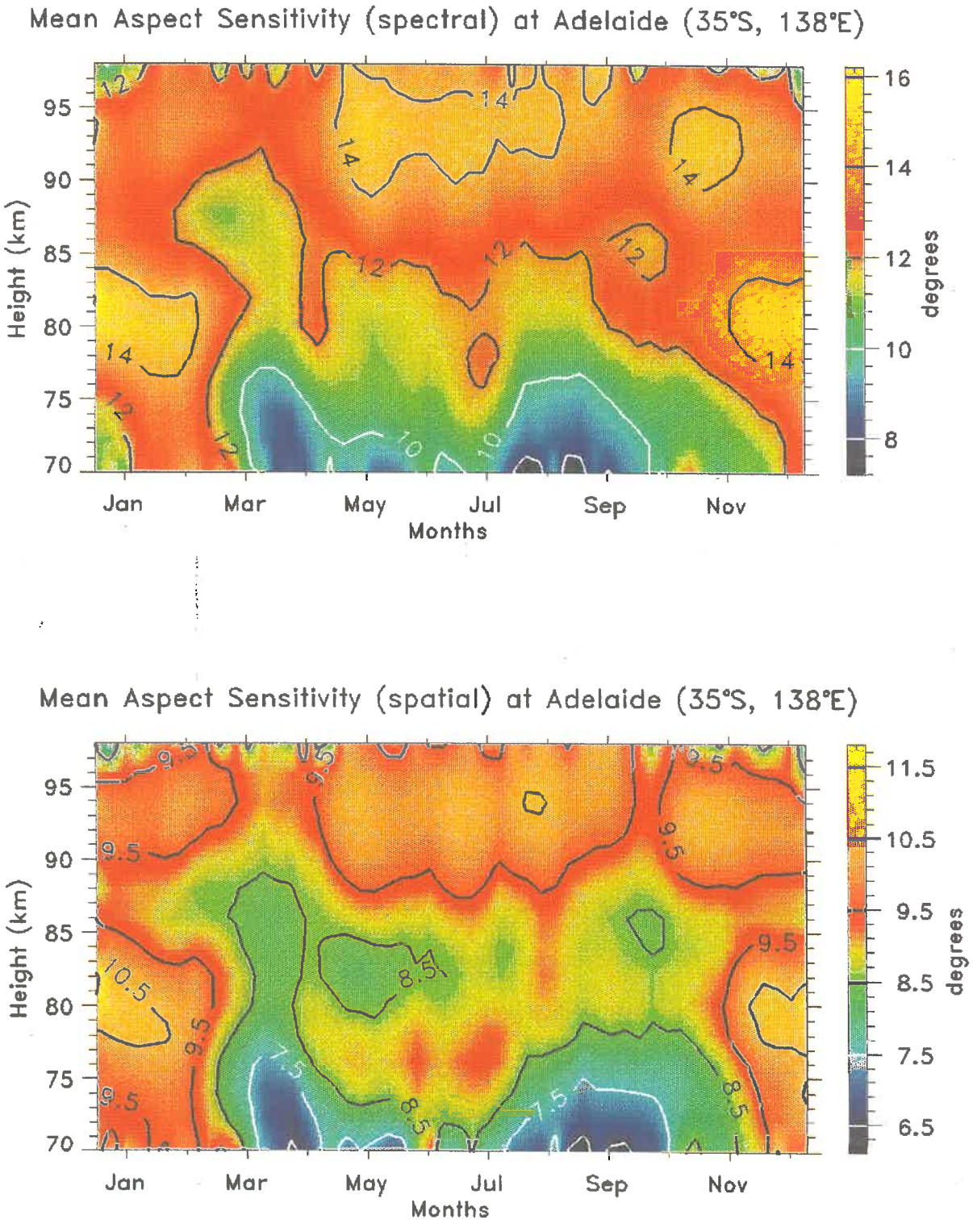

Figure 6.6: Weekly mean averages of the aspect sensitivity calculated by the spectral (top) and the spatial correlation method (bottom) at Adelaide. Three years of data were used in the analysis, 1986–1988. The contours are in degrees.

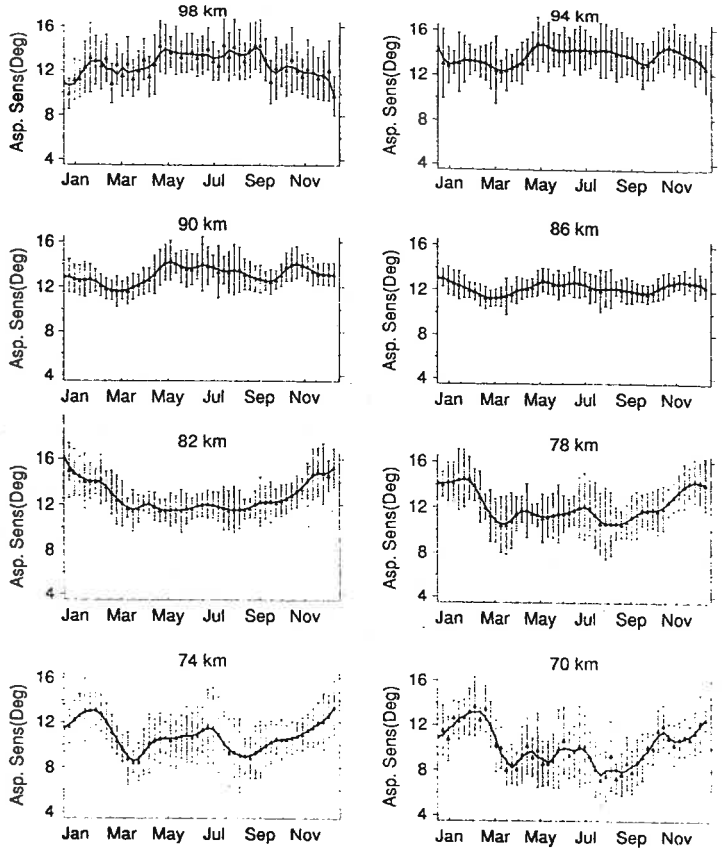

Figure 6.7: One–week averages of θ_s for heights of 70, 74, 78, 82, 86, 90, 94, and 98 km. θ_s was calculated using the spectral–width method. The error bars are the standard deviations of the plotted values.

of θ_s are smaller by several degrees, falling below 7.5° at the equinoxes, and reaching a 11° maximum. This reinforces the view that the major cause of the spectral width is indeed beam broadening. In addition, the fading time is determined from the cross–section of the characteristic ellipse. As this scale is horizontally anisotropic, the fading time may vary by as much as 50 percent, depending on the orientation of the ellipse with respect to the mean wind, since the spectral width is determined in the direction of motion. Thus θ_s determined by the spectral–width method is an upper limit only, while that measured by the spatial–correlation method is a much better statistical average.

Figure 6.8 shows θ_s, calculated by the spatial–correlation method, plotted at discrete heights. Again the error bars are the standard deviations of the plotted values. This not only shows that the seasonal behaviour of θ_s is real, but that the variability of θ_s is smallest around the

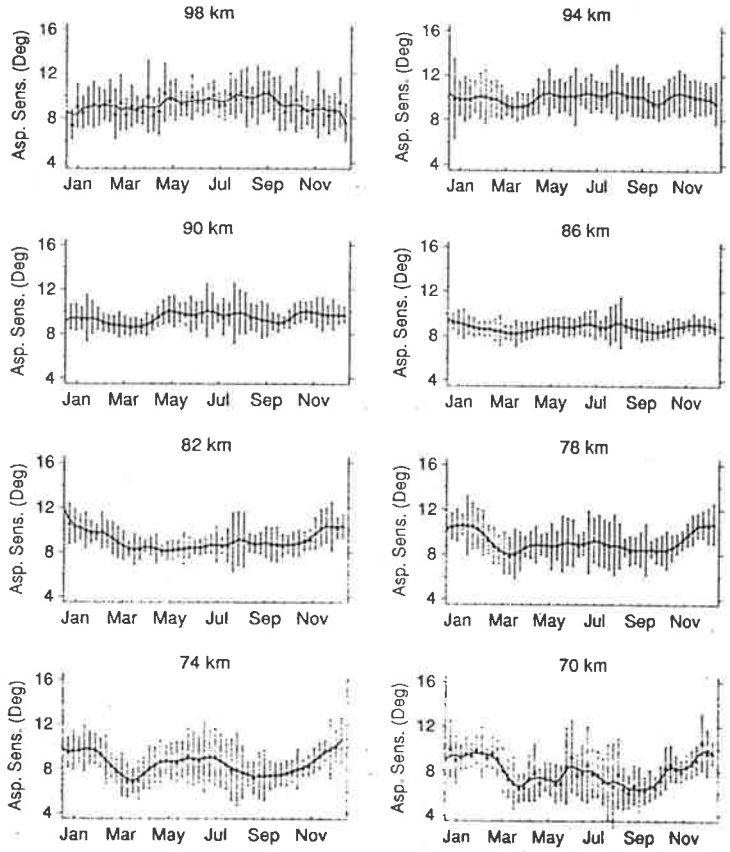

Figure 6.8: Same as figure 6.7, but with θ_s calculated by the spatial–correlation method.

mesopause.

Velocity–ratio method

Although data were routinely collected by the spaced–antenna system, every 2.5 to 3 hours the program switched to a different mode. In that mode, not only were the winds calculated but also spectra were calculated for one of the spaced–antenna beams, a narrow vertical beam, and an 11.6° off–vertical beam pointing eastward. Subsequent fitting of a Gaussian function to each of the spectra allowed the spectral width, mean frequency offset, and the signal–to–noise ratio to be measured. The mean frequency offset was then used to determine the radial velocities in the narrow beams, thus allowing determination of the horizontal component for an off–vertical beam [*Hocking*, 1988a]. In addition, the spectra underwent an effective chi–square test, which indicated the goodness of fit; those spectra with large chi–square values were rejected. Although

this reduced the data rates somewhat, it made sure that no spurious events were included.

Both the spaced–antenna horizontal velocity and the off–vertical Doppler radial velocity were measured simultaneously. However, there were often gaps in the data from the spaced–antenna measurements. The data rates where both the off–vertical Doppler radial velocity and the spaced–antenna horizontal velocity were accepted were found to be greatly improved if the mean horizontal winds using the spaced–antenna system were determined using the previous 20 minutes of data. A comparison between the velocity determined using one reading or a 20 minute average showed very little difference, and the same overall general trends. Subsequently this was the procedure adopted for the remainder of this work. It should be noted that in fact the antenna array is not aligned perfectly in the cardinal directions, but is in fact aligned 4° west of north. The spaced–antenna program automatically corrects for this, but this feature was not available on the off–vertical Doppler. This meant that the spaced–antenna horizontal velocity had to be re–corrected by 4 degrees. Thus the direction quoted hereafter is not perfectly eastward, although it will be referred to as such.

Figure 6.9 shows histograms of the horizontal velocity in the eastward direction, for 2 km height steps ranging from 96 to 80 km, measured by the spaced–antenna method using 20 minute averages. Figure 6.10 shows the radial eastward velocity measured by the off–vertical Doppler method. In both plots, a fair spread of velocities is evident, with the largest grouping of data available in the 82 to 90 km range. A first inspection,when comparing the Doppler with the spaced–antenna histograms, shows that the spread in velocities of the latter is about 5 times that of the Doppler. Since the off–vertical beam is pointed 11.6° from the vertical, it should measure a velocity roughly one–fifth of that measured by the spaced–antenna system; thereby showing that, to a first approximation, the two velocities are of the same order. The histograms also indicate that the range of velocities is quite "normal", i.e. there are no large fluctuations or "out–liers".

Until now we have assumed that there was no vertical velocity, an assumption that is usually false, and the Doppler off–vertical radial velocity has to be corrected for the effects of vertical

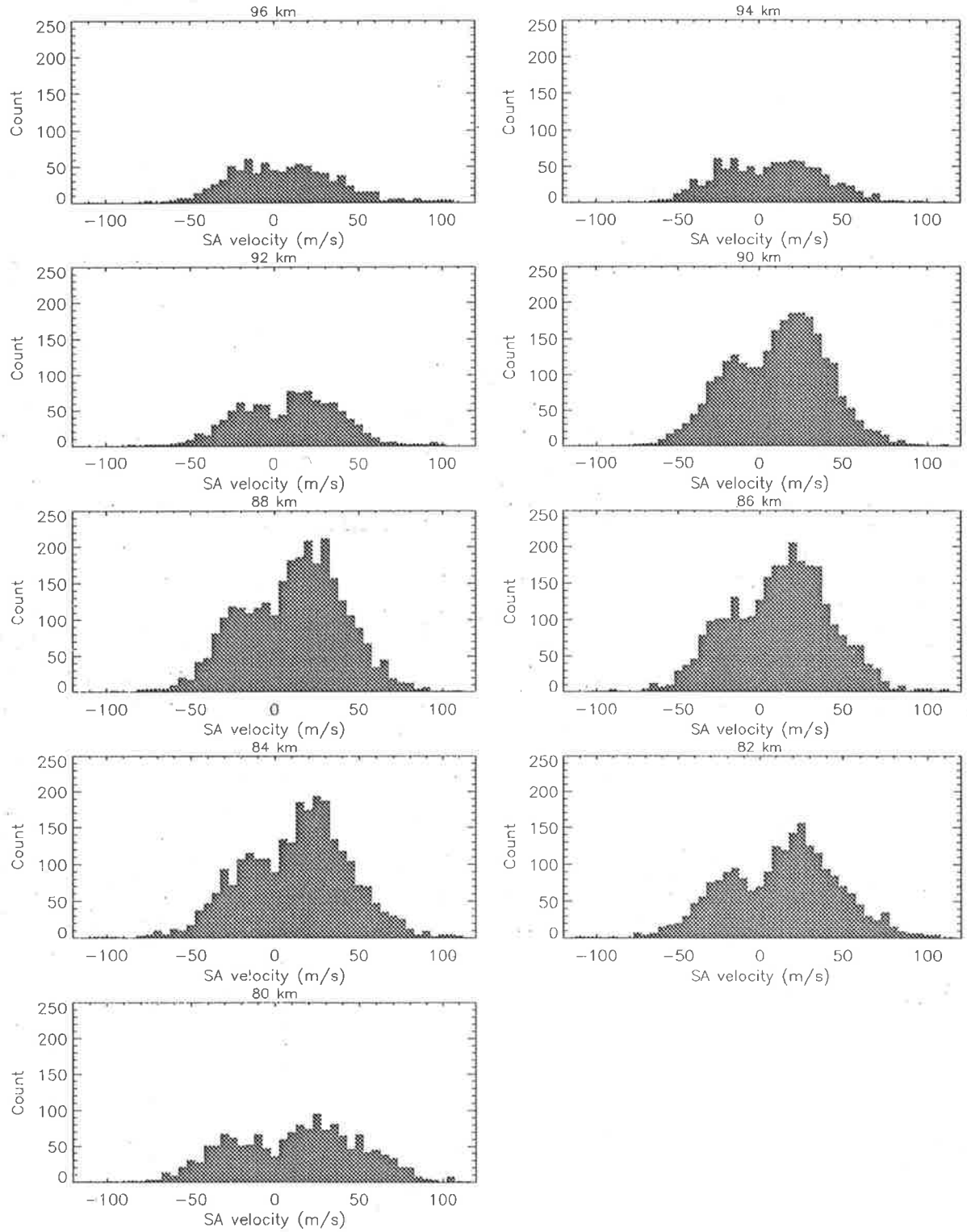

Figure 6.9: Histograms of 20 minute averages of the spaced–antenna eastward horizontal velocity using three years of data (1986–1988). The data is grouped into bins of width 5ms^{-1}.

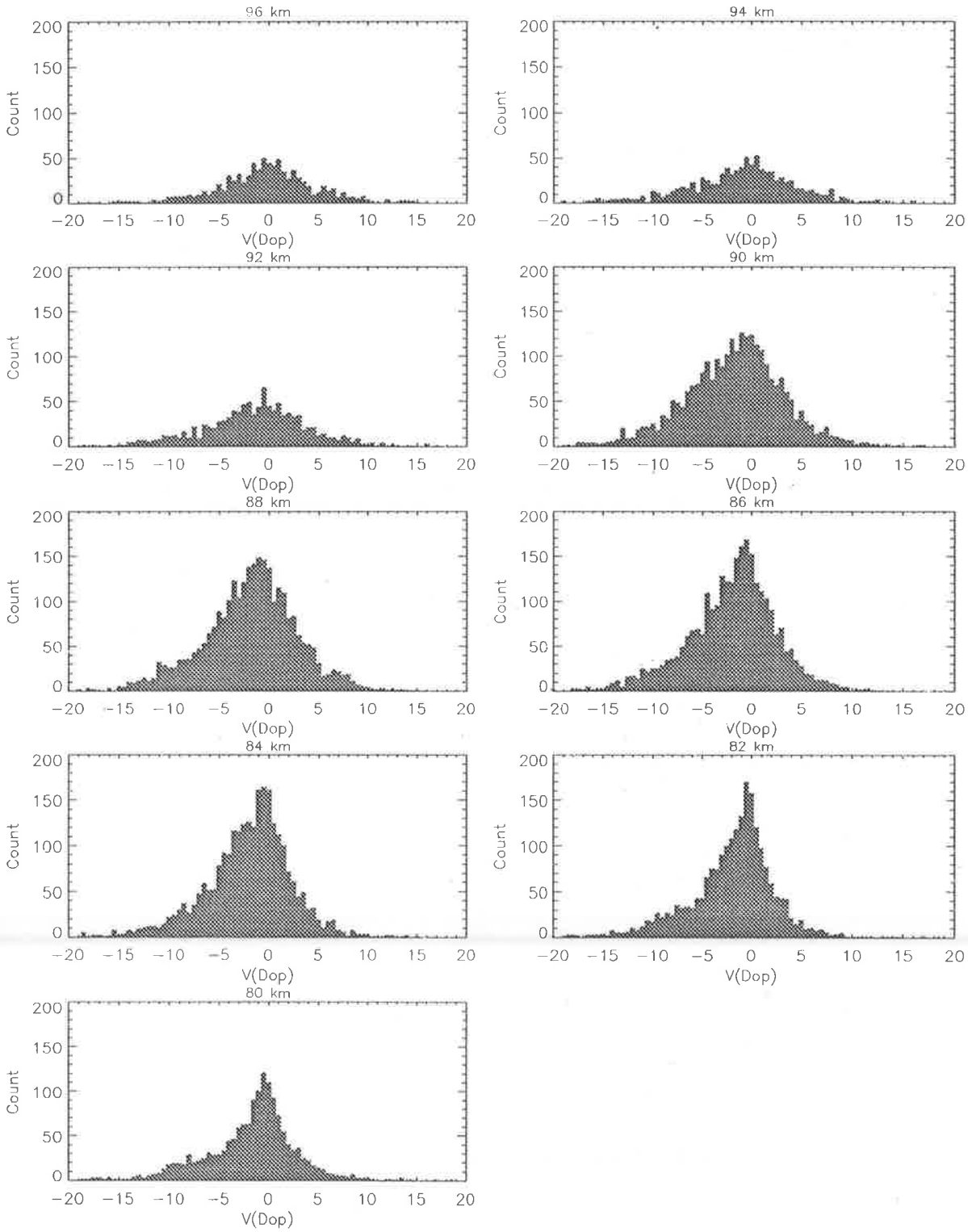

Figure 6.10: Histograms of the Doppler eastward radial velocity measured by the narrow off-vertical beam pointed at 11.6° eastward using three years of data (1986–1988). The data is grouped into bins of width 0.5ms^{-1}.

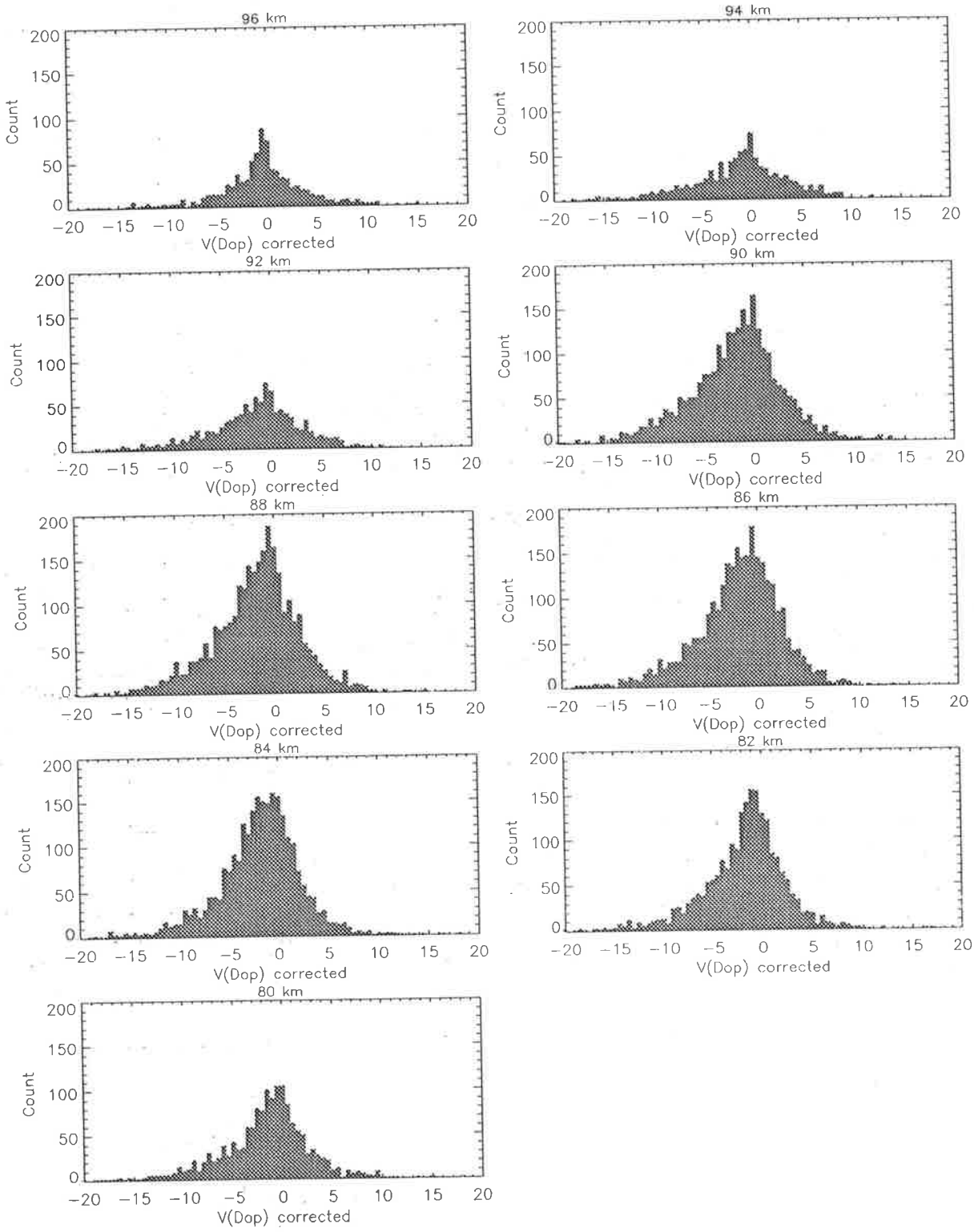

Figure 6.11: Histograms of the eastward radial velocity measured by the Doppler off–vertical beam but corrected for the vertical velocity. The data is grouped into bins of width $0.5 \mathrm{ms}^{-1}$.

motions (by equation 3.21). The Doppler off–vertical radial velocities corrected for the effect of vertical motion are plotted as height histograms in figure 6.11. No obvious differences can be seen between the corrected and the uncorrected radial velocities, although the histograms of the corrected radial velocities are slightly narrower. This method does assume that the vertical velocity in the sampling volume of the vertical beam is the same as that within the sampling volume of the off–vertical beam. This may not always be true for, at approximately 80km, the physical separation between the volume sampled vertically and that at 11.6° off–vertical is about 16 km; sufficiently large that local wave activity might cause the vertical velocity to differ at the two sampling volumes. In this work, however, the averaging of the velocities will improve these assumptions.

A comparison of the horizontal velocities measured by the spaced–antenna system and an off–vertical Doppler beam has been performed by *Reid* [1988], and in some detail by *Murphy* [1990]. *Murphy* [1990] found that there was a systematic difference between the spaced–antenna and the Doppler derived velocities. This suggests that the effective pointing angle was not 11.6°but smaller. As noted earlier (see chapter 5), the effective polar diagram of the radar is the product of the transmitting, receiving and scattering polar diagrams. If the transmitting and receiving polar diagrams are broad, than the effective pointing angle is mainly due to the scatterers' polar diagram.

The next part of the analysis was to compare the ratio of the radial velocities from the 11.6° off–vertical beam with the "true" horizontal wind speeds determined from the spaced–antenna method If the scatterers possessed no preferential scattering angle, i.e. they were not specular, then the expected ratio should be around 0.2. Figure 6.12 shows histograms of the velocity ratios at various heaights. Most of the ratios are concentrated in the range of -0.1 to -0.2 indicating that the off–vertically derived horizontal velocities are smaller than the spaced–antenna horizontal velocities, thus implying that the scatterers possess some specularity. In addition, whereas a negative[4] ratio implies that the velocities measured were in the same direction, positive values indicate an opposite direction. The positive values, especially large

[4]An eastward radial velocity was in this case denoted by a negative Doppler velocity

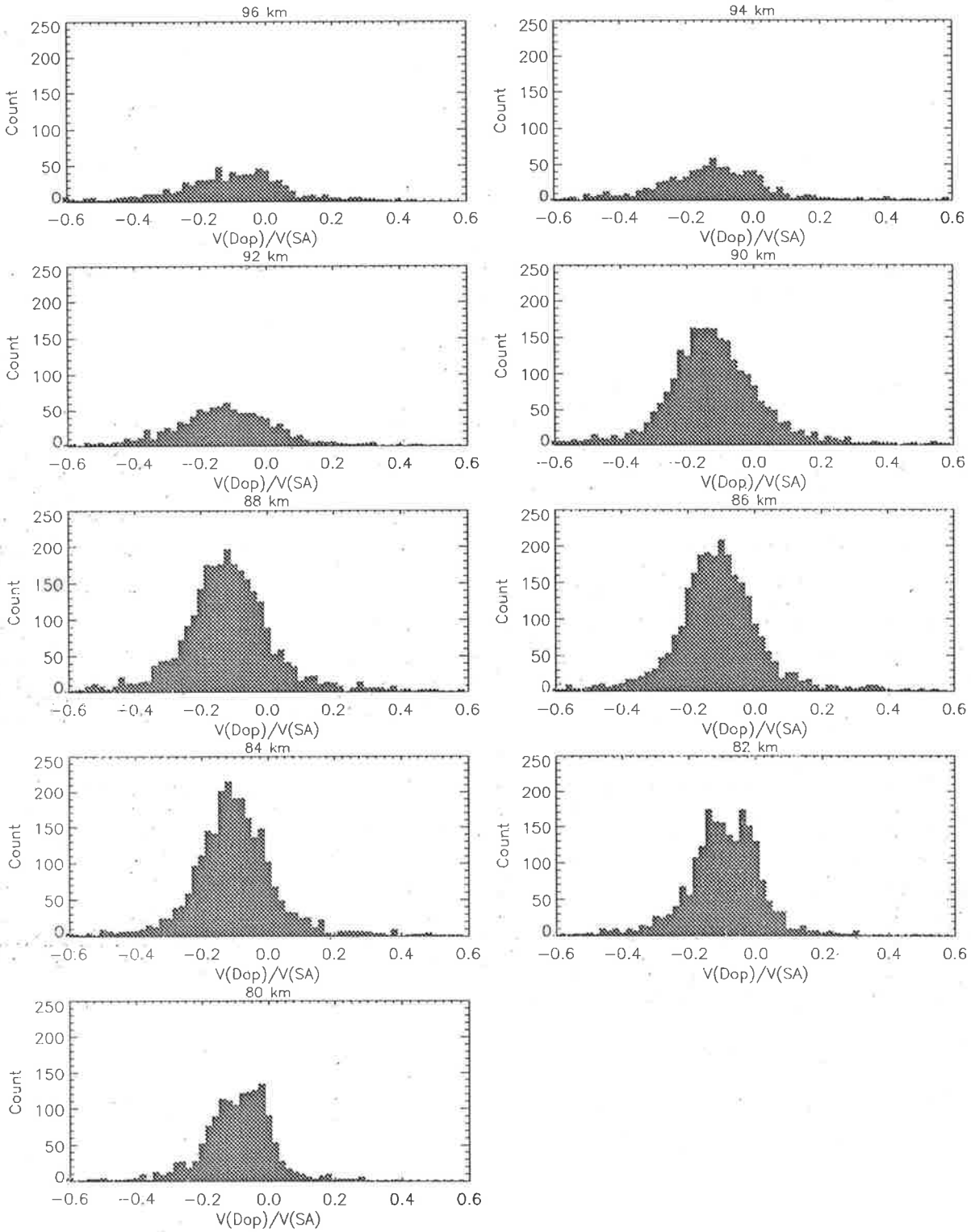

Figure 6.12: Histograms of the ratio of the Doppler eastward radial velocity measured by the off–vertical beam to the eastward horizontal spaced–antenna velocity using three years of data (1986–1988). The data is grouped into bins of width 0.02.

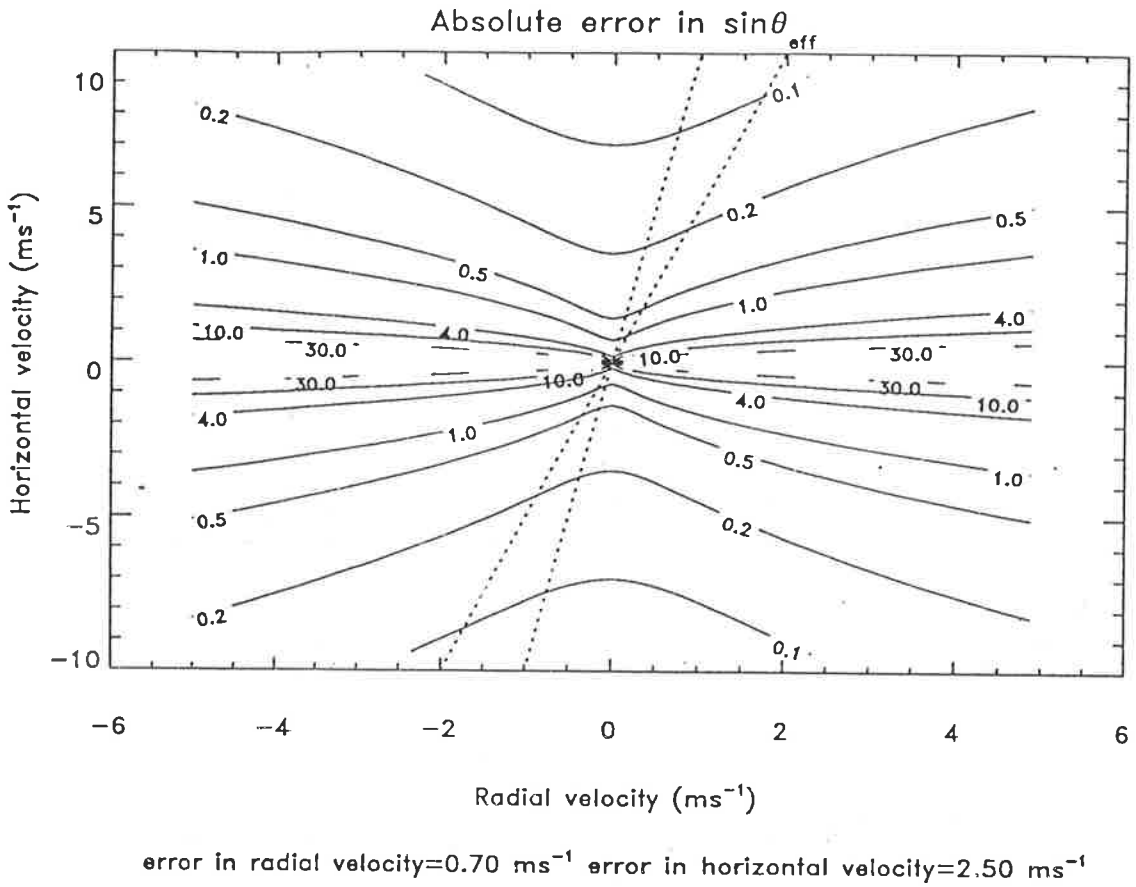

Figure 6.13: Contour plot of the error in $\sin\theta_{eff}$, which was calculated using equation 6.1 [from *Murphy*, 1990].

ones, may be caused by a number of factors. These may include leakage of stong signal through the sidelobes and edges of the main beam, and the fact that the spaced–antenna and the Doppler method examine spatially separated volumes of the atmosphere where the velocity difference may be entirely natural.

The error in the effective pointing angle has been considered by *Murphy* [1990] who used standard error analysis to find the absolute error in $\sin\theta_{eff}$ viz

$$\Delta \sin\theta_{eff} = \sqrt{\frac{(\Delta V_{rad})^2}{V_{hor}^2} + \frac{V_{rad}^2(\Delta V_{hor})^2}{V_{hor}^4}} \quad , \tag{6.1}$$

(Δ indicates the error of the component) and assuming that the covariance between V_{rad} and V_{hor} is zero. Since these measurements are made independently, the covariance is zero, and we consider the error in $\sin\theta_{eff}$ attributable to errors in the velocity measurements.

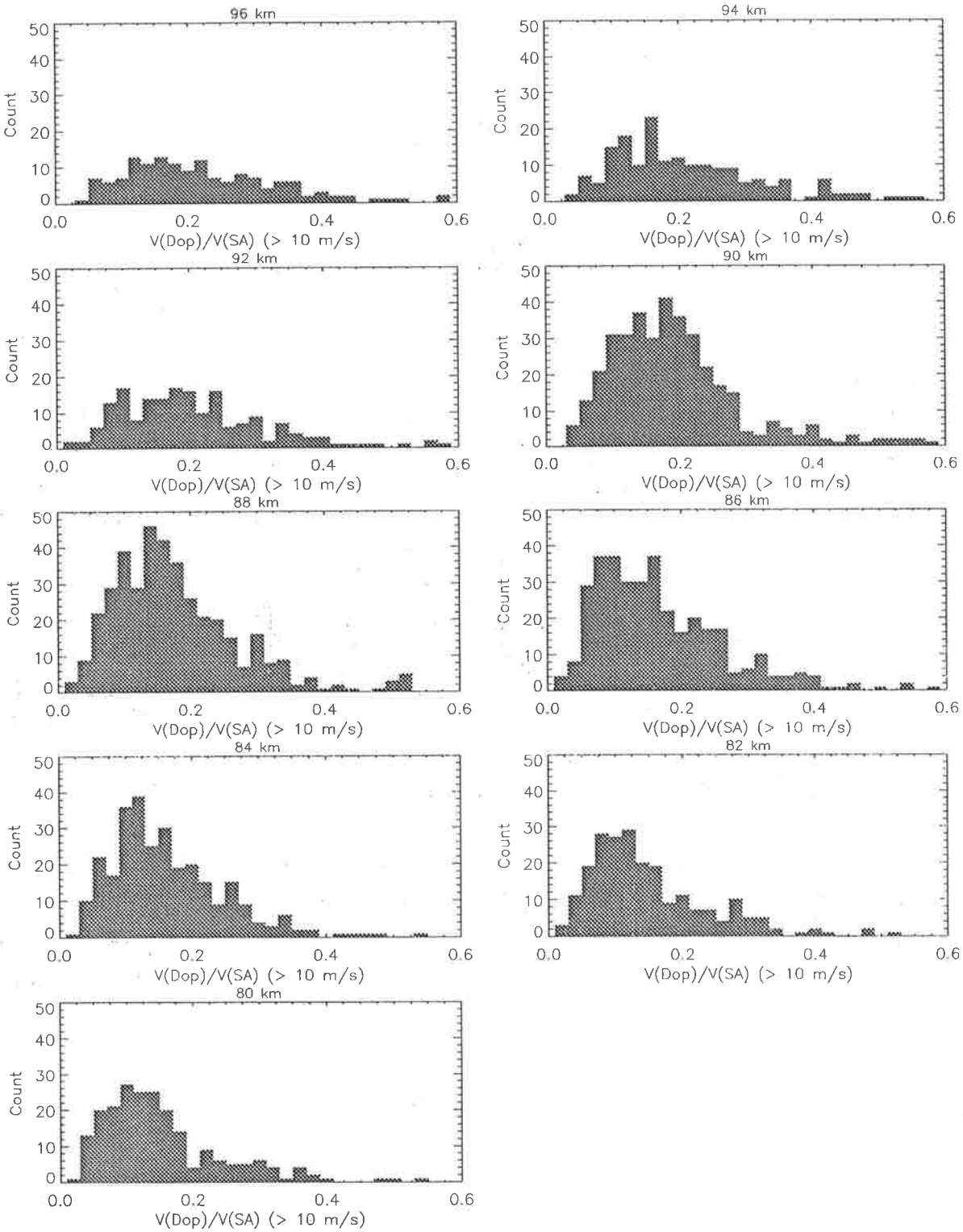

Figure 6.14: Histograms of the ratio of the Doppler eastward radial velocity measured by the off–vertical beam to the eastward horizontal spaced–antenna velocity for $V_{hor} > 10\text{ms}^{-1}$. The data is grouped into bins of width 0.02.

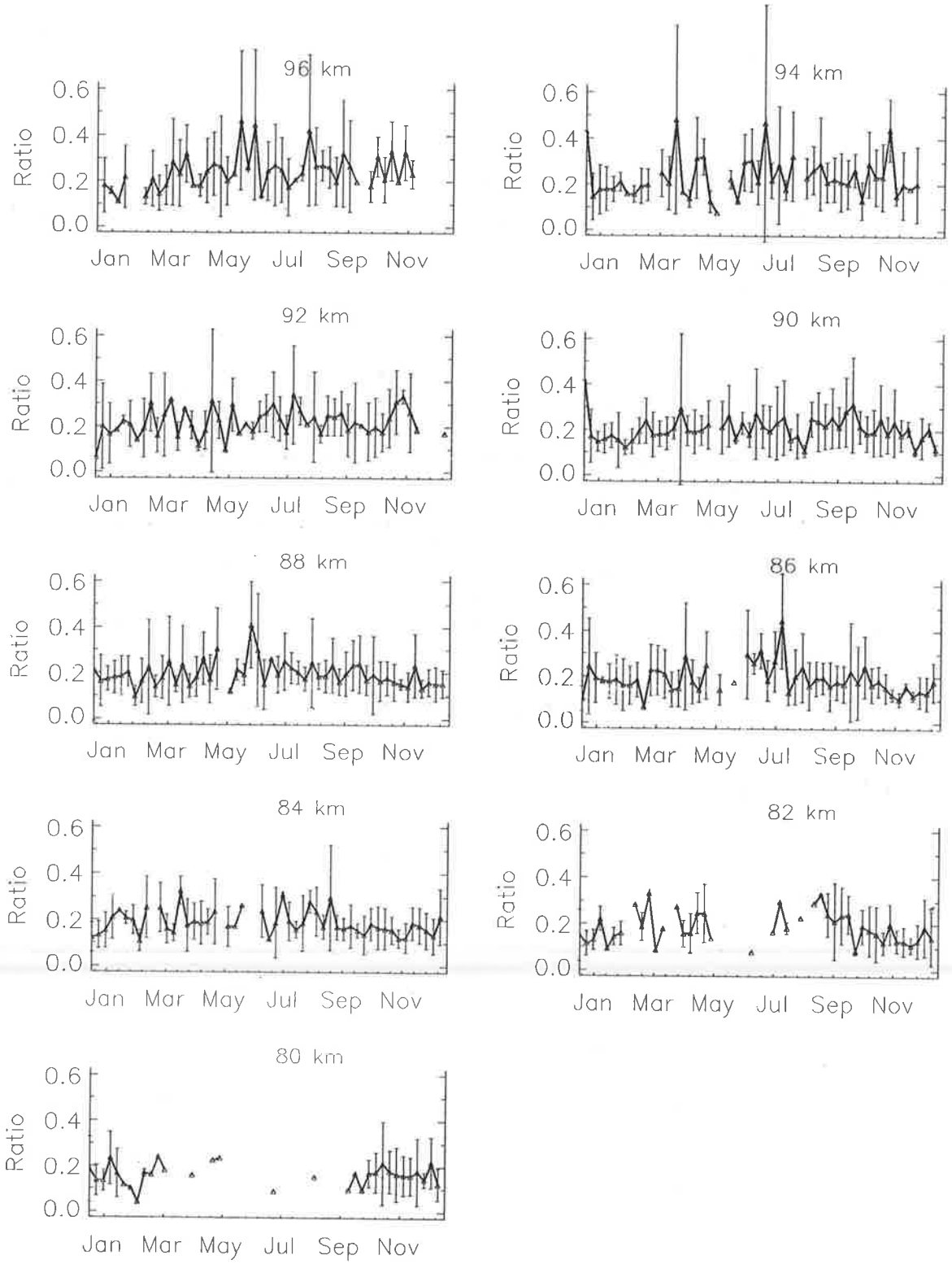

Figure 6.15: Weekly–mean ratio of the radial Doppler velocity to the horizontal spaced–antenna velocity using three years of data (1986–1988). Error bars indicate the standard deviations of the means.

Contours of the absolute error in $\sin\theta_{eff}$ for values of $\Delta V_{hor} = 2.5\text{ms}^{-1}$ and $V_{rad} = 0.7\text{ms}^{-1}$ are plotted in figure 6.13 [from *Murphy*, 1990]. The error of 2.5 ms^{-1} in the horizontal velocity is the mid value of the uncertainty range as deduced by *May* [1988], while the error in the radial velocity of 0.7 ms^{-1} comes from the work of *Reid & Vincent*, [1987]. We consider the region where $V_{rad} = (0.1 \text{ to } 0.2)V_{hor}$ (area bounded by the dotted lines in figure 6.13). In this region, errors in $\sin\theta_{eff}$ where $|V_{hor}| < 10\text{ms}^{-1}$ are of the order of 0.1. This suggests that horizontal velocities whose magnitude is less than 10 ms^{-1} should be rejected.

Figure 6.14 is a histogram of the absolute ratio of the Doppler to the spaced–antenna wind velocity where horizontal velocities less than 10 ms^{-1} have been rejected, grouped into bins of width 0.02. Overall around 70 percent of total data collected was rejected solely on the velocity criterion. This might bias the data somewhat, but it should make little difference when looking at long term averages. In addition, ratios where the velocities measured by the spaced–antenna method and the Doppler method were in the opposite directions were rejected.

Several features should be noted about figure 6.12. The means of the histograms are always less than 0.2, and are positively skewed. They also tend to be smaller with decreasing altitude, i.e. the mean at 96 km is closer to 0.2 than that at 80 km. The shift in the mean with altitude may be interpreted as due to the increasing specularity of the scatterers with decreasing altitude (as discussed in chapter 5). The other features are more difficult to interpret, not only because of the relative scarcity of data, but due to other possible errors; measuring vertical velocities, systematic errors in the spaced–antenna technique, and errors in the polar–diagram pointing angle. These may or may not contribute to the overall result. However, as this study looks at general trends and not the fine detail, the histograms are thought to be representative. What is of more interest is the seasonal behaviour of the velocity ratio, rather than qualitative measurements. We shall use this ratio to determine θ_s and thence compare those results with the seasonal variation in θ_s deduced by the spatial correlation and spectral width techniques.

Figure 6.15 shows the weekly means of the corrected velocity ratios, and the associated standard deviations, for 2 km height steps from 80–96 km. The data were corrected for vertical

motions and rejected where $V_{hor} < 10$ metres per second. No seasonal variation is evident. This strongly suggests that the scatterers observed by the off–vertical beam differ from those sampled by the vertical beam, since θ_s measured by the spatial correlation and the spectral width methods exhibited clear seasonal variations.

6.7 Horizontal correlation lengths

From calculations of θ_s by the spectral–width and the spatial–correlation methods, it is relatively easy to determine the length–to–depth (L/h) ratio of the scatterers. The mathematical groundwork for this has already been covered in chapter 5 and only the results and conclusions will be presented here.

L/h results calculated from the spectral–width method are shown in figure 6.16 (top), while those calculated from the spatial–correlation method are shown in figure 6.16 (bottom). Both of these show quite clearly that the scatterers possess the greatest length–to–depth ratio at the equinoxes, that is, late March to early April, and late August to early September, where the average ratio reaches 5.0–5.5. This seasonal variation seems to disappear above the mesopause, and the length–to–depth ratio falls by nearly 50%, to values around 3.0–3.5. In other words, if one thinks of the scatterers as possessing ellipsoidal structure, which may perhaps be due to anisotropic turbulence, then at the lower heights they have the greatest horizontal to vertical extent at the equinoxes. This would suggest that at these times there should be least dynamical activity. In absolute terms, with a wavelength of 150 metres (2 MHz), one can infer that the structures selected by the radar possess a vertical extent (2h) of around 70 metres, with the horizontal length varying from 200 to 400 metres. The latter values are quite consistant with typical values for the diffraction pattern formed over the ground.

Conclusion

Both the spectral–width and the spatial–correlation method of determining θ_s support the existence of anisotropic and even quasi–specular scatter, while that measured by the velocity ratio

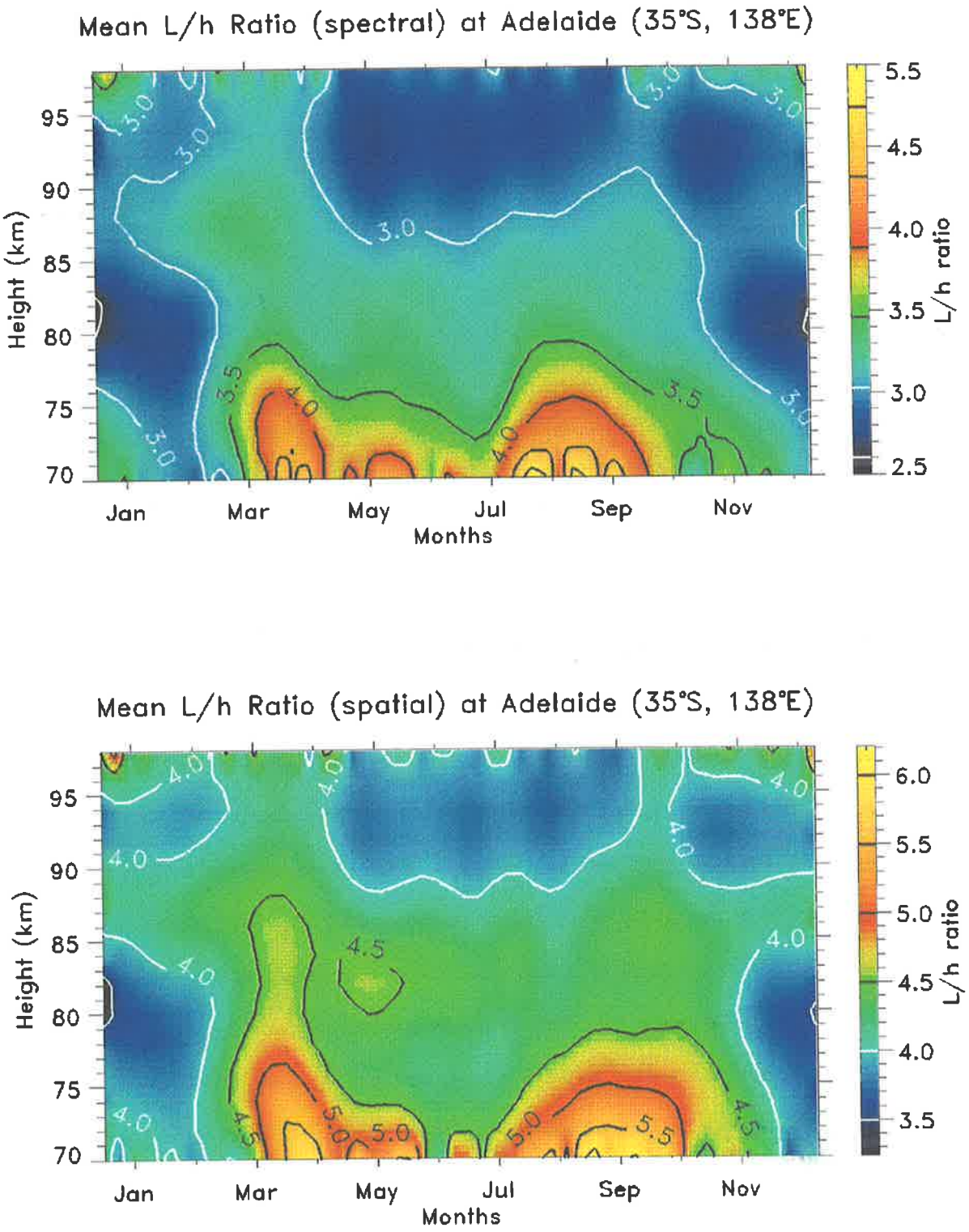

Figure 6.16: Mean weekly averages of the length–to–depth ratio of the partial reflection radar scatterers calculated by the spectral (top) and the spatial–correlation method (bottom) at Adelaide using three years of data (1986–1988). The contours are the ratio of the horizontal to the vertical depth.

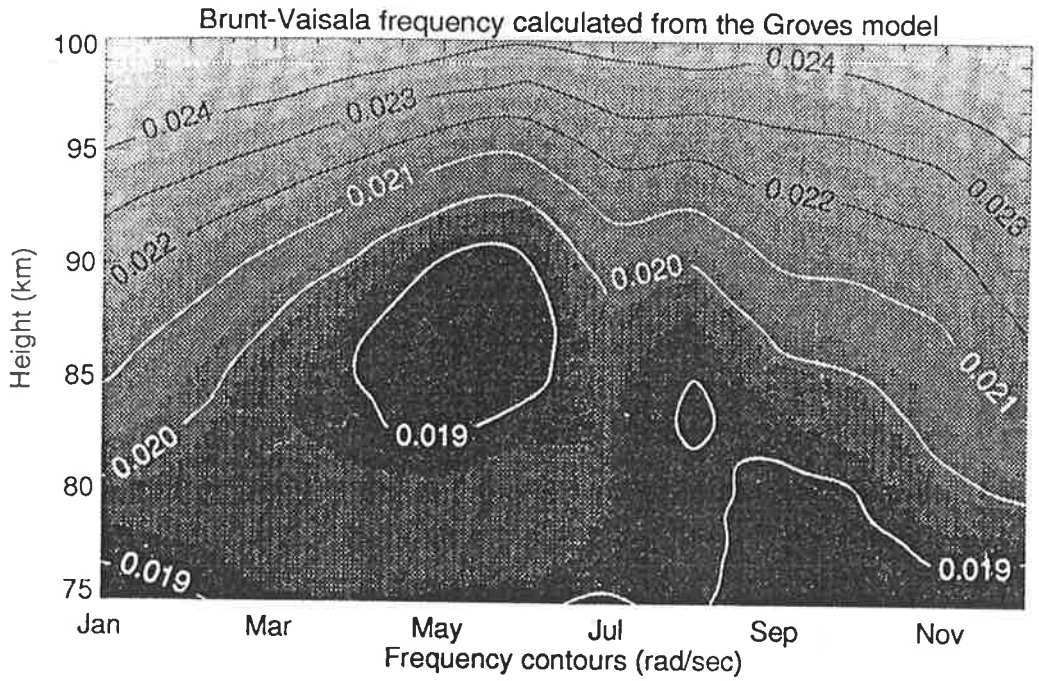

Figure 6.17: Contour plot of the Brunt-Väisälä frequency as a function of height in the mesosphere. The data were calculated from the Groves model. There seems to be no evidence to support a seasonal variation, especially below the mesopause.

method indicates more isotropic scatter. This tends to support the notion that the mesosphere contains at least two distinct types of scatterers (or a continuum) when probed by an MF radar. In addition, the anisotropic scatterers exhibit clear, well–defined seasonal variation, which is especially strong below the mesopause. The scattering model, discussed earlier in chapter 5, which proposes at least two types of scattering structures co–existing, is supported by these observations. Although at times evidence of highly aspect–sensitive and stable echoes have been found elsewhere and reported in the literature [see e.g. *Gregory & Vincent*, 1970; *Hocking*, 1979], these cases were chosen on the basis of their unusual behaviour, and are probably atypical. Furthermore, initially these types of echoes would have been rejected by the spaced–antenna analysis because of their slow fading echoes. Thus the results described above are representative of the majority of echoes, and although at times stable and mirror–like reflectors occur in the atmosphere, they account for only a few percent of the total echoes observed. Although the cause of the aspect–sensitivity reported above is still a matter of speculation,

there are a number of other parameters which are known to vary seasonally in the mesosphere. These include gravity–wave amplitudes, temperatures, and turbulence energy dissipation rates [see e.g. *Hocking*, 1988a; *Vincent & Fritts*, 1987; *Clancy & Rusch*, 1989; *Reid*, 1990]. It should then not be too surprising that θ_s exhibits seasonal variability.

It could be argued that the spaced–antenna method is in fact measuring propagating gravity waves, and not turbulent structures (which may of course be produced by the dissipation of gravity waves). This point has already been addressed in a previous chapter, where this scenario was found to be highly unlikely. However, if it were true then it would be reasonable to expect that variation in θ_s should be similar in character to that in the Brunt-Väisälä frequency at mesospheric heights, and could thus be the cause of the observed effects. Figure 6.17 is a contour plot of the Brunt-Väisälä frequency calculated from the Groves model [*Groves*, 1985]. There seems to be no strong or clear seasonal variation to affect the scatterers significantly at the MF scale.

6.8 Turbulent energy dissipation rates

The techniques for determining turbulent energy dissipation rates have already been discussed in chapter 3. Briefly, one uses the spectral width of the backscattered radar signal which, once effects like beam broadening have been removed, gives an estimate of the root mean square (RMS) velocity of the scatterers. This RMS velocity can then be used to determine the turbulent energy dissipation rate, ϵ. The parameter $T_{\frac{1}{2}}$, which is defined as the natural fading of the signal and is calculated by the full correlation analysis, can also be used to determine the scatterers RMS velocity and thus ϵ [see e.g. *Briggs*, 1980; *Manson & Meek*, 1980, *Manson et al.*, 1981].

Figure 6.18 is a plot of the energy dissipation rates determined from $T_{\frac{1}{2}}$ at Adelaide using three years of data (1986–1988). The energy dissipation rates vary from $\sim$ 0.025 Wkg^{-1} to greater than 0.125 Wkg^{-1}. There is a clear seasonal variation, with the minima occurring during the equinoxes, and maxima during the winter and summer periods. In addition, the

summer maximum tends to be higher than the winter one. At heights above 80 km there seems to be little variation with increasing height.

However, most spaced–antenna systems use wide radar beams, and this has the effect of resulting in over–estimates of ϵ, since gravity wave motions act to broaden the spectrum. Thus the above results are, at best, upper estimates of ϵ. *Hocking* [1983b], using the same radar system as in this work, has made estimates of the fraction of experimentally observed spectral widths which are due to turbulence; the remainder is taken to be due to short–wave gravity waves. He found that below around 84 km, turbulence accounted for less than 50% of the observed spectral width, while above that height turbulence contributed more than 50% of the fluctuating vertical velocity component. For short data sets (102 seconds), (the same length as used to derive figure 6.18), the fractions of the squared spectral half–power half–width due to turbulence were given as 0.76 at 84 km, 0.80 at 86 km, 0.70 at 88 km, and 0.64 at 92 km. *Hocking* [1983b] presented one week averages of the "corrected" turbulent energy dissipation rates, calculated over several years. The smallest values of ϵ were found to occur most often at the equinoxes, and there was some evidence of a seasonal variation above 84 km. The values of ϵ presented in figure 6.18 have not been corrected for gravity–wave contamination. Although estimates of the gravity–wave contribution to the spectral widths have been made, it is not certain that this contribution does not change both seasonally and latitudinally. It is felt that "uncorrected" estimates of the upper limit might be preferred. Furthermore, the data presented here are meant to represent general trends, rather than be quantitative measurements.

Previous measurements of ϵ have ranged between 0.05 and 0.1 Wkg^{-1}, with the 16% and 84% percentiles being typically at 0.02 and 0.2 Wkg^{-1} [*Hocking*, 1988a]. Thus the data presented in figure 6.18 fall well within this range. Other measurements of the seasonal variation in turbulent energy dissipation rates have produced somewhat mixed results. While *Muller* [1968] found a seasonal variation peaking in summer and winter and with minima at the equinoxes, *Elford & Roper* [1967] using a meteor technique, found the converse to be true. They used data collected in 1961, which showed maxima at the equinoxes. A later study by *Hocking* [1988a] found only

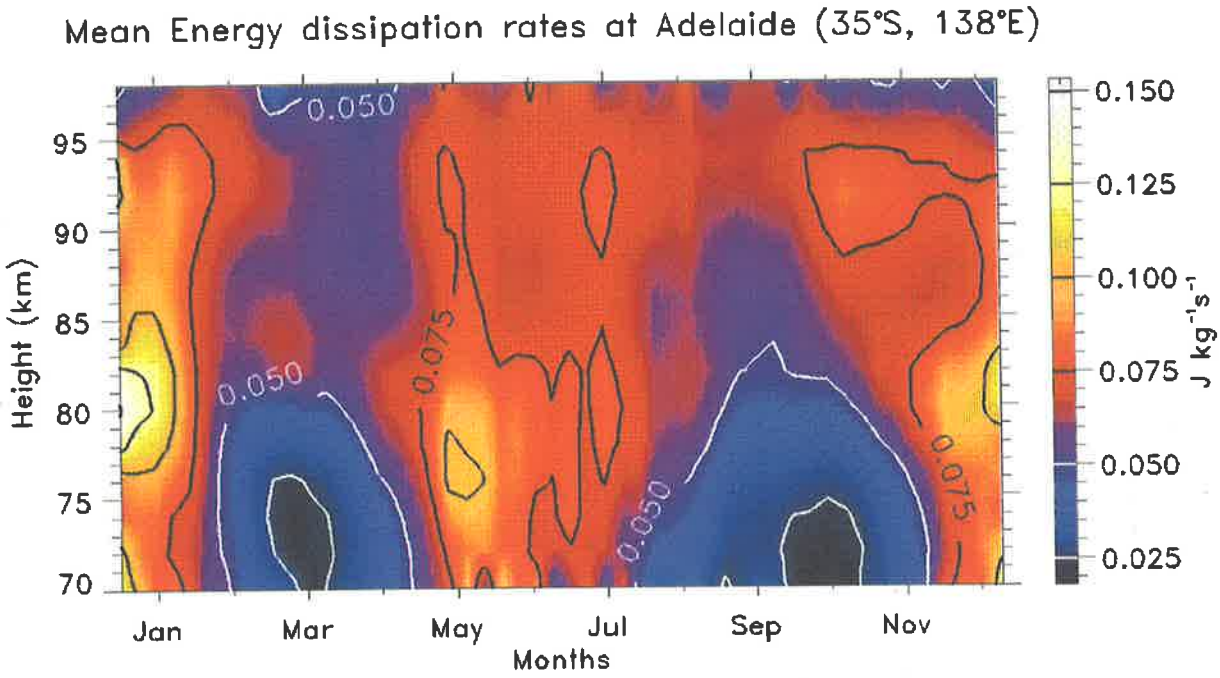

Figure 6.18: Weekly–mean energy dissipation rates calculated at Adelaide using three years of data (1986–1988). Contours are labelled in units of Wkg^{-1}.

weak evidence of a seasonal variation, although his study was able to explain the results of *Elford & Roper* [1967] as being consistant with his data provided allowance was made for the short data sets used in that earlier study. Other studies, both experimental and modelled, have examined the turbulence diffusion coefficient, which was found to exhibit seasonal variation. Turbulence activity was found to be at a minimum at the equinoxes, especially below 80 km [see e.g. *Thomas et al.*, 1984; *Garcia & Solomon*, 1985; *Meek et al.*, 1985; *Vincent & Fritts*, 1987].

Chapter 7

Seasonal results from Christmas Island

7.1 Introduction

In January 1990, a partial reflection radar was installed and successfully commissioned on Christmas Island (2° N and 157° W), an island located in the central Pacific, and part of the Republic of Kiribati. One of the major reasons for building a MF radar on this particular site was that there are very few studies of the dynamics of the equatorial mesosphere and lower thermosphere. Although the mean circulation and large–scale wave activity of the equatorial regions have previously been studied by both rockets and satellites, both methods have severe limitations. Rocket observations which reach altitudes of 90 km or more are limited by the low sounding rate, usually no more than a few a week, while those made by satellite–borne instruments, like the LIMS[1] instrument (which has provided data used to study planetary scale instabilities, Kelvin waves and tides [see e.g. *Salby et al.*, 1984; *Hitchman and Leovy*, 1988]) render poor temporal and horizontal spatial resolution and are unsuitable for studies of small scale structures and motions, particularly gravity waves.

The selection of Christmas Island was based on several reasons. Foremost it is located in

[1] Limb Infrared Monitor of the Stratosphere

a region of relatively low convective activity, is a flat atoll and is far removed from any large land mass. The last is probably one of the more important features since most radars are continent based and have to contend with potentially large locally–generated gravity waves. The island is also the location of a Stratosphere–Troposphere (ST) VHF wind–profiler operated by the Tropical Atmospheric Group, Aeronomy Laboratory, National Oceanic and Atmospheric Administration (NOAA), and through their cooperation it was possible to share buildings and power. The NOAA wind–profiler can also be used as a meteor wind radar, providing mesospheric wind measurements in the 80–100 km range [*Avery et al.*, 1990], and thus enabling direct comparisons with the results of our radar system.

The author's involvment in this project was as a member of a team of three people who installed and commissioned the radar system on Christmas Island. This involved the construction of antennas, and the logistics of moving all the necessary equipment and peripherals to the island.

This chapter discusses the general characteristics of the radar system, and presents long–term studies of the equatorial mesosphere. Short–term results are examined in the following chapter. Finally, a brief overview of Christmas Island is discussed in Appendix *B*.

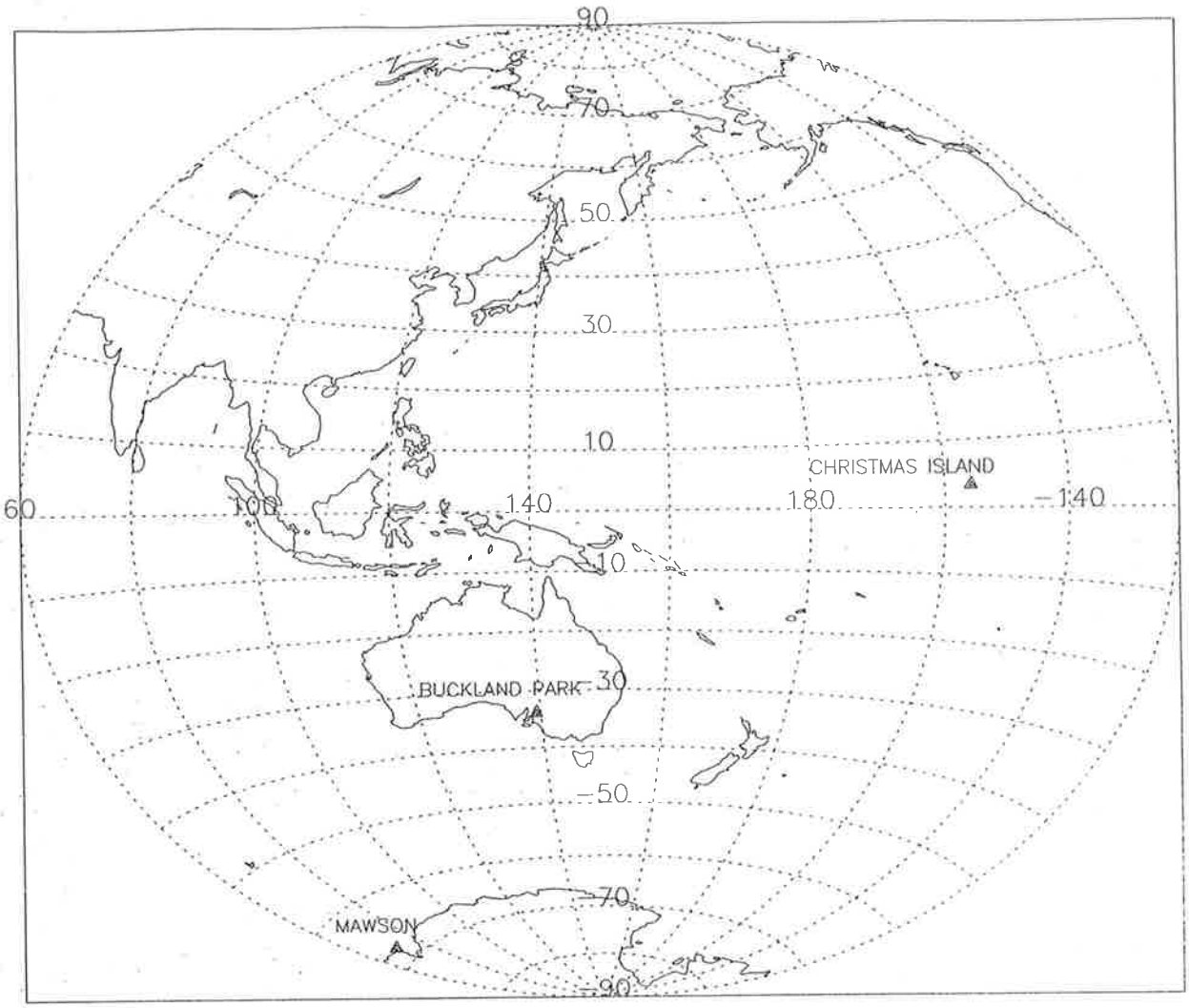

Figure 7.1: Map of the world showing the location of Kiritimati (Christmas Island), where the University of Adelaide has constructed a 2 MHz partial reflection radar. Also shown are the locations of two other partial reflection radars, one at Adelaide (Buckland Park), and the other at Mawson (Antarctica). The three radars together provide coverage of mesospheric winds and dynamics in the southern hemisphere between 60 and 100 km (108 km at Mawson).

See opposite page (221)

Figure 7.2: Map of Kiritimati (Christmas Island), Republic of Kiribati, The island is the worlds largest coral atoll, comprising over 300 km^2 of land area. The shadowed area on the bottom right--hand side is prone to flooding. The partial reflection radar system is marked on the map by the red dot. [from Lands and Surveys Division, Republic of Kiribati, published by the Government of the United Kingdom for the Government of Kiribati, 1984].


KIRITIMATI
(CHRISTMAS ISLAND)
REPUBLIC OF KIRIBATI
NORTH
PACIFIC
OCEAN
BAY
OF
WRECKS
Scale 1: 50,000

7.2 About the radar

Due to the remoteness of Christmas Island several criteria needed to be met to install the 2 MHz radar. The radar system had to be relatively light, portable, and reliable under various conditions. Since no technical support for the radar was available, the system had to be easy to operate and require minimum maintenance. It had to consist of modules which were easily replaceable and which could be shipped by mail for easy replacement. The system had to be power efficient since all power is generated on site by generators supplied by NOAA [see *Avery*, 1990].

The system can basically be split into three sections; the transmitting and receiving antennas, the transmitter and data acquisition system, and the computer software which subsequently analyses the data. We will briefly consider each of these in turn.

7.2.1 Transmitting and receiving antennas

The Christmas Island MF radar system is shown schematically in figure 7.3. The site is located next to the NOAA VHF radar. It is flat semi–sandy area, with a few local dense clumps of vegetation. Both the transmitting and receiving antennas are mounted on wooden telegraph poles which were buried to a depth of approximately 1.5 m, and rise up to a height of about 6–7 m. The erection of the poles and some laying out of cables was done by sub–contracting the local population, who also cleared some of the dense vegetation to minimize the total length of cabling required to reach both the transmitting and receiving towers.

The transmitting array is arranged in a square, and consists of four centre–fed half–wave dipoles, approximately 75 m in length, and suspended between wooden telegraph poles at a height of about 10 m. The antennas are constructed from 7 mm^2 hand–drawn copper wire, which was stretched by several metres using a line–belt to avoid the usual sag. One set of dipoles is arranged parallel to the Earth's magnetic field while the other is arranged orthogonally to it. This is because Christmas Island is situated close to the magnetic equator and the Ordinary (O) and the Extraordinary (E) rays are linearly polarized parallel to, and at right angles to,

the magnetic field respectively. The O–mode dipoles are used for day–time transmission while the E–mode are used at night–time. This geometrical arrangement also applies to the three receiving antennas.

The ideal height of the transmitting antennas is one quarter of the transmitting wavelength above the ground plane[2], which for an MF radar operating at 1.98 MHz is about 35 m. Three–stage telescopic towers were intended to be used at Christmas Island, which would have raised the antennas to about 30 m above ground level. In fact, a whole tower system was prepared with all the necessary rigging, but it was discovered that it was not possible to load the towers into the regular aircraft which services the island weekly, since they were a fraction too long. The other option involved shipping the towers to the island, but as shipping services were infrequent and irregular, this would have set back the installation by too long a time. Fortunately, during the building of the NOAA VHF radar, a number of telegraph poles which were shipped in for that project were not used and were made available for our radar system. The transmitting antenna baluns are fed from a central antenna tuning unit by co–axial cables each half a wavelength in length. Even at a height of about 6–7 m, the impedance of the antennas was found to be about 100 Ω (ideally 50 Ω), but by using an antenna tuning unit it was possible to match the antennas to the foamflex cable feeder from the transmitter.

The receiving antennas are of the inverted–V type, and are situated at the vertices of an equilateral triangle whose basic spacing is 180 m [see figure 7.3]. The centres of both the transmitting and receiving arrays coincide, making this a truly monostatic system. The impedence of each receiving antenna was 50 Ω to match the coaxial cable taking the signal back to the receiving system.

Figure 7.5 shows one of the three receiving poles, and the scaffolding which was used to reach the top of the poles. The balun box can be seen as a small black box at top of the pole. The transmitting antennas also used four identical poles. Figure 7.6 shows the view of the transmitting array as taken from the top of the scaffolding [as in figure 7.5]. The VHF system operated by NOAA can just be seen in the top right hand side of that photograph.

[2]At Christmas Island the effective ground plane is thought to fluctuate seasonally to some extent.

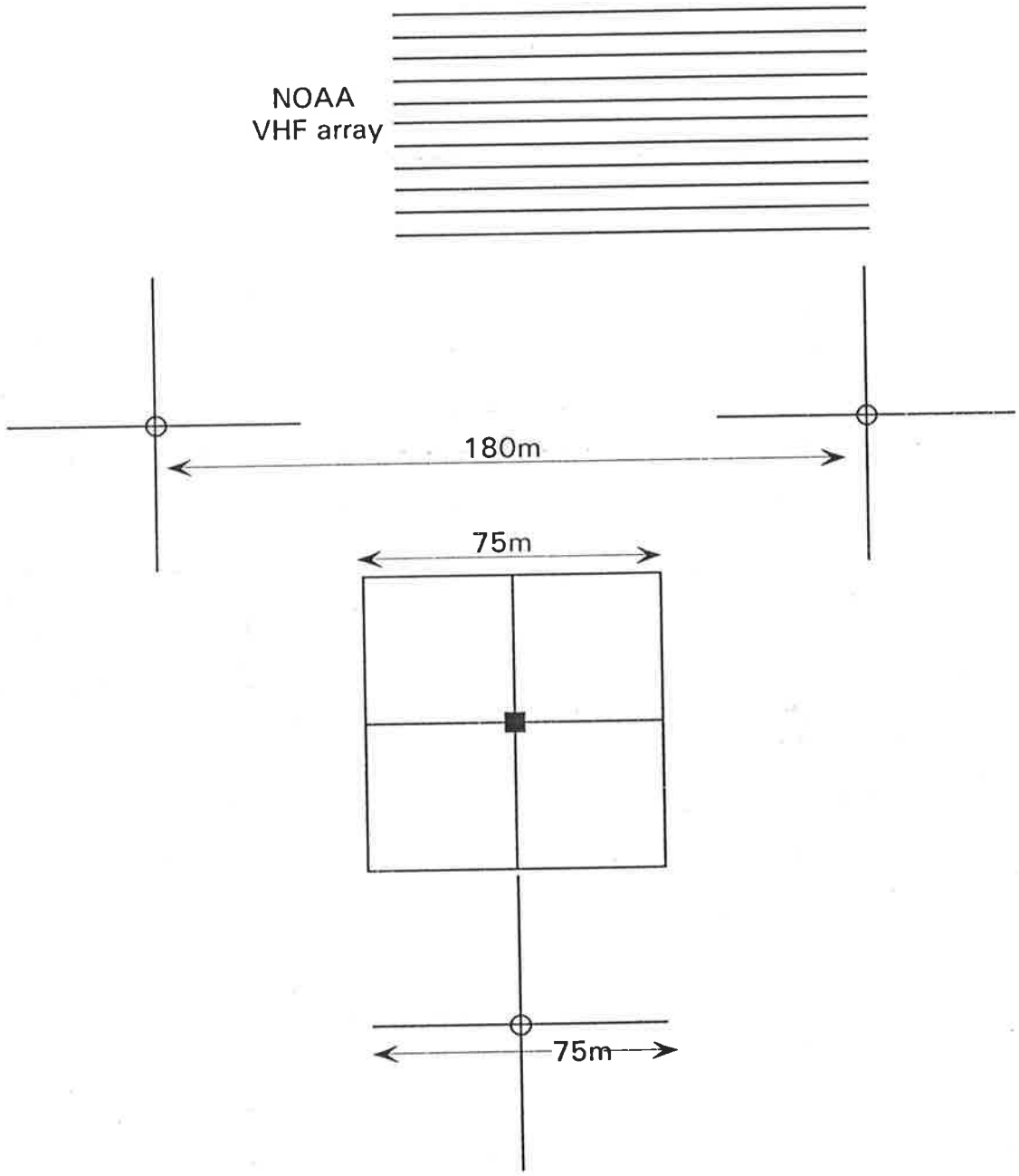

Figure 7.3: Schematic diagram of the Christmas Island partial reflection radar system showing the geometry of the transmitting and receiving antennas.

Peak transmit power	25 kW RMS
Maximum mean transmit power	200 W
Output stage efficiency	65%
Operating frequency	2.0 ± 0.2 MHz
Pulse length	10–50 μS, continuously variable
Pulse rise & fall times	5–25 μS, continuously variable
Harmonics	3rd: -52 dB, 5th: -63dB, even less than -65 dB
Output impedance	50 or 100 Ω unbalanced
Antenna impedance	transmitter shut down if VSWR $\succeq$ 1.5
Mains supply	110–120V, 60 Hz, 2 A
Dimensions	1200 mm Height x 500 mm Width x 500 mm Depth
Weight	50 kg approx.

Table 7.1: The specifications of the 2 MHz pulsed radar transmitter installed and commissioned on Christmas Island in January 1990.

7.2.2 The transmitter, receiving and data acquisition system, and computer controller

The heart of the system consists of the transmitter, the receiving and data acquisition system, and the computer which ultimately controls the system. The transmitter produces pulses at the desired frequency, pulse length and pulse repetition frequency. The receiving and data acquisition system controls the transmitter and collects the data from three receivers which it temporarily stores. The computer controller controls the receiving and data acquisition system, and analyses the raw data collected by it. Finally it stores the processed data, usually in binary form.

All three units are housed in a small room contained within a larger hut which houses the NOAA radar system [see figure 7.7]. The room is air–conditioned keeping the temperature constant and the air fairly dry. The main hut is located within a larger fenced–off compound enclosing a small shed for the diesel power generators, as well as four large fuel tanks.

We will discuss each of the individual units in turn.

The transmitter

Although the University of Adelaide has operated a MF radar system for several decades, one of the novel features about the transmitting system commissioned on Christmas Island is that it

uses a totally solid–state transmitter which has been developed and built within the Atmospheric Physics Group. The complete transmitter system is contained in a small rack, which contains a combiner unit, 10 power amplifier modules, a fan unit, a driver unit and a power supply unit. The transmitter operates at a frequency of 1.98 MHz, although this is adjustable by $\sim$ 0.2 MHz, and is fully phase coherent. The transmitter power is 25 kW, with a variable pulse length of 10–50 μs, usually operated at 25 μs which corresponds to a 4 km height resolution. The pulse repetition frequency is 80 Hz with 32 point integration during day–time. This is reduced to either 20 or 40 Hz during night–time (with the appropriate shorter integration), to avoid problems arising from nultiple reflections from equatorial spread F. Table 7.1 lists the common characteristics of the transmitting system.

The radar data acquisition system

The Radar Data Acquisition System (RDAS) is shown in block diagram form in figure 7.4, while table 7.2 lists the general characteristics of the receiving system. The system is controlled by a microprocessor which both controls the transmitter and acquires data. The data are subsequently transferred to a host personal computer, both for analysis and subsequent storage. The 1.98 MHz transmitter pulses are derived from the master oscillator and frequency synthesis module. The transmitted signal is linearly polarized.

The three receivers are of the superheterodyne type. In each receiver, the received 1.98 MHz signal is mixed with a 2.475 MHz local oscillator to produce a 495 kHz intermediate frequency (IF), which is then fed to the signal processor modules. The signal processors are phase sensitive: the 495 kHz IF signals are mixed with in–phase and quadrature local oscillators to produce in–phase and quadrature components, which are then digitized to 8–bit resolution.

The RDAS acquires and stores in its memory a complete data set. A data set at Christmas Island comprises 256 points of 20 consecutive height samples at 2 km intervals, thus providing a 40 km range coverage. Each data sample is the result of integrating the digitized data over a number of consecutive transmitter pulses. During the day the transmitter is usually pulsed at 80 Hz and the data from 32 consecutive transmitter pulses are coherently averaged to produce a

Recording Config.	Receivers	3
	Sampling start height	60 km night, 70 km daytime
	Sampling interval	2 km
	Pulse Repetition frequency	20, 40 , 80 Hz
	Coherent Integrations	4, 8, 16, 32
	Samples per data set	256
Receivers	Centre Frequency	1.98 MHz
	Bandwidth (3dB)	$\approx$ 39 kHz
	Sensitivity	$< 0.3\ \mu V$
	Maximum Gain	$\sim 10^5$
	Gain Control	Programmable in steps of unit dB
	Gain Control Range	60 dB
	Input Impedance	50 Ω
	Input Filtering	Bandpassed

Table 7.2: The specifications of the radar data acquisition system operating at Christmas Island.

mean data point every 0.4 seconds. A complete data set is therefore acquired in 102.4 seconds, and is then transferred to the host computer.

The recording information which is programmable by the host computer include the number of heights per sample, transmitter pulse repetition frequency, integrations (Tx pulses) per sample point, sample points per data set and receiver gains. Different recording configurations are used for day–time and night–time. The receiver gains are dynamically adjusted by the analysis program before the start of each data set. The RDAS system has been designed and built by the Electronic Services Group within the University of Adelaide and by private contractors.

Computer and analysis software

The computer used at Christmas Island is an Olivetti M28 personal computer with a 40Mb hard disk. After each data acquisition run, the computer performs a full correlation analysis on the 256 point complex data set to determine mean winds and various other parameters. The system runs continuously, barring power failures. Approximately every two weeks, the system is interrupted to allow data to be downloaded to 1.2 Mb floppy disks which are then flown by air mail back to Adelaide. During this time approximately 5 Mb of data are collected. The data are checked in Adelaide and when several copies have been made for safe–keeping, the old data files on the M28 are deleted. On Christmas Island this is all performed by a local resident,

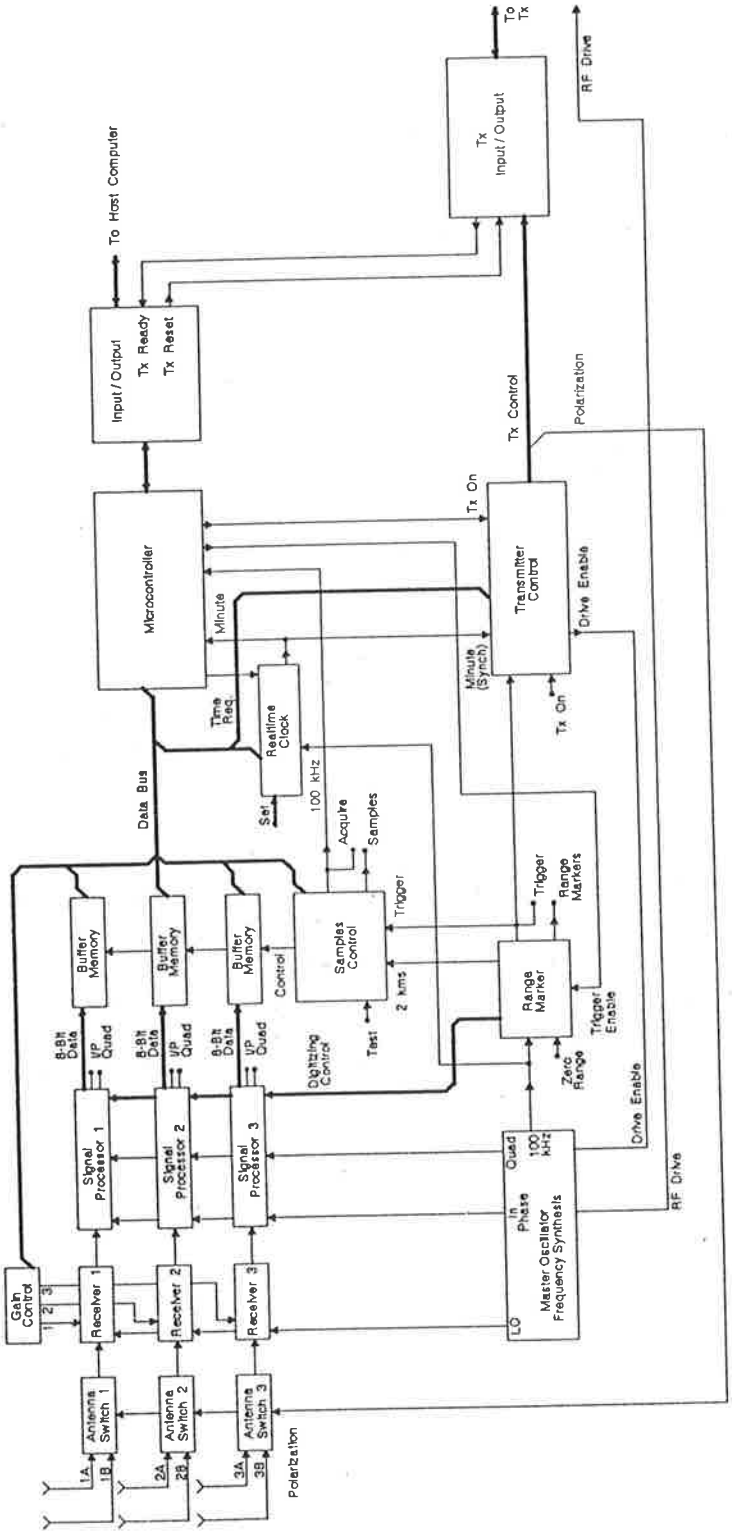

Figure 7.4: Block diagram of the radar data acquisition system, which controls the 2 MHz transmitter, and collects data which are subsequently passed to a host computer.

who also checks the system several times a day, restarts the system after data downloading, and does general maintenance.

See page 233

Figure 7.5: One of the three receiving poles, and the scaffolding which was used to access the receiving antennas. The balun box can be seen as a small black box at top of the pole. The transmitting antennas were mounted on four identical poles.

See page 235

Figure 7.6: A panoramic view of the transmitting array installed on Christmas Island. On the top right hand side of the photo one can also see the VHF radar operated by NOAA.

See page 237

Figure 7.7: Picture of the compound that houses the electronics that drive and control the radar. The compound was constructed by NOAA to house their meteor radar system. Their cooperation enabled us to use the smaller room in the main hut (white hut). The smaller room thus houses the transmitter, the receiver and the data acquisition system, as well as the host computer. The shed on the left houses the power generation equipment, consisting of three diesel generators; a primary one, an equivalent emergency backup, and a further smaller backup in case both of the larger ones fail. The fuel for the generators is stored in the four large tanks to the right of the shed. The antenna on top of the main hut is a satellite link used by NOAA to automatically download the data from the VHF radar.

See page 239

Figure 7.8: The heart of the MF radar system installed at Christmas Island. The transmitter is located on the floor on the right hand side of the room. The ten individual power modules can be seen in the two racks. The radar data acquisition system is located on the bench behind the Cathode Ray Oscilloscope. One can easily see the three receiver channels, one for each of the receiver antennas. The computer which ultimately controls the system is an Olivetti M28, which acquires data from the data acquisition system, analyses it using the full correlation analysis, and finally stores accepted data onto the hard disk in binary form.


Transmitter Pole
Transmitter Pole
NOAA VHF array
Transmitter Pole

Error Code	Meaning	Function
0	Analysis OK	
1	Signal level too low	Main
2	Signal/Noise too low	Interpolate
3	Fading too slow	Tau_fit
4	Time delays too long (slow velocity)	Delay
5	PTD > 50	Main
6	$V_c^2 < 0$ (data accepted)	True_vel
7	Pattern analysis breaks down	True_vel
8	$V_a > 250$ ms^{-1}	True_vel
9	$\|\theta_a - \theta_v\| > 40°$	Main
10	$V_a > 4V_t$	Main
11	$V_t > 1.5V_a$	Main
12	Bad fit to cross-correlation function	Ccf_fit
13	ρ_{max} less than 0.2	Ccf_fit
14	Hardware floating point error	Fphandler
15	Maths error (Log, Log10)	Matherr
16	Other maths errors	Matherr

Table 7.3: The error codes in the full correlation analysis which is being used at Christmas Island.

7.2.3 Experimental technique

The radar system was installed and successfully commissioned in late January 1990, and has collected data ever since. Operating in the spaced–antenna mode with full correlation analysis, horizontal wind velocities are obtained every 2 minutes, and at 2 km height intervals. A total of 20 heights are sampled, extending over the height range of 60 to 98 km. The only time when the system is interrupted is due to general maintenance and downloading of data which occurs at approximately fortnightly intervals. However, the time taken to perform this is relatively small, usually less than 30 minutes. Thus the data is of a very good temporal quality. A problem did, however, occur both in November 1990 and January 1991 when old data files were not deleted from the computer hard disk. The disk subsequently became completely full and no data could be written to it, even though it was collected by the system. Altogether about two weeks of data were lost on each of those occasions.

The data used in this work spans over about 60 weeks; from January 1990 to March 1992, and (apart from the times when no data were written to the disk), was of an excellent temporal resolution. The full correlation analyses rejected data for various reasons [see section 3.5.4].

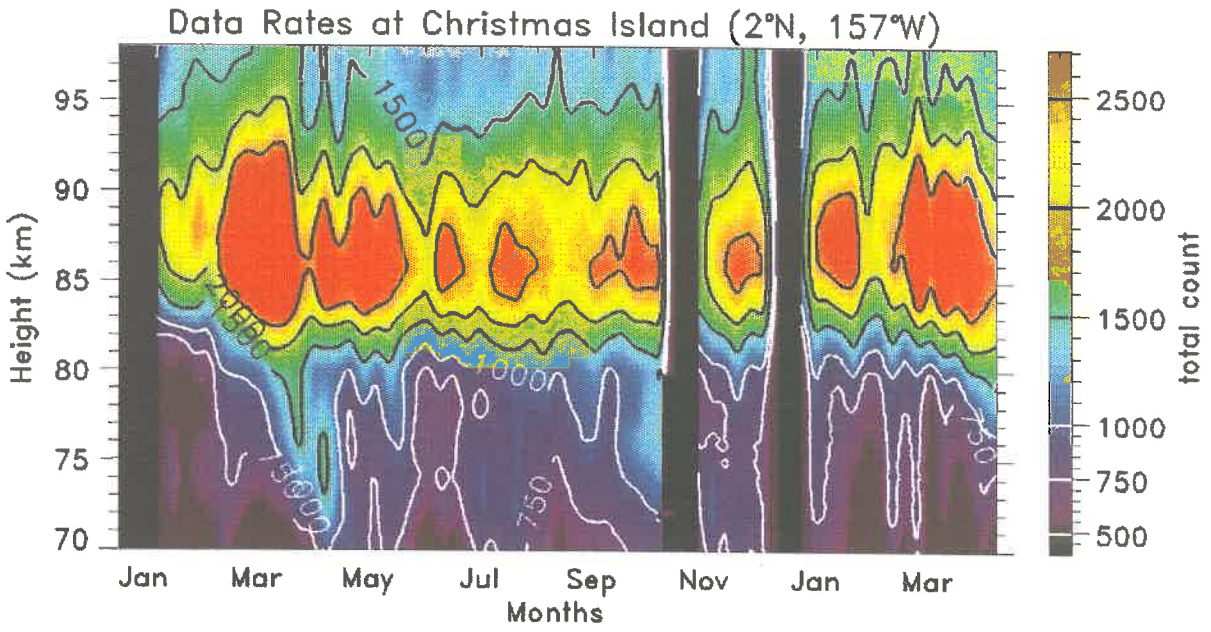

Figure 7.9: Total data collected by the Christmas Island MF radar from January 1990 to March 1991. The contours are labelled in the number of observations per week that were accepted by the full correlation analysis and subsequently used in further analysis. The black areas during October and early January indicate no data collected.

Table 7.4 lists the different acceptance and rejection codes and the relative percentage of data that were deemed suitable or not by the specific error codes. The data are binned into four different height distributions viz. 60–68 km, 70–78 km, 80–88 km, and 90–98 km. Error codes of 0 and 6 indicate that the data were accepted.

As can be seen from table 7.4, within the height range of 60–68 km, only 6.6% of total data were accepted by the full correlation analysis program. The majority of data were rejected due to error codes 3 (about 40%), 4 (about 15%), and 5 (about 30%); slow fading, time delays too long, and PTD > 50 respectively. It is not surprising that the majority of data were rejected due to slow fading as this region of the atmosphere is less turbulent than above 70 km. Since so little data were suitable from this height range it was excluded from any further analysis.

The data acceptance rate improved in the region of 70–78 km to about 15%. Within this height range data rejection due to slow fading fell dramatically to just over 19%, while the

rejection due to long time delays and PTD > 50 also fell; ≈ 11% and 22% respectively. However, more data were rejected due to the signal to noise level being too low (error code 2), accounting for ≈ 18% of total data being rejected.

Error Code	Meaning	Percentage seen per height range in km			
		60–68 km	70–78 km	80–88 km	90–98 km
0	Analysis OK (data accepted)	6.3	14.8	36.3	31.8
1	Signal level too low	$\ll 0.05$	0.1	$\ll 0.05$	$\ll 0.05$
2	Signal/Noise too low	0.5	18.4	5.8	0.06
3	Fading too slow	39.3	19.1	14.8	4.8
4	Time delays too long	15.4	10.9	8.0	14.6
5	PTD > 50	30.3	21.9	19.0	24.7
6	$V_c^2 < 0$ (data accepted)	0.3	0.3	0.8	0.9
7	Pattern analysis breaks down	0.9	1.0	1.4	4.2
8	$V_a > 250ms^{-1}$	0.3	0.7	1.0	1.1
9	$\|\theta_a - \theta_v\| > 40°$	0.9	1.3	2.6	4.5
10	$V_a > 4V_t$	0.6	1.6	4.9	3.9
11	$V_t > 1.5V_a$	1.4	1.7	2.4	4.5
12	Bad fit to cross-corr. function	0.7	4.9	1.4	0.6
13	ρ_{max} less than 0.2	2.9	1.7	0.9	4.0
14	Hardware floating point error	$\ll 0.05$	$\ll 0.05$	$\ll 0.05$	$\ll 0.05$
15	Maths error (Log, Log10)	0.05	0.07	0.2	0.2
16	Other maths errors	0.1	1.3	0.4	$\ll 0.05$

Table 7.4: The full correlation analysis performs on–line analysis of data which may be accepted and rejected according to stringent parameters. The table above lists the different acceptance and rejection codes, and the relative percentage of data that was deemed suitable or not by the specific error code. The data is binned into four different height distributions. As can bee seen from the table heights below 70 km produced very little accepted data, and this height range was subsequently not used in any analysis.

In the region of 80–88 km the percentage of data accepted increased markedly to about 37%. Data rejected due to low signal/noise ratio, slow fading, long time delays, and large PTD all fell to ≈ 6%, 15%, 8%, and 19% respectively. Within this height range other full correlation analysis rejection parameters start to be important. For example, error codes of 8, 9, 10, and 11, which test the apparent velocity and its relationship with the true velocity [see section 3.5] rejected just under 11% of all data collected, a marked increase from the lower heights.

Between 90–98 km the total percentage of data accepted was slightly less than that between 80–88 km. However, it was still more than double that of the 70–78 km region. Within the 90–98 km height range the rejection due to low signal/noise ratio was virtually non–existent, while

that due to slow fading continued in its downward trend to account for less than 5% of data rejected. In contrast, more data were rejected due to long time delays and long PTD's, while the rejection due to the differences between the apparent and true velocities again increased to around 14%.

Figure 7.9 shows the total number of data points collected per week by the Christmas Island radar system over a continuous period of 14 months, from January 1990 to March 1991. All these data were accepted by the full correlation analysis, having passed all the relevant rejection criteria. The regions where no data were collected are shown as black on the diagram. Clearly evident is the low data rates which are experienced below about 80 km. Whilst lower data rates are also evident above 92 km, they are still approximately double those below 80 km. It is known that the scatterers are more specular below 80 km [*Lesicar & Hocking*, 1992], thus causing slow fading, while above 92 km the receivers are saturated due to the close proximity of the E region. Another feature to note is the increase in data rates during March to May, but with no clear seasonal effects. This is in contrast to data collected at Adelaide [see figure 6.2] which exhibits a clear seasonal effect. The diurnal variation in the number of useful echoes at Christmas Island will be considered in chapter 10.

A factor which had to be considered when analyzing the data was the effect of strong backscatter from ocean waves. These were observed by the radar up to a distance of 80 km, in all directions. The backscatter was due to Fourier components in the sea surface whose scale was half the radar wavelength (75 metres). Since this backscatter produces a well defined shifts at ± 0.143 Hz, the data were band–pass filtered prior to performing the full correlation analysis. The sea–clutter was found to be strongest below 70 km, where the ionospheric back–scatter is weak; this was another reason not to include data below 70 km.

The data above 70 km were subsequently averaged into both hourly and 24 hour blocks. The 24 hour blocks averaged out any small–period atmospheric (and oceanic) wave motions which were still present in the hoiurly averages. Weekly means were then constructed from the 24 hr averages, thus removing the effects of medium–period wave motions.

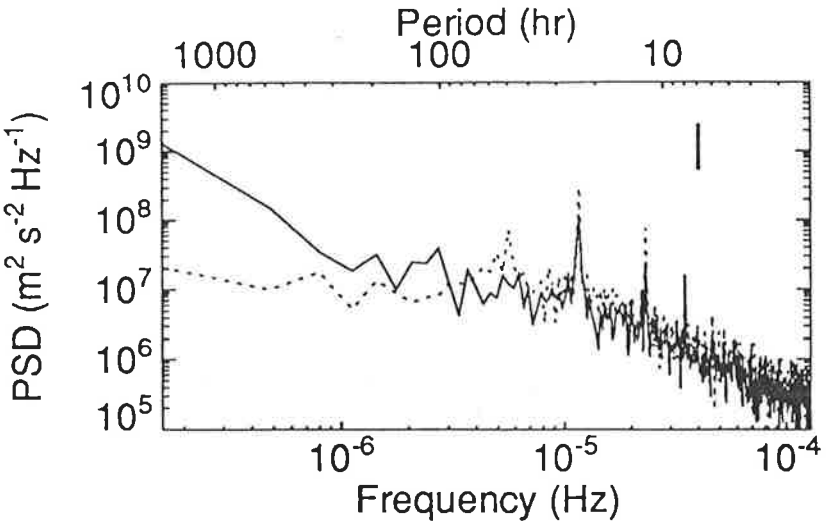

Figure 7.10: Power spectra of the zonal (solid line) and the meridional (dashed line) winds at an altitude of 86 km. The vertical line indicates the 95% confidence limits [from *Vincent & Lesicar*, 1991].

In the following sections we will discuss the long–term behaviour of mean winds and other full correlation analysis parameters; the latter are subsequently used to determine the aspect sensitivity and L/h ratios of the mesospheric scatterers. Some of the work presented here has already been published [see e.g. *Vincent & Lesicar*, 1991; *Lesicar et al.*, 1993].

7.3 Mean winds and dynamics at Christmas Island

Figure 7.11 (top) shows image–contours of the weekly–mean zonal wind at Christmas Island constructed from 14 months of data. The main feature of the mean zonal wind is a prevailing westward (easterly) flow which exhibits long–term variations with scales of months. The largest westward flow occurs during mid–March, when velocities of -40 ms^{-1} are found around 85 km altitude. The flow briefly reverses to eastward in May, and again for a longer period in June around and above the mesopause. An interesting feature is the downward descent of the wind contours at an approximate rate of a kilometre per day.

Figure 7.11 (bottom) shows image–contours of the weekly–mean meridional wind. Unlike the zonal component, the magnitude of the prevailing meridional component is rather small,

and seldom exceeds 7 ms^{-1}. Below the mesopause the flow is predominantly southward, while above about 80 km a northward flow is evident between September and March, peaking in January. Unlike the zonal flow there is no clear downwards descent of the wind contours.

In conclusion, the data presented above show that the equatorial mesosphere has a prevailing zonal wind, with long term descending wind contours. This long term variation, which is characteristic of a wave driven circulation, is consistent with that expected of a mesospheric semi–annual oscillation. This was first reported by *Hirota* [1978] for Ascension Island (8° S), and later by *Hamilton* [1982] for Kwajalein (9° N). Hirota's study covered the altitude range of 30–90 km while Hamilton's looked at the 40–80 km altitude range. Studies of satellite temperature data by *Hitchman & Leovy* [1986] and *Fleming & Chandra* [1989] have also found a semiannual oscillation in the zonal wind. The results presented here are also consistent with those found by the Christmas Island VHF meteor wind observations of *Avery et al.* [1990].

Figure 7.10 [from *Vincent & Lesicar*, 1991] illustrates the power spectra computed from hourly averages of each wind component at a height of 86 km and for about 6 months of observation. The atmospheric tidal periods of 24, 12 and 8 hours are seen as quite strong spectral peaks on a continuous background, which varies approximately as $f^{-\frac{3}{2}}$ for periods less than one day (f being the frequency). In addition to the tidal peaks, another peak is noticeable in the spectra of the meridional wind at a period of about 50 hours.

By band–pass filtering 6 months of wind data it was found by *Vincent & Lesicar* [1991], that for periods longer than a few days, variations in the zonal wind component are most marked early in the year, and absent in the meridional component. For zonal wind variations in the 3–12 day period range, the zonal wind variation exhibited a quasi–periodic oscillation with peak amplitude of $\sim 20 ms^{-1}$ and a period of about 7–8 days. The contours were found to possess a downward mean slope of about 15 km per day above, and 5 km per day below 85 km. This is equivalent to vertical wavelengths of the order of 40–110 km. Since the oscillations appear only in the zonal wind component they are most probably due to ultra–fast Kelvin waves [see *Salby et al.*, 1984]. Daily variations in the mean winds and dynamics are discussed in more detail in

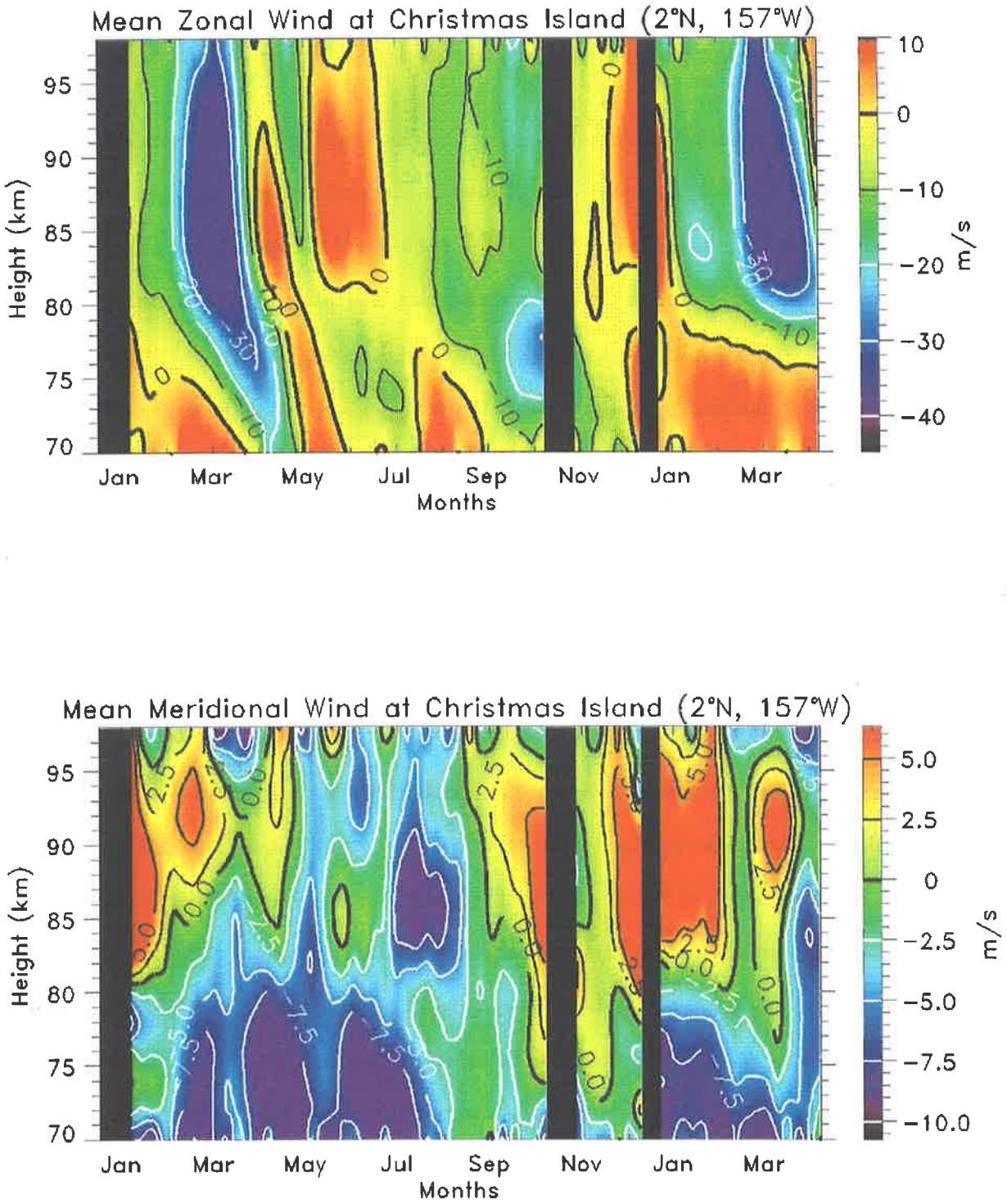

Figure 7.11: Mean zonal (top) and meridional (bottom) winds measured at Christmas Island by a MF partial reflection radar system over a period of 14 months, from January 1990 to March 1991. The contours are labelled in ms^{-1}, positive for eastward (westerly) and northward (southerly) respectively. The black areas are times and heights for which no data were collected.

chapter 10.

7.4 Seasonal behaviour of spaced–antenna parameters

The full correlation analysis provides a number of other useful parameters besides the mean winds [see chapter 3]. In this section we will present these other parameters and discuss their usefulness in providing a deeper understanding of the state of the mesosphere. We concentrate on their seasonal behaviour and present no mathematical derivations or equations. For these the reader is referred to chapter 3. The format of the following sections is identical to that employed in chapter 6 which examines the seasonal behaviour of full correlation analysis parameters at Adelaide. The short term behaviour of the parameters will be discussed in a later chapter.

Fading time

Figure 7.12 (top) is an image–contour plot of the weekly–mean fading time, $\tau_{0.5}$, the time for which the directly observable auto–correlation function falls to 0.5 of its peak value [see equation 3.54]. There is no clear seasonal variation in the fading time. An exception is March through to April, when there is a decrease in the fading time observed at all heights. The contours show a rapid downward propagation from about 90 to 75 km. The striking feature of the figure is the variation of fading time with altitude. While it is a fairly constant value of between 2.2 to 2.4 seconds below the mesopause, and with a maximum just above 2.4 seconds at the mesopause, at greater heights there is a marked reduction in the fading time over a height range of only 8 km. From about 86 to 94 km the fading time changes from more than 2.4 seconds to around 1.4 seconds, a change of more than one second. Since the mean value is around 2 seconds this represents a change of more than 50 percent.

The variation in the fading time could be, and is generally attributed to, a variation in the wind speed. With an increase in wind velocity, there is a reciprocal decrease in the fading time. However, unlike the results from Adelaide where the fading time was seen to be inversely related to the mean winds [figure 6.3 and figure 6.4], the mean winds at Christmas Island exhibit no

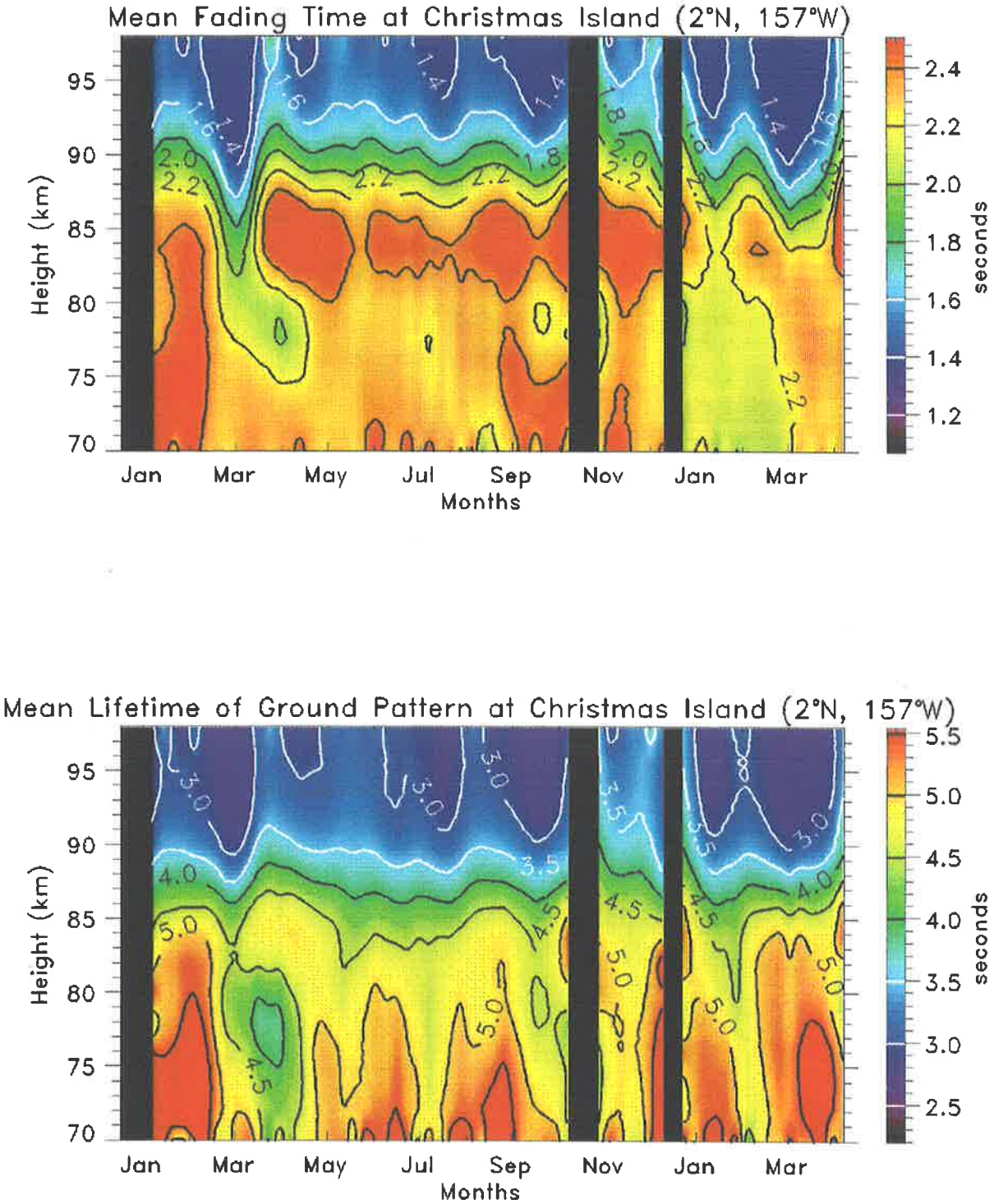

Figure 7.12: Weekly–mean fading time (top) and lifetime of ground pattern (bottom) at Christmas Island measured over 14 months, starting from January 1990. The contours are in seconds. The black areas indicate no data were collected.

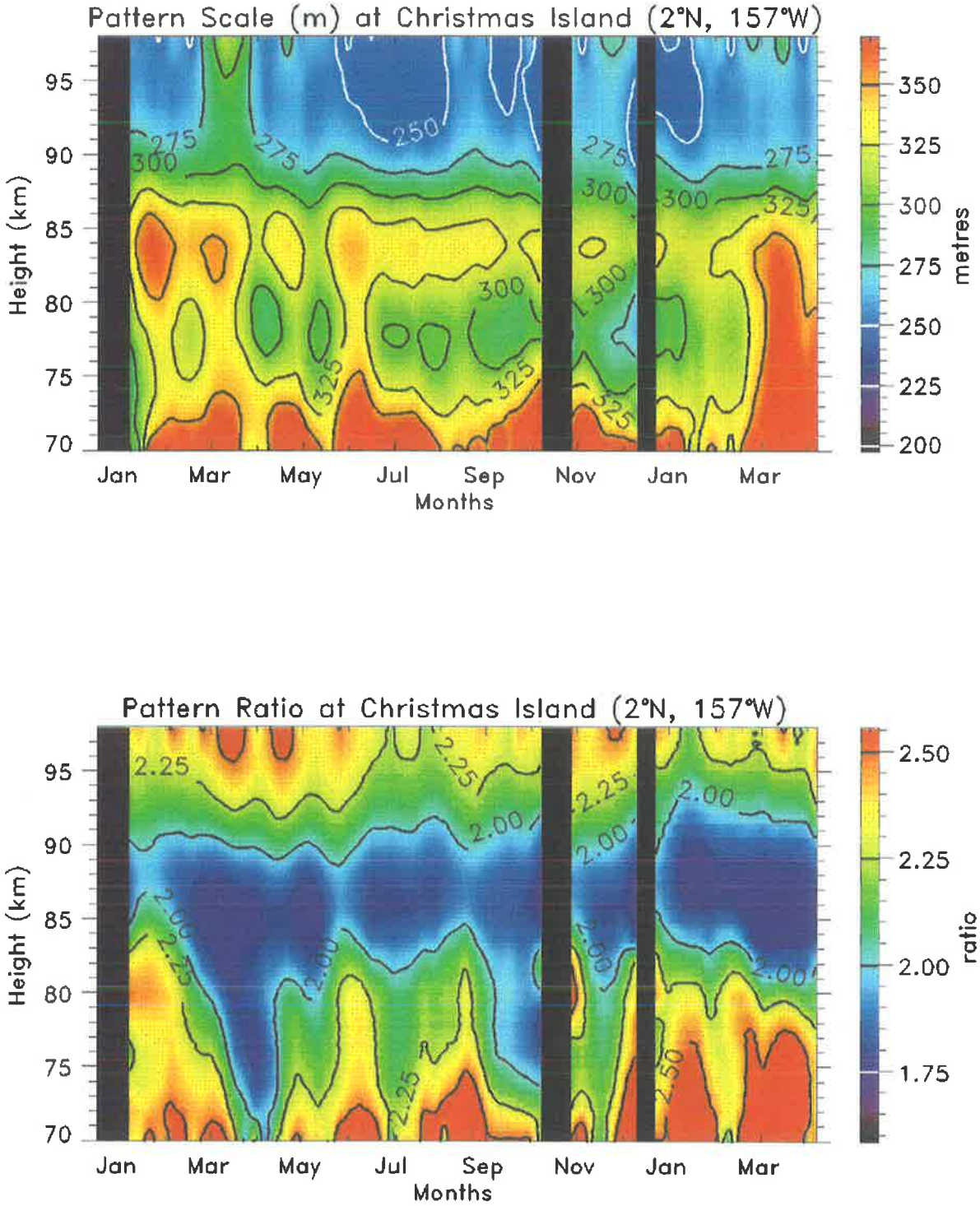

Figure 7.13: Weekly–mean pattern size (top) and pattern ratio (bottom) at Christmas Island measured over 14 months, starting from January 1990. The contours of the pattern size are in metres while the axial ratio is the ratio of the semi–major to the semi–minor axis. The black areas indicate no data collected.

clear height variation. The only time when the mean wind and fading time are inversely related occurs during late March to April when a decrease in the fading time is associated with a strong westward flow. However, the aspect sensitivity of scatterers also affects the fading times. Aspect sensitive scatterers result in large fading times due to their specularity. Since the radar partially reflects from scatterers whose vertical extent is $\sim \lambda/2$, the more aspect sensitive the scatterers, the larger their horizontal extent, and thus longer fading times. Similarly, the more isotropic the scatterers, the shorter the fading times. The aspect sensitivity of the scatterers will be discussed shortly.

Lifetime of ground pattern

Unlike the fading time, the lifetime of the ground pattern, $T_{0.5}$, is a parameter which has the effects of the mean wind motion removed, and hence represents the random changes of the scattering echoes only. This parameter can therefore be used to infer, or obtain a feel for the stability of the reflecting medium. It can also be used to give estimates of the turbulent energy dissipation rates: this will be discussed shortly.

Figure 7.12 (bottom) is a weekly–mean image–contour of the lifetime parameter, using 14 months of data. As for the fading time, there is no strong seasonal variation, but a clear height dependence. The mean lifetime at heights below 80 km is approximately 5 seconds. This decreases uniformly to about 3 seconds above 90 km. There is also a minimum occurring from March through to April with lifetimes decreasing by over one second to less than 4 seconds at just below 80 km. The striking feature is the rapid decrease of lifetime between 85 to 90 km. In addition there seems to be some evidence of another minimum below the mesopause during October. This seems to be in contrast to the fading time which exhibits no such behaviour.

Pattern size

Figure 7.13 (top) is an image–contour diagram of the weekly–mean of the pattern scale using 14 months of data. Similarly to $\tau_{0.5}$ and $T_{0.5}$, there exists a clear height variation, with the pattern scale decreasing with increasing altitude. While below 75 km the pattern scale is greater than

350 metres, this decreases at a fairly constant rate to around 300 metres at 85 km. Above 85 km there is a large change in the pattern scale within a 5 km height range, where it decreases to less than 275 metres. Above 90 km the pattern scale is fairly constant at around 250 metres. Otherwise, there is no clear seasonal variation in the data, although March again seems to be the odd month when the pattern scale seems somewhat slightly larger than during other times of the year. The smaller pattern scales at greater heights is also consistant with faster fading times at greater heights, assuming the mean wind is relatively stable.

Pattern axial ratio

Figure 7.13 (bottom) is an image–contour diagram of the weekly–mean pattern axial ratio at Christmas Island calculated over 14 months of data. The pattern ratio is clearly different to both the fading time, lifetime and pattern scale. A seasonal variation is quite noticeable. During March through to April the ratio contours propagate downward at a rate of approximately 5 km per week. For example, at 72 km the ratio changes from over 2.5 to less than 2.0 within 4 weeks. A local minimum is also evident during October, albeit a weaker effect. Superimposed on this seasonal behaviour is a strong altitude dependence. A minimum of less than 2.0 is prevalent within the 80 to 85 km range. The ratio subsequently increase both below and above this height range, being slightly larger at the lower height range.

Conclusion

The above examples clearly indicate that long–term averages of various diffraction parameters, with the exception of the pattern ratio, in the equatorial region exhibit no strong seasonal behaviour. They do, however, indicate a strong dependence on height, with all the parameters varying markedly between 70 to 98 km. This is in contrast to the results observed at Adelaide where the seasonal variation in the diffraction parameters was quite noticeable [see figures 6.4, 6.5]. In general, all of the parameters exhibited a decrease with increasing altitude, with the exception of the pattern ratio which also increased below the mesopause. In addition, within the range of 85 to 90 km all the parameters bar one, the pattern ratio, changed quite rapidly.

The pattern ratio in fact was most stable through this altitude range.

7.5 Aspect sensitivity

While the previous section examined the raw parameters which are deduced as by–products of the full correlation analysis, it was shown in chapter 5 how these various parameters could be used to make qualitative calculations of other atmospheric quantities. One of these was the aspect sensitivity, θ_s, which could be calculated by using either the fading time of the signal, or the spatial correlation size. Here we discuss the seasonal and height behaviour of aspect sensitivity calculated at Christmas Island using 14 months of data. This work has already been published, although detailing the spatial–correlation results only [see *Lesicar et al.*, 1993].

Spectral–width method

Figure 7.14 (top) is an image–contour diagram of the weekly–mean aspect sensitivity calculated by the spectral–width method. The values of θ_s range from between 13 to 26 degrees. There are several important features to note. First, the aspect sensitivity increases continuously from 85 km upwards. However, this increase is not constant and markedly accelerates between 88 and 94 km, changing within this range by over 6 degrees. Secondly, the aspect sensitivity between 80 to 85 km fluctuates around a constant value of 16 degrees. Below 80 km the aspect sensitivity slightly increases, with the exception of late March to April where there is no obvious increase. There also seems to be a slight increase in January by several degrees.

Spatial–correlation method

Figure 7.14 (bottom) is an image–contour plot of the weekly–mean aspect sensitivity calculated by the spatial–correlation method. The main features are very similar to those displayed by the aspect sensitivity calculated by the spectral–width method. However, the absolute values are much smaller, (ranging from 8° through to 15°), when compared to those calculated by the spectral–width method where the values range from 13° through to 26°. The difference between

the aspect sensitivity measured using the fading time as compared to that calculated using the pattern size may in part be due to the contribution by turbulence to the spectral–width, which may not always be primarily due to beam–broadening. Another factor contributing to the difference between the two methods is the way that we calculate the fading time. The fading time is calculated by the full correlation analysis and depends on the orientation of the scattering medium relative to the wind. If the scattering medium possesses elliptical geometry, the fading time measured depends on the orientation of this ellipse with respect to the mean wind direction. As such, the aspect sensitivity is inversely dependent on the fading time. A smaller fading time therefore leads to a larger aspect sensitivity. Conversely, a larger fading time leads to a smaller aspect sensitivity. This bias is avoided when the spatial correlation method is used where a geometric mean of the ellipse major and minor axis is used. As such the use of the pattern scale is a much more robust and realistic method when the scattering medium is anisotropic. A discussion of the anisotropy of the scattering media will be presented in later chapters, whilst that pertaining to the Christmas Island data will be tackled in chapter 10.

7.6 Horizontal correlation lengths

The calculated values of θ_s were then used to determine the length–to–depth (L/h) ratio of the scatterers. Again, the reader is referred to chapter 5 for the mathematical groundwork. Figure 7.15 (top) is an image–contour of the weekly–mean L/h ratio calculated from the spectral–width θ_s [shown in figure 7.14 (top)], while figure 7.15 (bottom) is an image–contour of the weekly–mean L/h ratio calculated from the spatial–correlation θ_s [shown in figure 7.14].

Both of the L/h results show a clear height dependence, with the L/h ratio possessing a maximum around 85 km and decreasing both above and below this height. However, the decrease is more marked at heights above 85 km where, by about 92 km, the L/h ratio drops to around 1.5 in the case of the spectral–width data, and down to less than 2.75 in the case of the spatial–correlation data. From 92 up to 98 km the L/h ratios are quite stable, and show very little change.

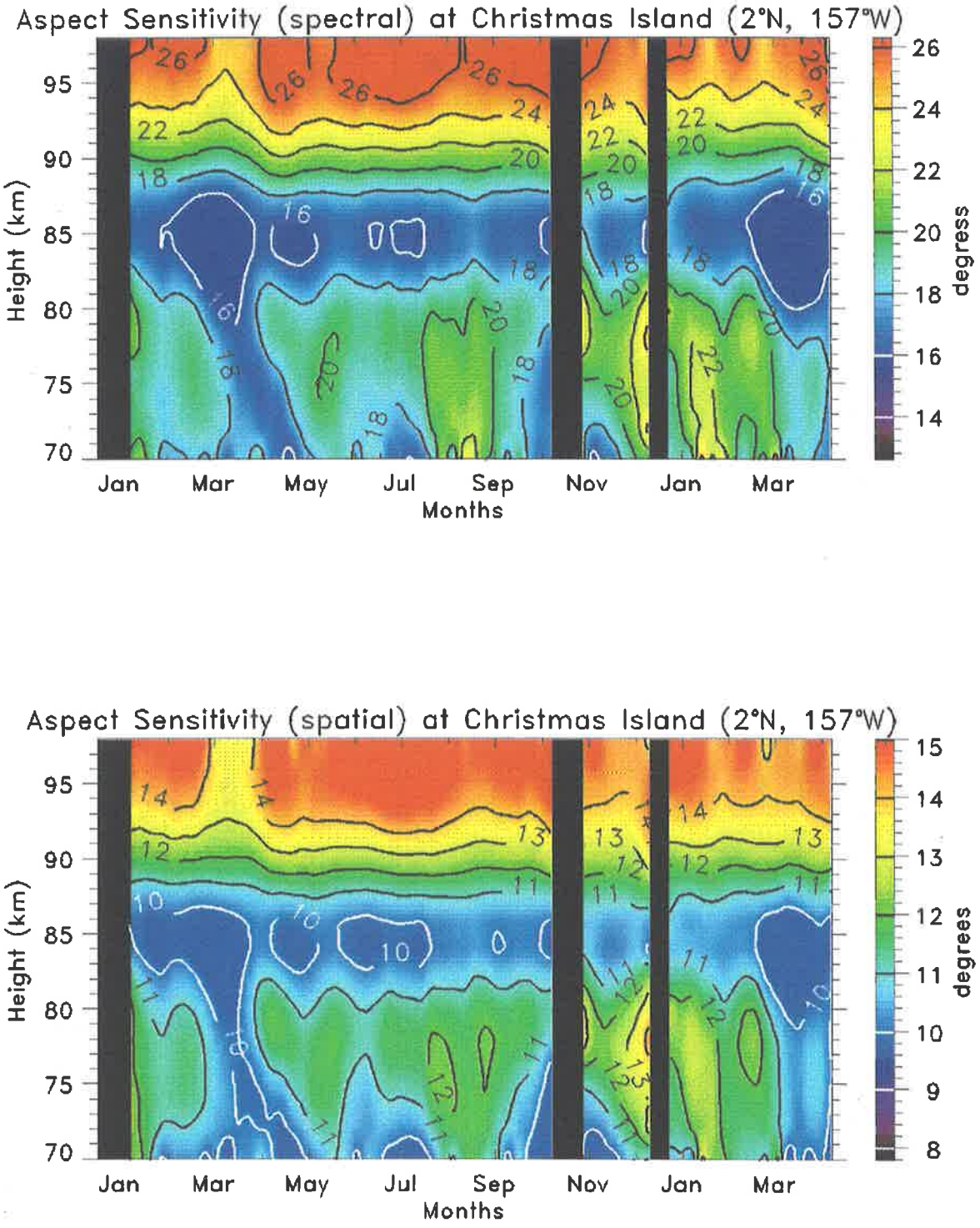

Figure 7.14: Weekly–mean aspect sensitivity calculated by the spectral–width method (top) and the spatial–correlation method (bottom) at Christmas Island using 14 months of data. The contours are in degrees.

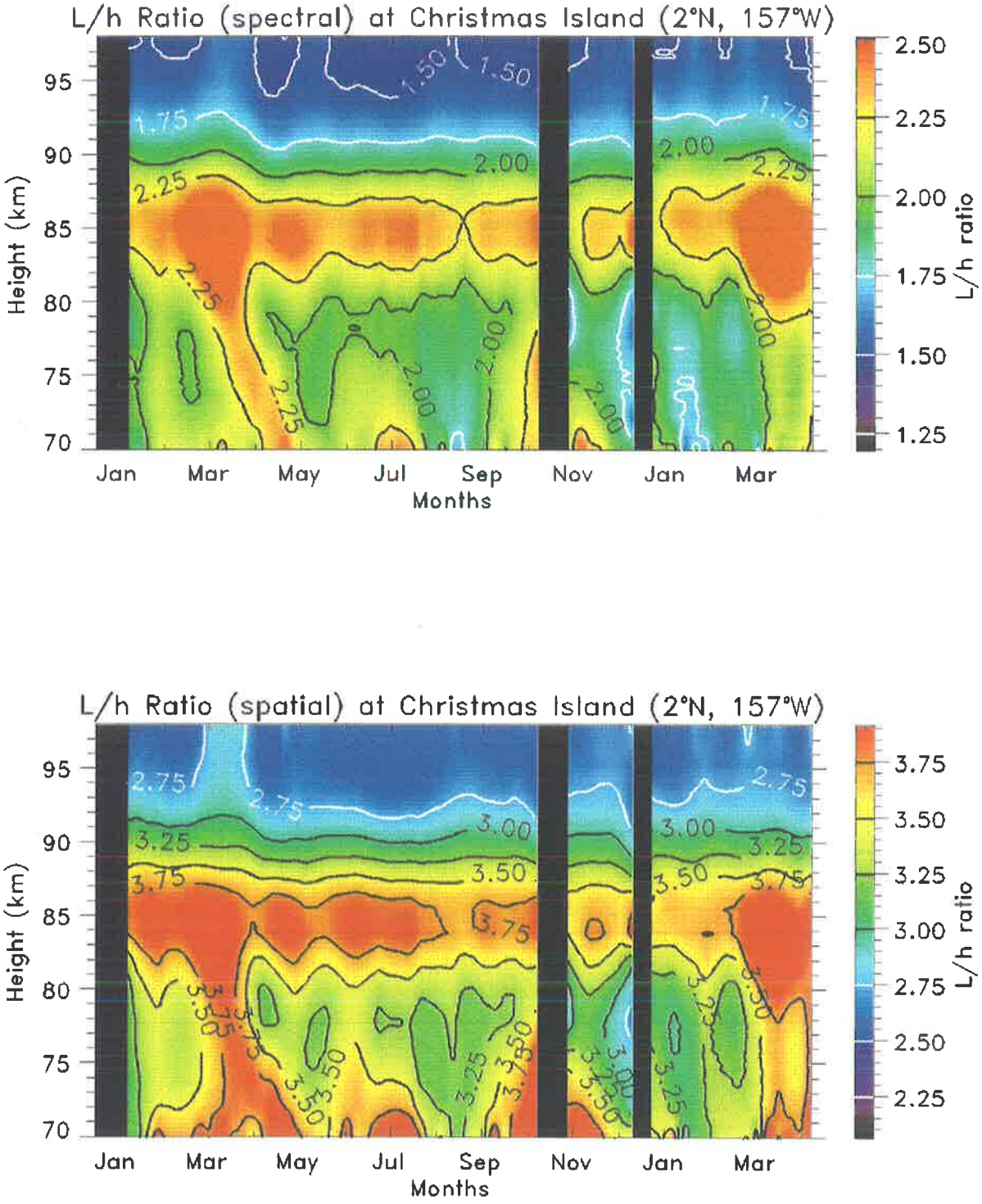

Figure 7.15: Weekly–mean L/h ratio, calculated by the spectral–width (top) and the spatial–correlation method at Christmas Island using 14 months of data. The contours are the ratio of the length to height.

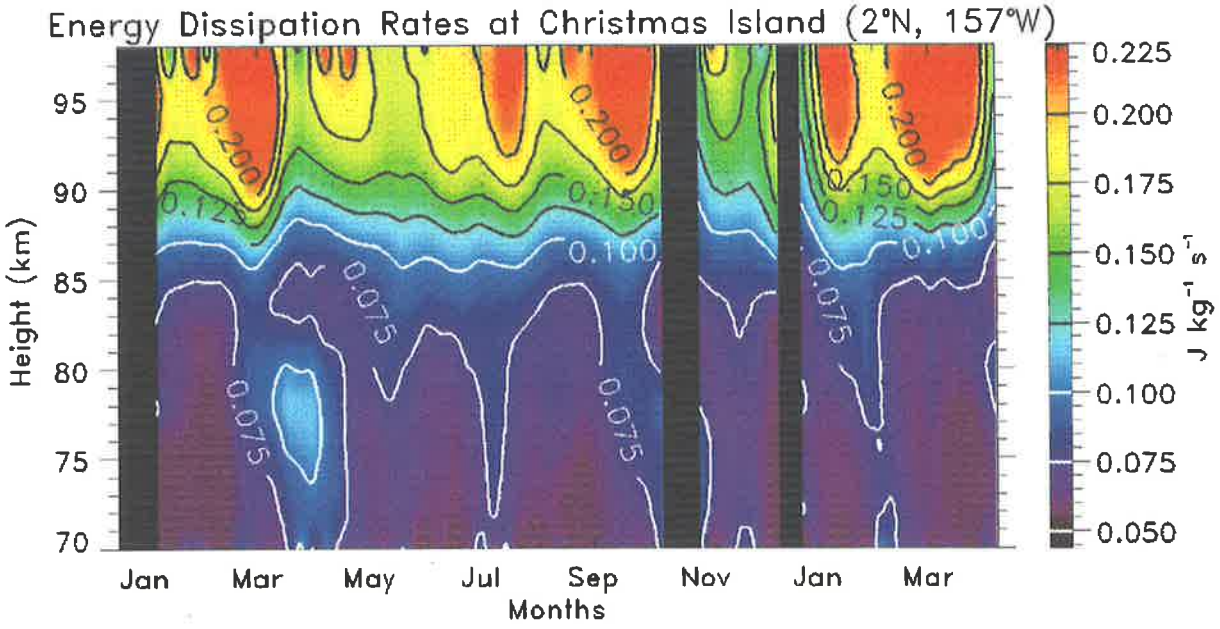

Figure 7.16: Weekly–mean energy dissipation rate calculated at Christmas Island using 14 months of data. The contours are in Wkg^{-1}.

However, below about 82 km, while there is only a small variation with height, there seems to be an increase in the L/h ratio during March to April where the ratio contours propagate downwards at a rate of several kilometres per week. In addition there seems to be a minimum occurring during late December through to early January. While this effect is noticeable in both the spectral–width and spatial–correlation data it is much more evident in the latter.

If the scatterers possess an ellipsoidal structure then the above data suggests that the structures are more anisotropic around the mesopause and tend to isotropy at heights above 90 km. If this was correlated with dynamical activity this could then be interpreted to mean that above the mesopause there is much more turbulent activity.

7.7 Turbulent energy dissipation rates

Estimates of turbulent energy dissipation rates can be derived by using the spectral width of the returned signal. For a review of the method see chapter 3. Figure 7.16 is an image–contour

plot of the weekly–mean energy dissipation rate, ϵ, calculated at Christmas Island by using the spectral width of the backscaterred signal. Again, 14 months of data were used to observe heights of 70 to 98 km. The ϵ rates are seen to vary from $\sim$ 0.05 Wkg^{-1} to greater than 0.2 Wkg^{-1}. There is a clear height variation where below about 85 km ϵ is approximately 0.075 Wkg^{-1}. Above 85 km ϵ doubles within a 5 km range to 0.15 Wkg^{-1}, while above 92 km the rate seems to be fairly uniform with height but exhibits a weak seasonal variation with small maxima during March and September. In addition, below 80 km during March, there is a small localized maximum where the energy dissipation rate increases by more than 0.025 Wkg^{-1}.

However, the data collected at Christmas Island used a wide radar beam. This tends to result in over–estimation of ϵ, due to the action of gravity wave motions which act to broaden the spectrum. Unlike the energy dissipation rate calculations for Adelaide, discussed in section 6.8, there are no estimates of the gravity wave contribution at Christmas Island. The results above should therefore be treated with great caution, and are, at best, only upper limits.

7.8 Conclusion

Since it was installed in January 1990, the MF partial reflection radar system has provided data of a good temporal and spatial resolution. By this time the system has provided several years of continuous data which is currently being analyzed to observe the seasonal variation of wave activity and to study the role of waves in driving the equatorial circulation, as well as other phenomena such as the QBO, and gravity wave sources.

Chapter 8

Seasonal results from Mawson

8.1 Introduction

Although regular measurements of Antarctic upper atmosphere winds had previously been made at Molodezhnaya (68°\$S, 45°\$E) prior to 1980, these utilized a meteor radar which had no height discriminatory capabilities, and the results were simply assumed to refer to a mean height of 94 km [*Lysenko et al.*, 1979]. During the late 1950's meteor wind measurements were carried out by *Elford and Murray*, [1960] but were restricted by low data rates. A spaced–antenna system was also set up at Scott Base (78°\$S, 168°\$ E) and measured winds in the 70–100 km range [see e.g. *Fraser*, 1984b]. The first spaced–antenna system installed by the University of Adelaide in Antarctica was constructed and operated at Mawson (67°\$S, 63°\$E) in the summer of 1981/82.

Seven weeks of continuous data were initially collected at Mawson during the summer of 1981/82 and provided the basis of the first study of the mean winds and atmospheric tides during the Antarctic summer [*MacLeod and Vincent*, 1985; *MacLeod*, 1986]. At the end of the summer the radar system (excluding the towers) was returned to Adelaide and rebuilt. In 1984, besides the installation of the new modified system, which included an on–line computer, both the transmitting and receiving antennas were rebuilt [*Phillips*, 1989]. The system underwent another major overhaul in the summer of 1988/89 when the computer was replaced and some maintenance of the antenna system carried out. The final stage occurred during 1991, when

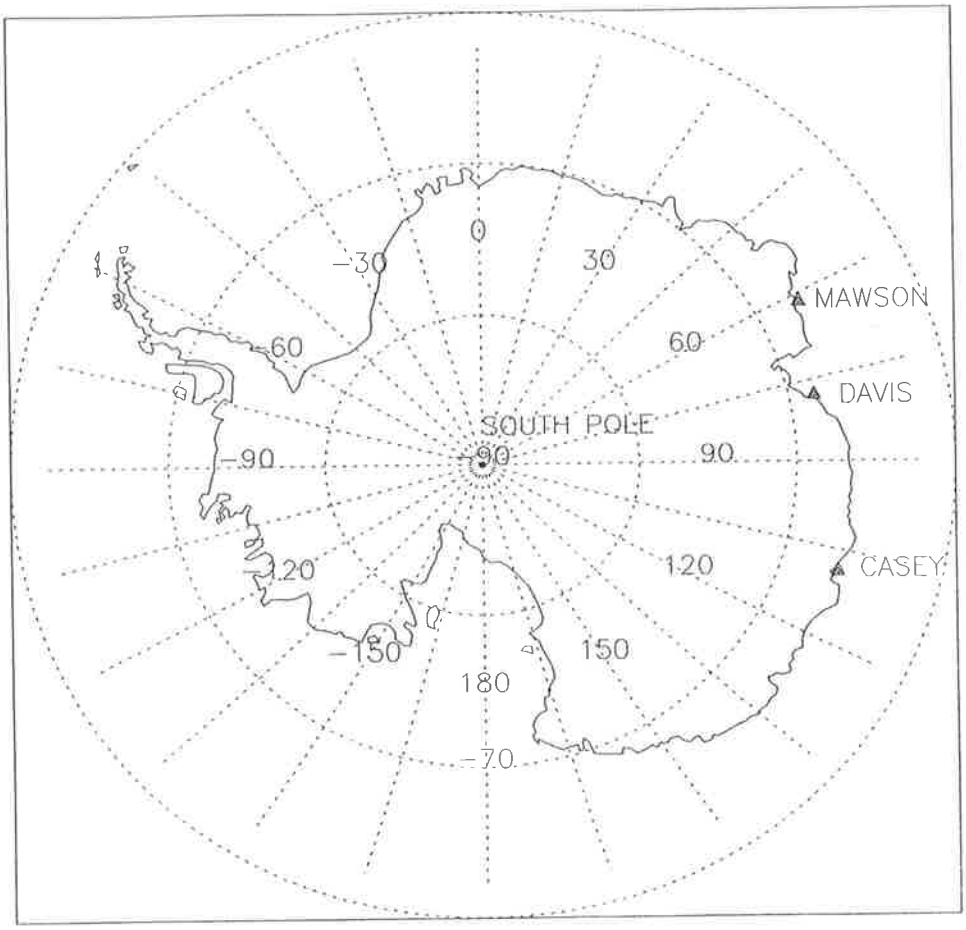

Figure 8.1: Map of Antarctica showing the location of the Mawson base where a partial reflection radar is located. Also indicated are two other Australian bases, Davis and Casey, which are also used for scientific research. All three bases are permanently staffed. During summer months Mawson houses over 60 personnel, which is reduced to 20–30 over the winter months.

a new solid state transmitter was installed. Apart from down–time due to system upgrades data have been continuously collected from July 1984, and this data set is one of the longest records of high–latitude antarctic upper mesosphere and lower thermosphere winds and other parameters. Figure 8.1 shows the position of the Mawson base operated by ANARE[1] which houses the partial reflection radar system.

This thesis uses data which were collected both by the old and the new improved system.

[1] Australian National Antarctic Research Expedition

While this chapter uses data collected over four years, from 1985–1988, and discusses the long–term behaviour of the atmosphere above Antarctica, data which were collected during 1991 by the improved system are used in chapter 11, where short–term variations are examined.

8.2 Radar overview

The radar system has been well documented elsewhere [see e.g. *Phillips*, 1989; *Price*, 1988], and only the salient features will be described here. The layout of the system is somewhat similar to the ones employed at Adelaide, and at Christmas Island.

Briefly, the transmitting array consists of 4 half–wave dipoles arranged in a square and elevated at about one–quarter wavelength; it can transmit on either the O or E mode. The antenna half–power beam–width is about 50 degrees. The transmitter used up until 1991 was a valve transmitter operating at 1.94 MHz, with a peak power of 4 kW, pulse width of 30 μs, and a pulse repetition frequency of 20 Hz.

The receiving array is a typical spaced–antenna system composed of 3 antennas each consisting of a crossed pair of inverted–V dipoles arranged in the form of an approximately equilateral triangle with sides of approximately 155 metres. The receiving antennas are phased to receive either E or O mode circular polarization. The three receivers are single conversion superheterodyne types with an IF of 485 kHz, a bandwidth of about 25 kHz, and gain of 100 dB. The receiving system is phase–sensitive; the detectors provide outputs in the form of in–phase and quadrature components. 10 heights are sampled at 2 km intervals every 5 minutes[2]. The height resolution is approximately 4 km.

Originally the system was controlled by a Data General NOVA 2 with a 32K core–type memory. Full correlation analysis was performed on–line. The data were then stored on magnetic tapes. The personal computer, which has replaced the NOVA, calculates winds and other parameters with a temporal resolution of 3 minutes, and stores the results on its hard disk.

[2]The new system samples 20 heights

8.3 Experimental technique

In the analysis described here, data used were collected over four years, from 1985 to 1988, and were the reuslt of joint collaboration between the Atmospheric Physics group and the Mawson Institute for Antarctic Research[3] both at the University of Adelaide. The system operated in the spaced–antenna mode and provided winds and other full correlation analysis parameters in the height range of 70 to 108 km. Under normal operating conditions between 20 and 40% of all data were deemed acceptable by the full correlation analysis. The other data were rejected due to the various rejection criteria. For example, the signal–to–noise criterion which rejects data where the signal–to–noise ratio falls below -6dB was responsible for rejecting a large percentage of data below about 76km. At times, the polar–cap–absorption can be quite strong, and reflections from the D and E regions may be absent for several days at a time. Other major contributors to data rejection were the percentage time discrepancy, slow fading

[3]The institute has recently been closed, and a new Mawson Centre for Environmental Studies established

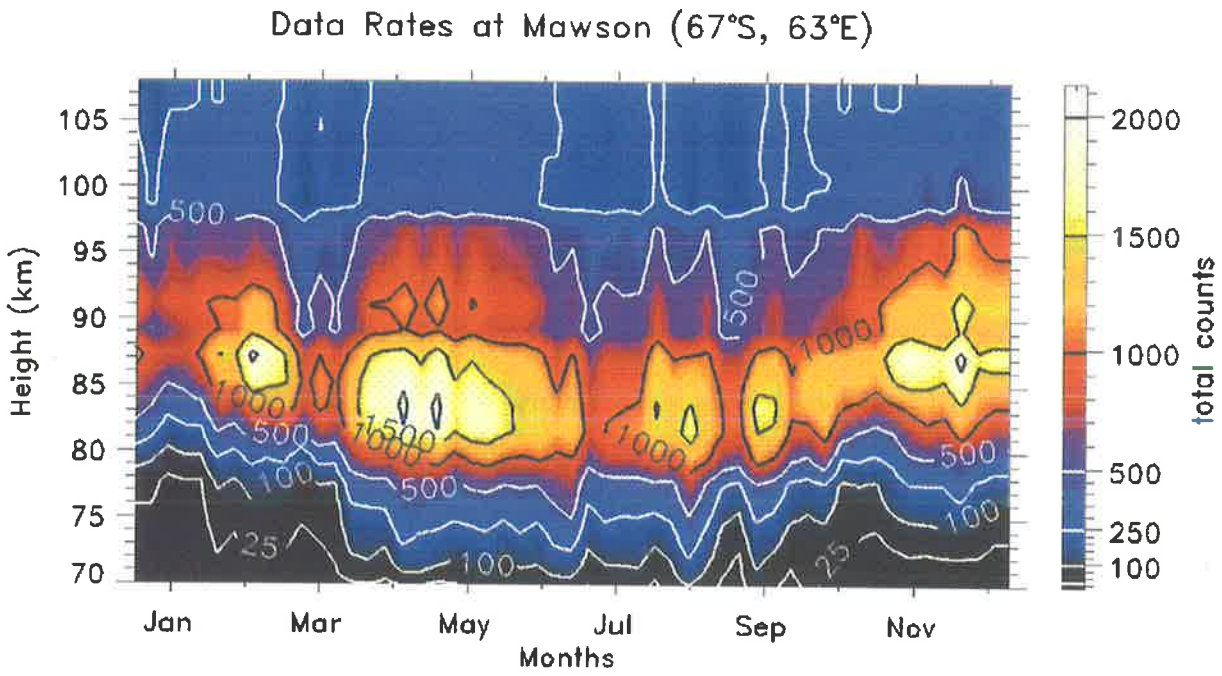

Figure 8.2: Total number of data points collected by the partial reflection radar at Mawson, over a period of four years (1985–1988).

time, and large differences between the apparent and true velocities. Another factor which affected the data acquisition rate was drifting snow during blizzards which carry static charge and produce excessive noise in the receivers.

Figure 8.2 shows the data rate, number of points per week per individual height range, collected over the four years, 1985–1988, at Mawson. The maximum rate is found between 80 and 95 km. Below 80 km the data rates are quite low, although they are higher during the winter months. Above 95 km the data rates are also smaller, but are relatively constant between 98 to 108 km. The data rejection criteria and their contribution to the total data rejected at Mawson are discussed in more detail in chapter 11.

In order to obtain long–term means the raw winds and other full correlation analysis parameters were first averaged into 24 hour blocks. Weekly means were then constructed from the daily averages using four years of data, from 1985 to 1988 inclusive. Finally, the weekly means from each year were combined together to produce "one" average year. These procedures filtered out any short–term wave motions. Therefore, it is implicit that all of the results presented in this chapter are derived from data collected over 1985–1988, and analyzed using the above procedure.

8.4 Mean winds at Mawson

Figure 8.3 (top) is an image–contour plot of the zonal weekly–mean circulation at Mawson as a function of time and height. The summer and winter circulation is clearly discernible. The zonal flow is generally similar to that found at Adelaide [see figure 6.3 (top)] with several exceptions. Firstly, the mean eastward circulation during winter is much weaker than at Adelaide reaching a maximum of only $15 ms^{-1}$. Secondly the westward flow during summer extends to slightly higher altitudes than at Adelaide. Thirdly, the reversal of flow during early spring and late autumn is very rapid at Mawson. At Adelaide, the wind contours descend at a rate of 10–20 km per month, while at Mawson this is much more rapid, with the wind reversal occurring almost immediately at all heights.

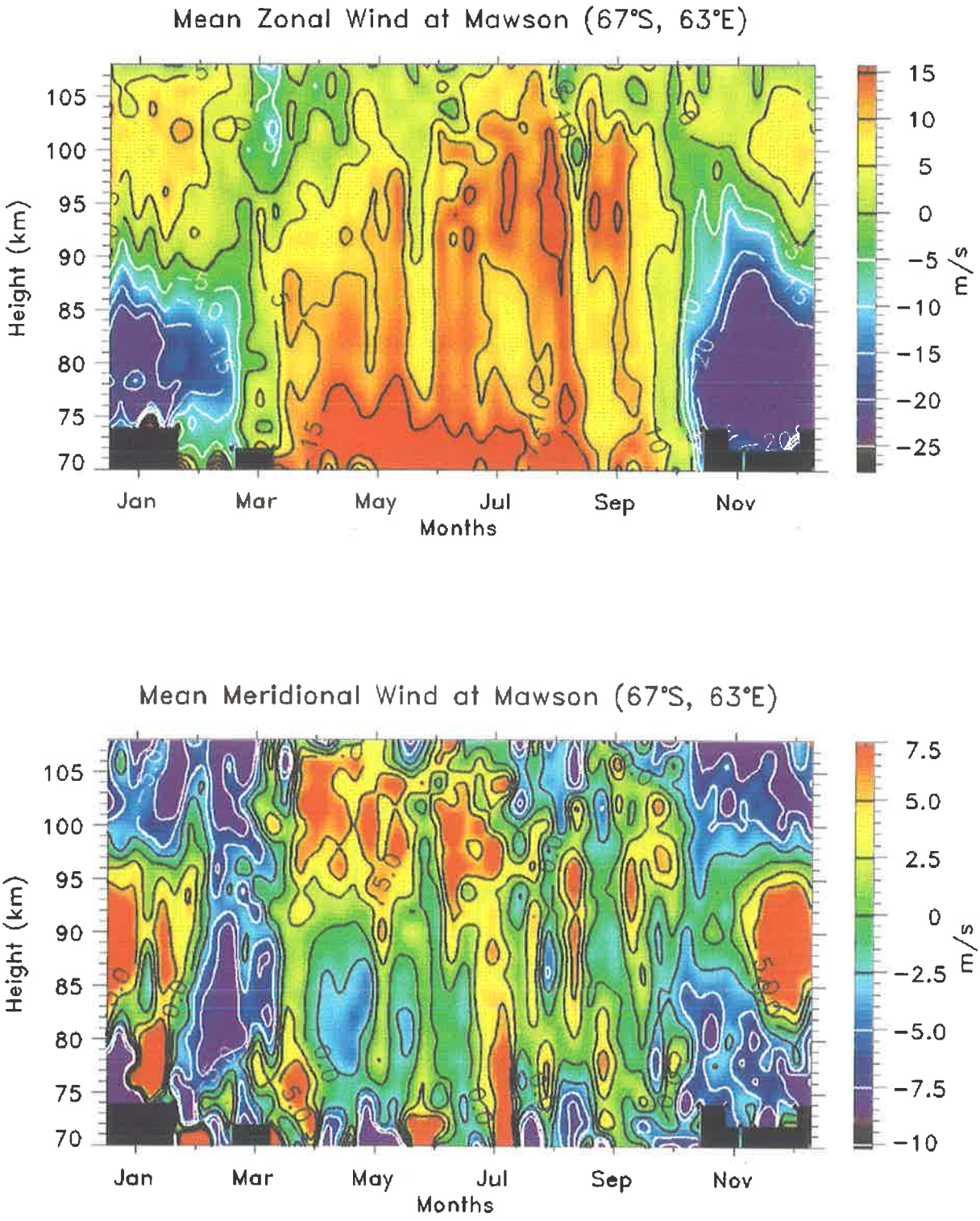

Figure 8.3: Weekly–mean zonal (top) and meridional (bottom) winds measured at Mawson by the partial reflection radar over four years, 1985–1988. The contours are labelled in ms^{-1}, positive for eastward and northward respectively.

Figure 8.3 (bottom) is an image–contour plot of the weekly–mean meridional circulation at Mawson. The meridional winds are not as seasonally structured as the zonal winds. During winter there is a strong equatorward flow of up to $7ms^{-1}$ above 90 km, while during early March and late October there is a maximum poleward flow of up to to $10ms^{-1}$. An interesting feature, and one also observed at Adelaide, is the strong "jet–like" equatorward flow during January between 85 and 95 km, which occurs just above the height at which the zonal winds undergo a reversal, and approaches a magnitude of nearly $7ms^{-1}$.

The winds measured at Mawson compare favorably with those reported for Scott Base [*Fraser*, 1984b], especially in the magnitude of the meridional "jet". A comparison of winds between Mawson, Adelaide and other sites has been discussed at length by *Phillips & Vincent* [1989], who also compared the measured winds with various model derived winds. Comparison of northern hemisphere winds measured at Poker Flat (65° N) [*Tetenbaum et al.*, 1986] show that while summer–time winds exhibit similar features, the spring reversal occurs earlier at Poker Flat.

8.5 Seasonal behaviour of spaced–antenna parameters

As in the previous chapters dealing with Adelaide and Christmas Island data, this section reviews the long–term, or seasonal variation of the various full correlation analysis parameters. Again no mathematical groundwork is covered. as this is discussed in detail in chapter 3.

Fading time

The fading time, or the time which would be measured by a ground–based observer, is shown in an image–contour weekly–mean plot in figure 8.4 (top). The fading time clearly shows both a seasonal and an altitude variation. During the summer months, September through to early April, the fading time is approximately around 3.5–4.0 below 85 km, decreasing to between 2.5–3.0 above that. During the winter months, April to September, the fading time reaches a minimum of less than 2.5 sec above 80 km and around 3.0 sec below this height. During

March the fading time exhibits a local maximum of about 3.0 seconds extending through all the heights, and persists for several weeks, and is probably due to the rapid reversal of wind during that time.

The fading time is partly attributed to the mean winds, and an increase in the mean winds results in a decreased fading time. Comparing the mean winds, shown in figure 8.3, with the fading times, one can see that during the winter months the zonal wind is strong and compares favorably with the fading time which is a minimum. Similarly, during the summer months, when the wind is a minimum the fading time is at its maximum. However, while the mean wind contours show no propagation with respect to time, the fading time contours propagate downwards at the beginning of winter and upwards at the end of it, at a rate of several km per month.

An investigation of fading time correlation with the K–index, where K is used to indicate the level of geomagnetic activity and depends on the strength and variability of the auroral electrojet, has been undertaken by *Price* [1988]. That study found that significant negative correlations were observed during spring time, i.e. the fading time decreased when geomagentic activity increased. No significant correlations were observed during summer and autumn, while winter observations showed no correlation.

Lifetime of ground pattern

The lifetime of the pattern, or the fading time as seen by an observer moving with the pattern, is shown as an image–contour weekly–mean plot in figure 8.4 (bottom). Similarly to the fading time there is a clear seasonal variation. The minimum occurs during the winter months with a mean value of around 3.0 seconds, although the extent of the minimum is not as broad as that for the fading time. The maximum values are found at heights below 85 km during September through to March where they increase to around 6 seconds. March is again the odd month out, when, for several weeks, the lifetime increases within all heights to more than 4 seconds.

Similarly to the fading time contours, the lifetime contours propagate downwards during autumn and upwards during summer. This is most obvious by following the 4 seconds contour

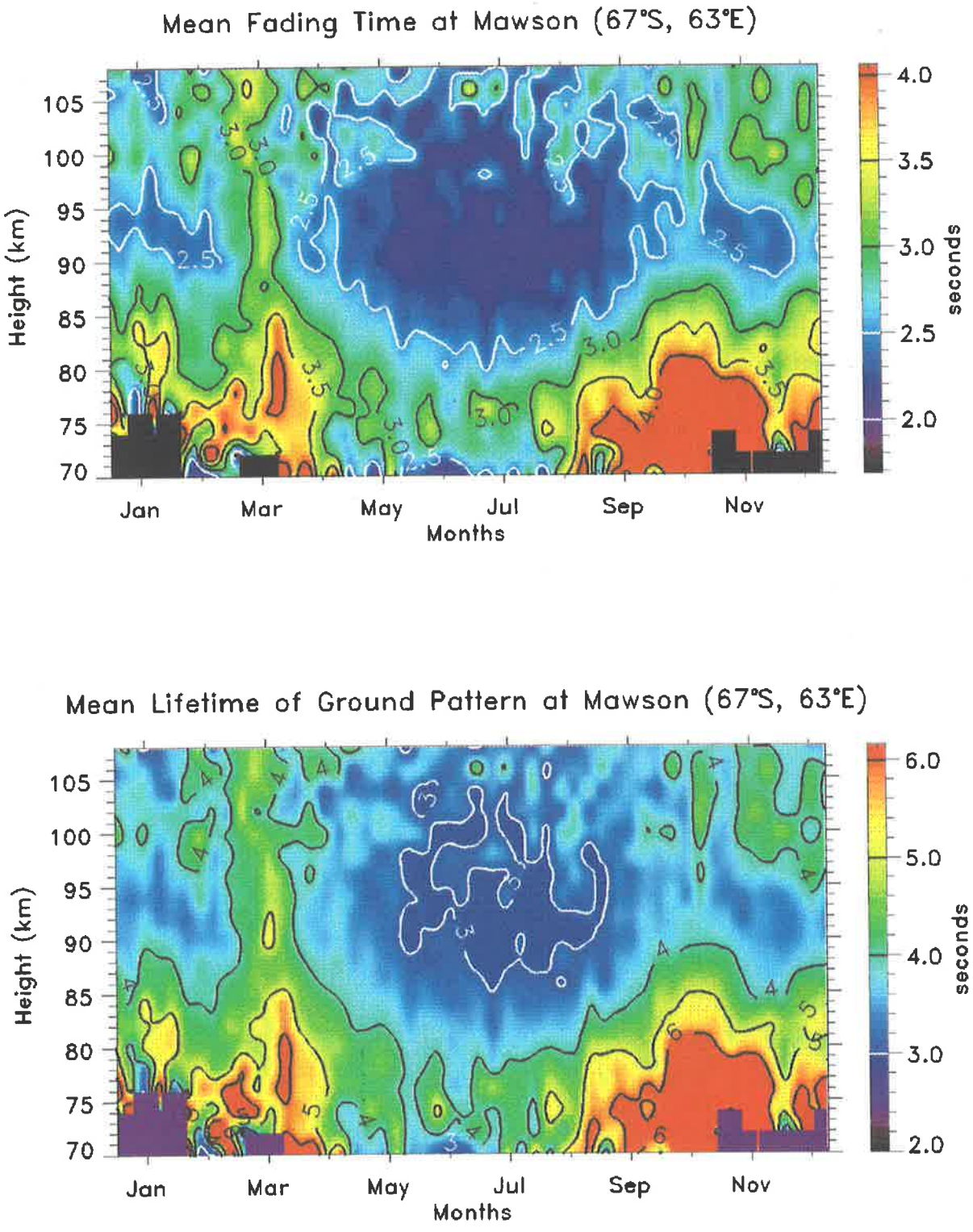

Figure 8.4: Weekly–mean fading time (top) and lifetime of ground pattern (bottom) at Mawson, constructed from four years of data, 1985–1988. The contours of both the fading time and lifetime are labelled in seconds.

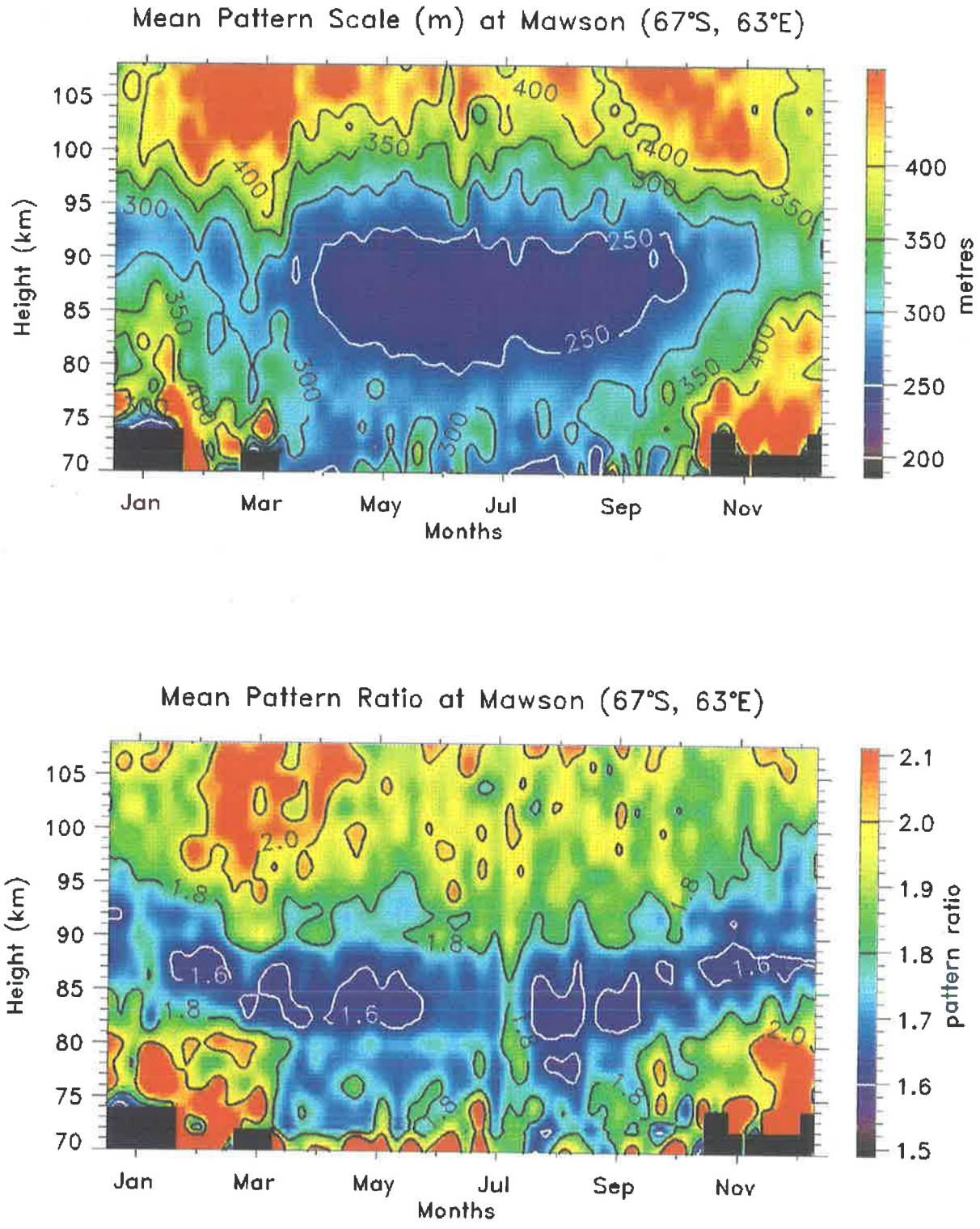

Figure 8.5: Weekly–mean size (top) and axial ratio (bottom) of the ground diffraction pattern at Mawson, constructed from four years of data, 1985–1988. The ellipse size contours are labelled in metres while the axial ratio is the ratio of the semi–major to the semi–minor axis of the ellipse.

which extends from 90 km in March to less than 80 km in June, and back to 90 km in late September.

Pattern size

Figure 8.5 (top) is an image–contour plot of the weekly–mean pattern size. Like the fading time and lifetime a clear seasonal behaviour is evident. The pattern size is a minimum during the winter months where its mean value is less than 250 metres between 80 and 92 km. During the summer months this increases to more than 400 metres at heights below 85 km. However, above 95 km the seasonal effect is not really evident with the mean pattern scale being constant throughout the year, fluctuating around 400 metres.

The interpretation of the pattern scale in terms of the scatterers is discussed in the aspect sensitivity section later on in this chapter. However, it is also important to remember that at Mawson there is total reflection from the bottom of the E region which begins at an altitude of approximately 95 km.

The variation of the pattern scale with height and against high, medium, and low geomagnetic activity has been studied by *Price* [1988]. That study found that a geomagnetic effect is evident in all seasons. The effect of geomagnetic activity was found to be more significant at lower heights in summer than in autumn or winter, while no apparent correlation was observed in spring.

Pattern axial ratio

The ratio of the pattern semi–major to the semi–minor axis is displayed as an image–contour weekly–mean plot in figure 8.5 (bottom). The pattern ratio is a minimum with a mean value of 1.6 to 1.7 during the summer months, between an altitude of 85 to 97 km. This minimum does not change during the winter months; what does change is the height range over which it occurs, which is between 80 to 90 km. The contours thus descend at a rate of approximately one kilometre per month. Above this minimum layer, the pattern ratio is greater than 1.8 with a local maxima during February to March where below 80 km and above 95 km the pattern

ratio is greater than 2.0. Below this layer the ratio is also a local maximum, but exists over a greater time span, throughout November to March.

8.6 Aspect sensitivity

As in the previous chapters dealing with data from Adelaide and Christmas Island here we present and discuss the seasonal behaviour of the aspect sensitivity of the partial reflection radar scatterers. Again we employ the two methods discussed in chapter 5. Some of this work has been published in *Lesicar et al.* [1993], and can be found in appendix *I*.

Spectral–width method

Figure 7.14 (top) is an image–contour plot of the weekly–mean aspect sensitivity, θ_s, calculated at Mawson using the spectral–width method. θ_s varies between 12 and more than 22°. There is a clear seasonal behaviour. Above 90 km θ_s is more than 22° during the winter months decreasing by several degrees during the summer months. Below 90 km θ_s is about 18° during the winter months, decreasing to less than 14° during the summer months. In addition, θ_s contours progress downwards during autumn and upwards during spring at a rate of several kilometres per month.

The scatterers are therefore seen to be more isotropic during the winter months, and more specular during the summer months, with the specularity increasing with decreasing altitude. Again, the results of θ_s calculated by the spectral–width method have to take into account the orientation of the ground pattern, since it is quite anisotropic (the degree of anisotropy being indicated by the pattern ratio). The spectral–width therefore depends on the orientation of the ellipse with respect to the direction of the mean wind. If the pattern ellipse major axis is orthogonal to the wind, the spectral–width measured will be quite small and will be interpreted as a higher θ_s. Conversely, a pattern aligned along the major axis will results in a larger spectral–width and thus a smaller θ_s. Therefore the results of θ_s presented are only upper estimates, and should be treated with caution.

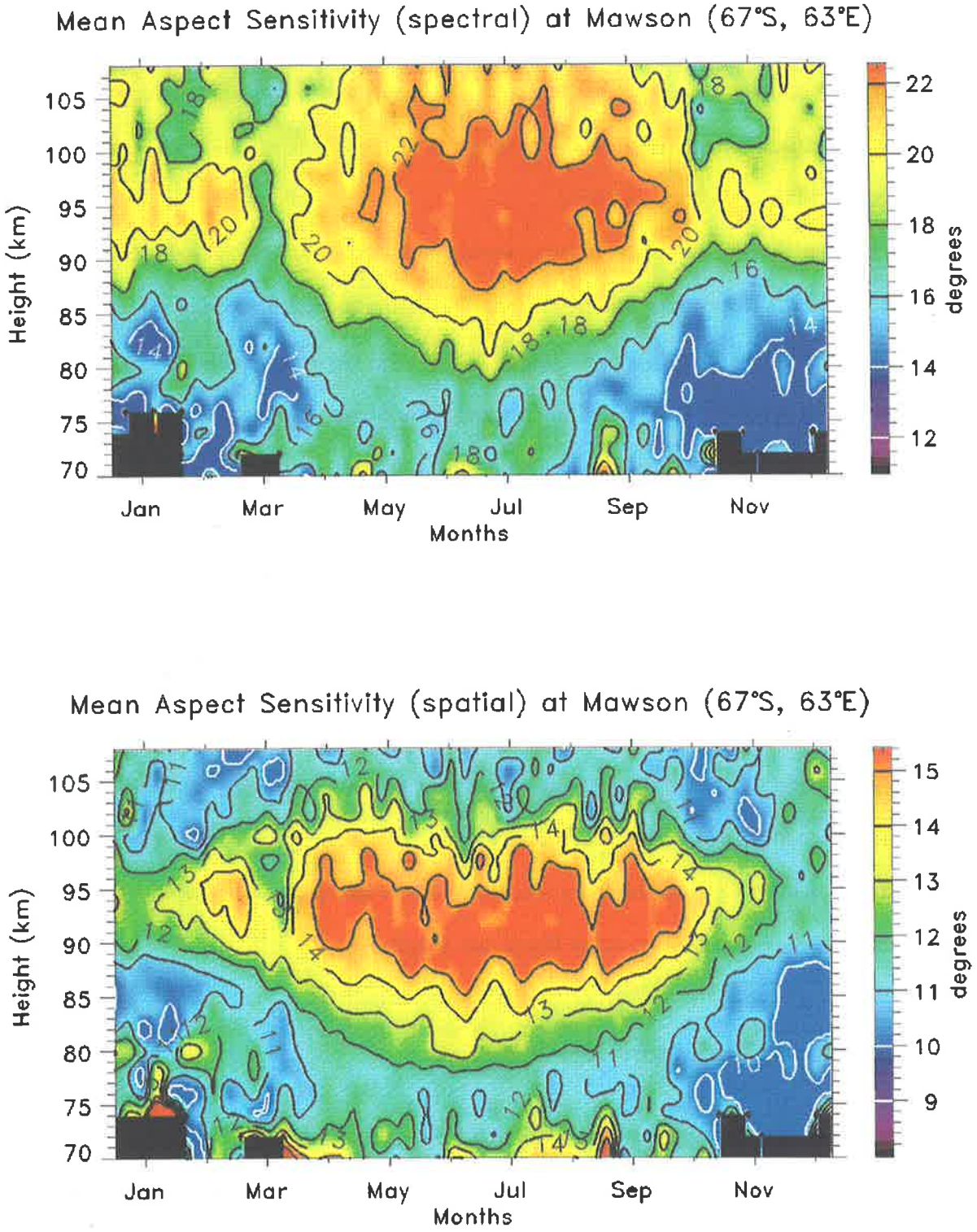

Figure 8.6: Weekly–mean aspect sensitivity calculated by the spectral–width method (top) and the spatial–correlation method (bottom) at Mawson. The contours are labelled in degrees and have been constructed from four years of data (1985–1988).

Spatial–correlation method

Unlike θ_s calculated by the spectral–width method, the spatial–correlation method is much more robust, for it uses the geometrical mean of the major and minor semi–axes of the correlation ellipse, and is not dependent on the orientation of the ellipse with respect to the various parameters like wind and geomagentism.

Figure 8.6 (bottom) is an image–contour weekly–mean plot of θ_s calculated by the spatial–correlation method. The results are very similar in their seasonal behaviour when compared with θ_s calculated by the spectral–width method. However, the actual values are much smaller than those by the spectral–width method, ranging from about 9 to more than 14°. Similarly to the spectral–width results there is a clear seasonal variation with a maximum during winter and a minimum during summer. However, the winter maximum does not extend above about 103 km where θ_s is approximately constant throughout the whole year. This is quite different to the spectral–width method, where the maximum extends up to 108 km. In general though, the two results show the same general characteristics below 90 km, including the propagation of contours; downwards during autumn and upwards during spring. Above 90 km, the contours of spatial–correlation θ_s propagate upwards at a rate of several kilometres per month unlike the spectral–width contours where this is not as evident.

Overall, the scattering structures are seen to be more isotropic during winter between 80 and 100 km, and more specular at other times and heights.

8.7 Horizontal correlation lengths

The above θ_s calculations were then used to calculate the length–to–depth ratios of the partial reflection radar scatterers. Figure 8.7 (top) is an image–contour weekly–mean of the length–to–depth ratio, L/h, using θ_s calculated by the spectral–width method. L/h ratios calculated by way of the spatial–correlation method are shown in figure 8.7 (bottom). Both of these show quite clearly a seasonal behaviour with the smallest L/h ratio occurring during the winter months, and a maximum L/h ratio during the summer months. As with the θ_s results the

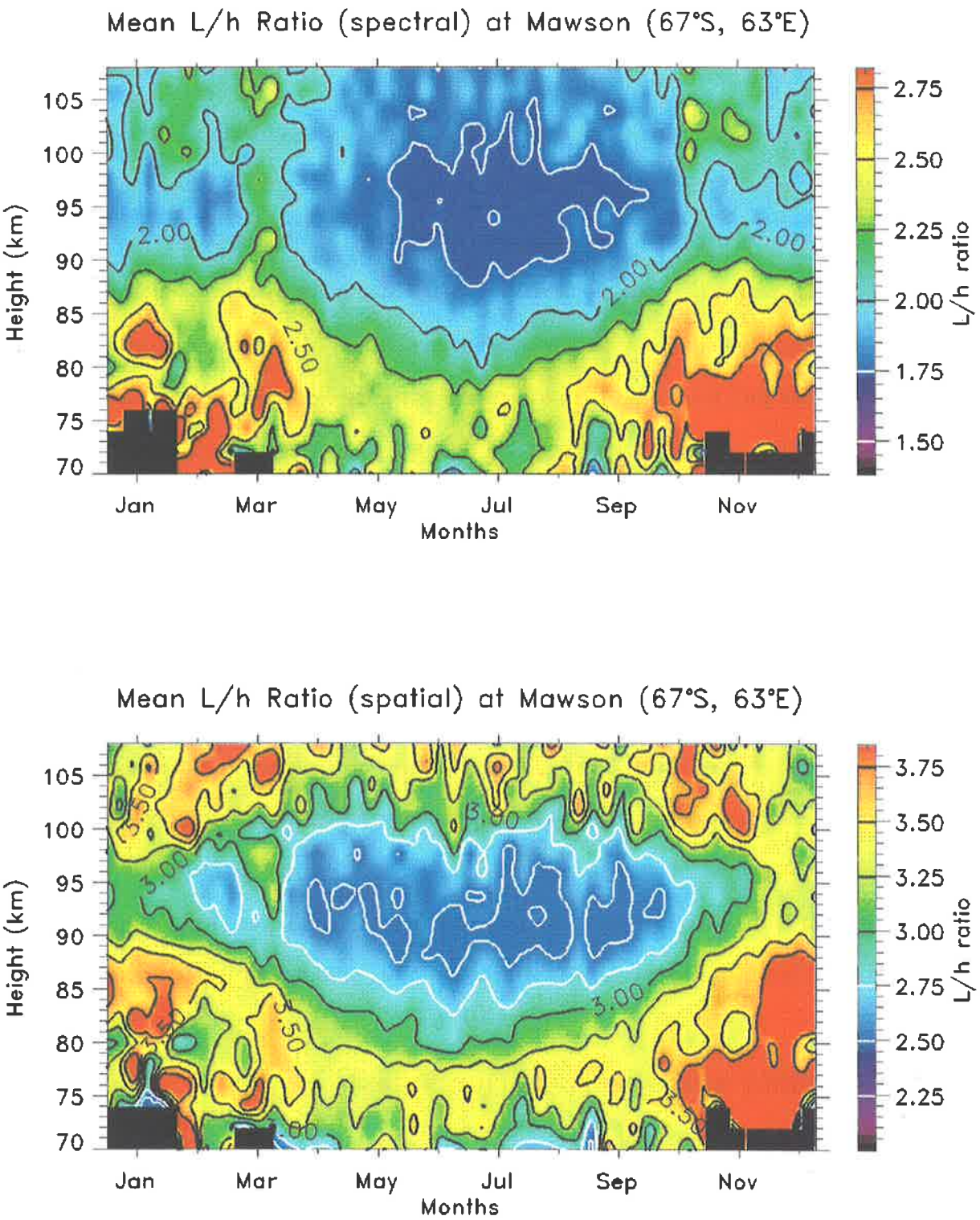

Figure 8.7: Weekly–mean length–to–depth ratios calculated by the spectral–width method (top), and the spatial–correlation method (bottom) at Mawson. The contours are the ratio of the horizontal to the vertical scattering depth. Four years of data were used (1985–1988).

actual values obtained by the two methods are different. The spectral–width L/h ratios range from 1.5 to more than 2.75, while the spatial–correlation L/h ratios range from about 2.25 to more than 3.75.

Both figures show that the minimum L/h ratio is centred around 95 km while the maximum generally occurs below 80 km. This is consistant with larger electron concentrations due to increased ionization by solar radiation, especially in summer. A noticeable difference between the two methods is that the spatial–correlation L/h ratios increase above 100 km while the spectral–width ones do not show such a marked change. This is difficult to interpret. The pattern scale increases with height due to two factors. Firstly the electron concentration increases, causing the scatterers to become more specular, because particle precipitation (in a disturbed ionosphere) enhances ionization at heights dependent on the energy spectrum of the incoming particles. The auroral spectrum[4] produces peak ionization in the 100–130 km range, while the solar hard proton spectrum[5] affects the 60–90 km region [see e.g. *Ratcliffe*, 1972; *Vallance Jones*, 1974]. Secondly, viscosity acts against small–scale motions. The spectral–width method takes into account the mean motion of the scatterers, so a changing wind field does not affect calculations of θ_s, and hence L/h. However, the spectral–width method is much more sensitive to the orientation of the pattern with respect to the mean wind. This therefore might bias the results whereas the spatial–correlation method is not so sensitive to that factor.

The variation of the pattern ellipse with respect to wind direction, and its general behaviour will be discussed in a later chapter dealing with short–term, or daily variations [see chapter 11].

8.8 Turbulent energy dissipation rates

Figure 8.8 is an image–contour plot of the weekly–mean energy dissipation rates, ϵ, calculated at Mawson. ϵ rates vary from ~ 0.05 Wkg^{-1} to greater than 0.15 Wkg^{-1}. Like all the other parameters discussed earlier in this chapter, ϵ also shows a seasonal variation with the maximum occurring during the winter months and the minimum during the summer months. In addition,

[4] of the order of 5–10 keV
[5] up to a few hundred MeV

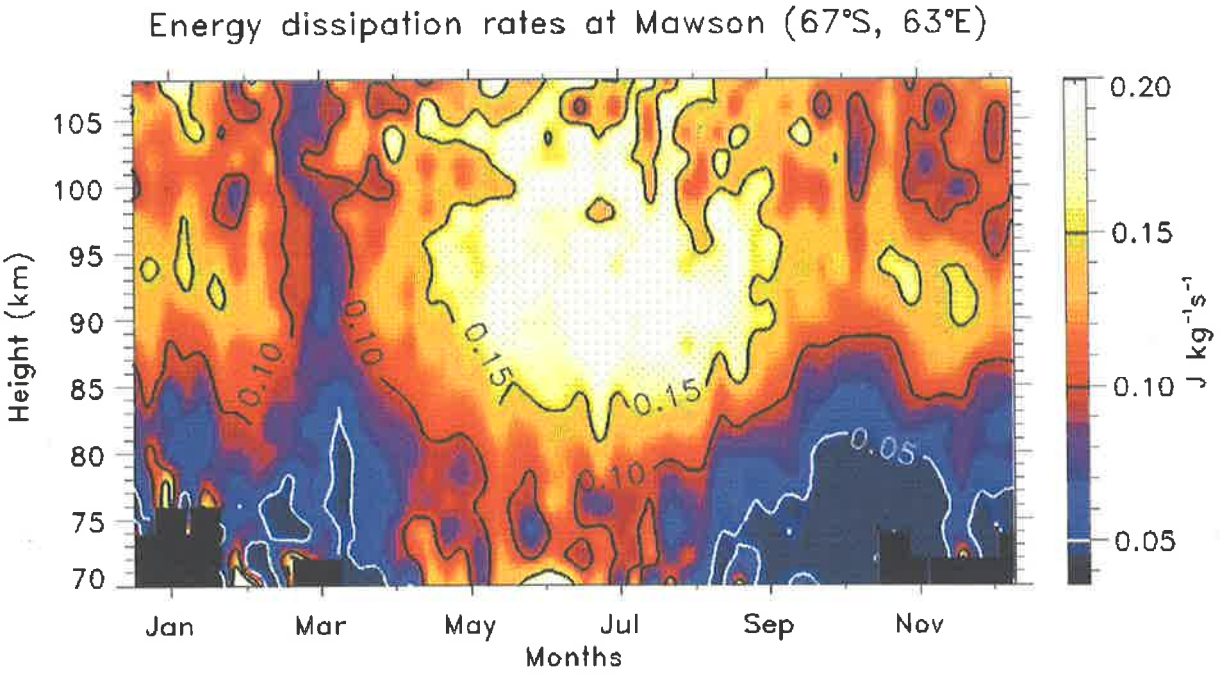

Figure 8.8: Weekly–mean energy dissipation rate at Mawson calculated by using the mean lifetime of the ground diffraction pattern at Mawson. The contours are in Joules per kilogram per second and have been constructed using four years of data (1985–1988). These calculated values are however at most the upper limits since the contribution to the spectra by gravity waves and turbulence could not be distinguished.

the winter maximum is concentrated above 85 km although it is somewhat smaller above 105 km. March is somewhat unique, for minimum values of ϵ extend through all heights observed.

However, like the radar systems at Adelaide and Christmas Island, this radar system also uses a wide radar beam. Therefore, these estimates of ϵ do not take into account the effect of gravity–wave spectrum broadening. The general shape of the spectra at Mawson has been calculated by *MacLeod*, [1986], who found that the results were quite similar to those presented by other authors for other sites [see e.g. *Vincent & Ball*, 1981; *Vincent*, 1984a; *Johnson & Luhmann*, 1985], who examined data from various sites, including Adelaide, Townsville, and Poker Flat. Therefore it is safe to assume that gravity–wave broadening of the spectrum does affect the spectral broadening to a significant degree and that turbulence is not the only contributor. What is yet to be determined is the percentage of this contribution. Therefore the results in figure 8.8 must be be regarded as the upper limit of the turbulence contribution to ϵ.

Chapter 9

Short–term results from Blanchetown

9.1 Introduction

Blanchetown (34° 21' S, 139° 38' E) is a small town located on the Murray River in South Australia at an altitude of 40 m above sea level. With an annual rainfall of 265 mm the climate is semi–arid[1]. The radar at Blanchetown is a monostatic partial reflection type operating at a frequency 1.98 MHz and is in fact a duplicate of the MF radar at Buckland Park, the only difference being that the transmitter used at Blanchetown is a much–improved solid state design. Figure 9.1 shows the location of the Blanchetown radar system in comparison both with the Buckland Park radar field station and Adelaide.

Initially earmarked as a training exercise for an installation of a radar which was to be erected at Christmas Island (see chapter 7), Blanchetown ended up as a semi–permanent field site in its own right because it proved difficult to arrange transportation of the main transmission towers to Christmas Island. The particular location for the radar was chosen for several reasons. It lies on the eastern side of the local Mount Lofty ranges, in comparison to the main field station at Buckland Park which lies to the west. This provides a good data set to examine the effects

[1]compared with Adelaide which has an annual rainfall of 585 mm

of local orography on gravity–waves and mesospheric dynamics. It is also relatively close to the University of Adelaide; at a distance of approximately 150 km day trips for system maintenance and installation are relatively easy and do not require the complex logistics associated with lengthy field station expeditions. Another contributing factor was that a local farming family allowed use of their land, and helped in providing support during the construction phase of the project. The major force in organizing and implementing this system at Blanchetown was Dr. W.K. Hocking.

9.2 Construction of the radar system

The radar was constructed in several separate stages. The chronological order of the work proceeded as follows: (1) Erection of both receiving and transmitting towers. (2) Preparation of transmitting and receiving antennas and rigging onto the towers, followed by subsequent tuning. (3) Installation of the transmitter, receiver and computer controller and software. We will discuss each of these stages individually.

Erection of the transmitting and receiving towers

The proposed site was initially surveyed in late 1987, when the positions of the transmitting and receiving towers were mapped out. The transmitting array is a square array, with a baseline tower spacing of 79 m. The three receiving antennas form an equilateral triangle encompassing the transmitting array and are spaced about 165 m apart. This therefore makes the radar a true monostatic type. A schematic of the relative position and geometry of both the transmitting and receiving arrays is shown in figure 9.2.

In December 1987, a small working party of three people, including the author, constructed the bases for the transmitting array towers. This involved excavating, and mixing as well as pouring concrete into the holes, four for each of the four towers. The concreted holes plus inserts acted as foundations for the tower construction. While one supported the base of the tower, and thus its weight, the other three, which are symmetrical at about 10 m from the base at 120°

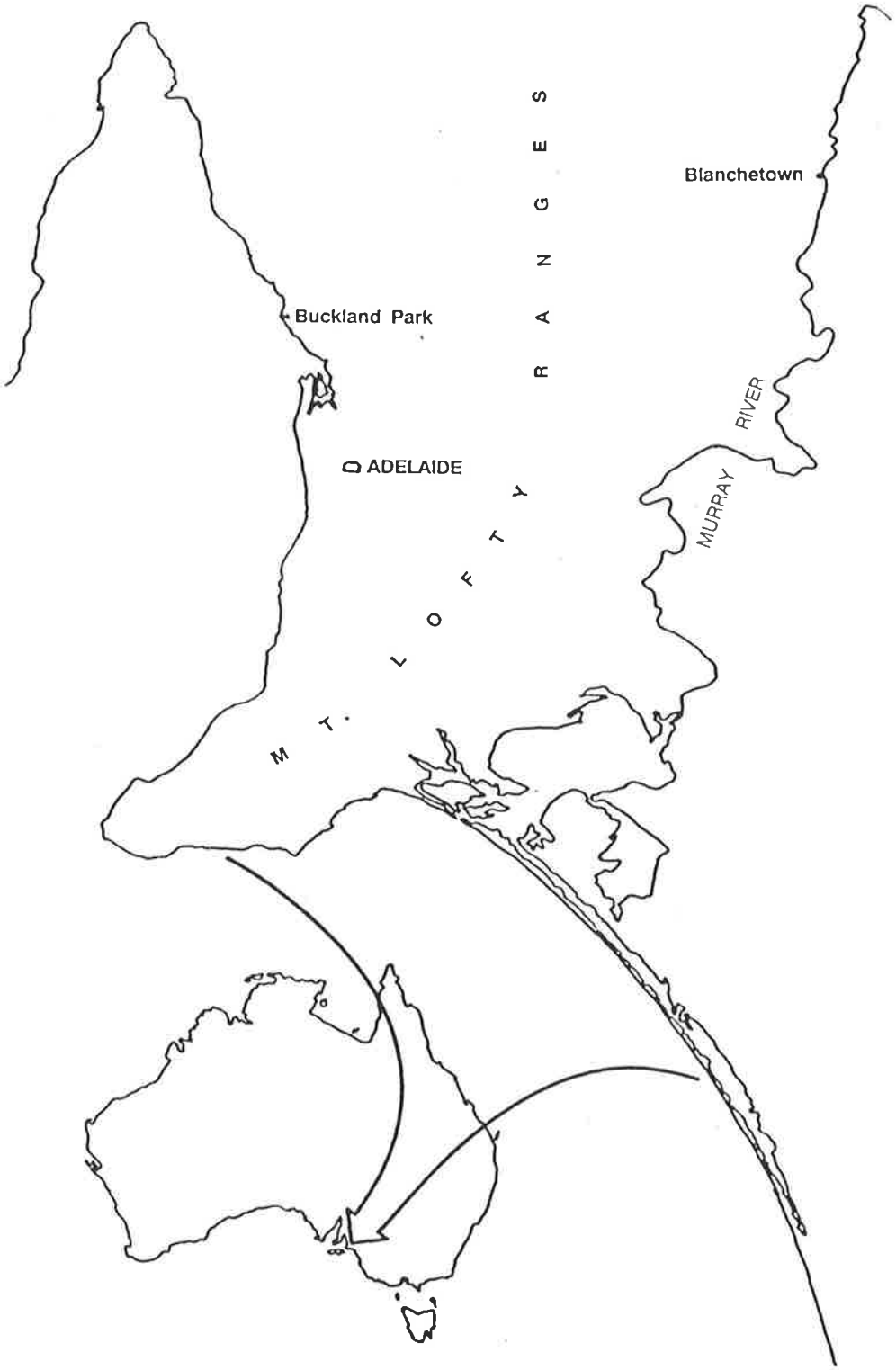

Figure 9.1: The location of the Blanchetown radar system, about 150 km north–east of Adelaide. The main field station is located at Buckland Park, about 40 km north of Adelaide where several radars are co–located.

intervals, act as anchors for the guys which hold the towers in place. Due to the sandy nature of the soil, the holes had to be at least 70 cm deep and of about the same width. Some limestone was encountered at a depth of ~60 cm but this did not prove to be a major problem. The base foundation of each tower had a steel footing of about 50 cm depth entombed in concrete, while the anchor footings had steel hoops embedded in concrete to which guy ropes could be securely tied. The site was then left for some time for the concrete foundations to settle, and to wait for cooler weather!

The towers used are of the three–section telescopic type, with the two top sections sliding into the bottom one. This makes them relatively easy to transport. In fact, these towers were originally used for a radar based at Townsville, in the far north–east of Australia, and were reconditioned for the new site. To erect the towers, each tower was hoisted up unextended and bolted to its base footing with the bottom tower section securely tied by guys to the anchor

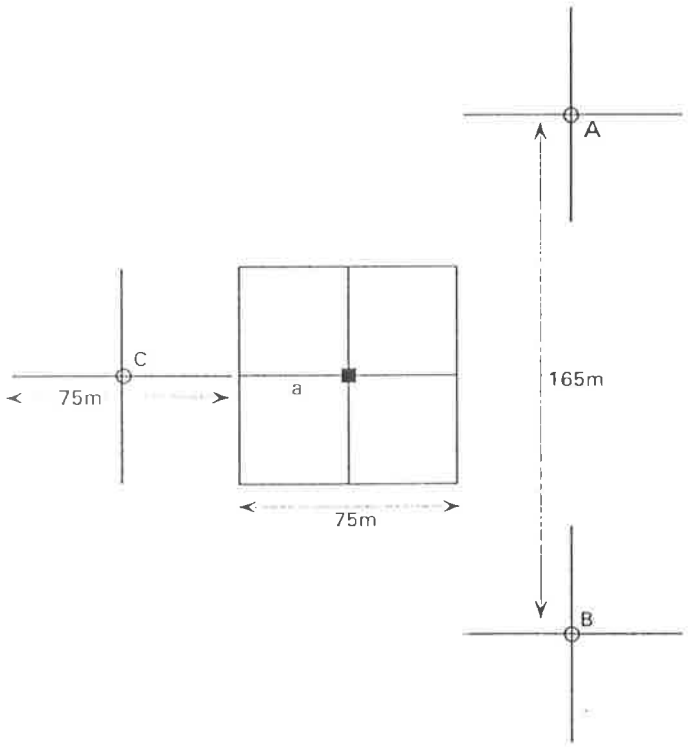

Figure 9.2: A schematic of the Blanchetown radar system showing the relative positions of the receiving and transmitting systems. The transmitting aerials are 4 folded half–wave dipoles suspended 30 m above ground, and 75 m long (half of the transmitting wavelength). The receiving aerials are 3 pairs of cross inverted–V dipoles, with the centre elevated about 10 m above ground level and also 75 m long.

points. The top section was extended next and bolted to the second section by climbing to the top of the bottom section. The middle section was extended last and bolted to the bottom section. At the top of each section the towers were securely fastened by guy ropes, so that each tower is held in its place by twelve individual steel guys. The hoisting of the towers was the most difficult operation to perform, involving co–ordination between 5–6 personnel, since there had to be at least two holding the guys at each anchor point in place. Figure 9.3 shows two of the four transmitting towers fully extended at a height of 30 m supported by twelve guy ropes. At the top of the towers one can also see one section of the transmitting antennas.

The receiving towers are just two sections of common galvanized plumbing pipe (50 mm diameter) which have been joined, and these extend to about 10 m in height. In a similar fashion to the transmitting towers, albeit much smaller, each receiving tower had a base upon which the tower rested, and three anchor points at 120° positions ~3 m from the centre to which the guy ropes were tied. Since the receiving towers were not extremely heavy, the foundations did not have to be constructed of concrete. A steel plate was therefore used, which, with a perpendicular metal spike, was hammered into the ground and found quite satisfactory. The symmetrical anchor points, on the other hand, were just common steel fencing posts hammered to a depth of about 50 cm.

The power for the radar needed to be drawn from the landowner's house, which is located some 300 m from the radar. This was done by hiring a local contractor to dig a trench between the house and radar site into which a 10 amp, 10 mm^2 copper power cable was laid. This was sufficient, since the radar does not draw more than 500 W, and the air conditioner, which was the only other electrical appliance, drew only several kilowatts.

Installation of antennas and feeders

Both the transmitting and receiving antenna systems, as well as all the cabling required, were constructed at Adelaide, and then installed at Blanchetown. Besides being logistically easier, since few facilities were available at Blanchetown, this was a good test run for the installation of the system at Christmas Island.

The transmitting array consists of four centre–fed half–wave dipoles, which are fed from the transmitter by one half–wavelength open–wire transmission line[2]. Each transmission line is supported by 1 m high permapine posts [see figure 9.4]. The receiving antennas consist of 3 pairs of inverted-V dipoles, and are connected to the receiving system by standard 50Ω coaxial cable. The transmitting and receiving systems are very similar to those employed at Buckland Park and at Mawson and will not be discussed here in any more detail.

Installation of the transmitter, receiver, and computer controller

The transmitter, receiver and data acquisition system, and the personal computer were the same as those subsequently employed at Christmas Island. Therefore, the reader is referred to chapter 7 for any of the details on the system. At Blanchetown, all three components which make up the radar system were housed in a caravan which was positioned right in the middle of the transmitting array. The caravan can be seen in figure 9.4, and besides housing the transmitter, receiver and data acquisition system, and computer, contained various tools, spares, and could be used as a small workshop for small repairs. The caravan was air–conditioned, since during summer the temperatures at Blanchetown commonly reach 40° C.

Although not continually used, the system at Blanchetown requires minimal maintenance and is routinely used as a testing site for the development of new solid state transmitters and receivers being developed by the University of Adelaide in co–operation with local industry.

[2]These have since been replaced by coaxial cables

See page 285

Figure 9.3: Two of the four transmission towers used for transmission at the Blanchetown site. The towers consist of three individual telescopic sections with each tower held in place by twelve guy ropes, and extend to a height of about thirty metres. The transmitting antennas, folded dipole types, can just be seen at the top of the towers, insulated from them by two ceramic insulators (600 mm apart). A caravan houses the transmitting and receiving gear as well as the computer controller, in this case a personal computer. The antenna feeders are held up on short posts and can be seen in line with the caravan. They feed the transmitting signal to the middle of the antennas into a balun box, seen on the picture as a little black dot just above the windmill water pump.

See page 287

Figure 9.4: All four of the transmitting towers used for transmission at the Blanchetown site. In the background between the two towers on the left can side, one of the three receiving towers can be just seen. They extend in height to about ten metres and hold up two orthogonal dipoles which do not physically touch (one passes underneath the other).

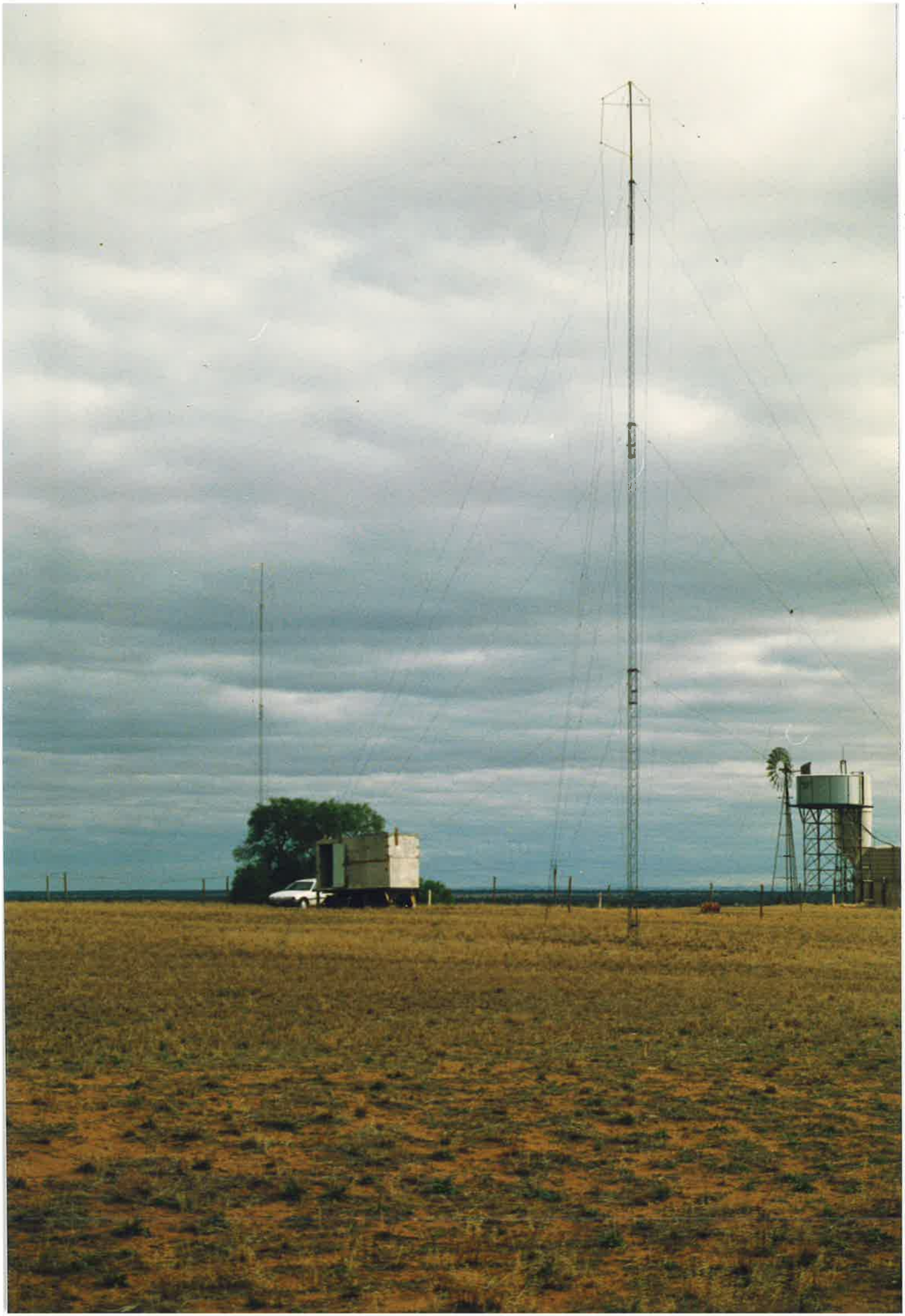

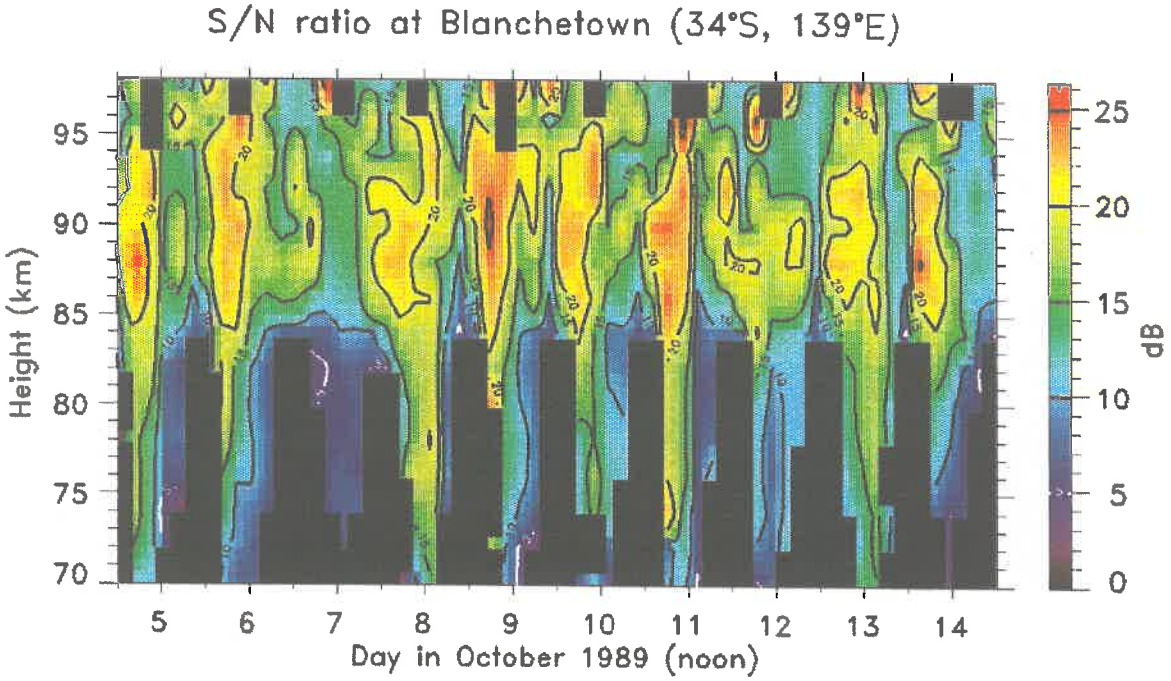

Figure 9.5: Four–hourly mean signal–to–noise ratio measured at Blanchetown over ten days in October 1989. The contours are labelled in dB. The black areas indicate times when no data were collected.

9.3 Experimental technique

The system initially ran from the September 5^{th} to November 4^{th} 1989. However, as the radar was essentially being tested, it was was continually stopped and re–started. This meant that the data were not continuous within this period, but consisted of runs. One of these was a 10 day period between October 5^{th} and the 15^{th}, and this time period is the one presented in this chapter. All the data within the 3 month period were analyzed, but the results were very similar to those for the data of early October. For this reason, only data from that period are presented here.

All data were analyzed in the following way. First all the data were grouped into four hourly intervals starting with midnight local time. A mean was then constructed from these four–hourly blocks. The individual value within this block whose magnitude deviated the most from the mean was discarded. A new mean was then constructed from the remaining data points, and this procedure was repeated four times, before the next four–hour block was analyzed. This

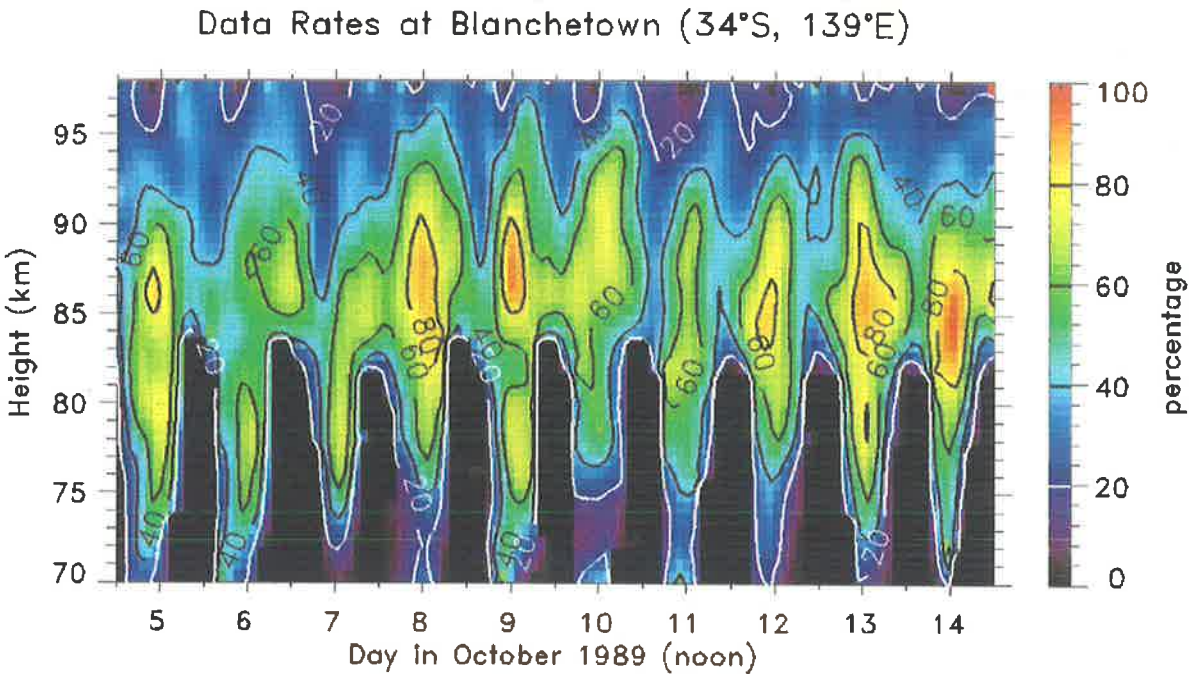

Figure 9.6: Four-hourly mean data rates measured at Blanchetown over ten days in October 1989. The contours are a percentage of the total data accepted by the analysis program. A maximum of 120 points can be collected per each four-hour block. The black areas, which occur during night-time at heights below about 82 km, indicate no data being collected.

procedure was adopted for each height of observation.

This method removed most of the outliers in the data, and although it probably removed some good data, the net effect was believed to improve the reliability of the means. Overall less than 10% of total data was removed.

9.3.1 Signal-to-noise ratios

During each radar sounding, a real-time coherent averaging of a number of successive received echoes is executed, enabling signals which are up to 6 dB below noise level to be detected. Providing that the noise is assumed to be constant, the signal-to-noise ratio, S/N, gives a rough indication of the echo strength. Noise is generally due to a combination of three sources; natural receiver noise, natural sources, and man-made noise. It is assumed that the receiver noise is constant, and the site at Blanchetown is well removed from any local man-made sources, so that outside interference does not vary. This is not strictly true at night-time when noise

can propagate large distances in the ionosphere. Another possible source of interference is due to maritime communications which use the frequency range around 1.98 MHz, but no evidence of this was found.

Figure 9.5 is an image–contour plot of four–hourly means of the S/N ratios measured at Blanchetown over 10 days in October 1989 over the 70–98 height range. When calculating S/N ratios one has to be careful not to use any simple arithmetic means since the S/N ratio distributions are non–Gaussian, and can show intense short bursts. These ratios were calculated by using the median values of the four–hourly blocks of data for each height range and for each of the three receivers. This method has the advantage of not being influenced by short intense bursts and is more representative of the typical S/N ratios observed. Only data from one receiver were presented here as data from all three were virtually identical.

The S/N ratios at Blanchetown show a clear diurnal variation, with a total absence of reflections below 80 km during night–time. A strong S/N ratio is observed during early mornings on all days, centred between 85 to 95 km.

9.3.2 Data rates

Figure 9.6 is an image–contour plot of the four–hourly mean percentage of data points for each individual height range collected by the Blanchetown radar system and accepted by the full correlation analysis. As the radar samples every 2 minutes, 120 data points are possible per four–hourly period. The data rates show a clear diurnal variation. Between the heights of 83 and 95 km about 40% of data is accepted during the night, while this figure increases to more than 60%, and even 80% during the day. Above this height range the data rates are only around 20%. At greater heights very few echoes are received during the day–time as the E layer causes total reflection at frequencies of 2 MHz. Below about 83 km, the day–time rates are quite good, only slightly smaller than those above this range. However, no night–time data are collected below 80 km, since no significant ionization occurs at these heights.

Besides the physical limitations, data are also rejected due to the various full correlation

analysis rejection criteria discussed earlier. It is generally found that data below 80 km are rejected not only as a consequence of low S/N ratios but because of slow fading, long time delays, and PTD > 50 as well. This is not surprising since that region of the atmosphere is known to be relatively stable. At greater heights, rejection due to slow fading, long time delays and PTD > 50 criteria all decrease in importance while the other criteria, like the various comparisons of apparent to true velocities, become much more important.

9.4 Mean winds at Blanchetown

Figure 9.7 (top) is an image–contour plot of four–hourly mean zonal winds measured with the partial–reflection radar at Blanchetown. The data have not been filtered to remove any tidal motions, and the diurnal tide is quite evident in the winds which oscillate between -40ms^{-1} and 40ms^{-1} (westward and eastward respectively). The winds are generally eastward during the day, and westward during the night, with the wind reversal occurring early in the morning and in the evening. However, after about the 11^{th} of October, the duration of the eastward flow decreases with the wind reversals occurring much later in the morning and earlier in the afternoon.

Figure 9.7 (bottom) is an image–contour plot of four–hourly mean meridional winds. Similarly to the zonal wind, a dominant tidal diurnal variation is observed in the wind, although the magnitude is slightly smaller, oscillating between 30 and -30ms^{-1}. The meridional wind is also less structured than the zonal, clearly evident around the 10th. In addition, the meridional component lags the zonal component by approximately 6 hr while both components exhibit a steady phase propagation with height. The diurnal wind vector thus rotates in an anticlockwise manner with time, as expected for tides in the Southern Hemisphere. Both the semi–diurnal and the ter–diurnal tidal modes also exist at Blanchetown, but their amplitudes are smaller than the dominant diurnal tide.

Mesospheric solar tides at Adelaide and other sites have been extensively investigated, and will be considered here no further. The reader is referred to the numerous publications on solar

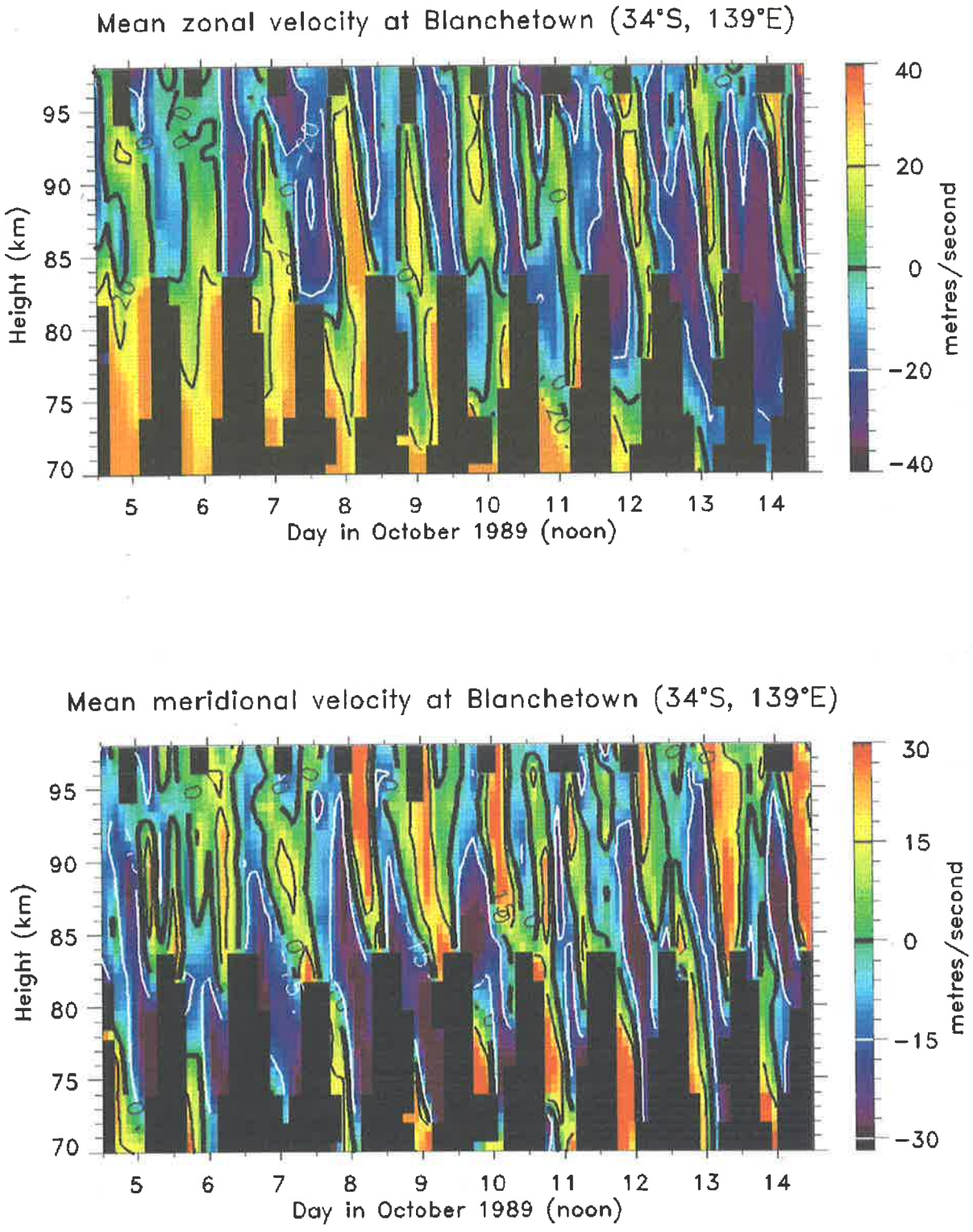

Figure 9.7: Four–hourly zonal (top) and meridional (bottom) winds measured at Blanchetown over ten days during October 1989. The contours are labelled in ms^{-1}.

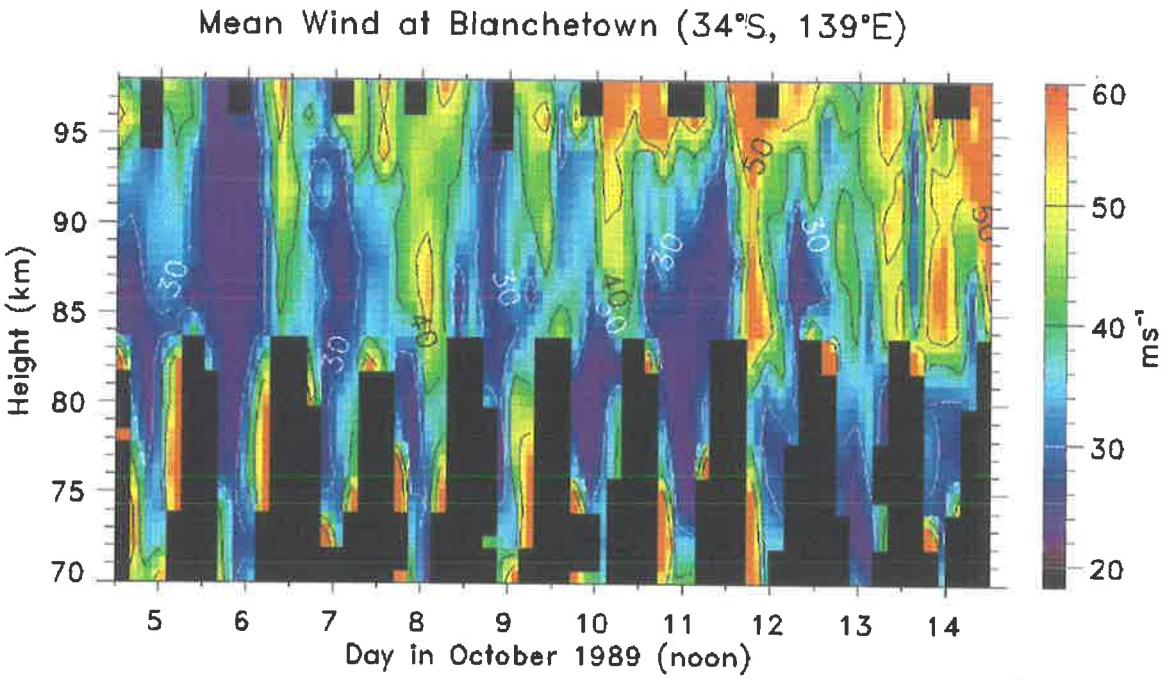

Figure 9.8: Four–hourly mean total wind magnitude measured at Blanchetown over ten days during October 1989. The contours are labelled in ms^{-1}.

tides, see e.g. *Groves* [1976], *Forbes* [1977, 1990], *Ball* [1981], *Vincent et al.* [1988] and the references contained therein.

The reason that the mean winds are of interest and are presented here, is to compare them with the various spaced–antenna parameters. These are presented in the following sections. Specifically, the short–term comparison of the mean winds with fading times, aspect sensitivities, and orientation of the correlation ellipse is a major objective of this study. When calculating the long–term circulation it was found that the zonal component is the dominant of the two, and it was sufficient to compare various full correlation analysis parameters against the zonal component only. However, when examining the daily winds, the meridional component is just as important. In that case, what is of more interest is not the separate meridional and zonal components, but rather the magnitude of the wind.

Figure 9.8 is an image–contour plot of the four–hourly means of the wind magnitude, i.e. irrespective of the wind direction. One can see that the wind speed is never less than $20ms^{-1}$ and at times approaches $60ms^{-1}$. In the early part of the data sample, a periodic variation is

clearly evident. In addition, the wind magnitude towards the latter part of the ten–day period approach much larger values.

9.5 Spaced–antenna parameters

The following sections discuss the daily behaviour of the various full correlation analysis parameters. These sections are mainly intended to provide information on the changes exhibited by the scattering structures. While the results can be taken to be reasonably accurate, they should not taken as being exact. Error bars have not been included with any of the data presented, although they have been calculated. The standard deviation of the means has been found to be no more, and usually less, than 20% of the mean value.

It was in a way fortunate that the time of these observations occurred during October, as this is the time when the seasonal winds undergo a reversal [see figure 6.3], and the other parameters show one of the semi–annual transitions. These results are presented in chapter 6.

Fading time

The fading time, as measured by a ground–based observer, is shown as an image–contour plot of four–hourly means in figure 9.9 (top). The fading time is seen to vary between about 1.5 and more than 5.0 seconds. The most obvious feature of the data is the change in fading time with height. The fading time between 70 and 75 km is approximately 5.0 seconds. This decreases at a reasonably constant rate to less then 2.0 seconds above 90 km, and is fairly constant thereafter.

There are a few anomalies. However, these can be accounted for by the wind magnitude. For example, during noon of the 8^{th} and 12^{th}, a small fading time of 2.0 seconds or less is observed above 85 km. This is directly related to the wind magnitude which is larger, more than $40 ms^{-1}$, during these times [see figure 9.8]. Similarly, during noon of the 6^{th}, a larger fading time is evident through all the heights, and again, this is reflected in the wind magnitude which is relatively low at this time. Therefore, the fading time above about 80 km is clearly dependent on the prevailing wind magnitude at that time.

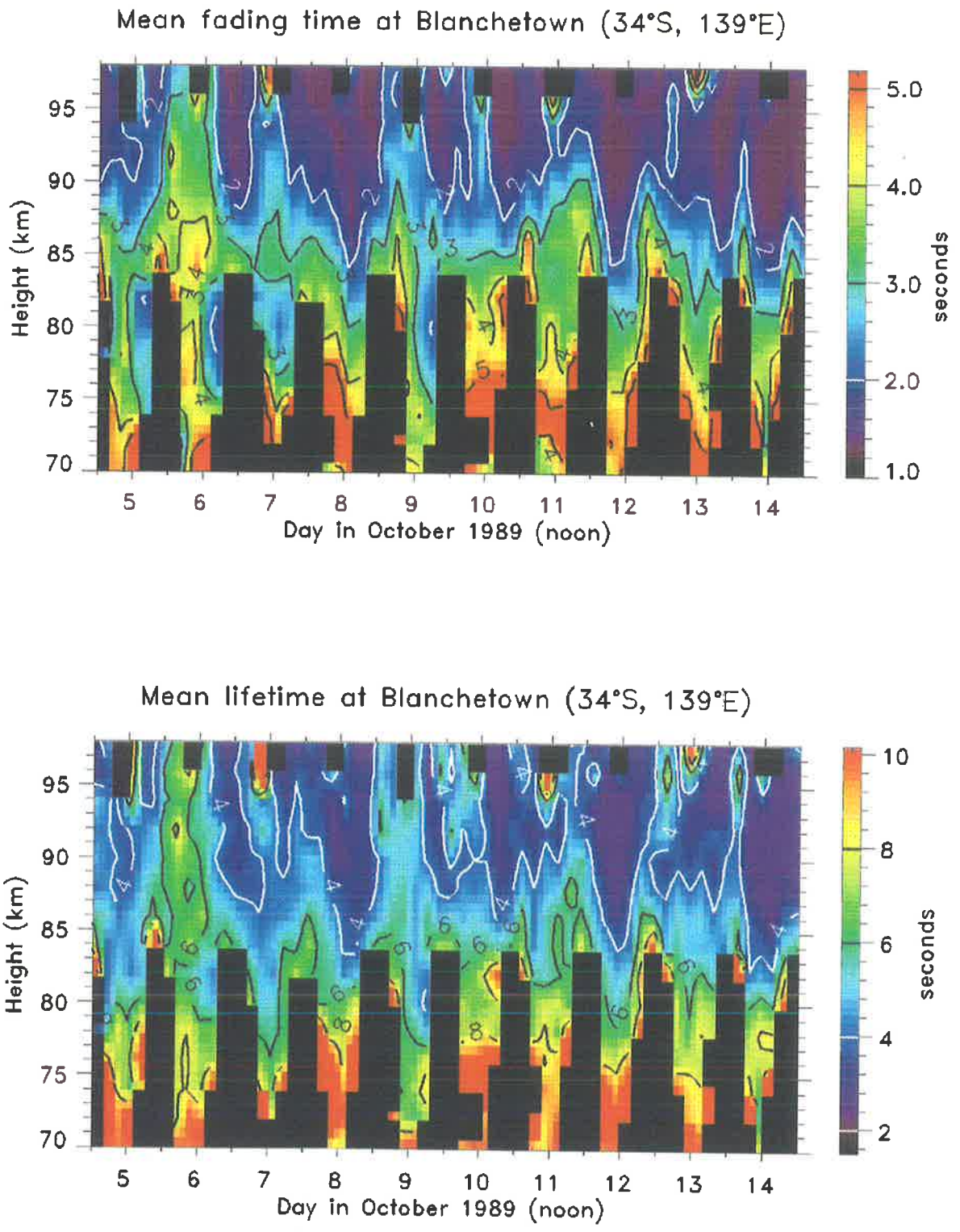

Figure 9.9: Four–hourly mean fading time (top) and lifetime of ground pattern (bottom) at Blanchetown over a one week period during October 1989. The contours are in seconds.

In contrast, while the fading times in the 70–80 km height range are relatively large, the wind magnitudes at these heights are also large. This implies that other physical processes besides the mean wind affect the fading times. In this case, the longer fading times can be traced to the aspect sensitivity, or spatial extent of the scatterers. This will be discussed shortly.

Lifetime of ground pattern

The lifetime of the ground pattern, which has had effects of the mean wind removed, is shown as an image–contour plot of four–hourly means in figure 9.9 (bottom). As expected, the values are significantly larger than the fading times, extending from 2.0 to around 10 seconds. The general tendency is for the lifetime to decrease with increasing height, a behaviour consistent with decreasing atmospheric stability. In addition, the lifetime behaviour is also somewhat similar to the wind magnitude. The best example of that occurs around noon of the 6th of October, when the prevailing wind was quite low, of the order of $20 ms^{-1}$, and extended through all the height range. At that time, the lifetimes were quite large, greater than 6.0 seconds, and also extended through all the heights measured.

The behaviour of the pattern lifetime can be loosely interpreted as a measure of atmospheric stability. In its primitive form, the lifetime is defined as the time taken for the auto–correlation fucntion of the ground diffraction pattern to fall to 0.5, as seen by an observer moving in its frame of reference. Therefore, the low lifetimes above 85 km can be taken as a measure of a disturbed atmosphere.

Pattern scale

The scale of the ground diffraction pattern is shown in an image–contour plot of four–hourly means in figure 9.10 (bottom). The pattern scale varies between 200 and more than 400 m, with the smaller pattern scales occurring at greater heights. A clear diurnal variation is observed between 75 and 85 km, where night–time pattern scales are greater than 400 m, while day–time pattern scales are less than 250 m. Furthermore, the small pattern scales which occur during the day–time are relatively long–lived.

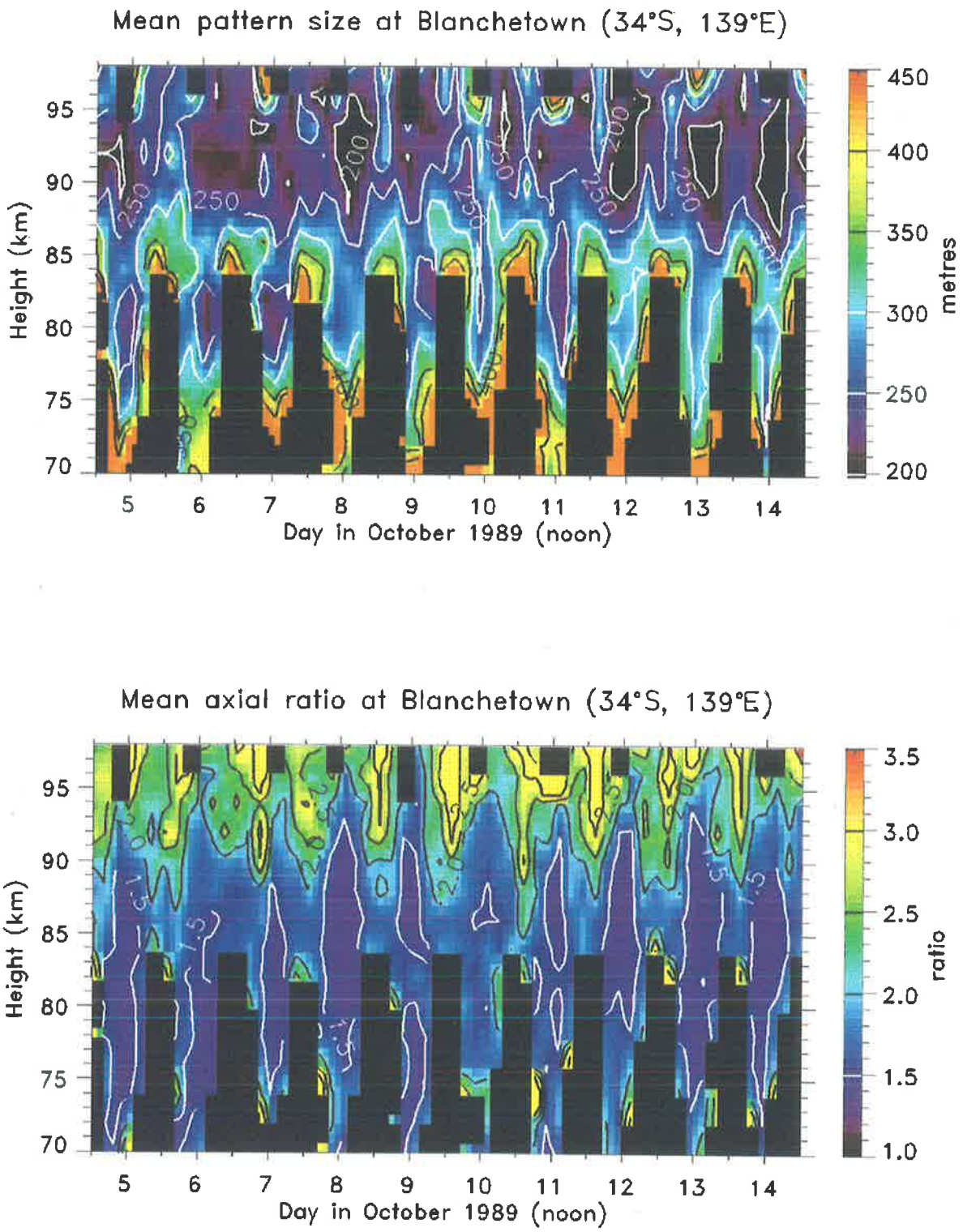

Figure 9.10: Four–hourly mean size (top) and axial ratio (bottom) of the ground pattern at Blanchetown over a one week period during October 1989. The contours for the pattern size are in metres while the ratio contours are a ratio of the semi–major to the semi–minor axis.

Above 88 km the scale of the ground diffraction patterns falls to less than 250 m. In contrast to the lower heights, the diurnal variation is hardly noticeable, and is only evident on the 12^{th}, 13^{th}, and the 14^{th}, where during day–time, the scales fall to their lowest values of less than 200 m. The small pattern scales are indicative of a more isotropic scatterers..

Pattern axial ratio

The ratios of the semi–major to the semi–minor axes of the ellipse which describes the ground diffraction pattern, as a function of height, are shown as an image–contour four–hourly mean plot in figure 9.10 (bottom). A pattern ratio of 1.0 indicates a circular diffraction pattern. In the data presented here the ratio varies between about 1.2 and more than 3.0.

While above 90 km the pattern ratio is in some instances greater than 3.0, below that height it is never much larger than 1.5. This increase in axial ratio with height has been found in other studies. Other studies have also found a constant increase in axial ratio with height [see e.g. *Clemesha*, 1963; *Stubbs*, 1977]. Superimposed on this height structure is a clear diurnal variation where the axial ratio is smaller during the day–time, and increases at night. The day–time ratios are less than 1.5, and are quite long–lived. The relationship between the axial ratio, and the pattern orientation will be discussed in a following section.

9.6 Aspect sensitivity

Using the full correlation analysis parameters discussed previously, it was once again possible to calculate the aspect sensitivity of the partial reflection radar scatterers. Again the two methods used were the spectral–width and the spatial–correlation method. Their results are presented as image–contour four–hourly means in figure 9.11 with the spectral–width results presented on the top and the spatial–correlation results on the bottom of the figure.

Both methods show that the general behaviour of θ_s is to vary both with height and on a daily basis. It is important to note, however, that although at first glance the two results appear

identical in magnitude, the spectral–width data vary between 10° and 40°, while the spatial–correlation data vary between 10° and 23°. Between 70 and 90 km θ_s varies only marginally around a mean value while it increases at a fairly rapid pace between 90 and 98 km. In the spectral–width case, θ_s varies by no more than ±5° around a mean of 15°, while in the spatial–correlation data θ_s varies by ±2.5° around a mean value of about 11°. In contrast, between 90 and 98 km, θ_s increases at a quite rapid pace, from 20° to 40° in the spectral–width case and from 15° to 23° in the spatial–correlation case. The increase in θ_s suggests that the structures which cause the partial radar reflections are more isotropic with increasing height. The difference in the actual values between the two can can be attributed to two factors. Firstly, turbulence can contaminate the measurements of the spectral–width, and can artificially increase θ_s. Secondly, the fading–time measurements are sensitive to the orientation of the correlation ellipse with respect to the mean wind. That is why the spectral–width calculations are, as always, upper limits and not meant to represent mean values.

The diurnal variation in θ_s is not as evident as it was in some of the previous parameters examined, e.g. the pattern size or the axial ratio. Above 90 km θ_s is larger during night–time and smaller during day–time. This is most evident around the 9^{th}, 10^{th}, 11^{th} and 12^{th} of October, especially so at 90 km altitude. Below 90 km, it is very difficult to say with any confidence that a diurnal variation is present, although on some nights, a minimum is experienced around 85 km. This is especially evident in the spectral–width estimates.

9.7 Horizontal correlation lengths

Figure 9.12 (top) is the length–to–depth ratio, L/h, of the scatterers as calculated using the spectral–width method while that calculated using the spatial–correlation method is shown in figure 9.12 (bottom). Both are exhibited as image–contour four–hourly mean plots. However, unlike the case for θ_s, the L/h ratios use the same colour range for the different data periods, ranging from 1.0 up to 4.0. This enables at first glance to show the difference between the two

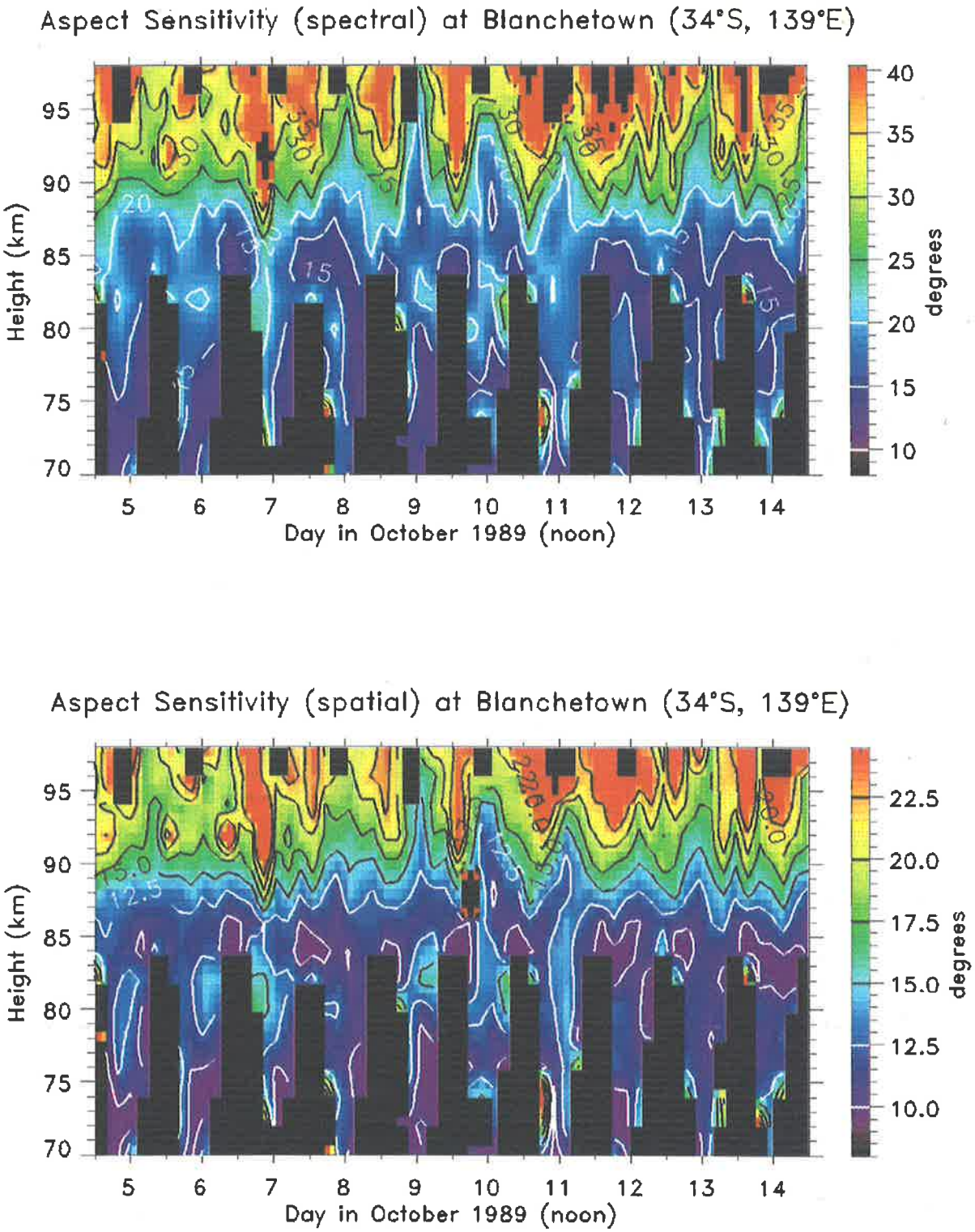

Figure 9.11: Four–hourly mean aspect sensitivity measured by the spectral (top) and the spatial correlation methods (bottom) for one week at Blanchetown for one week in October, 1989. The contours are in degrees.

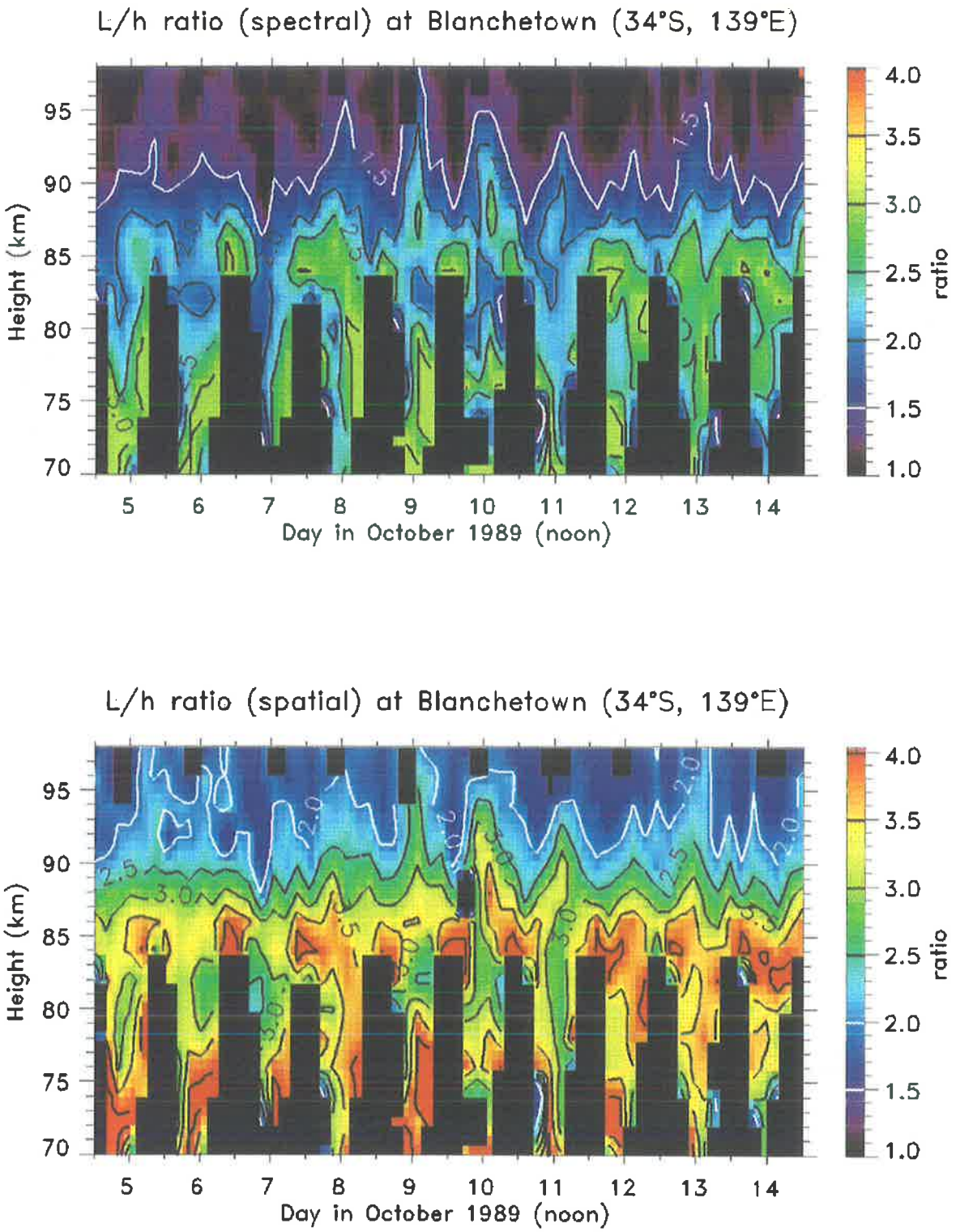

Figure 9.12: Four-hourly mean length-to-depth ratios of the radar scatterers measured by the spectral (top) and the spatial correlation methods (bottom) for one week at Blanchetown for one week in October, 1989. The contours are just the length-to-depth ratios.

methods. Whilst the spatial–correlation method ranges from around 2.0 to 4.0, the spectral–width ranges from less than 1.5 to around 3.0, on the average about 30% larger.

In general though, the L/h ratios calculated by the two methods show very similar trends. Up to a height of about 85 km, the L/h ratios are relatively stable. They do, however, show a diurnal variation, especially so around 85 km where night–time ratios are large, 3.0 in the spectral–width case and 4.0 in the spatial–correlation case. Between 85 and 90 km, the L/h ratios change quite rapidly falling down to 1.5 in the spectral–width case and down to 2.5 in the spatial–correlation case. In some instances, these local maximum contours propagate to greater heights. For example, on the 9^{th}, 10^{th} and 11^{th}, the L/h ratios increase between 85–90 km, and show a clear diurnal variation. However, the L/h ratios above 90 km are generally quite stable and show very little day–to–day variability.

If these L/h ratios are indicative of the structure of the radar scatterers, then these scatterers possess the greatest length–to-depth ratio below about 85 km, and are relatively isotropic above 90 km. In absolute terms, since the radar is sampling at a wavelength of 150 m, and is reflected by structures whole vertical extent is of the order of 75 m, the horizontal length of these structures varies from 100 to 280 m.

9.8 Two dimensional nature of the scatterers

In the previous sections data have been presented and discussed which suggested that the scattering structures possessed an anisotropic geometry. The length–to–depth ratio of the scatterers was seen to vary from nearly circular to be, in some instances, greater than 4.0. While the spectral–width and the spatial–correlation method both showed similar results, they differed in their magnitudes. This was attributed to the fact that the spectral–width method might be contaminated by turbuelnce. In addition, the spatial–correlation method uses the geometrical mean of the major and the minor axis of the correlation ellipse, while the spectral–width method relies on the fading time measured in the direction of the mean wind. If, however, the correlation ellipse is aligned with the mean wind, the fading time measured would be much

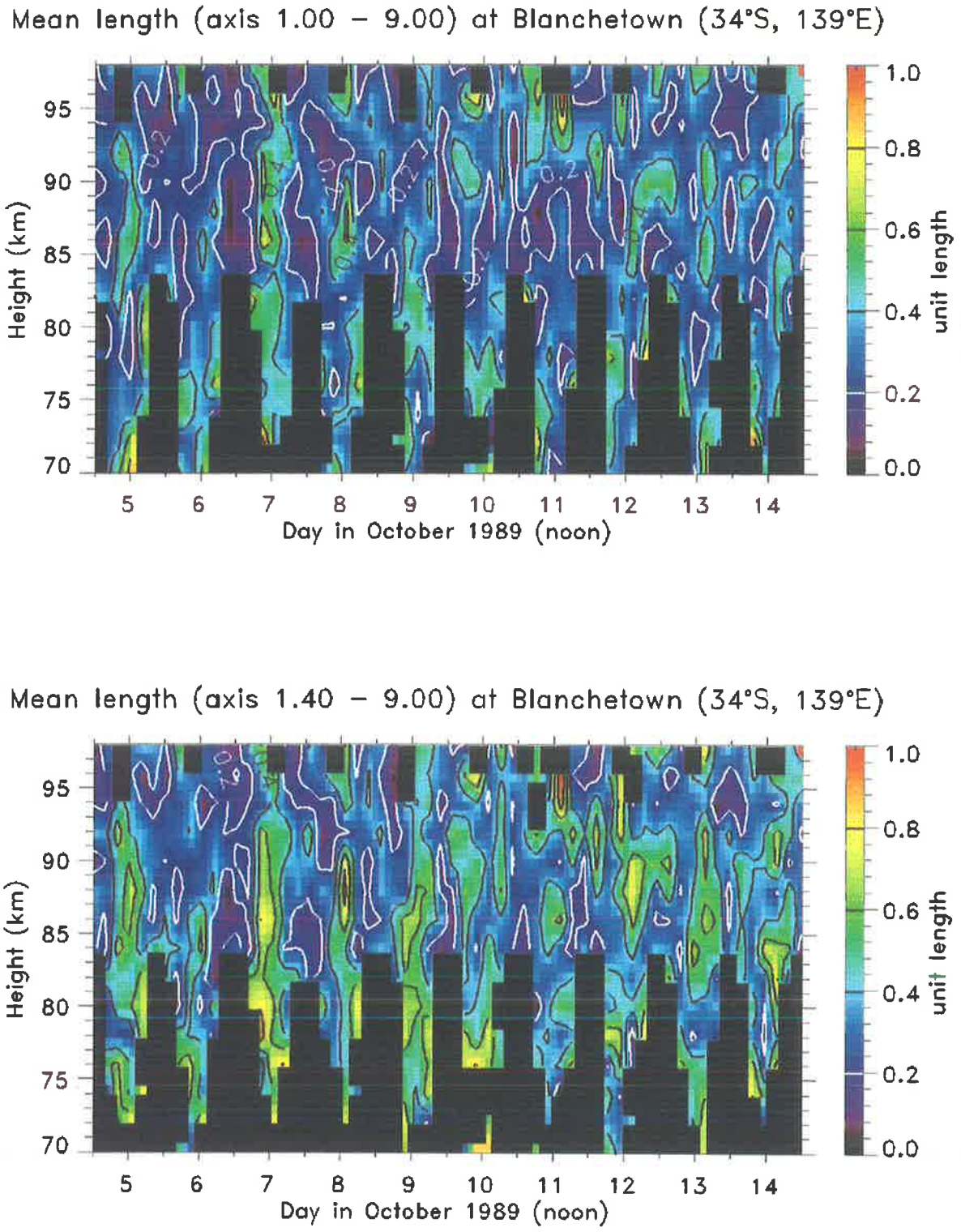

Figure 9.13: Four–hourly mean normalized lengths of the ground pattern for axial ratios of 1.0–9.0 (top) and 1.4–9.0 (bottom) at Blanchetown for one week in October 1989. The contours are the normalized length when direction has been taken into account.

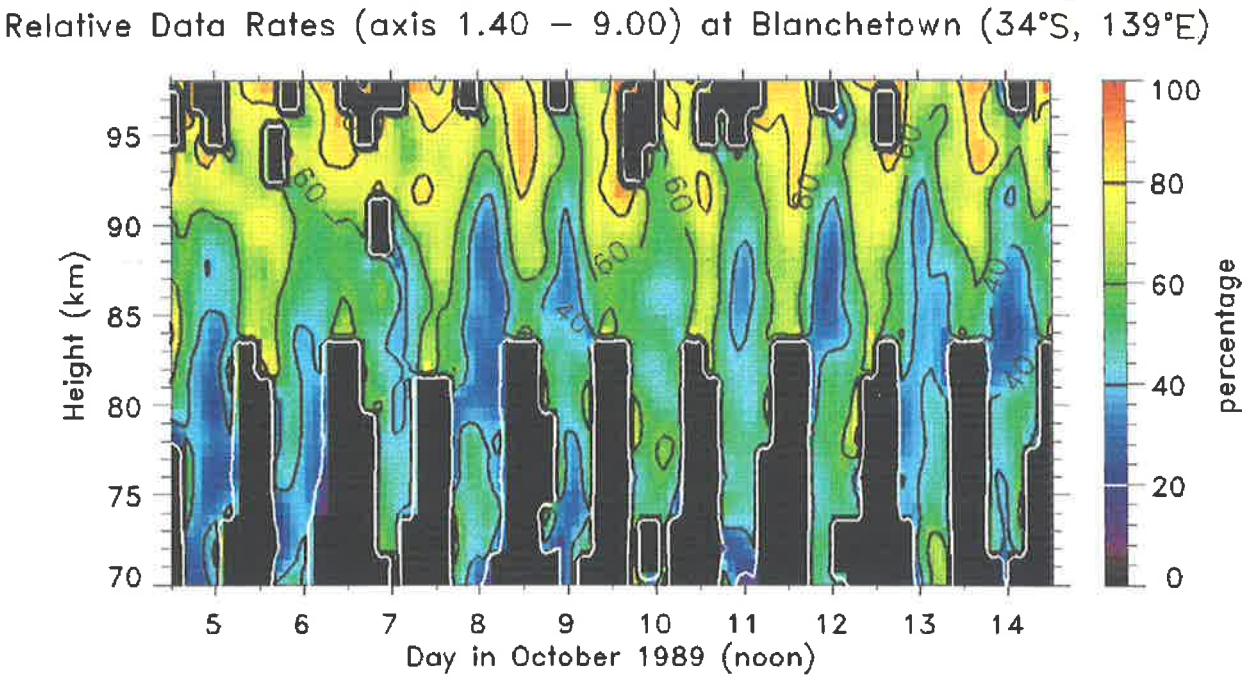

Figure 9.14: Four–hourly mean relative data rates for axial ratios of 1.4–9.0 at Blanchetown for one week in October 1989. The contours are percentages of the total data in that axial range to the total data accepted by the analysis program.

greater than if the minor axis were aligned with the mean wind. This dependence on the geometrical arrangement of the ground diffraction pattern is translated into calculations of θ_s and subsequently L/h.

It is therefore fortunate that the full correlation analysis, besides providing the size and axial ratio of the ground diffraction pattern, also measures its physical orientation. This orientation of the ground ellipse, mean direction and variability is investigated here.

In the study of directional data, it makes no sense to utilize linear statistics which can lead to paradoxes. The data presented in this study was analyzed using circular statistics. This is covered in more detail in appendix C which follows on from *Mardia* [1972]. Briefly however, we calculate a mean unit length, which is a normalized vector constructed from a number of vectors. Thus, a unit length of 1 indicates that all the other vectors were oriented in the same direction, while a mean unit length of approximately 0.2 indicates that most of the vectors pointed in random directions. Care should be taken in this interpretation, since vectors

with a systematic variation in angle would still appear random in this situation. However, no systematic behaviour was observed in the data which would cause such small unit lengths.

Figure 9.13 (top) is the mean length of the correlation ellipses, for axial ratios of between 1.0 and 9.0. The diagram clearly illustrates that there is no clear preferential orientation of the major axis, and that most of the time their direction is quite random and successive values are independent of each other. An exception occurs for a few hours after noon between 85 and 90 km, especially evident on the 7^{th}, 8^{th} and 9^{th} when the mean unit length was greater than 0.4. Another subtle feature of the data is that the mean unit lengths below 80 km are, perhaps, systematically larger.

It has been suggested in a study by *Wright & Pitteway* [1978], that even diffraction patterns whose computed axial ratios are up to 1.3 may be considered as being circular, and as such their major axis direction would be suspect and not a real physical phenomena. For that reason, the data were accepted according to their axial ratio, so that any diffraction pattern whose axial ratio was less than 1.4 or greater than 9.0 was rejected. These filtered data are presented in figure 9.13 (bottom), while figure 9.14 show the relative percentage of data that fell within this range and were thus accepted. The filtered data diagram shows that, although the mean unit length has somewhat improved, it is still relatively random in its orientation, and not much grouping of data is seen. The three days described above, 7^{th}, 8^{th}, and 9^{th} again show a clear maximum, where the unit length this time is greater than 0.6. This suggests that the grouping of the diffraction pattern orientations is time–dependent with a diurnal variation. However, at these times, the percentage of data whose axial ratios were greater than 1.4 was relatively low, about 50%, and there is a chance that the data accepted on the basis of its axial ratio could be biased.

Since the data did indicate the possibility that the pattern orientations did possess some group structure, the next step involved constructing histograms and binning data according to three criteria. First of all, only patterns whose axial ratios were in the 1.4–9.0 range were accepted. Secondly, the data were separated into two height ranges, 70–84 km and 86–98 km.

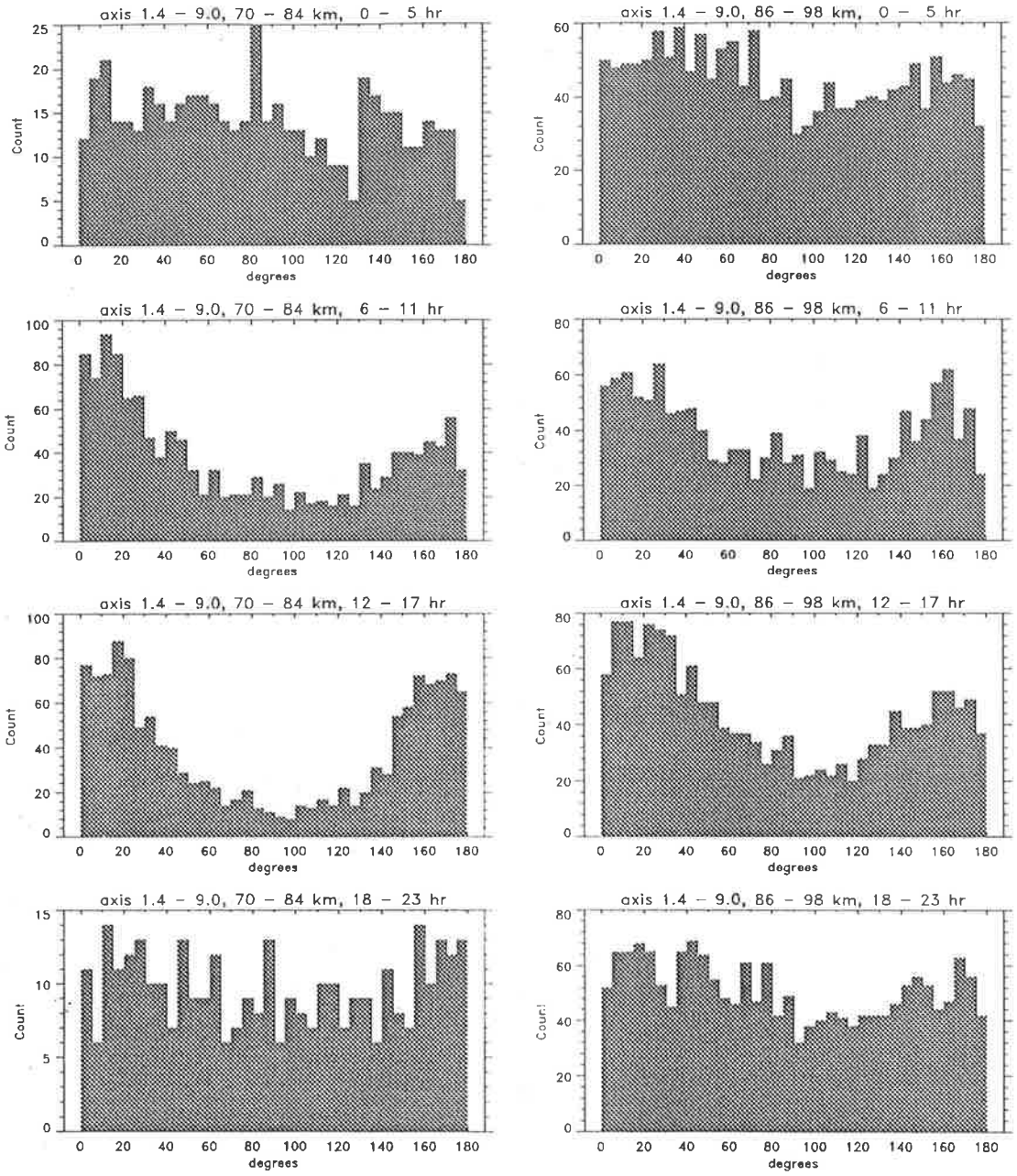

Figure 9.15: Histograms of the orientation of the major axis, filtered for patterns whose axis are greater than 1.4 and less than 9.0. The histograms are based on two height ranges. Those on the left examine the 70 to 84 km range, while those on the right look at the 86 to 98 km range. In addition the data is further grouped according to time. Starting from the top, each histogram looks at a six hour interval; 0:00 to 5:59, 6:00 to 11:59, 12:00 to 17:59, and 18:00 to 23:59 local time. The data are grouped into bins of width 5°.

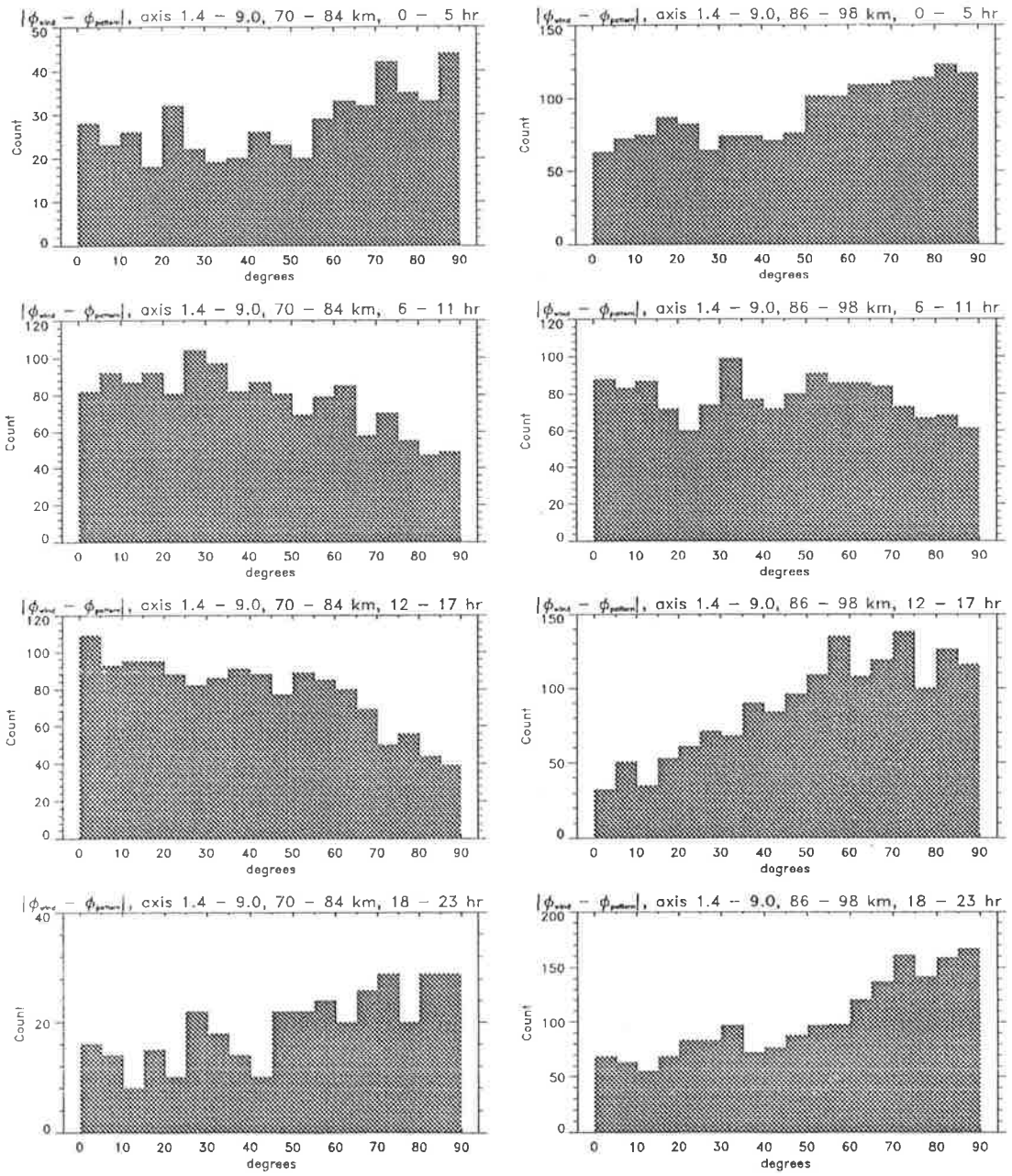

Figure 9.16: Histograms of the difference between the direction of the mean wind and the orientation of the diffraction pattern, filtered for patterns whose axis are greater than 1.4 and less than 9.0. The histograms are based on two height ranges. Those on the left examine the 70 to 84 km range, while those on the right look at the 86 to 98 km range. In addition the data is further grouped according to time. Starting from the top, each histogram looks at a six hour interval; 0:00 to 5:59, 6:00 to 11:59, 12:00 to 17:59, and 18:00 to 23:59 local time. The data are grouped into bins of width 5°.

Finally, the data were split into 4 time ranges; 0:00–5:59, 6:00–11:59, 12:00–17:59, and 18:00–23:59 local time. The data were binned into 5° intervals, and the orientation was measured clockwise with respect to North. These histograms are presented in figure 9.15. It is important to note that the y–axis range, which is the total count, differs between the histograms.

The histograms indicate that during the day–time hours the major axis is predominantly oriented within 25° of the north–south axis. This is especially so in the lower height range, but is also observed in the 86–98 km range. During the night–time hours, there is no evidence to suggest a preferential orientation of the pattern in the lower height range, although this could, in part, be due to the low sampling rate. However, in the 86–98 km range, it would be more accurate to suggest that the major axis is least likely to be oriented in the east–west plane.

With the establishment of the fact that there seems to be some sort of structure to the mean group orientation of the diffraction patterns, the question must be raised whether this is due to the mean wind, some sort of external forcing, or to the magnetic field lines. Figure 9.16 are histograms, constructed similarly to the ones discussed above. However, in this case what was binned was the mean difference between the wind direction and the major axis orientation, such that only the direction of the wind was used without regard to its absolute direction[3]. Thus, the algebraic difference between the two varies between 0°, indicating that they "faced" the same way, or 90°, indicating that the wind direction was orthogonal to the major axis of the pattern.

Several unusual results are found. Looking at the 70–84 km height range one sees that during the night–time hours, the difference between the two tends towards orthogonality, while during the day–time hours the reverse is true. However, within the 86–98 km height range all of the histograms except the one constructed for the 6–11 hr data show that in general the wind and the major axis size are more than 45° apart, i.e. tending towards orthogonality. This is a puzzling result, and cannot be simply explained. Since the effect is far less pronounced than that in figure 9.15, the preferred orientation of the scatterers seems to related to the north–east direction rather than the wind direction. This could partly be due to a geomagnetic effect, but

[3]i.e. it made no difference if the wind was eastward or westward

with no concurrent data for any geomagnetic indices, a clear conclusion cannot be reached. The comparison of pattern orientation and geomagnetic activity is further discussed in chapter 11.

Chapter 10

Short–term results from Christmas Island

10.1 Introduction

The Christmas Island radar system has already been discussed at length in Chapter 7 which examines both the radar and long–term results, and in Appendix *B* which discusses some general aspects of the island. This chapter will concentrate solely on the short–term results (four–hourly averages) obtained from the Christmas Island data. Since it would serve no purpose to present all the data collected, only four periods, each of one–week duration and spaced at equal periods are presented. The choice of the dates was made relatively easy, for during late March 1991, the Christmas Island radar was part of a global equatorial campaign, ALOHA–90[1], conducted in March–April 1990. This provided a unique opportunity to compare results obtained by several instruments. The data presented here cover the periods 19^{th}–26^{th} March, 1^{st}–8^{th} June, 1^{st}–8^{th} September and 1^{st}–8^{th} December.

Some of the work presented in this chapter, in particular connected with the ALOHA–90 campaign has been published in *Vincent & Lesicar* [1991] and *Hostetler et al.*, [1991]. These papers are located in Appendices *G* and *H*.

[1] Airborne Lidar and Observations of the Hawaiian Airglow–1990

10.2 ALOHA–90

ALOHA–90 was a program designed to study the horizontal density and temperature structure of the upper stratosphere (25–55 km altitude) and upper mesosphere (80–105 km) over the mid–Pacific equatorial regions, with an emphasis on wave activity. Internal gravity waves are common throughout the atmosphere and are thought to come from a variety of sources including tropospheric convection, wind shears, orography, and even large ocean swells. Generally propagating upwards, these waves dissipate their energy near the mesopause, contributing to both the momentum and turbulence energy budgets. The drag caused by these waves dissipating is now known to have a significant effect on the dynamics and thermal state of the middle atmosphere. However, the majority of gravity–wave observations are from *in situ* and remote–sensing instruments, and very few observations have been undertaken which study the geographic distribution of wave activity, characteristics of wave sources and the horizontal scales of the wave–induced density, wind, and temperature perturbations. ALOHA–90 attempted to address some of these issues, and involved nine research groups from the United States, Canada, United Kingdom, and Australia. It was based at Maui, Hawaii [*Gardner*, 1991]. Some initial results of the campaign were presented in an issue of *Geophysical Research Letters* [Volume 18, Number 7].

In the work presented here, we compare results obtained by the Christmas Island MF partial reflection radar with a VHF radar and several airborne instruments including a lidar, spectrometer and interferometer. The VHF radar is a VHF stratosphere–troposphere wind profiler, located on Christmas Island and operated by the University of Colorado and NOAA Aeronomy Laboratory (National Oceanographic and Atmospheric Administration). It provided measurements of the three–dimensional wind field [see e.g. *Gage et al.*, 1990]. The lidar, operated by the University of Illinois, was a Na/Rayleigh type. It measures atmospheric density and temperature profiles in the stratosphere (22–55 km) and Na density profiles near the mesopause (80–105 km) [see e.g. *Gardner et al.*, 1989]. The Ebert–Fastie visible and near–infrared spectrometer, operated by the University of Michigan, measures the intensities and rotational temperatures of

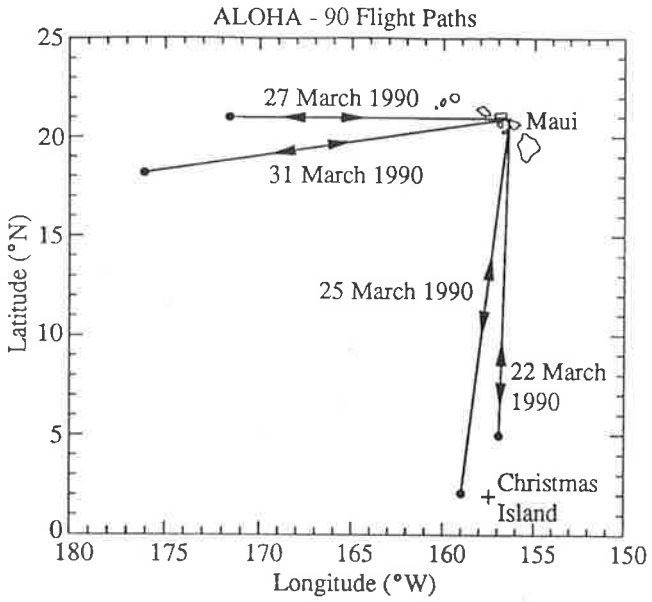

Figure 10.1: Flight paths for the Electra scientific missions on the 22^{nd}, 25^{th}, 27^{th} and 31^{st} March 1990 [from *Gardner*, 1991].

the O_2 Atmospheric (0–1) and OH Meinel (7–3 & 6–2) bands. The University of Michigan also operates a Michelson interferometer which senses the near infra–red region from approximately 1 to 1.7 μm. By obtaining nightglow emission measurements of the OH Meinel (4–2 & 3–1) bands the rotational temperatures can be deduced.

All three instruments were mounted on board an Electra 4–engine turbo–prop aircraft. Altogether, 6 night–time missions were flown. Of these, five were based in Hawaii, with two missions flying along an east–west path (27^{th} and 31^{st} March), two on a north–south flight path (22^{nd} and 25^{th} March) and one doing a local flight around Hawaii (29^{th} March). The two north–south missions approached very close to Christmas Island. The four north–south and east–west flight paths are shown in figure 10.1 [from *Gardner*, 1991].

This chapter is structured mainly to discuss the short–term behaviour of the mean winds, other full correlation analysis parameters, and the structure of the partial reflection radar scatterers through the calendar year. These results, and comparisons with the ALOHA–90 campaign, especially those on the 22^{nd} and 25^{th} March will be discussed where appropriate. However, some results pertaining to the other flight will also be noted where relevant. We start, however, with some general characteristics of the data at Christmas Island using a somewhat similar format to the previous chapters.

10.3 Experimental technique

All the data were analyzed in a similar fashion to those presented in chapter 9. That is, after grouping the data into four–hourly intervals, four points which showed maximum deviation from the mean were removed from the data sample, and a new mean computed. This resulted in a maximum of 10% data being rejected. As mentioned above, the data covered periods from 19^{th} to 26^{th} March, 1^{st} to 8^{th} June, 1^{st} to 8^{th} September, and 1^{st} to 8^{th} December, all during 1990. Hereafter, reference to each period shall be made on the basis of the month in which it occurs only.

10.3.1 Data rates

Figure 10.2 (top) is an image–contour plot of the four–hourly mean percentage of data points for each individual height range collected by the Christmas Island radar system and accepted by the full correlation analysis for March, while figure 10.2 (bottom) is the same for June. Similarly figure 10.3 (top) is for September while figure 10.2 (bottom) covers the first 8 days in December.

The radar samples each height range every 2 min, making it possible to collect a total of 120 points during four hours. All of the four months indicate good data rates between 80 and 90 km. However, March shows an exceptionally clear diurnal variation which is only weakly evident during the other three months. During March, the night–time data rates, especially between 82 and 93 km are very large. This maximum is less evident during June and December and even less so in September. Furthermore, while night–time data rates at around 80 km for June, September, and especially December were virtually zero, during March they were noticeably larger.

Another noticeable feature is that the data rates between 70–78 km during June, September and December are much larger than during March. Furthermore, these data rates change abruptly during night–time, unlike March where the data rate contours are more widely spaced indicating a slower change.

In addition, the nights of the $21^{st}/22^{nd}$ and $24^{th}/25^{th}$ March are quite different, with the data rates below 80 km for the $24^{th}/25^{th}$ significantly larger than the $21^{st}/22^{nd}$. These two dates are especially important, for these are the nights that the Electra aircraft flew very close to Christmas Island.

An unexpected results is that, above 80 km, the night–time data rates are far greater than those during the day–time, when the converse is expected to be true due to a lack of ionization [see e.g. the data rates for Blanchetown, figure 9.6]. To investigate this further, the raw data were binned according to three criteria. Firstly, the data were separated according to the full correlation acceptance and rejection rules. Secondly, the data were split into three height ranges; 70–78 km, 80–88 km, and 90–98 km. Finally, the data were separated according to the time of day into 6–hourly periods starting at midnight local time (LT). These results are tabled in tables 10.1 and 10.2, and the following discussion is based around the results displayed in these tables. For simplicity sake the 0:00–6:00 period will be referred to as night, the 6:00–12:00 period the morning, the 12:00–18:00 period the afternoon, and the 18:00–24:00 period the evening.

In the 70–78 km height range the data rates increased from less than 1% during the night to more than 20% during the morning and afternoon, and decreased to less than 5% in the evening. Most of the data were rejected due to one of four principal criteria, the S/N ratio, slow fading time, long time delays, and PTD's. While during the night and evening periods the dominant rejection was due to the low S/N ratios, during the morning and afternoon the dominant rejection occurred due to the slow fading and the PTD criteria. This shift in rejection can be attributed to the increase in ionization and the relative stability of the mesosphere at these heights.

However, in the 80–88 km height range the reverse is true. Whilst the data rates through all the time periods improve, this is most dramatic at night where around 55% of data are accepted. This number is slightly smaller in the morning, and decreases by nearly one–half in the afternoon. In this height range the rejections due to low S/N ratios decreased relatively

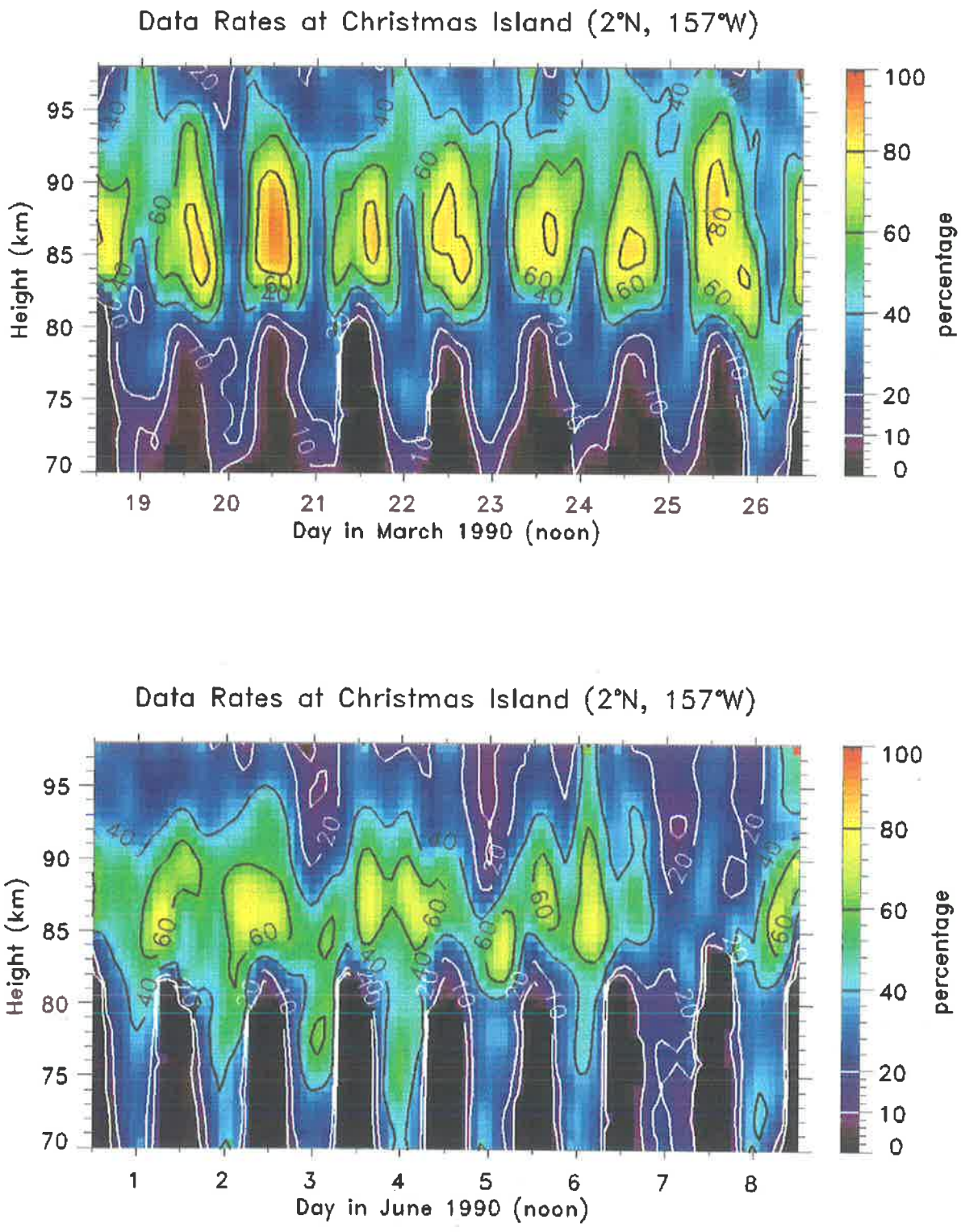

Figure 10.2: Four–hourly percentage of data accepted by the Christmas Island partial reflection radar per unit height for 8 days in March (top) and June (bottom), 1990.

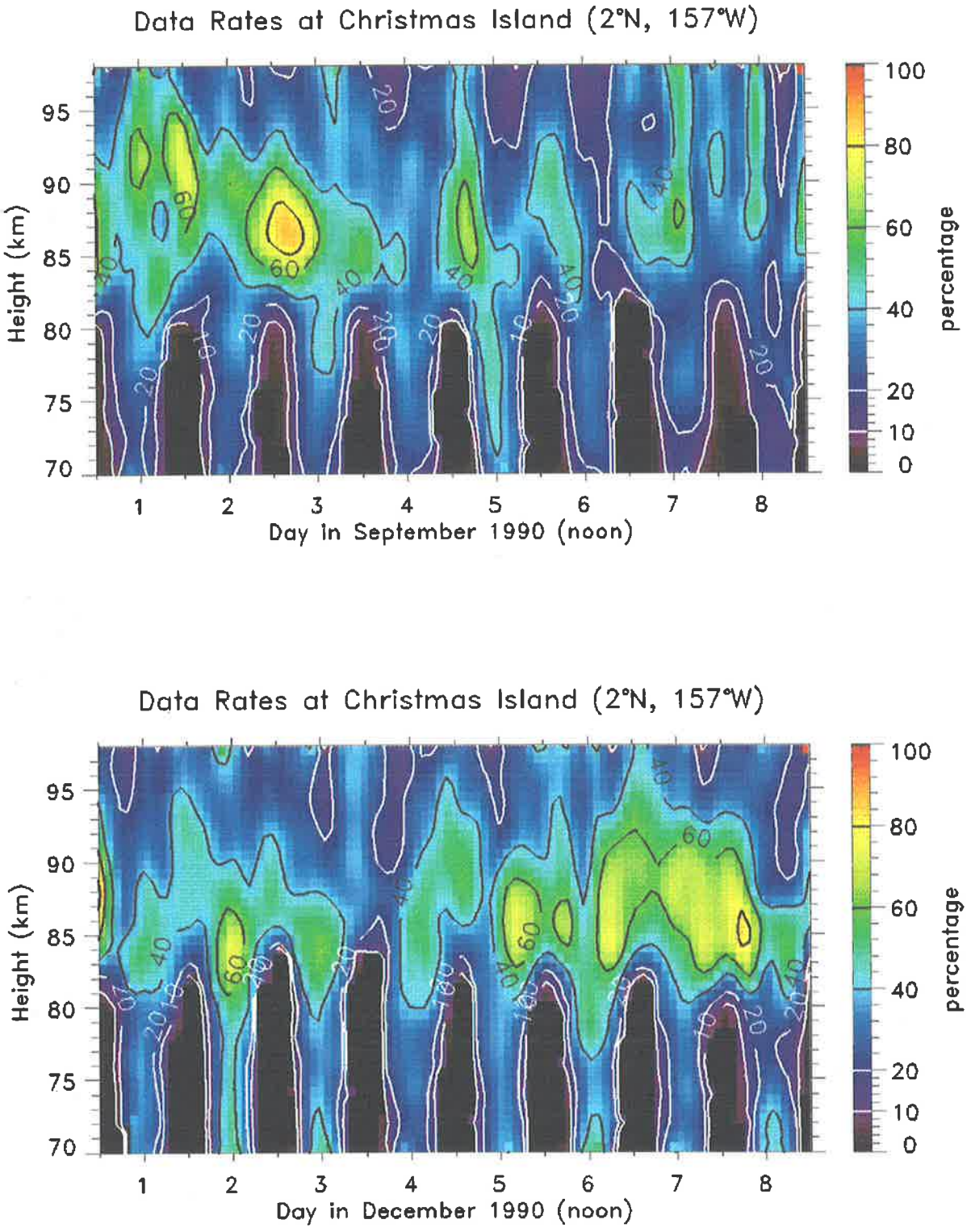

Figure 10.3: Four-hourly percentage of data accepted by the Christmas Island partial reflection radar for 8 days in September (top) and December (bottom), 1990.

Error Code	Meaning	0:00–6:00 LT			6:00–12:00 LT		
		70–78	80–88	90–98	70–78	80–88	90–98
0	Analysis OK (data accept)	0.8	52.8	36.3	22.3	44.4	34.5
1	Signal level too low	1.1	$\ll$0.05	0.0	0.0	0.0	0.0
2	Signal/Noise too low	31.0	5.6	0.0	0.6	0.2	$\ll$0.05
3	Fading too slow	17.1	12.7	2.1	34.3	18.0	2.8
4	Time delays too long	18.1	4.5	9.6	7.2	6.0	11.1
5	PTD > 50	19.1	12.1	27.0	25.1	17.0	21.2
6	$V_c^2 < 0$ (data accept)	0.2	1.8	1.7	0.2	0.5	0.6
7	Pattern analysis fails	0.8	1.2	5.1	0.9	1.4	5.0
8	$V_a > 250ms^{-1}$	0.1	0.4	0.8	1.0	1.0	2.5
9	$\|\theta_a - \theta_v\| > 40°$	0.2	2.1	3.5	2.6	3.1	8.1
10	$V_a > 4V_t$	$\ll$0.05	2.0	2.2	3.0	4.0	6.1
11	$V_t > 1.5V_a$	1.0	2.3	6.1	1.5	2.5	4.5
12	Bad fit to cross-corr. fn	7.9	1.6	0.2	0.5	0.4	0.2
13	ρ_{max} less than 0.2	0.4	0.1	5.1	0.7	0.4	3.1
14	Hardware fp error	$\ll$0.05	$\ll$0.05	$\ll$0.05	0.0	0.0	0.0
15	Maths error (Log, Log10)	0.2	0.3	0.2	$\ll$0.05	0.1	0.1
16	Other maths errors	2.0	0.3	0.0	0.1	$\ll$0.05	0.0

Table 10.1: The full correlation analysis performs on–line analysis of data which may be accepted and rejected according to stringent parameters. The table above lists the different acceptance and rejection codes, and the relative percentage of data that was deemed suitable or not by the specific error code. The data is binned into three different height distributions; 70–78 km, 80–88 km, and 90–98 km. In addition the data was separated according to the time of day, in this case for 0:00–6:00 and 6:00–12:00 LT.

quickly across all time periods, unlike that of the slow fading time and the PTD criteria whose contributions increase during the morning and afternoon periods, but at a smaller rate. This difference in rate explains the observed large night–time data acceptance rates.

In the 90–98 km height range, the data acceptance rates are very similar, fluctuating around 35%. The rejection due to the four principal criteria are relatively constant, with the exception of slow fading which is somewhat larger during the afternoon. In addition, the other eleven rejection criteria become much more important, contributing to the rejection of around 30% of the total data, as compared to the other two height ranges where their contribution varies around 10%.

10.3.2 Signal–to–noise ratios

As mentioned in the previous chapter, the S/N ratio is a good indicator of the echo strength provided that the receiver and natural noise is constant, and that there are no man–made radio

Error Code	Meaning	12:00–18:00 LT			18:00–24:00 LT		
		70–78	80–88	90–98	70–78	80–88	90–98
0	Analysis OK (data accept)	25.0	28.1	33.9	4.9	37.3	38.3
1	Signal level too low	0.0	0.0	$\ll$0.05	0.2	$\ll$0.05	0.0
2	Signal/Noise too low	0.1	0.1	$\ll$0.05	23.0	5.2	0.0
3	Fading too slow	33.5	27.8	8.7	20.0	13.1	1.7
4	Time delays too long	7.9	8.8	11.2	16.2	5.7	10.6
5	PTD > 50	23.8	22.1	17.9	21.1	17.5	23.1
6	$V_c^2 < 0$ (data accept)	0.2	0.2	0.3	0.3	0.6	0.9
7	Pattern analysis fails	0.7	1.1	5.0	1.1	1.6	4.9
8	$V_a > 250ms^{-1}$	1.1	1.4	1.4	0.3	2.2	1.2
9	$\|\theta_a - \theta_v\| > 40°$	2.4	2.8	9.0	0.7	3.5	5.4
10	$V_a > 4V_t$	3.2	5.2	6.2	0.3	7.7	3.6
11	$V_t > 1.5V_a$	1.5	1.8	4.4	1.2	2.5	5.0
12	Bad fit to cross-corr. fn	$\ll$0.05	0.2	1.1	7.3	1.8	0.4
13	ρ_{max} less than 0.2	0.4	0.3	0.7	1.8	0.9	4.5
14	Hardware fp error	0.0	0.0	0.0	$\ll$0.05	$\ll$0.05	$\ll$0.05
15	Maths error (Log, Log10)	0.0	0.1	0.2	0.1	0.2	0.2
16	Other maths errors	$\ll$0.05	$\ll$0.05	0.0	1.5	0.2	$\ll$0.05

Table 10.2: As for table 10.1 but for data collected during 12:00–18:00 and 18:00–24:00 LT.

sources nearby. Christmas Island is far removed from any large population centres, there are no radio sources on the island, and the receiver noise is constant. The S/N ratios, therefore, provide a crude indication of the echo strength.

Figure 10.4 (top and bottom) are image–contour plots of the four–hourly signal–to–noise (S/N) ratios for March and June respectively, while figure 10.5 (top and bottom) are for September and December respectively. The ratios were calculated by using the median values of the four–hourly blocks of data for each height range and for each of the three receivers. The medians were used instead of arithmetic means since they provided a much more robust result and were not influenced by large deviations in the data. Only data from one receiver are presented since the data from all three receivers were virtually identical. For ease of comparison all the data is colour–coded, and the same colour scheme is used for all the different data periods.

There are several interesting features exhibited by the S/N ratios. Below about 80 km, the S/N ratios are fairly constant and do not show any significant temporal variation. At greater heights, however, in June, September, and December there are clear diurnal variations with maximum S/N ratios approaching 25 dB during the day and dropping down to less than 5 dB

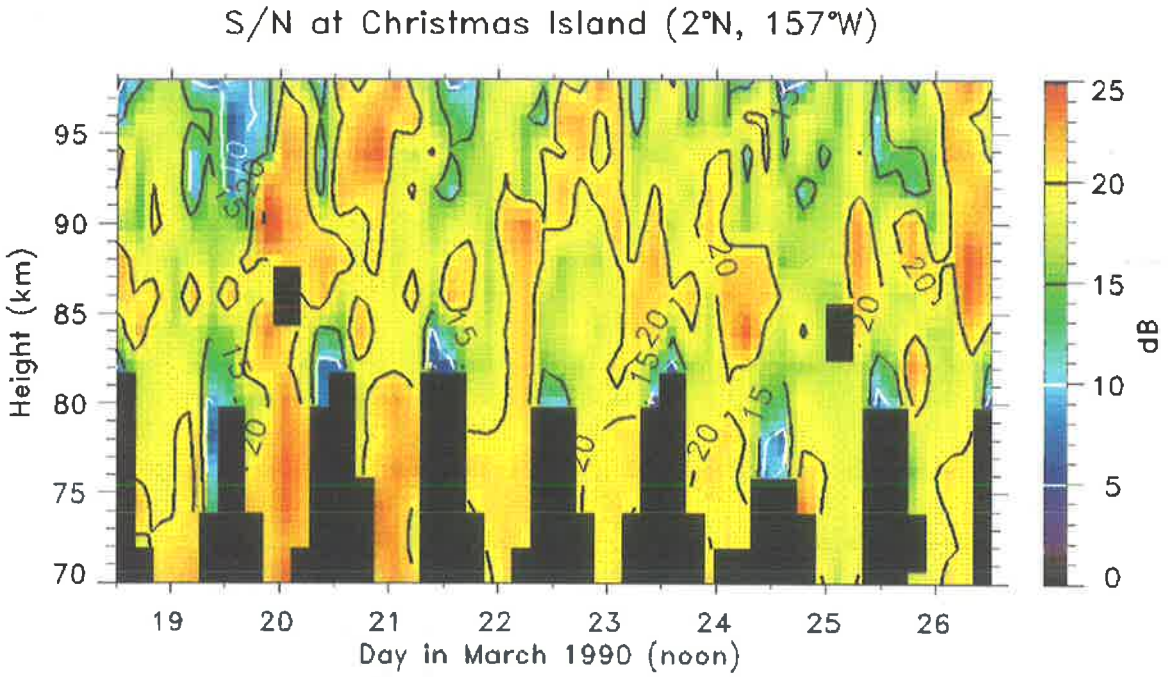

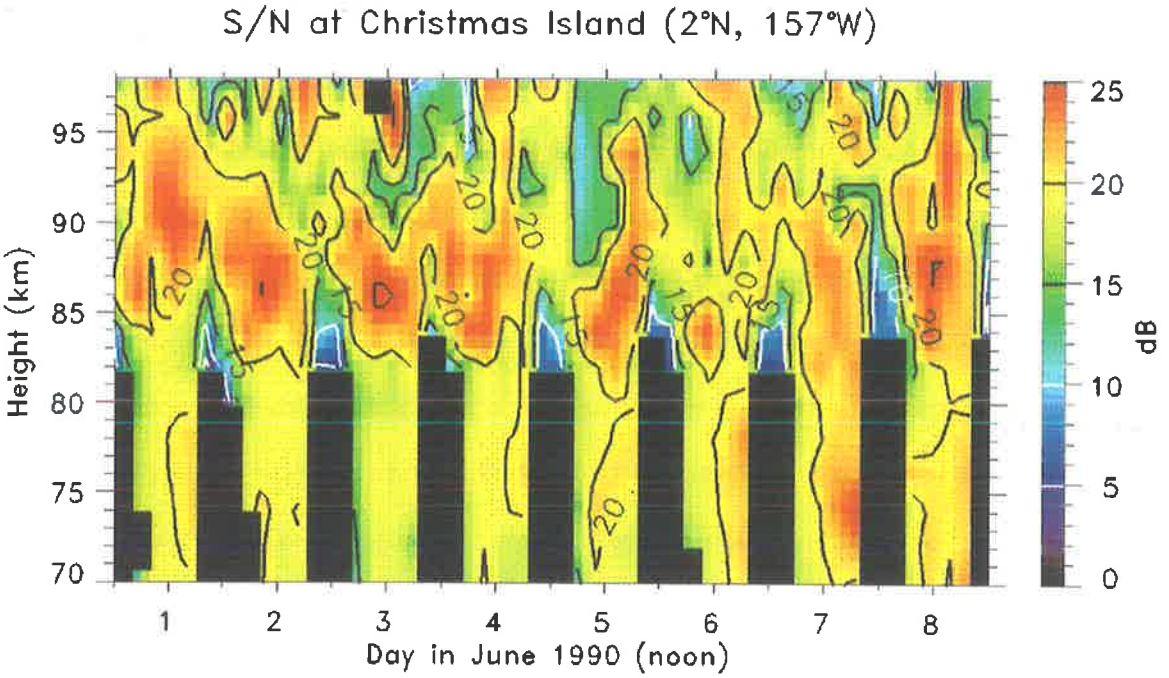

Figure 10.4: Four–hourly mean signal–to–noise ratios per unit height for one week at Christmas Island during March (top) and June (bottom), 1990.

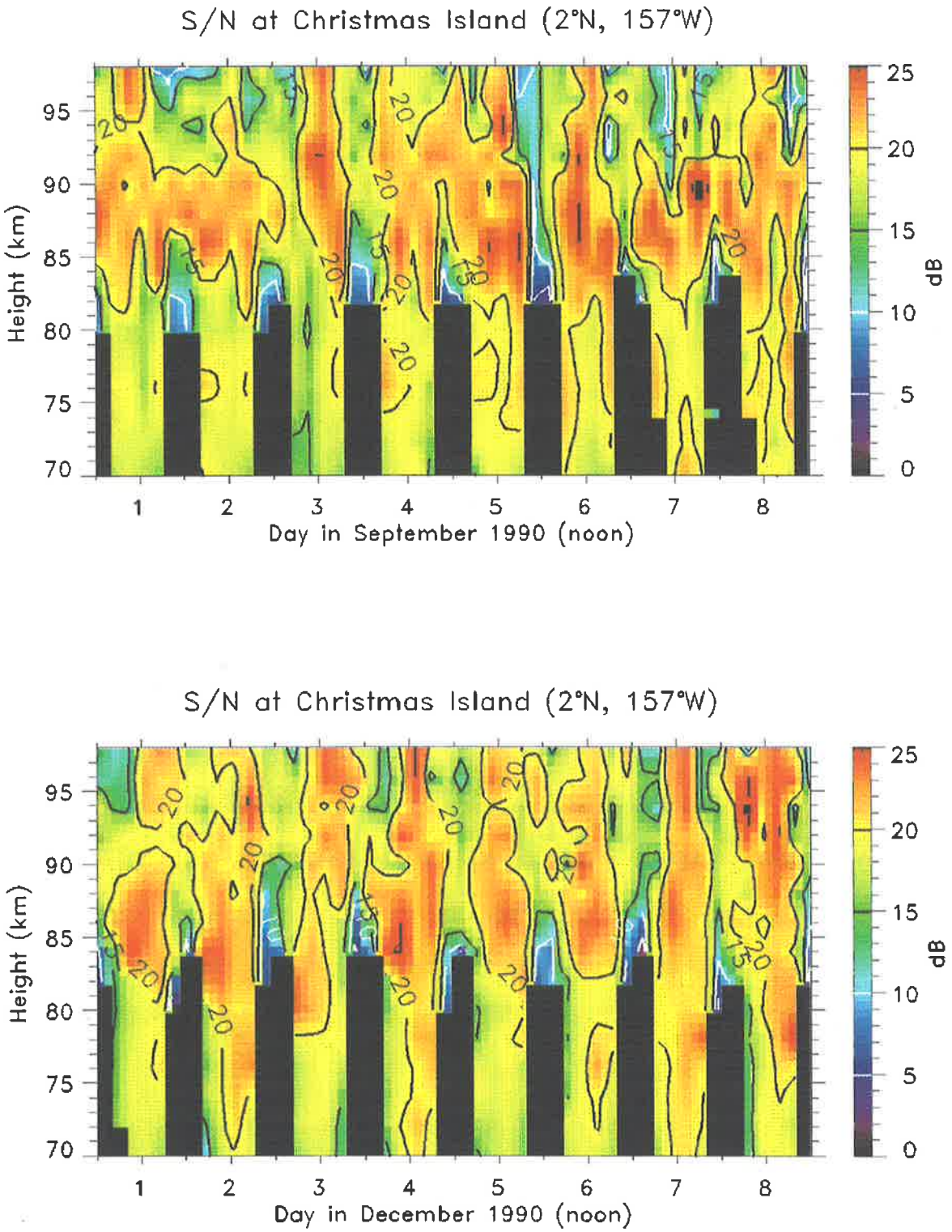

Figure 10.5: Four-hourly mean signal-to-noise ratios per unit height, for one week at Christmas Island during September (top) and December (bottom), 1990.

at night. In contrast the S/N ratios at these heights during March are systematically smaller by approximately 5 dB, and the diurnal variation so evident in the other months is weak. However, the diurnal variation can also be an artifact of the variation in noise level which increases at night and is not evident below 80 km due to lack of night–time data.

The S/N ratios during the nights of the $21^{st}/22^{nd}$ and the $24^{th}/25^{th}$ March, the time of the ALOHA–90 flights, are interesting. The S/N ratios during the $21^{st}/22^{nd}$ are approximately 5 dB at 82 km increasing to 15 dB at 85 km. During the $24^{th}/25^{th}$, however, the S/N ratios are markedly different, approximately 5 dB at 76 km and nearly 20 dB at 85 km. This is a difference of nearly 10 dB at a height of 82 km, and is quite significant.

10.4 Mean winds and dynamics

The mean four–hourly zonal and meridional winds are shown as image–contour plots in figures 10.6, 10.7, 10.8, and 10.9, for March, June, September, and December respectively. While the data were not filtered to remove wave motions, the four–hourly data blocks ensured that the effects of short–period waves were removed.

During March, the mean zonal winds are generally westward (easterlies) at all heights above 75 km, and are close to zero or slightly eastward at lower heights. The maximum westward flow occurs at heights near 85 km, where values up to -80 ms^{-1} are observed. The meridional wind shows an influence of an oscillation near the 2–day period, with the winds on the nights of the $20^{th}/21^{st}$, $22^{nd}/23^{rd}$ and $24^{th}/25^{th}$ being more northward than those on the nights of the $19^{th}/20^{th}$, $21^{st}/22^{nd}$ and the $23^{rd}/24^{th}$ March.

In June the mean zonal winds above 80 km are generally eastward, upon which is superimposed a clear oscillation with a period of approximately 2 days. The maximum eastward flow occurs at heights between 85–90 km, reaching values greater than 40 ms^{-1}. Between 75–80 km, the wind is generally westward with values around -20 ms^{-1}, while below this height they turn eastwards. The mean meridional winds are influenced by a 2–day oscillation with the winds being eastward on the 2^{nd}, 4^{th}, 6^{th} and 8^{th}, and westward on the alternate days, changing by

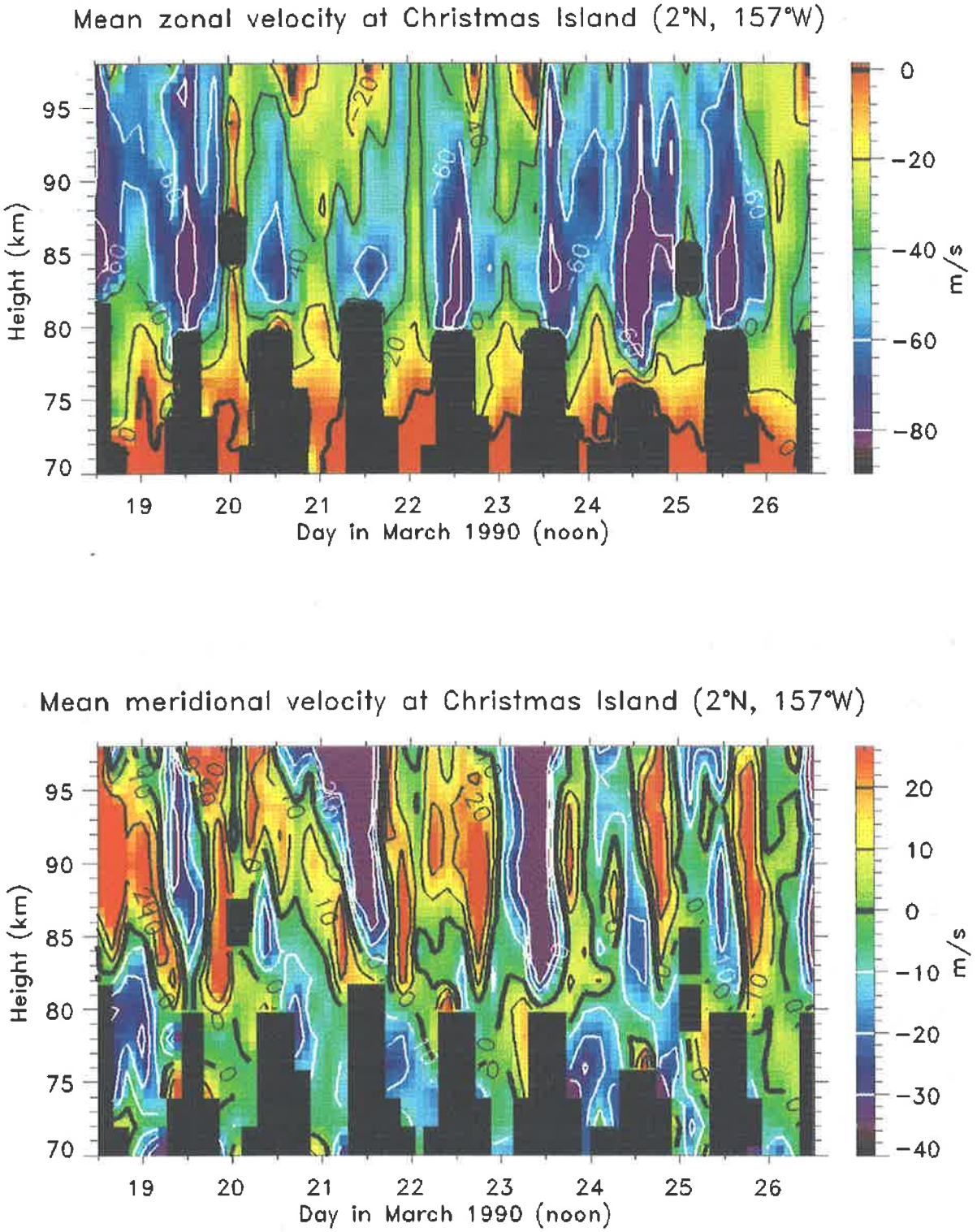

Figure 10.6: Four–hourly mean zonal (top) and meridional (bottom) wind at Christmas Island over one week during March 1990.

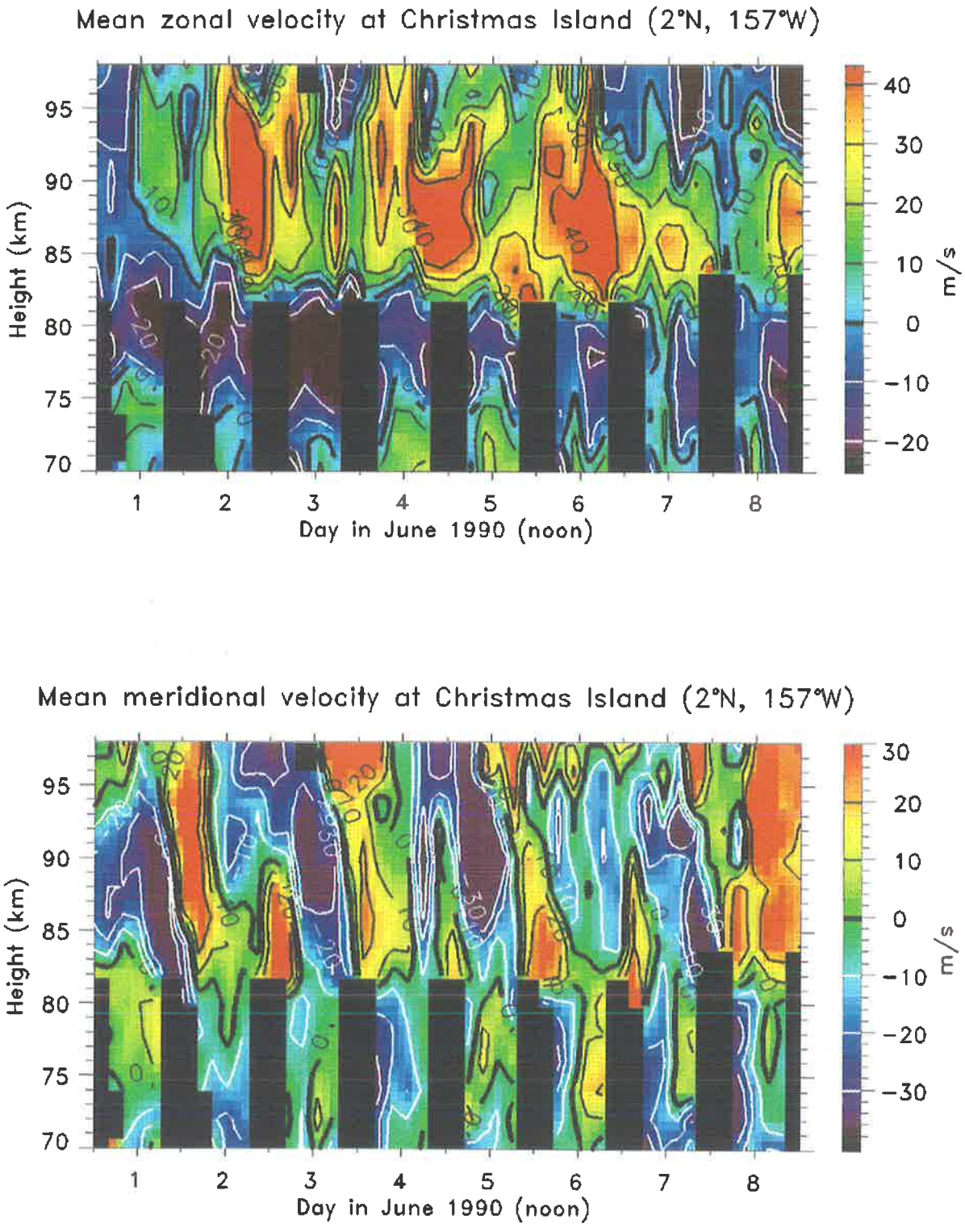

Figure 10.7: Four–hourly mean zonal (top) and meridional (bottom) wind at Christmas Island over one week during June 1990.

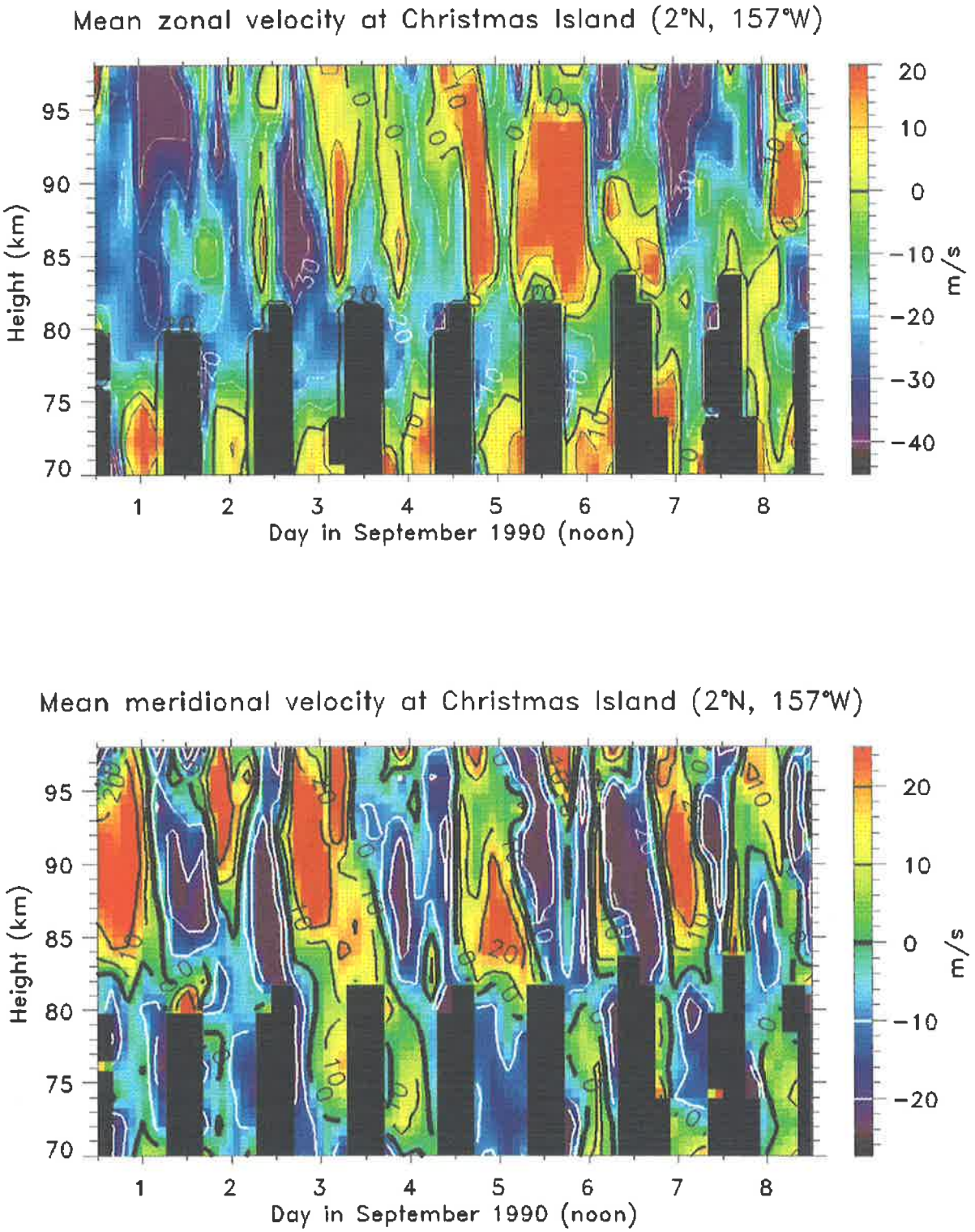

Figure 10.8: Four–hourly mean zonal (top) and meridional (bottom) wind at Christmas Island over one week during September 1990.

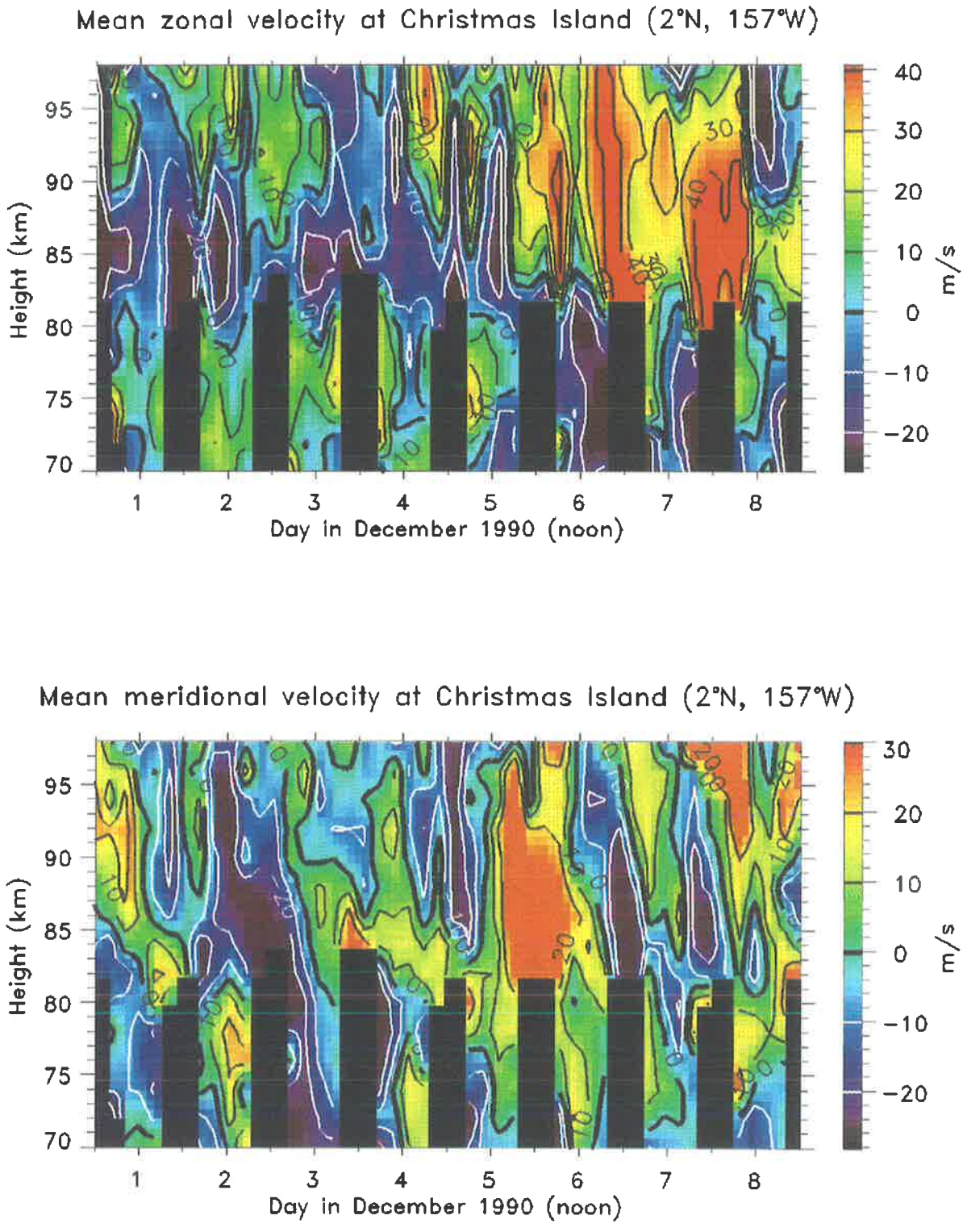

Figure 10.9: Four-hourly mean zonal (top) and meridional (bottom) wind at Christmas Island over one week during December 1990.

60 ms^{-1}, from 30 to -30 ms^{-1}. In addition, between 80 and 90 km a diurnal oscillation is quite clear.

In September, the mean zonal winds above 75 km are generally westward, although at times a strong eastward flow is observed (on the $5^{th}/6^{th}$). Below 75 km the flow is close to zero or slightly westward. The mean meridional winds are clearly influenced by oscillations with periods of approximately 1 and close to 2 days oscillating in value between -20 and 20 ms^{-1}.

During December, the zonal winds exhibit no simple temporal structure. Above 80 km during the first few days in December the flow is relatively weak and fluctuates in direction. However, from the 5^{th} to the 8^{th}, the flow is strongly eastward, reaching values of up to 40 ms^{-1}. Below this height the flow is initially weakly westward changing to eastward at the same time that the wind above 80 km exhibits a reversal. The meridional mean flow indicates some temporal structure, again with oscillations of around one and two days.

All of the observations of the mean zonal and meridional winds show that wave activity is significant in the equatorial mesosphere. Power spectral analysis has shown that wave activity occurs at all time scales [*Vincent & Lesicar*, 1991]. One scale in particular is the two–day wave which has been found to be strong at equatorial and tropical latitudes [see e.g. *Vincent & Lesicar*, 1991; *Fritts & Isler*, 1992; *Harris & Vincent*, 1993]. In fact, the partial reflection radar data used in this thesis has been analyzed for the 2–day wave motions by *Harris & Vincent* [1993], who found that a meridional quasi–two–day wave is present almost continuously in the 80–100 km height range, although its amplitude varies with season, being largest one month after solstices and smallest during April. The two–day wave exhibited downwards phase propagation, consistent with upwards energy propagation, a feature easily observable in the meridional winds presented above. In addition, at periods near two days, most of the variance is concentrated in the meridional component. A satisfactory explanation of the mechanism producing the 2–day wave has not yet been proposed, although several theories do exist [see e.g. *Salby*, 1981; *Plumb*, 1983; *Pfister*, 1985].

An examination of long–term periods (3–10 days) in the equatorial mesosphere has recently

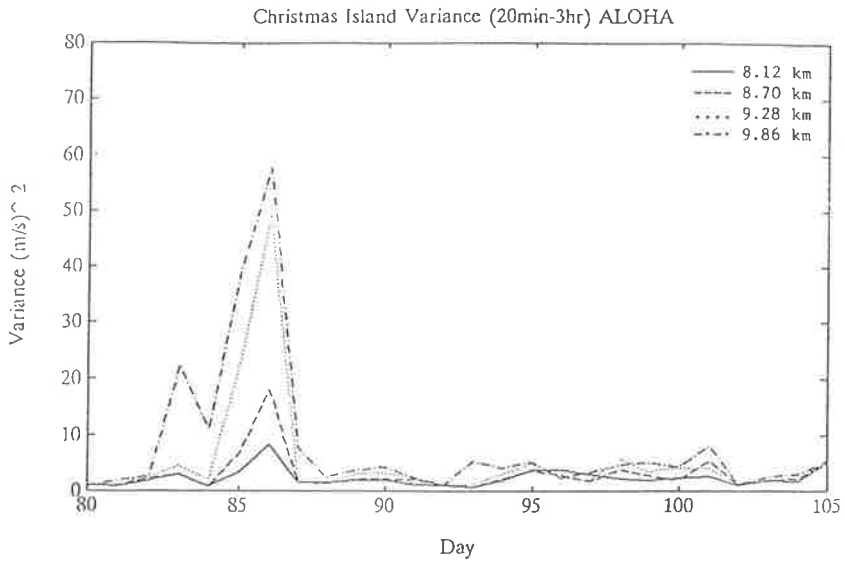

Figure 10.10: The time evolution of the sum of the daily variance in the zonal and meridional wind fields for wave motions with periods between 20 min and 3 hours [from *Avery & Palo*, 1991].

been completed by *Vincent* [1993], who, using Christmas Island data, found that motions within these periods occur mainly in the zonal winds. This is attributed to eastward propagating Kelvin waves, which are evanescent waves causing oscillations in the zonal wind component only. These Kelvin waves exhibit a semiannual variation in their activity, reaching maximum amplitudes at the mesopause in January/February, and August/September.

ALOHA–90

In this section we examine the results obtained during the ALOHA–90 campaign, concentrating in particular on two nights, the $21^{st}/22^{nd}$ and $24^{th}/25^{th}$ March, when the Electra aircraft carrying the Illinois lidar made its closest approach to Christmas Island. We start first with the results obtained with the ST radar located adjacent to our partial reflection radar on Christmas Island. These have been published by *Avery & Palo* [1991].

The ST radar measures the three-dimensional wind field over the height range of 2–16 km, with a temporal resolution of 4 min, and a height resolution of 1.2 km. Over days 80–86 (March 21^{st}–27^{th}) the zonal winds were generally westward throughout the troposphere with a slight eastward component above 10 km on days 80–83 (March 21^{st}–24^{th}). The meridional winds

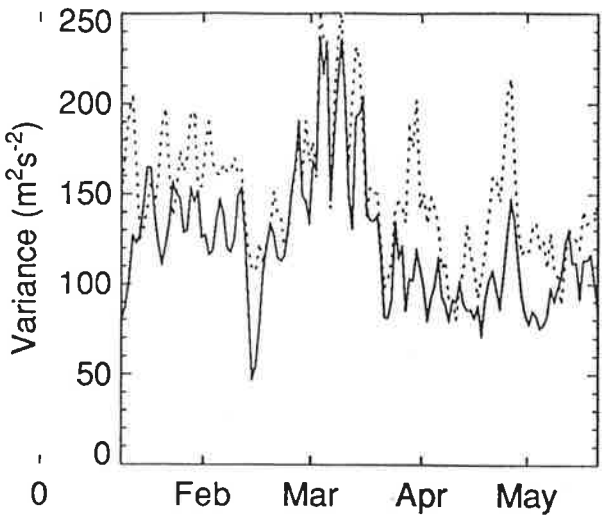

Figure 10.11: Daily values of the gravity wave variances in the 4 min to 1 hr period band for both the zonal (solid) and meridional (dotted) wind components [from *Vincent & Lesicar*, 1991].

were weaker than the zonal on average. Superimposed on these wind fields are low and high–frequency wave motions. The sum of the zonal and meridional variance in the wind field for four heights between 8 and 10 km bandpassed for wave motions between 20 min and 3 hours is shown in figure 10.10 [from *Avery & Palo*, 1991]. The diagram clearly shows that an increase in variance is observed starting at day 82 and peaking at day 85. The variance is also seen to increase with increasing height. Clearly this indicates that the troposphere had considerable high–frequency wave activity during this time, generated by convective activity and/or wind shears.

The results from the MF partial reflection radar show that the ALOHA–90 campaign occurred at a time when the equatorial mesosphere was dynamically active. Figure 10.11 shows the daily values of the gravity–wave variances in the 4 min to 1 hr period band. It is clearly apparent that the variances reach their largest values at the time of the ALOHA–90 campaign. In addition, significant daily variations are also shown, with the variances in each wind component varying by as much as 100 m^2s^{-2}.

Observations with the airborne Na/Rayleigh lidar, which measured Na density profiles, have shown strong wave activity near Christmas Island on March 25^{th}, with measured wind variances between 1000 and almost 1400 m^2s^{-2} [*Hostetler et al.*, 1991]. During the 2 hr period of closest

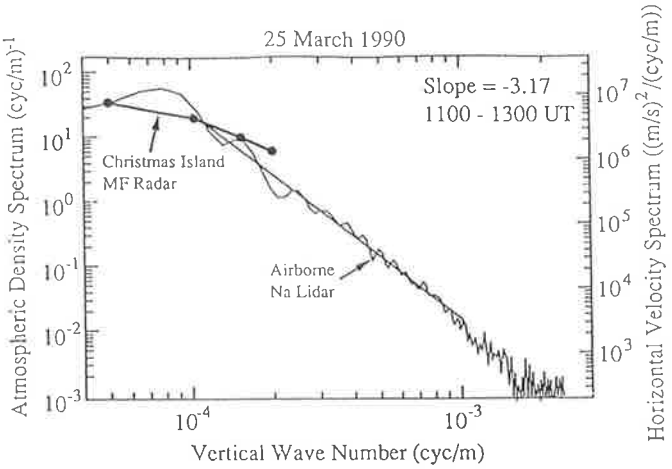

Figure 10.12: Comparison of the average vertical wave number spectra measured by the airborne lidar and MF radar during the period 1100–1300 UT on 25^{th} March. The radar data represent the scalar wind spectrum obtained by adding the zonal and meridional spectra [from *Hostetler et al.*, 1991].

approach to Christmas Island (around 0215 LT), the rms horizontal wind perturbations inferred from the lidar measurements was 37 ms^{-1} while the MF partial reflection radar measured 31 ms^{-1}. The higher lidar values were attributed to the averaging, since the peak rms winds occurred at 4° N, and the lidar results were averaged between 2° N and 7° N. The vertical wave number spectrum measured by the lidar was also comparable to that obtained with the MF radar [see figure 10.12].

A Fourier transform spectrometer and a 1/4 m grating spectrometer, both sensitive to the nocturnal airglow, were also flown on the Electra. These instruments provide complementary measurements of the rotational temperatures of OH and O_2. *Niciejewski & Yee* [1991] examined the temperatures from the 22^{nd} March (west–to–east) and 31^{st} March (north–to–south) flights [see figure 10.1]. They found that temperatures inferred from the OH and O_2 emissions on March 31^{st} were equal, $T(OH) \sim T(O_2)$, (within the error bars), during the start of the east–to–west flight, while $T(OH) > T(O_2)$ during the latter part of the flight. For the March 22^{nd} mission, the reverse was true. $T(OH) > T(O_2)$ during the first part of the north–to–south flight, and similar temperatures at the end.

Rocket photometry can be used to determine the peak altitude of emission for any airglow feature. The mean altitude of the peak hydroxyl emission has been determined to be ~87 km [*Baker & Stair*, 1988]. Similarly the peak altitude of the O_2 emission has been found to be

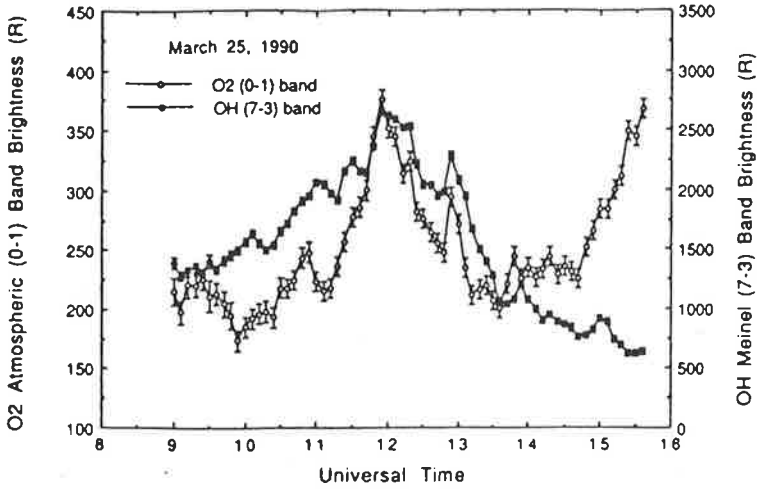

Figure 10.13: Measured brightness of the O_2 Atmospheric (0–1) band and the OH (7–3) band emissions on March 25 [from *Yee et al.*, 1991]. The Electra was at its closest approach to the equator at 12:00 UT.

around 94 km [*Greer et al.*, 1984]. This difference in mean height between the layers allows a crude determination of the temperature profile.

The conclusion reached by *Niciejewski & Yee* [1991], assuming the usually accepted altitudes for peak airglow emissions, was that the mesopause was high during the ALOHA campaign, and lay above 90 km, with the temperature gradient close to zero or negative with increasing altitude. An increase in the hydroxyl temperatures above Hawaii for the same observing period has also been reported [*Turnbull & Lowe*, 1990], while recent modelling [*Hedin*, 1991] has also shown a high mesopause in April at equatorial latitudes. The observed variations in the temperatures as a function of position are an indicator of dynamical influences in the 85–95 km region.

The 1/4 m spectrometer and the interferometer were also used to measure the O_2 and OH brightnesses for the March 25^{th} and March 31^{st} flights. These results have been discussed by *Yee et al.* [1991]. On both occasions, wave-like oscillations in both O_2 and OH brightness were clearly present. A noticeable feature was the enhanced brightness in both O_2 and OH during the March 25^{th} flight when the Electra was closest to the equator and Christmas Island at around 12:00 UT [see figure 10.13].

Sporadic Na layers were observed with the lidar during the 22^{nd}, 25^{th} and the 27^{th} March flights [*Gardner et al.*, 1991]. A correlation between the airglow and the sodium column density,

as measured by the lidar, was evident, especially so for the OH brightness. The most striking correlation occurred on the northbound leg of the March 25^{th} flight when the O_2 Atmospheric band intensities and temperatures above the Electra increased substantially during the sporadic Na event. A sporadic Na (Na_s) layer was formed at ~90.7 km, while the aircraft was between 500 and 750 km from Hawaii, while the O_2 temperatures near 95 km were observed to increase by about 45° K. Furthermore, this increase was not only observed by the instruments aboard the Electra, but by those stationed on Haleakala as well [*Hecht & Walterscheid*, 1991]. The data suggest that there is a connection between the observed Na_s and a large–scale wave, which is probably tidal in nature.

A connection between the Na_s layer formation and O_2 temperatures is as yet unclear. It has been observed though, that the formation of Na_s is accompanied by sporadic E (E_s) layers, and that the height of E_s layers is correlated with the intensity of O_2 emissions [*Gorbunova et al.*, 1982; *Beatty et al.*, 1989]. If the Na_s layers are, as suggested by some workers, related to upper atmospheric dust, the increased temperatures encourage the release of Na, as well as increase the O_2 emissions [see e.g. *Beatty et al*, 1989; *Hansen & von Zahn*, 1990]. The increase in temperatures on the March 25^{th} flight have been attributed to a large–scale zonally propagating wave [*Gardner et al.*, 1991].

Mean wind speed

As discussed in the previous chapter, a major part of this study is to investigate the temporal and spatial behaviour of the various spaced–antenna parameters. For this purpose, it is necessary to examine not only the separate zonal and meridional wind components, but the actual wind magnitude as well, especially since it has a direct bearing on the pattern fading time.

Figures 10.14 (top and bottom) and 10.15 (top and bottom) are image–contour four–hourly plots of the wind magnitude for March, June, September, and December respectively. During March a clear diurnal variation above 80 km in the wind magnitude is apparent, varying between 40 and 90 ms^{-1}, with maximum winds observed during night–time, and minimum during day–time. The wind is especially strong on the night of the $24^{th}/25^{th}$ where speeds in excess of 90

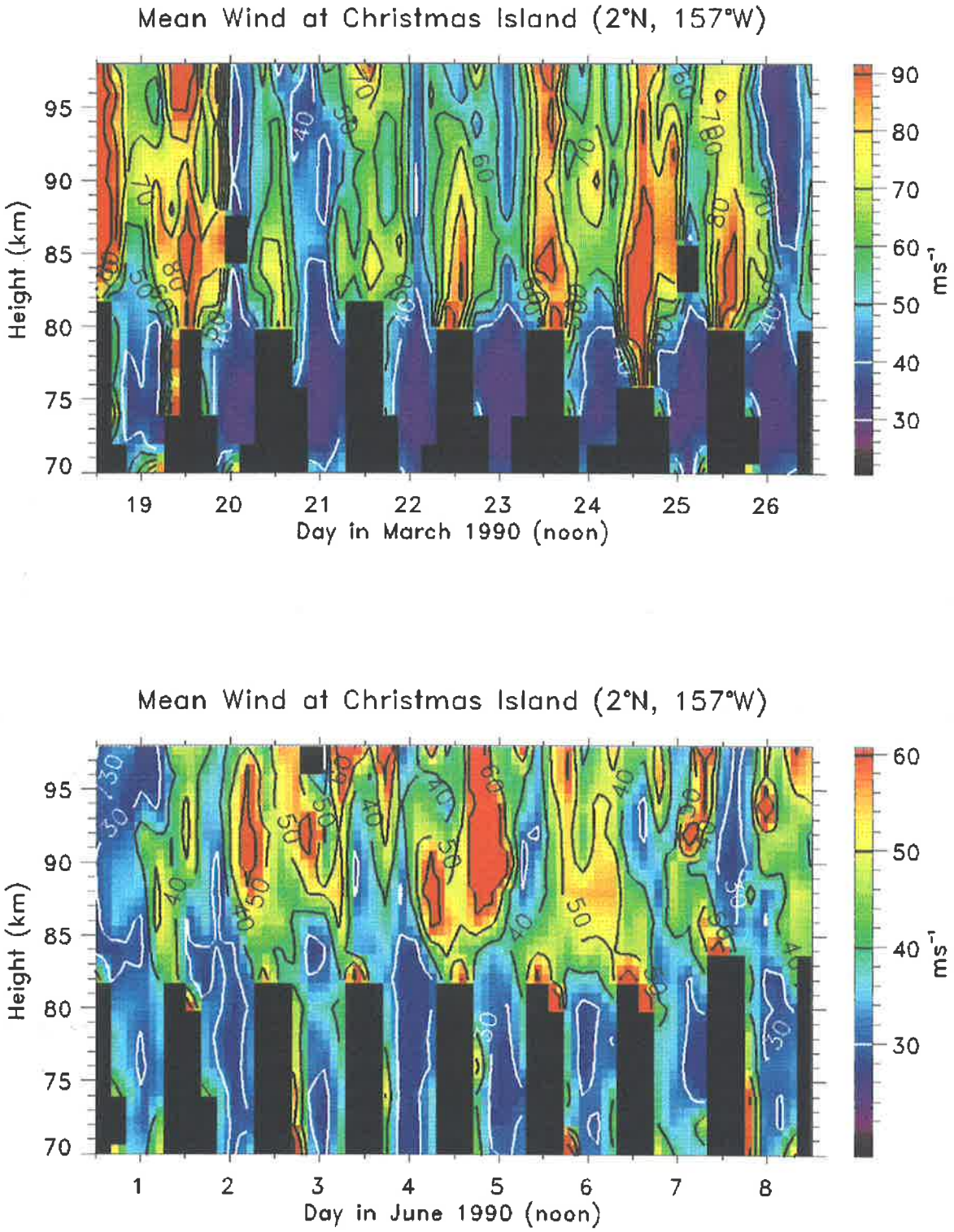

Figure 10.14: Four-hourly mean wind speed at Christmas Island over one week during March (top) and June (bottom) 1990.

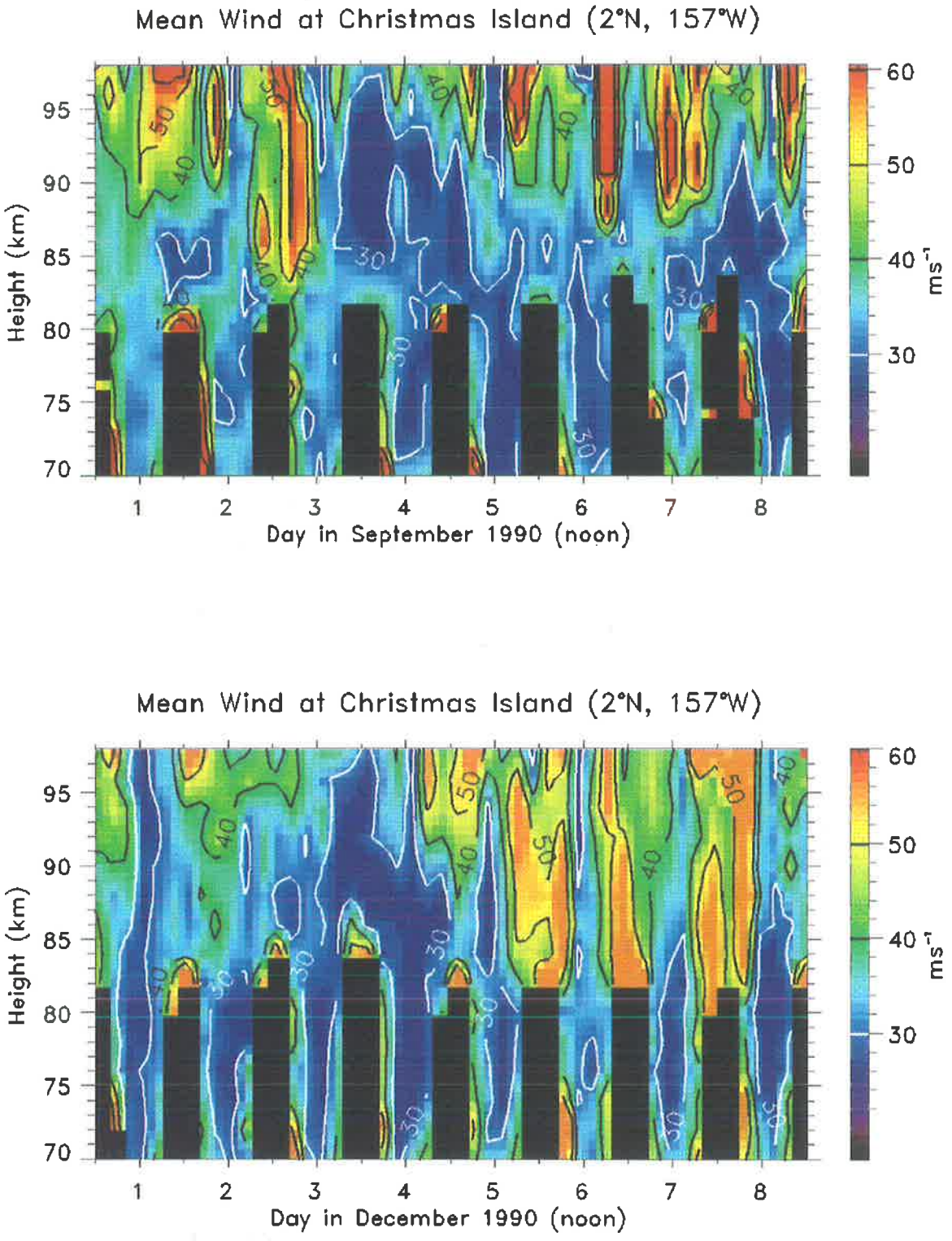

Figure 10.15: Four–hourly mean wind speed at Christmas Island over one week during September (top) and December (bottom) 1990.

ms^{-1} are observed at heights of 76–90 km. In comparison, during the night of the $21^{st}/22^{nd}$ the winds are only of the order of 60 ms^{-1}.

During June, the wind magnitude is not as structured although a quasi–diurnal variation is present. However, it is not as convincing as that observed in March, and its range is smaller, varying between 20–60 ms^{-1}. The maximum winds are still, however, centered around night–time. In September, the wind magnitude range is similar to that in June, with it varying between 20–60 ms^{-1}. The contours are more structured than those in June, although there are times when a diurnal variation is completely absent, e.g. the period of 3^{rd}–5^{th} September. During December, the magnitude of the winds is weakest, varying between 20–55 ms^{-1}. A diurnal variation is observed from the 5^{th}–8^{th}, with maxima occurring at night–time.

10.5 Spaced–antenna parameters

As in the previous chapters, the various full correlation analysis parameters will be presented in this section, with emphasis placed on their short–term temporal and altitude variation for various times of the year. For easier comparison of the four time periods, all of the data presented as image–contour plots share a common colour loading. That means that the values represented by a particular colour in one time period are the same as those presented in another.

Fading times

Figures 10.16 (top and bottom) and 10.17 (top and bottom) are image–contour plots of the four–hourly mean fading times for March, June, September, and December respectively, in the 70–90 km range calculated by the full correlation analysis. Generally the fading time falls within the 1.0–3.5 seconds range.

Initial investigation shows that the fading time in all four months generally decreases with increasing height. Above 90 km, the fading times are generally less than 1.5 seconds, and even less than 1.0 seconds in March. However, the minimum fading times are interspersed with sharp local maxima. Below 90 km while all four months show an increase in fading time with

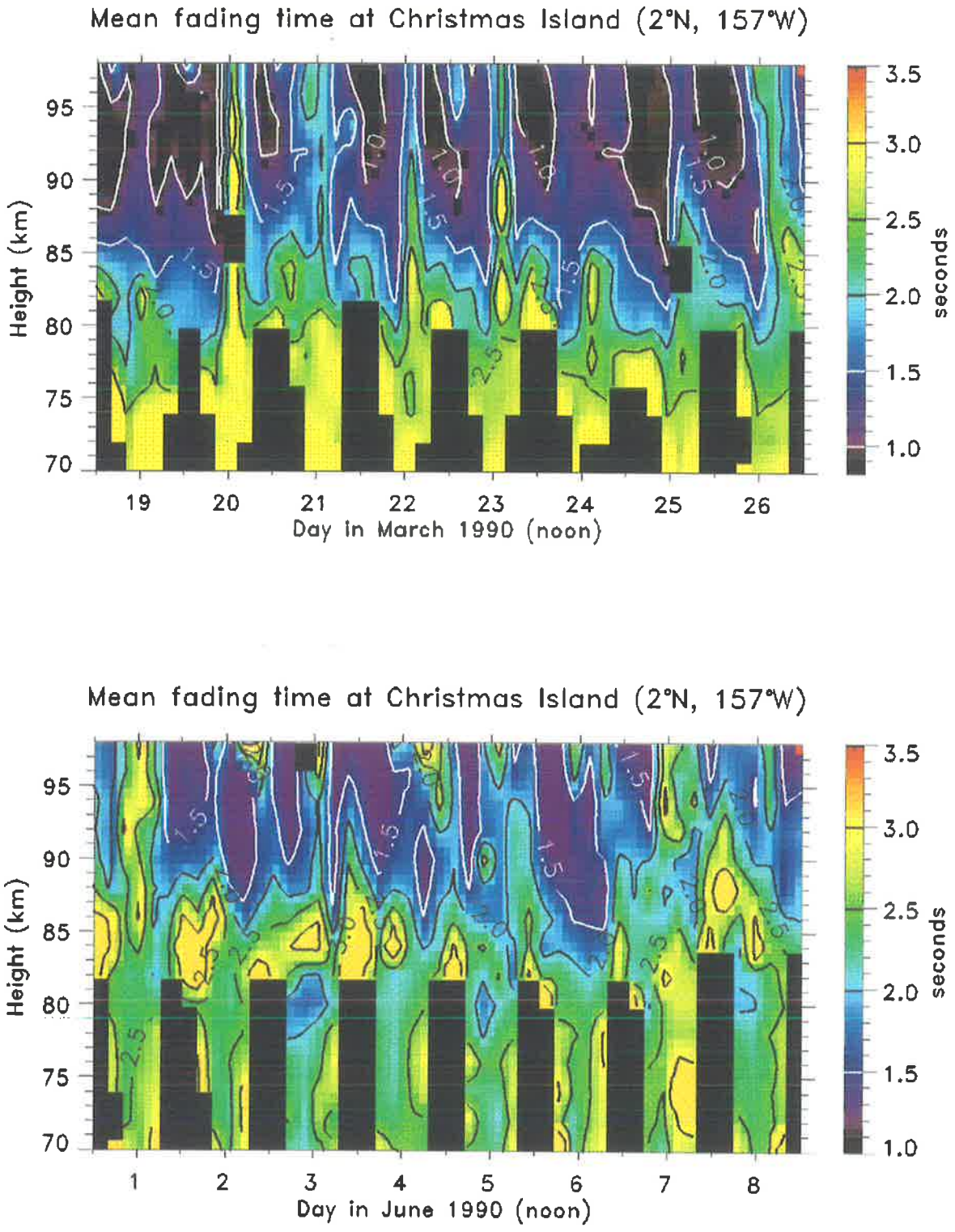

Figure 10.16: Four–hourly mean fading time (seconds) at Christmas island, during one week in March and June, 1990.

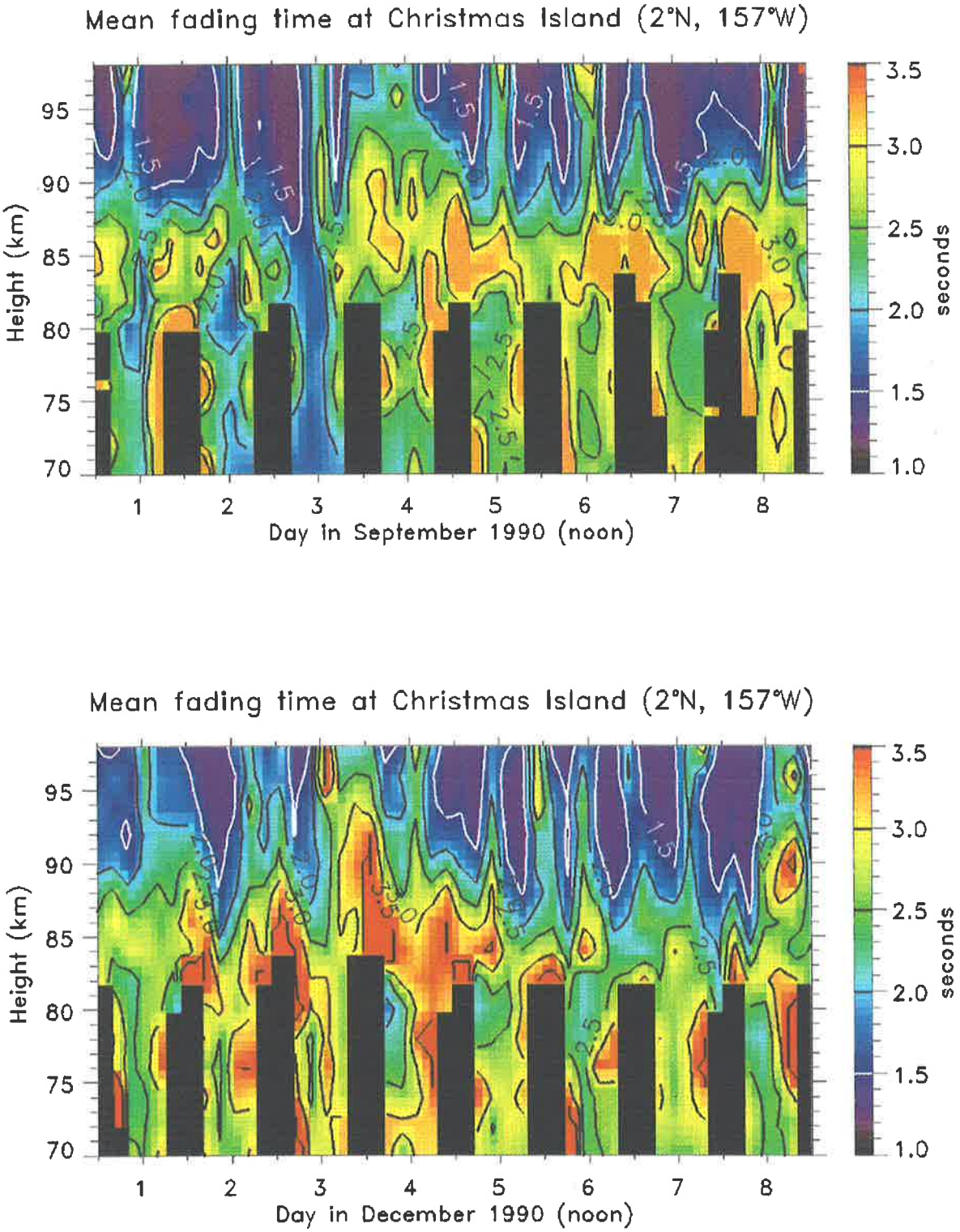

Figure 10.17: Four-hourly mean fading time (seconds) at Christmas island during one week in September and December, 1990.

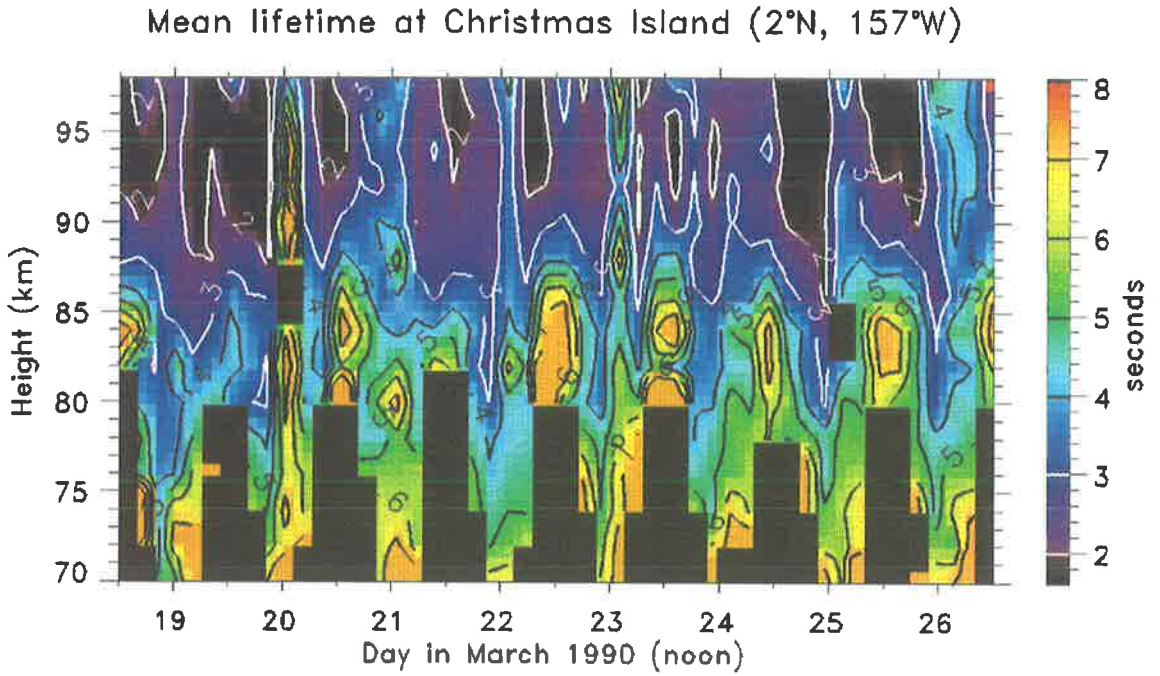

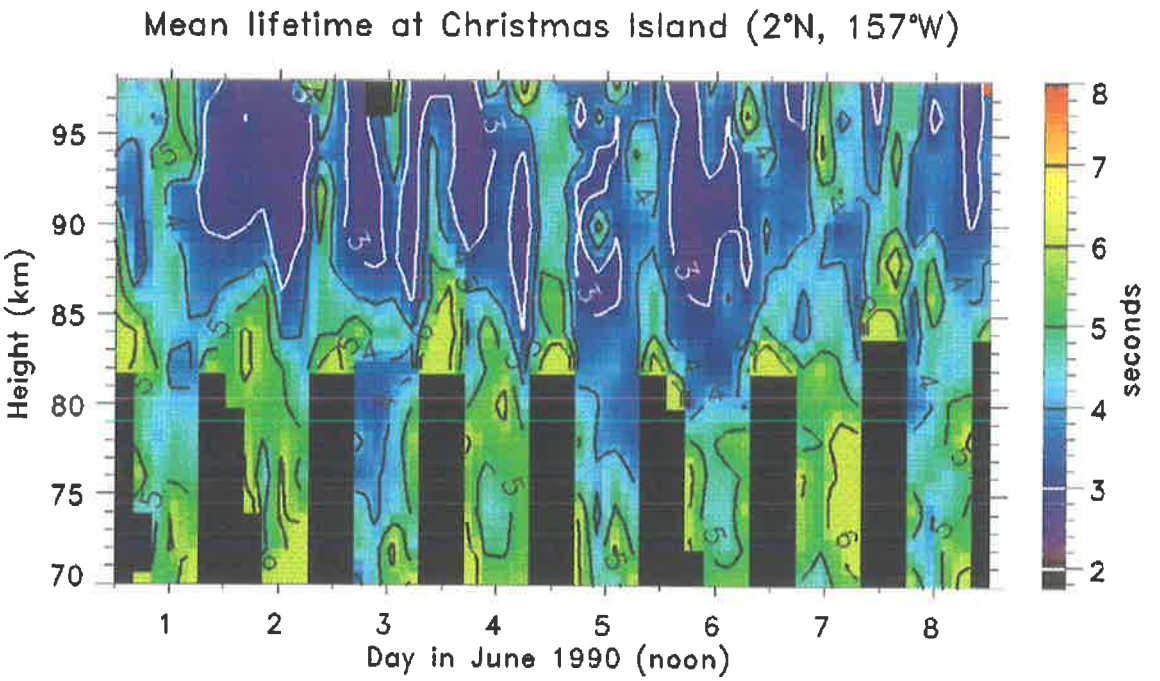

Figure 10.18: Four–hourly mean lifetime (seconds) of ground pattern at Christmas Island during one week in March and June, 1990.

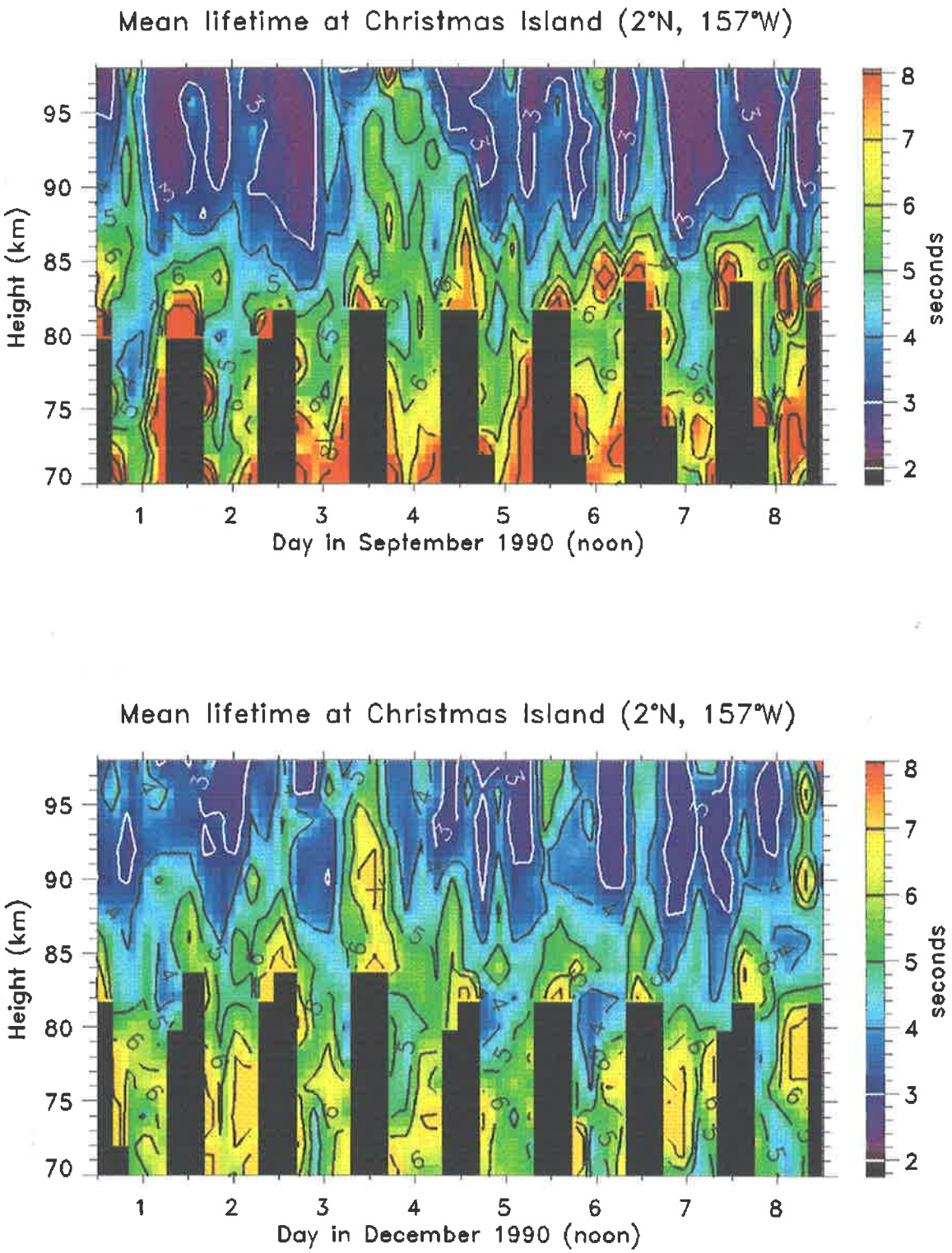

Figure 10.19: Four–hourly mean lifetime (seconds) of ground pattern at Christmas Island during one week in September and December, 1990.

decreasing height, the rate of increase and the temporal variation varies between the different months sampled.

In March, the fading time below 80 km is generally constant, and is above 2.5 seconds. June fading times at this height range are slightly smaller and show a diurnal variation with larger fading times occurring at night–time. The lack of night–time data below 80 km, however, does not allow a firm conclusion to be reached. In September and December, the same behaviour is noted with several differences. Firstly, the maximum fading times are longer, around 3.0 seconds in September and 3.5 seconds in December. Secondly, the temporal variation is not as cleanly structured.

Between 80–90 km the fading times between the four time periods exhibit quite different behaviour. March shows a diurnal variation with strong but very narrow maxima of more than 2.5 seconds, which generally occur at noon. In June, maxima are also observed, but occur at night–time, and are slightly larger and persist for longer times. The increase and broadening of the night–time maxima carries on through both September and December, with fading times in excess of 3.5 seconds observed during December. The large fading times found at lower heights are in step with the rejection criteria results discussed earlier. Below 80 km the percentage of data rejected solely due to long fading times exceeded at times 30%, and this percentage dropped very quickly to only a few percent above 90 km.

At times though, large fading times are observed during large mean winds. This is interpreted as being due to the increased specularity of the scatterers, and is reflected in larger values of θ_s. This issue will be considered shortly.

Lifetime of ground pattern

The lifetimes of the ground patterns are shown as image–contour four–hourly plots in figures 10.18 (top and bottom) and 10.19 (top and bottom) for March, June, September, and December respectively. The lifetimes are seen to vary between 2.0–8.0 seconds. The minimum of around 2.0 seconds is observed above 90 km during March while the maximum of around 8.0 seconds occurs around and below 80 km at night–time in September.

The lifetimes are seen to generally decrease with increasing height. Superimposed on this height dependence is a diurnal variation which is quite evident between 80–85 km. The maximum lifetimes occur at night and reach their maxima relatively quickly. For example, on the $22^{nd}/23^{rd}$ March, the lifetimes increased from less than 4.0 to more than 6.0 seconds in the space of a few hours, although the subsequent decrease occurred over a longer time period. During September, the lifetimes are about 8.0 seconds during the night, and decrease to nearly 4.0 seconds during the day. This is a dramatic change, and indicates that the dynamical activity in the mesosphere is quite variable. Another important feature to note is the range of lifetime values encompassed within each time period. During June and December, the lifetimes vary by about 4–5 seconds, while in March and September this range is larger, about 5–6 seconds.

The lifetimes measured by the full correlation analysis have the effect of the mean wind motion removed, unlike those of the fading times. They therefore, ideally, are an indicator of the random change within the pattern. It could be argued that this is not the case, for the mean wind motion might still "creep" into the measurements. However, the data above show that this is clearly not the case. Take for example the month of September. We compare three variables, the mean wind speed, fading times, and lifetimes [figures 10.15, 10.17, 10.19]. While the changes in the fading time are seen to mirror those of the wind magnitude, the same is not true for the lifetimes. Generally, the behaviour of the lifetimes are similar to those of the fading times, but there are large differences at times. On the 3^{rd} September, below 80 km, while the fading times exhibits a local minimum of less than 2.0 seconds, the lifetimes are actually a maximum of nearly 8.0 seconds. Similar examples can be found at other times. During March $22^{nd}/23^{rd}$ and December $3^{rd}/4^{th}$, the fading times and lifetime show different temporal characteristics.

Pattern scale

Figures 10.20 (top and bottom) and 10.21 (top and bottom) are image–contour four–hourly means of the ground diffraction pattern scale as a function of height and time. The pattern scales vary between 200–500 m, although most of the time fall in the 250–450 m range. The

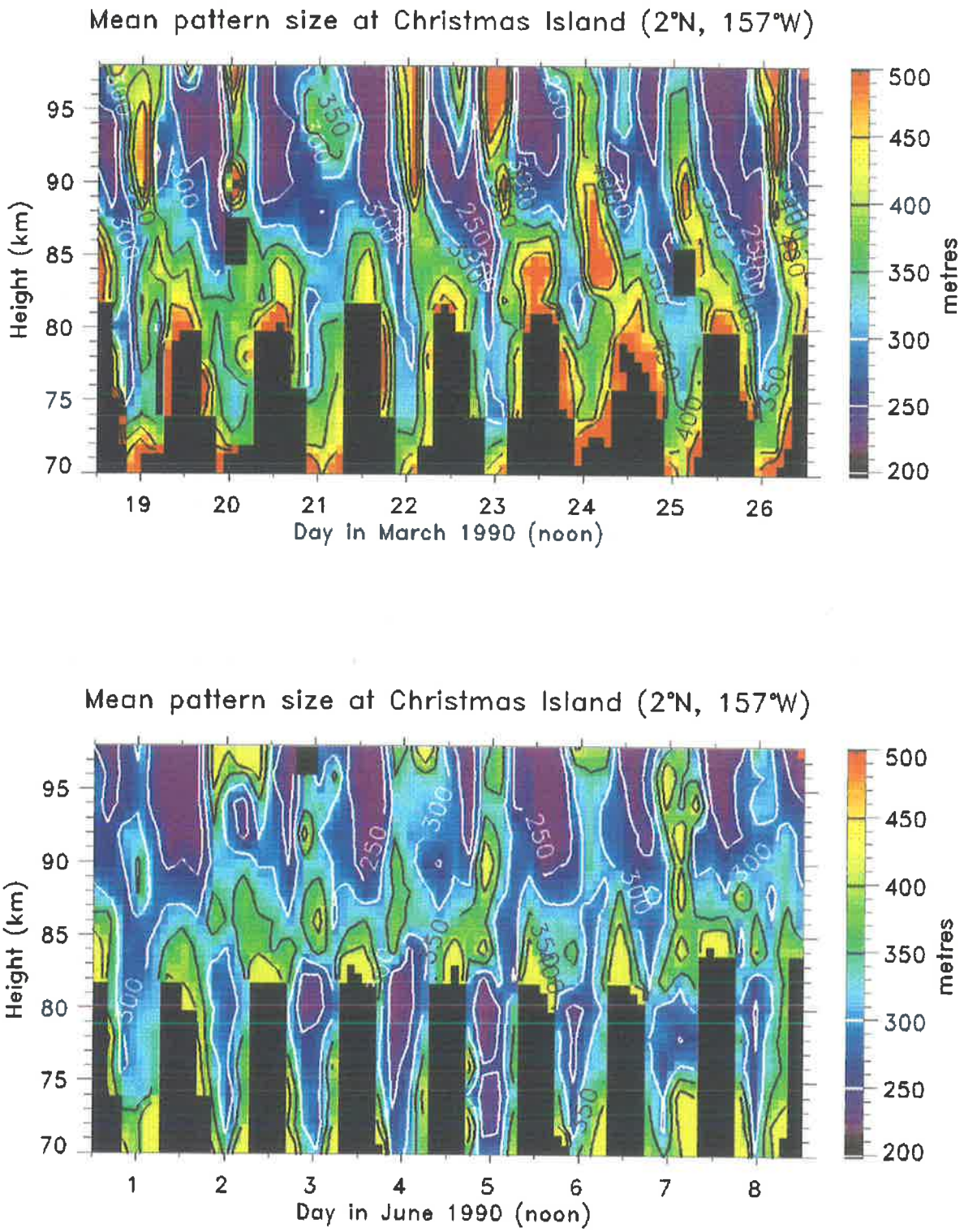

Figure 10.20: Four–hourly mean ellipse size (seconds) for one week at Christmas Island, during March and June, 1990.

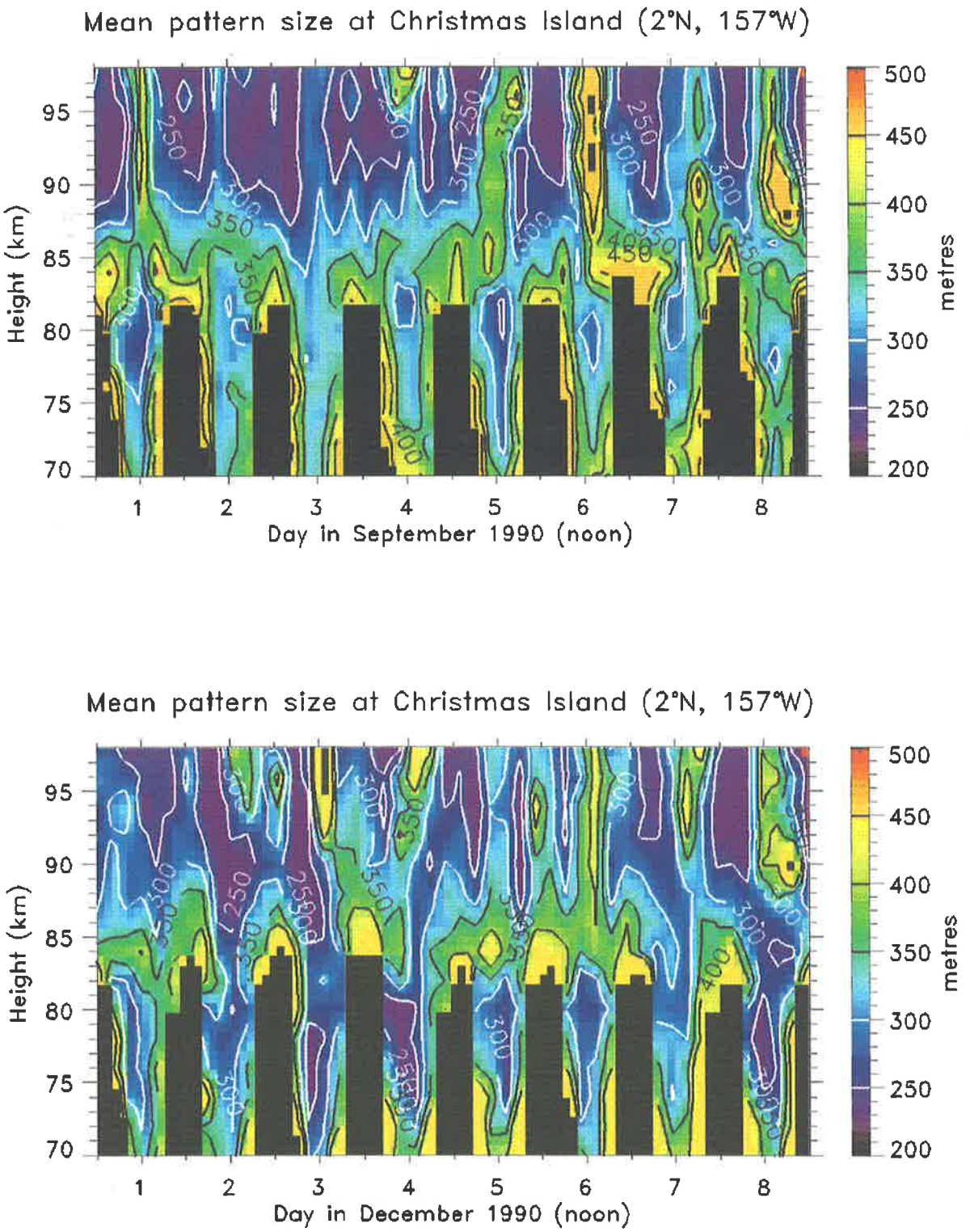

Figure 10.21: Four–hourly mean ellipse size (metres) for one week at Christmas Island, during September and December, 1990.

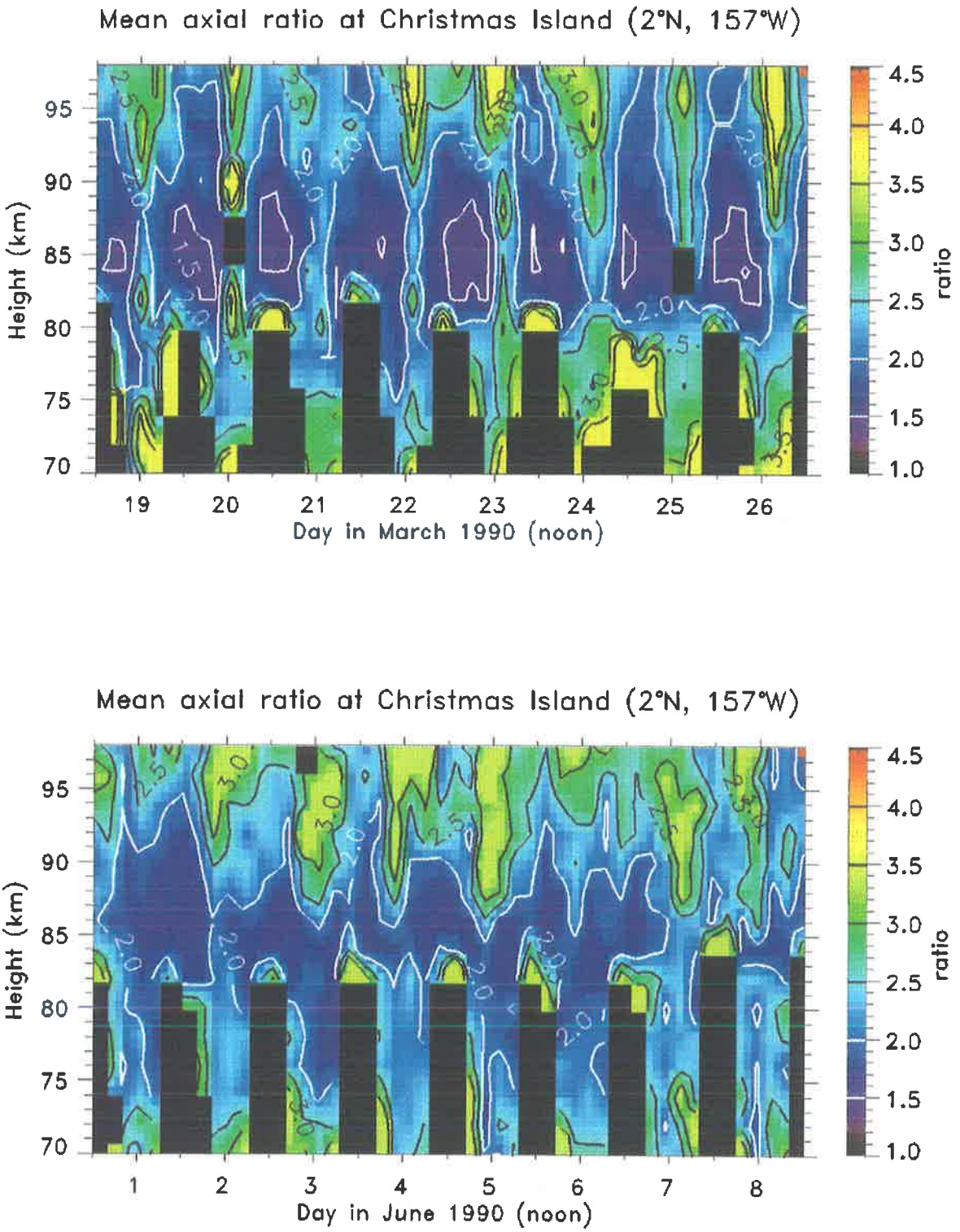

Figure 10.22: Four–hourly mean pattern ratio for one week at Christmas Island, during March and June, 1990.

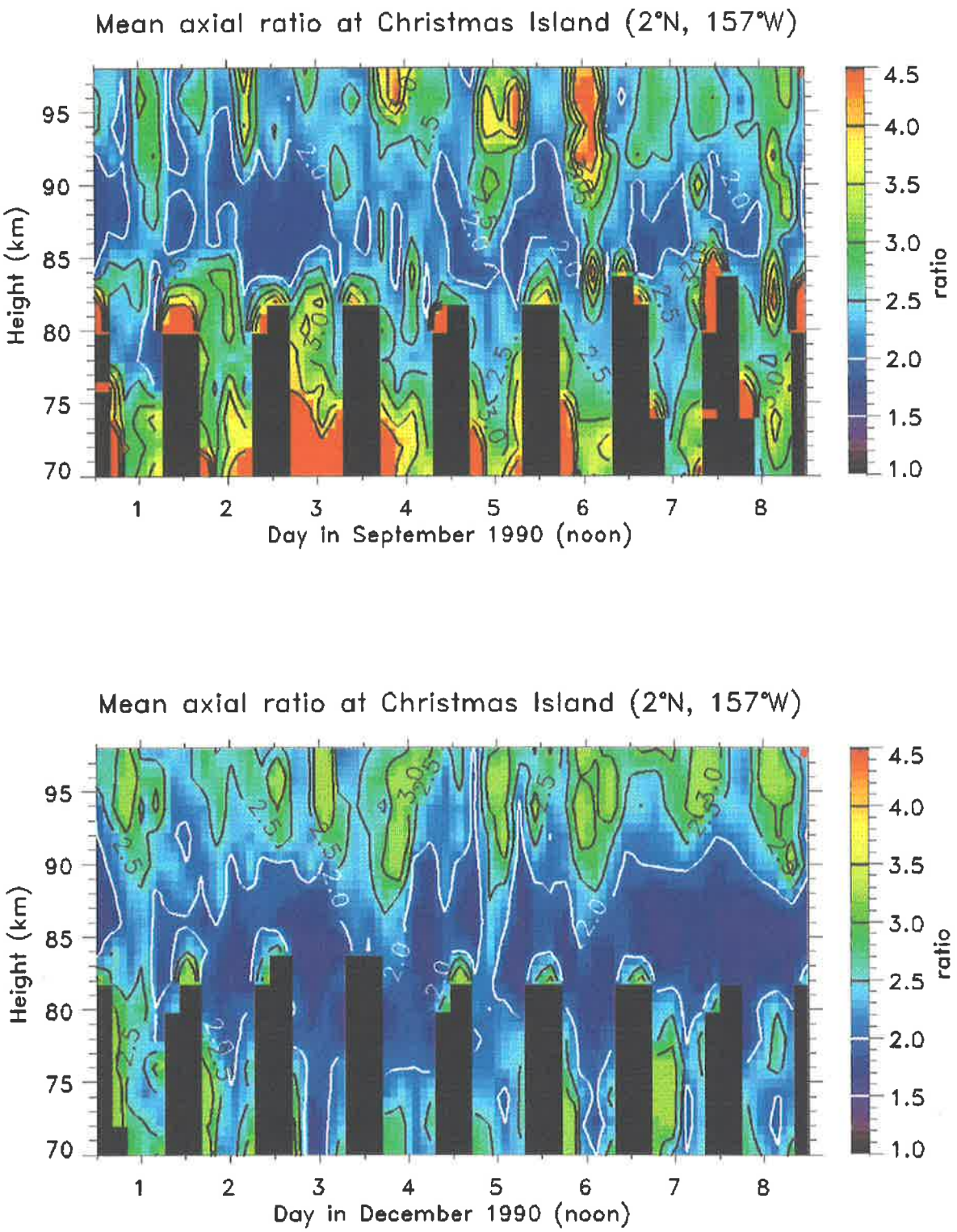

Figure 10.23: Four–hourly mean pattern ratio for one week at Christmas Island, during September and December, 1990.

maximum pattern scales are observed in March.

Unlike the fading and lifetimes a clear diurnal variation in the pattern scale is observed in all of the time periods. However, the time of the daily maximum seems to be dependent on height. For example, while between 80–85 km the maximum scales occur around midnight, the time of maxima occurs earlier at higher heights, so that above 90 km the maximum generally occurs at noon. This can be observed in all the data, but is extremely clear in March.

With reference to the ALOHA–90 campaign, it is interesting to note that during $24^{th}/25^{th}$ March when large gravity–wave activity was observed in both the troposphere and mesosphere, the pattern scale was extremely large, around 500 m. In addition, these large values persisted over the whole night.

Pattern axial ratio

The pattern axial ratios calculated for the four time periods are shown as image–contour four–hourly means in figures 10.22 (top and bottom) and 10.23 (top and bottom). Above 90 km, the axial ratios show a clear diurnal variation with the largest ratios occurring around noon. This can be easily seen on the 22^{nd}, 23^{rd} and 24^{th} March, and especially so on the 4^{th}, 5^{th} and 6^{th} September. Between 85–90 km the mean axial ratio varies around 2.0 with no clear diurnal variation except during March when sharp maxima are observed at noon.

At around 80 km, a night–time maximum is observable during all months. This maximum occurs relatively quickly, with axial ratios nearly doubling over a few hours. Below 80 km, it appears that larger axial ratios occur during night–time. It is also below this height that the largest values of axial ratio are observed in September. As with the pattern scale, March and September values of axial ratio span the biggest range, increasing at times by a factor of 3. from 1.5 to 4.5. December is the least variable month, with the axial ratios ranging from just under 2.0 to about 3.0.

On March $21^{st}/22^{nd}$, during the ALOHA–90 campaign the axial ratios at 82 km are more than 3.5 while on the $24^{th}/25^{th}$ they are less than 2.0. However, below this height, the axial ratios on the $24^{th}/25^{th}$ increase to more than 3.5, with this large values persisting for nearly 10

hours.

It is also interesting to closely examine the 3^{rd}–4^{th} September. It was found in the previous sections that below 80 km the fading times are small, while the lifetimes are large. The pattern scale was also found to be relatively small. However, the axial ratios at this height are extremely large, greater than 4.0. So we have a situation where the ground diffraction pattern, and thus the partial reflection scatterers are small, but extremely stable and elongated.

10.6 Aspect sensitivity

The aspect sensitivity of the scatterers was calculated by both the spectral–width and spatial–correlation methods discussed earlier. The spectral-width results are shown as image–contour plots in figures 10.24 (top and bottom) and 10.25 for March, June September and December respectively, while the spatial–correlation results, which follow the same format, are shown in figures 10.26 and 10.27. We will discuss the spectral–width results first.

During March, θ_s varied between ~12–25°, while in June, September, and December θ_s values were not only higher, but spanned a bigger range of between 15–32°. All four time periods exhibit a similar height structure, with smallest values of θ_s occurring between 80–90 km. Values of θ_s are larger both below and above this height range, but much more so above 90 km.

Superimposed on this height variation is a temporal variation where, in the height range of 80–90 km, a diurnal variation is quite evident, especially so in March and December. In March, values of θ_s vary between around 12° at night, to more than 20° during the day, although the night–time minima persist for more than 12 hours. During the other three times sampled here, a diurnal variation is also observed, albeit not as strong. The diurnal variation is also hinted at the lower height range of 70–80 km, although the lack of night–time data allows no firm conclusion.

Above 90 km, however, the structure seems a lot more complicated. At times a diurnal variation is quite clear, for example throughout all the December data. During other times

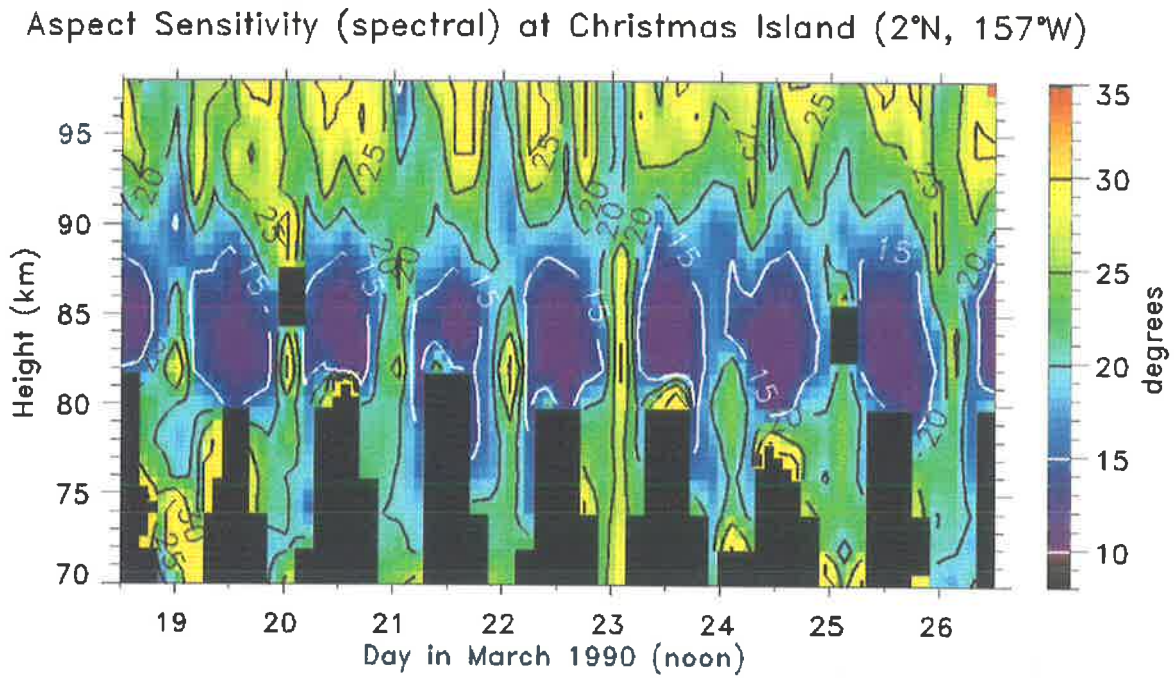

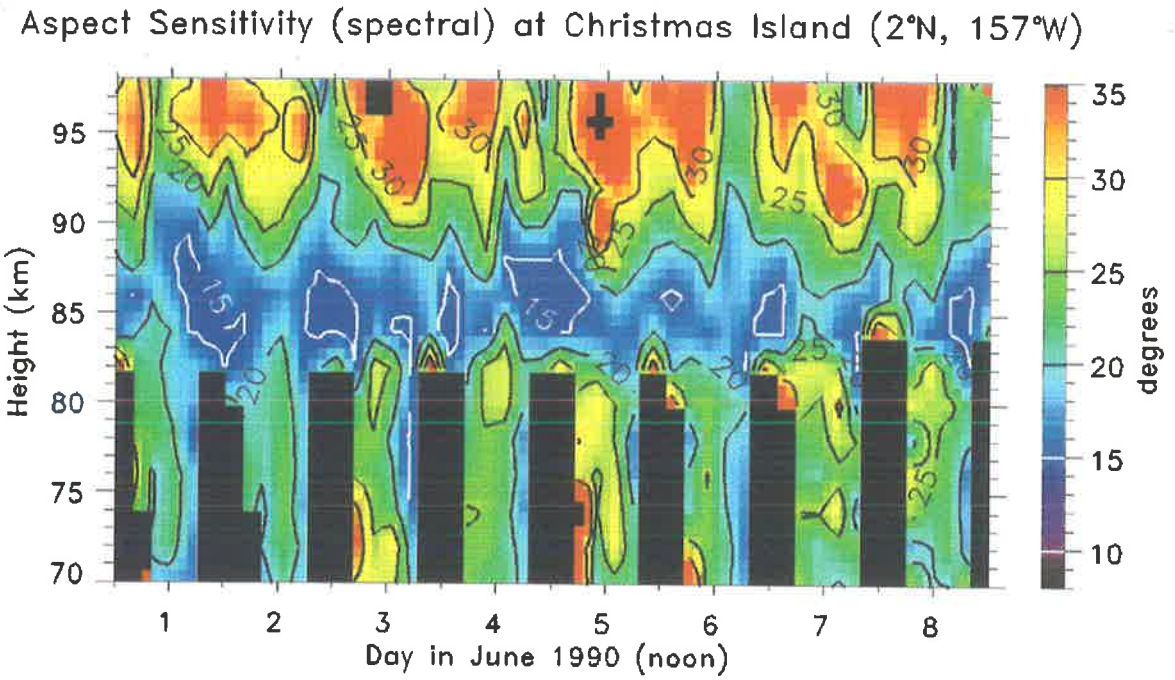

Figure 10.24: Four–hourly mean aspect sensitivity (spectral) for one week at Christmas Island, during March and June, 1990.

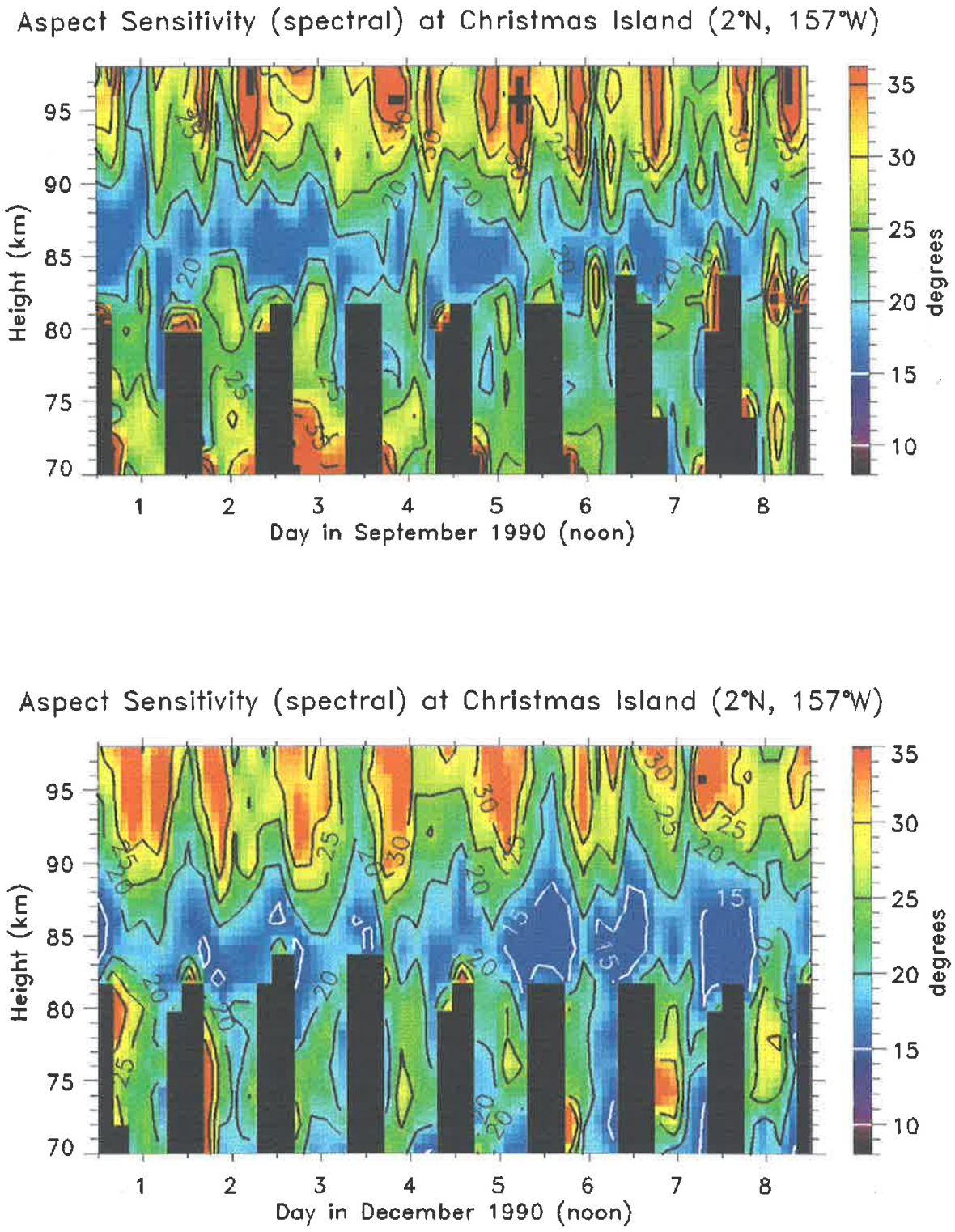

Figure 10.25: Four–hourly mean aspect sensitivity (spectral) for one week at Christmas Island, during September and December, 1990.

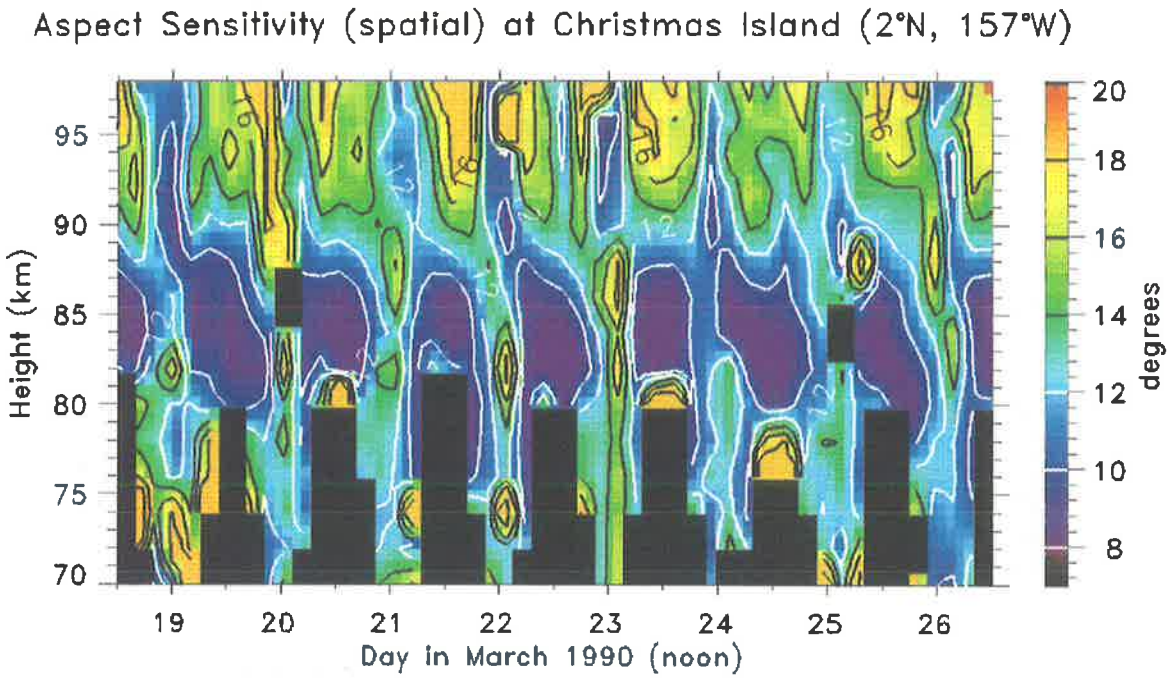

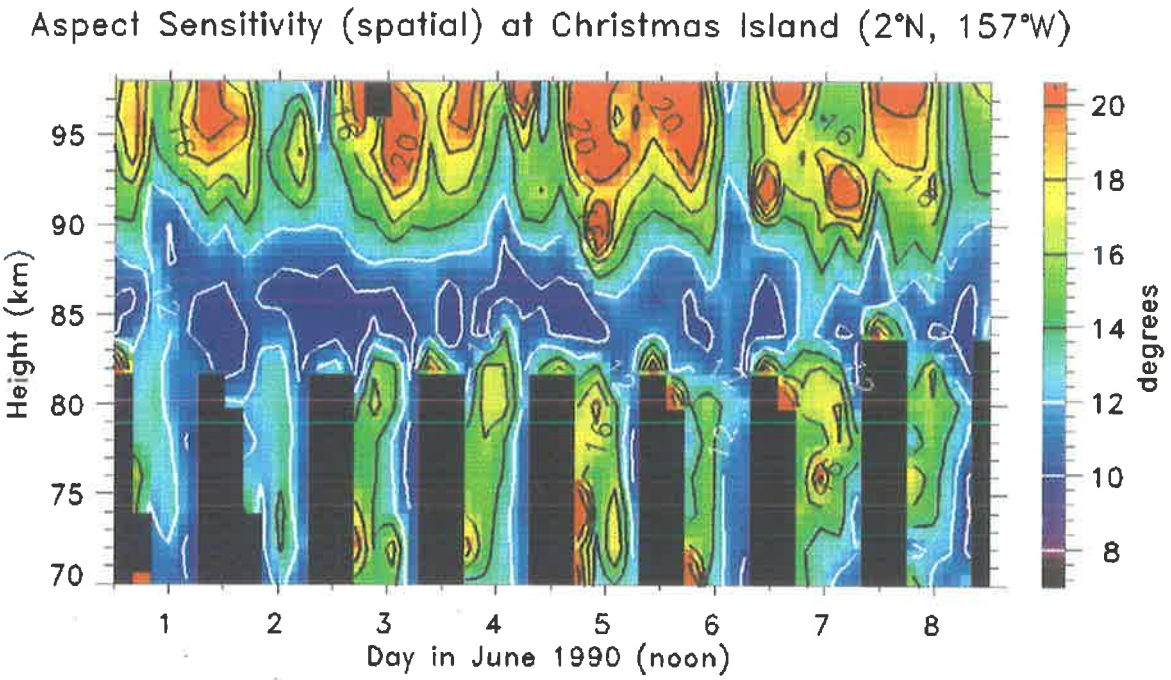

Figure 10.26: Four–hourly mean aspect sensitivity (spatial) for one week at Christmas Island, during March and June, 1990.

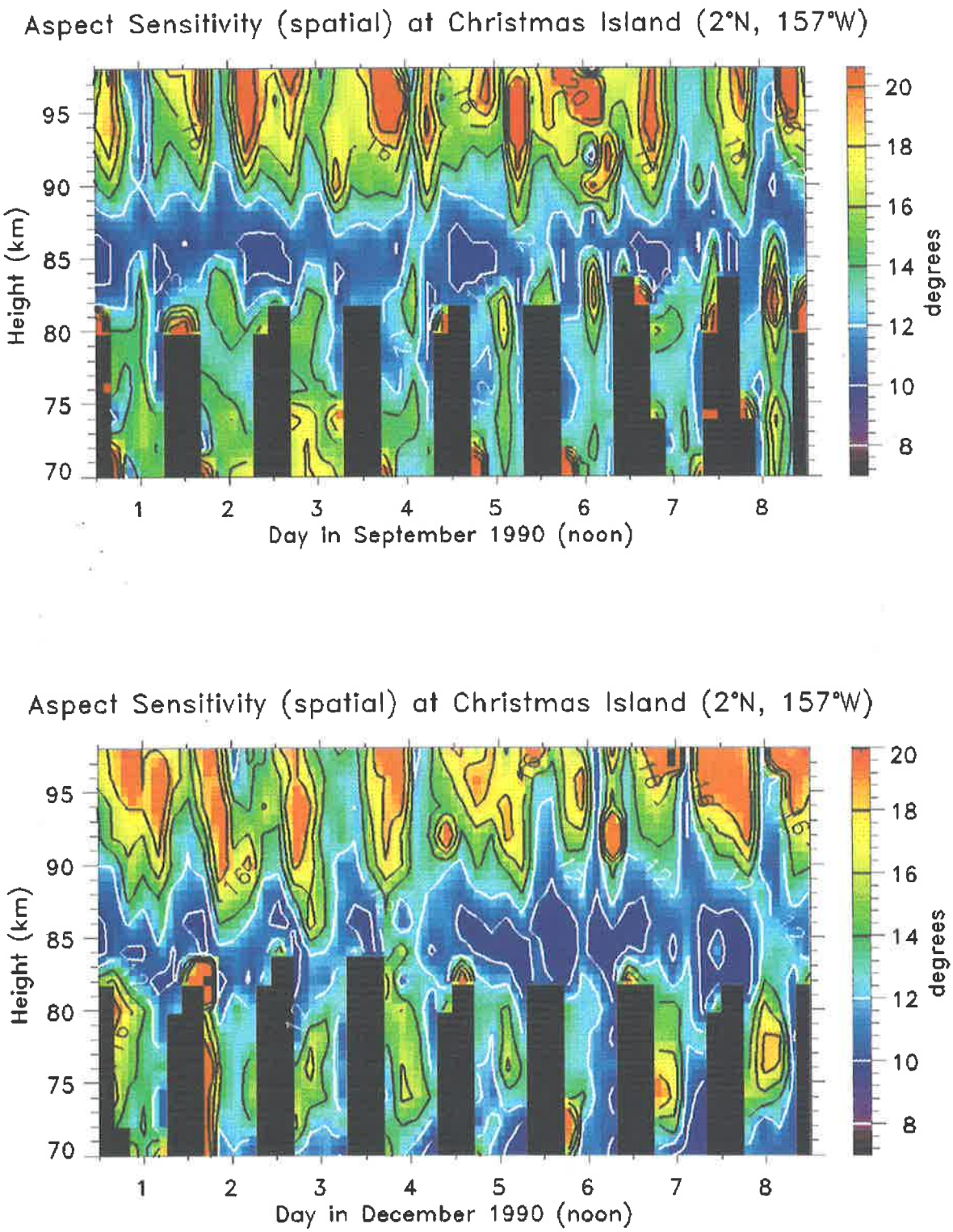

Figure 10.27: Four–hourly mean aspect sensitivity (spatial) for one week at Christmas Island, during September and December, 1990.

however, although maxima and minima are observed, there is no clear evidence of any temporal structure. In addition, the June data seems to suggest a two–day peridiocity.

When examining values of θ_s calculated by the spatial–correlation method, the gross features are consistent with those calculated by the spectral–width method, but there are some differences. One major difference is the absolute range of values of θ_s, which vary from less than 8° to just over 20°; the values are typically much smaller than those measured by the spectral–width method. This is not surprising, since not only does the spectral–width method rely on the two–dimensional geometry of the diffraction patterns' orientation, it is also affected by the turbulent energy dissipation rate. This is in contrast to the spatial–correlation method uses the area of the pattern ellipse. As discussed earlier, in the case where the pattern's semi–major axis is orthogonal to the mean wind direction, the fading time measured will be smaller than if the semi–major axis is parallel to it. This then makes calculations of θ_s dependent on the orientation of the diffraction ellipse. The two–dimensionality of the scatterers will be discussed shortly. For now, the point of interest remains the temporal variation of θ_s.

Another difference is observed in March, where contours of θ_s in the spatial–correlation calculations propagate downwards between 95 and 80 km at a rate of about one km per hour. This behaviour seems absent in the spectral–width data, but is in step with the pattern scale measurements.

10.7 Horizontal correlation lengths

The length–to–depth (L/h) ratios of the scatterers were calculated from the above θ_s values. They are shown as image–contour four–hourly plots in figures 10.28 (top and bottom) and 10.29 (top and bottom) for the spectral–width method, and in figures 10.30 and 10.31 for the spatial–correlation data. As before, the data are a function of height and four eight–day periods in March, June, September, and December.

The L/h ratios calculated by the two methods are generally very similar although, like the θ_s values above, there are two characteristic features. One of these is the absolute range of values

that L/h encompasses, between 1.0 and 3.5 in the spectral–width case, and between 2.0 and 4.5 in the spatial–correlation case. This can be attributed to the effect of the energy dissipation rate on the spectral–width results. The other difference between the two methods is seen in March when the spatial–correlation method produces L/h ratios which have contours showing a downward propagation from 95 to 80 km.

In general though, the two methods are quite complementary. Above 90 km the L/h ratios are quite small, less than 1.5 for the spectral–width data and around 2–2.5 for the spatial-correlation data. At this height, the scatterers are thus basically isotropic in their length–to–depth ratios, although when examining the pattern axial ratios, one can see that they are quite anisotropic in the horizontal plane. This will be examined more in the following section.

Between 80 and 90 km, the partial–reflection radio wave scatterers at Christmas Island exhibit large L/h ratios which suggests strong anisotropy. This anisotropy is also found to be strongly diurnal in March, when the values of L/h at night are about double those measured during the day (1.5–3.5 in the spectral–width data and 2.5–4.5 in the spatial–correlation data). At other times of the year the diurnal variation is not as evident, although the maximum L/h ratios are still found within this height range (about 2.5 in the spectral–width case and 3.5 in the spatial–correlation case).

Below 80 km, the L/h ratios decrease again, but not as much as those above 90 km. Some diurnal variation is hinted at but with no night–time data no conclusion can be drawn. In general the L/h ratios are around 2.5–3.5 in the spatial–correlation case and 1.5–2.0 in the spectral–width case.

During the time of the ALOHA–90 campaign, the L/h ratios show a rapid increase around 80 km during the night. For example, on the $23^{rd}/24^{th}$ the spatial–correlation L/h ratios increase from less than 2.0 to over 4.5 within a space of just 2 km. On the night of the $24^{th}/25^{th}$ March, when strong wave–activity was reported, the L/h ratio is less than 2.0 below 80 km, and between 4.0–4.5 from 80–88 km. In addition, although the ratio decreases above 90 km, the minimum is not as severe as that found during the other days in March.

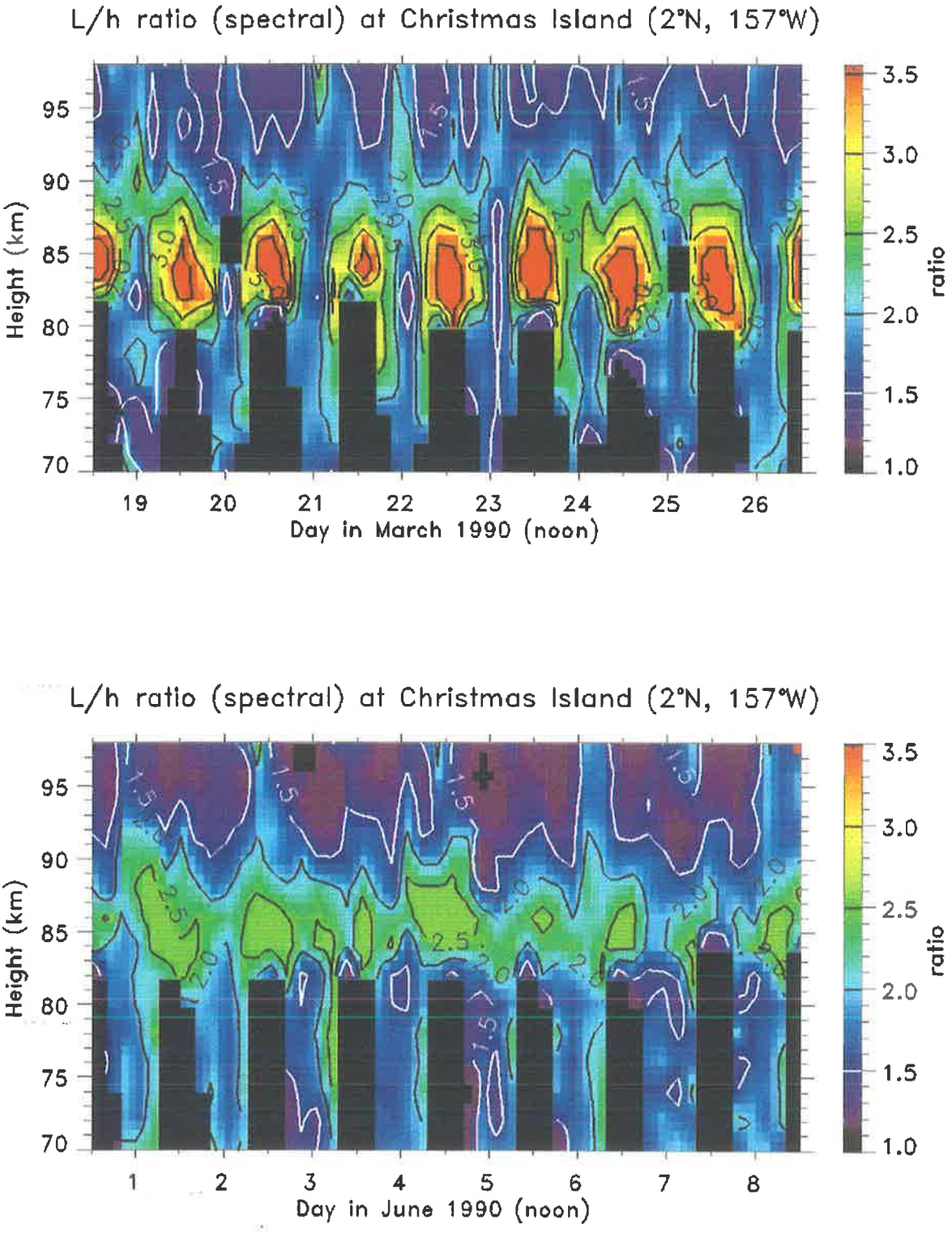

Figure 10.28: Four–hourly mean L/h ratios calculated at Christmas Island by the spectral–width method over one week in March and June, 1990.

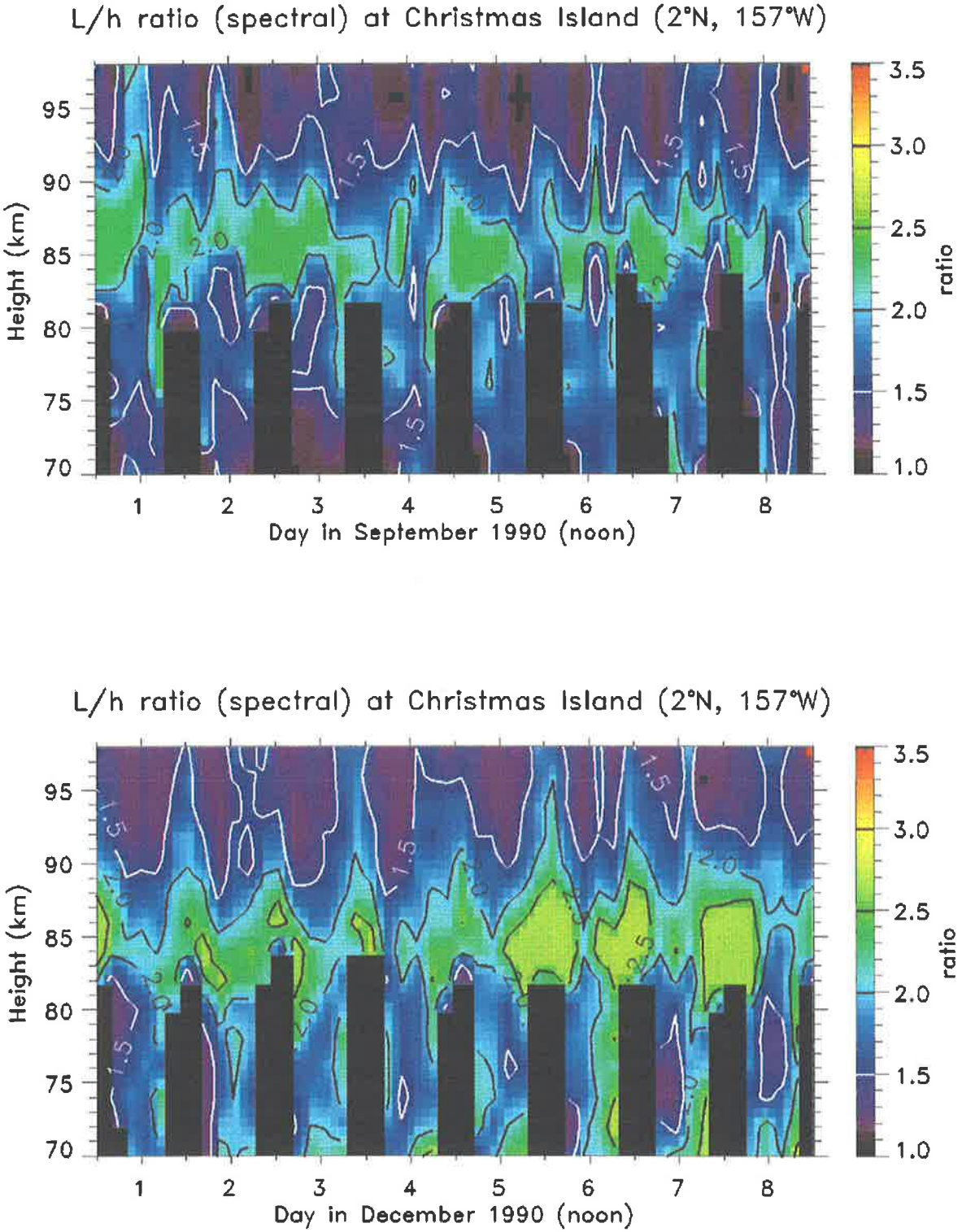

Figure 10.29: Four–hourly mean L/h ratios calculated at Christmas Island by the spectral–width method over one week in September and December, 1990.

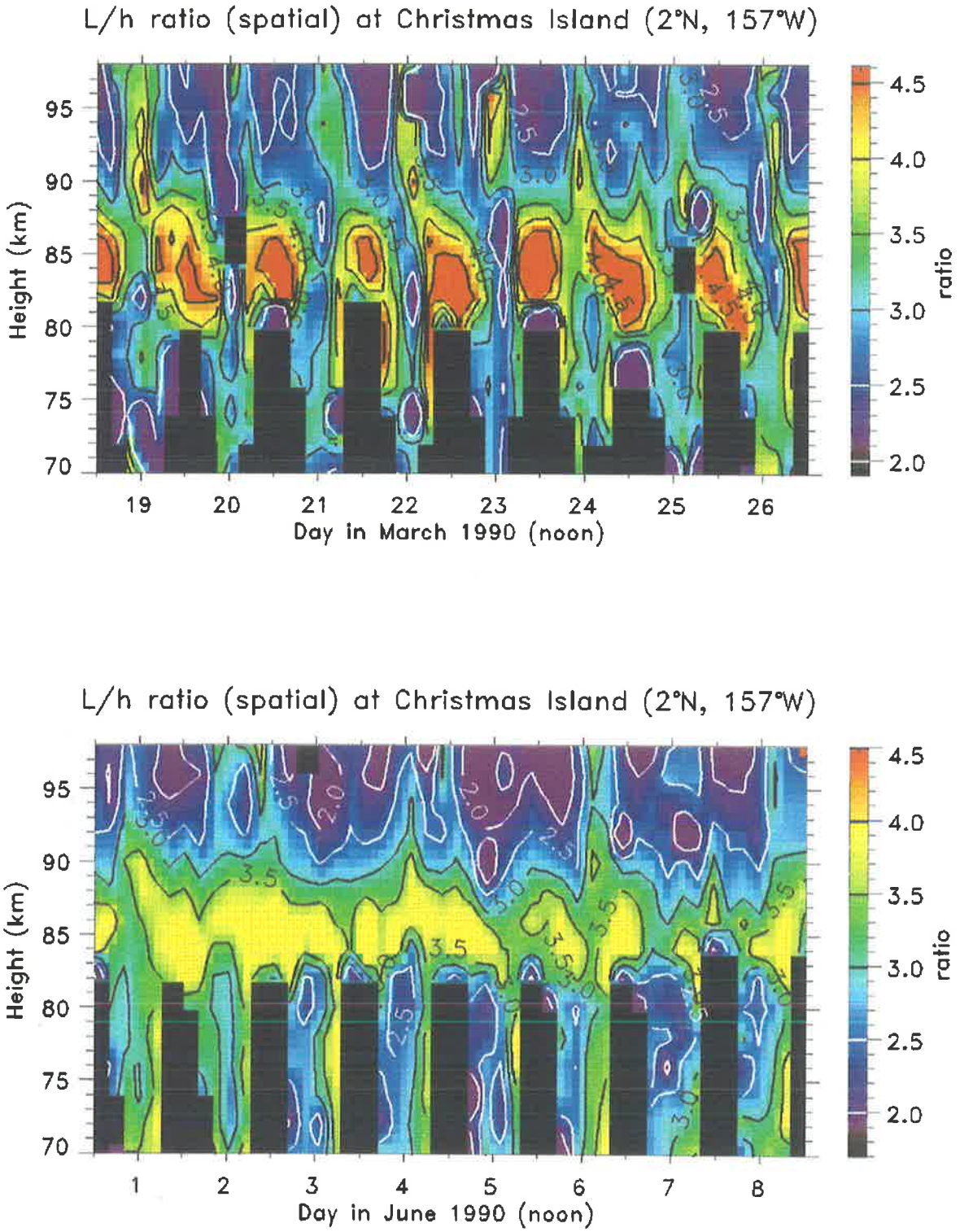

Figure 10.30: Four-hourly mean L/h ratios calculated at Christmas Island by the spatial-correlation method over one week in March and June, 1990.

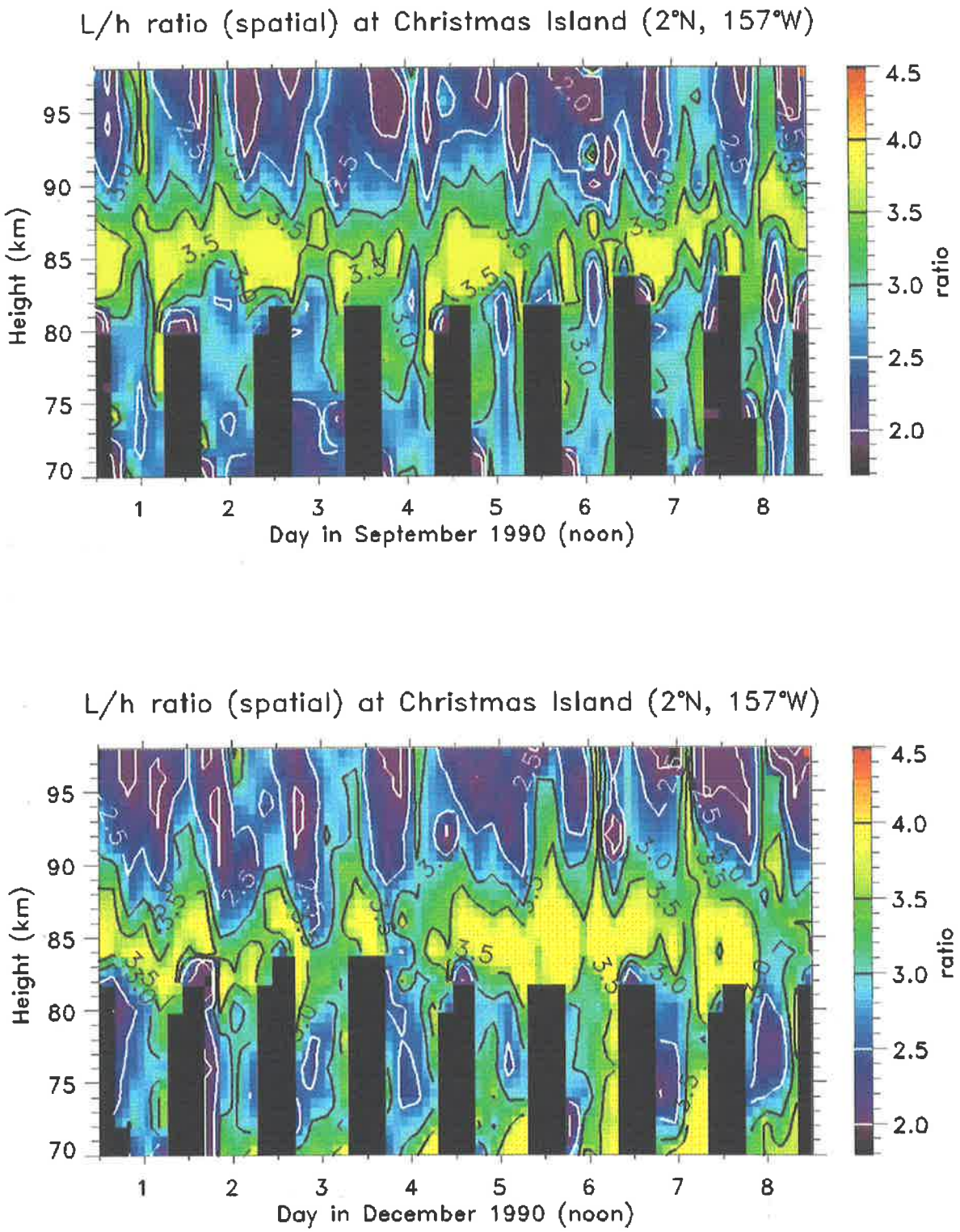

Figure 10.31: Four–hourly mean L/h ratios calculated at Christmas Island by the spatial–correlation method over one week in September and December, 1990.

10.8 Two–dimensional nature of the scatterers

The above results (which examined the length–to–depth ratio of the scatterers) clearly showed that the scatterers are anisotropic in their horizontal to vertical extent, varying from nearly circular to at times be greater than 4.5. However, the use of the ground diffraction pattern also allows us to examine the horizontal anisotropy of the diffraction pattern. The orientation of the ground diffraction pattern, its stability in direction and temporal variability both alone and with respect to the magnetic North and mean wind are investigated in this section.

Two–dimensional circular statistics are used in this analysis, and follow that of *Mardia* [1972]. The details are discussed in appendix C, and are the same as those used in the previous chapter. A vector whose mean unit length approaches 1.0 indicates that all the measurements are oriented in the same direction. Similarly, the standard deviation gives a feel to the spread of the measurements in actual degrees. The data were grouped into four–hourly periods for which a mean was constructed. The data point which deviated most from this mean was then rejected form the data sample, and a new mean re–computed. This was performed a total of four times. This resulted in spurious points being removed, and although some good data would have been rejected as well, the total percentage was quite small.

In this section, as mentioned earlier, we examine various angular characteristics of the pattern orientations like the mean pattern stability, mean orientation with respect to magnetic North, and its relationship with the mean wind direction. We start off, however, examining the stability of the pattern orientation.

Stability of the mean pattern orientation

The normalized mean length of the correlation ellipses for all axial ratios, as a function of height and time, and the corresponding circular standard deviations (in degrees), are shown as image–contour four–hourly mean plots in figure 10.32 (top and bottom) for March, while figures 10.33, 10.34, and 10.35 are for data in June, September, and December respectively. All the data share a common colour table, with the mean–lengths spanning 0.0–1.0, while the

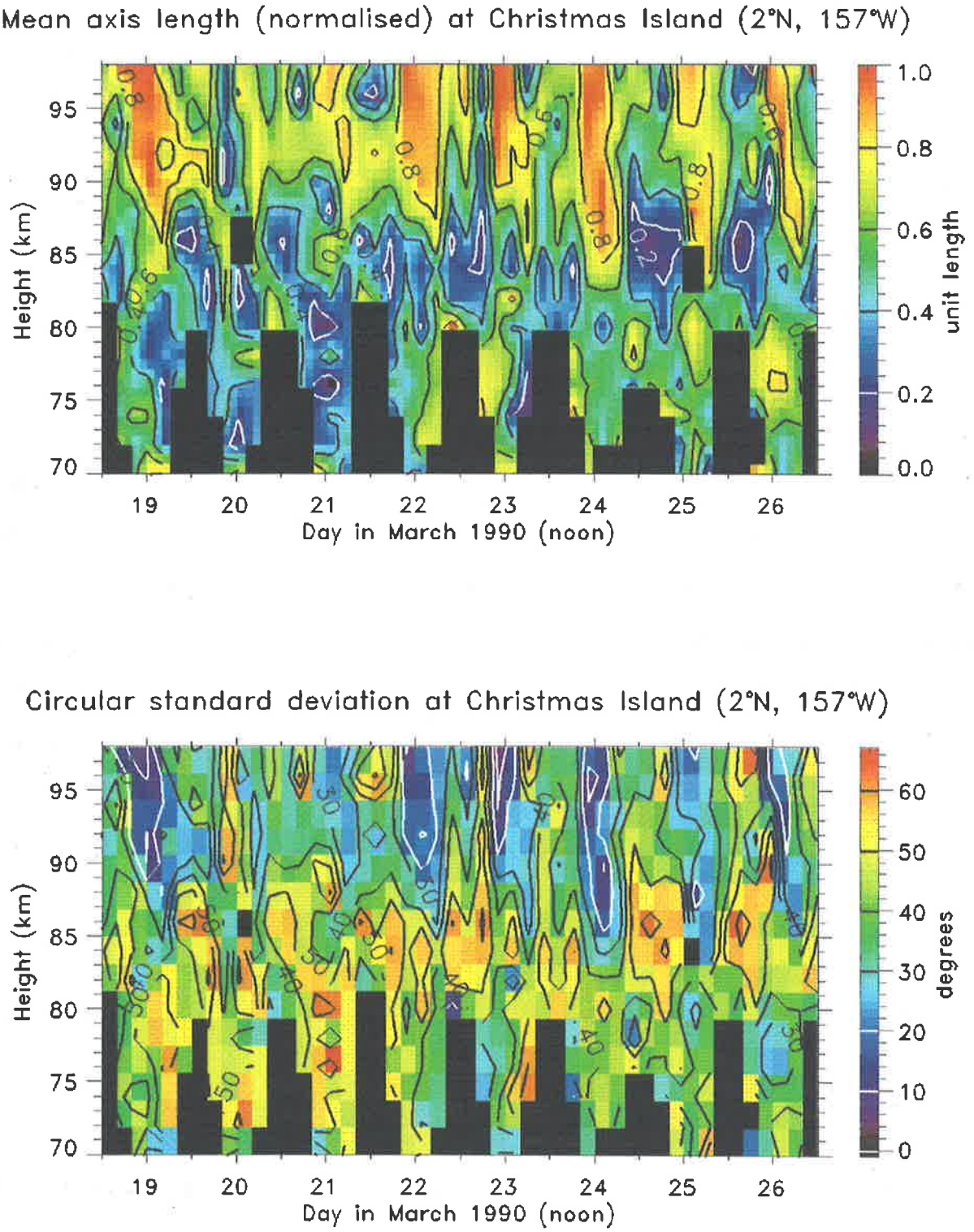

Figure 10.32: Four–hourly mean normalized lengths of the ground diffraction pattern for all axial ratios (top) and their circular standard deviation (bottom) for an eight–day period in March, 1990. The contours are the normalized length taking direction into account, while the standard deviation is in degrees.

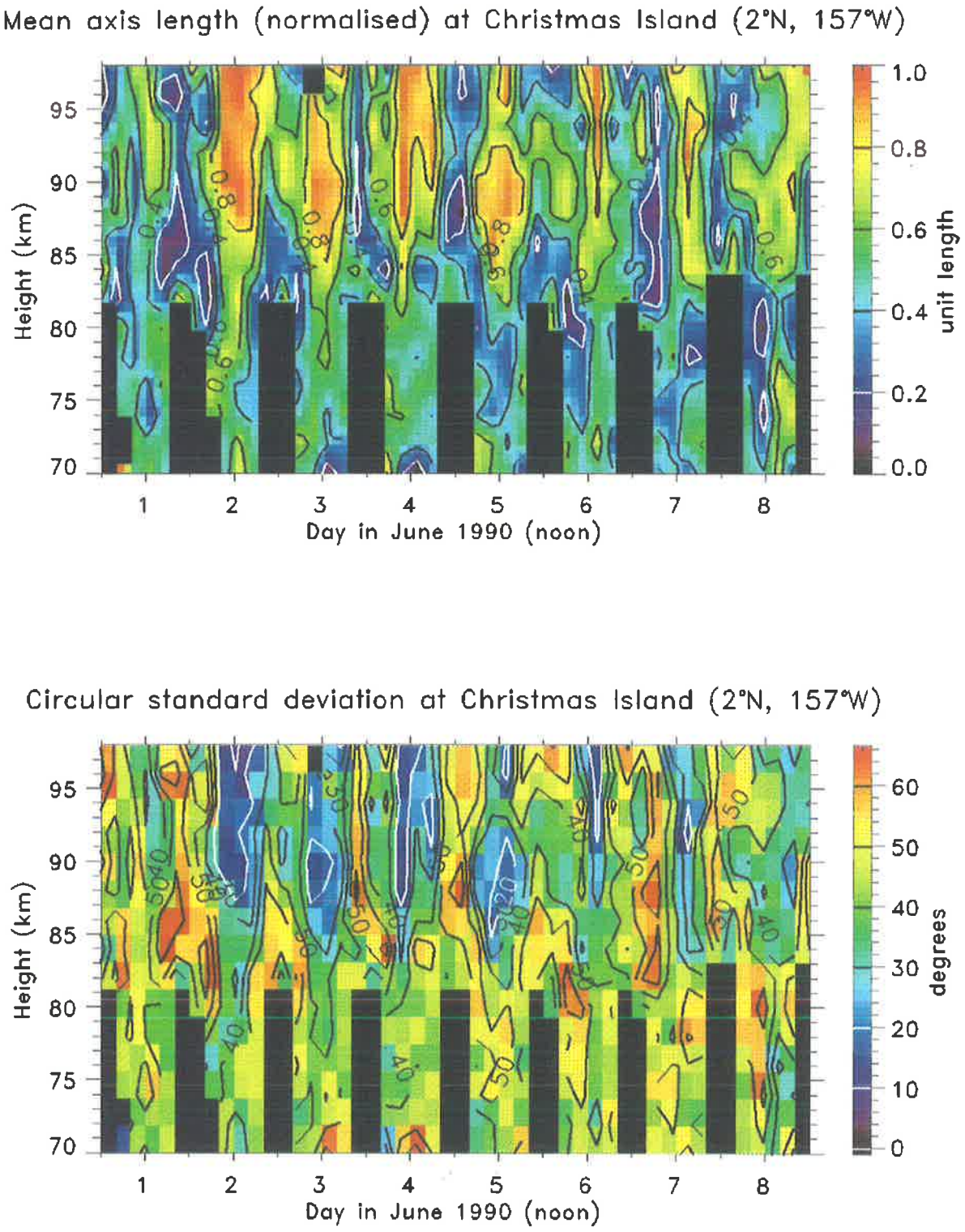

Figure 10.33: Four-hourly mean normalized lengths of the ground diffraction pattern for all axial ratios (top) and their circular standard deviation (bottom) for an eight-day period in June, 1990. The contours are the normalized length taking direction into account, while the standard deviation is in degrees.

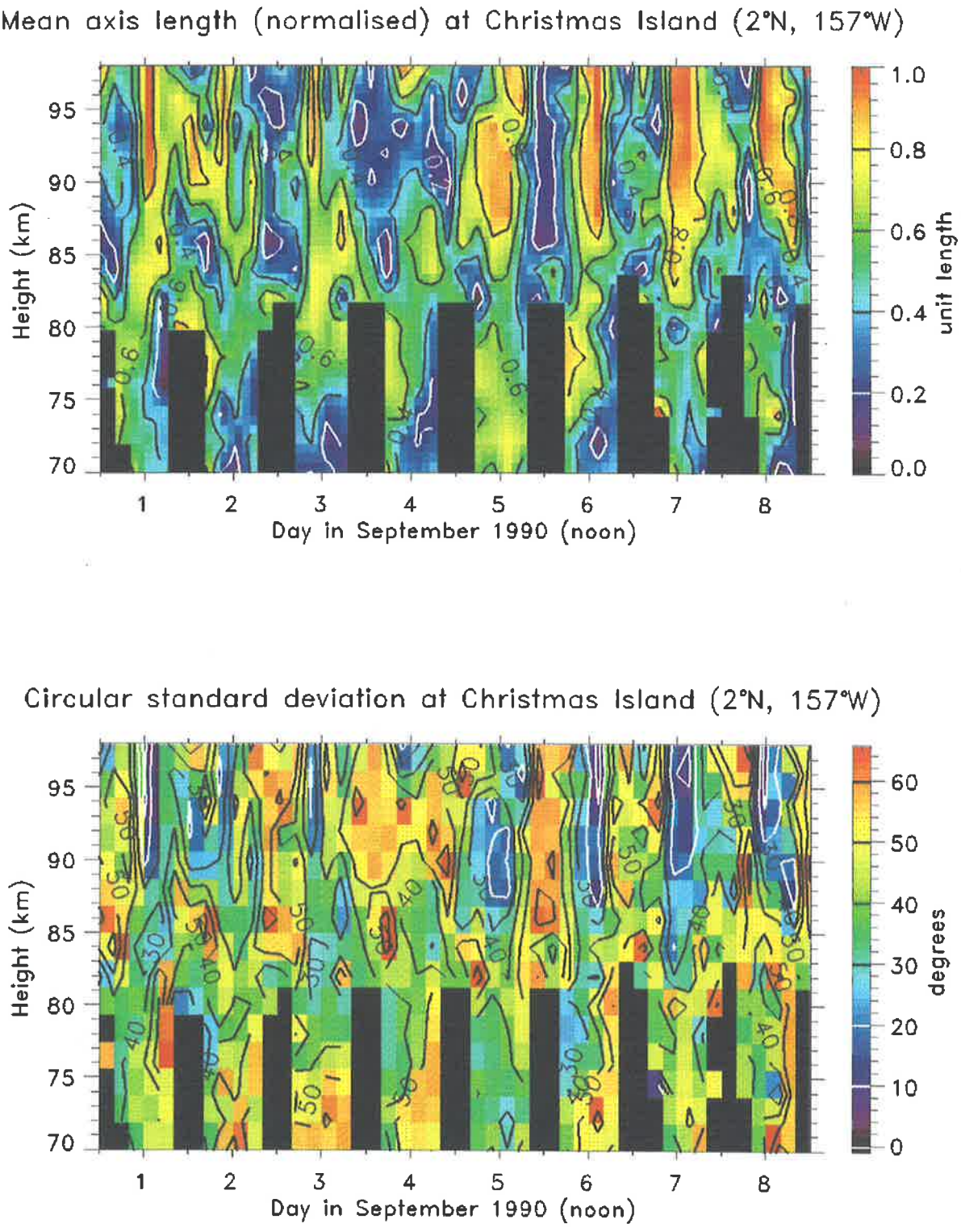

Figure 10.34: Four–hourly mean normalized lengths of the ground diffraction pattern for all axial ratios (top) and their circular standard deviation (bottom) for an eight–day period in September, 1990. The contours are the normalized length taking direction into account, while the standard deviation is in degrees.

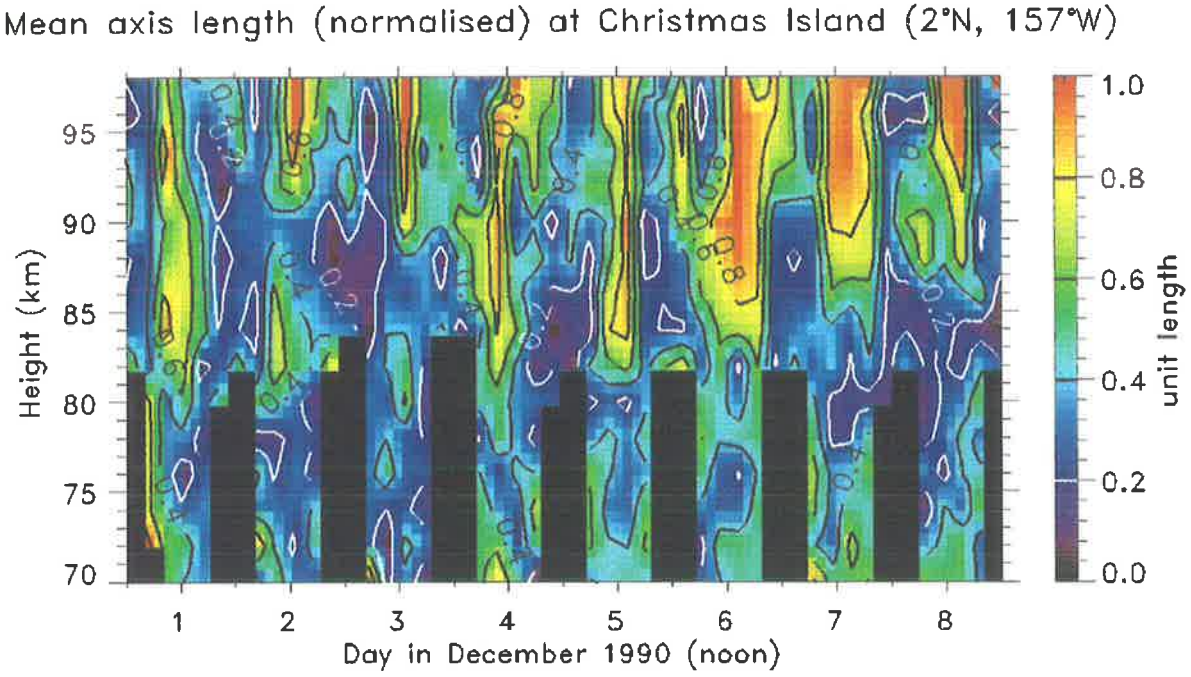

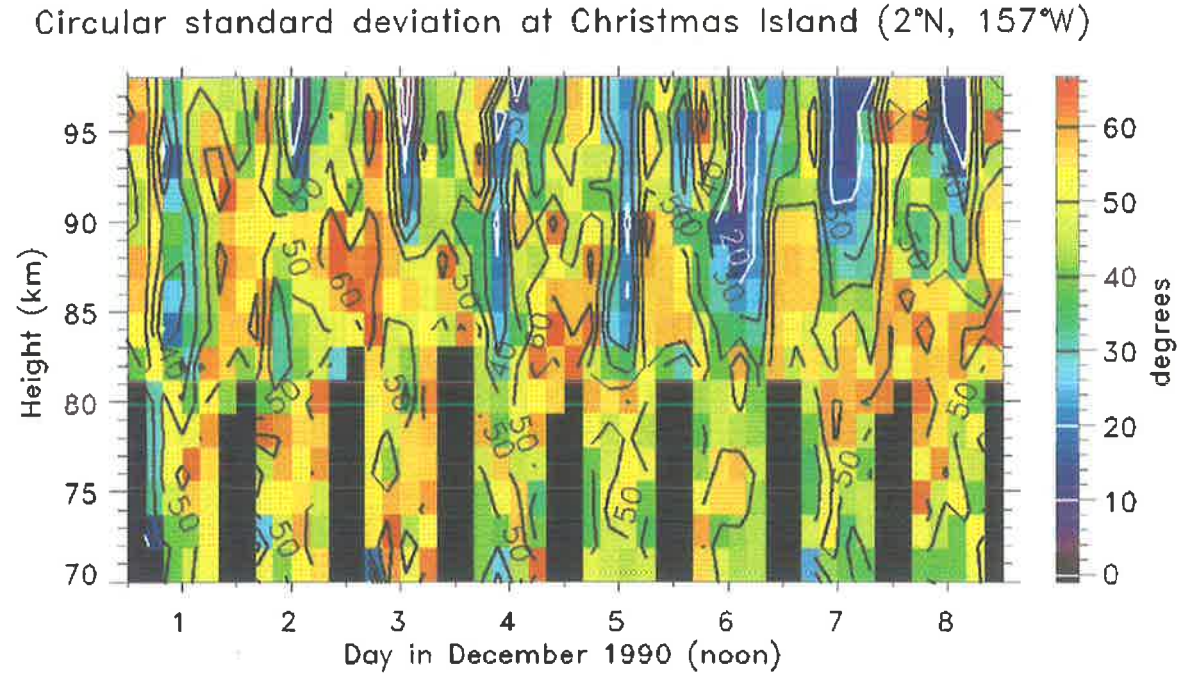

Figure 10.35: Four-hourly mean normalized lengths of the ground diffraction pattern for all axial ratios (top) and their circular standard deviations (bottom) for an eight-day period in December, 1990. The contours are the normalized length taking direction into account, while the standard deviation is in degrees.

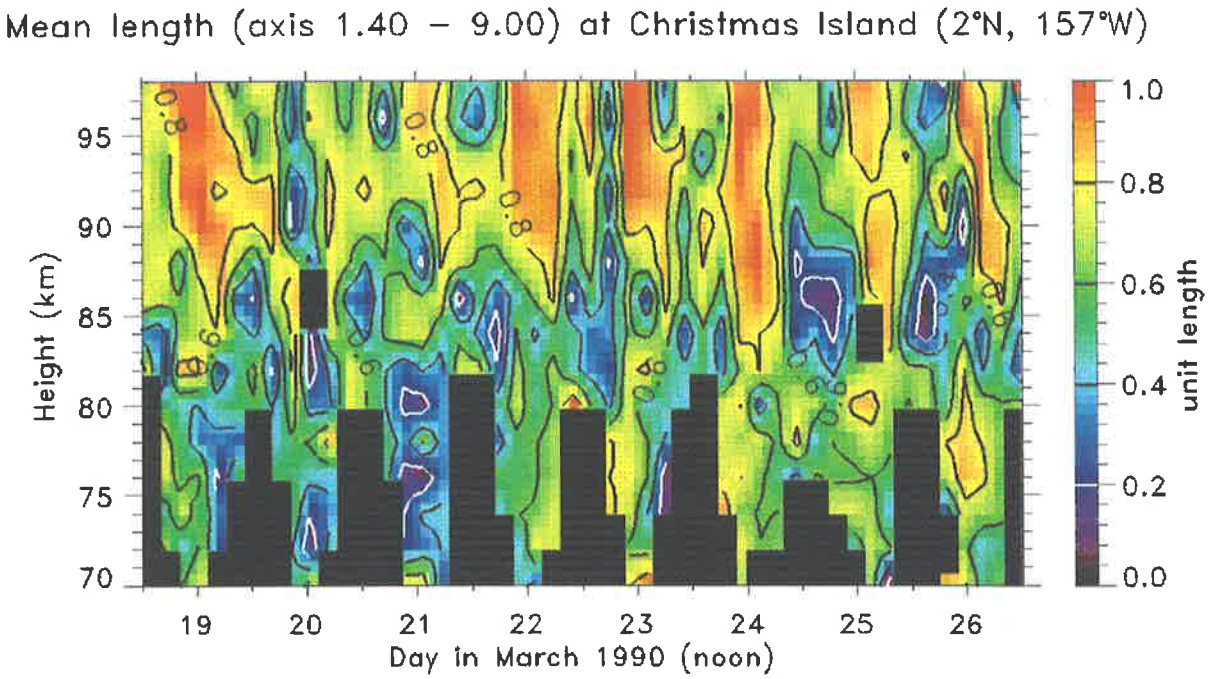

Figure 10.36: Four–hourly mean lengths of the ground diffraction pattern as for figure 10.32 but filtered for axial ratios of 1.4–9.0 for March 1990.

circular standard deviations span 0°–66°. For brevity the normalized mean axis length shall be denoted as L_n, while the standard deviation will be denoted as σ. A L_n of 0.2 is equivalent to a σ of about 60°, a L_n of 0.4 reflects a σ of about 50°, a L_n of 0.6 is a σ of about 40°, while a L_n greater than 0.8 translates into a σ of less than 20°.

On first inspection, both L_n and σ show large variability where, at times, L_n is greater than 0.8 and approaches 1.0. Similarly σ shows reciprocal behaviour, with low values occurring in step with large L_n. There is not a lot of difference in the range of values encompassed by L_n within the four different time periods, which vary between 0.2–0.8, However, during December, the total time when low L_n's were observed is greater than for the other three periods.

The data show that there are roughly two different height regimes, 70–85 km and 85–98 km, where different behaviour in L_n and σ is observed. However, the height separation is not rigid, and is used only as a rough guide. It is not clear why the difference occurs at approximately 85 km. One might initially attribute this to the mesopause which is normally thought to occur around this height. However, as discussed earlier, during ALOHA–90 the mesopause was

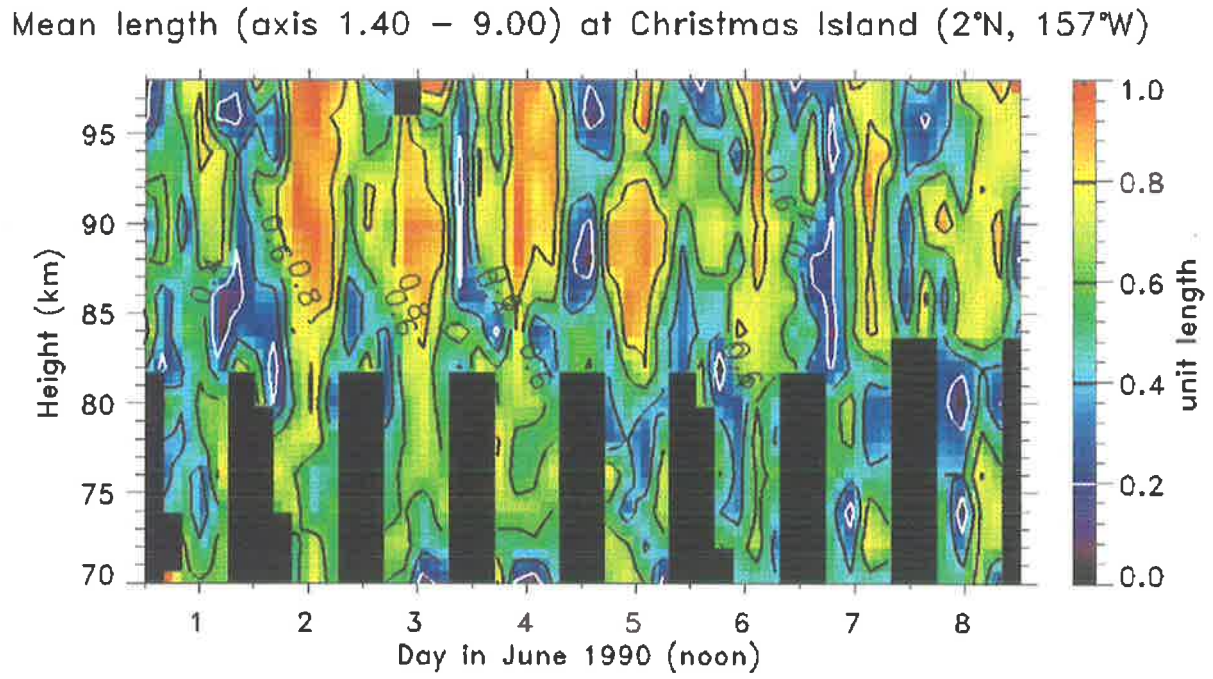

Figure 10.37: Four hourly mean lengths of the ground diffraction pattern as for figure 10.33 but filtered for axial ratios of 1.4–9.0 for June 1990.

observed to be higher than 90 km, and in the data presented here no consistent difference is found within the four time periods. The conclusion that therefore must be drawn is that the height of the mesopause does not affect these results.

In the 70–85 km region, L_n generally varies between 0.2–0.6 during all months except December when L_n rarely exceeds 0.4. That means that during December the orientations of the pattern vary by around 50° around some mean value, while during the other three months it varies by around 40°. In this height region, there is no clear temporal variation exhibited by the data, although at times L_n is larger for several days at a time, maybe hinting at some longer–term variability. This is clearly seen from the 22^{nd}–26^{th} March, and during the 3^{rd} and 5^{th} of September.

Unlike the 70–85 km range, a clear temporal variation exists within the 85–98 km range. In addition, the L_n values are, on average, larger, varying from 0.5–0.9. This translates into a σ at most about 30°, and at times less than 10°. The temporal variation is diurnal in character, with the maximum values of L_n occurring a few hours after local noon. This diurnal variation

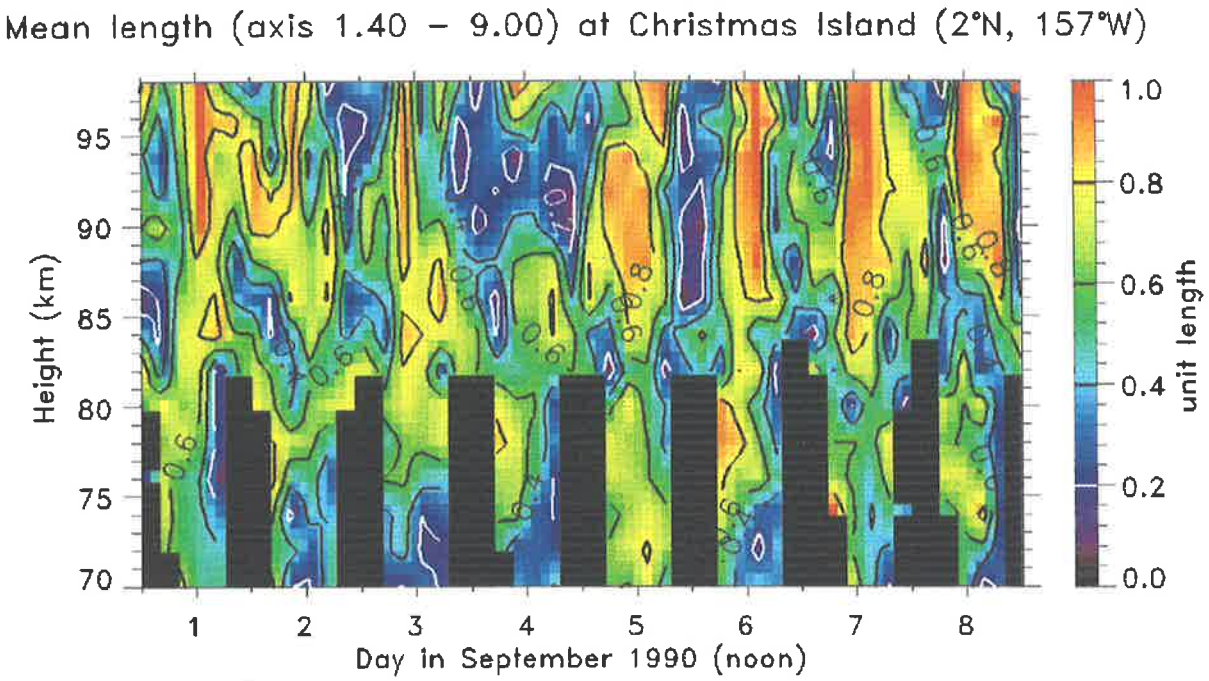

Figure 10.38: Four–hourly mean lengths of the ground diffraction pattern as for figure 10.34 but filtered for axial ratios of 1.4–9.0 for September 1990.

persists well into the late afternoon–evening time. The L_n contours are not height dependent, and occur simultaneously throughout this height range.

December seems to be the unusual month, for, in the 70–85 km height range, the daily maxima persist for a much shorter time than during the other three months. Furthermore, the height at which the maxima occur seem to propagate downwards from day to day. For example, on the 2^{nd} December, the maximum occurs above 93 km. This height decreases to about 90km on the 3^{rd}, 82 km on the 4^{th}, and starts increasing from the 5^{th} to the 8^{th}.

Up till now, all of the data used in the analysis were unfiltered for axial ratios. However, patterns whose axial ratios are less than or around 1.3 can be classified, according to a study by *Wright & Pitteway* [1978], to be essentially isotropic. In that case, their orientation should in principle be random. For this reason, the mean axis–lengths were re–analyzed, in such a way that all the patterns whose axial ratios were less than 1.4 and greater than 9.0 were rejected. As before, four data points which deviated the most from the data mean were rejected. The filtered data are presented in figure 10.36 for March, 10.37 for June, 10.38 for September, and

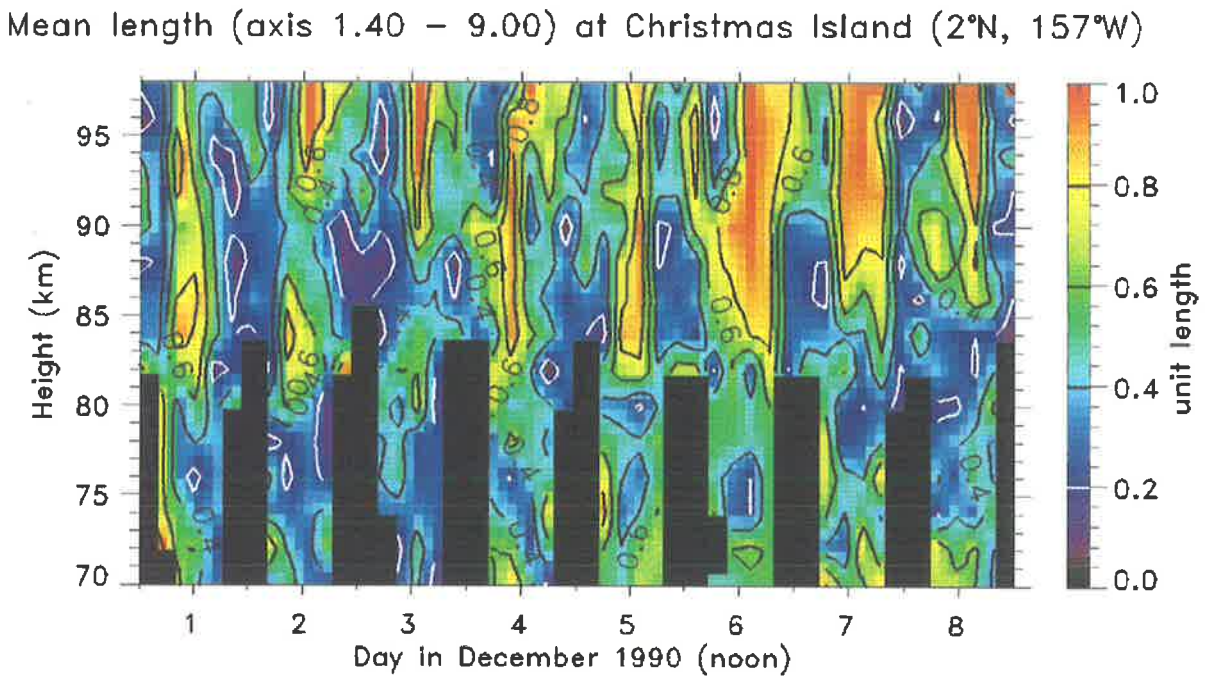

Figure 10.39: Four–hourly mean lengths as for figure 10.35 but filtered for axial ratios of 1.4–9.0 for December 1990.

10.39 for December.

Overall, the general temporal and spatial behaviour of the mean axis lengths has not changed. Below about 85 km, no temporal variation is observed, although some long–term variability is hinted at during March and June. What has clearly changed is the mean value of L_n which, after filtering for axis ratios, has increased by between 0.05 and 0.1. This occurred for all values of L_n, except those that were already large (more than 0.9). The overall increase translates into an improvement of σ of about 5°, statistically not significant.

Therefore, the conclusion reached is that below about 85 km, the patterns seem to be fairly randomly oriented within some mean value. Above 85 km however, this changes markedly, with the day–time patterns all possessing nearly the same orientation, while the stability of the night–time patterns is not much different from that below 85 km. In addition, although filtering for small axial ratios improved the overall stability, the general characteristics have not changed much. This strongly suggests that even patterns whose axial ratios are less than 1.4 are truly anisotropic, and not just a statistical by–product of the full correlation analysis.

Mean pattern orientation with respect to North

In the last section, the stability of the pattern orientations was investigated. It was found that there is both a temporal and spatial variation in the stability of the pattern orientations. For this reason, histograms of the data were constructed but according to the following rules. Firstly, all the data were separated into two height regions of 70–84 km, and 86–98 km. Secondly, the data were grouped according to the local time of day into four time zones of 0:00–6:00, 6:00–12:00, 12:00–18:00, and 18:00–24:00. Thirdly, the data were binned into 5° intervals. Finally, all the data were filtered according to their axial ratios of either 1.0–1.4, or 1.4–9.0.

Figure 10.40 are histograms of the orientation of the pattern[2] for the eight days in March. The left–hand side are histograms for data in the 70–84 km range, while the right–hand side are for those in the 86–98 km height range. In addition, starting from the top downwards, the data are separated into the four time periods described before. Similarly, figures 10.41, 10.42, and 10.43 are histograms for the June, September, and December data. It is important to note that the total number of counts is different between the different histograms.

In the 70–84 km range, the data clearly show that the pattern angle is dependent on the time of day. From midnight to 6:00 LT, the patterns tend to orientate themselves so that the centre of the distribution is approximately 80° with respect to North, although the distribution is not by any means narrow. This is observed in all the four months except during December, when the distribution is not clear. However, during December, the total number of counts in this height and time frame is less than at other months. In the 6:00–12:00 time frame, the orientation changes quite dramatically so that most of the pattern orientations are within 40° of North, a significant change in orientation. However, the distribution is slightly wider in June and December. In the afternoon, from 12:00–18:00, there is not much change from the preceding 6 hours, although the June and December distribution are slightly narrower. An interesting event is the development of a secondary maximum at approximately 45° during June. Finally, the 18:00–24:00 time period shows that the pattern orientations change in their preferential

[2]the orientation of the pattern is defined as the orientation of the semi–major axis. mesured clockwise from north

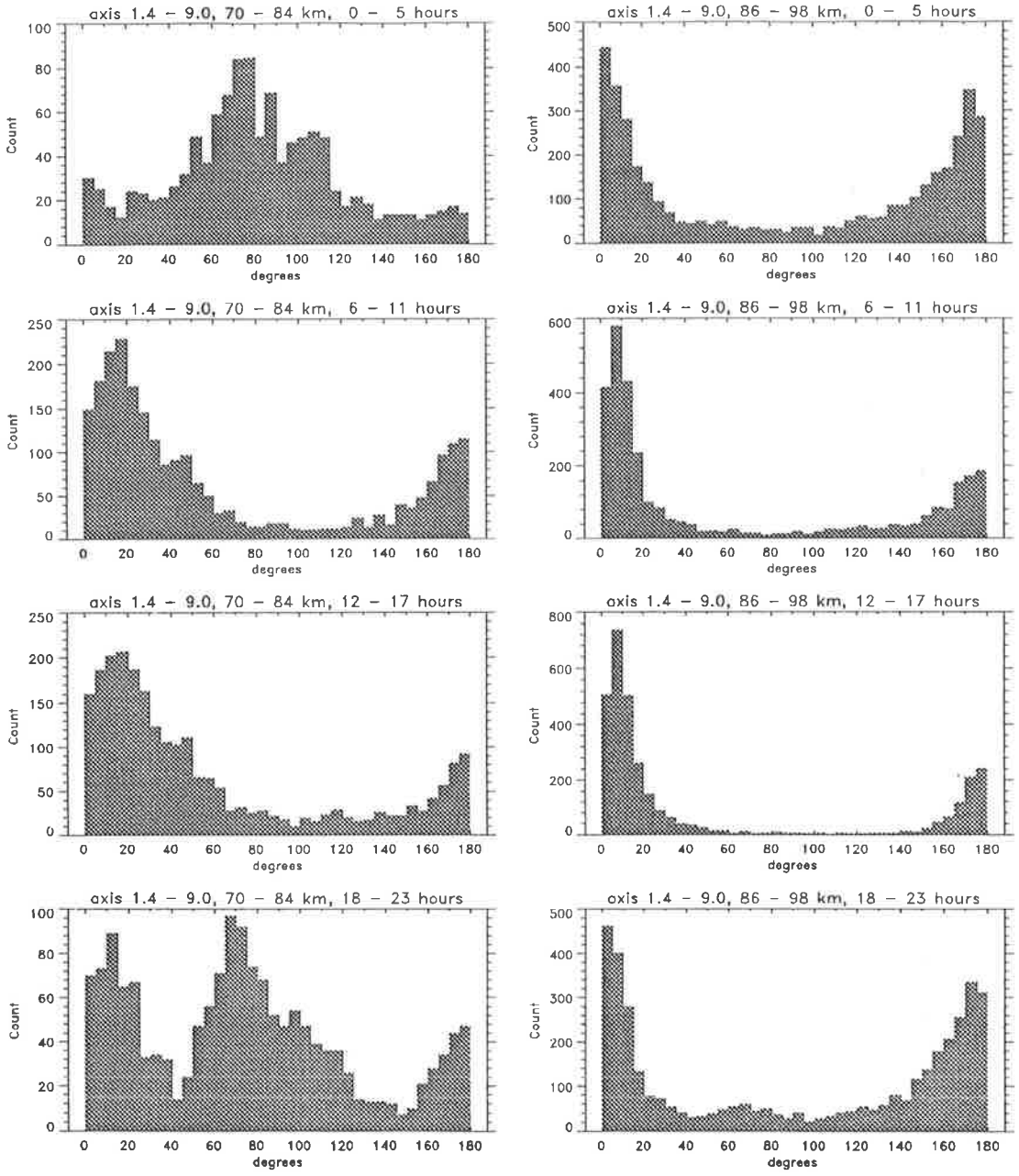

Figure 10.40: Histograms of the orientations of the ground diffraction patterns whose axial ratio is between 1.4–9.0. The histograms are based on two height ranges of 70–84 km (left hand side) and 86–98 km (right hand side). The data is further binned according to time. Starting from the top, each histogram looks at a six–hourly interval beginning at midnight local time. The data are separated into bins of 5° width, and are those collected at Christmas Island for an eight–day period in March 1990.

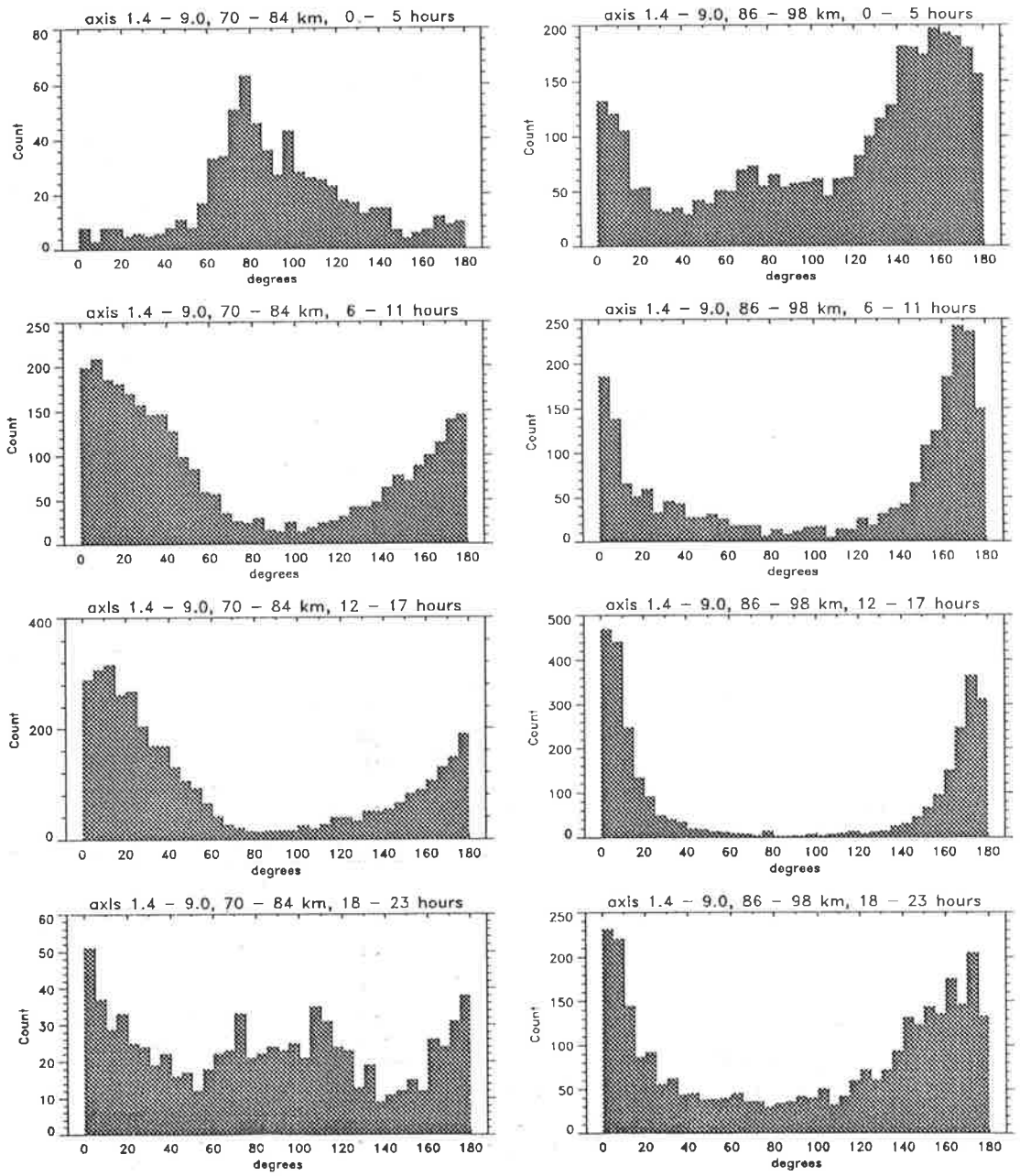

Figure 10.41: As for figure 10.40, but for data collected in June 1990.

orientations back to about 80° from North, although a large number are still oriented north–south.

In the height range of 86–98 km the orientation of the pattern is much more anisotropic. All four time periods show that the patterns are generally oriented north–south. However, the distributions in the 0:00–6:00 and 18:00–24:00 time frames are slightly broader than those obtained in the day–time, when there is a slight hint of an east–west distribution. During the

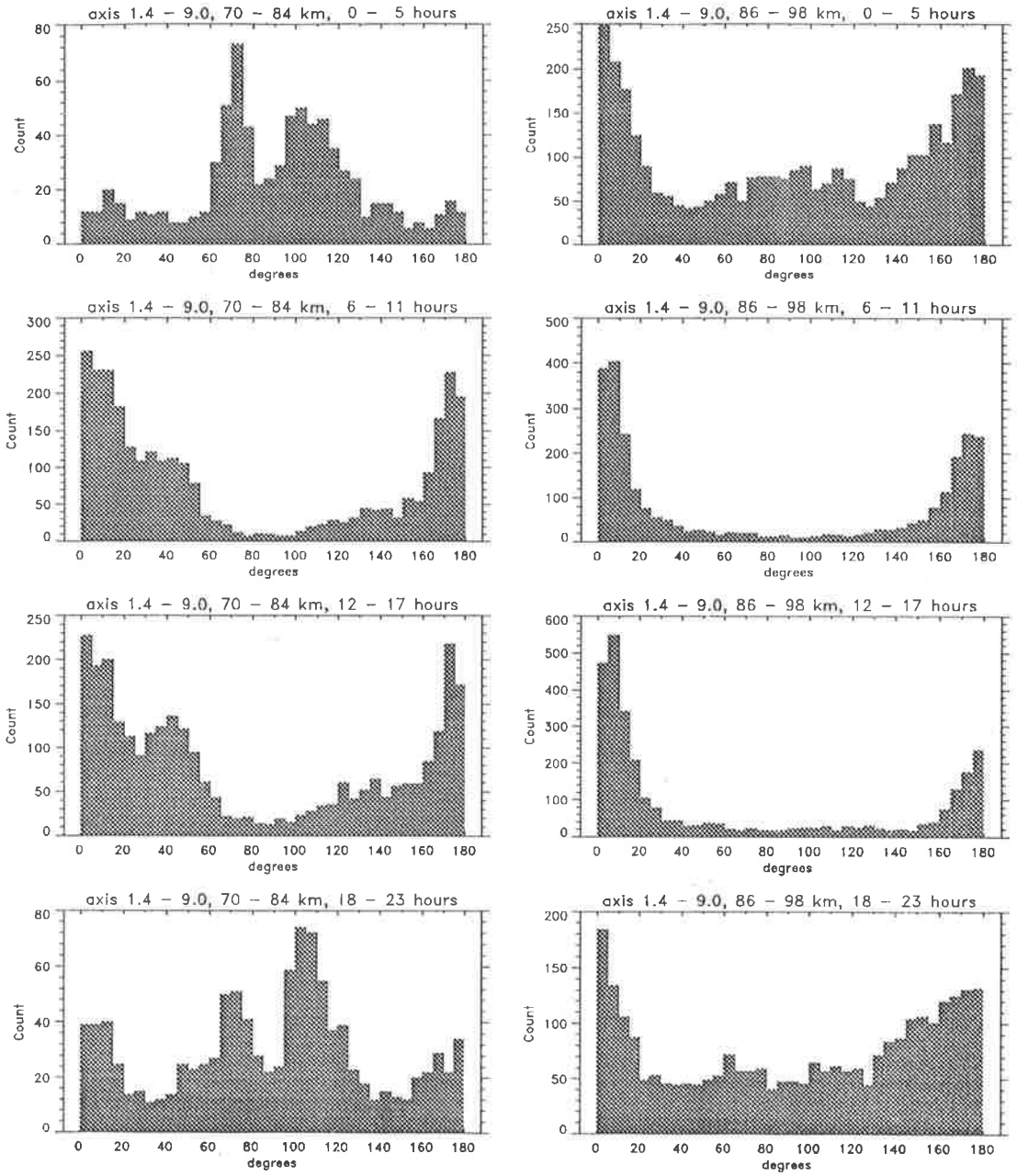

Figure 10.42: As for figure 10.40, but for data collected in September 1990.

day–time, however, the distribution are very narrow, contained within 20°. The anisotropy becomes even clearer if one looks at the total number of data points in the histograms. For example, during December, the 12:00–18:00 time period has several thousand individual data points which are within 20° of North, while only about several hundred points are contained in the rest of the bins.

The data presented in these histograms are those which have been filtered for axial ratios

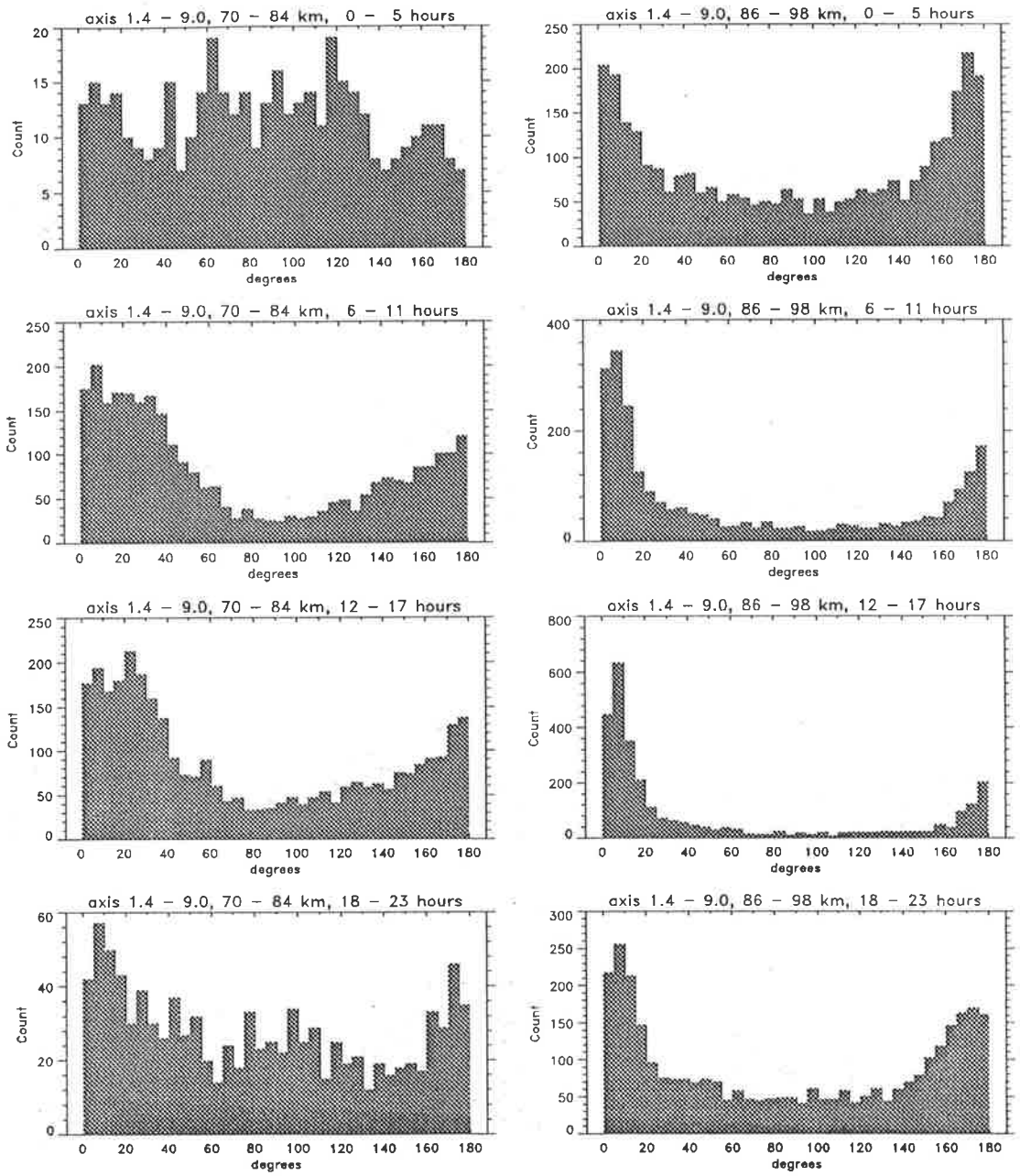

Figure 10.43: As for figure 10.40, but for data collected in December 1990.

of between 1.4–9.0. Earlier it was found that even those patterns whose axial ratios were less than 1.4 showed similar spatial and temporal characteristics, and at times strong stability in the mean pattern orientations. For this reason, it is interesting to examine the raw distributions of the pattern orientations whose axial ratios are less than 1.4. Figure 10.44 shows the March distributions of the pattern orientations for various times of day and height regions, but whose axial ratios fall between 1.0–1.4. The other three months are not shown since they are all very

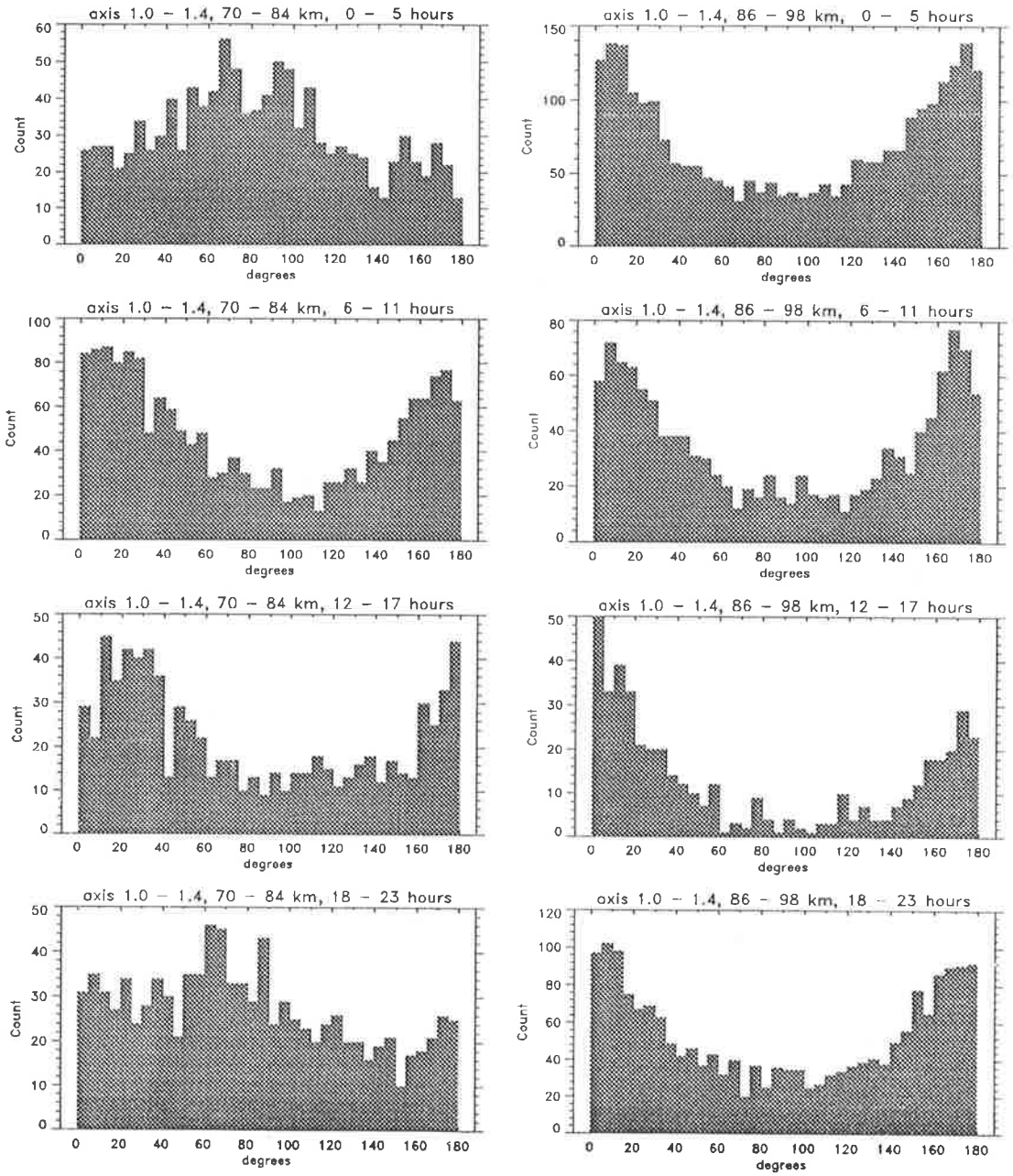

Figure 10.44: As for figure 10.40, but for patterns whose axial ratio is less than 1.4.

similar in character and it would serve nó purpose to present them here. The surprising thing is that the gross features of the angular distribution of patterns whose axial ratios are less than 1.4 is not very different from those whose axial ratios are greater than 1.4. Although the distributions are more spread, the night–time 70–84 km height range still show patterns aligned more often along the east–west axis, while day–time orientations tend towards a north–south distribution. Similarly, in the 86–98 km height range the angular distributions of the pattern

orientations favour a north–south orientation. This is again good evidence that even those patterns whose axial ratios approach 1.0 are genuinely anisotropic and the anisotropy is not an artifact of the analysis.

It is worth noting that out of all of the four different time distributions, March seems to be the time when the distributions are relatively narrower than the other three months examined. This is interesting since we may recall that during March, extremely strong westward winds which at times approach 100 ms^{-1} are found. Both this fact and the fact that the patterns are so clearly anisotropic leads to the question of the cause of this anisotropy. The logical initial choice must be the direction of the wind. This factor shall now be investigated.

Mean pattern orientation with respect to the wind direction

The difference in direction between the mean wind and mean pattern orientation is shown in figures 10.45, 10.46, 10.47, and 10.48 for March, June, September, and December respectively. Within each figure, the histograms are constructed according to the same criteria as those which were used when investigating the pattern orientation only. However, since the absolute direction of the wind is irrelevant, i.e. there is no distinction made between a wind blowing towards or away from an observer, the difference between the pattern orientation and the mean wind is at most 90°. We shall refer to the difference in angles as ϕ_{diff}.

All of the four individual time periods show very similar behaviour, with the exception, at times, of March. The following discussion therefore will pertain to all the data, and specific differences found in March will be commented upon where appropriate. We start off investigating the 70–84 km range. In the early morning, 0:00–6:00, the pattern orientation tends to be more orthogonal than parallel to the mean wind direction. In March, however, the reverse seems to be true, although this is not very convincing. During the morning, 6:00-12:00, ϕ_{diff} tends to change and is centred around 30°–40°, although during March, the distribution is somewhat skewed towards 90°. In the afternoon, 12:00–18:00, all of the months show that ϕ_{diff} is centred around 40°. This is especially apparent in September. During the evening, 18:00–24:00, ϕ_{diff} once again tends towards larger angles.

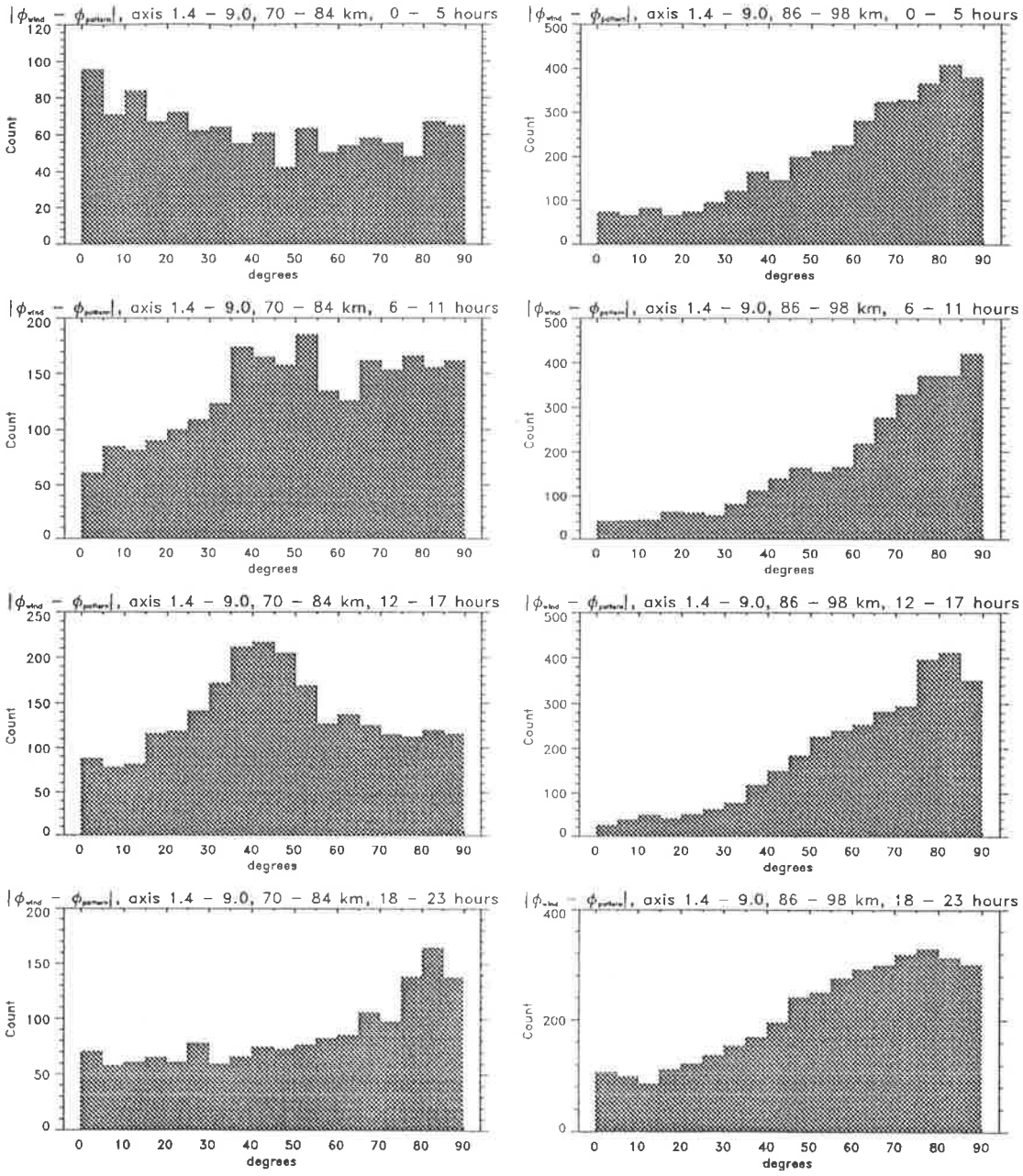

Figure 10.45: Histograms of the angular difference between the orientation of the ground diffraction pattern whose axial ratio is between 1.4–9.0 and the wind direction. The histograms are based on two height ranges of 70–84 km (left hand side) and 86–98 km (right hand side). The data is further binned according to time. Starting from the top, each histogram looks at a six–hourly interval beginning at midnight local time. The data are separated into bins of 5° width, and are those collected at Christmas Island for an eight–day period in March 1990.

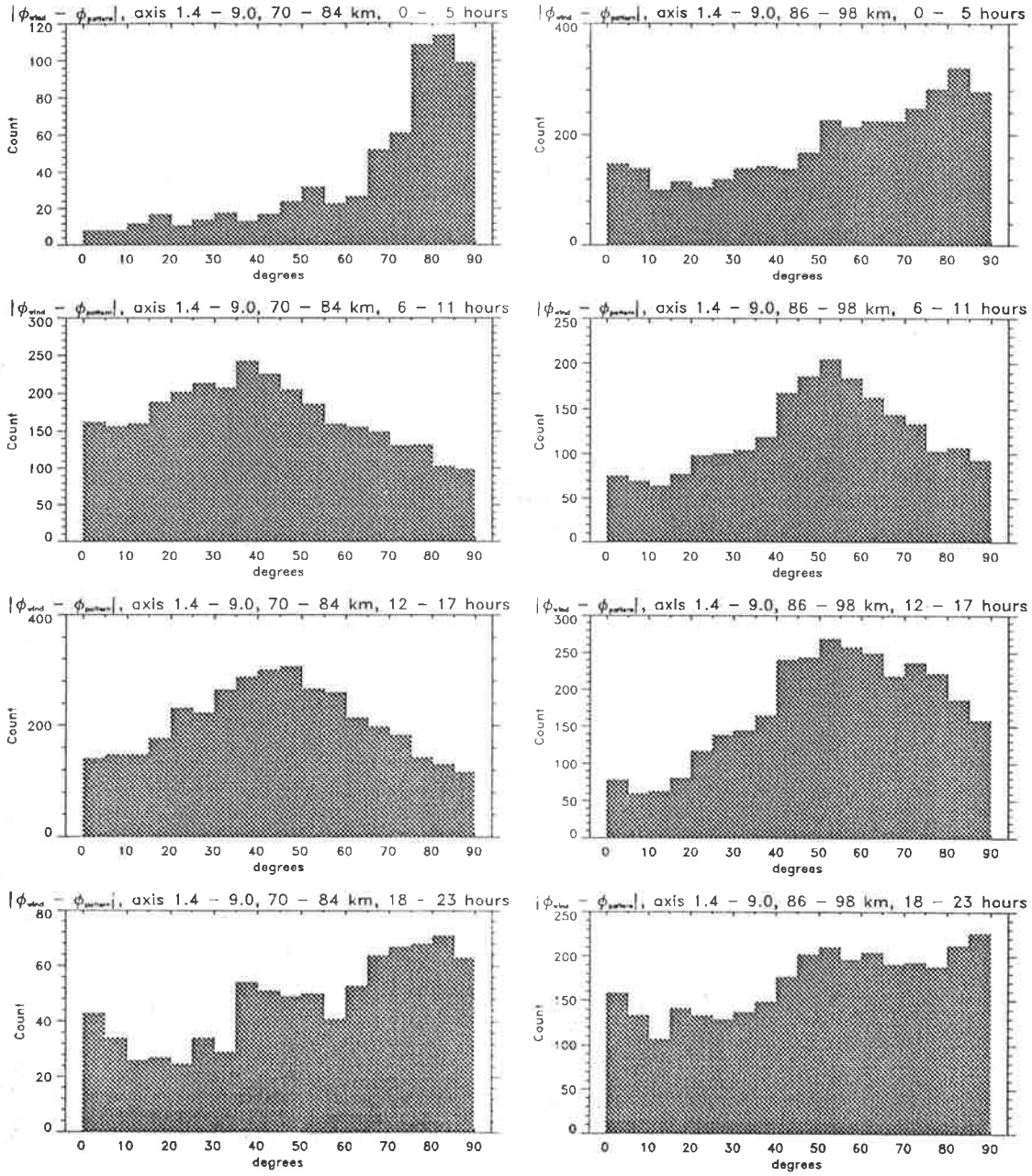

Figure 10.46: As for figure 10.45, but for data collected in June 1990.

In the upper height range, 86–98 km, March is clearly the odd month out with ϕ_{diff} approaching 90° in all of the four times of day. While the other three months also exhibit a bias with ϕ_{diff} tending to larger angles, the 16:00–18:00 time period shows that the ϕ_{diff} values are centred around 50°–60°.

Although a systematic difference in ϕ_{diff} is clearly observed in the data it is difficult to ascertain whether this difference is due to a real physical relationship or is just due to the

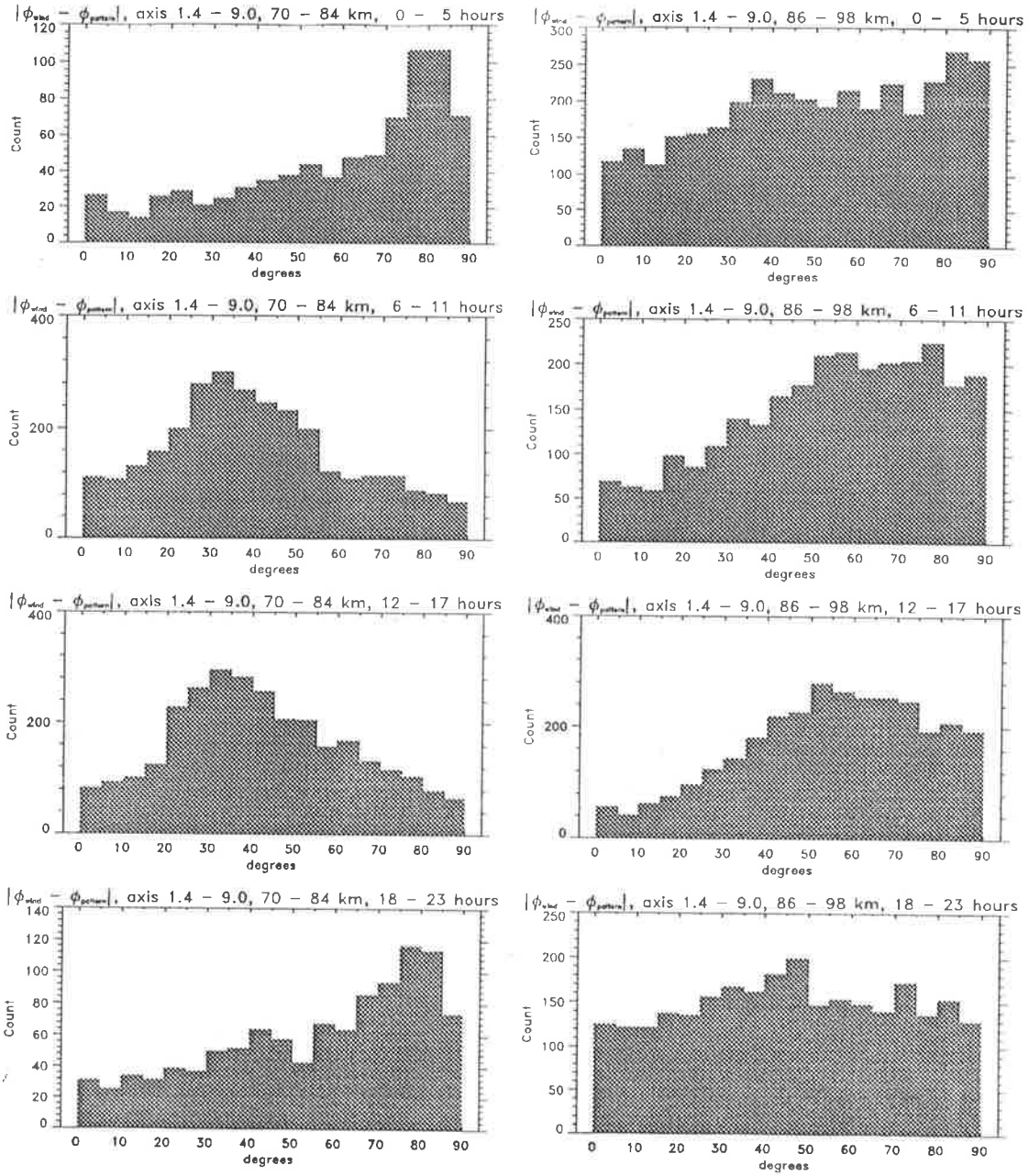

Figure 10.47: As for figure 10.45, but for data collected in September 1990.

change in the wind direction with time and height. In addition, the wind magnitude might also have an effect. To investigate this, it is necessary to visually compare the wind strengths and directions with the pattern orientations.

Figures 10.49, 10.50, 10.51, and 10.52 show the four–hourly mean wind directions and the mean pattern orientations as individual vector plots, as a function of time and height. The length of the wind vectors are proportional to the wind magnitude, where the maximum

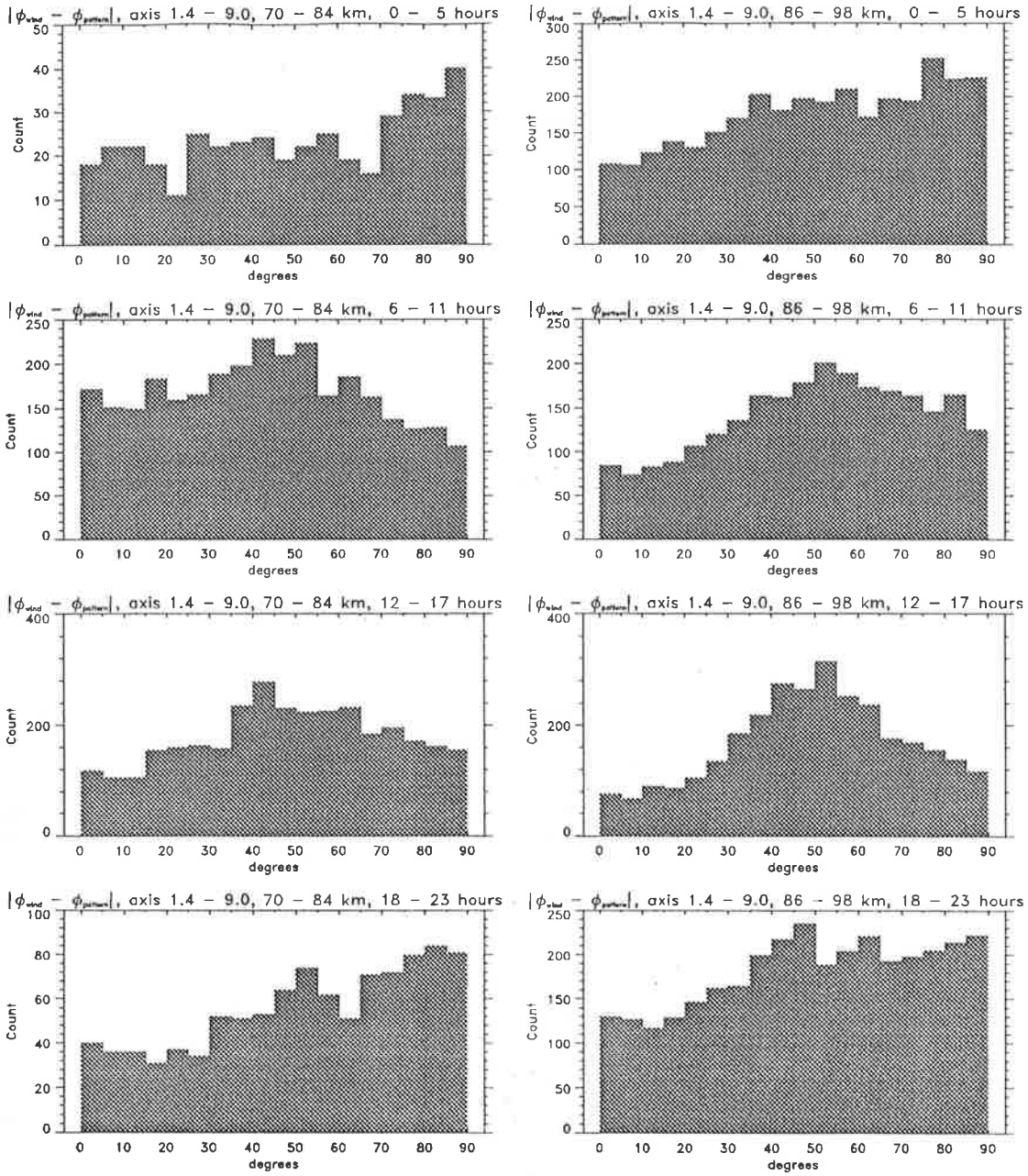

Figure 10.48: As for figure 10.45, but for data collected in December 1990.

length of the vector corresponds to a velocity of 80 ms^{-1} during March, and 50 ms^{-1} for June, September and December.

The mean pattern orientations (denoted as θ_p) in all four months show very similar general characteristics, although differences based upon time of day and height are found. During the day–time, θ_p above 85 km are oriented almost exclusively in the north–south plane. Below 85 km, they are more random but in general are aligned approximately 10°–20° eastward from the

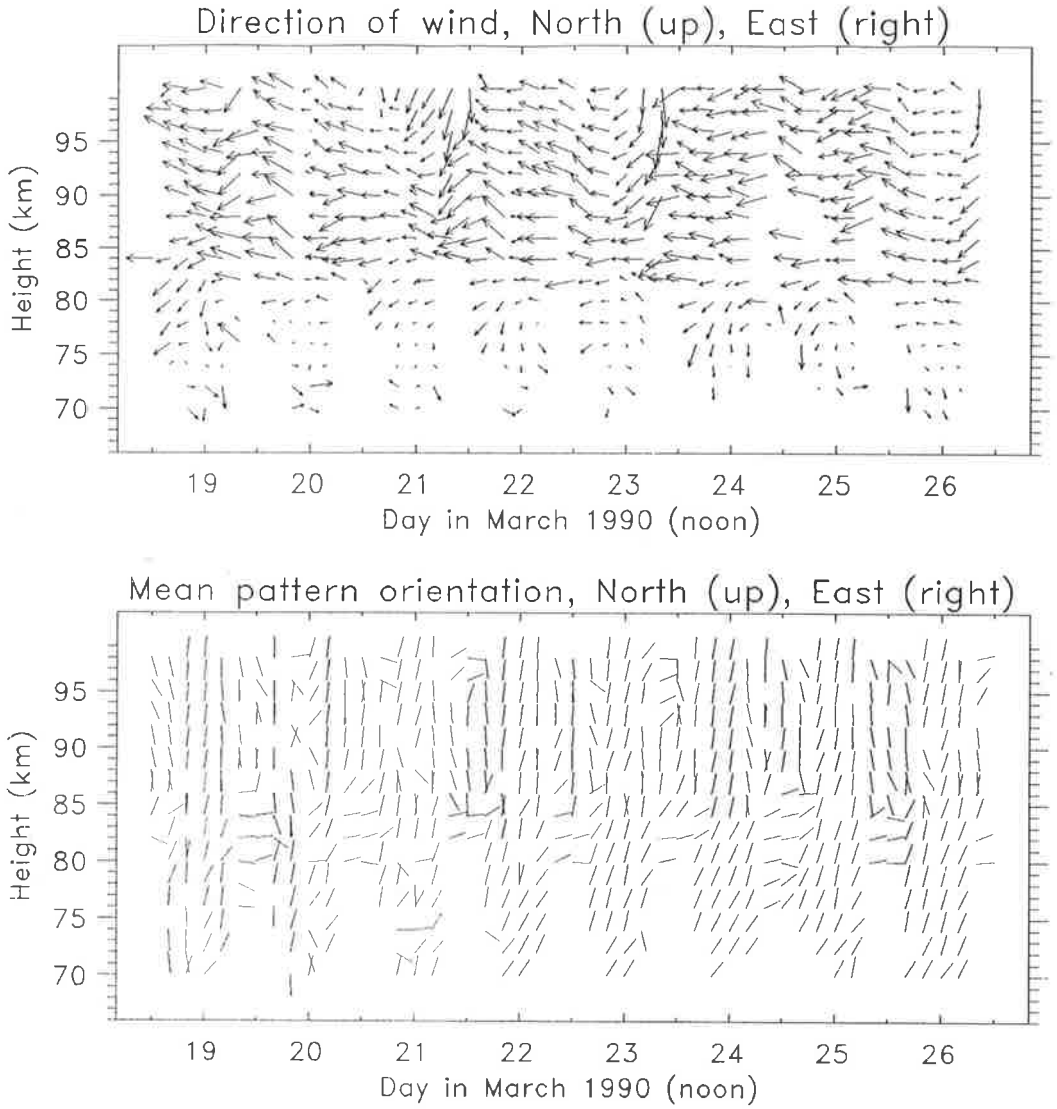

Figure 10.49: Four-hourly mean direction of wind (top) and pattern orientation (bottom) at Christmas Island during March 1990.

north-south plane (although there are a few exceptions to this). Night-time pattern orientations below 85 km are clearly different from the day-time ones, and are principally oriented in the east-west plane. Above 85 km they change their alignment to be more oriented in the north-south plane, although above 95 km they are occasionally more random. There can be no doubt that the pattern orientations exhibit a clear structure, for there is an inherent smoothness in the data. θ_p varies relatively smoothly between each data point with respect to both height and time. It is also worth remembering that the stability of the pattern orientations, investigated earlier, showed that at times all the patterns in a four-hourly period were virtually identical in

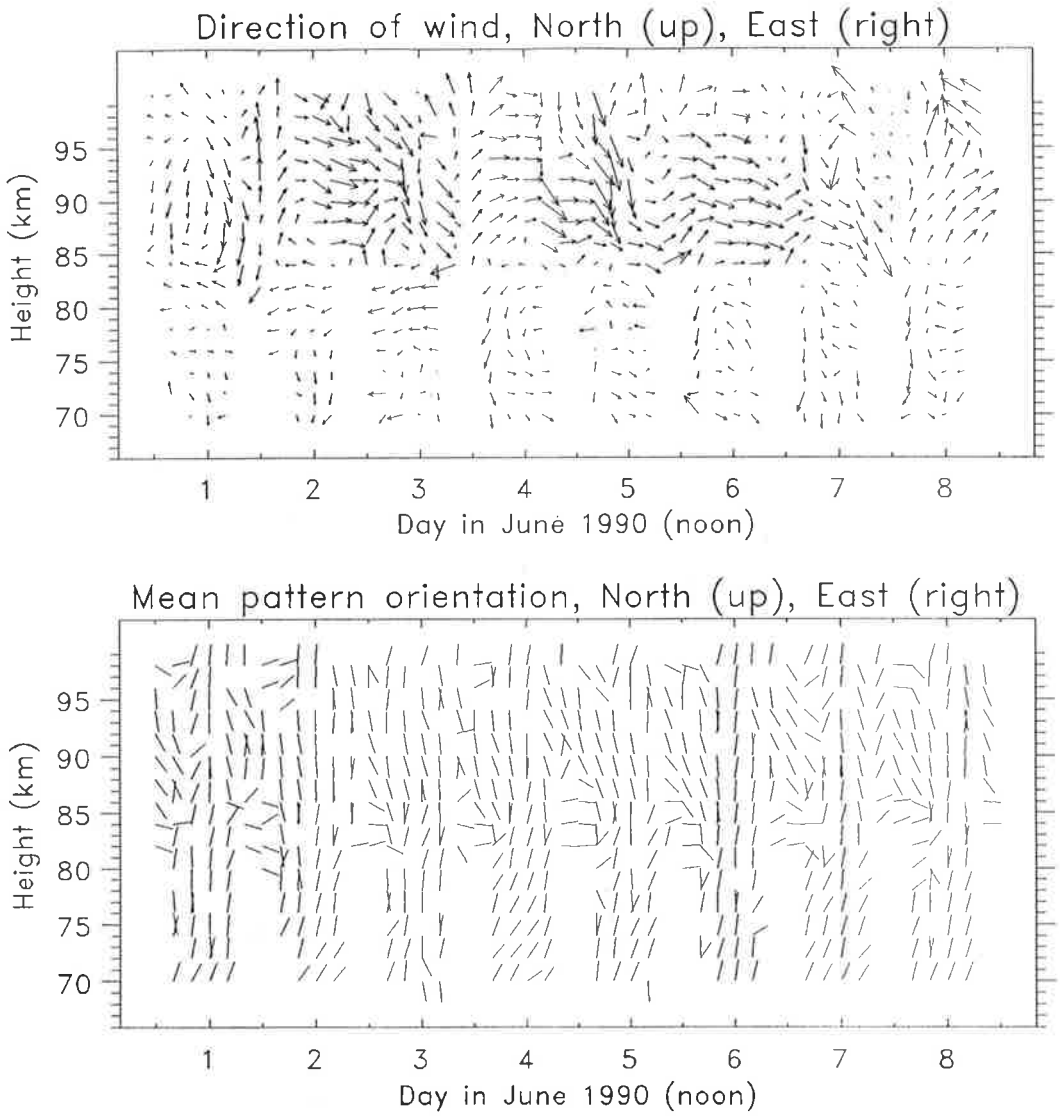

Figure 10.50: Four-hourly mean direction of wind (top) and pattern orientation (bottom) at Christmas Island during June 1990.

their direction, while at other times θ_p was within $\pm 40°$.

While the pattern orientations are clearly not dependent upon the time of year, this is not true for the wind direction (denoted as θ_w) and magnitude. During March, θ_w is predominantly westward, and the wind is extremely strong, especially above 85 km (up to 80 ms^{-1}). In June, θ_w is generally eastward although more variable in its direction, and the wind is weaker (up to $\sim$50 ms^{-1}). During September and December, θ_w varies with no particularly dominant direction, and the wind is weaker still , although large velocities are exhibited during some days. This variability in θ_w and wind magnitude between the different times of the year provides a

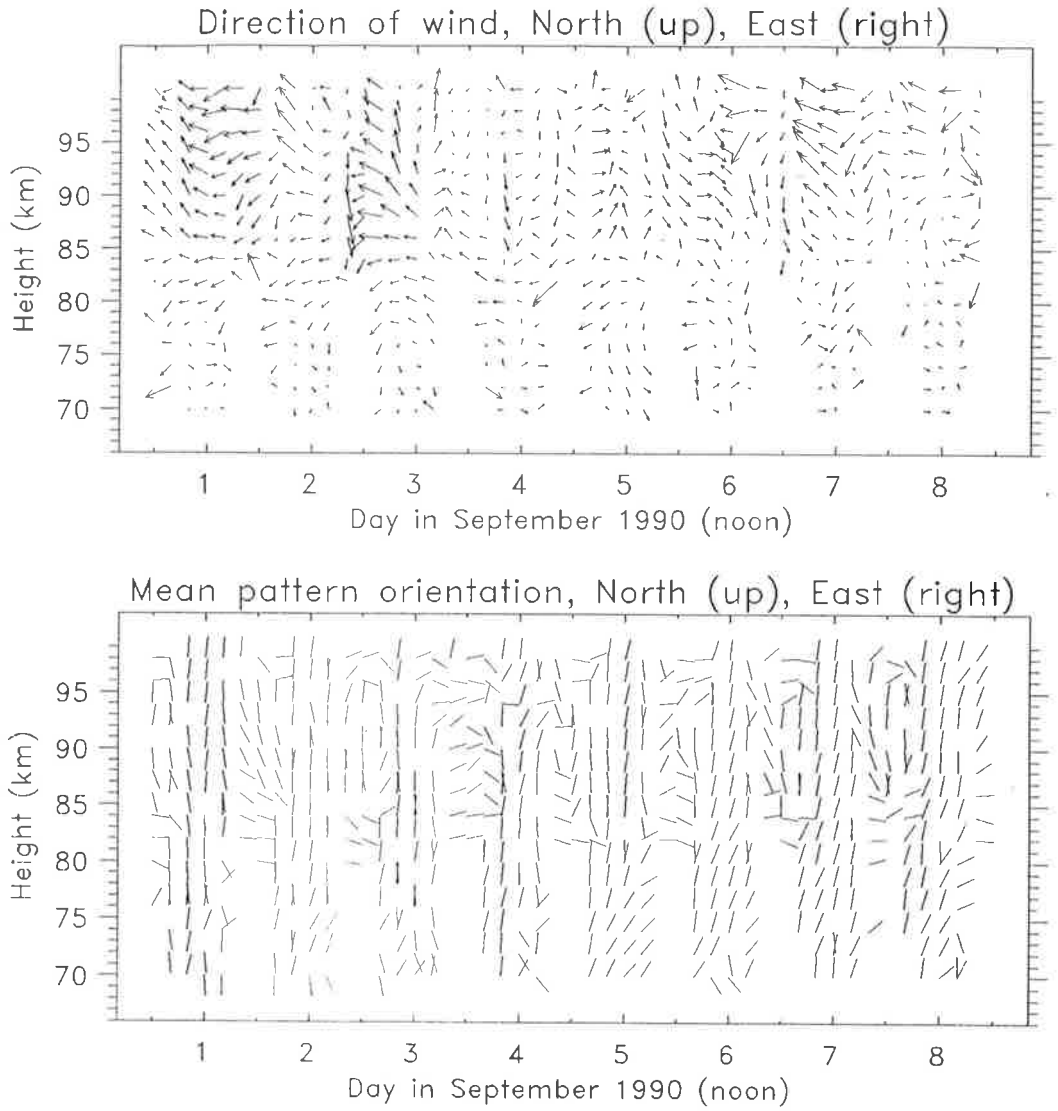

Figure 10.51: Four–hourly mean direction of wind (top) and pattern orientation (bottom) at Christmas Island during September 1990.

good opportunity to examine any correlation between θ_w and θ_p.

We start with the March data. Above 85 km, while values of θ_p are generally in the north–south plane, θ_w changes markedly. For example, between the 21^{st} and 24^{th}, θ_w changes by over 90° on several occasions, while at these times values of θ_p are fairly stable. This does not seem to be dependent on the wind magnitude although around noon on the 20^{th} values of θ_p are relatively disturbed, at a time when the wind magnitude was quite small. Below 85 km the day–time values of θ_p between the 22^{nd}–26^{th} are almost identical, while θ_w and the wind magnitude are again quite different for the individual days. The results for night–time

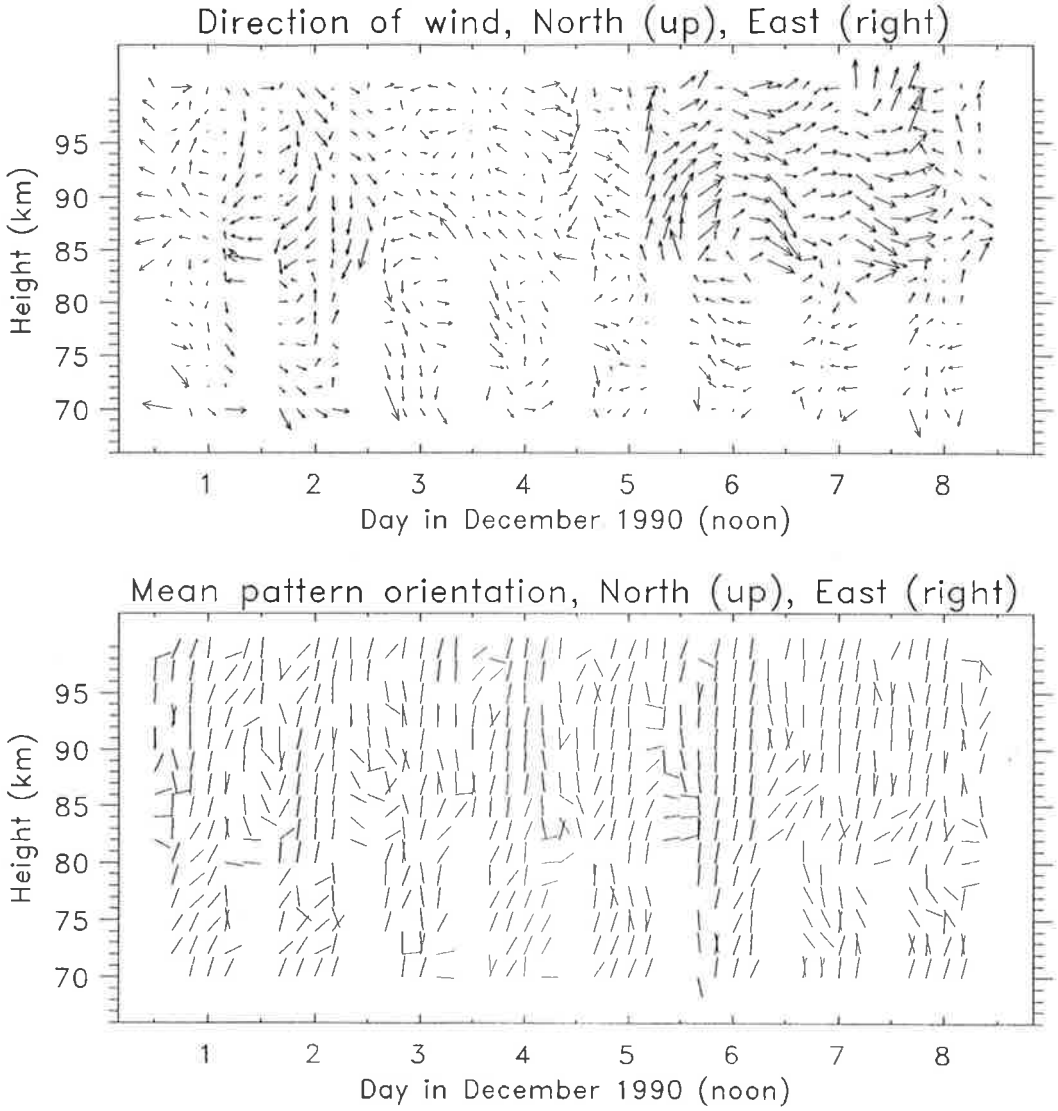

Figure 10.52: Four–hourly mean direction of wind (top) and pattern orientation (bottom) at Christmas Island during December 1990.

for heights of below 85 km are quite interesting in their consistent differences. Although θ_w at 85 and 90 km are virtually identical, values of θ_p change within several km by 90° to be in the east–west orientation (e.g. the night of the $20^{th}/21^{st}$). A final interesting event during March is the behaviour of θ_p around 95 km during the nights of the $21^{st}/22^{nd}$ and $23^{rd}/24^{th}$. At these heights values of θ_w were strongly southward while values of θ_p swung around towards the east–west plane.

During June, values of θ_p are remarkably similar in their spatial and temporal behaviour to those in March. The values of θ_w and the wind magnitude, on the other hand, are generally

eastward, and more variable. Just to cite one example, above 85 km on the 2^{nd}, θ_w changes from being northward to south–eastward, while values of θ_p remains in the north–south plane. Below 85 km, θ_w is southward while θ_p are generally oriented east–west. The same scenario is observed during September, with a good example of the typical relationship between θ_w and θ_p observed on the 1^{st}.

Perhaps the best example of the lack of correlation between θ_w and θ_p is seen on the $5^{th}/6^{th}$ December. On the early morning of the 5^{th}, θ_w is northward and swings around over the course of the day to be south-eastward on the night on the 6^{th}. During the day–time on the 6^{th}, θ_p is north–south through all the heights, while during the night of the $5^{th}/6^{th}$ it is east–west below about 86 km.

The conclusion that must be reached is that the wind does not affect the orientation of the pattern. Therefore, the day–time stability and north–south orientation of the patterns must be due to some other dynamical process. What makes this more interesting is that at lower heights at night–time, the pattern orientations are consistently in the east–west orientation. An initial explanation may be that this is in some way due to sea–wave scatter which may dominate the signal when the night–time atmospheric returns at lower heights are weak. However, if that was the case, then this should also affect the lower day–time height pattern orientations, which is clearly not the case. The reasons as to why the pattern orientations are dependent on height and time of day only are therefore as yet unknown.

Chapter 11

Short–term results from Mawson

11.1 Introduction

The Mawson radar system, and its history, has already been discussed in chapter 8. It was noted, amongst other things, that the system underwent several major upgrades. The last of these was performed during 1991 when the radar transmitter was upgraded to a completely solid–state system. This means that three virtually identical systems at three distinct sites were operating within a similar time period, and enables comparisons to be made between results from the sites at Blanchetown, Christmas Island and Mawson without the fear of instrumental bias. However, due to the restrictions of the computing system, the data sampling time at Mawson was 4 minutes as compared to Christmas Island and Blanchetown where it was 2 minutes.

This chapter examines the short–term behaviour of the polar upper atmosphere (70–108 km) during mid–winter (24^{th} June to 1^{st} July) and early summer (13^{th}–20^{th} December). These two periods were chosen since long–term studies of the polar mesosphere had shown that an annual oscillation existed in all the various full correlation analysis parameters [see chapter 8]. The mid–winter data suffers from some data gaps, due to both environmental conditions and the fact that the radar was undergoing an update.

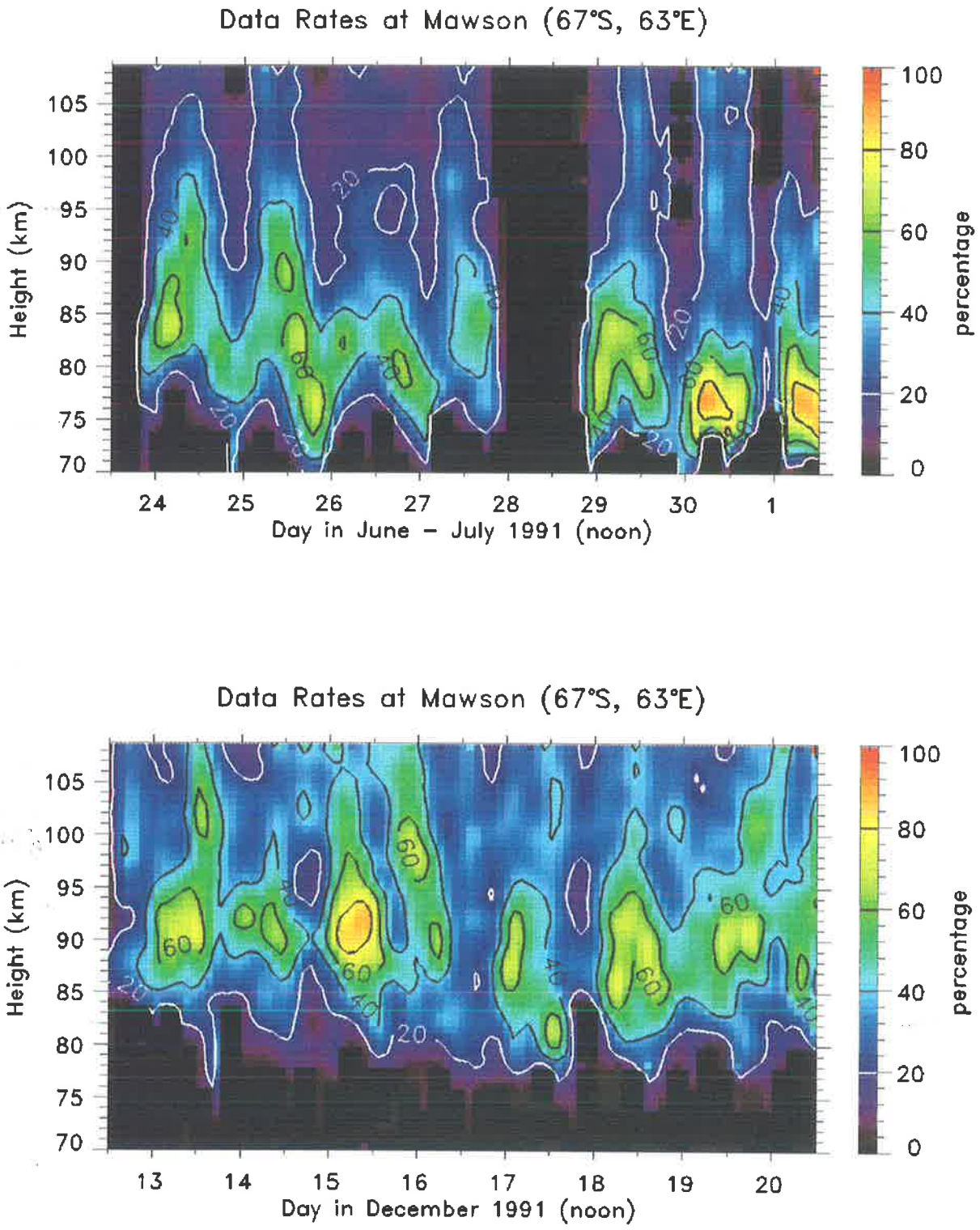

Figure 11.1: Four–hourly mean data rates at Mawson during one week in June (top) and a week in December (bottom). The contours are in percentage of useful echoes obtained as a function of the total sampling

11.2 Experimental technique

As with the short–term data from Blanchetown and Christmas Island, four–hourly means were constructed for the various full correlation analysis parameters. Again, the data were filtered so that four of the most outlying points were rejected from the sample mean. Although the data only covers two eight–day periods of 24^{th} June to 1^{st} July, and 13^{th}–20^{th} December hereafter, the two periods shall be referred to the month in which they occur. The times at which no or very few data were collected are completely black in all of the following image–contour diagrams.

11.2.1 Data rates

Figure 11.1 is an image–contour four–hourly mean plot of the percentage of data accepted as suitable by the full correlation analysis for June (top) and December (bottom). Since the radar sampled each height range every 4 min, a maximum number of 60 points could be collected in any four–hour period.

Both June and December exhibited a diurnal variation in the data rates with the maximum rates occurring at night at all the heights. However, the height of the night–time maxima for June occurred between 75 and 85 km, while those of December occurred somewhat higher, between 85 and 95 km. While the maximum data rates in both months exceeded, at times, 80%, the overall data rates above 90 km for June (15-20%) were significantly lower than those during December (~30%). Finally, while during December no data were collected below 80 km at night, in June this only occurred below 75 km and even then some data were collected around noon (although for a few hours only).

The night–time data rates are larger than the day–time ones. It must be remembered that in mid–winter the upper atmosphere is still illuminated by sunlight. This is because, at a height of 100 km, the sun will still rise approximately 10° above the horizon, unlike in mid–summer, when the daylight is continuous. To investigate this further it is necessary to find which of the rejection criteria rejected data during what period. Tables 11.1 and 11.2 list the various rejection criteria and the percentage of data rejected by them based upon four height regions;

Error Code	Meaning	June-July data			
		70–78 km	80–88 km	90–98 km	100–108 km
0	Analysis OK (data accept)	29.8	42.3	33.2	10.8
1	Signal level too low	$\ll$0.05	$\ll$0.05	0.2	1.9
2	Signal/Noise too low	2.3	0.7	3.9	27.8
3	Fading too slow	6.6	7.5	24.7	23.2
4	Time delays too long	3.9	2.4	2.0	7.1
5	PTD > 50	26.8	14.5	8.8	14.4
6	$V_c^2 < 0$ (data accept)	$\ll$0.05	$\ll$0.05	0.1	0.1
7	Pattern analysis fails	1.9	0.5	0.2	0.2
8	$V_a > 250ms^{-1}$	7.4	10.3	4.6	0.1
9	$\|\theta_a - \theta_v\| > 40°$	1.7	1.0	0.4	$\ll$0.05
10	$V_a > 4V_t$	9.1	15.7	17.4	7.2
11	$V_t > 1.5V_a$	1.8	1.1	0.2	0.4
12	Bad fit to cross-corr. fn	4.0	3.4	2.0	1.5
13	ρ_{max} less than 0.2	3.5	0.1	1.3	3.8
14	Hardware fp error	$\ll$0.05	$\ll$0.05	$\ll$0.05	$\ll$0.05
15	Maths error (Log, Log10)	0.2	0.1	0.1	$\ll$0.05
16	Other maths errors	0.7	$\ll$0.05	0.9	1.3

Table 11.1: The full correlation analysis performs on–line analysis of data which may be accepted and rejected according to stringent parameters. The table above lists the different acceptance and rejection codes, and the relative percentage of data that was deemed suitable or not by the specific error code for a period of eight days in June–July 1991 at Mawson. The data is binned into four different height distributions; 70–78 km, 80–88 km, 90–98 km, and 100–108 km.

70–78 km, 80–88 km, 90–98 km, and 100–108 km.

We first discuss the data from June. Between 70–78 km, ~30% of data were accepted. The rejection due to low S/N ratios, slow fading times and long time delays were relatively minor, altogether accounting for only 12%. A large percentage of data were rejected due to large PTD's (~27%). Perhaps the most surprising was the percentage of data rejected by errors 8–11 (we shall refer to these errors collectively as E_{app}), which test for the magnitude and direction of the apparent velocity and compare it to the true velocity (as defined by the full correlation analysis). Here E_{app} rejected about 20% of data, with the bulk of the rejections due to either an apparent velocity greater than 250 ms^{-1}, or one that was more than four times larger than the true velocity. This could perhaps be due to intense turbulence.

Between 80–88 km, the percentage of accepted data increased to about 42%. This was due to a decrease in data rejected by large PTD's to less than 15%. However, the rejection due to E_{app} and slow fading slightly increased, while the other parameters slightly decreased or

Error Code	Meaning	December data			
		70–78 km	80–88 km	90–98 km	100–108 km
0	Analysis OK (data accept)	18.0	31.8	47.1	21.8
1	Signal level too low	0.0	0.0	0.0	$\ll$0.05
2	Signal/Noise too low	4.0	0.8	0.5	23.6
3	Fading too slow	3.5	2.9	4.1	20.3
4	Time delays too long	5.0	5.9	7.3	6.3
5	PTD > 50	30.3	27.3	25.0	15.1
6	$V_c^2 < 0$ (data accept)	0.5	0.7	0.9	4.0
7	Pattern analysis fails	1.0	2.1	1 1	0.6
8	$V_a > 250ms^{-1}$	16.7	6.2	0.5	0.3
9	$\|\theta_a - \theta_v\| > 40°$	1.4	1.6	1.0	1.0
10	$V_a > 4V_t$	8.0	7.5	6.3	5.2
11	$V_t > 1.5V_a$	1.2	2.4	2.7	0.5
12	Bad fit to cross-corr. fn	1.3	$\ll$0.05	$\ll$0.05	$\ll$0.05
13	ρ_{max} less than 0.2	8.0	10.0	3.0	1.0
14	Hardware fp error	0.0	$\ll$0.05	0.0	$\ll$0.05
15	Maths error (Log, Log10)	$\ll$0.05	$\ll$0.05	0.0	$\ll$0.05
16	Other maths errors	0.4	$\ll$0.05	$\ll$0.05	0.0

Table 11.2: As for table 11.1 but for an eight day period during December 1991.

essentially remained constant. Between 90–98 km, total data accepted fell to about 33%. The trends by all the other error criteria remained the same, with the exception of slow fading which now accounted for nearly a quarter of all data being rejected. Above 100 km, only 11% of data were accepted, with low S/N ratios, and slow fading times each rejecting around 25% of data, and long PTD's about 15%.

In December, less data were accepted in the lower heights, and more in the upper height ranges than during June. The percentage of data accepted, for the four height ranges, are about 18%, 32%, 47%, and 22% for the 70–78km, 80–88 km, 90–98 km and 100–108 km height ranges respectively. The general trends of rejection in December are similar to those during June, but somewhat displaced in height. For example, whereas slow fading is the cause of the rejection of the data in June collected above 80 km, during December this only applies applies to heights above 100 km. At low heights (70–78 km), however, more data are rejected during December than June on the basis of the E_{app} criteria. In addition, 8% of data during December are rejected by the $\rho_{max} < 0.2$ rejection criterion.

It must be noted that the error rejections based upon the apparent velocity test are the last

checks that the full correlation analysis undertakes, i.e. the data have passed through all of the other rejection codes first. Therefore, all of the mathematical algorithms have been passed, and only the physical interpretation of the results makes us reject the data. This large percentage of data rejected at greater heights is similar to that found at Christmas Island, where, at times, up to 20% of the data were rejected above 90 km.

As to the cause of the descent of maximum number of the data rates during winter, this is probably due to the winter anomaly (discussed earlier), where, due to an increase in low level ionization more reflections occur at lower heights [see e.g. *Scwentek*, 1963]. The increase in the D–region ionization during winter is attributed to either a temperature rise which alters the chemical production/loss mechanisms, or an increase in the concentration of NO which is easily ionized by the Lyman–α radiation.

11.2.2 Signal–to–noise ratios

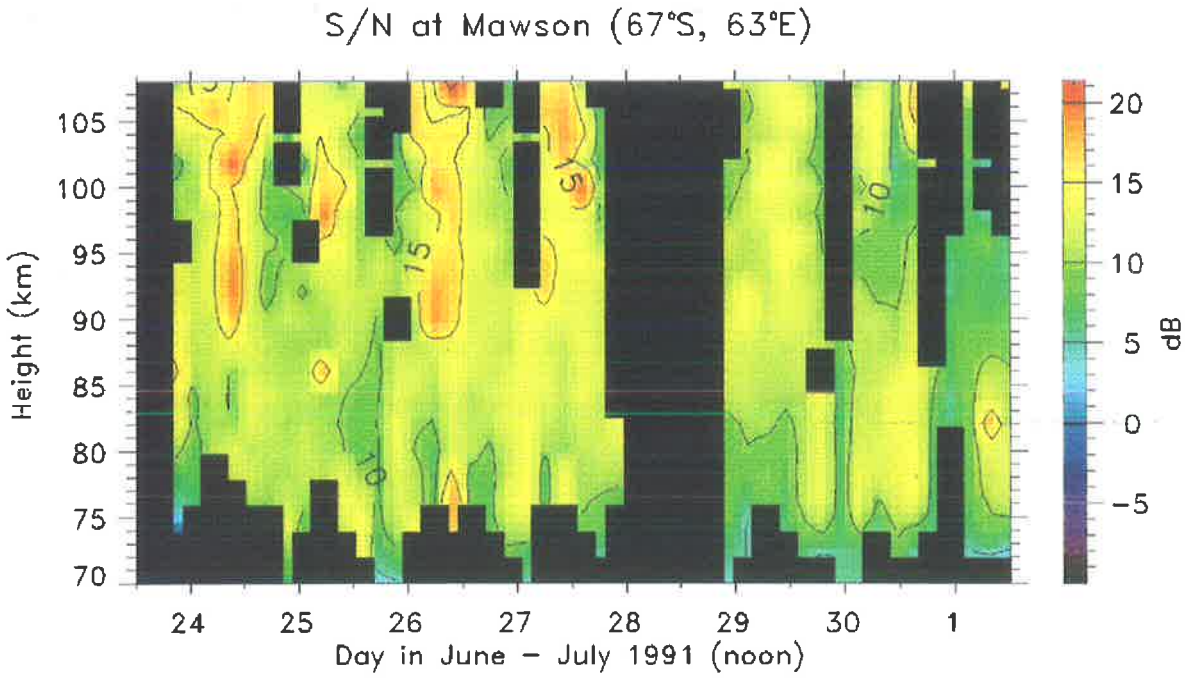

Figure 11.2: Four–hourly mean signal–to–noise ratios per unit height at Mawson during June 1991.

As in the previous chapters, an investigation into the S/N ratios hopefully provides some information on the echo field strengths. Although not an ideal parameter to use, the mean S/N ratios (over several hours) do provide a rough indicator of the relative power being reflected from the ionosphere. However, it must always be remembered that the noise probably shows a larger diurnal variation than the signal, with the night–time noise greatly exceeding the day–time noise due to extra absorption of noise in day–time. Four–hourly mean signal–to–noise ratios are plotted in figures 11.2 and 11.3 for June (winter) and December (summer) 1991 respectively. There is one difference between the two diagrams. Whereas the June S/N ratios are only those which have been accepted by the full correlation analysis programs, this is not so for December. The S/N ratios presented for December include all of the reflections obtained by the radar, whether or not accepted by the full correlation analysis. The reason for doing this is to investigate the S/N ratios below 80 km, since the December data rates below 80 km are low compared with those in June. In addition, below 100 km, only a few percent of the data are rejected on the basis of the S/N ratios, whereas above 100 km, that criteria rejects

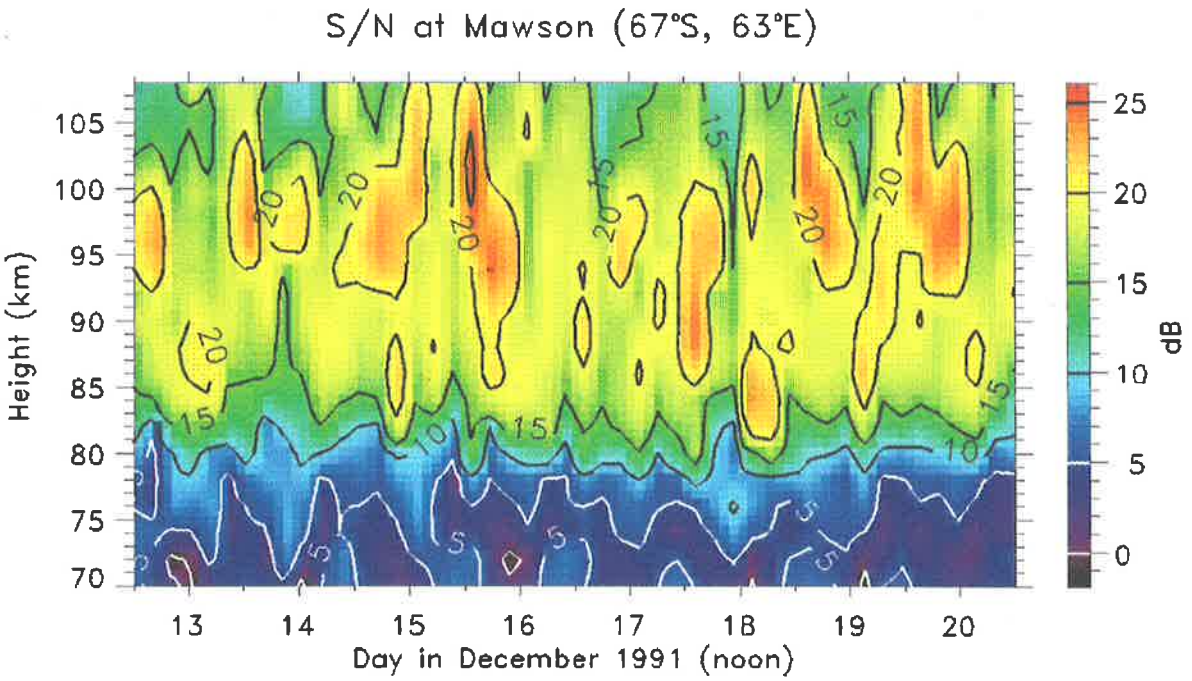

Figure 11.3: Four–hourly mean signal–to–noise ratios per unit height at Mawson during December 1991.

approximately a quarter of the total data possible.

As can be seen from the two figures, the S/N ratios below 80 km are quite large in June, with a mean value around 10 dB. On the other hand, the December S/N ratios are quite low and are on average 5 dB lower, with a mean value which varies around 5 dB. However, above 80 km, there is a reversal. Whereas the winter S/N ratios only slightly increase above 80 km, reaching at times more than 15 dB, during summer the mean S/N ratios are greater than 15 dB, with peak values of more than 25 dB.

The two seasons do share a common trait, which is a clear diurnal variation, although the June variation is clearly not as strong as the December one. The maximum S/N ratios are observed in the early morning, In addition, closer examination of the December S/N ratios reveal a semi–diurnal variation, especially evident at 95 km from the 16^{th} onwards. This semi–diurnal variation has also been found by *Phillips* [1988], who investigated the relationship between the reflected signal strengths and geomagnetic activity. This study found that during disturbed conditions, there is large attenuation of the signal around midday. In another words, during quiet conditions, the low level echo strengths increase around midday, whereas during disturbed conditions they decrease. However, in the data presented here the semi–diurnal variations are not very clear. This is however mainly due to the fact that the data have been averaged into four hour blocks.

11.3 Mean winds at Mawson

The zonal and meridional four–hourly mean winds are presented as image–contour plots in figure 11.4 (top and bottom) for June, and in figure 11.5 for December 1991. As before, the data have not been filtered to remove wave motions, except for periods less than the four–hour averaging time. The following discussion pertains to these data.

Both the winter and summer zonal and meridional flows show a complicated structure dominated by long–term wave motions and tides. During winter, the flow is generally eastward reaching velocities up to 40 ms^{-1}, although above 85 km it is around zero or slightly negative in

the mid–afternoon, probably due to the diurnal tide. The zonal winds in summer are generally westward below 85 km, with speeds over 30 ms^{-1}. Above 85 km, the flow varies from being slightly westward to strongly eastward up to 25 ms^{-1}. The eastwards winds generally dominate. No obvious periodicity is seen although perhaps a wave motion of around 40–60 hr is hinted at.

Unlike the zonal flow, the winter meridional flow clearly shows a dominating quasi–two–day wave motion, especially below 95 km, oscillating between –25 to +25 ms^{-1}. Above 95 km, the quasi–two–day wave motion is still evident, but with an additional diurnal variation. During summer, the meridional flow structure is complicated, although hints of both a quasi–two–day wave and diurnal variation are seen. The wind is large, varying at times between –30 to +30 ms^{-1}. A study of the dominant wave motions has been carried out by *Phillips* [1988] who found that the meridional component of the diurnal and semi–diurnal tides is significantly larger than that of the zonal component for all heights (70–108 km) and during all seasons. This dominance of the meridional component may be an artifact of the spaced–antenna technique, especially at greater heights (up to 100 km) and during high geomagnetic activity, since the radar may be observing charged–particle drift which is not necessarily coupled with the neutral wind motions. It has been estimated that drifts of at least 10 ms^{-1} are induced down to altitudes of 90 km in the meridional direction and down to 100 km in the zonal direction, increasing rapidly with increasing height for both components [*Reid*, 1983]. Thus spaced antenna measurements may be increased and shift away from the direction of the Hall drift (ExB) towards the direction of the electric field (E) when the electric field strength increases. However, until long–term comparisons between spaced–antenna winds and other instrument measurements are made, the net effect may not be estimated. It has been found, though, that the amplitude of the meridional diurnal wind component has a distinct connection with times of high geomagnetic disturbances, increasing in step with increasing geomagnetic conditions [*Phillips*, 1988]. This was not true for the zonal component or any component of the semi–diurnal tide. Another study also found a significant correlation between the raw wind and geomagnetic activity as well as a polarization of the high and medium frequency wind components in the geographic meridional direction

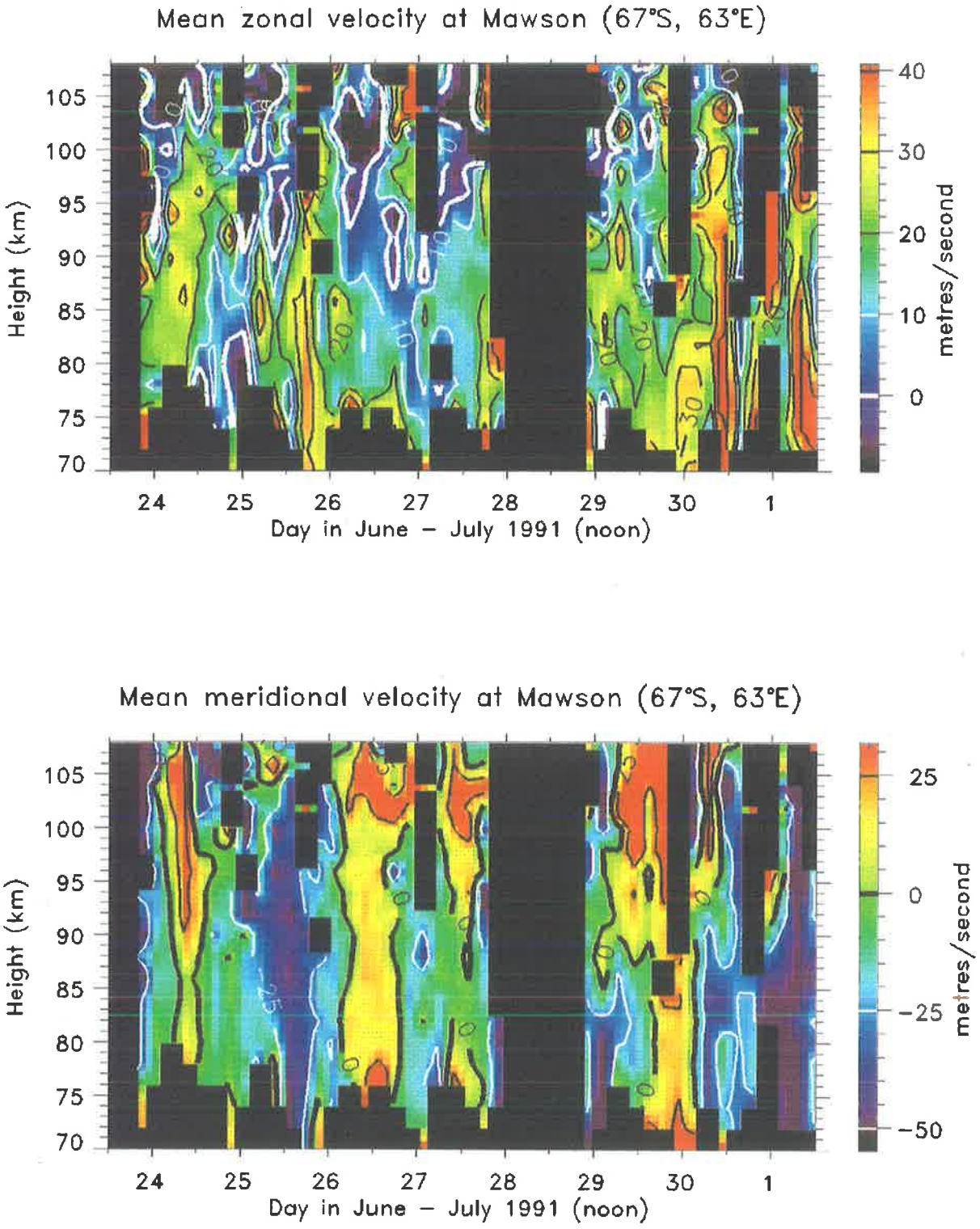

Figure 11.4: Four-hourly mean zonal (top) and meridional (bottom) winds at Mawson during one week in June 1991. The contours are labelled in ms^{-1}.

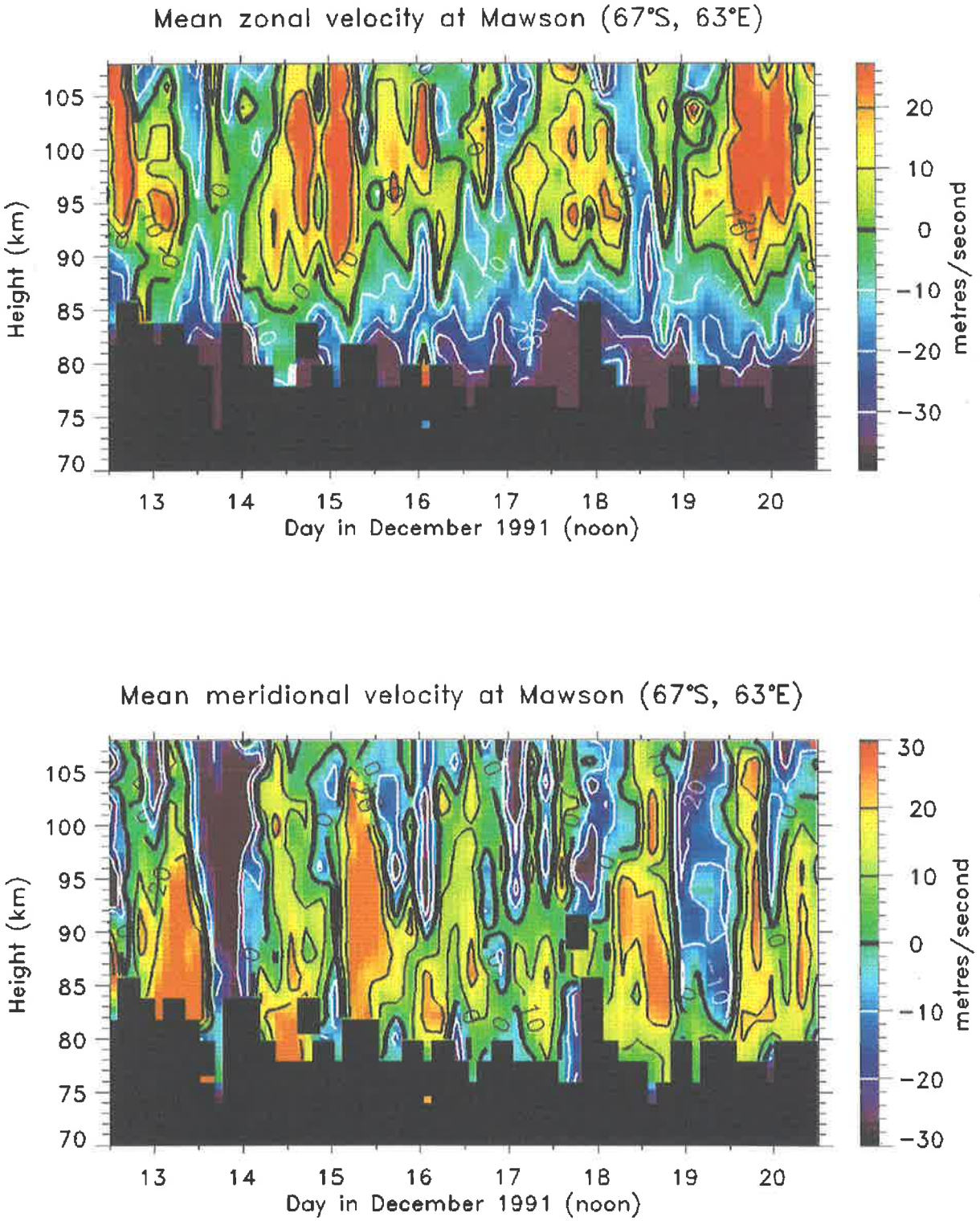

Figure 11.5: Four–hourly mean zonal (top) and meridional (bottom) winds at Mawson during one week in December 1991. The contours are in ms^{-1}.

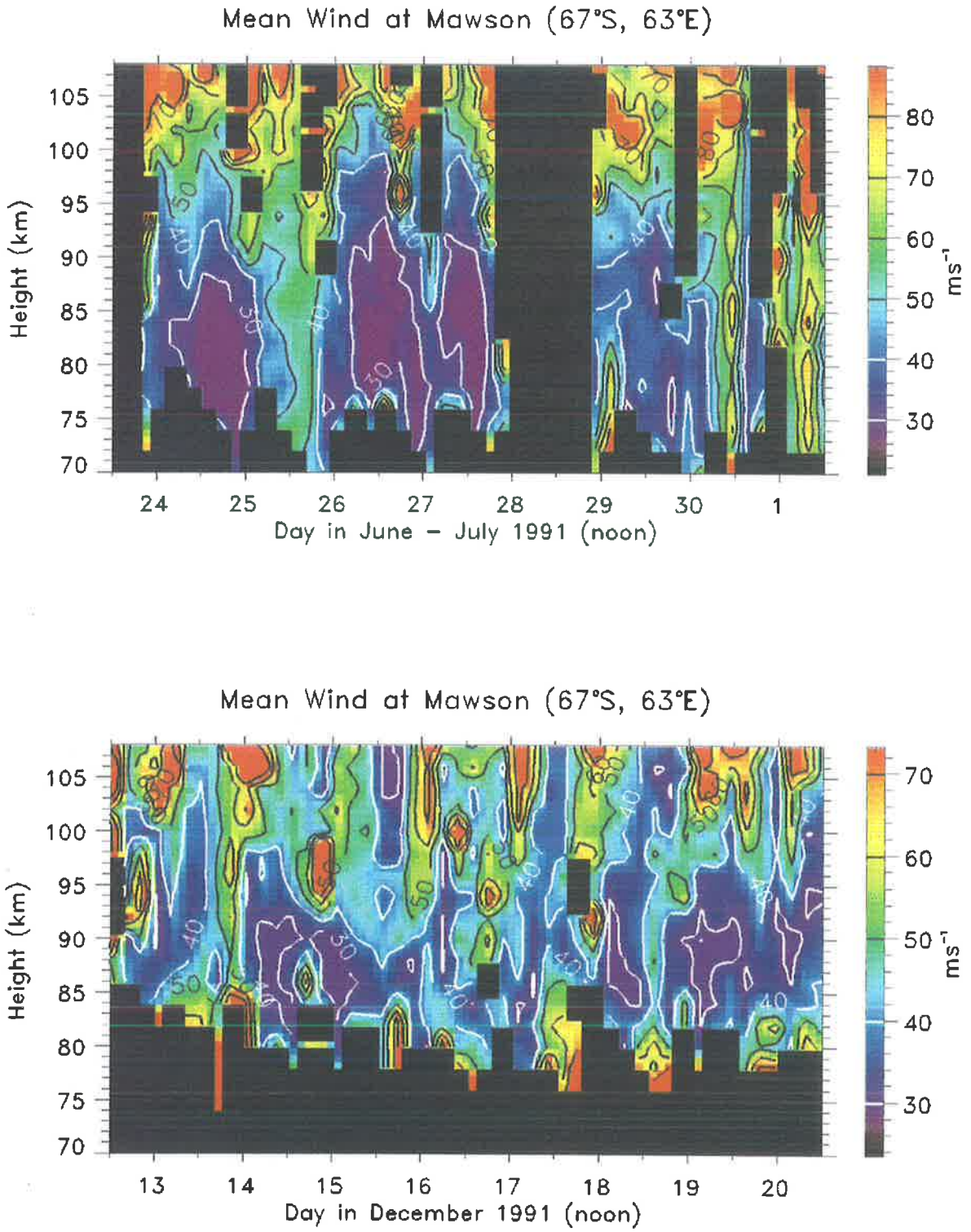

Figure 11.6: Four–hourly mean wind speed at Mawson for June (top) and December (bottom) 1991. The contours are labelled in ms^{-1}.

greatest in the 80–88 km range [*Price*, 1988].

It is not the intention here to discuss these motions in any detail. That has been investigated in other studies [see e.g. *Phillips & Vincent*, 1989] . The reason for their inclusion is to note the complexity of the wind both spatially and temporally. In this way, the investigation into the other parameters of full correlation analysis, and the structure of the scatterers can take into account any influence of the prevailing dynamical conditions. For that reason, it is useful to determine the mean wind magnitude, regardless of its direction. This is plotted in figure 11.6 for both June (top) and December (bottom). These diagrams show that during both summer and winter the wind velocity is larger at upper heights. During winter, the wind below 95 km varies between 20–30 ms^{-1} increasing to between 50–80 ms^{-1} above 100 km. During summer the increase in wind speed with altitude is also observed, but is not constant through the day, showing a clear diurnal variation, which peaks in magnitude around noon. In addition, large velocities are also observed at times around below 85 km, but with no obvious temporal structure.

11.4 Seasonal behaviour of spaced–antenna parameters

The following sections describe the various parameters of full correlation analysis and their temporal and spatial behaviour. As before, all the data are presented as image–contour plots and share a common colour coding for the two different time periods. We start off with the mean fading times and lifetimes of the ground diffraction pattern.

Fading times and lifetimes of the ground diffraction pattern

The four–hourly mean fading times and lifetimes as a function of time and height are presented in figures 11.7 and 11.8 for June and December respectively. In both figures, the top diagram represents the fading times while the bottom represents the lifetime of the pattern.

The fading times vary from less than 1.5 sec to around 3 sec in June, and up to 4 sec during December. However, during June, the fading times above 85 km, with the exception of the night

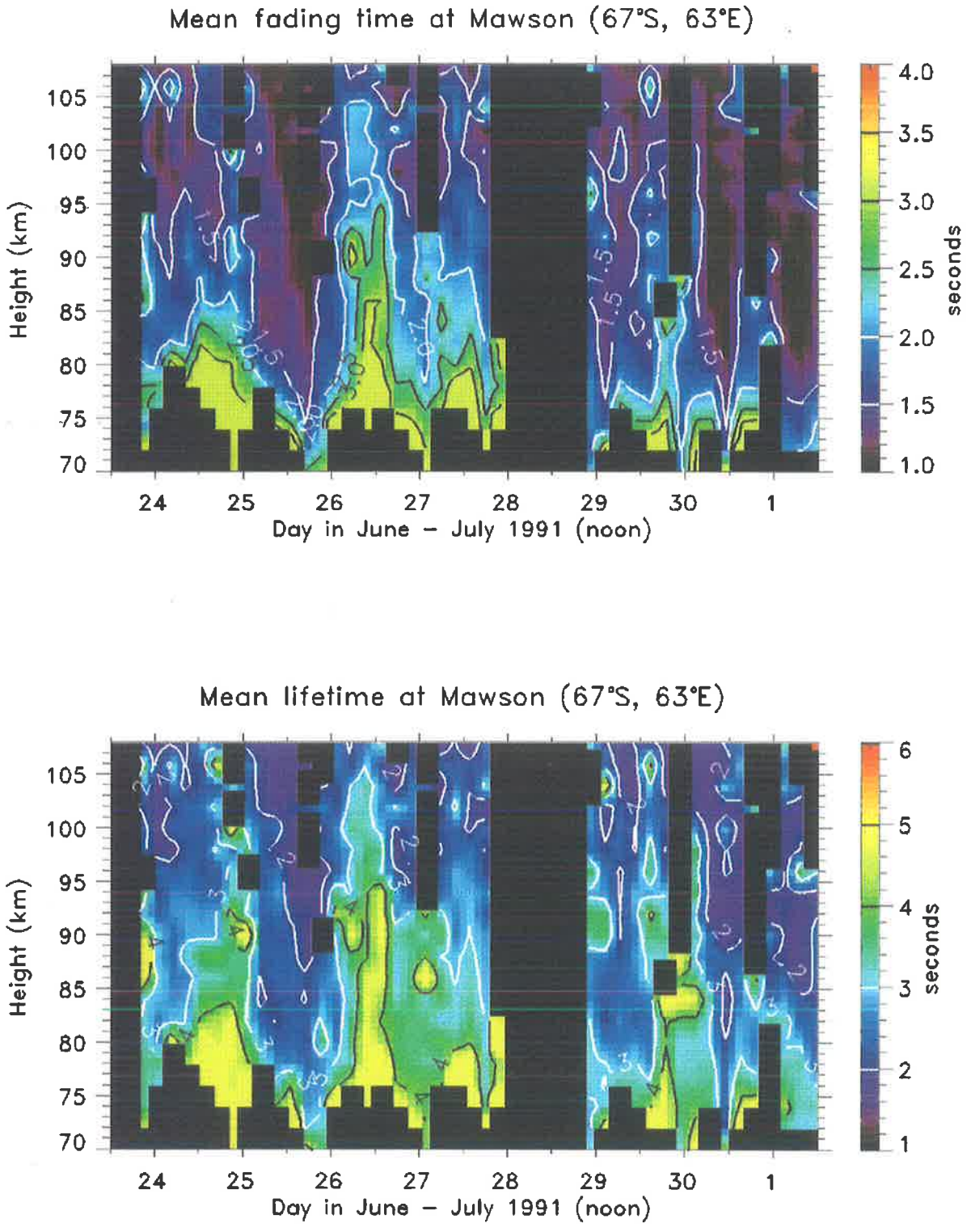

Figure 11.7: Four–hourly mean fading times (top) and lifetimes of the ground pattern (bottom), for one week at Mawson in June 1991. The contours are labelled in ms^{-1}.

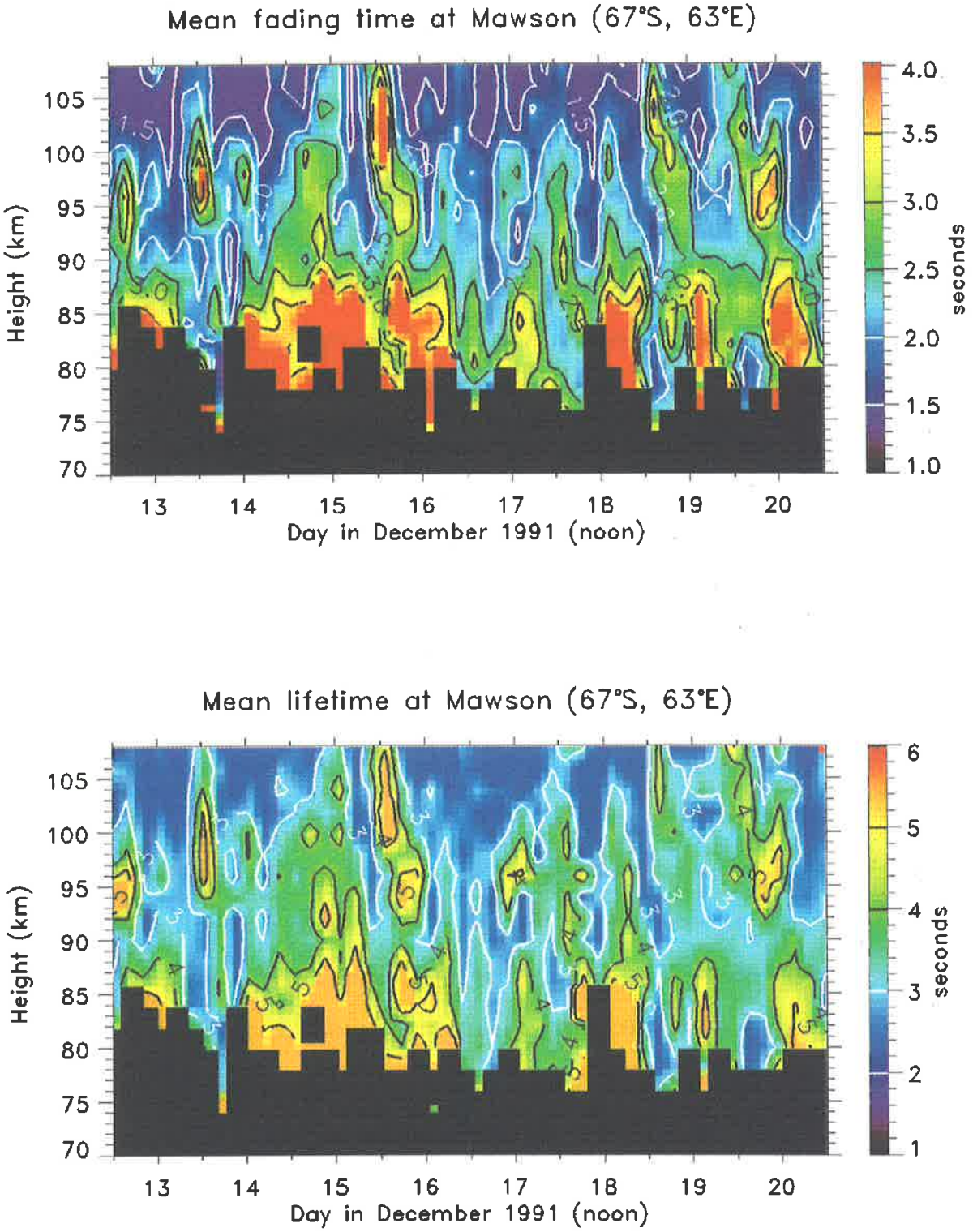

Figure 11.8: Four-hourly mean fading time (top) and lifetime of ground pattern (bottom), for one week at Mawson in December 1991. The contours are in labelled in ms^{-1}.

of the 26^{th} to 27^{th}, is rarely more than 1.5 sec. In contrast, this height boundary is around the 100 km mark for December. Below 85 km, the fading times in summer are generally high, with a diurnal variation with maxima occurring in the afternoon. Fading times in June do not exhibit such clear diurnal variations but do show broad maxima, with periods of perhaps several days. The fading times should vary in a similar way to the mean winds. When the wind magnitude is large the fading times should be correspondingly small. Comparison of the wind magnitude with the fading times shows that this is generally the case, for when the wind is small the fading times increase. However, at times this is not true and larger fading times occur during large wind speeds. For example, on the 15^{th} of December, the mean wind speed around 95 km is large, up to 50 ms^{-1}. At the same time the fading times, which should be small, are relatively large. This and other examples may then be due to the shape of the scatterers or their aspect sensitivity. As before, the scatterer shapes will be discussed shortly.

The lifetimes, which are fading times but with the effect of the wind removed, represent the relative stability of the ground diffraction pattern. They exhibit similar behaviour to the fading times, but are somewhat larger, varying between 2.0–4.5 sec in winter, and 3.0–5.5 sec during summer. The lifetimes in winter show some long–term structure, while the lifetimes in summer follow a strong diurnal variation with maxima during the afternoon. It is somewhat surprising that the character of both the fading times and lifetimes are in step with each other. This strongly suggests that the mechanisms for the local dynamical conditions also produce or interfere with the partial reflection radar scatterers. In the preceding sections it was mentioned that some studies have found a correlation between geomagnetic activity and the wind. Therefore, it might be expected that geomagnetic activity also affects the radar scatterers. This will be discussed in a later section. For now we turn to the geometrical description of the ground diffraction pattern.

Pattern scale and axial ratio

Figures 11.9 and 11.10 show the mean pattern scale (top) and axial ratio (bottom) for June and December respectively. The pattern scales in winter vary between 200–300 m. They are

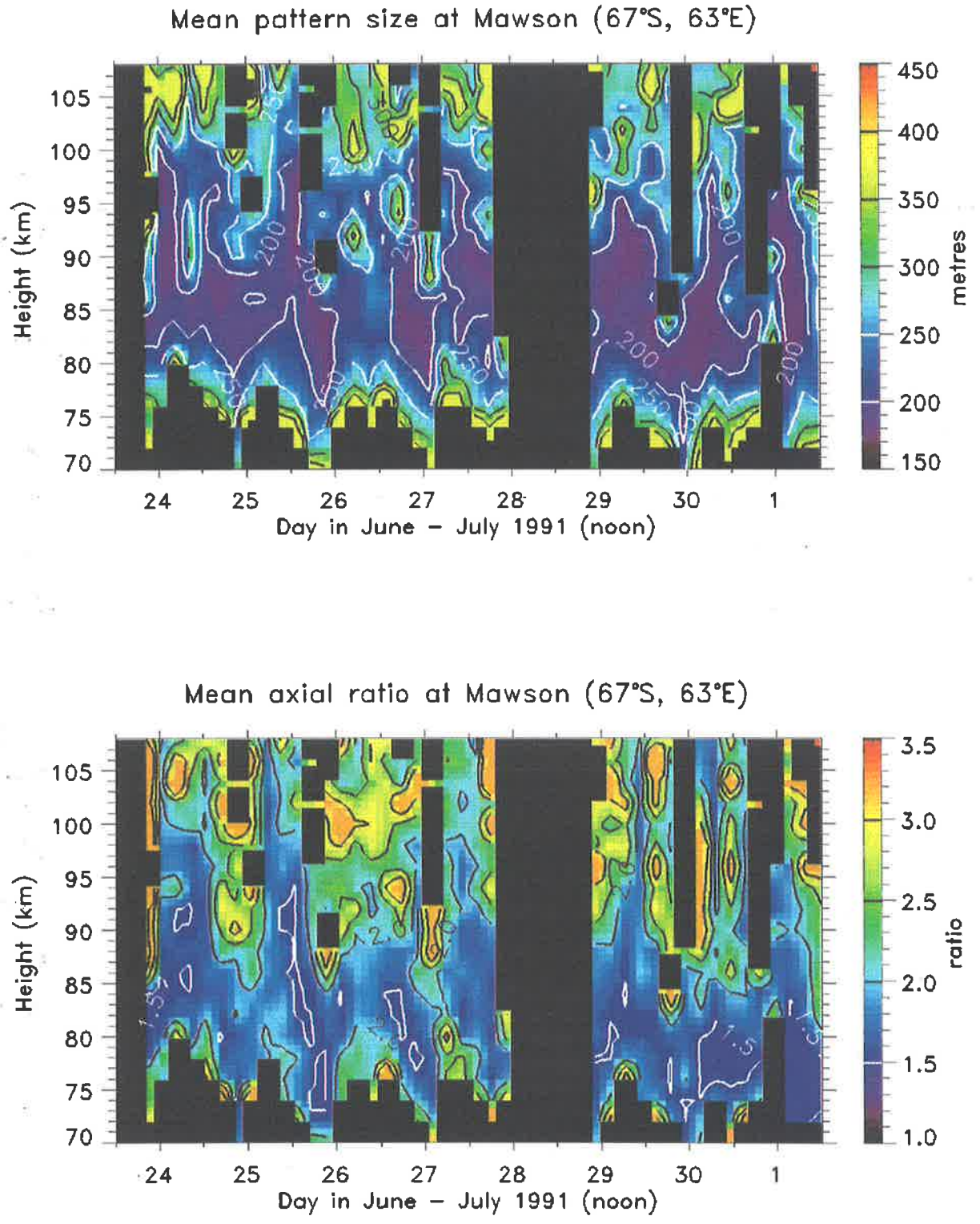

Figure 11.9: Four-hourly mean pattern size (top) and axial ratio (bottom), for one week at Mawson in June 1991. The contours are in seconds.

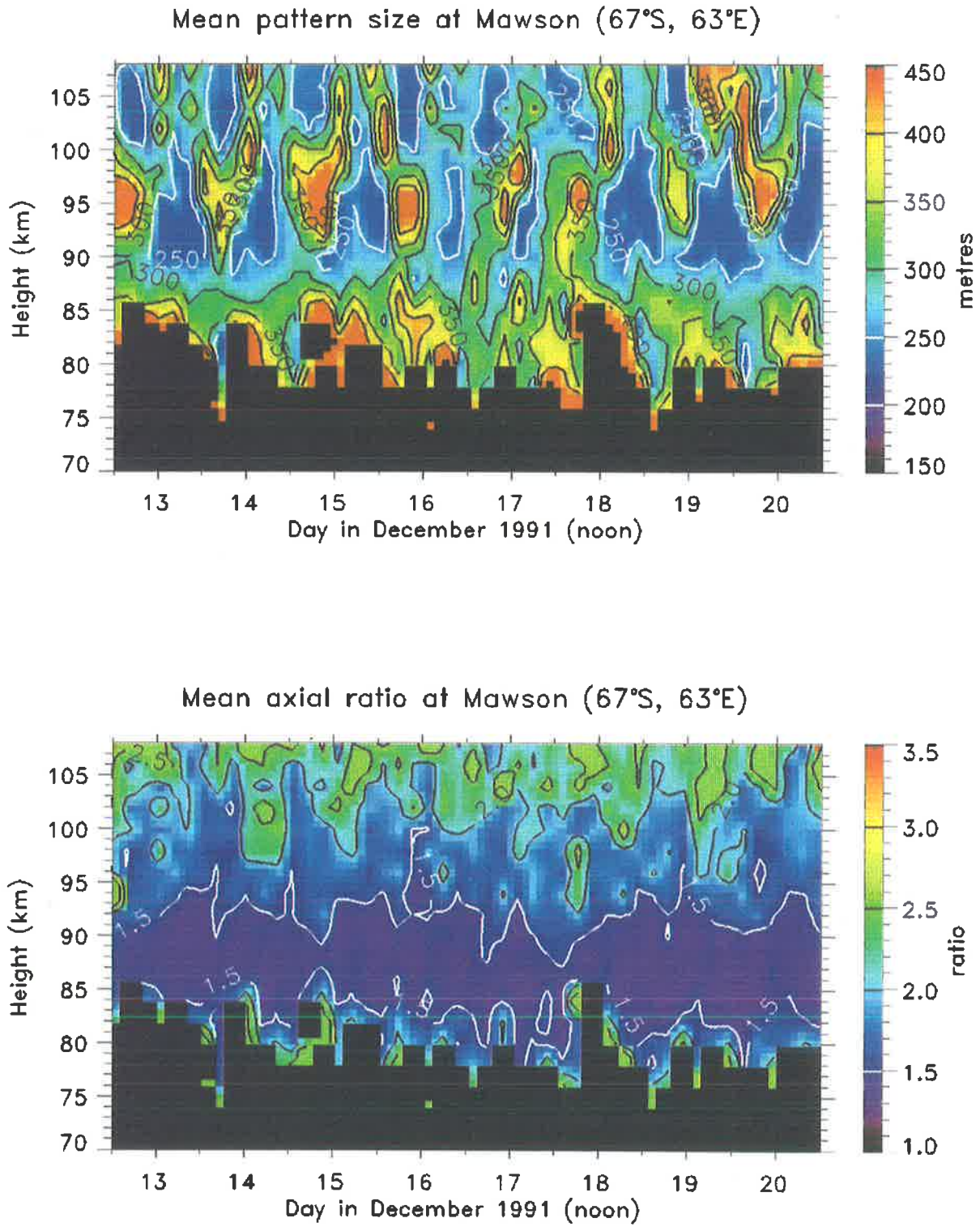

Figure 11.10: Four-hourly mean pattern size (top) and axial ratio (bottom), for one week at Mawson in December 1991. The contours are labelled in seconds.

relatively stable around the 200 m mark between 80–100 km although some local increases do occur. Both above 100 km and below 80 km, the pattern scales increase. In addition a diurnal variation exists below 80 km with minima occurring at noon. During summer, the pattern scales vary from 250 to 450 m. A clear diurnal variation is observed above 90 km with early morning minima of less than 250 m, and late afternoon maxima of more than 400 m. Above 100 km the afternoon maxima seems to split up into a short minimum surrounded by two short maxima, acting somewhat like a semi–diurnal variation.

The pattern axial ratios during winter range from 1.5–3.0. A clear diurnal variation is seen with maxima centred around noon above 85 km, which shift towards night–time below about 80 km. The summer axial ratios are quite different. No diurnal behaviour is seen at all below 95 km, and only some weak evidence of it occurs above that height. The axial ratios, which vary from ~1.25–2.5 are extremely stable in the 85–95 km region with values less than 1.5.

The correlation between the pattern scale as a function of height and geomagnetic activity has been investigated by *Price* [1988]. That study found that below 80 km the pattern scale increased with increasing geomagnetic activity, was relatively constant between 80–85 km, and decreased with increasing geomagnetic activity above 85 km. This effect was found to be strongest during winter. Geomagnetic activity measured during spring and summer was found to be low between noon and evening, and high for several hours after midnight. Therefore, this supports the results of this study where, during summer, large pattern scales are found after noon local time and small pattern scales occur in the early morning.

11.5 Aspect sensitivity

Taking the aforementioned values of the fading times, mean wind speeds, and ground diffraction pattern parameters, the aspect sensitivity of the Antarctic partial reflection scatterers was calculated by the two methods described earlier in this thesis, the spectral–width and the spatial–correlation method. The results of these calculations of the aspect sensitivity (θ_s) are shown in figures 11.11 and 11.12 for June and December respectively, with the spectral–width

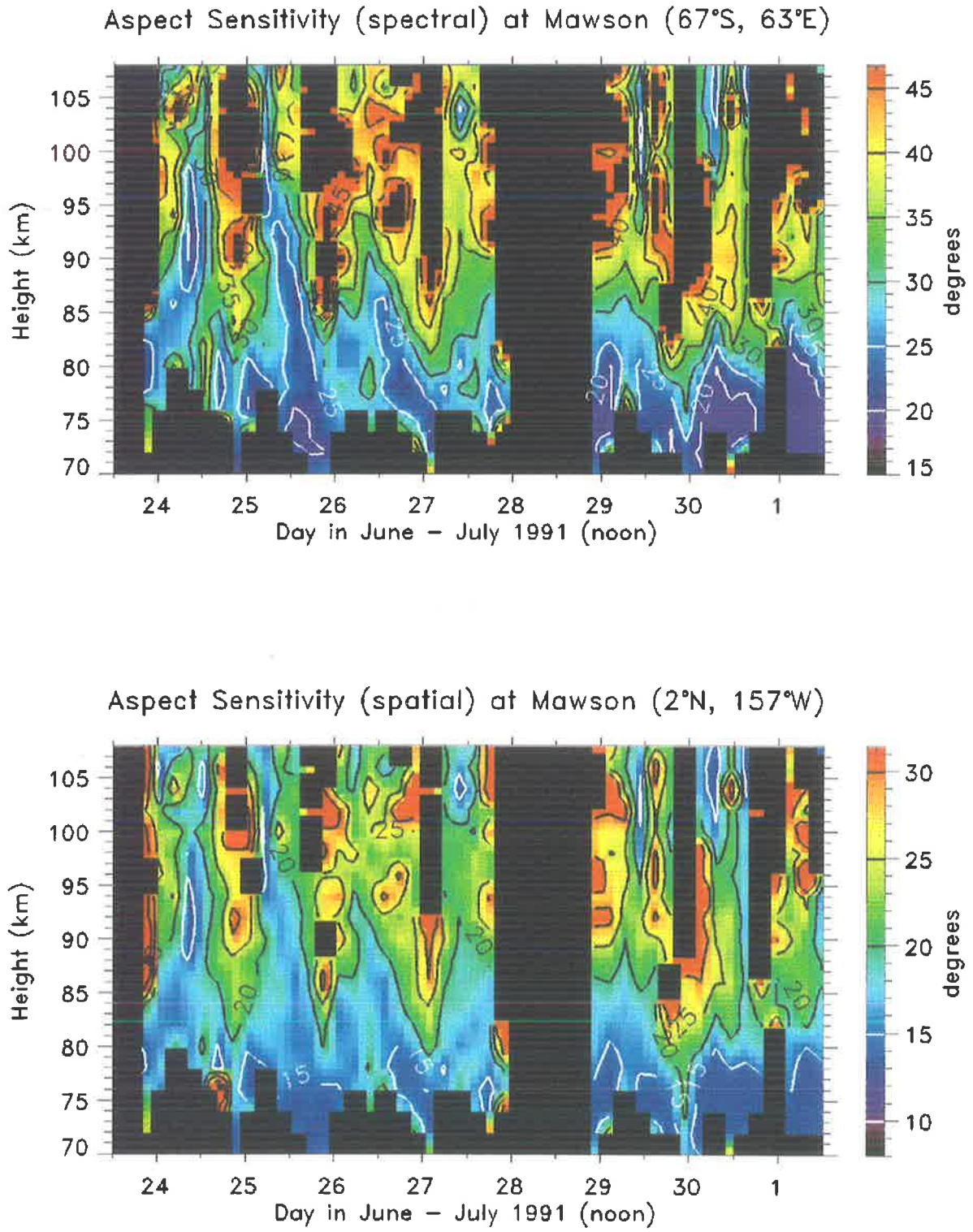

Figure 11.11: Four-hourly mean aspect sensitivity calculated by the spectral width method (top) and the spatial method (bottom) for one week during June 1991 at Mawson.

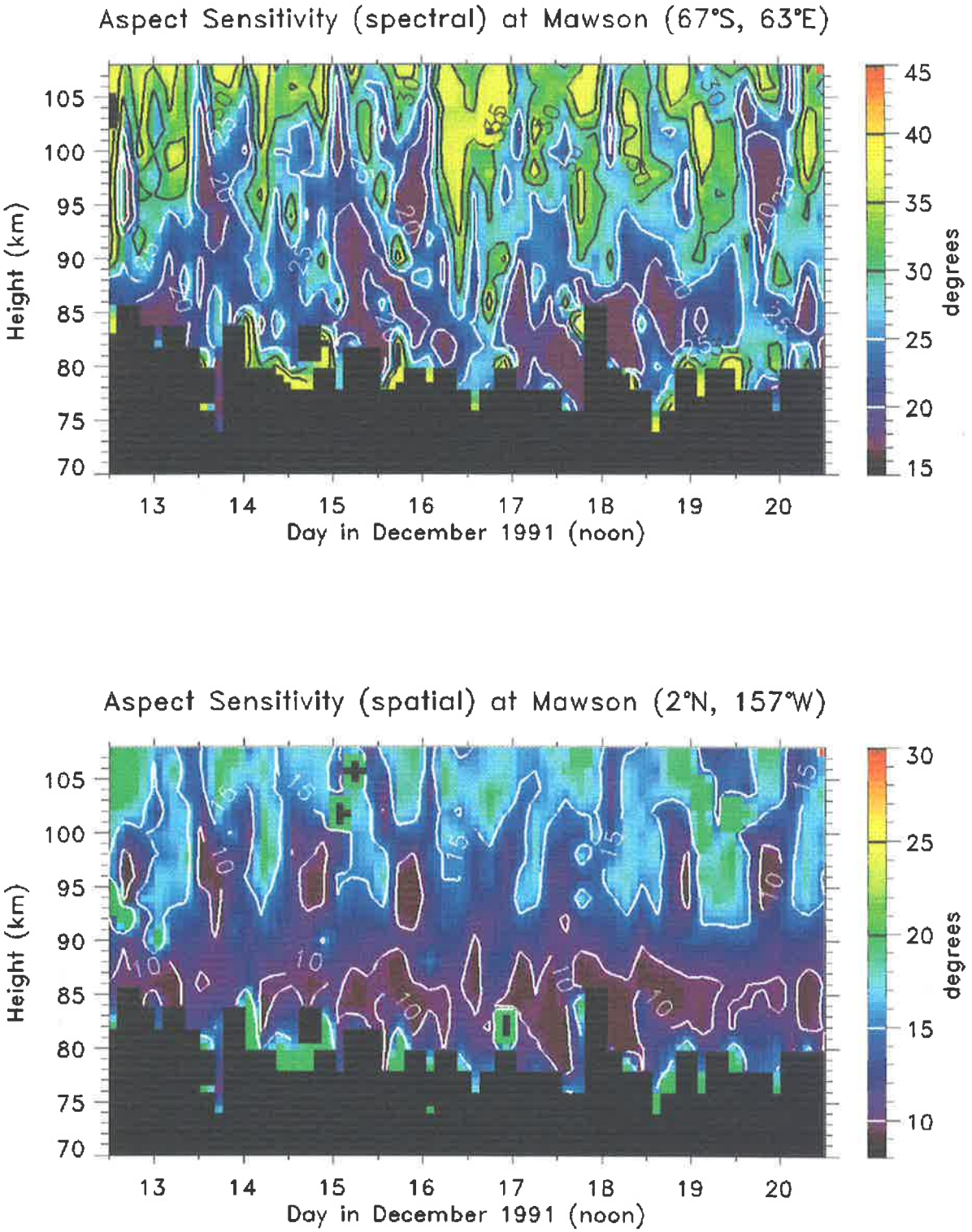

Figure 11.12: Four–hourly mean aspect sensitivity calculated by the spectral width method (top) and the spatial method (bottom) for one week during December 1991 at Mawson. The contours are labelled in degrees.

data on the top and the spatial-correlation data on the bottom of the diagrams.

Comparison of the aspect sensitivity calculations shows, as expected, that the two techniques show very similar characteristics although the absolute values of θ_s calculated by the spectral-width method are much larger than those calculated by the spatial-correlation method. Again, this can be traced to the calculation of the fading time. The spectral-width calculations of θ_s include a turbulence effect and are also affected by the orientation of the ground diffraction pattern with respect to the wind direction. If the orientation of the correlation ellipse is not random, then this makes the spectral-width method biased. The relationship of the geometry of the ground diffraction pattern with respect to geographical north and the wind direction will be investigated later on in this chapter. For now, we concentrate on the mean values of θ_s.

During winter, values of θ_s range from around 20°–45° in the spectral-width case, and from 15°–30° in the spatial-correlation case. A clear diurnal variation exists in values of θ_s measured by both methods. It extends through all the heights, although it is not as strong below 80 km. In addition, θ_s contours descend with increasing time, the rate of descent averaging several kilometres per hour. At greater heights the minima are centred in the late morning, shifting in time with descending height to be centred in the afternoon at lower heights. Strong maxima are observed around noon local time, and persist over several hours. Below 80 km, values of θ_s are generally low, indicative of more specular structures. One could argue that this is due in part to the low data rates; however, as seen earlier, the data rates, (for example on the morning of June 26^{th}), are quite large.

In summer, the mean values of θ_s are very much lower than those found during winter. The spectral-width values of θ_s extend from less than 20° to about 35°, while the spatial-correlation values are lower, ranging from less than 10° to more than 15° (around 18°). A diurnal variation is exhibited by values of θ_s, although only in the range of 90–100 km. In this height range, low minima are observed which persist for more than 12 hours and are centred in the early morning. Above 100 km there is weak evidence of a semi-diurnal variation with narrower local maxima occurring simultaneously with the times of local minima in the 90–100 km height range.

11.6 Horizontal correlation lengths

The length–to–depth ratios of the partial reflection radar scatterers were calculated from the above values of θ_s, and are shown as image–contour plots in figure 11.13 for June and figure 11.14 for December. As before the spectral–width results are on the top of the figures while the spatial–correlation results are on the bottom.

Once again, the two methods show similar characteristics, although different absolute ranges due to the contamination of a turbulence effect. The spectral–width L/h ratios range from less than 1.0 to nearly 2.0 during summer, increasing to be within 1.25–2.25 in summer. The spatial–correlation L/h ratios range from 1.5–2.5 during winter, and 2.0–4.0 during summer. Since the spatial–correlation method is more robust we will discuss those results only.

An initial inspection shows that the winter time L/h ratios are very much lower than those found during summer. This is in step with the much earlier result which investigated the seasonal behaviour of L/h at Mawson [see figure 8.7], where it was found that during winter, the mean L/h ratios were much lower than those found calculated for the summer months.

Superimposed on both the summer and winter results is a diurnal variation in L/h ratios, which, however, shows different characteristics between the two data samples. The winter diurnal variation in L/h ratios extends throughout all the heights although it is most evident in the 80–100 km height range. In general, at night, the L/h ratios increase to values between 2.0–2.5, decreasing to less than 1.5 during the day–time. The minimum peak is quite broad above 85 km, and increases and decreases over the 80–90 km height range in a regular pattern (especially on the 25^{th}, 26^{th} and 27^{th} June). During summer the situation is quite different. Although a diurnal variation is clear, the maxima are contained in the height range of approximately 90–100 km. In this range, the L/h ratios vary from a minimum around 2.5 during the late afternoon, and a maxima at times exceeding 4.0 during the early morning. Below this height range, the ratios are more constant, around 3.5–4.0. Above approximately 100 km, the diurnal variation changes into a quasi–semi–diurnal variation. The maxima in the 90–100 km range occurs at the same time as the minima below 90 km, albeit for a much shorter time. Maxima now tend

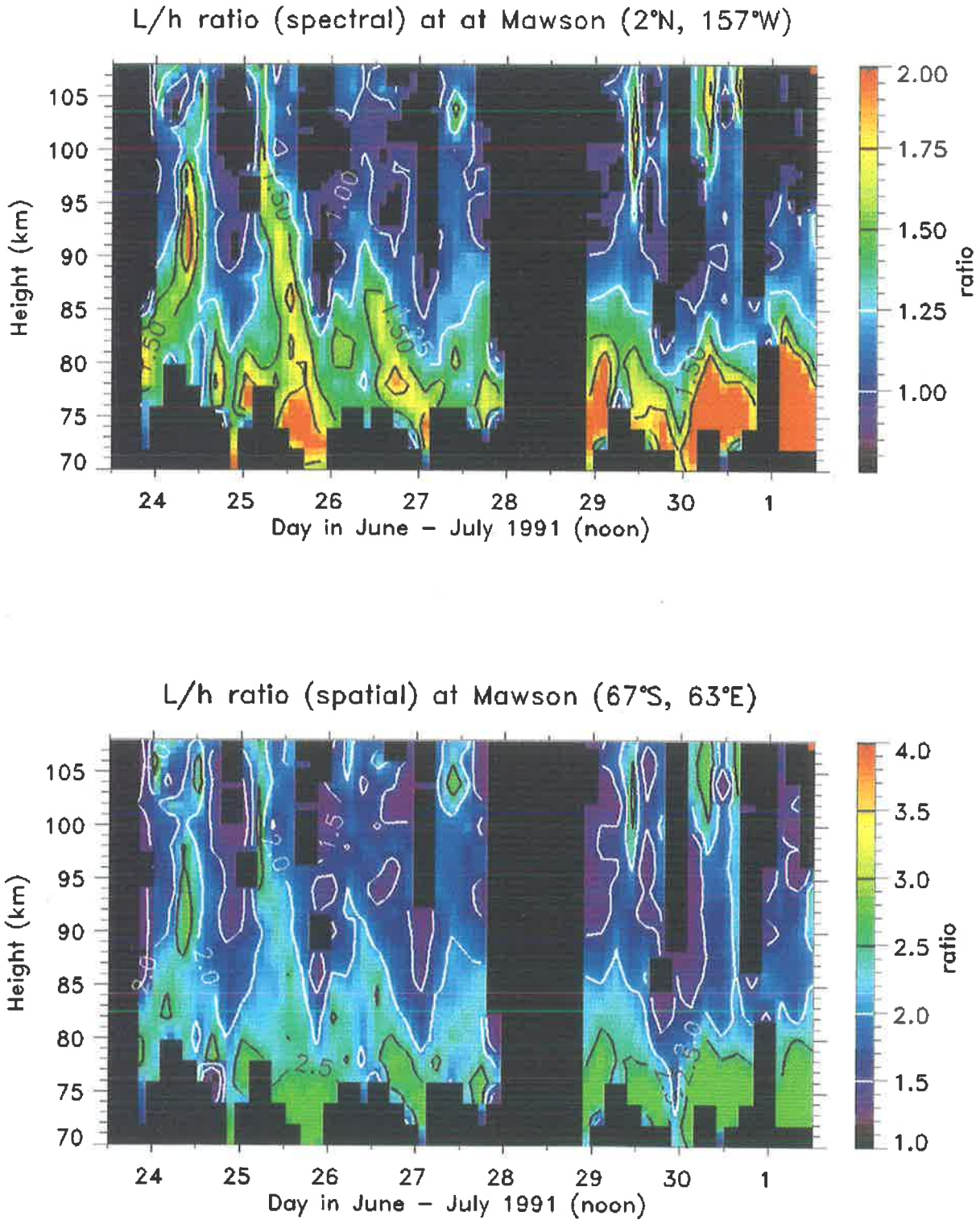

Figure 11.13: Four–hourly mean L/h ratios calculated by the spectral width method (top) and the spatial method (bottom) for one week during June 1991 at Mawson. The contours are the ratios of the horizontal to vertical extent of the irregularities.

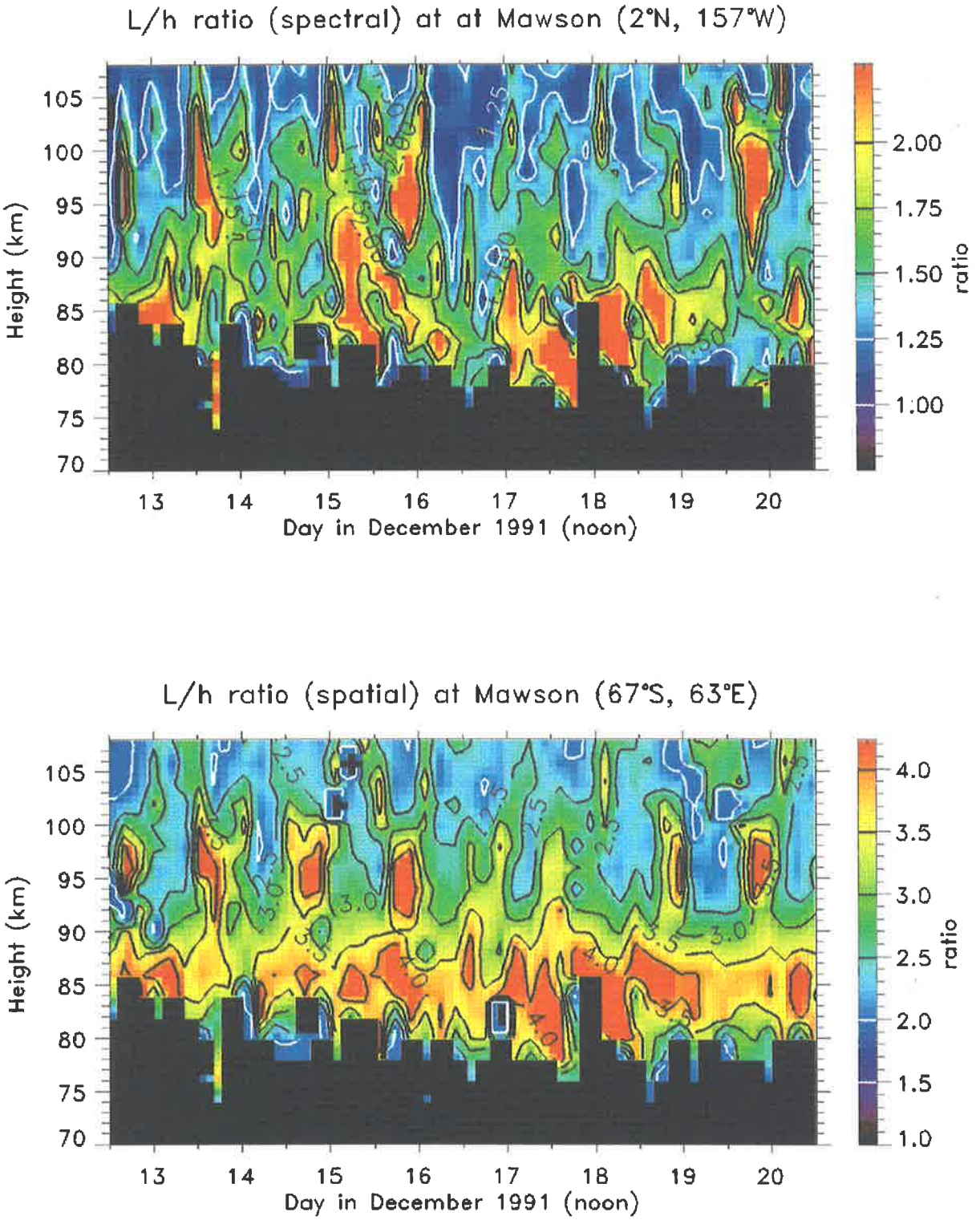

Figure 11.14: Four–hourly mean L/h ratios calculated by the spectral width method (top) and the spatial method (bottom) for one week during December 1991 at Mawson. The contours are the ratios of the horizontal to vertical extent of the irregularities.

to occur twice a day, around noon and midnight local time. Finally, it appears that below 80 km, the L/h ratios tend to decrease in values, at times by one–half, to 2.0.

The L/h ratios give an approximation of the horizontal to the vertical extent, on average, of the structures which are responsible for the partial reflection radar scatter. The above investigation suggests that besides the increase in anisotropy during the summer months, there is a clear diurnal variation in anisotropy both during winter and summer. However, the increase in summer is larger than that during winter, and its structure with respect to height is also different. This result is somewhat unusual since it was found that the pattern axial ratios were not only larger during winter than during summer, but they also exhibited a diurnal variation which was not present during December.

It is also interesting to compare the lifetimes of the ground diffraction pattern to the L/h ratios. During winter, the lifetimes exhibited no evidence of a diurnal variation. In fact a strong quasi–two–day variation was observed with, for example, maxima found on the $24^{th}/25^{th}$ and $26^{th}/27^{th}$, while a strong minimum occurred on the $25^{th}/26^{th}$ of June. This implies that the scatterers were relatively short–lived on the $25^{th}/26^{th}$, and long–lived on the other two dates. During the $25^{th}/26^{th}$ however, the values of the L/h ratios reached a local maxima. So it appears that the stability of the scatterers orientations is unrelated to stability of their existence, somewhat of a paradox, for it is natural to assume that the mechanism which produces these structures should also affect their geometry. This puzzling result is also true for December when the lifetimes appear unrelated to values of L/h as well.

11.7 Two–dimensional nature of the scatterers

The L/h ratios of the scatterers presented above showed that, at times, the L/h ratios were quite anisotropic, more so during the summer than winter. It was also found that the pattern axial ratios during winter were not only larger than those during summer, but also exhibited a strong diurnal variation. In this section we investigate this horizontal anisotropy of the ground diffraction pattern using the circular statistics used and discussed in previous chapters and

which is described in appendix C. We first investigate the stability of the pattern orientations, using the mean normalized length, which would be equal to 1.0 for patterns which are all oriented in the same direction.

Stability of the mean pattern orientation

The normalized mean lengths (denoted as L_n) of the June pattern correlation ellipses for all axial ratios less than 9.0 are shown in figure 11.15. The values of L_n generally vary between about 0.2 up to more than 0.8. Two characteristics are evident from the image–contour. First, values of L_n are generally larger below heights of 85 km, where they peak with maximum values greater than 0.8. These maxima generally occur over night–times and persist for periods up to 12 hours. The minima correspondingly occur around noon, although they persist over a shorter time.

As discussed in the previous chapter, an L_n of about 0.8 corresponds to a circular standard deviation of less than 20°, while an L_n of around 0.2 corresponds to a deviation of about 60° . Above about 85 km, the overall stability of the pattern orientation decreases. However, a diurnal variation still exists, albeit shifted in time. If one were to draw a line of best fit through the mean length maxima with respect to height, the line would have a negative slope, so that the maxima values ($\sim$0.6) at a height of 100 km occurred earlier, around noon. This data therefore implies that the pattern stability is maximum around noon at greater heights, shifting in time with descending height so that at around 80 km, all the pattern orientations are within 20° of each other, a pretty stable result. Since the data rates around this height region are substantial, these results are a real effect, and not an artifact of low data rates.

To remove those data points which could be considered to be horizontally isotropic, pattern orientations whose axial ratios were less than 1.4 were removed from the data and the mean lengths recalculated. These recalculated lengths are shown in figure 11.16 (top). The percentage of data that fell within this category with respect to the total data (but only that accepted by the full correlation analysis) is shown at the bottom of the same figure. The data rates are generally high and of the order of 50%, although somewhat higher above 95 km reaching

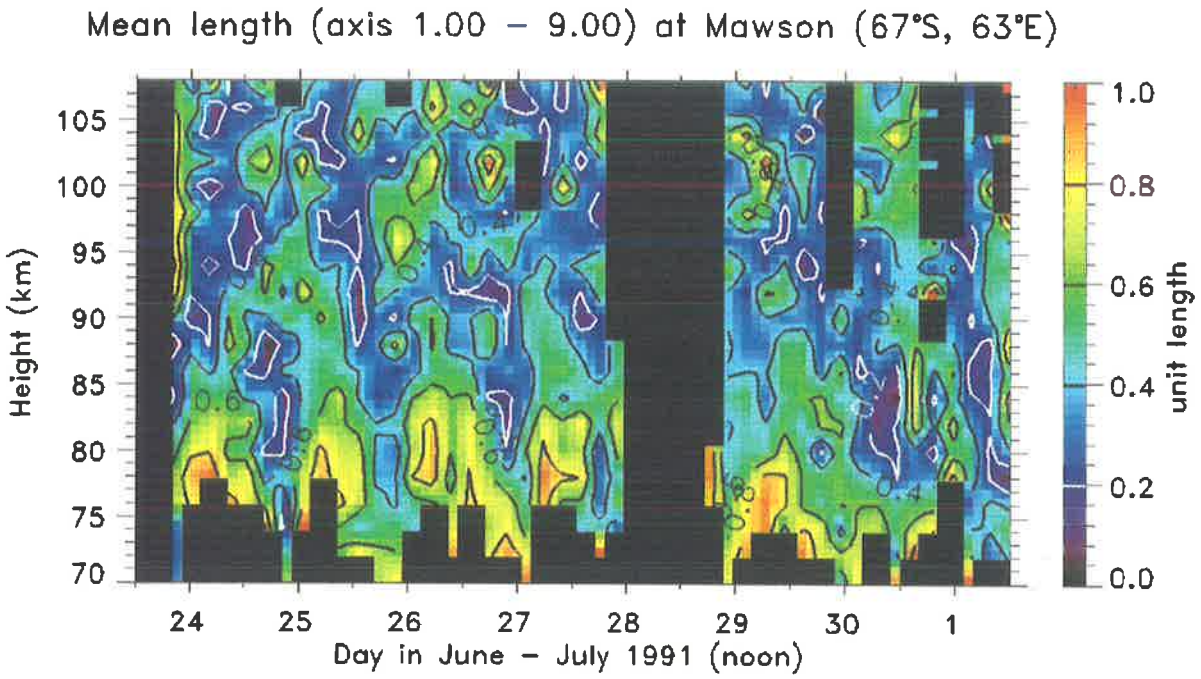

Figure 11.15: Four–hourly mean normalized lengths of the ground diffraction pattern for all axial ratios for an eight–day period during June 1991. The contours are the normalized length taking into account the direction of the semi–major axis.

80%. There is a diurnal variation for these data rates which can be clearly traced to the diurnal variation in the pattern axial ratio [see figure 11.9 (bottom)].

Examination of the stability of the axial–filtered pattern orientations shows that it has markedly improved. A broad night–time maxima now extends past 85 km and persists for more than 12 hours. The stability at greater heights has also improved, although low L_n are still observed at times. The big improver is the height range of 75–80 km where the majority of L_n values are now greater than 0.8.

The above discussion related to the data collected during June, or winter time. We now investigate the pattern directional stability during the southern hemisphere summer. The mean lengths of the pattern orientations during December are shown in figure 11.17, unfiltered for any pattern axial ratios, and in figure 11.18 (top) for patterns whose axial ratios are between 1.4 and 9.0. The corresponding data rates for patterns whose axial ratios are in that 1.4–9.0 range is shown in figure 11.18 (bottom).

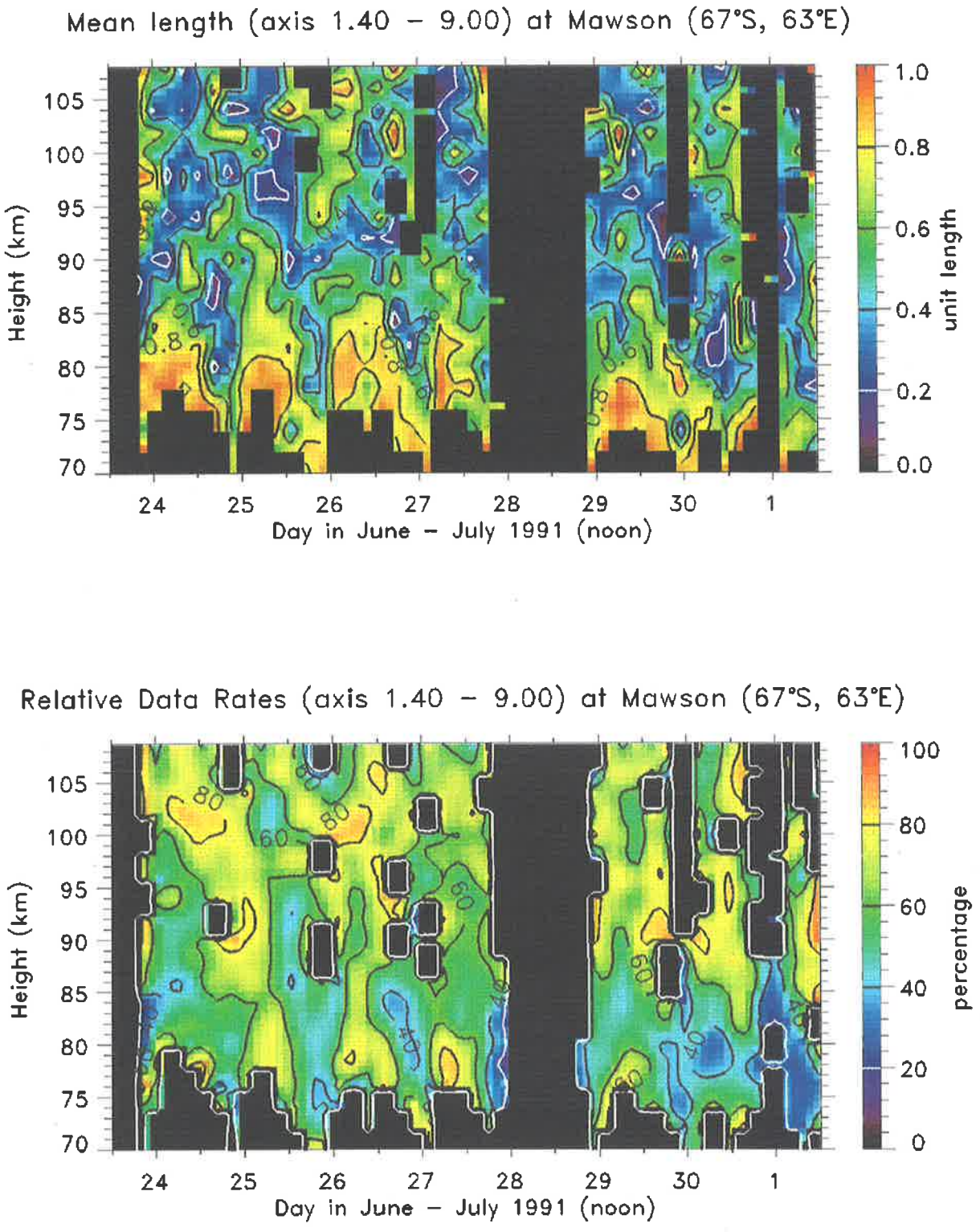

Figure 11.16: The top diagram is as for figure 11.15 but only for patterns whose axial ratio lies between 1.4 and 9.0. The bottom diagram are the relative percentages of data within that axial range.

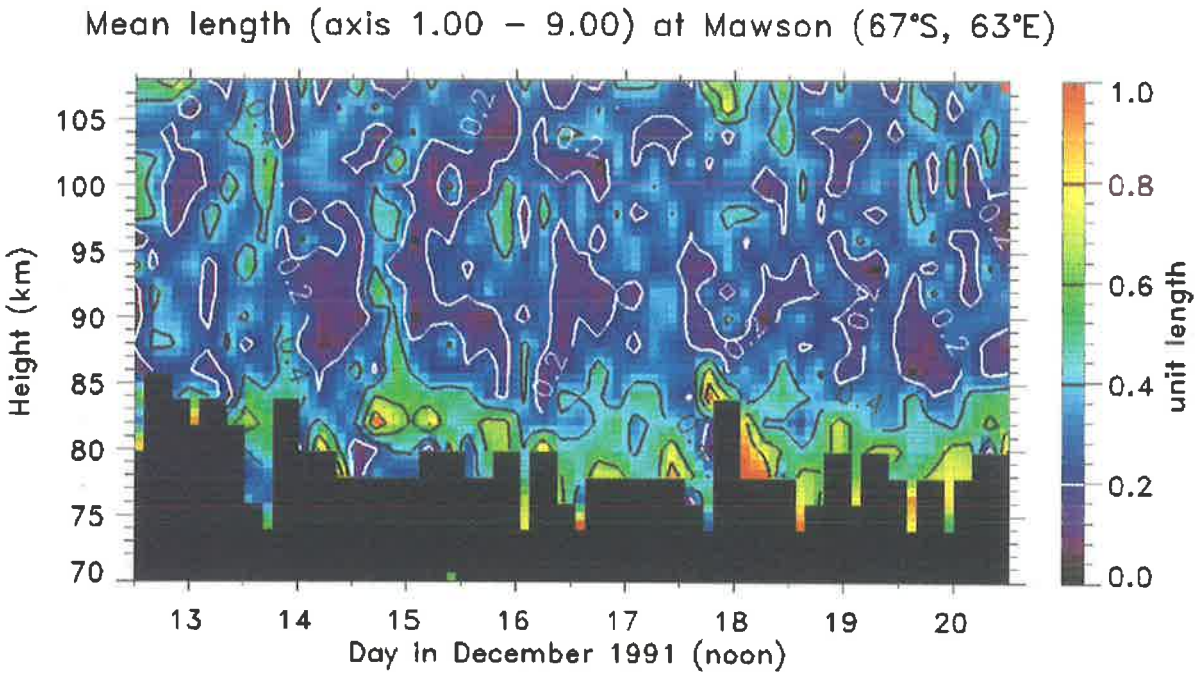

Figure 11.17: As for figure 11.15 but for data collected during an eight–day period in December 1991.

The unfiltered values of L_n are relatively small, varying from less than 0.2 to about 0.6 with only a few localized values larger. A very weak hint of a diurnal variation is observed above 85 km with values of L_n slightly higher in the mornings. Below 85 km, the average values of L_n increase but are still relatively small and range between 0.4–0.5. This translates into a circular standard deviation of between 40°–60°. Above 85 km, the values of L_n do not generally exceed 0.4 and the orientations can thus be treated as relatively random.

When the data were filtered, a general improvement in the values of L_n, implying a greater stability in the pattern orientations was found to occur throughout all heights. The relative data rates during this period were quite different than those during winter, with only 40% of data accepted in the range of 80–90 km. The data rates improve with increasing height to be more than 60% above about 95 km. Again, this is in step with the pattern axial ratios which were previously found to be low (less than 1.5) in the mid–height range and increased with increasing height. However, the values of L_n above 85 km are still in the 0.2–0.4 range, and about 0.6 below 85 km. A weak diurnal variation around 95 km (which is also the height at

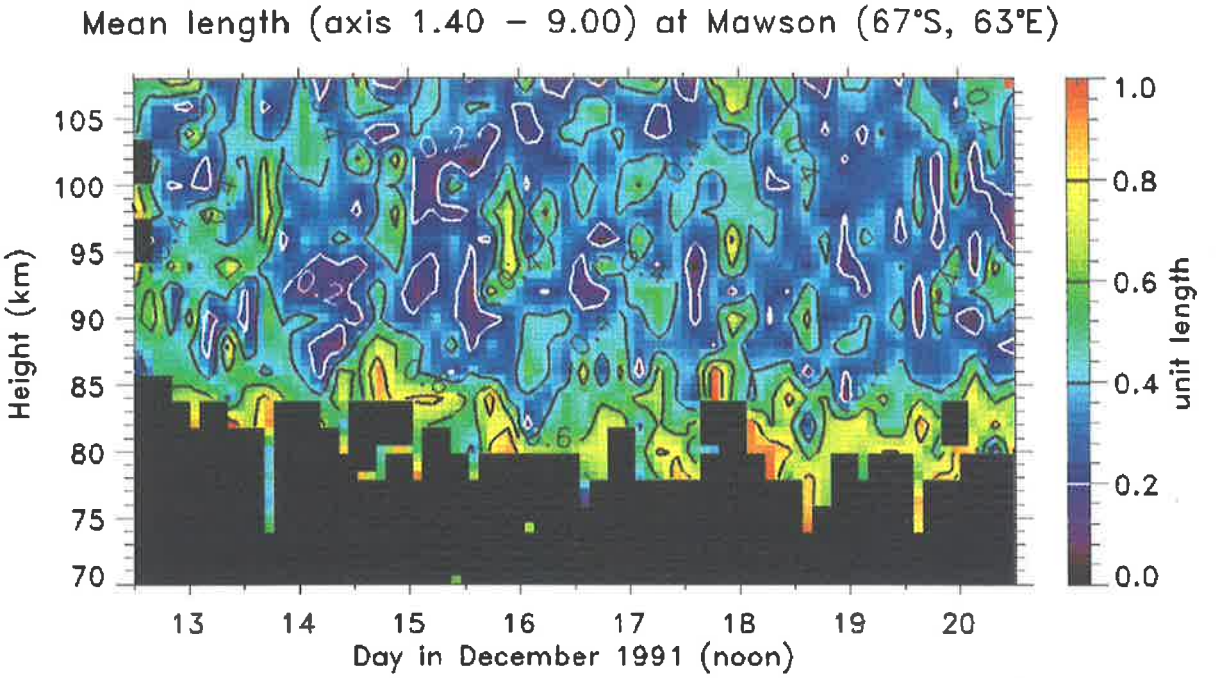

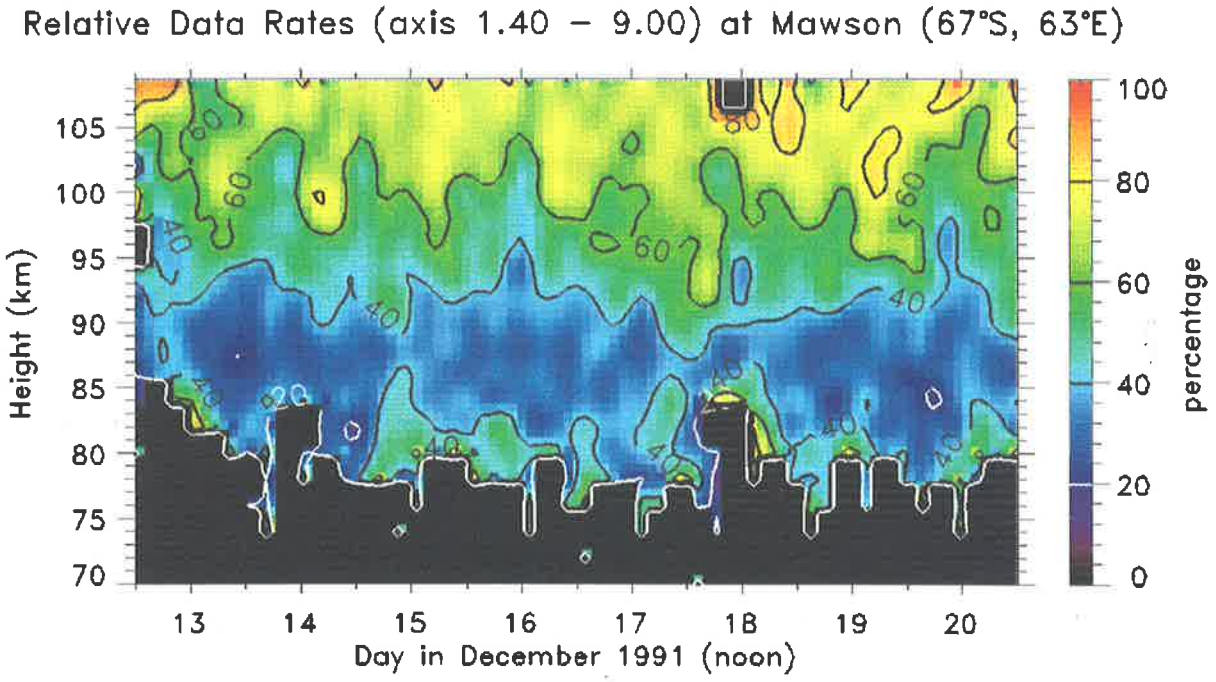

Figure 11.18: As for figure 11.16 but for data collected during an eight–day period in December 1991.

which the total data rates were high) is evident in the mornings of the 14^{th}, 15^{th} and 16^{th}, but only for a few hours.

Therefore, in conclusion, the patterns are much more stable in their four-hourly orientation with respect to each other during winter than during summer. In addition, the winter values of L_n exhibit a clear diurnal variation, which is only very weakly, if at all, evident during summer.

Mean pattern orientation with respect to geographic North

The last section investigated the pattern stability and showed that the patterns were stable at some periods and completely random at others. Here we investigate the pattern orientations with respect to geographic north, as opposed to magnetic north since at Mawson the magnetic north is ~65° west of geographic north. The individual pattern orientations are grouped into 5° bins according to the same criteria as those used for Christmas Island data. First they were separated into two groups whose pattern axial ratios ranged from 1.0–1.4 and 1.4–9.0. Then these data were separated into two height regions of 70–88 km and 90–108 km, and finally they were separated into four time intervals of 0:00–6:00, 6:00–12:00, 12:00–18:00, and 18:00–24:00 local time.

Figure 11.19 shows histograms of the orientations of the June ground diffraction patterns (clockwise with respect to geographic north) whose axial ratios lie within the 1.4–9.0 range, and separated according to the above criteria. Similarly, figure 11.20 shows histograms for the December data. In both diagrams, the left–hand side refers to the 70–88 km height range while the right–hand side encompasses the 90–108 km height range.

Even an initial glance at the distributions clearly show that the pattern orientations are preferentially distributed both with respect to time and height. In the 70–88 km height range the June patterns are oriented so that the bulk of the patterns are oriented ±25° from north. In addition, a hint of a secondary peak at around 100°–120° occurs but only between 18:00-6:00. In the 90–108 km height range, the orientations change to be broader through all the angles. However, a peak still occurs centred around 50°, and broader at night. In addition, the secondary peak is just observable at around 100°–102° but, unlike during night–time, occurs

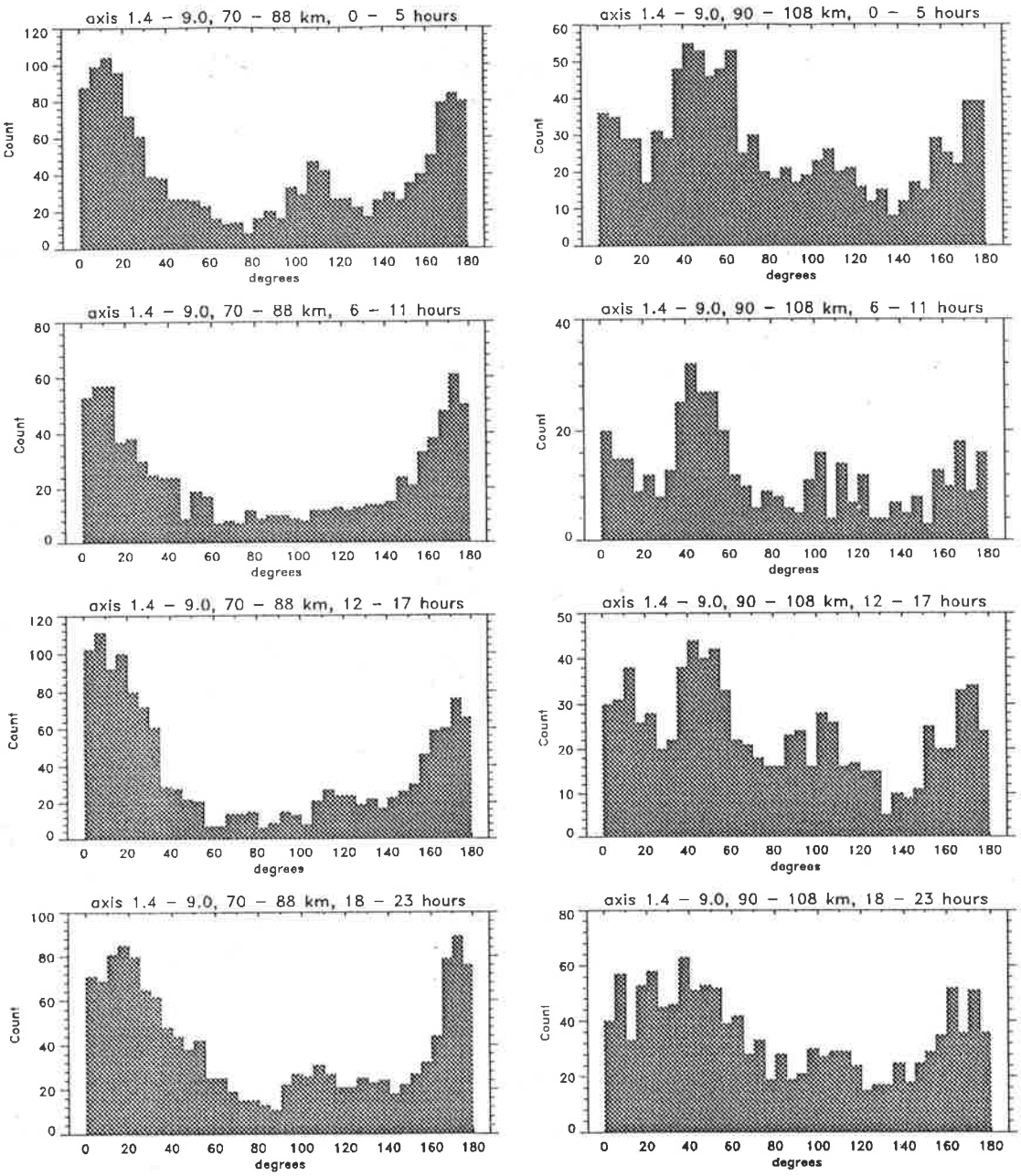

Figure 11.19: Histograms of the orientation of the ground diffraction patterns for two height regions, 70–88 km and 90–108 km, four 6–hour time periods, starting at midnight local time, and whose axial ratios are between 1.4–9.0. The data are grouped into bins of 5° width, and are those collected over an eight–day period during June 1991.

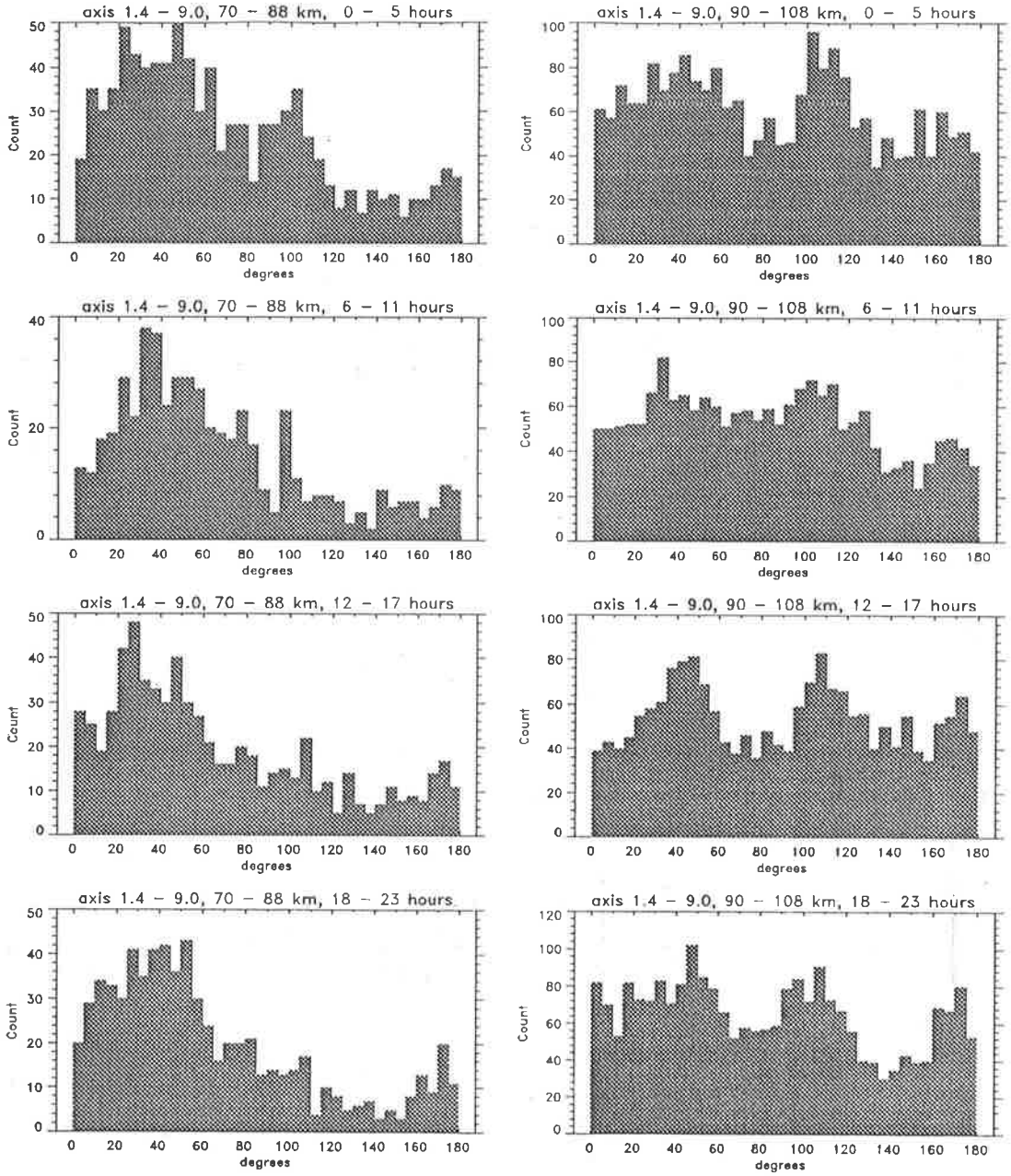

Figure 11.20: As for figure 11.19 but for data collected during December 1991.

through all the height ranges.

The December distributions also show directional anisotropy but broader than those of June. In the lower height range, the centre of the distributions lie between 20°–60°, and are somewhat skewed towards larger angles, although few orientations are greater than 120°. There is no distinction in the distributions of the different time periods, with the exception of, perhaps, the early morning, when the distribution is broadest. In the upper height range, all the different

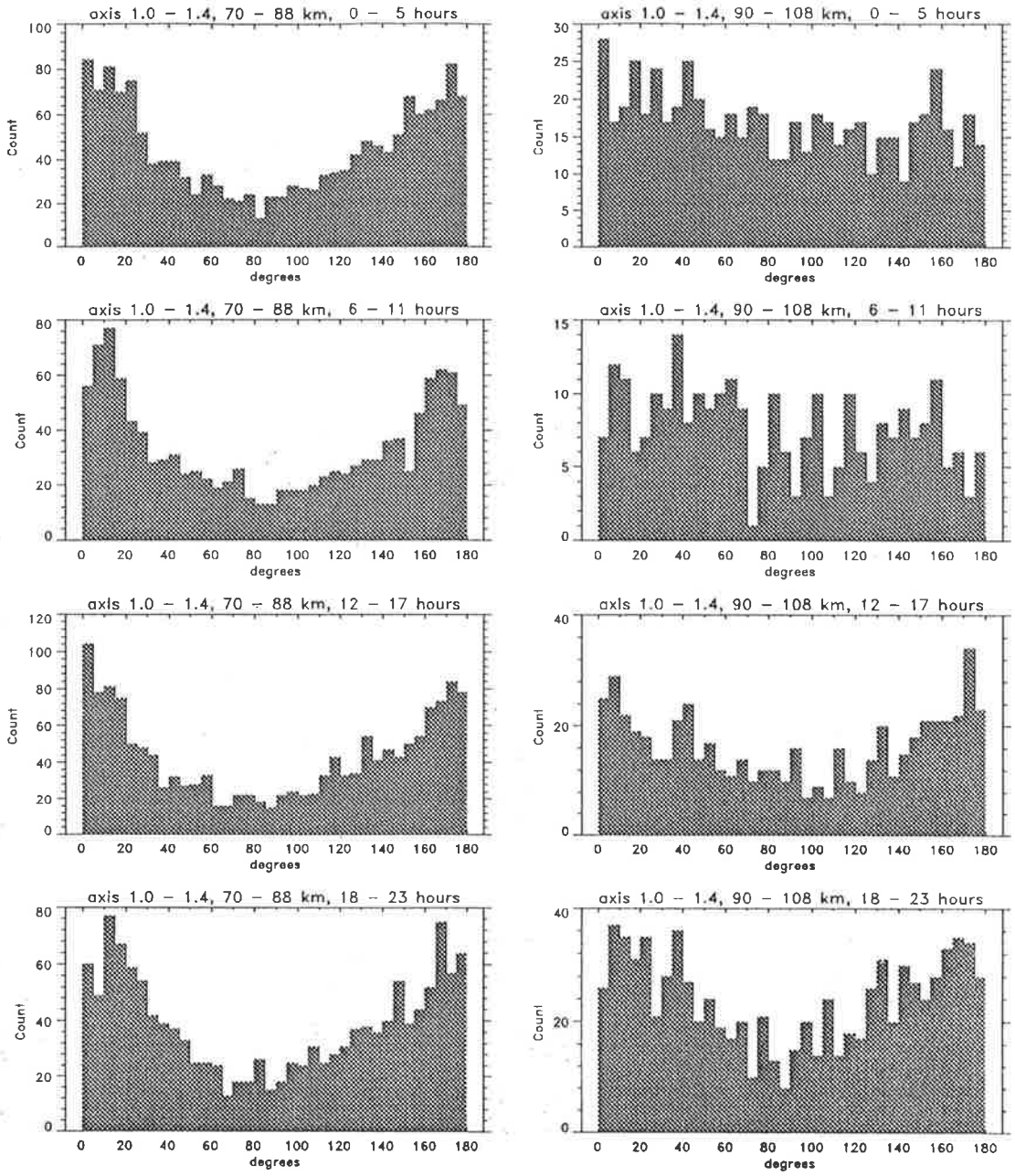

Figure 11.21: As for figure 11.19 but for patterns whose axial ratios lie between 1.0–1.4.

time periods show the same characteristic broad distribution with two peaks centred around 40°–60° and 100°–120°.

So far only patterns whose axial ratios were greater than 1.4 have been examined due to the fact, as discussed in the previous chapter, that patterns whose axial ratios are less than this can essentially be considered isotropic and their orientation should therefore be random. However, as seen in the last chapter for the Christmas Island data, even those patterns whose

axial ratios are less than 1.4 showed the same characteristics as those that are greater than 1.4. Figure 11.21 contains the June histograms of the pattern orientations binned in the same way as the histograms discussed above, but only for those patterns whose axial ratios fall within 1.0–1.4. The pattern distributions are clearly anisotropic, with the distributions, in the lower height range, preferentially oriented in the north–south plane, although much broader than the ones for patterns whose axial ratios are greater than 1.4. In the upper height range this is weakly true for the two periods from noon to midnight, and not really so for the midnight–noon histograms. Similar behaviour was found in the December data (although not presented here), where the lower height range mimicked the 1.4–9.0 axial ratio distributions, albeit much broader, while the upper height range was very weakly anisotropic, if at all.

Perhaps narrower distributions could have been obtained if the data had been binned for smaller height ranges. However, this gain would have been offset by the lower total number of counts within each distribution. Even with such large height ranges it is clear that the pattern orientations are preferential. The distribution of the orientation of the pattern angles during high and low geomagnetic active times has been previously investigated by *Price* [1988] who found no obvious difference between histograms corresponding to low and high geomagnetic activity over any height range and for any season. That study concluded that the pattern orientation is therefore not affected by geomagnetic activity. Therefore, as before, the obvious parameter with which to compare the pattern orientations is the wind direction.

Mean pattern orientation with respect to the wind direction

The distributions of the difference in directions between the mean wind and the pattern orientation are plotted as histograms in figures 11.22 and 11.23 for June and December respectively. The histograms are only for data whose axial ratios lie in the 1.4–9.0 range, and are binned according to the same height and time criteria as above.

During winter, it is very difficult to say with any conviction that any correlation exists in the lower 70–88 km height range. The instantaneous angles between the pattern orientation and the wind, θ_{diff}, is on the whole distributed randomly, with perhaps a tendency to be slightly more

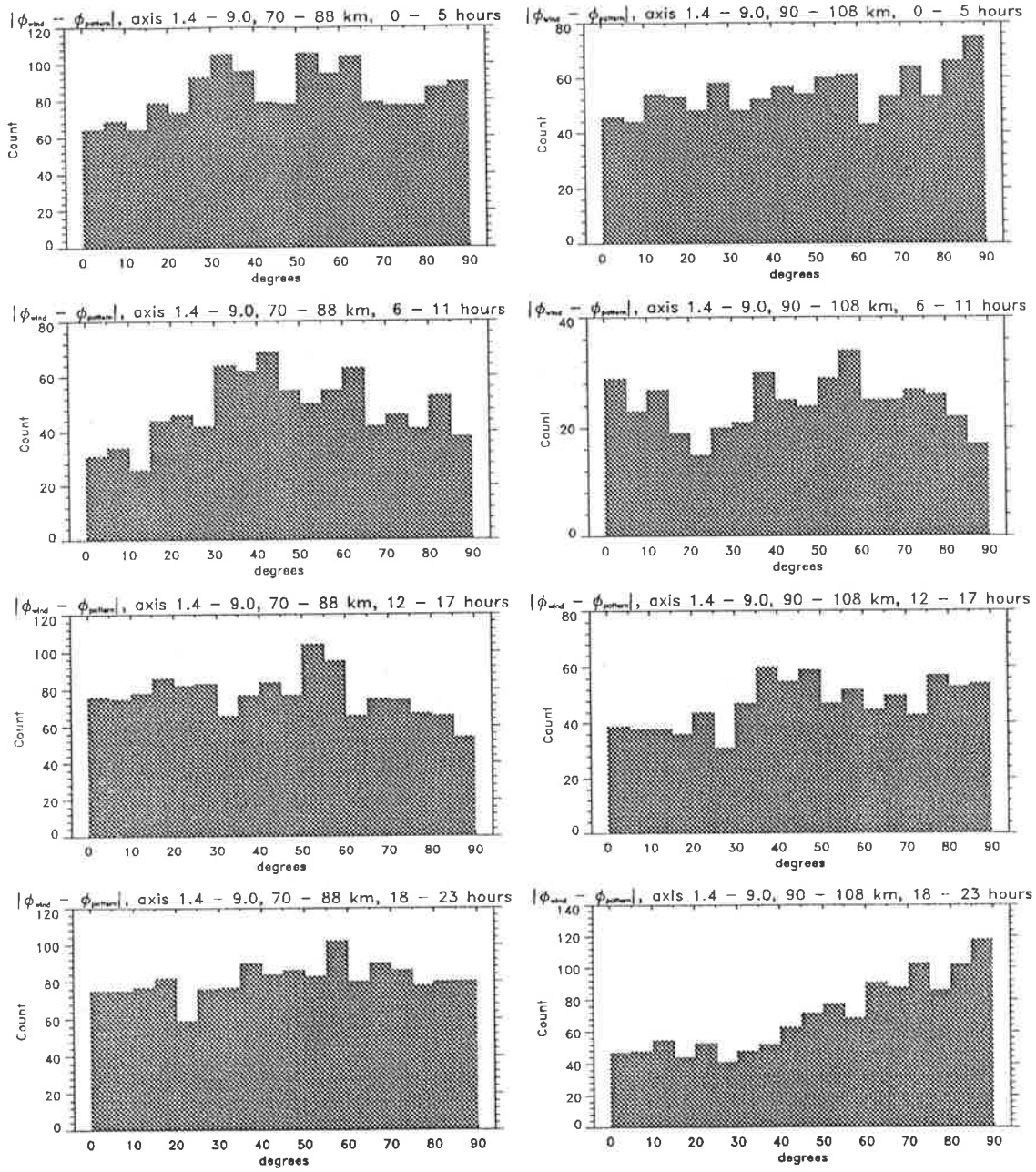

Figure 11.22: Histograms of the angular difference between the orientation of the ground diffraction pattern whose axial ratio is between 1.4–9.0 and the wind direction. The histograms are based on two height ranges of 70–84 km (left hand side) and 86–98 km (right hand side). The data is further binned according to time. Starting from the top, each histogram looks at a six–hourly interval beginning at midnight local time. The data are separated into bins of 5° width, and are those collected at Mawson for an eight–day period in June 1991.

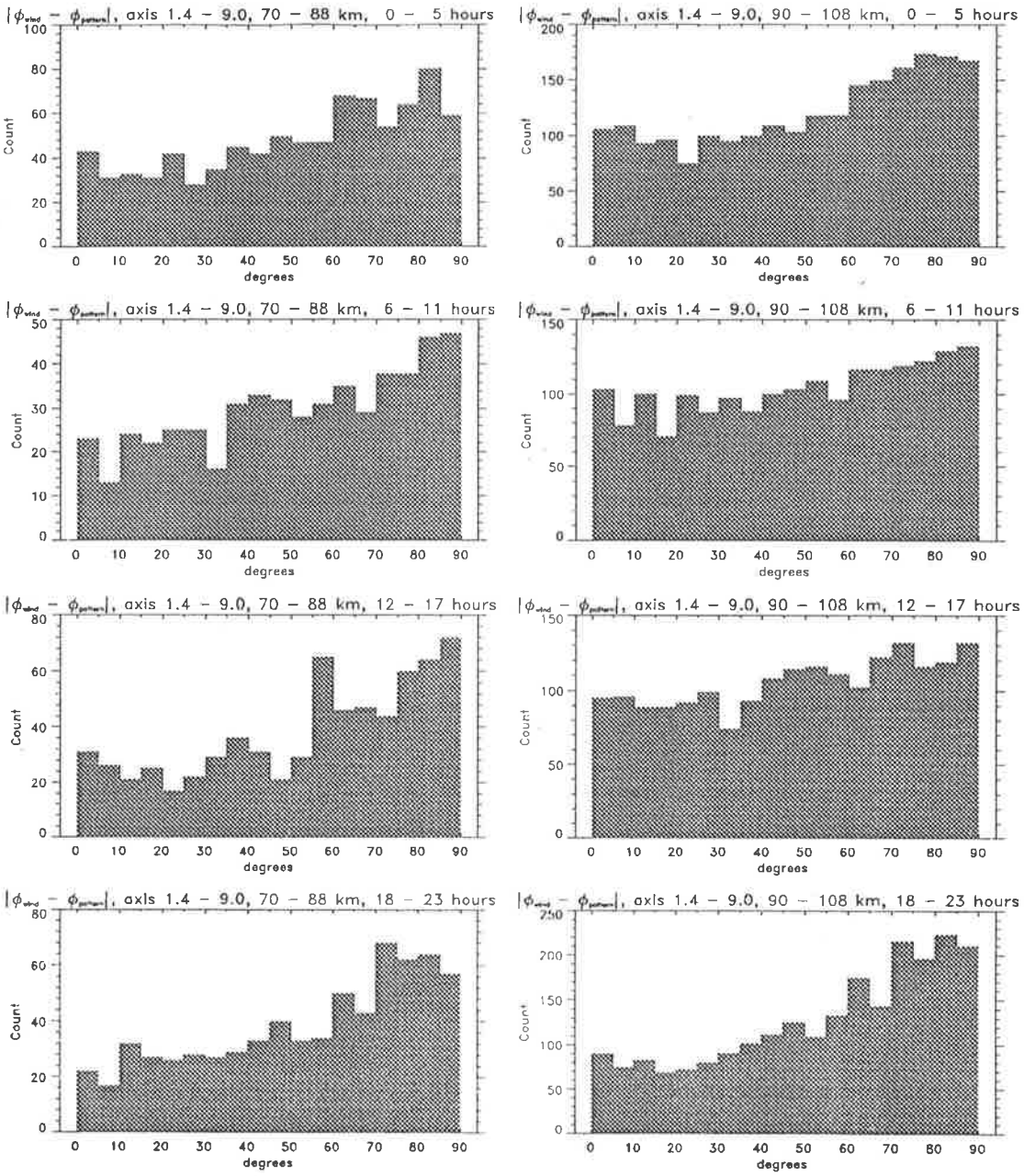

Figure 11.23: As for figure 11.22, but for data collected in December 1991.

concentrated in the 30°–70° range in the early morning. In the higher height range of 90–108 km, θ_{diff} tends towards larger angles, especially obvious in the 18:00–24:00 time period. The distributions of θ_{diff} for patterns within the 1.0–1.4 axial range show similar characteristics (and are thus not presented).

In December, θ_{diff} does show a common trend towards larger angles through both height ranges and all four time periods. This is most evident in the 18:00–24:00 hr time period when

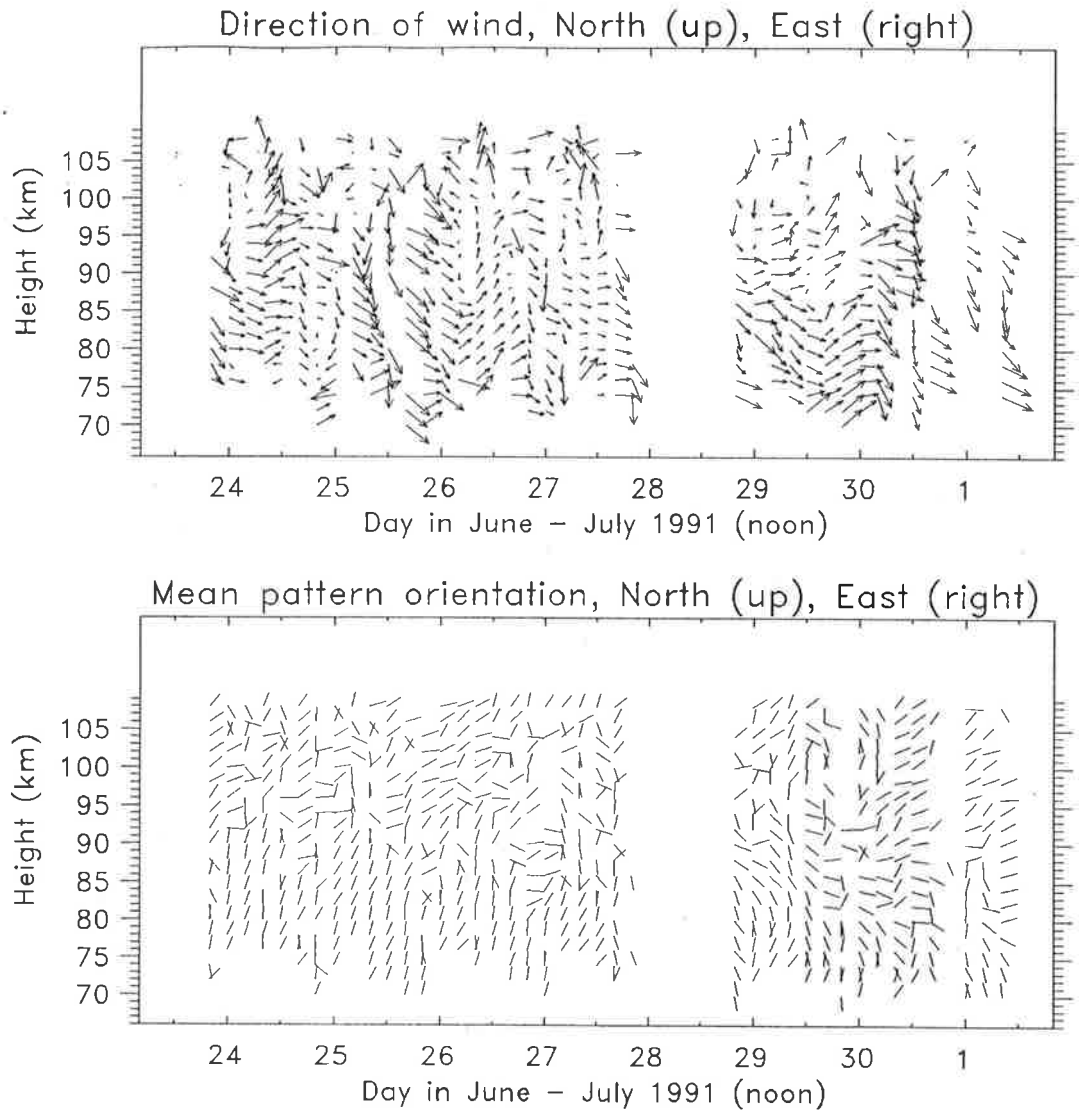

Figure 11.24: Four–hourly mean direction of wind (top) and pattern orientation (bottom) at Mawson during June 1991.

the number of θ_{diff} around 90° is up to four times larger than those around 0°, and only weakly evident in the two time periods encompassing the 6:00–18:00 hours.

Therefore, a systematic difference exists in the upper height region during both the summer and winter night, while only occurring at other times and heights during summer. To investigate this further, we look at the relationship between the mean four–hourly wind direction (θ_w) and wind magnitude with the pattern orientations (θ_p), shown as vector plots in figure 11.24 for June and 11.25 for December. The maximum length of the wind vector corresponds to a velocity of 50 ms^{-1}. At this time it is important to recall that below 85 km, θ_p are relatively

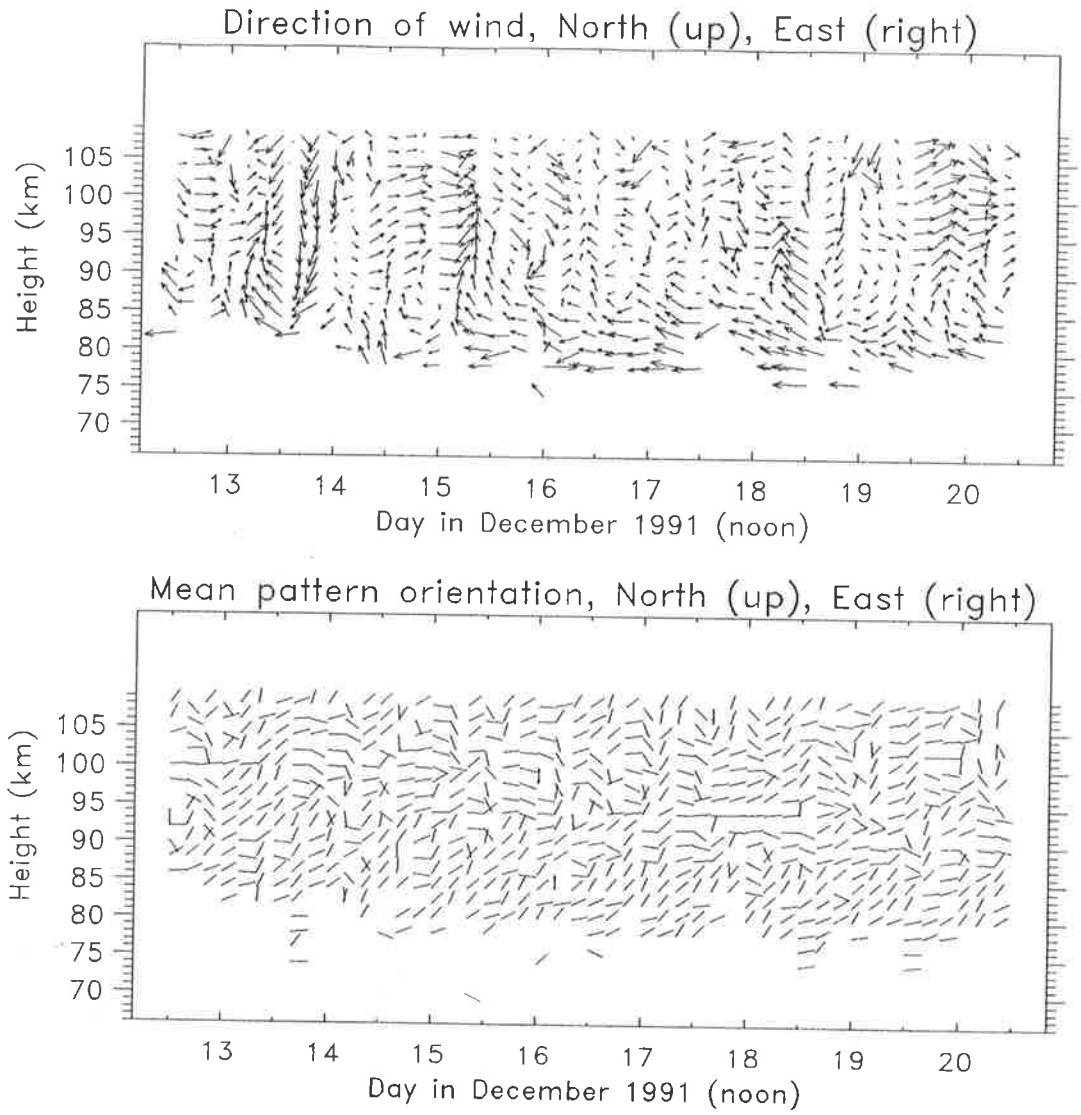

Figure 11.25: Four-hourly mean direction of wind (top) and pattern orientation (bottom) at Mawson during December 1991.

stable during both June and December although more so during June.

In June, mean values of θ_p are generally in the north–south plane below 85 km, and shift towards an easterly direction at greater heights. During this time, the wind vectors change in direction by over 180° and by several factors in magnitude over all the heights. The best example of this is seen below 85 km on the 24^{th}, 25^{th}, and 26^{th}, when the wind changed directions several times from eastward to south–westward. An interesting behaviour in θ_p is observed on the 29^{th} when it changes in direction down from 90 km from a north–westerly to a south–easterly direction, although the wind is fairly constant in direction and magnitude over

this time and height. Another interesting event occurs at night on the $30^{th}/1^{st}$ when the wind is strongly southward, while θ_p is in an east–west plane.

During December, θ_p values are more inclined to be oriented 45° eastward from the north–south plane, although at times, are in clearly in the east–west direction. A unique example is found on the 18^{th} December, when, at a height of 94 km θ_p is purely aligned east–west, while θ_w varies by 90°. Although an exact behaviour is not predictable it does appear like at heights below about 85 θ_p is more likely to be in the east–west plane.

Therefore, it appears that the wind is not the cause of the angular distribution of the pattern orientation, although, at times some correlation may exist. This is similar to the result found at Christmas Island, where the pattern orientations were extremely anisotropic in their horizontal plane, and where the wind was not seen to be the cause.

Chapter 12

Conclusion

This thesis focuses on the study of lower and middle atmosphere dynamics, with particular emphasis being placed on the small dynamical regime. The main focus of this work has been to examine in detail the spatial and temporal characteristics of the southern hemisphere mesosphere as observed by MF radars.

Chapter 1 started with a general description of both the structure and dynamics of the atmosphere as currently understood. The second chapter discussed atmospheric turbulence and concentrated in particular on two areas of interest, namely mesospheric and anisotropic turbulence. The description of the Doppler and the full correlation analysis techniques, the two primary data acquisition techniques used in this thesis was tackled in Chapter 3.

Chapter 4 presented computer simulations of a mesospheric MF partial-reflection radar system which was used to show that a spaced-antenna system using the full correlation analysis does extract relatively accurate (less than $\pm 10\%$) velocities of the atmosphere under various degrees of mean motion, turbulence, antenna spacing and different radar polar diagrams. In addition, other parameters extracted by the full correlation analysis, for example the pattern axial ratio, showed that the full correlation analysis does not suffer any bias in its calculations. In fact, the accuracy of the various parameters improves if means are used rather than individual measurements. This work therefore validated the use of the spaced-antenna derived results which are subsequently used in this thesis.

The nature and current knowledge of atmospheric radar scatterers was discussed at length in chapter 5. Various proposed models used to explain the cause of mesospheric partial radar reflections were described. In particular, the aspect sensitivity observed in radar scatterers was elaborated upon, followed by an in–depth look at the various methods that have been used to determine the aspect sensitivity. A brief discussion was also presented on radar measurements of turbulent energy dissipation rates. Finally, it was shown how the aspect sensitivity calculations can be used to infer the horizontal correlation lengths of the scatterers.

Chapters 6, 7, and 8, began the analysis of experimental data at Buckland Park, Christmas Island, and Mawson respectively. All of the chapters followed the same presentation and discussion formats. The first data to be discussed were the mean winds, followed by the full correlation analysis parameters and then calculations of the aspect sensitivities and horizontal correlation lengths. The aspect sensitivities at all three sites were calculated by both the spectral–width and the spatial–correlation methods.

In general the structure of the scatterers at all three sites was found to be aspect sensitive, with the horizontal correlation lengths varying between 2.5–5.5. In addition, the scatterers at Mawson and Buckland Park showed a clear seasonal behavior, especially below the mesopause, with maxima occurring during the local summer. The scatterers horizontal to vertical structure was seen to vary by nearly a factor of 2. With a wavelength of approximately 150 m, the structures selected by the radars possess a vertical extent of around 60 m. Therefore, since the L/h ratios have been found to range from between 2.5 to 5.5 this implies a horizontal correlation length of 150 to 350 m, a clear case of quasi–specular scatter. Meanwhile, although the scatterers at the low–latitude site (Christmas Island) were found to exhibit no clear seasonal behavior, they did show a remarkable increase in isotropiness with increasing height, such that the horizontal correlation lengths decreased at a fairly uniform rate from 4.0 to 2.5, all within a height of 10 km.

At Adelaide some data were also available which were collected by using a vertical and an off-vertical Doppler beams. This enabled the aspect sensitivities to be calculated using

the velocity–ratio method. Scatterers which were probed by the off–vertical beam showed no obvious seasonal behavior either below or above the mesopause. This evidence tends to support the notion that the atmosphere contains at least two distinct types of scatterers as seen by a MF radar. One type seems to be quasi–specular while the other is more isotropic.

Short–term results of the mean winds, full correlation analysis parameters, aspect sensitivities and horizontal correlation lengths were studied in Chapters 9, 10, and 11 for the radar systems located at Blanchetown, Christmas Island, and Mawson respectively. All of the radars employed the same type of radar and data analysis. Thus any variation between data collected by the three radars is a geophysical and not an experimental effect. In addition, the Christmas Island radar took part in the ALOHA–90 campaign which was designed to study the horizontal density and temperature structure of the upper stratosphere and upper mesosphere. During one particular night of the campaign the signal–to–noise ratio of the radar correlated strongly with gravity wave activity as observed by an airborne lidar. At the same time, the spatial correlation function was relatively large indicating specular scatter; a puzzling result since one would expect an increase in turbulence during high gravity–wave activity and thus more isotropic structures.

The study of the short–term results using data from the above three sites can be separated into two sections. In the first section what was investigated and discussed were winds, full correlation analysis parameters, aspect sensitivities and horizontal correlation lengths. All of these parameters exhibited a strong temporal daily variation which tended to be more complicated at higher heights. For example, data from all three sites showed that the L/h ratios decreased with increasing altitude. This can be interpreted to mean that the MF scatterers tend to be more isotropic with increasing height, especially so above 90 km.

In the second section use was made of that fact that the spatial–correlation method is a two–dimensional feature and information on the horizontal anisotropy of the scattering structures is also available. At Blanchetown it was found that not only is the pattern elongated well above what is expected from a random statistical distribution, but that it is preferentially oriented during the day–time to be within 25° of the north–south axis, and yet no such preferred

orientation was observed during night–times. This was also observed at Mawson where again the pattern orientations were clearly anisotropic. The most remarkable results were observed at Christmas Island where the orientations were very anisotropic with, at times, all of the patterns oriented within 10° of the north–south axis.

To ascertain whether or not the wind was a contributing factor in the horizontal anisotropy of the scatterers, all the data were analyzed for different time periods and heights where the difference between the wind direction and spatial correlation pattern orientation was examined. This was done by examining both instantaneous values which were binned into histograms and by comparing four–hourly averages. It was found that at none of the sites was the wind a contributing factor to the orientation of the spatial–correlation pattern. It was also found that the night–time patterns were preferentially oriented in the east–west plane at lower heights.

At this stage the cause of the preferential pattern orientations is unknown. The wind direction is clearly not a significant factor. While geomagnetic activity was not eliminated as a factor and might be a substantial cause of anisotropy at Mawson, it can not explain the highly anisotropic results at Christmas Island. Perhaps the anisotropy is caused by preffered gravity wave propagation due to selective filtering at lower heights. As gravity–waves propagate upwards they impart their anisotropy to the scatterers as they break and produce turbulence which is observed by the partial–reflection radars.

12.0.1 Suggestions for further work

A number of factors raised in this thesis should be looked into further. Firstly the spaced–antenna computer model should be used to determine the impact of other variables on the accuracy of the full correlation analysis. This includes such things as introducing vertical velocities and turbulences and including gravity–waves propagating through the scattering field. In addition an important test would be to have at least two type of scatterers co–existing and moving at different velocities to see what velocity is in fact extracted by the model.

In relation to the experimental data, the question as to why the scatterers are anisotropic,

especially so in their horizontal plane should be investigated further. Having eliminated the mean wind as a cause of anisotropy, a study on the correlation of the scatterers anisotropy and preffered gravity–wave propagation is the next obvious step.

Although the work presented herein has dealt exclusively with the mesosphere, some preliminary work not presented in this thesis did look at tropospheric data where the scatterers observed using VHF radars were also found to exhibit aspect sensitivity. It would be an interesting avenue to examine the structure of VHF tropospheric scatterers in detail and relate them to gravity–wave propagations, especially since in the troposphere the scales are significantly smaller. Simultaneous comparisons with mesospheric scatterers should also be performed to see what if any relation exists between tropospheric and mesospheric scatterers.

Appendix A

Historical Review

A.1 Introduction

This thesis concerns the study of the structure of the atmosphere, utilizing the remote sensing capabilities of radars[1]. Whilst this is an explicit area of study, I feel that it is important to be familiar with the history of atmospheric research and to recognize the place of any detailed study in the general scheme of things. In this endeavor it is equally important to recognize the various ingenious tools and apparatus used to facilitate the study of the atmosphere. For these reasons this appendix will deal with the history of atmospheric research, and the development of various atmospheric instruments.

The study of the atmosphere is divided into at least two distinct areas, which although distinct, are not separable. The first deals with the study of the behaviour of the atmosphere, its response to forcing and weather forecasting. The second deals with the actual composition of the air, its variability and stability. Both of these are coupled together since different dynamic conditions can affect the composition of the atmosphere, which in turn affects the dynamics of the atmosphere.

[1] Radio Detection and Ranging

A.2 First observations

The study of the atmosphere is one of the oldest physical sciences studied by man. Its behaviour has been studied since ancient times by farmers and sailors whose everyday activities were directly related to the weather, which was so important that it was deeply ingrained in the cultures of most primitive societies [*Frazer*, 1923]. The study of the first great civilizations, which developed along the great rivers of Asia and Africa[2] has failed to provide much information about their culture and science. The current knowledge of the Pre-Hellenistic[3] period is largely limited to the Babylonian and Egyptian cultures. It is fortunate for us that the Babylonians wrote on clay tablets exclusively, because of the unavailability of suitable plants. These clay tablets, of which thousands have been found and deciphered, have given an insight in to the Babylonian culture. Amongst other things, Babylonians tried to correlate atmospheric and astrological phenomena and produced forecasts such as, [*Frisinger*, 1977]:

When a dark halo surrounds the moon, the month will bring rain or will gather clouds.

The ancient Greeks were the first people to keep systematic weather records and used the past weather to predict the future climate. However, their primary concern was observations of the wind for navigational purposes. Changing weather patterns and phenomena were still attributed to ancient lore: lightning was due to the wrath of Zeus; the rainbow was the many-coloured robe of Iris; heat or drought were attributed to the carelessness of Phoebus, and Typhoon, in his underground prison, produced earthquakes and volcanoes. *Empedocles*, a fifth century Sicilian philosopher was the first to propose that air was one of four basic elements, the other three being earth, fire and water. He was able to show that air is a substance which occupies space and displaces water. This was the first time that an attempt was made to describe the substance of air, but without any instruments, the experiments were rather limited, and the scholars concerned themselves mainly with philosophical debate.

[2] Nile, Tigris, Euphrates, Indus ,Ganges, Hwang-Ho, and Yangtze

[3] Hellinitic - from the death of *Alexander the Great*, [323 B.C.] to the defeat of *Anthony and Cleopatra*, [30 B.C.]

The earliest recorded treatise on the subject of meteorology was the *Meteorologica*[4] of *Aristotle* [384-322 B.C.], where meteorology was the term used to describe all phenomena occurring in air[5]. *Aristotle* was the first to attempt to construct a coupled picture of the atmosphere, expanding on *Empedocles* and drawing on other philosophers who concerned themselves with particular isolated phenomena. He postulated that the terrestrial region consisted of four elements; earth, air, water and fire, which were stratified as in figure *A*.1. But this stratification was not rigid, and all the elements were thought to be interchanging. Dry land rose above water and the fire burned earth. The sun's heat reached the surface, and by mixing with cold and moist water formed moist air. The sun also acted on the cold and dry earth and produced another warm and dry substance, lime fire. Motion occurred when the different elements attempted to move to their natural position. Thus the two sorts of evaporations were responsible for the weather; a dry and hot exhalation and a warm moist vapour. The former was responsible for thunder, lighting, winds, earthquakes, comets and other fiery phenomena, while the latter was responsible for clouds, rain, snow, fog, dew, hail and mist. Rainbows, halos and multiple suns were thought to be due to the reflection of celestial bodies by miscellaneous vapour formations [*Heninger*, 1960]. *Aristotle* also carried out experiments to measure the weight of air, using a leather bag which he weighed as the bag was filled with air. However, since the volume of the bag also changes, a fact which he did not appreciate, he wrongly concluded that air did not possess any weight.

Thus, this was the age where the disdain for observable evidence, lack of any experimental instruments, and preference for symmetrical theories, resulted in the study of the atmosphere not progressing for several thousand years. *Aristotle's Meteorologica* was the undisputed authority on the atmosphere and its processes, and any new ideas were just an extension of his work. It was not until experimentation became an important facet of science that real gains in atmospheric science were made. The beginnings of the scientific revolution can be traced back to the thirteenth century.

[4]Consisting of four volumes
[5]This included comets

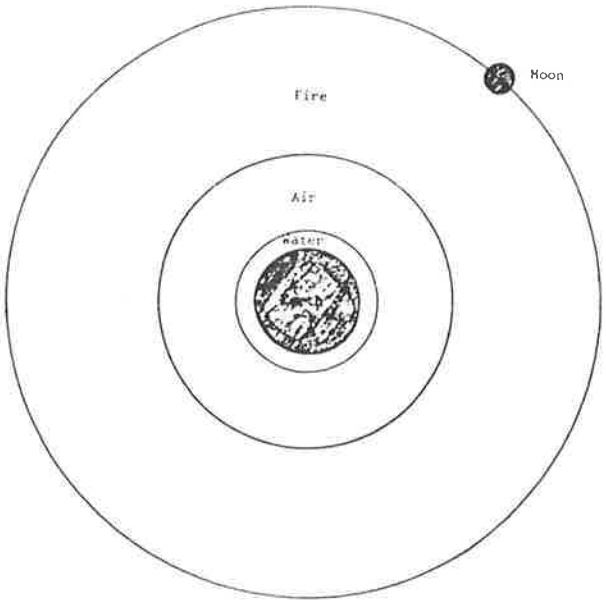

Figure A.1: Aristotle's concept of the terrestrial atmosphere [from *Heninger*, 1960].

A.3 Meteorology as a Science

Roger Bacon, [1214–1294] [*Binke*, 1928] was an English scholar whose greatest contribution to science was the advocation of experimentation rather than philosophical speculation. Although essentially following *Aristotle's* work on meteorology, his ideas on experimentation rather than philosophical descriptions marked the beginnings of scientific research. This process, however, did not clearly emerge until the seventeenth century.

By the middle of the sixteenth century, meteorology had split along two lines; one still followed *Aristotle's* treatise, while the other believed in weather prediction by natural phenomena, or Astrometeorology[6]. The first questioning of *Aristotle* was made by *Girolama Cardano* [1501-1576], an algebraist who argued that there were only three basic elements, not four, since fire produced nothing, required nothing and needed food to sustain itself. However, all of these were still qualitative statements, and it was not until properties of the atmosphere could be measured that further advances were made. It was the invention of the three most basic instruments that marked the beginning of the real study of the physics of the atmosphere.

[6]This was favoured by the church and royalty

A.3.1 The Thermometer

The basic principle of the expansion of air by heat was known since the third century B.C., when *Philo of Byzantium* constructed an apparatus which illustrated the expansion and contraction properties of air and later by *Hero of Alexandria* who constructed a primitive steam engine. They, however, failed to see the potential of this property to measure temperature, and construct a temperature measuring device. Although the exact date is uncertain, the thermometer[7] was invented by *Galileo Galilei* around 1593. He used this to determine relative temperatures of different places, and temperatures of places as a function of day and season, but because his thermometers were not sealed they were influenced by atmospheric pressure. Other scientists soon began constructing their own thermometers, and in the first half of the seventeenth century a number of different thermometers were designed. The first to produce a thermometer sealed at the end, and thus independent of atmospheric pressure was *Ferdinand II, Grand Duke of Tuscany.* The next step involved the standardization of the scale, a feat which began with *Robert Boyle* and was completed by *Robert Hooke*, who marked as zero the temperature of freezing distilled water. That the second point should be that of boiling water was then suggested by *Christian Huygens.* In 1714, *Fahrenheit* constructed the first mercury thermometers. His scale had three divisions, the first being the temperature of a mixture of ice, water and sea-salt, the second when water and ice are mixed without the sea-salt (32 deg), and the third the temperature when a man puts the thermometer in his mouth or the arm-pit (96 degrees). In 1742, *Anders Celsius* proposed a scale which had two fixed points; the temperature of boiling water (which he defined as 0 degrees) and the temperature of melting ice (100 degrees). The inversion of 0 as the freezing point was introduced by *Jean Pierre Christin* in 1743, thus defining a temperature scale which is in common use today.

[7]Thermo, Greek for heat, and meter, for measure

A.3.2 The Barometer

The barometer[8] measures the pressure of air, or atmospheric weight (per unit area). In the 4th century B.C. *Aristotle* demonstrated that air had body, by showing that a vessel had to be emptied of air before it could be filled with water. Although he also suspected that air had weight, his experiments on weighing a leather bag filled and empty with air showed no difference, and he concluded that air was weightless.[9] The Grand Duke of Tuscany, having fountains built upon his palace, found that his pumps could not make the water rise more than 32 feet, a fact which in 1640 he conveyed to *Galileo*. *Galileo* understood the fact of the existence of a vacuum, which he thought exerted a pulling force on water and which was somehow limited to 32 feet. This problem of the finite height he passed on to his assistant *Evangelista Torricelli*, [1608-1647], who first simplified the problem by using a heavier liquid, initially sea water, then honey and finally settling on mercury. He found that a column of mercury reached a maximum height of 30 inches and concluded that it was not the vacuum which sucked it up, but rather the weight of the atmosphere that pushed it up. He had invented the barometer. For the next hundred years, the barometer underwent intensive development, including a two-liquid barometer, the dial barometer. Finally in the nineteenth century corrections for temperature, the standardization and the capillarity were incorporated into the barometer, which was now a common meteorological instrument.

With the barometer, it was *Pascal* who finally proved conclusively that air had weight. Familiar with *Torricellis'* work, he put forward the idea that if the air did indeed have weight, and that the upper air pressing on the lower increased its pressure, then pressure should decrease with altitude. To this end, he engaged his brother–in–law to carry a barometer to the summit of a local mountain, where a barometric pressure reading was taken. The result clearly showed that pressure decreased with altitude, and that air is an elastic substance.

[8] Pressure measuring
[9] He did not understand that the volume of the bag changed

A.3.3 The Hygrometer

The water cycle of evaporation followed by precipitation was understood by the ancient Greeks. They, however, could not explain why in this process the water became invisible, and assumed that some of the water turned to air. Although a satisfactory explanation was not given until *Bernoulli* in his *Hydrodynamica*, [1738], attempts to measure the amount of water vapour in the atmosphere were made centuries before. The first successful invention of the hygrometer[10] is credited to the German, *Cardinal Nicholas de Cusa*, [1401-1464], who by balancing wool with stones, found that when the air is damp the weight of the wool increases and the reverse when air is drier. This type of hygrometer was not improved for several hundred years. At this stage the improvement came from the use of different materials which included catgut, and wild oat beards. The greatest development is attributed to *Johann Lambert* [1728-1777], who improved on the catgut, and made monthly and seasonal measurements of atmospheric humidity. Simultaneously measuring the temperature *Lambert* appears to have been the first person to present his data in a graphical format, an important contribution in itself. In the next fifty years many different hygrometers were proposed and built, including some utilizing whale–bone and human hair. Finally, the wet and dry bulb thermometers were invented in the eighteenth and improved in the nineteenth century. These are still used to measure humidity today.

A.3.4 Other instruments

The latter part of this millennium was the age of invention and other instruments or apparatus were developed which proved invaluable in atmospheric research. In 1650, *Otto de Guéricke*, burgomaster at Magdebury, invented the air pump. In that same year, using a glass globe, he conclusively showed that air has weight. This finally laid to rest *Aristotle's* idea that air had no weight. He also invented the Magdebury hemispheres, two hollow hemispheres made from copper, with a diameter of 4 inches, and connected to an air pump. He performed a number of

[10] humidity measuring device

experiments testing the strength required to pull them apart as a function of varying degrees of vacuum. In one of his famous experiments, using spheres of a diameter of 2 feet, two teams of 15 horses each could not pry the hemispheres apart[11].

Other instruments developed around this time included the rain gauge and the anemometer[12]. The psychrometer which measures the rate of evaporation and humidity of the air also became a much used instrument. Another important development was the automation of measurements with the introduction of the weather clock, which was able to take readings of the temperature, pressure and humidity at fifteen minute intervals while at the same time employing a rain bucket to measure the rainfall.

A.4 Chemistry of the atmosphere

The early Greeks thought that air was a homogeneous single substance, and that water turned to air as it evaporated. This idea remained until *Rene Descartes* [1596-1650], in his *Discourse on Method* proposed that all the earthly substances were in fact composed of a single fundamental substance. He ascribed the different states of matter to the intertwining of these particles. In solids these particles were hooked and intertwined together, while in air they just lay one on top of the other without being intertwined. The change from liquid to vapour of water depended on the strength of the intertwining, and evaporation was the result of the particles being strongly agitated thus breaking the bonds. This new idea inspired the next area of research which turned to the isolation and discovery of these individual constituents.

The French chemist *Lavoisier* was the first to study the properties of air. In 1777, after a lengthy experiment he found that air was composed of two elastic fluids of different and even opposite natures[13], one which is unable to support life and the other which is better adapted to respiration than atmospheric air. Although this experiment was a replication of one done by *Priestley*, it was *Lavoisier* who correctly interpreted the results. He deduced that there were two

[11] This corresponds to about 3.75 tons of atmospheric weight
[12] measures both the strength and direction of wind
[13] by heating mercury he absorbed all the oxygen in a chamber leaving behind nitrogen

parts to air; a pure part which supports life and burning, and another which supports neither. Assuming that the pure air was the basis of acids he named it oxygen, Greek for acid producer. Air which was produced by the respiration of animals was soon known to be produced by the combination of carbon and oxygen, and was eventually renamed carbon dioxide. Although prevalent throughout the whole atmosphere, the quantities were too small to be measured. *Rutherford* is credited with isolating nitrogen, long before *Lavoisiers* work, although he did not seem to understand his own discovery. The composition of air was thus known to consist of oxygen, nitrogen, and carbon dioxide, and this perception existed for well over a hundred years.

The discovery of the next component of the atmospheric air came in 1892. *Rayleigh* found a discrepancy of 0.5% by comparing the weight of nitrogen manufactured from pure ammonia with that obtained from the atmosphere. Two years later, *Rayleigh* and, independently, *Ramsay*, managed to isolate this new gas, and by using spectroscopy [14] discovered argon. Using similar techniques *Ramsay* discovered helium, krypton, neon and xenon.

A.5 Structure of the atmosphere

After the invention of the thermometer and the barometer, 18th century scientists conclusively showed by taking measurements from sea level to the highest accessible mountains, that both temperature and pressure steadily decreased with increasing height. They assumed that this trend continued until the atmosphere merged with interplanetary space. The major problem faced was the remoteness of the atmosphere and its inaccessibility to scientists. The invention of the balloon and the use of kites in meteorological studies soon changed this.

A.5.1 The troposphere and stratosphere

The first manned balloon flight occurred over Paris in 1783. Within a short time scientists, using both warm air and hydrogen[15] balloons began to carry instruments on the ascent. It was in 1804 that *Gay-Lussac* retrieved an air sample at a height of 23,000 feet, and subsequently

[14] *Bunsen* and *Kirchoff* were the first to realize that gases could be identified by their discrete spectra
[15] hydrogen was discovered in 1782 by *Cavallo*

discovered that the proportion of oxygen to nitrogen was no different from that at sea level. In 1862, *Glaucher* and *Coxwell* reached an altitude of 37,000 feet. These balloon ascents were not without their dangers, and several aeronauts died in the ascents[16]. Then, in 1892, *Hermite* was the first person to launch a barometer on an unmanned balloon flight. The first person to make routine measurements using balloons and kites was *Teisserenc do Bort* a French meteorologist. In the late nineteenth and early twentieth centuries he launched a number of payloads carrying kites and balloons. He used two balloons made from varnished paper. One was a main balloon which was filled with just sufficient hydrogen to support the instruments, and the other was a guide balloon which, by filling it with a specified pre–determined amount of hydrogen, burst at a particular altitude. The instruments on board[17] were driven by clockwork, and he was able to obtain measurements of pressure, temperature and humidity as a function of both height and time. He also tracked the balloons using two theodolites and was able to gather both wind and altitude measurements every minute. Finally after 3 years of research and 236 balloon soundings, on April 28th, 1902, he presented the results of his research for heights between 6 and 9 miles, to the French Academy of Sciences. His results showed that, contrary to common belief of the time, the atmospheric temperature does not decrease indefinitely with height, but that it levels off at a height of about seven miles above the surface of the earth. Assuming that above this height the temperature remained constant, he proposed that the various gases, in the absence of wind and convection currents, settled into distinct layers, the ordering of which was determined by their molecular weight. Thus there were two distinct zones of the atmosphere. The first zone where the temperature decreases with height he called the *troposphere*[18]. The second zone he called the *stratosphere*[19]. The boundary between the two zones soon became known as the tropopause, the so–called ceiling on the world's weather. At this time there was basic understanding of warm air rising, expanding and growing colder due to the lower pressure. On reaching the tropopause, where the temperature is constant, the temperature

[16] Lack of oxygen accentuated by the cold
[17] all weighing less than one pound, an achievement in itself
[18] Greek translation of "to turn over"
[19] consisting of strata of different gases

of the air parcel no longer differs from that of the surroundings, and the air rises no further. Evidence for this can be seen by the formation of anvil clouds observed at the top of summer thunderstorms.

A.6 The stratosphere

Although balloon soundings only extended to heights of 15 miles, in the early part of this century, it was assumed that the stratosphere extended indefinitely until it reached into space. At that stage direct measurements of different parameters at higher heights were not yet technologically feasible. Studying meteors and their trails, *Lindemann* and *Dobson* [1922], derived mathematical relationships which calculated the density of air, and thus its temperature, by knowing the altitude, length and brightness of a meteor trail. Gathering data from a number of amateur observers their initial calculation showed that the temperature at an altitude of approximately 30 miles was approximately 70 degrees Fahrenheit. This seemed a complete contradiction to the idea of an extensive stratosphere, which should have had a temperature at that height of -60 degrees Fahrenheit, and suggested that the atmosphere at that height was being heated. Although the result was treated with initial skepticism, it was used by a British scientist *Whipple*, to explain an acoustical phenomena first observed in World War I (see figure *A*.2). The sound from the large guns could sometimes be heard hundreds of kilometers from the front, and yet there existed an area, closer to the front where they were not heard and which was called the *zone of silence. Whipple* compiled observations and enlisted the help of the army to conduct experiments using stations at varying distances from a gun to measure the length of time taken to hear its blast. From his experiment he concluded that the sound waves reached an altitude of between 25 and 37 miles before bending back earthward. Several explanations were proposed to explain this phenomena. One involved the presence of a velocity gradient of wind at high altitudes. This, however, did not explain all of the observed properties; the circularity of the audible and silent zones, and the lack of correlation with wind velocity. Another explanation hypothesized the presence of lighter gases in the middle atmosphere. It

was however soon shown that the atmospheric gases are quite uniformly mixed, up to an altitude of 100 km. The only other possible explanation was the presence of a warmer layer of air which at that height gradually refracted the sound back to earth. The *zone of silence* was the region between the points where all the sound waves were refracted up and the region where they first started returning back to earth.

A decade later it was finally discovered that the heating can be related to ozone[20], which absorbs the sun's ultraviolet radiation very strongly. The u–v radiation splits a diatomic molecule of oxygen which then attaches itself to an existing molecule of oxygen, to form ozone. On further absorption of u–v radiation, ozone is split again. The creation and destruction of ozone is in equilibrium at the top of the layer. At lower heights, less u–v radiation comes through and thus less ozone is destroyed. That is why the stratosphere warms at higher altitudes.

A.7 The mesosphere

In the late 1940's and early 50's experiments utilizing rockets were performed in order to study the atmosphere at even higher heights. There were two popular methods used to obtain information about the atmosphere at those heights. One used rocketborne grenades which were released and detonated at different altitudes. Measurements of the velocity of the sound waves were used to calculate the wind speed, air density and temperature. The other method involved the release of spheres at particular heights. Tracking the spheres as they descended, the wind velocity, the air density and hence the temperature could be calculated. These experiments showed that at heights above the stratopause, the temperature steadily decreased for about 20 miles. It was also discovered that this region of the atmosphere, known as the mesosphere[21], was at its coldest during the summer months, due to a process not then understood. The upper boundary of the mesosphere is around 80 km altitude. Here there is very little absorption of solar radiation. However, there is strong radiation by CO_2 in the infra–red region.

[20] Greek for odour
[21] middle sphere

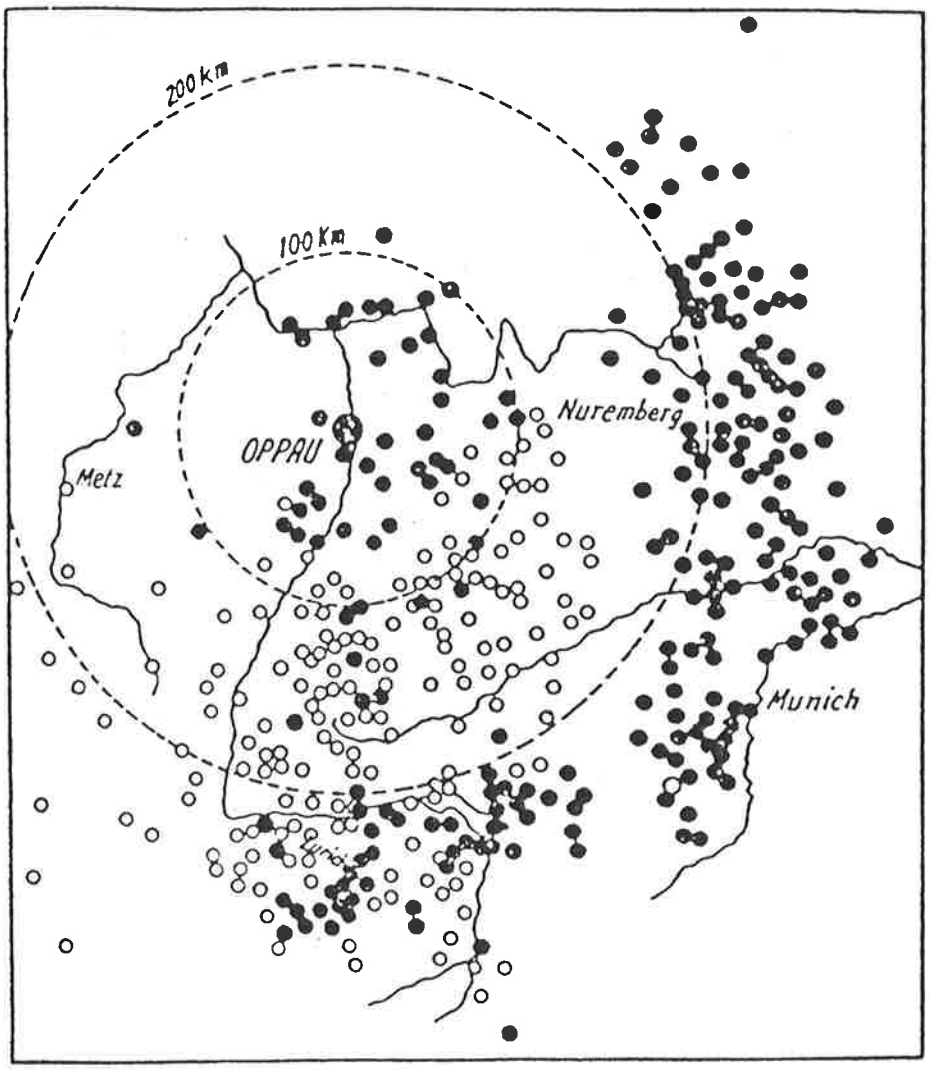

Figure A.2: The zones of audibility and of silence for an explosion at Oppau, Germany, on September 21, 1921. The open circles represent observers who did not hear any sound while the solid circles represent those that did hear the explosion. Towards the east and south, there is a zone of audibility of approximately 100km, followed by a zone of silence between 100-200km. Beyond 200km, there is again a zone of audibility [from *Mitra* [1952].

A.8 The thermosphere and exosphere

The region of the atmosphere above an altitude of about 50 miles was first investigated in the late 1950's by measuring the drag and perturbations of orbiting satellites. The atmosphere at this height was found to be quite rare, and very absorbant in the short ultra-violet range. Due to this absorption, mainly by molecular and atomic oxygen, the temperature increases quite rapidly up to 2000 degrees Kelvin, although this maximum varies dramatically between night and day. It was also found that the neutral atmospheric dynamics are strongly influenced by plasma motions at these upper heights. Unlike the lower atmosphere, molecular diffusion becomes important in the high altitudes and plays the dominant role for both the transfer of molecules themselves and in the transfer of heat. This results in the constituent gases each settling into their own exponentially decreasing height profile, the scale heights of which are determined by their molecular weight. Denoted as the *thermosphere* this region of the atmosphere was found to extend to over a thousand kilometers above the Earth's surface.

The region of the atmosphere where the density is so rare that molecular escape from the atmosphere becomes significant, is called the *exosphere*. Calculations of the height where this occurs have been attempted since the early 1920's, but as it is dependent on the density, which in itself varies, only an approximate height of upwards of one thousand km can be given.

A.9 Beyond the exosphere

Even by the late 1950's the general perception amongst the scientific community was that beyond the exosphere was a region devoid of anything except an occasional meteorite, interstellar cosmic ray or energetic bursts of particles from the sun. First evidence to the contrary was obtained with the launching of scientific satellites. The satellite Explorer I, launched in 1958, had a variety of instruments on board, one of which was a Geiger counter, measuring the frequency of charged particle collisions. The group of scientists headed by *Van Allen* found that a region of intense radiation existed above the equator, while radiation was essentially non-existent over the poles. With the launching of other satellites and gathering of further

data, two belts were eventually found to exist, the *Van Allen radiation belts.* The charged particles contained within the belts mainly arise from the solar wind and from cosmic rays. Moving at a high velocity, they follow a helical motion around the Earth's magnetic field, and spiral towards the poles. Another natural phenomena that was explained was due to collisions between solar particles and the atmosphere producing several glows, one of which is the famous aurora, observed over both the poles.

A.10 The ionosphere

The major atmosphere classification through the ages was on the basis of temperature. There do exist, however, several other structure classifications. These came about in the late nineteenth and early twentieth centuries, with the advent of other major physical discoveries. First it was *Herschel* who showed that there were rays beyond the red-end of the visible spectrum, which were called infra-red rays. Then *Maxwell* made his great breakthrough when he finally concluded that light is an electromagnetic wave, and he further postulated that visible light is just a small part of the electromagnetic spectrum. Other researchers soon expanded on this theory, and in 1888 *Hertz* made radio waves in his laboratory.

Marconi was the first person to study these radio waves and use them for long-distance radio communication. In 1901 he succeeded in sending a radio signal from England to Newfoundland. Although he was unable to produce a satisfactory explanation of how the radio waves followed the curvature of the earth, one was soon provided by *Heaviside*, who proposed that there may exist a conducting layer in the upper air, and that the radio waves were guided by this layer and the sea surface[22]. This was the discovery of the *ionosphere*, later found to consist of a number of layers, a region consisting of free electrons and ions in sufficient quantities to affect the propagation of radio waves. It was this discovery which eventually led to remote–sensing as we know it today.

[22]This conclusion was independently reached by *Kennelly*

A.11 Development of radars

The major advances in the understanding of the atmosphere came about both with the increase in the knowledge of other physical sciences and the availability of better and new remote sensing instruments. Although all the atmosphere could be probed to an altitude of at least a hundred kilometres, this was mainly by *in situ* methods which were very infrequent, labor intensive and expensive. This soon changed with the advent of radars which were one of the first remote–sensing tools.

The use of scattering of electro–magnetic waves by atmospheric constituents for research preceded the advent of radars by more than fifty years. Scattering of light from aerosols was initially studied by *Tyndall* in 1869. Although many other workers studied light scattering by various particles, the principal investigators were *Rayleigh* (1871–1918), *Mie* (1906) and *Debye* (1915) [see e.g. *Berne and Pecora*, 1976]. The relevance of the study of optical scattering to the radar case is found in the terminology used. When the dimensions of the scattering objects is smaller than the wavelength one refers to *Rayleigh* scattering. Scattering from targets whose size is comparable to the wavelength is referred to as *Mie* or resonance scatter. As the target sizes increase to be much larger than the wavelength, one refers to the *optical* region. Although the detection of objects using electro–magnetic theory seems implicit in their theoretical understanding, the first formal idea seems to have come from *Tesla*, who in the *Century Illustrated Monthly Magazine* [1900], wrote the following [after *Papović et al.*, 1956]

When we raise the voice and hear an echo in reply, we know that the sound of the voice must have reached a distant wall, or boundary, and must have been reflected from the same. Exactly as the sound, so an electrical wave is reflected, and the same evidence which is afforded by an echo is afforded by an electrical phenomenon known as a 'stationary wave' – that is, a wave with fixed nodal and central regions...Stationary waves in the earth will mean something more than mere telegraphy without wires to any distance. They will enable us to attain many important specific results, impossible otherwise. For instance, by their use we may produce at will, from a sending station, an electrical effect in any particular region of the globe; we may determine the

relative position or course of a moving object, such as a vessel at sea, the distance traveled by same, or its speed.....

Although the idea of producing an electrical effect anywhere in the world is still an ambitious one, one might wonder whether Tesla would have been surprised by the latest mobile phones and satellite positioning!

It is difficult to credit anyone or any group with the invention of the radar, and in fact it seems that it was invented independently and simultaneously by groups working in the United States, United Kingdom, and Germany [for a brief history see e.g. *Hill*, 1990], although other groups in France, Italy, and Japan also had an active research programme. Furthermore there seems to be a major contention in the definition of radar. The first idea for using radio waves to measure distance was proposed in 1924 by Appleton, who together with Barnett, determined the height of the E–layer at around 100 km [*Appleton and Barnett*, 1926]. The following year, ionospheric physicists were using pulse–modulated techniques to study the ionosphere [*Tuve and Breit*, 1925]. However, according to *Watson-Watt* [1957], who claims to be the father of radar, this did not constitute a radar for two reasons; firstly the transmitter and receiver were widely separated, and secondly, there was no individual ionospheric feature for which a real direction and range were determined. According to *Page* [1962], however, it was *Breit and Tuve* [1926] who sampled direct and reflected pulses, and found, without resolving the reflected from the direct pulse, that the decaying side of a direct pulse was affected when an aircraft flew across the radio beam. *Page* asserts that *Watson-Watt* did not detect aircraft until June, 1935.

Regardless of the exact origins and time of the first experiments utilizing scattering of electro–magnetic radiation to detect objects, it was the threat and growing speed of military aircraft which ensured a rapid growth in radar research. In fact the acronym radar, was only coined in 1940 by the United States Navy, well after radars were first used in the Second World War [*Swords*, 1986], which saw the emergence of all manner of systems quite diverse in function and frequency. It was also during this time that the use of secondary radar emerged. This is a combined receiver and transmitter unit which, when prompted by a ground radar signal,

transmits a weak encoded signal back and enables identification of friendly or enemy aircraft. Other developments included the use of several ground stations to create radio–navigational position lines enabling aircraft or ships to determine their position.

After the war, although the radar continued to be used and widely applied both in military and commercial applications, it was also being applied in scientific research, especially in radio meteorology and radio astronomy. In fact it was right after the war, in 1946, that the first radar echoes were reflected from the moon, and the structure of hurricanes and thunderstorms first studied [*Mofensen*, 1946; *Brooks*, 1946; *Wexler*, 1947]. The now common Doppler radar did not however emerge until 1957, when simultaneous measurements of amplitude and phase were recorded [*Brantley and Barczys*, 1957]. Besides measuring the Doppler velocity of the atmosphere and other objects, the Doppler radar was also used by aircraft to compute true velocity and track, unaided by ground based radars. Radio meteorology has since become a tool for studying all kinds of atmospheric phenomena, including rain, hail and clear air turbulence. In addition, radars have been employed on spacecraft; for example the Magellan spacecraft uses a radar which has mapped most of the surface area of Venus. Radio astronomy has also made use of radar to study many other areas, including auroral phenomena, meteor trails, and distant planets. Even though conventionalradio astronomy relies on passive rather than active systems, many of the general principles used are the same as those used in radars. It was radio astronomy that eventually led to the discovery of radio stars, quasars and pulsars.

In conclusion, the radar has opened up areas of research which until now were generally unattainable, and has led to many new scientific discoveries. For example it was the need for efficient crystal mixers that concentrated research on germanium and silicon, and led to better understanding on the injection of impurities into semi–conductors. This research led to the emergence in 1948 of the transistor. Furthermore, the need for radar controllers led to advances in both control algorithms and electronics.

Appendix B

About Christmas Island

Christmas Island, locally known as *Kiritimati*, is located at 2°North, 157°West, [see figure 7.1] and is the world's largest coral atoll covering an area of some 250 square miles, interspersed with numerous lagoons (about 140 square miles of land area) [see figure 7.2 and figure $B.1$]. It rests just above the waves of an ancient reef located at the summit of an undersea volcano rising 3 miles from the ocean floor. The topography is fairly flat, with a mean height above sea level of approximately five feet and the highest point on the island being approximately 12 feet. The island was first explored by Captain James Cook on Christmas Eve 1777, and was found to be uninhabited although teeming with birdlife. During the next two centuries, Americans, Australians, and Europeans all attempted to develop the island as a commercial venture, including the planting of half a million coconut palms.

In the 1950's the island was used as a staging area for British and American airborne nuclear tests, and this was when most of the island's existing road network was constructed. It was also during this time that the current residents, Gilbertese Islanders of Micronesian descent, first established permanent residency. Under colonial rule education became compulsory resulting in a 100% literacy rate. Although Gilbertese is the local language, English is used within the government structure and is taught in all schools. The current population numbers approximately 1600, most of whom are in their late twenties, being the first generation after permanent settlement.

See page 451

Figure B.1: Christmas Island as seen from the air. Main feature of the photograph is the numerous lagoons which cover the island. These lagoons and the reef on which the island rests provide both the staple diet of the local population and one of the few local industries, the export of fish and granting of commercial fishing licenses, especially to Asian fishing fleets. Since the island is only a few feet elevation from mean sea level, the islanders are quite concerned and aware of the disastrous consequences a greenhouse effect would have on the island.

See page 453

Figure B.2: Cassidy International airport, located 5 feet above mean sea level, provides the only semi–regular link between Christmas island and the outside world. Most of the necessities that are not locally grown and produced are usually flown in. Besides staple foods like rice, sugar milk and fresh fruits other goods can include motor vehicles, bicycles and household goods. The island, in return, exports by air several tons of fish and lobsters, most of which are destined for the American market. The principal passengers of the air service are American sports–fishermen who have come to the island for a week at a time to indulge in their sport. The airport was constructed in the 1950's when the island was used as a base for both British and American nuclear airborne tests. There are still visible remnants of military occupation both from that time and from World War II when the island was used as a staging area for Allied troops. Rows of military housing with corrugated iron roofs are used as dwellings by the local population, although these are generally being transformed into the open style housing favoured by the Gilbertese.


ARRIVALS
CASSIDY INTERNATIONAL AIRPORT
CHRISTMAS ISLAND
REPUBLIC OF KIRIBATI
ARRIVALS

Christmas Island became part of the *Republic of Kiribati* (capital of Tarawa), when a number of islands, 33 in total, gained independence from colonial rule in 1979, and is considered the capital of a local group of islands, the *Phoenix* and *Line Islands.* Although the Gilbertese are mostly self-sufficient, some foreign currency is earned from the rich fishing grounds and granting of commercial fishing licenses as well as production of copra and limited tourism.

Transport to and from the island is either by boat which only comes once every four months, or a somewhat irregular weekly flight from Hawaii [see figure $B.2$] which brings in a variety of goods[1] and up to several dozen tourists who come to the island as sport-fishermen, something the island is infamous for.

The climate is very mild, with day time average air temperatures being about 26°C, dropping to 22°C at night. Average rainfall is $\approx$ 750 mm, mostly afternoon and evening showers, except during periods of El Nino[2]. The surface winds are mostly easterly, averaging about 10–12 knots.

[1] Motor vehicles can and are also flown in

[2] El Nino is an event when the Pacific ocean current circulation changes, affecting global weather patterns, especially rainfall rates

Appendix C

Directional statistics

When dealing with directional data, it makes no sense to utilise linear statistics which can lead to paradoxes; for example it is intuitive that the mean of two angles at 1° and 359° is 0°, and not 180° as obtained by arithmetic means. Here we present some of the simple ideas that have been used in directional analysis in this thesis; for a detailed description see *Mardia* [1972].

We assume that $\theta_1, ..., \theta_n$ is a sample of size n, where each angle represents a vector of unit length $\overline{OP_i}$, where P_i is the point θ_i on the unit circle. Then the centre of gravity $(\overline{C}, \overline{S})$ of these points is given in Cartesian co–ordinates as

$$\overline{C} = \frac{1}{n}\sum_{i=1}^{n} cos\theta_i, \qquad \overline{S} = \frac{1}{n}\sum_{i=1}^{n} sin\theta_i \quad ,$$

such that if

$$\overline{R} = (\overline{C}^2 + \overline{S}^2)^{\frac{1}{2}},$$

then, $R = \overline{R}n$ is defined as the length of the resultant, and $\overline{x}_0$ is the mean direction obtained by solving the above equations. Then

$$cos\overline{x}_0 = \frac{\overline{C}}{\overline{R}} \quad , \qquad sin\overline{x}_0 = \frac{\overline{s}}{\overline{R}} \quad ,$$

with the following conditions

$$\overline{x}_0 = \begin{cases} \overline{x}'_0 & \text{if } \overline{S} > 0, \overline{C} > 0, \\ \overline{x}'_0 + \pi & \text{if } \overline{C} < 0, \\ \overline{x}'_0 + 2\pi & \text{if } \overline{S} < 0, \overline{C} > 0, \end{cases}$$

where

$$\overline{x}'_0 = arctan\left(\frac{\overline{S}}{\overline{C}}\right) \quad , \qquad -\frac{\pi}{2} < \overline{x}'_0 < \frac{\pi}{2} \quad .$$

If we denote α as a fixed direction we can show that a measure of dispersion of P_i is defined as

$$D = \frac{1}{n}\sum_{i=1}^{n} 1 - cos(\theta_i - \alpha) \quad .$$

Furthermore, this D is minimized at $\alpha = \overline{x}_0$, such that the dispersion, around a mean value $\overline{x}_0$, is now defined as

$$S_0 = 1 - \frac{1}{n}\sum_{i=1}^{n} cos(\theta_i - \overline{x}_0) \quad ,$$

where S_0 is defined as the circular variance and is related to $\overline{R}_0$ by

$$S_0 = 1 - \overline{R}_0, \qquad 0 \leq S_0 \geq 1 \quad .$$

This is intuitive because if all the angles are tightly clustered about the mean, then the length R will be large and S_0 will approach 0, whereas if the angles are widely dispersed, S_0 aproaches 1.

Since S_0 lies in the range of $(0, 1)$, we relate it to the linear standard deviation, assuming a wrapped normal distribution, by

$$1 - S_0 = e^{\frac{1}{2}\sigma^2} \quad .$$

σ, or s_0, is defined as the circular standard deviation where

$$\sigma_0 = -2\, ln(1 - S_0)^{\frac{1}{2}} \quad , \qquad 0 \leq \sigma \geq \infty \quad .$$

For the case where the range of angles is between $(0, 2\pi/l)$, we find that

$$s_0 = -2ln(1 - S_0)^{\frac{1}{2}}/l \ .$$

Appendix D

Relating spectral width to fading time

The full correlation analysis applied to a triangle of three spaced antennae, primarily calculates the horizontal velocity of the scatterers (as dicussed in chapter 3). However, it also calculates a number of other parameters including the fading time of the signal, $\tau_{0.5}$, which is defined as the time taken for an auto–correlation function to fall to 0.5.

If the spectrum is approximately Gaussian then the spectral width can be related to the fading time. Firstly, denoting the auto–correlation function as $\rho(t)$ and the spectrum as $F(n)$, we know that a Gaussian function has the following form in the time domain

$$\rho(\tau) = \exp[\frac{-\pi t^2}{\sigma^2}] \ , \tag{D.1}$$

whilst in the frequency domain $F(n)$ has the form

$$F(n) = \sigma e^{-\pi\sigma^2 n^2} \ . \tag{D.2}$$

Examining the case of half–time and half–spectrum we find that

$$\begin{aligned} ln2 &= \frac{-\pi\tau_{0.5}^2}{\sigma^2} \ln 2 \ , \\ ln2 &= \pi\sigma^2 n_{0.5}^2 \ . \end{aligned} \tag{D.3}$$

Equating the two σ^2 terms gives

$$\begin{aligned} \sigma^2 &= \frac{\pi}{ln2}\tau_{0.5}^2 \ , \\ \sigma^2 &= \frac{ln2}{\pi n_{0.5}^2} \ , \end{aligned} \tag{D.4}$$

so we find that the fading time is related to the spectral width by the simple direct relationship

$$f_{0.5} = \frac{0.22}{\tau_{0.5}} \ . \tag{D.5}$$

Appendix E

Studies of seasonal behaviour of the shape of mesospheric scatterers using a 1.98 MHz radar

This is a reprint of a paper by D. Lesicar and W.K. Hocking, published in *J. Atmos. Terr. Physics*, *54*, 295–309, 1992.

Lesicar, D., and Hocking, W.K., (1992) Studies of seasonal behaviour of the shape of mesospheric scatterers using a 1.98 MHz radar.
Journal of Atmospheric and Terrestrial Physics, v. 54 (3-4), pp. 295-303, 305-309.

Appendix F

Dynamics of the equatorial mesosphere: First results with a new generation partial reflection radar

This is a reprint of a paper by R.A. Vincent and D. Lesicar, published in *Geophys. Res. Letters*, *18*, 825–828, 1991.

Vincent, R.A., and Lesicar, D., (1991) Dynamics of the equatorial mesosphere: first results with a new generation partial reflection radar.
Geophysical Research Letters, v. 18 (5), pp. 825-828.

Appendix G

Mean winds, tides and gravity waves in the upper middle atmosphere during ALOHA–90

This is a preprint of a paper by R.A. Vincent and D. Lesicar, published in *Geophys. Res. Letters*, *18*, 1321–1324, 1991.

Vincent, R.A., and Lesicar, D., (1991) Mean winds, tides and gravity waves in the upper middle atmosphere during ALOHA-90.
Geophysical Research Letters, v. 18 (7), pp. 1321-1324.

Appendix H

Spectra of gravity wave density and wind perturbations observed during ALOHA–90 on the 25 March flight between Maui and Christmas Island

This is a preprint of a paper by C.A. Hostetler, C.S. Gardner, R.A. Vincent, and D. Lesicar, published in *Geophys. Res. Letters*, *18*, 1325–1328, 1991.

Hostetler, C.A., Gardner, C.S., Vincent, R.A., and Lesicar, D., (1991) Spectra of gravity wave density and wind perturbations observed during ALOHA-90 on the 25 March flight between Maui and Christmas Island.
Geophysical Research Letter, v. 18 (7), pp. 1325-1328.

Appendix I

Comparative studies of scatterers observed by MF radars in the Southern Hemisphere mesosphere

This is a paper by D. Lesicar, W.K. Hocking, and R.A. Vincent, accepted for publication by the *Journal of Atmospheric and Terrestrial Physics*, 1993.

Lesicar, D., Hocking, W.K., and Vincent, R.A., (1994) Comparative studies of scatterers observed by MF radars in the southern hemisphere mesosphere. *Journal of Atmospheric and Terrestrial Physics, v. 56 (5), pp. 581-587, 589-591.*

References

Adams, G.W., D.P. Edwards, and J.W. Brosnahan, The imaging Doppler interferometer; Data analysis, *Radio Science*, *20*, 1481–1492, 1985.

Adams, G.W., J.W. Brosnahan, and R.E. Johnson, Aspect sensitivity of 2.66 MHz radar returns from the mesosphere, *Radio Science*, *24*, 127–132, 1989.

Anandarao, B.G., R. Raghavarao, J.N. Desai, and G. Haerendel, Vertical winds and turbulence over Thumbs, *Journal of Atmospheric and Terrestrial Physics*, *40*, 157–163, 1978.

Andrews, D.G., and M.E. McIntyre, An exact theory for nonlinear waves on a Lagrangian–mean flow, *Journal of Fluid Mechanics*, *89*, 609–646. 1978.

Andrews, D.G., J.R. Holton, and C.B. Leovy, *Middle Atmosphere Dynamics*, Vol. *40*, International Geophysics Series, Academic Press, 1987.

Appleton, E.V., and M.A.F. Barnett, On some direct evidence for downward reflection of electric rays, *Proceedings of the Royal Society, London*, *109*, 621–641, 1926.

Atlas, D., *Advances in Geophysics*, *10*, 317–483 pp, Academic New York, 1964.

Atlas, D., R.C. Srevestava, and P.W. Sloss, Wind shear and reflectivity gradient effects on Doppler radar spectra, II, *Journal of Applied Meteorology*, *8*, 384–388, 1969.

Avery, S.K., and S.E. Palo, Mean winds and waves in the troposphere during ALOHA–90, *Geophysical Research Letters*, *18*, 1317–1320, 1991.

Avery, S.K., J.P. Avery, T.A. Valentic, S.E. Palo, M.J. Leary, and R.L. Obert, A new meteor echo detection and collection system: Christmas Island mesospheric wind measurements, *Radio Science*, *25*, 657–669, 1990.

Awe, O., Errors in correlation between time series, *Journal of Atmospheric and Terrestrial Physics*, *26*, 1239–1255, 1964a.

Awe, O., Effects if errors in correlation on the analysis of the fading of radio waves, *Journal of Atmospheric and Terrestrial Physics*, *26*, 1257–1271, 1964b.

Baker, D.J., and A.T. Stair Jr., Rocket measurements of the altitude distributions of the hydroxyl airglow, *Physica Scripta*, *37*, 611, 1988.

Ball, S.M., *Upper atmosphere tides and gravity waves at mid- and low-latitudes*, Ph.D. Thesis, Department of Physics, University of Adelaide, Adelaide, Australia, 1981.

Balsley, B.B., The MST technique - A brief review, *Journal of Atmospheric and Terrestrial Physics*, *43*, 495–509, 1981.

Balsley, B.B., W. Ecklund, and D.C. Fritts, VHF echoes from the high latitude mesosphere and lower thermosphere: Observations and interpretations, *Journal of the Atmospheric Sciences*, *40*, 2451–2466, 1983.

Barakat, R., Sums of independent logonormally distributed random variables, *Journal of the Optical Society of America*, *66*, 211–216, 1976.

Barnett, J.J., and M. Corney, Middle atmosphere reference model derived from satellite data, *Handbook for MAP*, *16*, 47–85, 1985.

Barsis, A.P., J.W. Herbstreit, and K.O. Hornberg, The Cheyenne mountain tropospheric propagation experiments, *National Bureau of Standards Circular*, 554, Washington, D.C., December, 1954.

Batchelor, G.K., *Theory of Homogenous Turbulence*, Cambridge University Press, 1953.

Batchelor, G.K., *An introduction to fluid dynamics*, Cambridge University Press, 1967.

Bean, B.R., and E.J. Dutton, *Radio Meteorology*, Dover, New York, 1968.

Beatty, T.J., R.L. Collins, C.S. Gardner, C.A. Hostetler, C.F., Sechrist Jr., and C.A. Tepley, Simultaneous radar and lidar observations of sporadic E and Na layers at Arecibo, *Geophysical Research Letters*, *16*, 1019–1022, 1989.

Beckmann, P., Statistical distribution of the amplitude and phase of a multiply scattered field, *Journal of Research of the National Bureau of Standards and Technology*, *66D*, 231, 1962.

Berggren, R., and K. Labitzke, The distribution of ozone on pressure surfaces, *Tellus*, *20*, 88, 1968.

Berne, B.J., and R. Pecora, *Dynamic light scattering*, John Wiley, New York, 1976.

Bevilacqua, R.M., D.F. Strobel, M.E. Summers, J.J. Olivero, and M. Allen, The seasonal variation of water vapour and ozone in the upper mesosphere: implications for vertical transport

and ozone photochemistry, *Journal of Geophysical Research*, *95*, 883–893, 1990.

Beynon, W.J.G., and J.C. Wright, Ionospheric drift measurements on adjacent aerial arrays, *Journal of Atmospheric and Terrestrial Physics*, *31*, 119–133, 1969.

Bills, R.E., C.S. Gardner, and S.J. Franke, Na Doppler/Temperature Lidar: Initial mesopause region observations and comparisons with the Urbana medium frequency radar, *Journal of Geophysical Research*, *96*, 22701, 1991.

Binke, R.B., *Roger Bacon. The Opus Majus of Roger Bacon (trans.)*, Philadelphia: University of Pennsylvania Press, 1928, 1:116.

Blamont, J., *Planetary and Space Science*, *10*, 89–101, 1963.

Blamont, J.E., and J. Barat, Dynamical structure of the atmosphere between 80 and 120 km, *Aurora and Airglow*, ed. B.M. McCormac, Reinhold Publishing Co., 159pp, 1967.

Blix, T.A., *In–situ studies of turbulence in the middle atmosphere by means of electrostatic ion probes.* Technical report NDRE/PUBL-88/1002, Norwegian Defence Research Establishment, P.O. Box 25-N-2007 Kjeller, Norway, April 1988.

Blix, T.A., E.V. Thrane, D.C. Fritts, U. von Zahn, F.J. Lübken, W. Hillert, S.P. Blood, J.D. Mitchell, G.A. Kokin, and S.V. Pakhomov, Small–scale structure observed *in–situ* during MAC/EPSILON, *Journal of Atmospheric and Terrestrial Physics*, *52*, 835–854, 1990.

Bolgiano, R. Jr., Structure of turbulence in stratified media, *Journal of Geophysical Research*, *67*, 3015–3023, 1962.

Bolgiano, R. Jr., The General Theory of Turbulence – Turbulence in the Atmosphere, p371–400, from *Winds and Turbulence in the Stratosphere, Mesosphere and Ionosphere*, Ed. K. Rawer, North–Holland, 421pp, 1968.

Booker, H.G., A theory of scattering by non-isotropic irregularities with application to radar reflections from the aurora, *Journal of Atmospheric and Terrestrial Physics*, *8*, 204–221, 1956.

Booker, J.R., and F.P. Bretherton, The critical layer for internal gravity waves in a shear flow, *Journal of Fluid Mechanics*, *27*, 513, 1967.

Booker, H.G., and W.E. Gordon, Theory of radio scattering in the troposphere, *Proceedings of IEEE*, *64*, 401–412, 1950.

Bowman, M.R., L. Thomas, and R.H. Thomas, The propagation of gravity waves through a critical layer for conditions of moderate wind shear, *Planetary and Space Science*, *28*, 119–133, 1980.

Bracewell, R.N., *The Fourier Transform and its Applications*, McGraw-Hill, New York, 444pp., 1978.

Bradshaw, P., *An Introduction to Turbulence and its Measurement*, Pergamon Press, 218pp., 1971.

Brantley, J.Q., and D.A. Barczys, Some weather observations with CW Doppler radar, *Proceedings of the Sixth Weather Radar Conference*, Boston: American Meteorological Society, 297, 1957.

Brasseur, G., and M. Nicolet, Chemospheric processes of nitric oxide in the mesosphere and stratosphere, *Planetary and Space Science*, *21*, 939, 1973.

Brasseur, G., and S. Solomon, *Aeronomy of the middle atmosphere, Chemistry and Physics of the Stratosphere and Mesosphere*, 2nd. ed., Reidel, Dordrecht, Holland, 1986.

Breit, G., and M.A. Tuve, A test of the existence of the conducting layer, *Physical Review*, *28*. 1926.

Briggs, B.H., Ionospheric Drifts, *Journal of Atmospheric and Terrestrial Physics*, *39*, 1023–1033, 1977.

Briggs, B.H., Radar observations of atmospheric winds and turbulence: A comparison of techniques, *Journal of Atmospheric and Terrestrial Physics*, *42*, 823–833, 1980.

Briggs, B.H., The analysis of spaced sensor records by correlation techniques, *Handbook for MAP*, *13*, 166–186, 1984.

Briggs, B.H., Radar measurements of aspect sensitivity of atmospheric scatterers using spaced-antenna correlation techniques, *Journal of Atmospheric and Terrestrial Physics*, *54*, 153–165, 1992.

Briggs, B.H., and R.A. Vincent, Some theoretical considerations on remote probing of weakly scattering irregularities, *Australian Journal of Physics*, *26*, 805–814, 1973.

Briggs, B.H., G. J. Phillips, and D. H. Shinn, The analysis of observations on spaced receivers of the fading of radio signals, *Proceedings of the Physical Society*, *63B*, 106–121, 1950.

Briggs, B.H., W.G. Elford, D.G. Felgate, M.G. Golley, D.E. Rossiter, and J.W. Smith, Buckland Park aerial array, *Nature*, *223*: 1321–1325, 1969.

Brooks, A summary of some radar thunderstorm observations, *Bulletin of the American Meteorological Society*, *27*, 557, 1946.

Brown, G.M., and J.I. John, Vertical penetration of planetary waves into the lower ionosphere, *Journal of Atmospheric and Terrestrial Physics*, *41*, 379–386, 1979.

Brownlie, G.P., L.G. Dryburgh, and J.D. Whitehead, Measurement of the velocity of waves in the ionosphere; A comparison of the ray theory approach and diffraction theory, *Journal of Atmospheric and Terrestrial Physics*, *35*, 2147–2162, 1973.

Buckley, R., Some notes on practical digital power spectral and auto– and cross–correlation analysis using the FFT, Department of Physics report, University of Adelaide, 1971.

Cardano Girolamo, De Subtiliate 3rd. ed., (Basel: 1569).

Caughey, S.J., B.A. Crease, D.N., Asimakapoulos, and R.S. Cole, Quantitative bistatic acoustic sounding of the atmospheric boundary layer, *Quarterly Journal of the Royal Meteorological Society*, *104*, 147–161, 1980.

Chakrabarty, D.K., P. Chakrabarty, and G. Witt, A theoretical attempt to explain some observed features of the D region, *Journal of Geophysical Research*, *83*, 5763–5767, 1978.

Chakrabarty, D.K., G. Dutta, and H. Chandra, *Journal of Atmospheric and Terrestrial Physics*, *43*, 217–220, 1981.

Chamberlain, M.T., and F. Jacka, Optical evidence for mid-latitude charged particle precipitation, *Journal of Atmospheric and Terrestrial Physics*, *41*, 111–118, 1979.

Chandra, H., On triangle size effect in spaced receiver drift experiments, *Indian Journal of Radio Space Physics*, *7*, 13–15, 1978.

Chandra, H., and R.A. Vincent, Radio wave scattering from the southern hemisphere D region, *Journal of Atmospheric and Terrestrial Physics*, *39*, 1011, 1977.

Chandra, H., M.R. Deshpande, and R.C. Rastogi, Errors in the correlation analysis of ionospheric drift records, *Journal of the Institution of Telecommunication Engineers, New Delhi*, *18*, 340, 1972.

Chang, N.J.F., Precision of tropospheric/stratospheric winds measured by the Chatanika radar, *Radio Science*, *15*, 371–382, 1980.

Chapman, S., and R.S. Lindzen, *Atmospheric Tides*, D. Reidel Pub. Co., 1970.

Charney, J.G., and P.G. Drazin, Propagation of planetary-scale disturbances from the lower into the upper atmosphere, *Journal of the Atmospheric Sciences*, *66*, 83–109, 1961.

Chisholm, J.H., P.A. Portmann, J.T. DeBettencourt, and J.F. Roche, Investigations of angular scattering and multipath properties of tropospheric propagation of short radio waves beyond the horizon, *Proceedings of IEEE*, *43*, 1317–1335, 1955.

Clancy, R. T., and D.W. Rusch, Climatology and trends of mesospheric (58-90 km) temperatures based upon 1982–1986 SME limb scattering profiles, *Journal of Geophysical Research*, *94*, 3377–3393, 1989.

Clemesha, B.R., The elongation of irregularities in the equatorial ionosphere, *Journal of Geophysical Research*, *68*, 2363, 1963.

Countryman, I.D., P.K. Rastogi, S.A. Bowhill, and P.M. Dalas, Short–period gravity–wave observations in the equatorial mesosphere, *Handbook for MAP*, *2*, 301–310, 1981.

Craig, R.L., R.A. Vincent, G.J. Fraser, and M.J. Smith, The quasi 2–day wave in the southern hemisphere mesosphere, *Nature: Physical Science*, *287*, 319–320, 1980.

Crane, R.K., A review of radar observations of turbulence in the lower stratosphere, *Radio Science*, *15*, 177–193, 1980.

Croft, T.A., Sky-wave backscatter; a means of observing our environment at great distances, *Reviews of Geophysics and Space Physics*, *10*, 73–155, 1972.

Cunnold, D.M., Vertical transport coefficients in the mesosphere obtained from radar observations, *Journal of the Atmospheric Sciences*, *32*, 2191, 1975.

Czechowsky, P., R. Rüster, and G. Schmidt, Variations of mesospheric structures at different seasons, *Geophysical Research Letters*, *6*, 459–462, 1979.

Czechowsky P., G. Schmidt, and R. Rüseter, The mobile SOUSY Doppler radar: technical design and first results, *Radio Science*, *19*, 441–450, 1984.

Czechowsky, P., I. M. Reid, and R. Rüster, VHF radar measurements of the aspect sensitivity of the summer polar mesopause echoes over Andenes Norway *Geophysical Research Letters*, *15*, 1259-1262, 1988.

Czechowsky, P., I.M. Reid, R. Rüster, and G. Schmidt, VHF radar echoes observed in the summer and winter polar mesosphere over Andøya, Norway, *Journal of Geophysical Research*, *94*, 5199–5217, 1989.

Dalaudier, F., and C. Sidi, Evidence and interpretation of a spectral gap in the turbulent atmospheric temperature structure, *Journal of the Atmospheric Sciences*, *44*, 3121–3126, 1987.

Daley, R., and D.L. Williamson, The existence of free Rossby waves during January 1979, *Journal of the Atmospheric Sciences*, *42*, 2121–2141, 1985.

Dewan, E.M., N. Grossbard, A.F. Quesada, and R.E. Good, Saturation and the "universal" spectrum for vertical profiles of horizontal scalar winds in the atmosphere, *Geophysical Research Letters*, *11*, 80–83, 1984. (correction, *Geophysical Research Letters*, *11*, 624, 1984.)

Doviak, R.J., and D.S. Zrnić, Reflection and scatter formula for anisotropically turbulent air, *Radio Science*, *19*, 325–336, 1984.

Driscoll, R.J., and L.A. Kennedy, A model for the spectrum of passive scalars in an isotropic turbulence field, *Physics of Fluids*, *28*, 72–80, 1985.

Du Castel, F., *Tropospheric radio Wave Propagation Beyond the Horizon*, Engl. ed., 236pp., Pregamon, New York, 1966.

Dunkerton, T.J., On the mean meridional mass motions of the stratosphere and mesosphere, *Journal of the Atmospheric Sciences*, *35*, 2325, 1978.

Dunkerton, T.J., Theory of the mesopause semiannual oscillation, *Journal of the Atmospheric Sciences*, *39*, 2681–2690, 1982.

Dutton, J.A., and H.A. Panofsky, Clear air turbulence: a mystery may be unfolding, *Science*, *167*, 937, 1970.

Eckermann, S.D., *Atmospheric gravity waves: Observations and theory*, Ph.D. Thesis, Department of Physics and Mathematical Physics, University of Adelaide, 1990.

Ecklund, W.L., D.A. Carter, and B.B. Balsley, Continuous measurement of upper atmospheric winds and turbulence using a VHF Doppler radar: Preliminary results, *Journal of Atmospheric and Terrestrial Physics*, *41*, 983–994, 1979.

Elford, W.G., and R.G. Roper, Turbulence in the lower thermosphere, *Space Research VII*, p42, ed. R.L. Smith–Rose, North–Holland, Amsterdam, 1967.

Elford, W.G., and E.L. Murray, Upper Atmosphere wind measurements in the Antarctic, *International Space Research Symposium*, Space Research I, Kallmann, H. ed., 158–163, 1960.

Eliassen, A., and E. Palm, On the transfer of energy in stationary mountain waves. *Geophysica Norvegica*, *12*, 1–23, 1960.

Farley, D.T., H.M. Ierkic, and B.G. Fejer, Radar interferometry: a new technique for studying plasma turbulence in the ionosphere, *Journal of Geophysical Research*, *86*, 1467–1472, 1981.

Fedor, L.S., A statistical approach to the determination of 3–dimensional ionospheric drifts, *Journal of Geophysical Research*, *72*, 5401–5415, 1967.

Fedor, L.S., and W. Plywaski, The interpretation of ionospheric radio drift measurements, IV, The effects of signal coupling among spaced sensor channels, *Journal of Atmospheric and Terrestrial Physics*, *34*, 1285–1303, 1972.

Felgate, D.G., On the point source effect in the measurement of ionospheric drifts, *Journal of Atmospheric and Terrestrial Physics*, *32*, 241–245, 1970.

Felgate, D.G., and M.G. Golley, Ionospheric irregularities and movements observed with a large aerial array, *Journal of Atmospheric and Terrestrial Physics*, *33*, 1353–1369, 1971.

Fellous, J.L, and M.E. Frezal, The random wind component in the lower thermosphere, *Handbook for MAP. 2*, 323–332, 1981.

Ferguson, E.E., *Ion-molecule reactions in the atmosphere*, pp. 377–403, in: Auslos, P. (ed.) *Kinetics of ion-molecule reactions*, Plenum Press, (New York), 1979.

Flammarion, C., *The atmosphere*, translated from the French, ed. James Glaisher, F.R.S. London, Sampson Low, Marston, Low and Searle, 1873.

Fleming, E.L., and S. Chandra, Equatorial zonal wind in the middle atmosphere derived from geopotential height and temperature data, *Journal of the Atmospheric Sciences*, *46*, 860–866, 1989.

Forbes, J.F., Middle atmosphere tides, *Journal of Atmospheric and Terrestrial Physics*, *39*, 1023–1033, 1977.

Forbes, J.F., Atmospheric tides between 80 km and 120 km, *Advances in Space Research*, *10*, (12)127–(12)140, 1990.

Forbes, J.F., and G.V. Groves, Atmospheric tides below 80 km, *Advances in Space Research*, *10*, (12)119–(12)125, 1990.

Fraser, G.J., Partial reflection spaced antenna wind measurements, *Handbook for MAP*, *13*, 233–247, 1984a.

Fraser, G.J., Summer circulation in the Antarctic middle atmosphere, *Journal of Atmospheric and Terrestrial Physics*, *46*, 143–146, 1984b.

Fraser, G.J., and A. Kochanski, Ionospheric drifts from 64–108 km altitudes at Birdlings Flat, *Annals de Geophysique*, *26*, 675–687, 1970.

Fraser, G.J., and U. Khan, Semidiurnal variations in the time scale of irregularities near the Antarctic summer mesopause, *Radio Science*, *25*, 997–1004, 1990.

Fraser, G.J., and R.A. Vincent, A study of D–region irregularities, *Journal of Atmospheric and Terrestrial Physics*, *32*, 1591–1607, 1970.

Frazer, James G., *The Golden Bough* (abridged ed.; London, 1923), pp.60–83, 1923.

Friend, A.W., Theory and practice of tropospheric sounding by radar, *Proceedings of the Institute of Radio Engineers*, *37*, 116–138, 1949.

Frisinger, H.H., *The History of Meteorology to 1800*, Science History Publications, American Meteorological Society, 1977.

Fritts, D.C., Gravity wave saturation in the middle atmosphere: A review of theory and observations, *Review of Geophysics*, *22*, 275–308, 1984.

Fritts, D.C., A review of gravity wave saturation processes, effects, and variability in the middle atmosphere, *Pure and Applied Geophysics*, *130*, 343–372, 1989.

Fritts, D.C., and M.A. Geller, Viscous stabilization of gravity wave critical level flows, *Journal of the Atmospheric Sciences*, *33*, 2276–2284, 1976.

Fritts, D.C., and J.R. Isler, First observations of mesospheric dynamics with a partial reflection radar in Hawaii (22° N, 160° W), *Geophysical Research Letters*, *19*, 409–412, 1992.

Fritts, D.C., and R.A. Vincent, Mesospheric momentum flux studies at Adelaide, Australia: Observations and a gravity wave–tidal interaction model, *Journal of the Atmospheric Sciences*, *44*, 605–619, 1987.

Fritts, D.C., S.A. Smith, B.B. Balsley, and C.R. Philbrick, Evidence of gravity wave saturation and local turbulence production in the summer mesosphere and lower thermosphere during the STATE experiment, *Journal of Geophysical Research*, *93*, 7015–7025, 1988a.

Fritts, D.C., T. Tsuda, T. Sato, S. Fukao, and S. Kato, Observational evidence of a saturated gravity wave spectrum in the troposphere and lower stratosphere, *Journal of the Atmospheric Sciences*, *45*, 1741–1759, 1988b.

Fukao, S., S. Kato, S. Yokoi, R.M. Harper, R.F. Woodman, and W.E. Gordon, One full–day radar measurement of lower stratosphere winds over Jicamarca, *Journal of Atmospheric and Terrestrial Physics*, *40*, 1331–1337, 1978.

Fukao, S., T. Sato, S. Kato, R.M. Harper, R.F. Woodman, W.E. Gordon, Mesospheric winds and waves over Jicamarca on 23–24 May 1974, *Journal of Geophysical Research*, *5*, 357–360,

1979.

Fukao, S., K. Wakasugi, and S. Kato, Radar measurement of short-period atmospheric waves and related scattering properties at the altitude of 13–25 km over Jicamarca, *Radio Science*, *15*, 431–438, 1980b.

Fukao, S., T. Sato, R.M. Harper, and S. Kato, Radio wave scattering from the tropical mesosphere observed with the Jicamarca radar, *Radio Science*, *15*, 447–457, 1980a.

Fukao, S., T. Sato, P.T. May, T. Tsuda, S. Kato, M. Inaba, and I. Kimura, A systematic error in MST/ST radar wind measurements induced by a finite range volume effect, 1. Observational results, *1*, 59–73, 1988a.

Fukao, S., M. Inaba, I. Kimura, P.T. May, T. Sato, T. Tsuda, and S. Kato, A systematic error in MST/ST radar wind measurements induced by a finite range volume effect, 2. Numerical considerations, *1*, 74–82, 1988b.

Gage, K.S., Evidence for a $k^{-\frac{5}{3}}$ law inertial range in mesoscale two dimensional turbulence, *Journal of the Atmospheric Sciences*, *36*, 1950–1954, 1979.

Gage, K.S., and B.B. Balsley, Doppler radar probing of the clear atmosphere, *Bulletin of the American Meteorological Society*, *59*, 1074, 1978.

Gage, K.S., and B.B. Balsley, On the scattering and reflection mechanisms contributing to clear air radar echoes from the troposphere, stratosphere and mesosphere, *Radio Science*, *15*, 243–258, 1980.

Gage, K.S., and J.L. Green, Evidence for specular reflection from monostatic VHF radar observations of the stratosphere, *Radio Science*, *13*, 991–1001, 1978.

Gage, K.S., and G.D. Nastrom, On the spectrum of atmospheric velocity fluctuations seen by MST/ST radars and their interpretation, *Radio Science*, *20*, 1339–1347, 1985.

Gage, K.S., B.B. Balsley, and J.L Green, Fresnel scattering model for the specular scattering echoes observed by VHF radars, *Radio Science*, *16*, 1447–1453, 1981.

Gage, K.S., B.B. Balsley, W.L. Ecklund, R.F. Woodman, and S.K. Avery, A trans–Pacific network of wind profiling Doppler radars for tropical atmospheric research. *EOS*, *71*, 1851–1854, 1990.

Garcia, R.R., and S. Solomon, The effect of breaking gravity waves on the dynamics and chemical composition of the mesosphere and lower thermosphere, *Journal of Geophysical Research*, *90*, 3850–3868, 1985.

Gardner, C.S., Introduction to ALOHA–90: The airborne lidar and observations of the Hawaiian airglow campaign, *Geophysical Research Letters*, *18*, 1313–1316, 1991.

Gardner, C.S., D.C. Senft, T.J. Beatty, R.E. Bills, and C.A. Hostetler, Rayleigh and sodium lidar techniques for measuring middle atmospheric density, temperature and wind perturbation and their spectra, *World Ionosphere/Thermosphere Study Handbook, 2*, edited by C.H. Liu, and B. Edwards, 1989.

Gardner, C.S., T.J. Kane, J.H. Hecht, R.L. Walterscheid, J.H. Yee, R.J. Niciejewski, R.P. Lowe, and D.N. Turnbull, Formation characteristics of sporadic Na layers observed simultaneously by lidar and airglow instruments during ALOHA–90, *Geophysical Research Letters*, *18*, 1369–1372, 1991.

Gavrilov, N.M., and G.M. Shved, Study of internal gravity waves in the lower thermosphere from observations of the nocturnal sky airglow [01] 5577 A in Ashkhabad, *Annals deGeophysique*, *38*, 789–803, 1982.

Gjessing, D.T., Determination of isotropy properties of the tropospheric permitivitty and wind velocity fields by radio–propagation methods, *Journal of Geophysical Research*, *69*, 569–581, 1964.

Golley, M.G., and D.E. Rossiter, Some tests of methods of analysis of ionospheric drifts records using an array of 89 aerials, *Journal of Atmospheric and Terrestrial Physics. 32*, 1215–1233, 1970.

Golley, M.G., and D.E. Rossiter, Some aspects of ionospheric drifts using partial and total reflections from the lower ionosphere, *Journal of Atmospheric and Terrestrial Physics*, *33*,

701–714, 1971.

Gorbunova, T.A., N.Y. Kuznetsova, and G.M. Shved, Investigation of the relation between perturbations of the altitude of the E_s–layer and the intensity of night–time luminescence at (0,1) 557.7 nm, *Geomagnetism and Aeronomy*, *22*, 357, 1982.

Gossard, E.E., and W.H. Hooke, *Waves in the atmosphere*, Elsevier, New York, 456pp., 1975.

Gossard, E.E., and J.H. Richter, The shape of internal waves of finite amplitude from finite resolution radar sounding of the lower atmosphere, *Journal of the Atmospheric Sciences*, *27*, 971–973, 1970.

Greenhow, J.S., and E.L. Neufeld, *Journal of Atmospheric and Terrestrial Physics*, *16*, 384, 1959.

Greer, R.G.H., E.J. Llewellyn, B.H. Solheim, and G. Witt, The excitation of O_2 in the nightglow, *Planetary and Space Science*, *29*, 383, 1984.

Gregory, J.B., Radio wave reflections from the mesosphere 1. Heights of occurrence, *Journal of Geophysical Research*, *66*, 429, 1961.

Gregory, J.B., and D.T. Rees, Wind profiles at 100 km near 53° N during 1969, *Journal of the Atmospheric Sciences*, *28*, 1079–1082, 1971.

Gregory, J.B., and R.A. Vincent, Structure of partially reflecting regions in the lower ionosphere, *Journal of Geophysical Research*, *75*, 6387, 1970.

Groves, G.V., Rocket studies of atmospheric tides, *Proceedings of the Physical Society*, *A351*, 437, 1976.

Groves, G.V., A global reference atmosphere from 18 to 80 km, Air Force Geophysics Laboratory, Hanscom A.F.B., Massachusetts, U.S.A., Report No. AFGL-TR-85-0129, 1985.

Gunther, P.T., *Early Science in Oxford*, (London: Dawsons of Pall Mall; 1967), 7:519–523.

Hamilton, K., Rocketsonde observations of the mesospheric semiannual oscillation at Kwajalein, *Atmosphere and Oceans*, *20*, 281–286, 1982.

Hansen, G., and U. von Zahn, Sudden sodium layers in polar latitudes, *Journal of Atmospheric and Terrestrial Physics*, *52*, 585–608, 1990.

Hardy, K.R., D. Atlas, and K.M. Glover, Multi wavelength backscatter from the clear atmosphere, *Journal of Geophysical Research*, *71*, 1537–1552, 1966.

Harnischmacher, E., *Winds and Turbulence in the Stratosphere, Mesosphere, and Ionosphere*, edited by K. Rawer, 277pp., North–Holland, Amsterdam, 1963.

Harper, R.M., and R.F. Woodman, Preliminary multiheight radar observations of waves and winds in the mesosphere over Jicamarca, *Journal of Atmospheric and Terrestrial Physics*, *39*, 959–963, 1977.

Harper, R.M., and W.E. Gordon, A review of radar studies of the middle atmosphere, *Radio Science*, *15*, 195, 1980.

Harris, T.J., and R.A. Vincent, The quasi–two–day wave observed in the equatorial middle atmosphere, *Journal of Atmospheric and Terrestrial Physics*, in press, 1993.

Haug, A., and H. Pettersen, An interpretation of asymmetric cross–correlation functions in D- and lower E–region drift measurements, *Journal of Atmospheric and Terrestrial Physics*, *32*, 397–403, 1970.

Hayashi, Y., A generalized method of resolving disturbances into progressive and retrogressive waves by space Fourier and time cross–spectral analyses, *Journal of Meteorological Society of Japan*, *49*, 125–128, 1971.

Hayashi, Y., Space–time power spectral analysis using the maximum entropy method, *Journal of Meteorological Society of Japan*, *55*, 415–420, 1977.

Heaps, M.G., A parameterization of cosmic ray ionization, *Planetary and Space Science*, *26*, 513, 1978.

Hecht, J.H., and R.L. Walterscheid, Observations of the OH Meinel (6,2) and O_2 atmospheric (0,1) nightglow emissions from Maui during the ALOHA–90 campaign, *Geophysical Research Letters*, *18*, 1341–1344, 1991.

Hedin, A.E., Extension of the MSIS thermosphere model into the middle and lower atmosphere, *Journal of Geophysical Research*, *96*, 1159, 1991.

Heninger, S.K., *Handbook of Renaissance Meteorology*, Duke, University Press, 1960.

Heppner, J.P., and M.L. Miller, Thermospheric winds at high latitudes from chemical release observations, *Journal of Geophysical Research*, *87*, 1633–1647, 1982.

Hill, R.D., Origins of radar, EOS, *Transactions, American Geophysical Union*, *71*, No. 27, 1990.

Hill, R.J., and S.F. Clifford, Modified spectrum of atmospheric temperature fluctuations and its application to optical propagation, *Journal of the Optical Society of America*, *68*, 892–899, 1978.

Hines, C.O., Internal gravity waves at ionospheric heights, *Canadian Journal of Physics*, *38*, 1441–1481, 1960.

Hines, C.O., Minimum vertical scale sizes in the wind structure above 100 kilometers, *Journal of Geophysical Research*, *69*, 2947–2848, 1964.

Hines, C.O., Some consequences of gravity–wave critical layers in the upper atmosphere, *Journal of Atmospheric and Terrestrial Physics*, *30*, 837–843, 1968.

Hines, C.O., Generalizations of the Richardson criterion for the onset of atmospheric turbulence, *Quarterly Journal of the Royal Meteorological Society*, *97*, 429–439, 1971.

Hines, C.O., Motions in the ionospheric D and E regions, *Philosphical Transactions of the Royal Society of London*, *A271*, 457–471, 1972.

Hines, C.O., Corrections to papers on ionospheric drifts, *Journal of Atmospheric and Terrestrial Physics*, *38*, 561–563, 1976.

Hines, C.O., The earlier days of gravity waves revisited, *Pure and Applied Geophysics*, *130*, 151–170, 1989.

Hines, C.O., and R.R. Rao, Validity of three–station methods of determining ionospheric motions, *Journal of Atmospheric and Terrestrial Physics*, *30*, 979–993, 1968.

Hines, C.O., G.W. Adams, J.W. Brosnahan, F.T. Djuth, M.P. Sulzer, C.A. Tepley, and J.S. Van Baelen, Mesospheric wind and partial reflection observations: Comparisons and observations, *Journal of Atmospheric and Terrestrial Physics*, in press, 1992.

Hinze, J.O., *Turbulence*, McGraw–Hill, New York, pp. 219–239, 1959.

Hirooka, T., and I. Hirota, Normal mode Rossby waves observed in the upper stratosphere. Part II: Second antisymmetric and symmetric modes of zonal wavenumbers 1 and 2, *Journal of the Atmospheric Sciences*, *42*, 536–548, 1985.

Hirooka, T., and I. Hirota, Evidence of normal mode Rossby waves, *Pure and Applied Geophysics*, *130*, 277–289, 1989.

Hirota, I., Equatorial waves in the upper stratosphere and mesosphere in relation to the semiannual oscillation of the zonal wind, *Journal of the Atmospheric Sciences*, *35*, 714–722, 1978.

Hirota, I., T. Hirooka, Normal mode Rossby waves observed in the upper stratosphere. Part I: First symmetric modes of zonal wavenumbers 1 and 2, *Journal of the Atmospheric Sciences*, *41*, 1253–1257, 1984.

Hitchamn, M.H., and C.B. Leovy, Evolution of the zonal mean state in the equatorial middle atmosphere during October 1978 – May 1979, *Journal of the Atmospheric Sciences*, *43*, 3159–3176, 1986.

Hitchman, M.H., and C.B. Leovy, Estimation of the Kelvin wave contribution to the semiannual oscillation, *Journal of the Atmospheric Sciences*, *45*, 1462–1475, 1988.

Hitschfield, W., and A.S. Dennis, Measurement and calculations of fluctuations in radar echoes from snow, Sci. Rep. MW-23, McGill Univ, Montreal, Canada, 1956.

Hocking, W.K., Angular and temporal characteristics of partial reflection from the D-region of the ionosphere, *Journal of Geophysical Research*, *84*, 845–852, 1979.

Hocking, W.K., On the extraction of atmospheric turbulence parameters from radar backscatter Doppler spectra I, Theory, *Journal of Atmospheric and Terrestrial Physics*, *45*, 89–102, 1983a.

Hocking, W.K., Mesospheric turbulence intensities measured with a HF radar at 35° S, II, Observations, *Journal of Atmospheric and Terrestrial Physics*, *45*, 103–114, 1983b.

Hocking, W.K., Measurement of turbulent energy dissipation rates in the middle atmosphere by radar techniques: a review, *Radio Science*, *20*, 1403–1422, 1985.

Hocking, W.K., Observation and measurement of turbulence in the middle atmosphere with a VHF radar, *Journal of Atmospheric and Terrestrial Physics*, *48*, 655–670, 1986.

Hocking, W.K., Turbulence in the region 80–120 km, *Advances in Space Research*, *7*, 171–181, 1987a.

Hocking, W.K., Radar studies of small scale structure in the upper middle atmosphere and lower ionosphere, *Advances in Space Research*, *7*, 327–338, 1987b.

Hocking, W.K., Reduction of the effects of non–stationarity in studies of amplitude statistics of radio wave backscatter, *Journal of Atmospheric and Terrestrial Physics*, *49*, 1119–1131, 1987c.

Hocking, W.K., Two years of continuous measurements of turbulence parameters in the upper mesosphere and lower thermosphere made with a 2-MHz radar, *Journal of Geophysical Research*, *93*, 2475–2491, 1988a.

Hocking, W.K., Lecture notes: Target parameter estimation, *International School on Atmospheric Radars*, ed. S. Fukao, Kyoto, 1988b.

Hocking, W.K., Seasonal variation of turbulence intensities in the upper mesosphere and lower thermosphere measured by radar techniques, in *Handbook for MAP*, 27, 427–438, SCOSTEP Secr., Univ. of Ill., Urbana, 1989.

Hocking, W.K., On the relationship between between the strength of atmospheric radar backscatter and the intensity of atmospheric turbulence, *Advances in Space Research*, *12*, (10), 207–213, 1992.

Hocking, W.K., and J. Röttger, Pulse length dependence of radar signal strengths for Fresnel backscatter, *Radio Science*, *18*, 1312–1324, 1983.

Hocking, W.K., and R.A. Vincent, Comparative observations of D region HF partial reflections at 2 and 6 MHz, *Journal of Geophysical Research*, *87*, 7615–7624, 1982.

Hocking, W.K., R. Rüster, and P. Czechowsky, Observation and measurement of turbulence and stability in the middle atmosphere with a VHF radar, University of Adelaide internal report, ADP-335, University of Adelaide, Adelaide, S.A. Australia, 1984.

Hocking, W.K., R. Rüster, and P. Czechowsky, Absolute reflectivities and aspect sensitivities of VHF radio wave scatterers measured with the SOUSY radar, *Journal of Atmospheric and*

Terrestrial Physics, *48*, 131–144, 1986.

Hocking, W.K., P.T. May, and J. Röttger, Interpretation, reliability and accuracies of parameters deduced by the spaced antenna method in middle atmosphere applications, *Pure and Applied Geophysics*, *130*, 571–604, 1989.

Hocking, W.K., S. Fukao, T. Tsuda, M. Yamamoto, T. Sato, and S. Kato, Aspect sensitivity of stratospheric VHF radiowave scatterers, particularly above 15 km altitude, *Radio Science*, *25*, 613–628, 1990.

Hocking, W.K., S. Fukao, M. Yamamoto, T. Tsuda, T. Sato, and S. Kato, Viscosity waves and thermal conduction waves as a cause of "specular" reflectors in radar studies of the atmosphere, *Radio Science*, *26*, 1281, 1991.

Holton, J.R., and X. Zhu, A further study of gravity wave induced drag and diffusion in the mesosphere, *Journal of the Atmospheric Sciences*, *41*, 2653–2662, 1984.

Hooke, W.H., and R.M. Jones, Dissipative waves excited by gravity–wave encounters with the stable stratified planetary boundary layer, *Journal of the Atmospheric Sciences*, *43*, 2048–2060, 1986.

Hostetler, C.A., C.S. Gardner, R.A. Vincent, and D. Lesicar, Spectra of gravity wave density and wind perturbations observed during ALOHA–90 on the 25 March flight between Maui and Christmas Island, *Geophysical Research Letters*, *18*, 1325–1328, 1991.

Houghton, J.T., The stratosphere and mesosphere, *Quarterly Journal of the Royal Meteorological Society*, *104*, 1–29, 1978.

Houghton, J.T., *The Physics of the Atmospheres*, Cambridge University Press., 271pp, 1986.

Howard, L.N., Note on a paper of John W. Miles, *Journal of Fluid Mechanics*, *10*, 509, 1961.

Hull, L.W.H., *History and Philosophy of Science, An introduction*, Longmans, Green and Co. Ltd. 1959.

Inhester, B., J.C. Ulwick, J. Cho, M.C. Kelley, and G. Schmidt, Consistency of rocket and radar electron density observations: implication about the anisotropy of mesospheric turbulence, *Journal of Atmospheric and Terrestrial Physics*, *52*, 855–873, 1990.

Inhester, B., and J.C. Ulwick, Combined rocket and radar observations of anisotropic fluctuations in the mesosphere, *Advances in Space Research*, *12*, (10)165–(10)168, 1992.

Johnson, R.M., and J.G. Luhmann, Neutral wind spectra at the auroral zone mesopause: Geomagnetic effect?, *Journal of Geophysical Research*, *90*, 1735–1743, 1985.

Jones, K.L., Keeping track of radio echoes from the D–region, *Journal of Atmospheric and Terrestrial Physics*, *44*, 55–60, 1982.

Jones, W.L., and D.D. Houghton, The coupling of momentum between internal gravity waves and mean flow: a numerical study, *Journal of the Atmospheric Sciences*, *28*, 604–608, 1971.

Justus, C.G., The eddy diffusivities, energy balance parameters, and heating rate of upper atmosphere turbulence, *Journal of Geophysical Research*, *72*, 1035–1039, 1967.

Kaimal, J.C., J.C. Wyngaard, Y. Izumi, and O.R. Cote, Spectral characteristics of surface layer turbulence, *Quarterly Journal of the Royal Meteorological Society*, *98*, 563, 1972.

Kato, S., *Dynamics of the Upper Atmosphere*, Developments in Earth and Planetary Sciences 01, D. Reidel, Tokyo, 1980.

Kawahira, K., An observational study of the D–region winter anomaly and sudden stratospheric warmings, *Journal of Atmospheric and Terrestrial Physics*, *44*, 947, 1982.

Kelleher, R.F., Some statistical properties of the ground diffraction patterns of vertically reflected radio waves, *Journal of Atmospheric and Terrestrial Physics*, *28*, 213–224, 1966.

Kelley, M.C., D.T. Farley, and J. Röttger, The effect of cluster ions on anomalous VHF backscatter from the summer polar mesosphere, *Geophysical Research Letters*, *14*, 1031–1034, 1987.

Klaassen, G.P., and W.R. Peltier, Evolution of finite amplitude Kelvin–Helmholtz billows in two spatial dimensions, *Journal of the Atmospheric Sciences*, em 42, 1321–1339, 1985.

Klostermeyer, J., Numerical calculation of gravity wave propagation in a realistic thermosphere, *Journal of Atmospheric and Terrestrial Physics*, *34*, 765–774, 1972.

Klostermeyer, J., Computation of acoustic-gravity waves, Kelvin-Helmholtz instabilities, and wave-induced eddy transport in realistic atmospheric models, *Journal of Geophysical Research*, *85*, 2829–2839, 1980.

Koshelev, V.V., Variations of transport conditions and winter anomaly in the ionospheric D–region, *Journal of Atmospheric and Terrestrial Physics*, *41*, 431–438, 1979.

Koshelkov, P., Observed winds and temperatures in the Southern Hemisphere, *Handbook for MAP*, *16*, 3–11, (eds. K. Labitzke, J.J. Barnett, and B. Edwards) (University of Illinois, Urbana, Illinois, U.S.A.), 1985.

Kropfli, R.A., I. Katz, T.G. Konrad, and E.B. Dobson, Simultaneous radar reflectivity measurements and refractive index spectra in the clear atmosphere, *Radio Science*, *3*, 991–994, 1968.

Kuo, F.S., C.C Chen, S.I. Liu, J. Röttger, and C.H. Liu, Systematic behaviour of signal statistics of MST radar echoes from clear air and their interpretation, *Radio Science*, *22*, 1043–1052, 1987.

Labitzke, K., K. Paetzoldt, and H. Schwentek, Planetary waves in the stratosphere and mesosphere during the Western European Winter anomaly campaign 1975/76 and their relation to ionospheric absorption, *Journal of Atmospheric and Terrestrial Physics*, *41*, 1149–1162, 1979.

Lane, J.A., Radar echoes from clear air in relation to refractive–index variations in the troposphere, *Proceedings of IEEE*, *116*, 1656–1660, 1969.

Lane, J.A., and P.W. Sollum, VHF transmission over distances of 140 and 300 km, *Proceedings of IEEE*, *112*, 254–258, 1965.

Larsen, M.F., Application of MST radars: Meteorological Applications, Lecture notes: Target parameter estimation, *International School on Atmospheric Radars*, ed. S. Fukao, Kyoto, 1988.

Larsen, M.F., and J. Röttger, The spaced antenna technique for wind profiling, *Journal of Atmospheric and Oceanic Technology*, *6*, 920–938, 1989.

Larsen, M.F., M.C. Kelly, and K.S. Gage, Turbulence spectra in the upper troposphere and lower stratosphere at periods between 2 hours and 40 days, *Journal of the Atmospheric Sciences*, *39*, 1035–1041, 1982.

Lesicar, D., and W.K. Hocking, Studies of seasonal behaviour of the shape of mesospheric scatterers using a 1.98 MHz radar, *Journal of Atmospheric and Terrestrial Physics*, *54*, 295–309, 1992.

Lesicar, D., W.K. Hocking, and R.A. Vincent, Comparative studies of scatterers observed by MF radars in the Southern Hemisphere mesosphere, accepted for publication in *Journal of Atmospheric and Terrestrial Physics*, 1993.

Liller, W., and F.L. Whipple, High altitude winds by meteor–train photography. In "Rocket Exploration of the Upper Atmosphere", special supplement to *Journal of Atmospheric and Terrestrial Physics*, *1*, Pergamon, New York, 1954.

Lilly, D.K., D.E. Waco, and S.I. Adelfang, Stratospheric mixing estimated from high-altitude turbulence measurements, *Journal of Applied Meteorology*, *13*, 448–493, 1974.

Lindemann, F.A., and G.M.B. Dobson, *Proceedings of the Royal Society A*, *102*, 411, 1922.

Lindner, B.C., The nature of D–region scattering of vertical incidence radio waves, I. Generalized statistical theory of diversity effects between spaced receiving antennas, *Australian Journal of Physics*, *28*, 163–170, 1975a.

Lindner, B.C., The nature of D-region scattering of vertical incidence radio waves, II. Experimental observation using spaced antenna reception, *Australian Journal of Physics*, *28*, 171–184, 1975b.

Lindzen, R.S., Tides and internal gravity waves in the atmosphere, from *Developments in atmospheric science, I. – Structure and Dynamics of the Upper Atmosphere*, ed. F. Vernieni, Elsevier Sci. Pub. co., Amsterdam-Oxford-NY, 1974.

Lindzen, R.S., Turbulence and stress owing to gravity wave and tidal breakdown, *Journal of Geophysical Research*, *86*, 9707–9714, 1981.

Liu, C.H., and K.C. Yeh, Scattering of VHF and UHF radar signals from turbulent air, *Radio Science*, *15*, 277–282, 1980.

Lloyd, K.H., C.H. Low, B.J. McAvaney, B.J. Rees, and R.G. Roper, Thermospheric observations combining chemical seeding and ground based techniques - I. Winds, turbulence and the

parameters of the neutral atmosphere, *Planetary and Space Science*, *20*, 761, 1972.

Lloyd, K.H., C.H. Low, and R.A. Vincent, Turbulence, billows and gravity waves in a high shear region of the upper atmosphere, *Planetary and Space Science*, *21*, 653, 1973.

Lübken, F–J, U. Von Zahn, E.V. Thrane, T. Blix, G.A. Kokin, and S.V. Pachomov, In–situ measurements of turbulent energy dissipation rates and eddy diffusion coefficients during MAP/WINE, *Journal of Atmospheric and Terrestrial Physics*, *49*, 763, 1987.

Lumley, J.L., The spectrum of nearly inertial turbulence in a stably stratified fluid, *Journal of the Atmospheric Sciences*, *21*, 99–102, 1964.

Lumley, J.L. (1965), Theoretical aspects of research on turbulence in stratified flows, in *Atmospheric Turbulence and Radio Waves Propagation*, eds. A.M. Yaglom, and V.I. Tatarsky, Nauka, Moscow, pp 105–109, 1967.

Lumley, J.L., and H.A. Panafosky, *The Structure of Atmospheric Turbulence*, Interscience Publishers, 239pp., 1964.

Lyons, R., H.A. Panofsky, and S. Wollaston, The critical Richardson number and its implications for forecast problems, *Journal of Applied Meteorology*, *3*, 136–142, 1965.

Lysenko, I.A., A.D. Orlyansky, and Yu.I. Portnyagin, Results of wind measurements at middle and high latitudes by the meteor radar method, *Journal of Geomagnetic Geoelectricity*, *31*, 411–418, 1979.

MacDougall, J.W., The interpretation of ionospheric drift measurements, *Journal of Atmospheric and Terrestrial Physics*, *28*, 1093, 1966.

MacLeod, R., *Dynamics of the Antarctic middle atmosphere*, Ph.D. Thesis, University of Adelaide, Adelaide, Australia, 1986.

MacLeod, R., and R.A. Vincent, Observations in the Antarctic summer mesosphere using the spaced antenna technique, *Journal of Atmospheric and Terrestrial Physics*, *47*, 567–574, 1985.

Madden, R.A., Further evidence of travelling planetary waves, *Journal of the Atmospheric Sciences*, *35*, 1605–1608, 1978.

Madden, R.A., and K. Labitzke, A free Rossby wave in the troposphere and stratosphere during January 1979, *Journal of Geophysical Research*, *86*, 1247–1254, 1981.

Manson, A.H., and C.E. Meek, Gravity waves of short period (5-90min), in the lower thermosphere at 52° N (Saskatoon, Canada), *Journal of Atmospheric and Terrestrial Physics*, *42*, 103–113, 1980.

Manson, A.H., C.E. Meek, and J.B. Gregory, Gravity waves of short period (5–90 min), in the lower thermosphere at 52° N (Saskatoon, Canada), 1978/1979, *Journal of Atmospheric and Terrestrial Physics*, *43*, 35–44, 1981.

Manson, A.H., C.E. Meek, M. Massebeuf, J.L. Fellous, W.G. Elford, R.A. Vincent, R.L. Craig, R.G. Roper, S.Avery, B.B. Balsley, G.J. Fraser, M.J. Smith, R.R. Clark, S. Kato, T. Tsuda, A. Ebel, Mean winds of the upper middle atmosphere (60–110km): A global distribution from radar systems (MF, Meteor, VHF),*Handbook for MAP*, 16, 239–268, SCOSTEP Secr., Univ. of Ill., Urbana, 1985.

Mardia, K.V., *Statistics of Directional Data*, Academic Press, London and New York, 1972.

Mathews, J.D., J.H. Shapiro, and B.S. Tanenbaum, Evidence for distribution scattering in D-region partial reflection processes, *Journal of Geophysical Research*, *78*, 8266–8275, 1973.

Matsuno, T., A quasi one-dimensional model of the middle atmosphere circulation interacting with internal gravity waves, *Journal of the Meteorological Society of Japan*, *60*, 215–226, 1982.

May, P.T., Statistical errors in the determination of wind velocities by the spaced antenna technique, *Journal of Atmospheric and Terrestrial Physics*, *50*, 21–32, 1988.

May, P.T., S. Fukao, T. Tsuda, T. Sato, and S. Kato, The effect of thin scattering layers on the determination of wind by Doppler radars, *Radio Science*, *23*, 83–94, 1988.

McAvaney, B.J., *Small scale wind structure in the upper atmosphere*, Ph.D. Thesis, University of Adelaide, Adelaide, Australia, 1970.

McCormack, F.G., and R.W. Smith, The influence of the Interplanetary Magnetic Field Y Component on Ino and Neutral Motions in the Polar Thermosphere, *Geophysical Research Letters*, *11*, 935–938, 1984.

McEwan, M.J., and L.F. Phillips, *Chemistry of the Atmosphere*, Edward Arnold, London, England, 1975.

McIntyre, M.E., Towards a Lagrangian mean description of stratospheric circulations and chemical transports, *Philosophical Transactions of the Royal Society London A*, *296*, 129–148, 1980.

Meek, C.E., Triangle size effect in spaced antenna wind measurements, *Radio Science*, *25*, 641–648, 1990.

Meek, C.E., I.M. Reid, and A.H. Manson, Observations of mesospheric wind velocities 2. Cross sections of power spectral density for 48–8 hours, 8–1 hour and 1 hour to 10 min over 60–110 km for 1981, *RS*, *20*, 1383–1402, 1985.

Megaw, E.C.S., Fundamental radio wave scatter propagation theory, *Proceedings of IEEE*, *104*, 441–456, 1957.

Miles, J.W., On the stability of heterogeneous shear flows, *Journal of Fluid Mechanics*, *10*, 496, 1961.

Miller, K.L., S.A. Bowhill, K.P. Gibbs, and I.D. Countryman, First measurements of mesospheric vertical velocities by VHF radar at temperate latitudes, *Geophysical Research Letters*, *5*, 939–942, 1978.

Mitra, S.K., A radio method of measuring winds in the ionosphere, *Proceedings of the Institute of Electrical Engineers*, *96*, 441, 1949.

Mitra, S.K., *The upper atmosphere*, The Asiatic Society, Monograph series, Vol 5, Calcutta, 1952.

Mofensen, J., Radar echoes from the moon, *Electronics*, *19*, 92, 1946.

Muller, H.G., Wind shears in the meteor zone, *Planetary and Space Science*, *16*, 61–90, 1968.

Murgatroyd, R.J., *The global circulation of the atmosphere*, G.A. Corby, Ed., Roy. Met. Soc., (London), 1969.

Murphy, D., *Measurements of energy and momentum in the mesosphere*, Ph.D. Thesis, University of Adelaide, Adelaide, Australia, 1990.

Myers, R.M., and M. Yanowitch, Small oscillations of a viscous isothermal atmosphere, *Journal of Computational Physics*, *8*, 241–357, 1971.

Newman, D.B.Jr., and A.J. Ferraro, Amplitude distributions of partially reflected signals from the mid-latitude D region, *Journal of Geophysical Research*, *81*, 2442–2444, 1976.

Niciejewski, R.J., and J.H. Yee, Airglow rotational measurements during the ALOHA campaign, *Geophysical Research Letters*, *18*, 1353–1356, 1991.

Offerman, D., An integrated GBR campaign for the study of the D region winter anomaly in western Europe 1975/76, *Journal of Atmospheric and Terrestrial Physics*, *41*, 1047–1050, 1979.

Ottersten H., Atmospheric structure and radar backscattering in clear air, *Radio Science*, *4*, 1179–1193, 1969a.

Ottersten H., Radar backscattering from the turbulent clear atmosphere, *Radio Science*, *4*, 1251–1255, 1969b.

Page, R.M., *The origin of radar*, Doubleday, New York, 1962.

Panafosky, H.A., and J.A. Dutton, *Atmospheric Turbulence: Models and Methods for Engineering Applications*, John Wiley & Sons, 397pp., 1984.

Papović, V., R. Horvat, and N. Nikolić, Nikola Tesla – Lectures, Patents, Articles, (Nikola Tesla Museum, Beograd, pp. A109–A152. Reprint available from MRG, Archer's Court, Stonestile Lane, Hastings, England), 1956.

Pawsey, J.L., Further investigations of the amplitude variations of downcoming wireless waves, *Proceedings of the Cambridge Philosophical Society*, *31*, 125–144, 1935.

Pedlosky, J., *Geophysical Fluid Dynamics*, 2nd ed., Springer-Verlag, New York, 1979.

Peltier, W.R., J. Halle, and T.L. Clark, The evolution of finite-amplitude Kelvin-Helmholtz Billows, *Geophysical and Astrophysical Fluid Dynamics 10*, 53–87, 1978.

Pfister, W., The wave-like nature of inhomogeneities in the E-region, *Journal of Atmospheric and Terrestrial Physics*, *33*, 999–1025, 1971.

Pfister, W., Baroclinic instability of easterly jets with applications to the summer mesosphere, *Journal of the Atmospheric Sciences*, *42*, 313–330, 1985.

Phillips, A., Simultaneous observations of the quasi 2–day wave at Mawson, Antarctica, and Adelaide, South Australia, *Journal of Atmospheric and Terrestrial Physics*, *51*, 119–124, 1988.

Phillips, A., *Dynamics of the Antarctic mesosphere and lower thermosphere*, Ph.D. Thesis, University of Adelaide, Adelaide, Australia, 1989.

Phillips, A., and R.A. Vincent, Radar observations of prevailing winds and waves in the southern hemisphere mesosphere and lower thermosphere, *Pure and Applied Geophysics*, *130*, 303–318, 1989.

Phillips, G.J., and M. Spencer, The effects of anisometric amplitude patterns in the measurement of ionospheric drifts, *Proceedings of the Physical Society*, *68B*, 481–492, 1955.

Pitteway, M.L.V., and C.O. Hines, The viscous damping of gravity atmospheric waves, *Canadian Journal of Physics*, *41*, 1935–1948, 1963.

Plumb, R.A., Baroclinic instability of the summer mesosphere: A mechanism for the 2–day wave, *Journal of the Atmospheric Sciences*, *40*, 262–270, 1983.

Price, G.D., *Upper atmosphere dynamics in the auroral zone*, Ph.D. Thesis, University of Adelaide, Adelaide, Australia, 1988.

Probert–Jones, J.R., The radar equation in meteorology, *Quarterly Journal of the Royal Meteorological Society*, *88*, 485, 1962.

Rastogi, P.K., and S.A. Bowhill, Scattering of radio waves from the mesosphere – 1. Theory and observations, *Journal of Atmospheric and Terrestrial Physics*, *38*, 399–412, 1976a.

Rastogi, P.K., and S.A. Bowhill, Scattering of radio waves from the mesosphere – 2. Evidence for intermittent mesospheric turbulence, *Journal of Atmospheric and Terrestrial Physics*, *38*, 449–462, 1976b.

Rastogi, P.K., and S.A. Bowhill, Gravity waves in the equatorial mesosphere, *Journal of Atmospheric and Terrestrial Physics*, *38*, 51–60, 1976c.

Rastogi, P.K., and O. Holt, On detecting reflections in presence of scattering from amplitude statistics with application to D–region partial reflections, *Radio Science*, *16*, 1431–1443, 1981.

Rastogi, P.K., and R.F. Woodman, Mesospheric studies using the Jicamarca incoherent–scatter radar, *Journal of Atmospheric and Terrestrial Physics*, *36*, 1217–1231, 1974.

Ratcliffe, J.A., Some aspects of diffraction theory and their application to the ionosphere, *Reports on Progress in Physics*, *19*, 188, 1956.

Ratcliffe, J.A., *An introduction to the ionosphere and magnetosphere*, Cambridge University Press, London, 1972.

Rees, D., R.G. Roper, K.H. Lloyd, and C.H. Low, Determination of the structure of the atmosphere between 90 and 250 km by means of contaminant releases at Woomera, May 1968, *Philosophical Transactions of the Royal Society*, *A 271*, 631, 1972.

Rees, M.H., On the interaction of auroral protons with the Earth's atmosphere, *Planetary and Space Science*, *30*, 463, 1982.

Rees, M.H., *Physics and chemistry of the upper atmosphere*, Cambridge University Press, Cambridge, 1989.

Reid, G.C., The influence of electric fields on radar measurements of winds in the upper mesosphere, *Radio Science*, *18*, 1028–1034, 1983.

Reid, G.C., Production and loss of electrons in the quiet daytime D–region of the Ionosphere, *Journal of Geophysical Research*, *75*, 2551, 1970.

Reid, I.M., *Radar studies of atmospheric gravity waves*, Ph.D. Thesis, University of Adelaide, Adelaide, Australia, 1984.

Reid, I.M., MF Doppler and spaced antenna radar measurements of upper middle atmosphere winds, *Journal of Atmospheric and Terrestrial Physics*, *50*, 117–134, 1988.

Reid, I.M., Radar observations of stratified layers in the mesosphere and lower thermosphere (50–100 km), *Advances in Space Research*, *10*, 107–119, 1990.

Reid, I.M., and R.A. Vincent, Measurements of mesospheric gravity wave momentum fluxes and mean flow accelerations at Adelaide, Australia, *Journal of Atmospheric and Terrestrial*

Physics, *49*, 443–460, 1987.

Reid, I.M., R. Rüster, P. Czechowsky, and G. Schmidt, VHF radar measurements of momentum flux in the summer polar mesosphere over Andenes, (69° N, 16° E), Norway, *Geophysical Research Letters*, *11*, 1263–1266, 1988.

Rice, S.O., Mathematical analysis of random noise, *Bell System technical journal*, *23*, 282–332, 1944.

Rice, S.O., Mathematical analysis of random noise, *Bell System technical journal*, *24*, 46–156, 1945.

Richmond, A.D., *The ionosphere*, Chapter 7 in it The Solar Wind and the Earth, S.I. Akasofu, and Y. Kamide (eds.), Terra, Tokyo, 1987.

Tatarski, V.I., *Wave Propagation in a turbulent medium*, McGraw–Hill, New York, 285pp., 1961.

Richmond, A.D., Tidal winds at ionospheric heights, *Radio Science*, *6*, 175–189, 1971.

Rind, D., R. Suozzo, N.K. Balachandran, A. Lacis, and G. Russell, The GISS global climate-middle atmosphere model, I; Model structure and climatology, *Journal of the Atmospheric Sciences*, *45*, 329–370, 1988.

Rodgers, C.D., and A.J. Prata, Evidence for a travelling two–day wave in the middle atmosphere, *Journal of Geophysical Research*, *86*, 9661–9664, 1981.

Roper, R.G., The semidiurnal tide in the lower thermosphere, *Journal of Geophysical Research*, *71*, 5746–5748, 1966.

Röttger, J., Reflection and scattering of VHF radar signals from atmospheric refractivity structures, *Radio Science*, *15*, 259–276, 1980a.

Röttger, J., Structure and dynamics of the stratosphere and the mesosphere revealed by VHF radar investigations, *Pure and Applied Geophysics*, *118*, 494–527, 1980b.

Röttger, J., Investigations of lower and middle atmosphere dynamics with spaced antenna drifts radars, *Journal of Atmospheric and Terrestrial Physics*, *43*, 277–292, 1981a.

Röttger, J., The capabilities of VHF radar for meteorological observations, Preprint of Nowcasting Symposium, *Third Scientific Assembly of International Association of Meteorology and Atmospheric Physics*, Hamburg, FRG, 17–28 August, 1981b.

Röttger, J., The correlation of winds measured with a spaced antenna VHF radar and radiosondes, Preprint, *21st Conference on Radar Meteorology*, 97–99, (published by the American Meteorological Society, Boston, Massechutes), 1983.

Röttger, J., The interpretation of MST radar echoes: The present knowledge of the scattering/reflection and the irregularity generation mechanism, *Handbook for MAP*, *28*, 68–82, 1989.

Röttger, J., and P. Czechowsky, Tropospheric and stratospheric wind measurements with the spaced antenna drifts technique and the Doppler beam swinging technique using a VHF radar, Preprint, *19th Conference on Radar Meteorology of the American Meteorological Society*, Miami, Florida, U.S.A., 15–18 April, pp. 577–584, 1980.

Röttger, J., and H.M. Ierkic, Postset beam steering and interferometer applications of VHF radars to study winds, waves, and turbulence in the lower and middle atmosphere, *Radio Science*, *20*, 1461–1480, 1985.

Röttger, J., and C.H. Liu, Partial reflection and scattering of VHF radar signals from the clear atmosphere, *Geophysical Research Letters*, *5*, 357–360, 1978.

Röttger, J., and R.A. Vincent, VHF radar studies of tropospheric velocities and irregularities using spaced antenna techniques, *Geophysical Research Letters*, *5*, 917–920, 1978.

Röttger, J., P.K. Rastogi, and R.F. Woodman, High-resolution VHF radar observations of turbulence structures in the mesosphere, *Geophysical Research Letters*, *6*, 617–620, 1979.

Röttger, J., P. Czechowsky, and G. Schmidt, First low–power VHF radar observations of tropospheric, stratospheric and mesospheric winds and turbulence at the Arecibo Observatory, *Journal of Atmospheric and Terrestrial Physics*, *43*, 789–800, 1981.

Royrvik, O., Drift and aspect sensitivity of scattering irregularities in the upper equatorial E region, *Journal of Geophysical Research*, *87*, 8338–8342, 1982.

Salby, M.L., The 2-day wave in the middle atmosphere: observations and theory, *Journal of Geophysical Research*, *86*, 9654–9660, 1981.

Salby, M.L., Survey of planetary scale travelling waves: The state of theory and observations, *Review of Geophysics and Space Physics*, *22*, 209–236, 1984.

Salby, M.L., D.L. Hartmann, P.L. Bailey, abd J.C. Gille, Evidence for equatorial Kelvin modes in Nimbus 7 LIMS, *Journal of the Atmospheric Sciences*, *40*, 220–235, 1984.

Sato, T., Radar principles, *Lecture notes: International School on Atmospheric Radars*, ed. S. Fukao, Kyoto, 1988.

Sato, T., T. Tsuda, S. Kato, S. Morimoto, S. Fukao, and I. Kimura, High resolution MST observations of turbulence using the MU radar, *Radio Science*, *20*, 1452–1460, 1985.

Schlegel, K., A. Brekke, and A. Haug, Some characteristics of the quiet polar D–region and mesosphere obtained with the partial reflection method, *Journal of Atmospheric and Terrestrial Physics*, *40*, 205–213, 1978.

Schmidt, M., The influence of large scale advection on the vertical distribution of stratospheric source gases in 44° and 41° north, *Journal of Geophysical Research*, *87*, 11239–11246, 1982.

Schwentek, H., The variation of ionospheric absorption from 1956 to 1963, *Journal of Atmospheric and Terrestrial Physics*, *25*, 733–734, 1963.

Sheen, D.R., C.H. Liu, and J. Röttger, A study of signal statistics of VHF radar echoes from clear air, *Journal of Atmospheric and Terrestrial Physics*, *47*, 675–684, 1985.

Shur, G.N., Experimental investigations of the energy spectrum of atmospheric turbulence, *Trudy*, *43*, 79–90, [trans. A.I.D. report T-63-65, Aerospace Information Division, Library of Congress], 1962.

Sidi, C., and F. Dalaudier, Temperature and heat flux spectra in the turbulent buoyancy subrange, *PAGEOPH*, *130 (2/3)*, 547–569, 1989.

Sidi, C., and F. Dalaudier, Turbulence in the stratified atmosphere: recent theoretical developments and experimental results, *Advances in Space Research*, *10*, (10), 25, 1990.

Sidi, C., and H. Teitelbaum, Thin shear turbulent layers within the lower thermosphere induced by non–linear interaction between tides and gravity waves, *Journal of Atmospheric and Terrestrial Physics*, *40*, 529–540, 1978.

Silverman, R.A. Turbulent mixing theory applied to radio scattering, *Journal of Applied Physics*, *27*, 699–705, 1956.

Sloss, P.W., and D. Atlas, Wind shear and reflectivity gradient effects on Doppler radar spectra, *Journal of the Atmospheric Sciences*, *25*, 1080–1089, 1968.

Smith, A.K., Wave transience and wave–mean flow interaction caused by the interference of stationary and travelling waves, *Journal of the Atmospheric Sciences*, *42*, 529–535, 1985.

Smith, S.A., D.C. Fritts, and T.E. VanZandt, Evidence of a saturated spectrum of atmospheric gravity waves, *Journal of the Atmospheric Sciences*, *44*, 1404–1410, 1987.

Solomon, S., and R.R. Garcia, Simulation of NO_x partitioning along isobaric parcel trajectories, *Journal of Geophysical Research*, *88*, 5497, 1983.

Stamnes, K., Analytic approach to auroral electron transport and energy degredation, *Planetary and Space Science*, *28*, 309–312, 1980.

Staras, H., Scattering of electromagnetic energy in a randomly inhomogeneous atmosphere, *Journal of Applied Physics*, *23*, 1152–1156, 1952.

Staras, H., Forward scattering of radio waves by anisotropic turbulence, *Proceedings of IRE*, *43*, 1374–1380, 1955.

Strobel, D.F., M.E. Summers, R.M. Bevilacqua, M.T. DeLand, and M. Allen, Vertical constituent transport in the mesosphere, *Journal of Geophysical Research*, *92*, 6691–6698, 1987.

Stubbs, T.J., The measurement of winds in the D–region of the ionosphere by the use of partially reflected radio waves, *Journal of Atmospheric and Terrestrial Physics*, *35*, 909–919, 1973.

Stubbs, T.J., A study of ground diffraction parameters associated with D-region partial reflections, *Journal of Atmospheric and Terrestrial Physics*, *39*, 589, 1977.

Stubbs, T.J., and R.A. Vincent, Studies of D–region drifts during the winters of 1970–1972, *Australian Journal of Physics*, *26*, 645–660, 1973.

Swords, S.S., *Technical history of the beginnings of RADAR*, Peter Peregrinus Ltd., IEE History of technology series 6, London, 1986.

Tatarskii, V.I., *Wave propagation in a turbulent medium*, McGraw-Hill Book Company, 1961.

Tatarskii, V.I., *The effects of the Turbulent Atmosphere on Wave propagation*, 5319 VDC 551. 510, translated from Russian, 471 pp., Israel Program for Scientific Translation, Jerusalem, 1971.

Teitelbaum, H., and C. Sidi, Formation of discontinuities in atmospheric gravity waves, *Journal of Atmospheric and Terrestrial Physics. 38*, 413–421, 1976.

Tennekes, H, and J.L. Lumley, *A first course in turbulence*, The MIT Press 300pp., 1972.

Tetenbaum, D., S.K. Avery, and A.C. Riddle, Observations of mean winds and tides in the upper mesosphere during 1980–1984, using Poker Flat, Alaska, MST radar as a meteor radar, *Journal of Geophysical Research*, *91*, 14539–14556, 1986.

Thomas, L., Recent developments and outstanding problems in the theory of the D–region, *Radio Science*, *9*, 121, 1974.

Thomas, R.J., C.A. Barth, and S. Solomon, Seasonal variations of ozone in the upper mesosphere and gravity waves, *Geophysical Research Letters*, *11*, 673–676, 1984.

Thrane, E.V., B. Grandal, T. Fla, and A. Brekke, *Nature*, *292*, 221, 1981.

Thrane, E.V., O. Andreassen, T. Blix, B. Grandal, A. Brekke, C.R. Philbrick, F.J. Schmidlin, H.U. Widdel. U. von Zahn, and F.J. Lübken, Neutral air turbulence in the upper atmosphere observed during the Energy Budget Campaign, *Journal of Atmospheric and Terrestrial Physics*, *47*, 243–264, 1985.

Thrane, E.V., T.A. Blix, C. Hall, T.L. Hansen, U. von Zahn, W. Meyer, P. Czechowsky, G. Schmidt, H.–U. Widdel, and A. Neumann, Small scale structure and turbulence in the mesosphere and lower thermosphere at high latitudes in winter, *Journal of Atmospheric and Terrestrial Physics*, *49*, 751–762, 1987.

Tsuda, T., T. Sato, K. Hirose, S. Fukao, and S. Kato, MU radar observations of the aspect sensitivity of backscattered VHF echo power in the troposphere and lower stratosphere, *Radio*

Science, *21*, 971–980, 1986.

Turnbull, D.N., and R.P. Lowe, A summary of the results obtained by The University of Western Ontario ground–based Michelson interferometer during ALOHA–90, *EOS Transactions*, *71*, 1501, 1990.

Tuve, M.A., and G. Breit, Note on radio method of estimating the height of the conducting layer, *Terrestrial Magnetism*, *30*, 1925.

Ulwick, J.C., K.D. Baker, M.C. Kelley, B.B. Balsley, and W.L. Ecklund, Comparison of simultaneous MST radar and electron density probe measurements during STATE, *Journal of Geophysical Research*, *93*, 6989–7000, 1988.

Vallance Jones, A.J., *Aurora*, D. Reidel Publishing Company, Dordrecht, Holland, 1974.

Vampola, A.L., and D.J. Gorney, Electron energy deposition in the middle atmosphere, *Journal of Geophysical Research*, *88*, 6267–6274, 1983.

Vandepeer, B.G.W., and W.K. Hocking, A comparison of Doppler and Spaced Antenna techniques for the measurement of turbulent energy dissipation rates, *Fifth SCOSTEP/URSI workshop on technical and scientific aspects of MST radar*, Aberystwyth, Paper 4.19, 1991.

VanZandt, T.E., and D.C. Fritts, A theory of enhanced saturation of the gravity wave spectrum due to increases in atmospheric instability, *Pure and Applied Geophysics*, *130*, 399–420, 1989.

VanZandt, T.E., and R.A. Vincent, Is VHF Fresnel reflectivity due to low frequency buoyancy waves?, *Proceedings of the 21st Conference on Radar Meteorology*, Edmenton, Alberta, Canada, Published by the American Meteorological Society, 126–158, 1983.

VanZandt, T.E., J.L Green, K.S.Gage, and W.L. Clark, Vertical profiles of refractivity turbulence structure constant: Comparison of observations by the Sunset radar with a new theoretical model, *Radio Science*, *13*, 819, 1978.

Vincent, R.A., Gravity–wave motions in the mesosphere, *Journal of Atmospheric and Terrestrial Physics*, *46*, 119–128, 1984.

Vincent, R.A., Long–period motions in the equatorial mesosphere, *Journal of Atmospheric and Terrestrial Physics*, *55*, 1067, 1993.

Vincent, R.A., and S.M. Ball, Mesospheric winds at low and mid–latitude in the Southern Hemisphere, *Journal of Geophysical Research*, *86*, 9159–9169, 1981.

Vincent, R.A., and J.S. Belrose, The angular distribution of radio waves partially reflected from the lower ionosphere, *Journal of Atmospheric and Terrestrial Physics*, *40*, 35–47, 1978.

Vincent, R.A., and S.D. Eckermann, VHF radar observations of mesoscale motions in the troposphere: Evidence for gravity wave Doppler shifting, *Radio Science*, *25*, 1019–1037, 1990.

Vincent, R.A., and D.C. Fritts, A climatology of gravity wave motions in the mesosphere at Adelaide, Australia, *Journal of the Atmospheric Sciences*, *44*, 748–760, 1987.

Vincent, R.A., and D. Lesicar, Dynamics of the equatorial mesosphere: First results with a new generation partial reflection radar, *Geophysical Research Letters*, *18*, 825–828, 1991.

Vincent, R.A., and I.M. Reid, HF Doppler measurements of mesospheric gravity wave momentum fluxes, *Journal of the Atmospheric Sciences*, *40*, 1321–1333, 1983.

Vincent, R.A., and J. Röttger, Spaced Antenna VHF radar observations of tropospheric velocities and irregularities, *Radio Science*, *15*, 319–336, 1980.

Vincent, R.A., and T.J. Stubbs, A study of motions in the winter mesosphere using the partial reflection drifts technique, *Planetary and Space Science*, *25*, 441, 1977.

Vincent, R.A., T.J. Stubbs, P.H.O. Pearson, K.H. Lloyd, and C.H. Low, A comparison of partial reflection drifts with winds determined by rocket techniques, *Journal of Atmospheric and Terrestrial Physics*, *39*, 813–821, 1977.

Vincent, R.A., P.T. May, W.K. Hocking, W.G. Elford, B.H. Candy, and B.H. Briggs, First results with the Adelaide VHF radar: Spaced antenna studies of tropospheric winds, *Journal of Atmospheric and Terrestrial Physics*, *49*, 353–366, 1987.

Vincent, R.A., T. Tsuda, and S. Kato, A comparative study of mesospheric solar tides observed at Adelaide and Kyoto, *Journal of Geophysical Research*, *93*, 699–708, 1988.

Von Biel, H.A., Amplitude distributions of D-region partial reflections, *Journal of Geophysical Research*, *76*, 8365–8367, 1971.

Von Biel, H.A., The phase–switched correlation polarimeter – a new approach to the partial reflection experiment, *Journal of Atmospheric and Terrestrial Physics*, *39*, 769–778, 1977.

Von Biel, H.A., A statistical assessment of synoptic D–region partial reflection data, *Journal of Atmospheric and Terrestrial Physics*, *43*, 225–230, 1981.

von Zahn, U., The project MAP/WINE: an overview, *Journal of Atmospheric and Terrestrial Physics*, *49*, 607–620, 1987.

Wakasugi, K., MST radar technique for remote sensing of the middle atmosphere, report, Kyoto Institute of Technology, Kyoto, Japan, 1981.

Walterscheid, R.L., and W.K. Hocking, Stokes diffusion by atmospheric internal gravity waves, *Journal of the Atmospheric Sciences*, *48*, 2213–2230, 1991.

Warnock, J.M., T.E. VanZandt, J.L. Green, and R.H. Winkler, Comparison between wind profiles measured by Doppler radar and by rawinsonde balloons, *Geophysical Research Letters*, *5*, 109–112, 1978.

Waterman, A.T., Techniques for measurement of vertical and horizontal velocities; monostatic vs. bistatic measurements, *Handbook for MAP*, *9*, 164–169, 1983.

Waterman, A.T., T.Z. Hu, P. Czechowsky, and J. Röttger, Measurement of anisotropic permittivity structure of upper troposphere with clear-air radar, *Radio Science*, *20*, 1580–1592, 1985.

Watson–Watt, R.A., *Three steps to victory*, Odham's Press, London, 1957.

Weinstock, J., On the theory of turbulence in the buoyancy subrange of stably stratified flows, *Journal of the Atmospheric Sciences*, *35*, 634–649, 1978a.

Weinstock, J., Vertical turbulent diffusion in a stably stratified fluid, *Journal of the Atmospheric Sciences*, *35*, 1022–1027, 1978b.

Weinstock, J. On the theory of temperature spectra in a stably stratified fluid, *Journal of Physical Oceanography*, *15*, 475–477, 1985.

Wernik, A.W., C.H. Liu, and K.C. Yeh, Modeling of spaced–receiver scintillation measurements, *Radio Science*, *18*, 743–764, 1983.

Wexler, H., Structure of hurricanes as determined by radar, *Annals of the New York Academy of Sciences*, *48*, 820, 1947.

Wheelon, A.D., Radio–wave scattering by tropospheric irregularities, *Journal of Research of the National Bureau of Standards*, *63D*, 205–233, 1959.

Wheelon, A.D., Relation of turbulence theory ti ionospheric forward scatter propagation experiments, *Journal of Research of the National Bureau of Standards*, *64D*, 301–309, 1960.

Woodman, R.F., Spectral moment estimation in MST radars, *Radio Science*, *20*, 1185–1195, 1985.

Woodman, R.F., and A. Guillen, Radar observations of winds and turbulence in the stratosphere and the mesosphere, *Journal of Atmospheric and Terrestrial Physics*, *31*, 493-505, 1974.

Woodman, R.F., and YY-H Chu, Aspect sensitivity measurements of VHF backscatter made with the Chung-Li radar: plausible mechanisms, *Radio Science*, *24*, 113–126, 1989.

Woods, J.D., On Richardson's number as a criterion for laminar-turbulent-laminar transition in the ocean and atmosphere, *Radio Science*, *4*, 1289, 1969.

Wright, J.W., and M.L.V. Pitteway, Computer simulation of ionospheric radio drift measurements and their analysis by correlation methods, *Radio Science*, *13*, 189–210, 1978.

Wright, J.W., M. Glass, and A. Spizzichino, The interpretation of ionospheric radio drift measurements-viii. Direct comparisons of meteor radar winds and Kinesonde measurements: Mean and random motions, *Journal of Atmospheric and Terrestrial Physics*, *38*, 713–729, 1976.

Yanowitch, M., Effect of viscosity on gravity waves and the upper boundary condition, *Journal of Fluid Mechanics*, *29*, 209–231, 1967a.

Yanowitch, M., Effect of viscosity on vertical oscillations of an isothermal atmosphere, *Canadian Journal of Physics*, *45*, 2003–2008, 1967b.

Yanowitch, M., A numerical study of vertically propagating waves in a viscous isothermal atmosphere, *Journal of Computational Physics*, *4*, 531–542, 1969.

Yee, J.H, R. Niciejewski, and M.Z. Luo, Observations of the O_2 and OH nightglow during the ALOHA–90 campaign, *Geophysical Research Letters, 1357–1360*, 1991.

Zimmerman, S.P., Discussion of paper by C.G. Justs "Energy balance of turbulence in the upper atmosphere, *Journal of Geophysical Research, 73*, 463–454, 1968.

Zrnić, D.S., Estimation of spectral moments for weather echoes, *Institute of Electrical and Electronics Engineers, transactions on geoscience and remote sensing, GE–17*, 113–128, 1979.